

Understanding The Influence of Microwave Heating on Biomass-Solvent Extraction

TAQI, Ali A. M. A.

Thesis submitted to the University of Nottingham in fulfilment of the requirements for the award of the degree of Doctor of Philosophy

November 2021

BLANK PAGE

ABSTRACT

Replacing fossil fuels with cleaner, more sustainable energy/chemical resources is key in tackling the current global challenges. Plant-based biomasses are an abundant resource offering direct access to a set of various fuels and platform chemicals. However, amongst many reasons, the lack of maturity of the available biomass processing techniques has hindered this sector from arriving at the envisaged industrial scales.

This thesis is concerned with biomass-solvent extraction, a process which returns high value-added components from plant-based biomass. Microwave heating is widely thought to enhance this process, but the cause of the enhancement is still unclear as the underpinning mechanisms are yet to be thoroughly described and quantified. Without such fundamental mechanistic understanding, it will not be possible to industrialise the process despite its promising prospects. The aim of this thesis is to characterise the influence of microwave heating on biomass-solvent extraction, thereby understanding whether/how microwaves enhance the process. A mathematical model is developed to quantify extraction at the cellular scale (i.e., $< 1\,mm$), delivering an unprecedented level of detail on how the various physical parameters affect the process.

Initially, a heat transfer model was developed, through which microwaves were shown to induce unique temperature gradients between biomass and solvent at thermal steady state. The magnitudes of these gradients depend on the size of the biomass-solvent system as well as the magnitudes of the various heating parameters. Furthermore, the model reasonably predicts the timeframes required to achieve thermal steady state, for a wide range of input microwave powers used in a variety of biomass processes, such as solvent extraction and liquid pyrolysis.

The relationship between temperature gradients and mass transfer was investigated using relevant principles of statistical mechanics and thermodynamics. It was deduced that temperature gradients act as a driving force for diffusion, where particles normally flow towards higher temperature regions. As such, to enable analysing mass transfer in systems exhibiting non-uniform temperatures, the diffusion driving forces including gradients in activity, pressure, and temperature were collectively expressed in a single

equation defining chemical potential (μ). The current analysis on diffusion and temperature gradients is useful in various fields and contexts, even beyond this thesis.

From this, the existing heat transfer model was expanded by introducing mass transfer and cell expansion mechanics. The resulting framework is the first of its kind, as it combines microwave heating, heat transfer, mass transfer, cell expansion mechanics, and geometrical features. All these elements collectively describe whether microwave heating improves the likelihood of cell rupture, a phenomenon widely perceived as the rate-limiting step in enhancing biomass-solvent extraction. Two hypotheses presented in literature, which describe how microwave heating enhances cell rupture, were assessed using the new model. The popular Steam-Rupturing hypothesis was investigated from a heat transfer viewpoint, showing that it only holds true at the extreme fringes of realistic physical parameters. In contrast, the recently proposed Temperature-Induced Diffusion hypothesis, entailing water diffusion against a temperature gradient, was shown to be entirely reasonable as an underpinning mechanism for enhanced cell rupture. This result alters many of the currently accepted views on how cell rupture is achieved in biomass-solvent systems.

A critical empirical analysis was conducted to screen for evidence of cell rupture influencing extraction trends. Pectin extraction from onion peels was investigated under two microwave heating modes, yet the yield patterns attained were not fully explicable with cell rupture. Therefore, the model developed earlier was further modified to drive away from cell rupture as a rate-limiting step in extraction. The resulting framework directly quantifies solute diffusion, showing that solutes possessing low solubility cannot be extracted in large quantities from the biomass, due to restrictions in mass transfer. However, microwave heating overcomes this limitation by interfering with the diffusion patterns, thereby driving more solutes towards the solvent phase. This mechanism is proposed for the first time in the current thesis, and it is presented with a significant level of detail. Various scenarios underpinned by this mechanism are demonstrated, to compare microwave and conventional heating but also to understand the effects of a multitude of physical parameters. This newly proposed mechanism describes extraction where cell rupture fails; hence, it challenges the currently prevailing perceptions on how biomass-solvent extraction occurs.

KEYWORDS: Biomass-Solvent Extraction; Microwaves; Mathematical Model; Heat Transfer; Temperature Gradient; Mass Transfer; Pressure; Chemical Potential.

CONTENTS

ACKNOWLEDGEMENTS IV

LIST OF FIGURES V

LIST OF TABLES XV

1 INTRODUCTION, AIM, OBJECTIVES, AND THESIS STRUCTURE 1

2 REVIEW: MICROWAVE THEORY AND BIOMASS EXTRACTION 8

3 MICROWAVE HEAT TRANSFER IN BIOMASS-SOLVENT SYSTEMS 56

4 MASS TRANSFER UNDER TEMPERATURE GRADIENT 88

5 TWO COMPETING HYPOTHESES TO EXPLAIN CELL RUPTURE 123

6 EVIDENCE FOR CELL RUPTURE – EMPIRICAL ANALYSIS 170

7 MICROWAVES IMPROVE EXTRACTION WITHOUT RUPTURE 191

8 GENERAL CONCLUSIONS AND RECOMMENDATIONS 285

APPENDIX A Validation for the model developed in Chapter 3 301

APPENDIX B Validation for the model developed in Chapter 5 307

APPENDIX C Validation for the model developed in Chapter 7 320

APPENDIX D Software implementation 331

REFERENCES 337

Subheadings are listed at the beginning of each chapter/appendix

ACKNOWLEDGEMENTS

I would like to thank every member of my family for their enduring support, without which this achievement would not have been possible. I am deeply grateful to my parents, Mrs. Nafisa Sulaiman and Mr. Ahmed Taqi, for their unconditional love, support, guidance, and encouragement throughout the years. Thanks parents, both of you are exceptional, and this is but one of your many accomplishments.

I would also like to thank my supervisors, Prof. John Robinson, Dr. Eleanor Binner, and Dr. Etienne Farcot, for their immense knowledge and extremely valuable support. They have not spared an opportunity to guide me throughout this research and in the preparation of this thesis, and for this I am deeply grateful to them. Their example continues to be a source of inspiration and motivation for myself. I am also deeply thankful to my assessors, Prof. Andrew Livingston and Prof. Sean Rigby, for their valuable feedback and highly constructive comments.

I extend my appreciation to all the staff and students at the University of Nottingham whose support has been extremely valuable.

LIST OF FIGURES

Chapter 1

N/A

Chapter 2

Figure 2.1 – Electromagnetic wave.....11

Figure 2.2 – Debye representation of (A) dielectric constant and (B) dielectric loss factor as functions of frequency (Equation (2.14)). Concept inspired by Metaxas et al. (Metaxas and Meredith, 1983). $\boldsymbol{\varepsilon dc = 70}$, $\boldsymbol{\varepsilon\infty = 10}$, and $\boldsymbol{t = 10 - 11\ s}$. These properties may describe pure water as this has a relaxation frequency of the order of 10 GHz at room temperature (Kaatze, 1989), and a dielectric constant close to 70 (Datta, Sumnu and Raghavan, 2005) 18

Figure 2.3 – Debye representation of (A) dielectric constant and (B) dielectric loss factor as functions of frequency (Equation (2.14)). $\boldsymbol{\varepsilon dc}$ is variable while $\boldsymbol{\varepsilon\infty = 10}$ and $\boldsymbol{t = 10 - 11\ s}$.....20

Figure 2.4 – Debye representation of dielectric constant (A) and dielectric loss factor (B) as functions of frequency (Equation (2.14)). $\boldsymbol{t}$ is variable while $\boldsymbol{\varepsilon dc = 70}$ and $\boldsymbol{\varepsilon\infty = 10}$ 21

Figure 2.5 – Attenuating electromagnetic wave. Concept inspired by Metaxas et al. (Metaxas and Meredith, 1983) 27

Figure 2.6 – Single-mode cavity setup.....32

Figure 2.7 – Multimode cavity setup 34

Figure 2.8 – Single-mode configuration with stub tuner and sliding short.....35

Figure 2.9 – Biomass microstructure 40

Figure 2.10 – Graphical representation of the Multinet-Growth hypothesis. Concept inspired by the description of the hypothesis (Roelofsen and Houwink, 1953). (A) microfibrils (black) are deposited orthogonal to the main growth axis; (B) a second layer of microfibrils (orange) is deposited while the former layer (black) gets pushed into the page and readjusted to an oblique orientation; (C) a third layer (green) is deposited while the former two layers are further pushed into the page, where the black microfibrils become tangential to the major growth axis and the orange microfibrils assume an oblique orientation 42

Figure 2.11 – Difference between microwave and conventional heating sources in terms of energy delivery to the biomass. (A) Conventional heat transfer incorporates the solvent as an intermediary phase, hence solvent temperature is higher than that of the biomass. (B) Microwaves deliver energy directly to the biomass, bypassing the solvent and constituting heat transfer in the opposite direction.....47

Chapter 3

Figure 3.1 - General model structure 58

Figure 3.2 - The geometry of a single cell; (A) XY cross-section; (B) XZ cross-section; (C) YZ cross-section.....59

Figure 3.3 - The geometry of a multicellular biomass cluster; (A) XY cross-section; (B) XZ cross-section; (C) YZ cross-section 59

Figure 3.4 - Differential heat transfer element. Directions of heat flow are arbitrary and used for demonstration purposes.....60

Figure 3.5 – 2-dimensional representation of model discretisation for heat transfer. Biomass phases are discretised with the method of lines, while the solvent is denoted a single mobile numerical point 64

Figure 3.6 – Taylor expansion framework for 3 unidimensional points.....64

Figure 3.7 – Numerical framework for the heat model.....67

Figure 3.8 – Temperature-time profile for a single-cell biomass-solvent system; (A) $\Delta\boldsymbol{\varepsilon}'' = \mathbf{25}$; (B) (A) $\Delta\boldsymbol{\varepsilon}'' = \mathbf{-25}$.....70

Figure 3.9 – Steady state temperature distribution of an XZ cross-section of 1000-cell biomass-solvent system. Dielectric loss factors of biomass and solvent are 20 and 5, respectively.....71

Figure 3.10 - Steady state temperature distribution of an XZ cross-section of 1000-cell biomass-solvent system; penetration depth = (A) 0.1 cm; (B) 1 cm; (C) 5 cm ..75

Figure 3.11 – Temperature-time plots for a 125-cell biomass-solvent system with variable biomass dielectric loss factor. Temperatures are shown for the solvent and a cell located at the middle of the cluster. Dielectric loss factor = (A) 0; (B) 10; (C) 25 83

Figure 3.12 – Temperature-time plots for a 125-cell biomass-solvent system with variable thermal conductivity. Temperatures are shown for the solvent and a cell

located at the middle of the cluster. Thermal conductivity = (A) 0.05 $Wm^{-1}K^{-1}$; (B) 0.2 $Wm^{-1}K^{-1}$; (C) 0.4 $Wm^{-1}K^{-1}$ 84

Figure 3.13 – Temperature-time plots for a 125-cell biomass-solvent system with variable incident electric field intensity. Temperatures are shown for the solvent and a cell located at the middle of the cluster. Electric field intensity = (A) 2000 Vm^{-1}; (B) 6000 Vm^{-1}; (C) 10000 Vm^{-1} 84

Chapter 4

Figure 4.1 – Binomial distribution for variable $\boldsymbol{\varepsilon}$ where (A) N = 50; (B) N = 10000. Concept inspired by Eastman and Reif (Eastman, 2019; Reif, 1965).....94

Figure 4.2 – Microcanonical ensemble 95

Figure 4.3 – Biomass solvent system under microwave heating. Energy cycle is induced where (A) biomass is heated directly with microwave radiation, and (B) energy is lost conventionally from biomass to solvent and then back to the environment.....102

Figure 4.4 – Three-way microcanonical ensemble comprising energy cycle. (1) direct energy delivery from C to A by microwave radiation; (2) conventional heat transfer from A to B; (3) energy removal from B back to C either by conventional heat transfer or through reflux (i.e., evaporation and condensation).....103

Figure 4.5 – Rough representation of $\boldsymbol{\partial ln\,\Omega \partial E}$, $\boldsymbol{\partial ln\,\Omega \partial V}$, and $\boldsymbol{\partial ln\,\Omega \partial N}$ as functions of $\boldsymbol{E}$. (A) $\boldsymbol{\partial ln\,\Omega \partial E \sim 1E}$; (B) $\boldsymbol{\partial ln\,\Omega \partial V}$ and $\boldsymbol{\partial ln\,\Omega \partial N \sim ln\,E}$.....109

Chapter 5

Figure 5.1 – Demonstration of how cell pressure rises due to vaporisation when (A) there is no cell wall; (B) there is a cell wall. In (A), boiling occurs at atmospheric pressure, which might or might not be sufficient for cell rupture. In (B), boiling is resisted by the surrounding cell walls, inducing pressure within the cell. This pressure increases together with temperature as the saturation condition, until cell rupture is achieved 128

Figure 5.2 – A cubic biomass cluster with 1x2x10 cells and particle size of 0.1 mm 130

Figure 5.3 – Steady state temperature distribution of a YZ cross-section of a 0.5 mm cubic biomass within a biomass-solvent system. Dielectric loss factor of biomass =

35; thermal conductivity = 0.1 $Wm^{-1}K^{-1}$; incident electric field intensity = 10000 Vm^{-1} 131

Figure 5.4 – Differential mass transfer element. Directions of mass flow are arbitrary and used for demonstration purposes 136

Figure 5.5 – Schematic demonstrating the interdependence between pressure and diffusion, where water influx to cells induces pressure, which then drives water to diffuse out of the cell.....140

Figure 5.6 – Computational stress-strain behaviour with Y_0 = 800 MPa (Equation (5.17)).....141

Figure 5.7 – Stress components acting on a cell wall fragment.....142

Figure 5.8 – Force balance between a cell and its surrounding cell wall. A_C and A_{CW} are the cross-sectional areas of the cell and surrounding cell wall, respectively, along the *x-direction* 143

Figure 5.9 – Numerical framework for cell expansion 144

Figure 5.10 – 2-dimensional representation of model discretisation for mass transfer. Biomass cells are discretised with the method of lines, while the solvent and cell walls are denoted a single mobile numerical point 146

Figure 5.11 – Numerical framework for the combined heat, mass, and mechanical model.....150

Figure 5.12 – Pressure induced in a single-cell biomass-solvent system with microwave and conventional heating. (A) Cell pressure against time; (B) temperature against time under microwave heating; (C) temperature against time under conventional heating 154

Figure 5.13 – Pressure distribution at mass equilibrium for a YZ cross-section of a 0.5 mm cubic biomass within a biomass-solvent system. Dielectric loss factor of biomass = 10; thermal conductivity = 0.2 $Wm^{-1}K^{-1}$; incident electric field intensity = 10000 Vm^{-1} 155

Chapter 6

Figure 6.1 – Example from Mao et al. (Mao et al., 2019) to demonstrate the dramatic drop in the input microwave power on approaching a desired temperature set-point. Figure from Mao et al. (Mao et al., 2019), cropped from a larger figure comprising four plots, but unmodified otherwise (© 2019 The Authors. Published by Elsevier Ltd.), available under CC BY 4.0 license

(https://creativecommons.org/licenses/by/4.0/) when obtained. Further use of this item is governed by the said license unless otherwise indicated by the copyright holders 173

Figure 6.2 – Single-cell biomass-solvent system being heated up to $\boldsymbol{T_{extraction} = 80}$ ℃. (A) Solvent boiling point equals $\boldsymbol{T_{extraction}}$ (i.e., continuous microwave heating); (B) $\boldsymbol{T_{extraction}}$ is lower than solvent boiling point (i.e., ramp microwave heating); (C) conventional heating 174

Figure 6.3 – Microwave extraction system enabling continuous power input. See Table 6.1 for description 177

Figure 6.4 – Average temperature-time profiles for different microwave extraction runs; (A) continuous heating experiments; (B) ramp heating experiments 183

Figure 6.5 – Results for the (A) continuous heating experiments; (B) ramp heating experiments 183

Figure 6.6 – Results for the room temperature experiments 187

Chapter 7

Figure 7.1 – Visual demonstration by Mao et al. (Mao, Robinson and Binner, 2021) of how extraction could be enhanced with temperature gradients without the need for cell rupture. Localised temperature gradients are thought to improve diffusion, solubilisation, hydrolysis, and pressure build-up, resulting in enhanced extraction of pectin in this case. Figure unmodified from Mao et al. (Mao, Robinson and Binner, 2021) (© 2021 The Authors. Published by Elsevier Ltd.), available under CC BY 4.0 license (https://creativecommons.org/licenses/by/4.0/) when obtained. Further use of this item is governed by the said license unless otherwise indicated by the copyright holders 194

Figure 7.2 – Infinitesimal domain/cuboid and its 6 adjacent phases of direct interaction 199

Figure 7.3 – Activity-mole fraction relationship described in Equation (7.5); (A) Plot of activity against mole fraction for different values of n; (B) Plot of activity coefficient against mole fraction for different values of n 203

Figure 7.4 – Demonstration of how the presence of undissolved solutes inhibits changes in mole fraction as mass transfer takes place. Cell wall fragment A: solute diffusing to the solvent is substituted by surplus dissolving solute. Cell wall fragment B: solute diffusing from the solvent precipitates out of solution 205

Figure 7.5 – Mole fraction as a function of mixture fraction/composition (Equation (7.6)). $\boldsymbol{XW *= 0.5}$ 206

Figure 7.6 – Demonstration of the shape that cell wall voids are assumed to take. Each cell wall fragment has a square-shaped concentration of voids running through the *x-direction* (into the page). Axial stress is applicable along the *x-direction* and is limited to areas adjacent to voids, so as to maintain a square-shaped area of mechanical influence.....209

Figure 7.7 – Numerical framework for cell wall expansion 211

Figure 7.8 – Numerical framework for the comprehensive extraction model 217

Figure 7.9 – A cubic biomass cluster with 1x2x2 cells and particle size of 0.1 mm 218

Figure 7.10 – Biomass cell cluster cross-section, demonstrating inner biomass and outer cell wall layers 221

Figure 7.11 – Yield-time plot for the room temperature extraction base case.....222

Figure 7.12 – Osmotic potential diagrams for the room temperature extraction base case. Diagrams show gradients in activities, pressure, temperature, and chemical potentials between solvent, outer cell wall layer, inner cell wall layer, and cells. (A) initial condition; (B) final/equilibrium condition. Diagrams are supplemented with water/solute activity-time plots, where each cell wall layer is represented by a single cell wall fragment.....223

Figure 7.13 – Schematic for the room temperature extraction base case. Mass transfer only takes place between the solvent phase and the outer layer of cell wall fragments. These solutes cannot be fully dissolved by the available water; hence, activities remain constant in the outer layer and uniform across the biomass, thereby inhibiting any intra-biomass diffusion and restricting extraction to the outer layer only.....224

Figure 7.14 – Yield-time plot for room temperature extraction where $\boldsymbol{Ss = 0.04\ gSgW - 1}$ (other parameters fixed as shown in Table 7.4).....226

Figure 7.15 – Osmotic potential diagrams for room temperature extraction with $\boldsymbol{Ss = 0.04\ gSgW - 1}$. Diagrams show gradients in activities, pressure, temperature, and chemical potentials between solvent, outer cell wall layer, inner cell wall layer, and cells. (A) initial condition; (B) complete dissolution of solutes in outer cell wall layer; (C) final/equilibrium condition. Diagrams are supplemented with water/solute activity-time plots, where each cell wall layer is represented by a single cell wall fragment 227

Figure 7.16 – Schematic for room temperature extraction under high $\boldsymbol{Ss}$; (A) initially, mass transfer only takes place between the solvent and the outer cell wall layer due to the presence of undissolved solutes; (B) mass equilibrium is not established even as all solutes in the outer cell wall layer get fully dissolved; hence, intra-biomass diffusion is triggered where solutes are extracted from the inner cell wall layer and from cells. Water/solute exchange within the inner biomass (cells/cell walls) depends on the established local gradients. Nonetheless, the overall diffusion process is regulated by the significant gradients between the outer layer and the inner biomass, which generally drive water diffusion deeper into the biomass and solutes towards the solvent phase. This occurs regardless of the specific pathways taken by water/solutes within the inner biomass 228

Figure 7.17 – Flow diagram summarising the layer-by-layer extraction process occurring at room temperature 229

Figure 7.18 – Osmotic potential diagrams for room temperature extraction with $\boldsymbol{Ds = 0\ m2s - 1}$ (i.e., solutes do not flow in the system; only water does). Diagrams show gradients in activities, pressure, temperature, and chemical potentials between solvent, outer cell wall layer, inner cell wall layer, and cells. (A) initial condition; (B) final/equilibrium condition 233

Figure 7.19 – Yield-time plots for $\boldsymbol{Ds1 = 10 - 10\ m2s - 1}$ and (A) $\boldsymbol{Ds2 = 10 - 10\ m2s - 1}$; (B) $\boldsymbol{Ds2 = 5 \times 10 - 11\ m2s - 1}$; (C) $\boldsymbol{Ds2 = 10 - 12\ m2s - 1}$ (other parameters fixed as shown in Table 7.4) 235

Figure 7.20 – Water activity-time plots for $\boldsymbol{Ss = 0.1\ gSgW - 1}$ and different cell wall solute contents (%$\boldsymbol{s - CW}$); (A) %$\boldsymbol{s - CW = 0.06}$; (B) %$\boldsymbol{s - CW = 0.2}$ (other parameters, except solvent-to-solid ratio, are fixed as shown in Table 7.4) .244

Figure 7.21 – Base results for the heating case presented as yield-time plots; (A) $\boldsymbol{\varepsilon'' biomass = 20}$ (microwave heating); (B) $\boldsymbol{\varepsilon'' biomass = 0}$ (conventional heating) (other parameters fixed as shown in Table 7.4) 245

Figure 7.22 – Base results for the heating case presented as temperature gradient-time plots (difference in temperature between biomass phases and solvent); (A) $\boldsymbol{\varepsilon'' biomass = 20}$ (microwave heating); (B) $\boldsymbol{\varepsilon'' biomass = 0}$ (conventional heating). Other parameters are fixed as shown in Table 7.4, and each cell wall layer is represented by a single fragment 246

Figure 7.23 – Osmotic potential diagrams for the microwave extraction base scenario. Diagrams show gradients in activities, pressure, temperature, and chemical potentials between solvent, outer cell wall layer, inner cell wall layer, and cells. (A) initial condition; (B) pressure build-up in the biomass leading to a fresh increase in the yield; (C) final/equilibrium condition. Diagrams are supplemented with water activity-time and biomass pressure-time plots, where each cell wall layer is represented by a single cell wall fragment 248

Figure 7.24 – Schematic describing extraction under microwave heating. In addition to normal mass transfer between solvent and outer biomass, water flows towards the inner biomass against the established temperature gradient, inducing high pressure and forcing solute extraction from the inner cell wall layer and cells. Water/solute exchange within the inner biomass (cells/cell walls) depends on the chemical potential gradients. Nonetheless, the overall water inward diffusion and solute extraction are governed by the temperature and pressure gradients, respectively, existing between the biomass and the solvent. Regardless of the specific pathways taken by water/solutes within the inner biomass, water generally diffuses into the biomass and solutes generally flow towards the solvent 250

Figure 7.25 – Steady state temperature distribution of a YZ cross-section of a 0.3 mm cubic biomass within a biomass-solvent system. $\boldsymbol{\varepsilon''biomass = 30}$; $\boldsymbol{k = 0.01\,Wm-1K-1}$; $\boldsymbol{Qs = 5\,Ks-1}$; and all other parameters are fixed as shown in Table 7.4. (A) general temperature map of the biomass including both cells and cell walls; (B) temperature map for the cell walls only. A maximum biomass temperature of around $\boldsymbol{145}$ ℃ occurs around the centre of the cluster 251

Figure 7.26 – (A) Temperature-time plot and (B) temperature gradient-time plot (difference in temperature between biomass phases and solvent) for a biomass-solvent system comprising a 0.1 mm cubic biomass material, with $\boldsymbol{\varepsilon''biomass = 30}$; $\boldsymbol{\varepsilon''solvent = 5}$ (i.e., $\Delta\boldsymbol{\varepsilon'' = 25}$); $\boldsymbol{Qs = 7.5\,Ks-1}$; and all other parameters fixed as shown in Table 7.4. Each cell wall layer is represented by a single cell wall fragment 254

Figure 7.27 – Temperature gradient-time plots (difference in temperature between biomass phases and solvent) for $\Delta\boldsymbol{\varepsilon'' = -2.5}$ and variable $\boldsymbol{D}$. (A) $\boldsymbol{DW, Ds = 10-10, 10-11\,m2s-1}$; (B) $\boldsymbol{DW, Ds = 10-8, 10-9\,m2s-1}$. All other parameters are as shown in Table 7.4. Each cell wall layer is represented by a single cell wall fragment.....256

Figure 7.28 – Temperature gradient-time plots (difference in temperature between biomass phases and solvent) for $\Delta\boldsymbol{\varepsilon'' = -2.5}$ and variable $\boldsymbol{Ss}$. (A) $\boldsymbol{Ss = 0.00075\,gsgW-1}$; (B) $\boldsymbol{Ss = 0.001\,gsgW-1}$; (C) $\boldsymbol{Ss = 0.1\,gsgW-1}$. All other parameters are as shown in Table 7.4. Each cell wall layer is represented by a single cell wall fragment 256

Figure 7.29 – Yield-time plots under (A) continuous microwave heating, (B) ramp microwave heating, and (C) conventional heating. $\boldsymbol{Qs = 1\,Ks-1}$; $\boldsymbol{Ss = 0.01\,gsgW-1}$; $\boldsymbol{Ds1 = Ds2 = DRs = 10-10\,m2s-1}$; other parameters fixed as shown in Table 7.4.....259

Figure 7.30 – Yield-time plots under (A) continuous microwave heating, (B) ramp microwave heating, and (C) conventional heating. $\boldsymbol{Qs = 5\,Ks-1}$; $\boldsymbol{Ss = 0.1\,gsgW-1}$; $\boldsymbol{Ds1 = Ds2 = DRs = 10-10\,m2s-1}$. Other parameters fixed as shown in Table 7.4.....263

Figure 7.31 – Yield-time plots under (A) continuous microwave heating, (B) ramp microwave heating, and (C) conventional heating. $\boldsymbol{Qs = 5\ Ks - 1}$; $\boldsymbol{Ss = 0.1\ gsgW - 1}$; $\boldsymbol{Ds1 = 10 - 10\ m2s - 1\ m2s - 1}$; $\boldsymbol{Ds2 = 10 - 11\ m2s - 1\ m2s - 1}$; $\boldsymbol{Ds1 = DRs1}$; $\boldsymbol{Ds2 = DRs2}$ 265

Chapter 8

N/A

Appendices

Figure A.1 – Temperature-time plots for the cell and solvent under the no-heating case and for different computational time intervals.....303

Figure A.2 – Temperature-time plots for the cell and solvent under conventional heating where $\boldsymbol{E0 = 5 \times 103\ Vm - 1}$ and $\boldsymbol{\varepsilon''solvent = 5}$, and for different computational time intervals.....305

Figure A.3 – Temperature-time plots for the cell and solvent under conventional heating where $\boldsymbol{E0 = 104\ Vm - 1}$ and $\boldsymbol{\varepsilon''solvent = 10}$, and for different computational time intervals.....306

Figure B.1 – Water activity-time and cell pressure-time plots under the no-heating case where $\boldsymbol{\alpha Winitial = 1}$, and for different computational time intervals 309

Figure B.2 – Water activity-time and cell pressure-time plots under the no-heating case where $\boldsymbol{\alpha Winitial = 0.99}$, and for different computational time intervals...311

Figure B.3 – Water activity-time and cell pressure-time plots under the no-heating case where $\boldsymbol{\alpha Winitial = 0.98}$, and for different computational time intervals...313

Figure B.4 – Water activity-time and cell pressure-time plots under the no-heating case where $\boldsymbol{\alpha Winitial = 0.98}$, where cell pressure is constrained to $\boldsymbol{0\ barg}$ regardless of water diffusion.....315

Figure B.5 – Water activity-time and cell pressure-time plots under a microwave heating case where $\boldsymbol{E0 = 104\ Vm - 1}$, $\boldsymbol{\alpha Winitial = 0.98}$, and for different computational time intervals.....317

Figure C.1 – Percentage yield-time and solute activity-time plots under the no-heating case where $\boldsymbol{Ss = 0.01\ gsgW - 1}$, and for different computational time intervals.....323

Figure C.2 – Water activity-time plots under the no-heating case where $\boldsymbol{Ss = 0.01\ gsgW - 1}$ and $\boldsymbol{0.03\ gsgW - 1}$, and for different computational time intervals 325

Figure C.3 – Water activity-time plots under the no-heating case where $\boldsymbol{\%W - CW = 0.01}$ and $\boldsymbol{0.1}$, and for different computational time intervals 327

Figure C.4 – Solute quantity-time plots under the no-heating case, for different computational time intervals 330

Figure D.1 – 2-dimensional structure showing perfect symmetry in the vertical and horizontal axes; therefore, the properties of the representative segment are identical to those throughout the other segments. Such symmetry can be utilised in the biomass-solvent extraction model to compute the relevant outcomes only in representative segments, thereby significantly reducing the demand for computational effort 332

Figure D.2 – Software structure mapping the links between the various model elements, which are connected in an object-oriented fashion 335

LIST OF TABLES

Chapter 1

N/A

Chapter 2

Table 2.1 – Some ISM frequency band allocations. This is an indicative highlight, and the relevant domestic/international laws and official documentation should still be referred to for accurate and up-to-date information 9

Table 2.2 – Examples of available microwave-assisted extraction models 51

Chapter 3

Table 3.1 – Typical value ranges and selected baseline values for the various model parameters 69

Table 3.2 – Maximum temperature difference between biomass and solvent at thermal steady state, and time required to achieve 95% of steady state, for variable dielectric loss factors and cell cluster size 72

Table 3.3 – Maximum temperature difference between biomass and solvent at thermal steady state, and time required to achieve 95% of steady state, for variable microwave penetration depths and cell cluster size 74

Table 3.4 – Maximum temperature difference between biomass and solvent at thermal steady state, and time required to achieve 95% of steady state, for variable thermal conductivity and cell cluster size 76

Table 3.5 – Maximum temperature difference between biomass and solvent at thermal steady state, and time required to achieve 95% of steady state, for variable specific heat capacity and cell cluster size 78

Table 3.6 – Maximum temperature difference between biomass and solvent at thermal steady state, and time required to achieve 95% of steady state, for variable solvent-to-solid ratio and cell cluster size 78

Table 3.7 – Maximum temperature difference between biomass and solvent at thermal steady state, and time required to achieve 95% of steady state, for variable density and cell cluster size 79

Table 3.8 – Maximum temperature difference between biomass and solvent at thermal steady state, and time required to achieve 95% of steady state, for variable cell dimensions and cell cluster size 80

Table 3.9 – Maximum temperature difference between biomass and solvent at thermal steady state, and time required to achieve 95% of steady state, for variable microwave frequency and cell cluster size.....81

Table 3.10 – Maximum temperature difference between biomass and solvent at thermal steady state, and time required to achieve 95% of steady state, for variable electric field intensity and cell cluster size 82

Chapter 4

Table 4.1 – Volume transfer scenarios when a system "i" possesses higher temperature than its surroundings "j" 106

Table 4.2 – Summary of the framework for transfer phenomena 114

Chapter 5

Table 5.1 – Key features, strengths, and limitations of the existing microwave cell rupture hypotheses 127

Table 5.2 - Input variables and constants for the Steam-Rupturing analysis.....130

Table 5.3 – Maximum temperature difference between biomass and solvent at thermal steady state, and time required to achieve 95% of steady state, for variable cell cluster size and (A) thermal conductivity; (B) dielectric loss factor of biomass 131

Table 5.4 – Typical value ranges for the various model parameters 152

Table 5.5 – Selected baseline values for the various model parameters.....153

Table 5.6 – Maximum cell pressure at mass equilibrium, and time required to achieve 95% of mass equilibrium, for variable biomass dielectric loss factor and particle size.....156

Table 5.7 – Maximum cell pressure at mass equilibrium, and time required to achieve 95% of mass equilibrium, for variable thermal conductivity and particle size 158

Table 5.8 – Maximum cell pressure at mass equilibrium, and time required to achieve 95% of mass equilibrium, for variable incident electric field intensity and particle size.....159

Table 5.9 – Maximum cell pressure at mass equilibrium, and time required to achieve 95% of mass equilibrium, for a collection of secondary input parameters. Particle size = 0.1 mm.....161

Table 5.10 – Threshold electric field intensities needed for cell rupture, for variable biomass dielectric loss factor, thermal conductivity, and biomass particle size. The condition for rupture is attaining a maximum equilibrium cell pressure of at least 70 bar within 5 minutes at most. Field intensity values are quoted to the nearest $\mathbf{500\ Vm-1}$. Cell rupture is deemed unachievable if a field intensity larger than $\mathbf{104\ Vm-1}$ is required, as this is the likely maximum under single-mode cavities (Robinson et al., 2010).....164

Chapter 6

Table 6.1 – Description of the parts incorporated in the microwave extraction system enabling continuous power input (Figure 6.3). Setup materials should withstand pressure gradients and be compatible with microwave heating.....178

Chapter 7

Table 7.1 – Existing limitations in the model from Chapter 5, along with the implications and methods to readdress 197

Table 7.2 – $\mathcal{H}i-j$ values corresponding to the different physical conditions governing mass transfer between two phases “i” and “j” 202

Table 7.3 – Typical value ranges for the various model parameters 219

Table 7.4 – Selected baseline values for the various model parameters.....220

Table 7.5 – Percentage yield and time required to achieve 95% of mass equilibrium, for variable solubility (other parameters fixed as shown in Table 7.4) 230

Table 7.6 – Percentage yield, time required to achieve 95% of mass equilibrium, and maximum biomass pressure, for variable solute diffusivity (other parameters fixed as shown in Table 7.4).....232

Table 7.7 – Percentage yield and time required to achieve 95% of mass equilibrium, for variable diffusivity of solute (2). $\boldsymbol{DW = 10-9\ m2s-1}$, $\boldsymbol{Ds1 = 10-}$

$\mathbf{10}\ \boldsymbol{m2s}-\mathbf{1}$, and $\boldsymbol{Ss}=\mathbf{0.01}\ \boldsymbol{gsgW}-\mathbf{1}$ (other parameters fixed as shown in Table 7.4) 234

Table 7.8 – Percentage yield and time required to achieve 95% of mass equilibrium, for variable diffusivity of solute (2). $\boldsymbol{Ds}\mathbf{1}=\mathbf{10}-\mathbf{11}\ \boldsymbol{m2s}-\mathbf{1}$ and $\boldsymbol{Ss}=\mathbf{0.02}\ \boldsymbol{gsgW}-\mathbf{1}$ (other parameters fixed as shown in Table 7.4).....236

Table 7.9 – Percentage yield and time required to achieve 95% of mass equilibrium, for variable solute-to-solvent ratio (other parameters fixed as shown in Table 7.4)237

Table 7.10 – Percentage yield and time required to achieve 95% of mass equilibrium, for variable biomass particle size (other parameters fixed as shown in Table 7.4) .238

Table 7.11 – Percentage yield and time required to achieve 95% of mass equilibrium, for variable activity-mole fraction relationship for solutes (other parameters fixed as shown in Table 7.4).....240

Table 7.12 – Percentage yield and time required to achieve 95% of mass equilibrium, for variable initial mass percentage of solutes in solvent (other parameters fixed as shown in Table 7.4).....240

Table 7.13 – Percentage yield and time required to achieve 95% of mass equilibrium, for variable initial mass percentage of solutes in cell wall. $\boldsymbol{Ss}=\mathbf{0.01}\ \boldsymbol{gSgW}-\mathbf{1}$. Other parameters, except solvent-to-solid ratio, are fixed as shown in Table 7.4)..242

Table 7.14 – Percentage yield and time required to achieve 95% of mass equilibrium, for variable initial mass percentage of solutes in cell wall. $\boldsymbol{Ss}=\mathbf{0.1}\ \boldsymbol{gSgW}-\mathbf{1}$. Other parameters, except solvent-to-solid ratio, are fixed as shown in Table 7.4)..243

Table 7.15 – Yield, time required to achieve 95% of mass equilibrium, and maximum temperature gradient between biomass and solvent, for variable solvent heating rate, dielectric loss factor of biomass, and thermal conductivity. Base case values: $\boldsymbol{Qs}=\mathbf{1}\ \boldsymbol{Ks}-\mathbf{1}$; $\boldsymbol{\varepsilon''biomass}=\mathbf{20}$; $\boldsymbol{k}=\mathbf{0.01}\ \boldsymbol{Wm}-\mathbf{1}\boldsymbol{K}-\mathbf{1}$ (other parameters fixed as shown in Table 7.4).....251

Table 7.16 – Threshold solvent heating rate ($\boldsymbol{Qs}$) required to maintain a temperature gradient of at least $\mathbf{0.25}$ ℃, between the representative inner cell wall fragment (blue line in Figure 7.28) and the solvent, during the heat-up phase. $\boldsymbol{Qs}$ values are shown in increments of $\mathbf{0.5}\ \boldsymbol{Ks}-\mathbf{1}$ for variable $\boldsymbol{D}$, $\boldsymbol{Ss}$, and $\boldsymbol{\varepsilon''biomass}$. If $\boldsymbol{Qs}>\mathbf{15}\ \boldsymbol{Ks}-\mathbf{1}$, the required temperature gradient is deemed unachievable. $\boldsymbol{\varepsilon''solvent}=\mathbf{5}$ throughout, and other parameters are fixed as shown in Table 7.4 257

Table 7.17 – Yields achieved after 1000 s of extraction, under ramp microwave heating and conventional heating, for variable $\boldsymbol{Qs}$. Other parameters fixed as shown in Table 7.4.....260

Table 7.18 – Yields achieved after 1000 s of extraction, under ramp microwave heating and conventional heating, for variable $\boldsymbol{Qs}$, and where $\boldsymbol{DRs1 = DRs2 = 10 - 9\,m2s - 1}$. Other parameters fixed as shown in Table 7.4.....262

Table 7.19 – Solubilities and diffusivities used in the various scenarios.....266

Table 7.20 – Yield-time plots for scenario 1.....267

Table 7.21 – Yield-time plots for scenario 2.....268

Table 7.22 – Yield-time plots for scenario 3.....269

Table 7.23 – Yield-time plots for scenario 4.....271

Table 7.24 – Yield-time plots for scenario 5.....272

Table 7.25 – Yield-time plots for scenario 6.....273

Table 7.26 – Yield-time plots for scenario 7.....274

Table 7.27 – Yield-time plots for scenario 8.....276

Chapter 8

N/A

Appendices

Table A.1 – Variables and constants for the current model validation.....301

Table B.1 – Variables and constants for the current model validation.....307

Table C.1 – Variables and constants for the current model validation.....320

Table D.1 – Python libraries used in this work.....336

1 INTRODUCTION, AIM, OBJECTIVES, AND THESIS STRUCTURE

The format of this chapter is as follows:

1.1 General introduction/background 2
1.2 Thesis aim and objectives 5
1.2.1 Aim 5
1.2.2 Objectives 6
1.3 Thesis structure 6
1.3.1 Chapter 2 6
1.3.2 Chapter 3 7
1.3.3 Chapter 4 7
1.3.4 Chapter 5 7
1.3.5 Chapter 6 7
1.3.6 Chapter 7 7
1.3.7 Chapter 8 7

1.1 General introduction/background

In 2019, the global demand for liquid fuels (e.g., oil) had been expected to increase slightly over the coming decades (BP, 2019); however, this shifted in 2020 to a more negative outlook, entailing a ~70% drop in demand by 2050 in the worst-case scenario for the sector, and a ~10% drop in the best-case scenario (BP, 2020). The predicted decrease in demand is due to multiple factors, including the different global events (e.g., COVID-19 pandemic (BP, 2020)), and the efforts towards substituting fossil fuels with cleaner, more sustainable energy sources. Various countries have introduced plans and legislation to accelerate their transition towards clean energy, especially in light of the Paris Agreement for climate (UN, 2015). For example, in 2020 the UK Government set out a 10-point plan outlining its intention to end the sale of new petrol/diesel cars/vans in the country by 2030 (UK Government, 2020). Such plans and incentives will undoubtedly affect the demand on liquid fuels, given that ~50% of such demand currently originates from the transportation sector (BP, 2020).

Despite the currently envisaged reduction in oil demand, the need for this commodity is generally expected to hold for non-combusted uses, such as in the petrochemical industries. This has been pointed out uniformly in the annual BP Energy Outlook reports 2016 – 2020 (BP, 2016, 2017, 2018, 2019, 2020), indicating that oil is still expected to cover the global needs for chemicals and other products in the coming decades. This is an interesting observation, as it stipulates a requirement for significant research to be conducted, to develop unconventional chemical production routes offering more sustainable alternatives to petrochemicals and fossil resources. In this regard, such alternatives can be achieved through plant-based biomass, which are considered a potential displacement to fossil reserves for the production of fuels and platform chemicals (Zhang et al., 2016). These materials exist in various forms, including both food-based products such as fruits/vegetables, and non-edible lignocellulosic biomass like wood, grass, etc (Hu and Ragauskas, 2012; Paudel et al., 2017). There is an abundance of biomass feedstocks, as the annual availability of cellulosic materials was recently estimated at 180 billion tons (Demain, Newcomb and Wu, 2005), and the wasted/lost fruits/vegetables were also estimated at ~50% of the global production (FAO, 2011).

Plant-based biomasses can be converted into various products including both liquid and gaseous fuels/chemicals (IEA, 2009a). It is often preferable to develop biomass

processing techniques that complement the "biorefinery concept," which is defined as the "sustainable processing of biomass into a spectrum of marketable products and energy" (IEA, 2009b). The biorefinery concept incorporates process synergy and integration, thereby enabling many valuable products to be attained, such as biomaterials, biofuels, waxes, acids, aromatics, proteins, fertilizers, and others. Various intermediary platforms can also be produced, including biogas, syngas, C5/C6 sugars, etc; moreover, heat, electricity, and steam can be generated (IEA, 2009b; Jong and Jungmeier, 2015; Kumar, Singh and Singh, 2008). Such biorefineries will undoubtedly enhance the economic prospects of biomass processing, since they combine the production of major fuels with further value-added by-products, thereby rendering the overall process more competitive in the market (Huang et al., 2008).

Biomass processing techniques can be categorised into the following: (i) thermochemical methods such as pyrolysis, gasification, and combustion; (ii) biochemical methods where enzymes and micro-organisms are utilised, such as in fermentation and anaerobic digestion; (iii) chemical methods involving the use of reagents to alter the chemical makeup of biomass, such as in transesterification, acid hydrolysis, etc; and (iv) mechanical methods like pressing, particle size reduction, extraction, and some pre-treatment techniques (Cherubini, 2010; IEA, 2009b; Jong and Jungmeier, 2015). Biorefineries should attempt to optimise production through combining/integrating these methods. For example, incorporating a pre-treatment step can upgrade feedstocks and overcome their recalcitrance, thus improving subsequent processes such as enzymatic conversions, pyrolysis, and others (Duan et al., 2018; Lynd, 1996; Puligundla, Oh and Mok, 2016; Wyman et al., 2005). This indicates the importance of working diversely to develop various biomass processing techniques, rather than focussing on a single processing method/route/form.

However, biomass processing still encounters various challenges that must be overcome, before biorefineries can be implemented at the envisaged industrial scales. For instance, notwithstanding their wide availability, biomass materials are naturally rigid and resistant to attempts for their degradation (Alcántara et al., 2016; Ohmiya et al., 2003). This is especially true for non-edible lignocellulosic materials, which although are favourable to use over edible feedstocks, they still lack the appropriate and mature technologies enabling their full utilisation (Cherubini, 2010; IEA, 2009a; Wainaina, Horváth and Taherzadeh, 2018). Furthermore, biomass materials are very

heterogeneous in nature, with features and compositions varying from one type of material to another (Carpenter et al., 2014; Jawaid, Paridah and Saba, 2017). Also, these materials are seasonally available (Clark and Deswarte, 2015), and their wide geographic distribution and significant water content can dramatically increase their transportation costs (Searcy et al., 2007). On the other hand, biomass processing gives rise to an alternative set of chemical processing routes, which may currently be unfamiliar to the petrochemical industries. This is due to the highly oxygenated and functionalised bonds existing within biomass, which demand reduction or hydrolysis-based reactions to arrive at the desired products, rather than the synthetic or oxygenation routes currently implemented in petro-refineries (Clark and Deswarte, 2015; Farmer and Mascal, 2015). Furthermore, the compositions of some platforms, like syngas, are very sensitive to feedstock properties and processing conditions (Ramachandriya et al., 2016), which constitutes further challenges for downstream operations. The challenges associated with biomass refining have rendered the achievable products generally expensive compared with their fossil-derived counterparts (Jong and Jungmeier, 2015). In turn, this stipulates the need for novel processing techniques to be developed, and for the existing technologies to be improved. These challenges should not only be addressed within the biorefinery itself, but also in the various upstream/downstream industries, which may require further capital investments to adapt to the new processes and chemical conversion routes. This is essential for developing comprehensive supply- and value-chains that support the envisaged biorefineries.

In light of the need to develop multiple novel biomass processing techniques, this thesis investigates biomass-solvent extraction, which denotes immersing biomass into a solvent (i.e., biomass-solvent system) and applying heat to facilitate the recovery of biomass components (Huang et al., 2008; Lee et al., 2015). Extraction results in various value-added products which can replace fossil-based compounds, but also serve as feedstocks in the food, pharmaceutical, cosmetic, and other industries (Flórez, Conde and Domínguez, 2015; Rodrigues et al., 2018; Tsubaki, Sakamoto and Azuma, 2010). However, despite the variety of valuable components achievable with extraction, this technique generally suffers from low yields and demands significant downstream separation steps (Farmer and Mascal, 2015). It is, therefore, vital to develop novel extraction techniques or improve existing ones, in order to enhance the

economic prospects and robustness of biomass-solvent extraction processes. In this regard, microwave heating has been put forward as a promising technology to enhance biomass-solvent extraction. Compared with conventional extraction techniques, microwave-assisted extraction is thought to accelerate the process, increase yields, reduce solvent consumption, and improve product quality/selectivity (Bagherian et al., 2011; Pan, Niu and Liu, 2003; Pandey and Shrivastava, 2018; Xiao, Han and Shi, 2008). Nevertheless, despite the multitude of research publications and patent filings made under this topic (Angiolillo, Del Nobile and Conte, 2015; Galan et al., 2017), microwave extraction is yet to be implemented industrially (Galan et al., 2017). One of the reasons for this shortage in large scale implementation, is a lack of fundamental understanding of how microwave interact with biomass materials, and, in turn, why they bring about enhanced extraction (Chapter 2; section 2.2). Such mechanistic understanding is essential to allow outcome prediction in different biomass-solvent systems, thereby enabling engineering design and process scale-up.

It is attempted in this thesis to develop a mechanistic understanding of the effect of microwaves on biomass-solvent extraction. A mathematical model incorporating key physical characteristics will be constructed, in order to understand microwave interactions and extraction patterns at the cellular scale (i.e., the scale of a few plant cells; $< 1\ mm$).

1.2 Thesis aim and objectives

1.2.1 Aim

The aim of this work is to understand the influence of microwave heating on extraction in biomass-solvent systems, and whether microwaves can fundamentally alter the extraction patterns in these systems compared with conventional heating techniques. This requires characterising the underlying link between electromagnetic heating, heat/mass transfer, and biomass mechanical properties, which currently constitutes a significant gap in knowledge. The intended link will be described through developing a mathematical model for biomass-solvent extraction, aimed to be constructed at the cellular scale (i.e., the scale of a few plant cells; $< 1\ mm$). This model will deliver unprecedented insight/details as to how the various physical parameters influence extraction, which is currently extremely challenging (if at all possible) through experimentation. This work is envisaged as a key first step towards

enabling large-scale implementation of the microwave technology for biomass-solvent extraction.

1.2.2 Objectives

The aim (section 1.2.1) is to be achieved through the following objectives:

- To construct a biomass-solvent model capable of depicting key geometrical features of a cluster of biomass cells immersed in a body of solvent. This model is to incorporate electromagnetic heating and heat transfer, and it should describe temperature build-up/distribution in the system.
- To establish the link between heat transfer and diffusion, and to incorporate this link into the existing heat transfer model, while also extending the model altogether to include mass transfer and biomass pressure build-up. This shall yield a sophisticated heat-mass-mechanical model for biomass-solvent extraction.
- To use the combined heat-mass-mechanical model for investigating the currently accepted hypotheses as to how microwaves enhance extraction in biomass-solvent systems. Such hypotheses claim enhanced microwave extraction to be caused by structural alterations and cell rupture within the biomass (see Chapter 5), but nonetheless, it will be necessary to understand which of these qualifies as the most viable explanation for the observable phenomena.
- To conduct a brief empirical analysis, screening for any evidence for cell rupture that may match the acquired model predictions. The model is to be further modified based on the attained outcomes.

1.3 Thesis structure

This thesis comprises 8 chapters including the current one. The following subsections summarise the goals of Chapters 2 – 8.

Note: Chapters 3 – 7 incorporate “thesis recap” sections to summarise the overall progress so far in each case.

1.3.1 Chapter 2

This chapter will review relevant background information for the current thesis, including aspects of the microwave theory, biomass-solvent systems, and thermal extraction in such systems.

1.3.2 Chapter 3

This chapter will develop a microwave heat transfer model for biomass-solvent systems at the cellular scale. This model shall provide quantitative understanding of the thermal patterns in these systems.

1.3.3 Chapter 4

This chapter will use relevant concepts of statistical mechanics and thermodynamics to characterise the effect of temperature on mass transfer. To aid readers from interdisciplinary backgrounds, a brief review of some relevant concepts of statistical mechanics is also offered.

Moreover, chemical potential will be expressed mathematically in this chapter, so it can be implemented later in kinetic mass transfer analyses.

1.3.4 Chapter 5

This chapter will validate and compare two of the most popular hypotheses attempted at explaining why microwave heating improves cell rupture and extraction in biomass-solvent systems. In doing so, the previously developed model (Chapter 3) will be extended to incorporate water diffusion and cell pressure build-up. The relationships between heat, mass, and pressure shall be defined here as per the discussions in Chapter 4 (i.e., with the chemical potential).

1.3.5 Chapter 6

This chapter will empirically screen for evidence with which enhanced microwave extraction can be attributed to cell rupture, as per discussed in Chapter 5.

1.3.6 Chapter 7

This chapter will propose a novel mechanism for understanding enhanced microwave extraction away from cell rupture. The intended mechanism will be incorporated into a modified version of the existing heat-mass-mechanical model (Chapter 5), where numerous existing assumptions and limitations are to be readdressed. As such, the existing model is to be further enhanced and made applicable to a wider range of conditions, including both room temperature and thermal extraction.

1.3.7 Chapter 8

This chapter will outline the conclusions of the current thesis, together with setting out recommendations for future work.

2 REVIEW: MICROWAVE THEORY AND BIOMASS EXTRACTION

The aim of this chapter is to review fundamental aspects of microwave theory and biomass-solvent extraction, thus providing context for the research carried out in this thesis.

The format of this chapter is as follows:

2.1 Microwave theory 9
2.1.1 Introduction 9
2.1.2 Microwave heating 10
2.1.2.1 Heating mechanisms 11
2.1.2.1.1 Polarisation 11
2.1.2.1.2 Ionic conduction 13
2.1.2.2 Dielectric properties 13
2.1.2.2.1 Relevant Maxwell's equations 14
2.1.2.2.2 Complex dielectric permittivity 16
2.1.2.2.3 Parameters influencing dielectric properties 16
2.1.2.3 Microwave power dissipation 23
2.1.2.4 Microwave attenuation 27
2.1.3 Microwave heating instruments 29
2.1.3.1 Generators 29
2.1.3.2 Transmitters/waveguides 29
2.1.3.3 Applicators 30
2.1.3.3.1 Single-mode cavities 31
2.1.3.3.2 Multimode cavities 32
2.1.3.4 Further instruments 34
2.1.3.4.1 Circulator: safeguarding the power source 34
2.1.3.4.2 Stub & sliding short: tuning 35
2.1.3.4.3 Directional coupler: power detection 36
2.1.4 Section summary 36
2.2 Biomass-solvent extraction 37
2.2.1 Introduction 37
2.2.2 Biomass-solvent systems 38
2.2.2.1 Biomass 38
2.2.2.1.1 General description 38
2.2.2.1.2 Efforts to quantify cell expansion 44
2.2.2.2 Solvent 45
2.2.3 Thermal extraction in biomass-solvent systems 46
2.2.3.1 Microwave versus conventional extraction 46
2.2.3.2 Attempts to model microwave extraction 48
2.2.4 Section summary 52
2.3 Nomenclature 54

2.1 Microwave theory

2.1.1 Introduction

Microwaves are electromagnetic radiation with frequency ranging from 300 MHz to 300 GHz, which can be used in heating applications such as in drying, food processing, and others (Menéndez et al., 2010). However, to avoid interference with telecommunication, there are certain "available" frequencies for industrial, scientific, and medical (ISM) applications, which include but are not limited to 0.915 GHz and 2.45 GHz (Osepchuk, 1984). Table 2.1 highlights some of the microwave bands allocated for ISM use in Europe (Electronic Communications Committee; ECC) and the USA (Federal Communications Commission; FCC). Relevant domestic and international laws and official documentation should still be referred to for accurate and up-to-date information.

ECC allocated (Europe) (Electronic Communications Committee, 2020)	**FCC allocated (USA)** (Federal Communications Commission, 2021)
433.05 – 434.79 MHz	902 – 928 MHz
2400 – 2500 MHz	2400 – 2500 MHz
5725 – 5925 MHz	5650 – 5925 MHz
24 – 24.25 GHz	24 – 24.25 GHz
59.3 – 64 GHz	59.3 – 64 GHz

Table 2.1 – Some ISM frequency band allocations. This is an indicative highlight, and the relevant domestic/international laws and official documentation should still be referred to for accurate and up-to-date information

Microwave heating has gained interest in various biomass processing applications including in the food industry, where the reported advantages incorporate higher product quality and reduced heating times (Salazar-González et al., 2012). These advantages can be attributed to the unique heating characteristics of microwave radiation, which include volumetric and selective heating. Volumetric heating refers to the ability of microwaves to heat materials in bulk, bypassing the need for gradual heat transfer from the surface inwards, which is a rate-limiting step in conventional heating techniques (Kappe, 2004; Oliveira and Franca, 2002). Moreover, selective heating denotes the tendency of microwaves to heat certain materials or portions thereof based on the specific dielectric properties (Clark, Folz and West, 2000), thus allowing preferential heating of "targeted" components. These unique microwave characteristics can be useful in various contexts, as they enable both rapid and targeted

heating which can overcome many of the existing process challenges. This is evident given the numerous reported case-specific process improvements, which include, e.g.: preserving some thermally fragile products of biomass pyrolysis, thus improving the quality of the overall process (Robinson et al., 2015); enhancing polymer and ceramic joining processes through selectively heating the joining interfaces (Thostenson and Chou, 1999); and, potentially offering a low-energy alternative for extracting oil from Oil Sands (Robinson et al., 2014). These examples clearly demonstrate a promising prospect for large-scale industrial utilisation of the microwave technology. However, this has not yet been attained as there remain numerous areas demanding further research and improvement. For instance, understanding, attaining data from, and reproducing microwave heating profiles can be challenging, because microwaves do not heat materials uniformly, and the absorption dynamics often depend on temperature (Mishra and Sharma, 2016). Furthermore, for biomass materials (which are the subject of interest in this thesis) there is a general lack in the available dielectric properties, coupled with a shortage of technical expertise, poor design of fit-for-purpose microwave cavities, and limited understanding of the microwave-induced heating trends (Kostas, Beneroso and Robinson, 2017).

It is aimed in this section to review aspects of the microwave theory that are relevant to the work presented in this thesis. This shall set the context and formulate the basis upon which further analyses are to be conducted.

2.1.2 Microwave heating

In biomass processing and other industrial contexts, microwaves are normally described using classical electromagnetism which is sufficient to underpin the observable phenomena. Microwaves are, therefore, a transverse propagation of alternating electric and magnetic fields, where the direction of wave propagation is perpendicular to the peaks and troughs of the fields themselves, and additionally the electric and magnetic components are orthogonal to each other (Figure 2.1). Depending on the physical condition, such wave configuration may result in energy dissipation when propagating through materials. This shall be expanded upon in the following subsections.

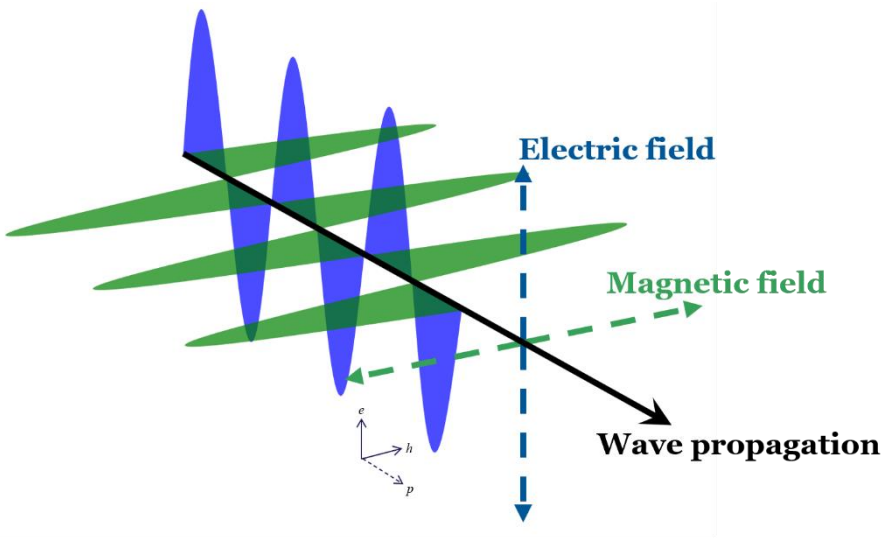


Figure 2.1 – Electromagnetic wave

2.1.2.1 Heating mechanisms

Materials can be classified into three categories based on their response to microwaves, namely conductors, which reflect any incident electromagnetic radiation; insulators through which the waves effectively propagate without being absorbed; and absorbers in which molecules interact with the propagating waves so as to absorb the electromagnetic energy (Jones et al., 2002). Materials are susceptible to interaction with both the electric and magnetic field components of a propagating wave (Figure 2.1). However, given that typical biomass materials (like foods) exhibit negligible magnetic responses (Datta, Sumnu and Raghavan, 2005), this work is exclusively focussed on interactions with the electric component.

As electromagnetic waves propagate through a material, the alternating electric field component (Figure 2.1) triggers polarisation and ionic conduction effects, which are responsible for heat dissipation in the material (Metaxas and Meredith, 1983). This is expanded upon in the following subsections.

2.1.2.1.1 Polarisation

In response to the alternating electric field, bound charges (e.g., atomic nuclei/electrons and molecular dipoles) get polarised, in that they abandon their equilibrium configurations and rotate/readjust continuously. However, the mechanisms by which polarisation effects induce energy dissipation (termed loss mechanisms) depend primarily on the frequency of the electromagnetic wave, and on the size/characteristics of the charged particles (Metaxas and Meredith, 1983). For instance, under microwave frequency only two polarisation effects are relevant in

inducing loss mechanisms, namely dipolar (reorientation) polarisation and interfacial (Maxwell-Wagner) polarisation (Peng and Hwang, 2015). In contrast, loss mechanisms due to atomic and electronic polarisations require higher frequency bands such as the infrared and visible spectra (Metaxas and Meredith, 1983), which is probably due to the smaller sizes of the particles involved.

Dipolar polarisation refers to a continuous readjustment of dipoles due to the alternating electric field, and the rate of such realignment can be as high as $10^{12}\ s^{-1}$ (Peng and Hwang, 2015). However, as the microwave frequency is raised, the rotating dipoles gradually fail to follow the rapidly alternating field, and this lag causes heat dissipation as a substitute to the reduced effective polarisation (Metaxas, 1991). This loss mechanism, amongst all others, is the most important for microwave heating, which is because dipolar polarisation dominates beyond 1 GHz. Nevertheless, the occurrence of such mechanism still depends on the existence of dipolar molecules and their characteristics in a material. Hence, the resulting heat-dissipating phase lag between polarisation and electric field, is usually characterised with a material-specific "relaxation time," a parameter also related to the microwave frequency at which heat dissipation is at its peak (termed relaxation frequency). Beyond this peak frequency, the dipoles lose their ability altogether to respond to the extremely rapid field alterations, let alone lagging behind such changes; therefore, as frequency is increased further, the dipoles gradually lose their ability to dissipate heat (Metaxas and Meredith, 1983).

Loss mechanisms due to interfacial polarisation are less common than those induced with dipolar polarisation. Nevertheless, interfacial polarisation occurs at the interfaces of heterogeneous media, where charged particles could accumulate and subsequently contribute towards heat dissipation due to field deformations (Peng and Hwang, 2015). Interfacial polarisation usually takes place in heterogeneous dielectric materials incorporating a conducting phase within (Metaxas and Meredith, 1983). This may be relevant in some biomass materials especially given the existence of cell/cell wall interfaces (section 2.2). However, dipolar polarisation and ionic conduction (section 2.1.2.1.2) are generally regarded as the dominant loss mechanisms in biomass materials like foods (Datta, Sumnu and Raghavan, 2005).

2.1.2.1.2 Ionic conduction

Free ions present in a material are subject to movement under the alternating electric field, and this results in heat dissipation due to ohmic effects (i.e., electrical resistance comprising molecular collisions) (Remya and Lin, 2011). Even small amounts of embedded free charges can be sufficient to enable the ionic conduction loss mechanism (Meredith, 1998), which is logical because ohmic resistance demands small electric conduction in an otherwise non-conducting medium.

Ionic conduction fades away with increasing microwave frequency, because given the sizes of free ions, these tend to lose their mobility in response to the increasingly rapid field alterations (Clark and Sutton, 1996). Ionic conduction typically dominates at frequencies below 0.1 GHz (Meredith, 1998); therefore, this mechanism is vital to consider in low-frequency microwave heating of biomass materials (e.g., agricultural products) (Jiang, Liu and Wang, 2018). On the other hand, the effectiveness of microwave heating of water typically increases with salinity, as ionic conduction further contributes towards heat dissipation (Datta, Sumnu and Raghavan, 2005).

2.1.2.2 Dielectric properties

Dielectric materials subjected to an electric field ($\vec{\boldsymbol{E}}$) experience charge repositioning (i.e., polarisation), and such repositioning is often characterised with an electric displacement vector ($\vec{\boldsymbol{D}}$). This displacement of charges depends upon the intensity of the applied electric field ($\vec{\boldsymbol{E}}$), but also on the ability of the material itself to respond to the field. The latter is characterised with a material property known as the dielectric permittivity (ε), where ε, $\vec{\boldsymbol{E}}$, and $\vec{\boldsymbol{D}}$ are collectively expressed thus (Huray, 2010; Sadeghi, Hassanzadeh and Harding, 2017):

$$\vec{\boldsymbol{D}} = \varepsilon\vec{\boldsymbol{E}} = \varepsilon'\varepsilon_0\vec{\boldsymbol{E}} \qquad \textbf{(2.1)}$$

ε_0 is the permittivity of free space (a universal constant), and ε' is a relative permittivity defining ε in terms of ε_0. Following common terminology, ε' shall be termed “dielectric constant” from this point forward.

Therefore, it can be deduced that the dielectric permittivity (ε) is a measure of the extent to which a material polarises in response to an applied electric field. Further characterisation of ε is required to quantify interactions between microwaves and

materials, leading to heat dissipation in the latter. Relevant aspects of this characterisation will be discussed in the following subsections.

2.1.2.2.1 Relevant Maxwell's equations

Of the four Maxwell's equations of electromagnetism, two are relevant in the intended discussions on dielectric permittivity (ε) and microwave power density (section 2.1.2.3). These equations are as follows (Huray, 2010):

$$\nabla \times \vec{\boldsymbol{E}} = -b\frac{\partial \vec{\boldsymbol{H}}}{\partial t} \tag{2.2}$$

$$\nabla \times \vec{\boldsymbol{H}} = \vec{\boldsymbol{I}} + \varepsilon\frac{\partial \vec{\boldsymbol{E}}}{\partial t} \tag{2.3}$$

$\vec{\boldsymbol{H}}$ is the magnetic field and b is the magnetic permeability (analogous to ε). Moreover, $\vec{\boldsymbol{I}}$ is the electric current vector.

Equations (2.2) and (2.3) highlight the fact that magnetic and electric fields coexist naturally, in that any change in the magnetic field induces a corresponding variation in the electric field, and vice versa. Put simply, the rate of change of a magnetic field passing through a plane is proportional (at constant b) to the induced electric field rotating around the plane (Equation (2.2)). Similarly, an electric current and the rate of change of an electric field passing through a plane, are collectively proportional (at constant ε) to the induced magnetic field rotating around the plane (Equation (2.3)).

The alternating electric and magnetic fields of a microwave (Figure 2.1) can be described mathematically as sinusoidal functions (Metaxas and Meredith, 1983). Hence, the following can be written (Huray, 2010):

$$\vec{\boldsymbol{E}} = \tilde{E}\,cos(\omega t - \beta p)\ \vec{\boldsymbol{e}} \tag{2.4}$$

$$\vec{\boldsymbol{H}} = \tilde{H}\,cos(\omega t - \beta p)\ \vec{\boldsymbol{h}} \tag{2.5}$$

$\tilde{E}\,cos(\omega t - \beta p)$ and $\tilde{H}\,cos(\omega t - \beta p)$ are the magnitudes of the electric and magnetic fields, respectively, as functions of time (t) and location along the wave

propagation axis (p). ω is the wave angular velocity and β is a displacement factor. $\tilde{E}$ and $\tilde{H}$ are the peak intensities of the electric and magnetic fields, respectively. $\vec{\boldsymbol{e}}$ and $\vec{\boldsymbol{h}}$ are unit vectors pointing in the directions of the electric and magnetic fields, respectively.

However, Equations (2.4) and (2.5) can be written as complex quantities incorporating real and imaginary parts (Ayappa et al., 1991; Huray, 2010; Metaxas and Meredith, 1983). As will be shown, this treatment simplifies further mathematical operations. Equations (2.4) and (2.5) can be expressed as follows:

$$\vec{\boldsymbol{E}} = Re\{\tilde{E}[cos(\omega t - \beta p) + jsin(\omega t - \beta p)]\,\vec{\boldsymbol{e}}\} = Re\{\tilde{E}e^{j(\omega t - \beta p)}\,\vec{\boldsymbol{e}}\} \quad \textbf{(2.6)}$$

$$\vec{\boldsymbol{H}} = Re\{\tilde{H}[cos(\omega t - \beta p) + jsin(\omega t - \beta p)]\,\vec{\boldsymbol{h}}\} = Re\{\tilde{H}e^{j(\omega t - \beta p)}\,\vec{\boldsymbol{h}}\} \quad \textbf{(2.7)}$$

$Re\{\ \}$ refers to the real part of the complex number enclosed within the brackets. Also, $j = \sqrt{-1}$.

Differentiating $\vec{\boldsymbol{E}}$ and $\vec{\boldsymbol{H}}$ with respect to time yields the following:

$$\frac{\partial \vec{\boldsymbol{E}}}{\partial t} = Re\{j\omega\tilde{E}e^{j(\omega t - \beta p)}\,\vec{\boldsymbol{e}}\} = Re\{j\omega\vec{\boldsymbol{E}}\} \quad \textbf{(2.8)}$$

$$\frac{\partial \vec{\boldsymbol{H}}}{\partial t} = Re\{j\omega\tilde{H}e^{j(\omega t - \beta p)}\,\vec{\boldsymbol{h}}\} = Re\{j\omega\vec{\boldsymbol{H}}\} \quad \textbf{(2.9)}$$

Dropping the $Re\{\ \}$ notation (since both $\vec{\boldsymbol{E}}$ and $\vec{\boldsymbol{H}}$ are now complex vectors), and substituting Equations (2.8) and (2.9) into the original Maxwell's expressions (Equations (2.2) and (2.3)), yields the following:

$$\nabla \times \vec{\boldsymbol{E}} = -j\omega b\vec{\boldsymbol{H}} \quad \textbf{(2.10)}$$

$$\nabla \times \vec{\boldsymbol{H}} = \vec{\boldsymbol{I}} + j\omega\varepsilon\vec{\boldsymbol{E}} \quad \textbf{(2.11)}$$

Equations (2.10) and (2.11) are known as the time-harmonic forms of the relevant Maxwell's equations (Datta, Sumnu and Raghavan, 2005; Huray, 2010). The complex form is a mathematical treatment that simplifies further operations, and this is evident given that Equations (2.10) and (2.11) do not incorporate time derivatives any longer.

2.1.2.2.2 Complex dielectric permittivity

Equation (2.11) can be rewritten as shown in Equation (2.12), where the electric current ($\vec{\boldsymbol{I}}$) is expressed in terms of $\vec{\boldsymbol{E}}$ (Metaxas and Meredith, 1983), which is analogous to Ohm's law.

$$\nabla \times \vec{\boldsymbol{H}} = (k_\alpha + j\omega\varepsilon'\varepsilon_0)\vec{\boldsymbol{E}} \tag{2.12}$$

k_α represents ohmic losses, and similarly, a term k_β can be introduced to represent polarisation losses like those caused by dipolar polarisation. Introducing this term and rearranging Equation (2.12) yields the following (Metaxas and Meredith, 1983):

$$\nabla \times \vec{\boldsymbol{H}} = j\omega\varepsilon_0\left(\varepsilon' - j\frac{k_\alpha + k_\beta}{\omega\varepsilon_0}\right)\vec{\boldsymbol{E}} = j\omega\varepsilon_0(\varepsilon' - j\varepsilon'')\vec{\boldsymbol{E}} = j\omega\varepsilon_0\hat{\varepsilon}\vec{\boldsymbol{E}} \tag{2.13}$$

Equation (2.13) defines the complex dielectric permittivity $\hat{\varepsilon} = \varepsilon' - j\varepsilon''$, whose real part quantifies the polarisability of a material in response to an electric field, and whose imaginary part describes the material's ability to dissipate electromagnetic energy as heat. The dielectric constant (ε') and dielectric loss factor (ε'') are together known as "dielectric properties" (Chandrasekaran, Ramanathan and Basak, 2012). Clearly, defining $\vec{\boldsymbol{E}}$ as a complex vector demands the dielectric permittivity also be defined as a complex number, where heat dissipation characteristics get isolated in the imaginary part.

2.1.2.2.3 Parameters influencing dielectric properties

Microwave frequency is perhaps the most relevant factor influencing dielectric properties, as it dictates the dominant loss mechanisms in a dielectric material. Section 2.1.2.1 briefly discussed the effect of frequency, stating that dipolar heating is introduced as polar molecules fail to follow the applied high-frequency waves, and that this heating peaks at a frequency corresponding to the material's relaxation time.

Additionally, ionic conduction was stated to dominate at lower microwave frequencies, dissipating heat in dielectric materials incorporating free ions.

Nevertheless, these concepts can be further illustrated quantitatively, thus highlighting the effects of various parameters on dielectric properties. The Debye equation, for instance, relates the dielectric properties to frequency and relaxation time (Metaxas and Meredith, 1983):

$$\hat{\varepsilon} = \varepsilon_\infty + \frac{\varepsilon_{dc} - \varepsilon_\infty}{1 + j\omega\ddot{t}} = \varepsilon_\infty + \frac{\varepsilon_{dc} - \varepsilon_\infty}{1 + \omega^2\ddot{t}^2} - j\frac{(\varepsilon_{dc} - \varepsilon_\infty)\omega\ddot{t}}{1 + \omega^2\ddot{t}^2} \quad \textbf{(2.14)}$$

ε_∞ and ε_{dc} are permittivity values at very high and static frequencies, respectively, and $\ddot{t}$ is the relaxation time. ε_{dc} occurs at frequencies lower than those needed to induce dipolar losses, whereas ε_∞ occurs at very high frequencies also incapable of inducing any further dipolar losses. Therefore, it is logical to have $\varepsilon_\infty < \varepsilon_{dc}$ for materials exhibiting dipolar loss mechanisms.

Differentiating the imaginary part of Equation (2.14) (i.e., loss factor) yields the following:

$$\frac{\partial\varepsilon''}{\partial\omega} = \frac{(\varepsilon_{dc} - \varepsilon_\infty)\ddot{t}}{1 + \omega^2\ddot{t}^2} - \frac{2(\varepsilon_{dc} - \varepsilon_\infty)\omega^2\ddot{t}^3}{(1 + \omega^2\ddot{t}^2)^2} \quad \textbf{(2.15)}$$

Equating Equation (2.15) to zero reduces it to the form $\omega\ddot{t} = 1$, showing that ε'' and, thereby, heat dissipation peak at a wave angular velocity equivalent to the reciprocal of the material's relaxation time. As stated earlier, the frequency corresponding to this ω value is termed "relaxation frequency." Equation (2.14) can be expressed graphically as shown in Figure 2.2.

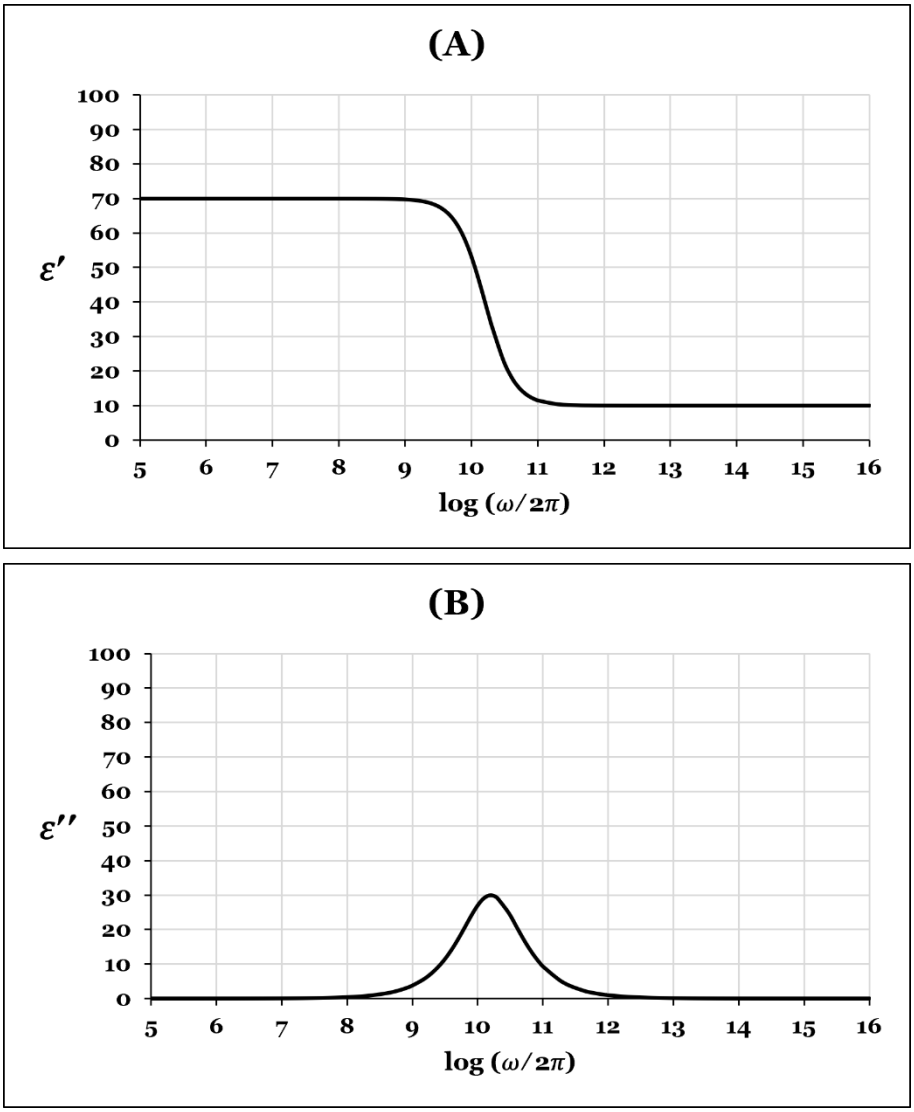


Figure 2.2 – Debye representation of (A) dielectric constant and (B) dielectric loss factor as functions of frequency (Equation (2.14)). Concept inspired by Metaxas et al. (Metaxas and Meredith, 1983)**. $\boldsymbol{\varepsilon_{dc} = 70}$, $\boldsymbol{\varepsilon_{\infty} = 10}$, and $\boldsymbol{\ddot{t} = 10^{-11}\ s}$. These properties may describe pure water as this has a relaxation frequency of the order of 10 GHz at room temperature** (Kaatze, 1989)**, and a dielectric constant close to 70** (Datta, Sumnu and Raghavan, 2005)

As seen in Figure 2.2, ε' drops from its low-frequency value $\varepsilon_{dc} = 70$ to its high-frequency value $\varepsilon_{\infty} = 10$, starting at some threshold frequency amounting to 1 GHz in this case, which matches the frequency at which dipolar polarisation starts to dominate (Metaxas and Meredith, 1983). The drop in ε' represents dipoles gradually lagging behind the alternating electric field, as they lose their ability to follow the ever-increasing wave frequency. The lag, indicating a reduction in the overall polarisation, enables energy to be dissipated as heat, which is why ε'' increases simultaneously with decreasing ε'. Eventually, ε'' peaks at the relaxation frequency of the material and

drops thereafter, as the dipoles lose their ability altogether to follow the extremely high frequency electric field (Metaxas and Meredith, 1983). The data used in Figure 2.2 may resemble pure water, as this possesses a relaxation frequency of the order of 10 GHz at room temperature (Kaatze, 1989), and a static ε' value close to 70 (Datta, Sumnu and Raghavan, 2005).

The events of Figure 2.2 demonstrate a significant dependence of dielectric properties on frequency. This is evident given that, dipolar heating is generally possible within a narrow frequency band, where molecules start to lose their polarisability in response to the applied electric field. This loss in polarisability (i.e., reduction in ε') causes heat dissipation in the material (i.e., increase in ε''), where the extent of such dissipation (i.e., peak value of ε'') depends on the overall reduction experienced in ε'. The decrease in polarisability is mathematically represented by the difference between ε_{dc} and ε_{∞} (Equation (2.14)), which simply communicates the change in the material's ε' from its low-frequency value to its high-frequency value. Figure 2.3 shows that, a wider gap between ε_{dc} and ε_{∞} results in a larger peak value for ε'' and, therefore, more heat dissipation in the material.

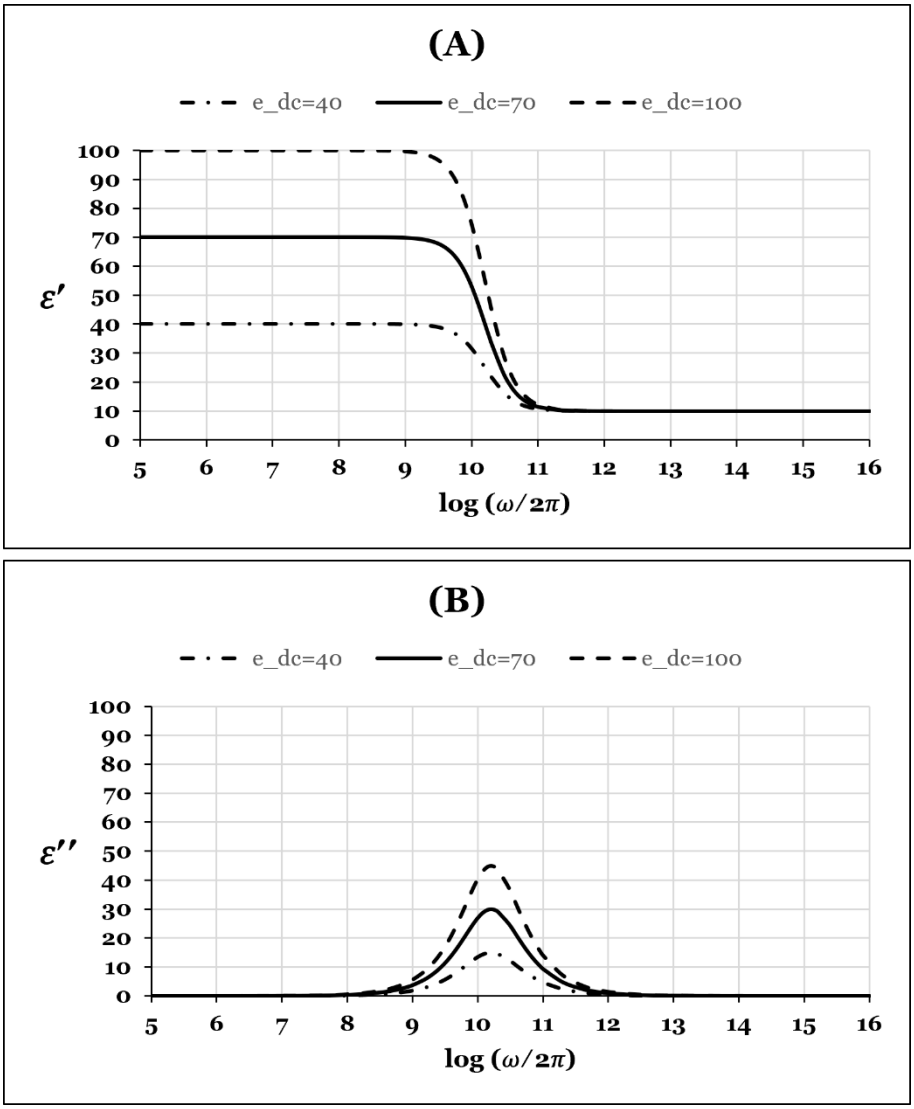


Figure 2.3 – Debye representation of (A) dielectric constant and (B) dielectric loss factor as functions of frequency (Equation (2.14)). ε_{dc} is variable while $\varepsilon_{\infty} = 10$ and $\ddot{t} = 10^{-11}\ s$

On the other hand, as expected from Equation (2.14), dielectric properties also depend on the material's relaxation time ($\ddot{t}$). Decreasing $\ddot{t}$ shifts the overall dielectric response towards higher frequencies (Figure 2.4). This is because, in such a case the dipolar molecules realign more efficiently (i.e., faster) with the alternating electric field, thereby requiring higher wave frequencies before they show any lag in their response.

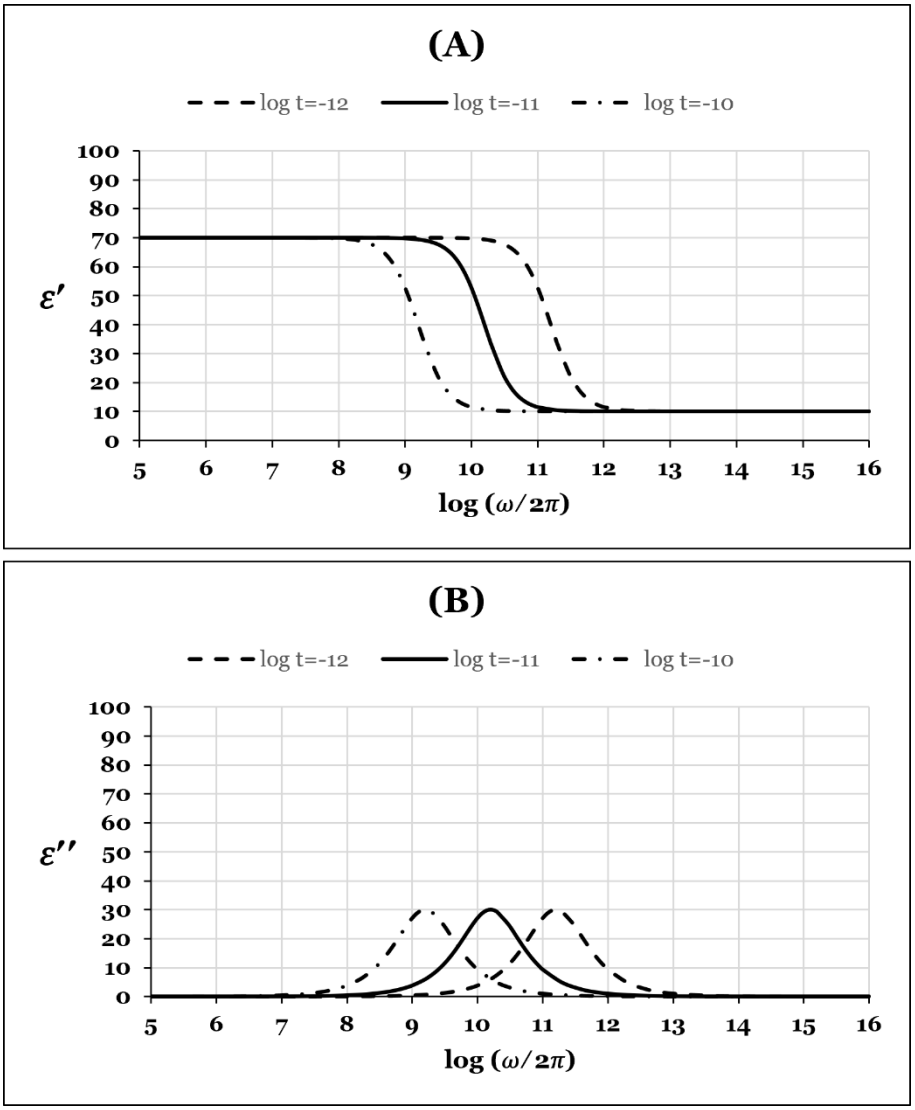


Figure 2.4 – Debye representation of dielectric constant (A) and dielectric loss factor (B) as functions of frequency (Equation (2.14)). $\ddot{t}$ is variable while $\varepsilon_{dc} = 70$ and $\varepsilon_{\infty} = 10$

A material's relaxation time ($\ddot{t}$) depends on the intermolecular forces within, which, in turn, are strongly related to temperature. As temperature increases, dipoles overcome the intermolecular forces holding them together, which enables them to respond faster and more efficiently to the alternating electric field. As a result, $\ddot{t}$ decreases with increasing temperature, and the overall dielectric response shifts to higher wave frequencies (Figure 2.4) (Gabriel et al., 1998). However, an increase in temperature also indicates higher kinetic energy acquired by the molecules, which can suppress their polarisability in return for more pronounced kinetic vibrations (Dinulovic´ and Rašuo, 2011). Therefore, the influence of temperature rise on

dielectric properties could comprise a combination of Figure 2.3 and Figure 2.4, entailing a shift to higher frequencies but also a reduction in the peak value of ε''.

Considering Figure 2.4, it can be seen that ε'' varies differently with temperature (through $\ddot{t}$) depending on the applied wave frequency. If the latter is lower than the relaxation frequency at the initial temperature, then ε'' decreases with increasing temperature. However, if the opposite is true then ε'' could increase with temperature up to a given temperature threshold, before pursuing a declining path as the temperature increases further. Such varying behavioural trends are important to understand in the case of biomass materials, which potentially incorporate different moisture contents exercising variable influences on the dielectric properties. At room temperature, the relaxation frequency of pure water is of the order of 10 GHz (Kaatze, 1989); therefore, ε'' is expected to decrease when heating pure water at 2.45 GHz, for instance. Thus, many biomass materials with significant moisture contents (such as foods) show a reduction in ε'' with increasing temperature (Datta, Sumnu and Raghavan, 2005). However, this is not always true, as in some cases the mobility of water molecules is suppressed due to binding, dissolution, adsorption, etc within the biomass matrix; hence, water's relaxation frequency is lowered and ε'' could increase with temperature (Venkatesh and Raghavan, 2004). In fact, the forms of water binding, dissolution, adsorption, etc differ from one material to another; therefore, it is inherently challenging to describe dielectric properties collectively for all materials from a single theoretical ground (Trabelsi and Nelson, 2006). Nevertheless, it is still accepted that the presence of bound water (as opposed to free water) in biomass materials like foods, generally contributes towards increasing ε'' with temperature (Datta, Sumnu and Raghavan, 2005).

The Debye model (Equation (2.14)) is quite useful in characterising dielectric properties generally; however, it still lacks the ability to fully depict dielectric responses. For instance, low-frequency losses due to ionic conduction (section 2.1.2.1.2) are not incorporated, yet they can be significant in some cases. As discussed previously, ionic conduction dominates at low microwave frequencies, meaning that ε'' would decrease with increasing frequency, before increasing once again as dipolar polarisation becomes effective (Metaxas and Meredith, 1983). On the other hand, increasing temperature generally improves the mobility of free ions, thus increasing heat dissipation due to ionic conduction. This is evident given that, ε'' increases with

temperature in salt solutions even though it decreases in pure water, and that ε'' also increases with temperature in foods containing high salt contents (Datta, Sumnu and Raghavan, 2005).

Further to frequency, temperature, and moisture content, dielectric properties are also influenced by other material properties. For example, higher bulk density can result in larger permittivity, since a smaller volume within the material will be occupied by microwave-transparent voids (Nelson, 1994). Dielectric properties of food materials are also influenced by the chemical makeup and physical attributes (Ryynänen, 1995).

2.1.2.3 Microwave power dissipation

Understanding dielectric properties is a significant step towards quantifying microwave power dissipation; nonetheless, the relationship between power and field magnitude should also be established.

The Poynting theorem describes electromagnetic power flux through a closed surface in terms of the propagating electric and magnetic fields (Metaxas and Meredith, 1983):

$$\vec{\boldsymbol{Q}}_{\boldsymbol{At}} = \vec{\boldsymbol{E}} \times \vec{\boldsymbol{H}} \qquad \textbf{(2.16)}$$

$\vec{\boldsymbol{Q}}_{\boldsymbol{At}}$ (Wm^{-2}) is the Poynting vector describing power dissipated per unit area of closed surface. As can be seen, $\vec{\boldsymbol{Q}}_{\boldsymbol{At}}$ is orthogonal to both $\vec{\boldsymbol{E}}$ and $\vec{\boldsymbol{H}}$; hence, it is parallel to the direction of wave propagation.

$\vec{\boldsymbol{Q}}_{\boldsymbol{At}}$ is variable with time since $\vec{\boldsymbol{E}}$ and $\vec{\boldsymbol{H}}$ are alternating fields; therefore, a time-averaged power dissipation ($\vec{\boldsymbol{Q}}_{\boldsymbol{A}}$) can be defined as follows (Sadeghi, Hassanzadeh and Harding, 2017):

$$\vec{\boldsymbol{Q}}_{\boldsymbol{A}} = \frac{1}{\bar{\bar{t}}} \int_0^{\bar{\bar{t}}} \vec{\boldsymbol{Q}}_{\boldsymbol{At}}\, dt \qquad \textbf{(2.17)}$$

$\bar{\bar{t}} = 2\pi/\omega$ is the wave periodic time.

However, since $\vec{\boldsymbol{E}}$ and $\vec{\boldsymbol{H}}$ have been defined here as complex vectors (Equations (2.6) and (2.7)), $\vec{\boldsymbol{Q}}_{\boldsymbol{A}}$ can be expressed thus (Ayappa et al., 1991; Metaxas and Meredith, 1983; Sadeghi, Hassanzadeh and Harding, 2017):

$$\vec{\boldsymbol{Q}}_{\boldsymbol{A}} = -\frac{1}{2} Re\{\vec{\boldsymbol{E}} \times \vec{\boldsymbol{H}}^*\} \tag{2.18}$$

Equation (2.18) is yet another demonstration of the simplification offered upon utilising complex notation. $\vec{\boldsymbol{E}}^*$ and $\vec{\boldsymbol{H}}^*$ are the complex conjugates of $\vec{\boldsymbol{E}}$ and $\vec{\boldsymbol{H}}$, respectively, and they can be defined as follows:

$$\vec{\boldsymbol{E}}^* = Re\{\tilde{E} e^{j(\beta p - \omega t)}\, \vec{\boldsymbol{e}}\} \tag{2.19}$$

$$\vec{\boldsymbol{H}}^* = Re\{\tilde{H} e^{j(\beta p - \omega t)}\, \vec{\boldsymbol{h}}\} \tag{2.20}$$

Hence, it can be shown that the vectors $\nabla \times \vec{\boldsymbol{E}}^*$ and $\nabla \times \vec{\boldsymbol{H}}^*$ equate to the following:

$$\nabla \times \vec{\boldsymbol{E}}^* = j\omega b \vec{\boldsymbol{H}}^* \tag{2.21}$$

$$\nabla \times \vec{\boldsymbol{H}}^* = -j\omega \varepsilon_0 \hat{\varepsilon}^* \vec{\boldsymbol{E}}^* \tag{2.22}$$

$\hat{\varepsilon}^* = \varepsilon' + j\varepsilon''$ is the complex conjugate of the complex permittivity $\hat{\varepsilon}$ defined in Equation (2.13).

To quantify the total absorbed power, $\vec{\boldsymbol{Q}}_{\boldsymbol{A}}$ should be integrated with respect to area; therefore, the final integral power expression can be written as follows (Metaxas and Meredith, 1983):

$$Q_M = \oint_0^A \vec{\boldsymbol{Q}}_{\boldsymbol{A}} \,.\, d\vec{\boldsymbol{a}} = -\frac{1}{2} \oint_0^A Re\{\vec{\boldsymbol{E}} \times \vec{\boldsymbol{H}}^*\} \,.\, d\vec{\boldsymbol{a}} \tag{2.23}$$

Q_M is the dissipated microwave power; A is the total area of the closed surface; and $\vec{\boldsymbol{a}}$ describes an infinitesimal surface area. $\vec{\boldsymbol{a}}$ is defined as a vector here to exclusively capture the $\vec{\boldsymbol{Q}}_{\boldsymbol{A}}$ component normal to the surface.

Equation (2.23) describes the power dissipated as microwaves propagate through a closed surface. The divergence theorem can be used to equate this to the power dissipated within the volume enclosed by the surface (Huray, 2010; Metaxas and Meredith, 1983):

$$Q_M = \oint_0^A \vec{\boldsymbol{Q}}_{\boldsymbol{A}} \,.\, d\vec{\boldsymbol{a}} = \int_0^V \left(\nabla \,.\, \vec{\boldsymbol{Q}}_{\boldsymbol{A}}\right) dv = -\frac{1}{2}\int_0^V Re\left\{\nabla \,.\, \left(\vec{\boldsymbol{E}} \times \vec{\boldsymbol{H}}^*\right)\right\} dv \qquad \textbf{(2.24)}$$

V is the volume enclosed by surface A, and v is describes an infinitesimal volume.

Further to Equation (2.24), the term $\nabla \,.\, \left(\vec{\boldsymbol{E}} \times \vec{\boldsymbol{H}}^*\right)$ can be re-expressed using basic vector identity, as follows:

$$\nabla \,.\, \left(\vec{\boldsymbol{E}} \times \vec{\boldsymbol{H}}^*\right) = \vec{\boldsymbol{H}}^* \,.\, \left(\nabla \times \vec{\boldsymbol{E}}\right) - \vec{\boldsymbol{E}} \,.\, \left(\nabla \times \vec{\boldsymbol{H}}^*\right) \qquad \textbf{(2.25)}$$

Based on the previous definitions of $\vec{\boldsymbol{E}}$ and $\vec{\boldsymbol{H}}$ and their respective complex conjugates, the terms in Equation (2.25) can be expressed thus (Metaxas and Meredith, 1983):

$$\vec{\boldsymbol{H}}^* \,.\, \left(\nabla \times \vec{\boldsymbol{E}}\right) = -j\omega b\left(\vec{\boldsymbol{H}}^* \,.\, \vec{\boldsymbol{H}}\right) = -j\omega b\tilde{H}^2 \qquad \textbf{(2.26)}$$

$$\vec{\boldsymbol{E}} \,.\, \left(\nabla \times \vec{\boldsymbol{H}}^*\right) = -j\omega\varepsilon_0\hat{\varepsilon}^*\left(\vec{\boldsymbol{E}} \,.\, \vec{\boldsymbol{E}}^*\right) = \omega\varepsilon_0\varepsilon''\tilde{E}^2 - j\omega\varepsilon_0\varepsilon'\tilde{E}^2 \qquad \textbf{(2.27)}$$

Substituting Equations (2.26) and (2.27) into Equation (2.25) yields the following (Ayappa et al., 1991; Metaxas and Meredith, 1983):

$$\nabla \,.\, \left(\vec{\boldsymbol{E}} \times \vec{\boldsymbol{H}}^*\right) = -\omega\varepsilon_0\varepsilon''\tilde{E}^2 + j\omega\left(\varepsilon_0\varepsilon'\tilde{E}^2 - b\tilde{H}^2\right) \qquad \textbf{(2.28)}$$

In turn, substituting Equation (2.28) into Equation (2.24) yields the following, assuming that $\vec{\boldsymbol{E}}$ does not change much within small volumes amounting to the plant-cell scales intended in this thesis (section 2.2) (Metaxas and Meredith, 1983):

$$Q_M = \frac{1}{2}\int_0^V \omega\varepsilon_0\varepsilon''\tilde{E}^2\, dv = \frac{1}{2}\omega\varepsilon_0\varepsilon''\tilde{E}^2 V \qquad \textbf{(2.29)}$$

The electric field intensity ($\tilde{E}$) can be expressed as a root-mean-squared value ($|E|$) where $\tilde{E}^2 = 2|E|^2$, and this yields the final expression for microwave power dissipation in a given volume (Metaxas and Meredith, 1983):

$$Q_M = \omega\varepsilon_0\varepsilon''|E|^2 V \qquad \textbf{(2.30)}$$

From this point forward, electric field intensity will be represented with the value $|E|$. The per-volume form of Equation (2.30) is as follows:

$$\dot{Q_M} = \omega\varepsilon_0\varepsilon''|E|^2 = 2\pi F\varepsilon_0\varepsilon''|E|^2 \qquad \textbf{(2.31)}$$

$\dot{Q_M}$ is the dissipated microwave power per unit volume.

Equation (2.31) is widely reported (Altarawneh et al., 2021; Robinson et al., 2009; Thomas-Hillman et al., 2018; Whittles, Kingman and Reddish, 2003), as it demonstrates the dependence of power dissipation on the loss factor, which matches the earlier definition of ε'' (section 2.1.2.2.2). Moreover, $\dot{Q_M}$ also depends on the characteristics of the imposed wave, including frequency and intensity of the electric field.

It is assumed in Equations (2.30) and (2.31) that ω, ε'', and $|E|$ are independent of the sample volume (i.e., as indicated in the integration step; Equation (2.29)). Effectively, therefore, ω and ε'' will be assumed homogeneous/constant throughout any given phase, as they will only vary from one phase to the other if controlled by an external parameter (e.g., phase type, water activity, temperature, etc). Given the small scale of the model intended in this thesis, this is seen as a valid and reasonable simplification. On the other hand, as will be discussed in section 2.1.2.4 $|E|$ will be

assumed to follow Lambert's law, thus waiving the need to consider the volume dependence of this parameter. Future developments of the intended model may require more detailed electromagnetic analysis depending on the desired scale, heating equipment/cavity considerations (section 2.1.3), and the required level of precision in the modelling of heat.

2.1.2.4 Microwave attenuation

Microwaves polarise materials and dissipate heat in them, and this energy transfer is coupled with an attenuation in the propagating waves, in adherence to the energy conservation principle.

Microwave attenuation is commonly described as an exponential decay in the amplitude of the propagating wave, which is expressed below and represented in Figure 2.5 (Metaxas and Meredith, 1983):

$$\vec{\boldsymbol{E}} = Re\left\{\tilde{E}e^{-\alpha p}e^{j(\omega t-\beta p)}\,\vec{\boldsymbol{e}}\right\} \quad \textbf{(2.32)}$$

$$\vec{\boldsymbol{H}} = Re\left\{\tilde{H}e^{-\alpha p}e^{j(\omega t-\beta p)}\,\vec{\boldsymbol{h}}\right\} \quad \textbf{(2.33)}$$

α is an attenuation factor for the electric and magnetic fields.

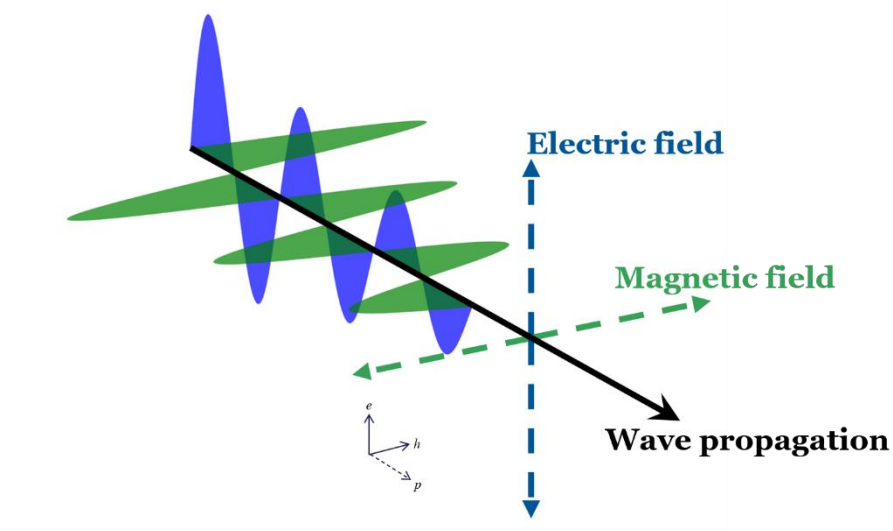


Figure 2.5 – Attenuating electromagnetic wave. Concept inspired by Metaxas et al. (Metaxas and Meredith, 1983)

Considering the electric field component exclusively, Equation (2.30) indicates a proportionality between microwave power dissipation (Q_M) and the squared electric

field intensity ($|E|^2$). Based on this, and given that $\vec{\boldsymbol{E}}$ decays exponentially (Equation (2.32)), Q_M is considered proportional to $e^{-2\alpha p}$ (Metaxas and Meredith, 1983). The latter enables Q_M to be estimated thus (Ayappa et al., 1991; Yang and Gunasekaran, 2004):

$$Q_M = Q_{M_0} e^{-2\alpha p} \tag{2.34}$$

Q_{M_0} is the power incident upon a material.

Equation (2.34) is otherwise known as Lambert's law, and it typically applies where the microwave wavelength is much smaller than the dimensions of the material (Ayappa et al., 1991; Oliveira and Franca, 2002).

Penetration depth (δ_p) is the distance within a medium that a wave should travel to reduce Q_M to e^{-1} (i.e., 36.8%) of its original value at the incidence point (Q_{M_0}). Hence, Equation (2.34) can be rewritten thus (Meredith, 1998):

$$Q_M = Q_{M_0} e^{-p/\delta_p} \tag{2.35}$$

Furthermore, δ_p can be expressed in terms of the dielectric properties, as follows (Meredith, 1998; Metaxas and Meredith, 1983):

$$\delta_p = \frac{c}{\omega\sqrt{2\varepsilon'}}\left[\sqrt{\left(1+\left(\frac{\varepsilon''}{\varepsilon'}\right)^2\right)}-1\right]^{-0.5} \tag{2.36}$$

c is the speed of light, and ω represents the wave angular velocity in free space.

δ_p is a material property as it depends on ε' and ε''. Therefore, the higher the dielectric properties the lower the value of δ_p, meaning that the wave attenuates more readily.

Attenuation is vital to consider in microwave systems comprising significant scales. High attenuation could result in non-uniform heating of the material, as microwaves get absorbed at quite shallow depths from the surface. Therefore, optimal microwave heating is governed by a trade-off between the desire for high dielectric properties,

and the need to ensure appropriate microwave penetration (Beneroso et al., 2016; Meredith, 1998).

Although microwave attenuation will be considered in this work, its effects should remain minor due to the plant-cell scales of the intended model (Chapter 3 onwards). For instance, the penetration depth of water, a strong microwave absorber (Meredith, 1998), is of the order of 1 cm (Pueschner, 2015) which is larger than the scales intended for most numerical investigations. Nevertheless, it is intended to incorporate microwave attenuation in this work through the use of Lambert's law, thereby offering a more comprehensive definition of microwave heating, but also enabling future uses of the model that demand access to larger scales.

2.1.3 Microwave heating instruments

This section offers a brief discussion of the main equipment required for microwave heating in typical settings.

2.1.3.1 Generators

Generators convert source energy into electromagnetic waves, and they can be classified either as power-tube devices (e.g., magnetrons and klystrons) or solid-state amplifiers. Magnetrons are perhaps the most common amongst generator types, with cost, efficiency, and high power-related advantages, and with numerous industrial applications (Brace, 2009; Meredith, 1998).

Magnetrons comprise a cylindrical cathode surrounded by a circular wheel entailing radial slots/openings which collectively act as the anode. The whole chamber is maintained at vacuum conditions and is subjected to a strong magnetic field orthogonal to the circular plane. The cathode heats up upon applying high-voltage power, releasing electrons which assume a spiral pathway as they approach the anode, due to the presence of the magnetic field. The radial slots/openings of the anode are designed to acquire natural frequencies matching the desired microwave frequency; therefore, as these structures resonate, microwaves are generated at the desired frequency and, subsequently, these waves get delivered to a waveguide through a transmission probe (Meredith, 1998; Thostenson and Chou, 1999).

2.1.3.2 Transmitters/waveguides

Transmission devices are required to transfer microwaves from the generator to the load, and waveguides are commonly used for this purpose. A waveguide is a hollow metallic tube commonly with a rectangular cross-section. It transmits high-frequency

waves (e.g., microwaves) while also minimising energy losses incurred from such transmission. Therefore, waveguides are a more suitable means of microwave transmission compared to coaxial probes/cables, which are used in transmitting lower-frequency waves (Metaxas and Meredith, 1983; Thostenson and Chou, 1999).

Unlike plane waves travelling freely, waves transmitted in waveguides are confined to small spaces. This induces numerous wavefront interferences and off-surface reflections which ultimately give rise to certain guided propagation "modes", hence the terminology "waveguide". These modes are controllable by the design of the waveguide, which dictates certain orientation and angle for wave propagation. This induces electric and magnetic field components in multiple dimensions within the waveguide, including in the direction of wave propagation itself. This aspect is different from plane waves travelling freely, where the electric and magnetic fields remain orthogonal to each other and to the direction of wave propagation (i.e., transverse electromagnetic or TEM waves; Figure 2.1). In contrast, due to reflection and interference patterns, the propagation modes assumed in waveguides can either be transverse-electric (TE) or transverse-magnetic (TM), as only one of the two fields remains fully orthogonal to wave propagation. In TE modes, all nonzero electric field components are transverse to the direction of wave propagation, whereas in TM modes, it is the magnetic field components that remain completely orthogonal. Further classification of TE and TM modes is conducted through defining the mode numbers "m" and "n" (i.e., TE_{mn} and TM_{mn}), which represent the number of sinusoidal half-cycles of the fields in directions normal to wave propagation. For example, the simplest and most common TE mode obtainable in a conventional rectangular waveguide is TE_{10}, where one electric field component and two magnetic field components are sustained. The wave patterns and field maxima, minima, and zero-points can be predicted based on knowledge of the wave properties and waveguide design, and such patterns are well-established for the TE_{10} mode for example (Meredith, 1998; Metaxas and Meredith, 1983; Thostenson and Chou, 1999).

2.1.3.3 Applicators

Applicators are metallic-walled closed chambers where microwave energy is received into the load (Bykov, Rybakov and Semenov, 2001). Although multimode cavities are the most common type of applicator, single-mode cavities and travelling wave applicators are also fairly common. Additionally, several other

types/hybrids/modifications with special designs exist to serve more specific purposes, and some of these include helix, radiator, rectangular TEM, ridged, and other applicators (Metaxas and Meredith, 1983).

Both single-mode and multimode cavities support resonant wave patterns, thereby sustaining high field intensities and enhancing heat dissipation into the load (Meredith, 1998). This is because, resonance entails a continuous passing of the waves within the cavity as they are reflected off the metallic boundaries, which leads to constructive wave interferences and ultimately higher field intensities. Yet, it should be noted that resonant patterns are only established upon applying waves with certain frequencies, which match the natural frequencies of the cavity resonator (Bykov, Rybakov and Semenov, 2001). The potential for high energy dissipation with single-mode and multimode cavities makes these popular for material processing (Thostenson and Chou, 1999); therefore, the following subsections further expand upon these two applicator types.

2.1.3.3.1 Single-mode cavities

As the name suggests, single-mode cavities are designed to accommodate a single resonant wave pattern. A given mode arises in the cavity when the applied wave frequency matches one of the natural frequencies of the resonator; hence, it is vital to design/select cavities based on the intended working frequency, and to maintain a narrow frequency band about this intended value during heating (Mehdizadeh, 2015; Thostenson and Chou, 1999).

For a given input microwave power, single-mode cavities generally sustain higher electric field intensities compared to other applicators, which is a key advantage when processing low-loss materials (Metaxas and Meredith, 1983). Such feature is available because, these cavities are purposely designed to concentrate the applied field into certain areas, which can then be occupied by the load thus optimising its power absorption, but also inducing a uniform electric field across the heated material (Chandrasekaran, Ramanathan and Basak, 2012; Mehdizadeh, 2015). However, acquiring an effective single-mode configuration demands small-scaled cavities, typically in the order of the intended microwave wavelength (Thostenson and Chou, 1999) (i.e., a size equivalent to half the wavelength). This is necessary to efficiently couple the field intensity maximum with the heated load, yet it poses a limitation as only small load volumes can be treated at any given time (Bykov, Rybakov and

Semenov, 2001). The size-related shortcomings of single-mode cavities have limited their industrial utilisation; however, where these cavities are feasible to use, they have proven effective (Clark and Sutton, 1996). Single-mode cavities are carefully designed to sustain quite specific wave patterns that are also uniform across a heated load, thereby allowing more efficient heat dissipation and enabling more predictable heating profiles (Mehdizadeh, 2015). Therefore, it is logically inferable that single-mode cavities are ideal to use in many experimental-scale processes. Nevertheless, every experiment will likely require case-specific coupling of the wave frequency with one of the natural frequencies of the cavity resonator, which is because the latter does not only vary with the cavity's design, but also with the dielectric properties of the load (Bykov, Rybakov and Semenov, 2001). The constraints suffered by single-mode cavities, including limited processing volumes and the need for detailed understanding/tuning, are largely overcome in multimode cavities.

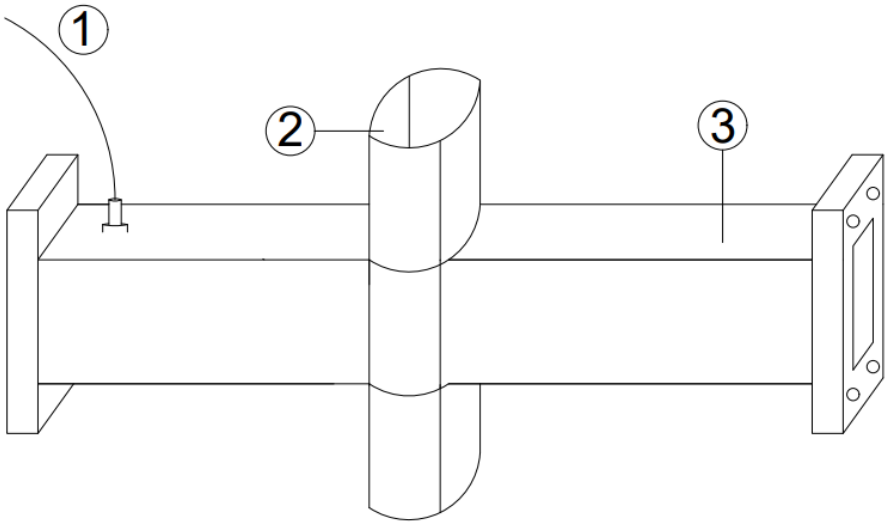


Figure 2.6 – Single-mode cavity setup

2.1.3.3.2 *Multimode cavities*

Increasing the size of a cavity enables it to accommodate multiple resonant wave patterns at the same time, yielding multimode cavities which are the most common type of applicator (Mehdizadeh, 2015; Meredith, 1998). Multimode cavities are used in domestic heating and in many continuous and batch processes (Chandrasekaran, Ramanathan and Basak, 2012). Unlike single-mode cavities where strict

understanding of wave patterns is required, designing multimode cavities tends to follow a more empirical approach, involving probing, experience, etc (Thostenson and Chou, 1999). Nevertheless, central to designing these cavities is the need to identify the natural frequencies of the cavity resonator corresponding to the intended modes, and then to pack as many of these modes as possible around the operating frequency (Metaxas and Meredith, 1983). This is key because, although an empty cavity constitutes very narrow natural frequency bands capable of exciting given modes, these bands tend to dilate upon introducing a load into the cavity. This means that, many of the modes initially packed around the operating frequency now get to overlap; hence, they can be excited and sustained in the cavity simultaneously under the same operating frequency, leading to improved heating conditions (Mehdizadeh, 2015; Metaxas and Meredith, 1983).

Multimode cavities are often regarded as simple and robust, with the ability to process a wide range of material types (Mehdizadeh, 2015; Meredith, 1998; Metaxas and Meredith, 1983). It is, therefore, unsurprising that these cavities lack the need for sophisticated tuning or specialised operating personnel (Mehdizadeh, 2015), and when this advantage is coupled with the larger cavity size, it becomes understandable why multimode cavities are in many cases preferable over their single-mode counterpart. However, this preference does not indicate superiority at every instance, for there remain some advantages in using single-mode cavities as described in section 2.1.3.3.1. For example, single-mode cavities sustain higher field intensities than other applicators for the same input power, allowing for more efficient heating (Metaxas and Meredith, 1983). In fact, multimode cavities are notorious for their non-uniform heating of the load, due to interfering wave patterns that induce local field maxima and minima across the cavity (Mehdizadeh, 2015). Such non-uniformity can be minimised either by enlarging the cavity hence increasing the number of overlapping modes, or by operating at higher wave frequencies thus narrowing the separation between field maxima and minima. However, the former option may contravene practical size limitations, and the latter can suppress volumetric heating due to increased microwave attenuation (Equation (2.36)) (Thostenson and Chou, 1999). Furthermore, as stated in section 2.1.1 there is a limitation in the frequencies available to utilise for industrial, scientific, and medical (ISM) applications of microwave heating. Instead, heating homogenisation is commonly attempted by introducing a set

of practical solutions into the cavity, such as turntables which mobilise the load across various field maxima and minima, and mode stirrers whose rotating blades agitate the standing modes by reflecting the input waves, thereby improving heating uniformity (Chandrasekaran, Ramanathan and Basak, 2012; Thostenson and Chou, 1999). These practical solutions emphasise the experiential aspect of multimode cavity design.

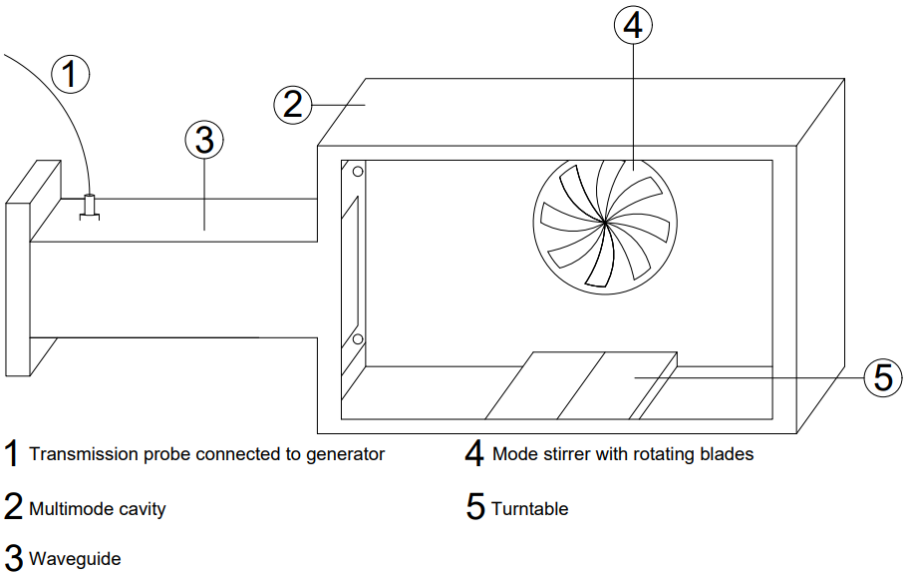


Figure 2.7 – Multimode cavity setup

2.1.3.4 Further instruments

2.1.3.4.1 Circulator: safeguarding the power source

The power generated within a microwave heating system is not always fully absorbed by the load, which gives rise to reflected power. Circulators direct the reflected power towards a dummy load (e.g., water), thereby safeguarding the generator against damage. Circulators typically consist of a three-port junction enforcing directional bias in the power flow. For example, the generated power flows from port A (generator side) to port B (applicator/load side); however, any reflected power is diverted towards port C (dummy load side) instead of port A, thereby protecting the power source (Meredith, 1998; Metaxas and Meredith, 1983).

Besides circulators, other devices can also be used to achieve the same goal of safeguarding the generator from reflected power. However, circulators are usually preferred due to their cost and practicality-related advantages (Metaxas and Meredith, 1983).

2.1.3.4.2 Stub & sliding short: tuning

In some applicators like single-mode cavities (section 2.1.3.3.1), achieving optimal heating requires coupling the generated waves with the intended load. This is because, changing the heated material may alter the natural frequencies of the cavity resonator (Bykov, Rybakov and Semenov, 2001), thereby altering the resonant wave patterns together with the locations of electric field maxima/minima/zero points within the cavity. As such, tuning is necessary to induce appropriate resonant wave patterns at the operating wave frequency, and to ensure the electric field maximum overlaps with the physical location of the load, thus optimising power absorption.

A sliding short is a piston installed at a termination point in the waveguide. It constitutes a short-circuit whose position can be altered to adjust the resonant frequencies of the loaded cavity, and match one of them with the desired operating frequency, thus optimising power absorption. Further matching can also be achieved with stub tuners, whose vertical lengths are adjustable so as to refine the wave patterns and optimise power absorption by the load. Some heating configurations comprise multiple stub tuners, while others feature automated tuners which readjust continuously based on the magnitude of the reflected power (Steer, 2008; Mehdizadeh, 2015; Meredith, 1998; Metaxas and Meredith, 1983).

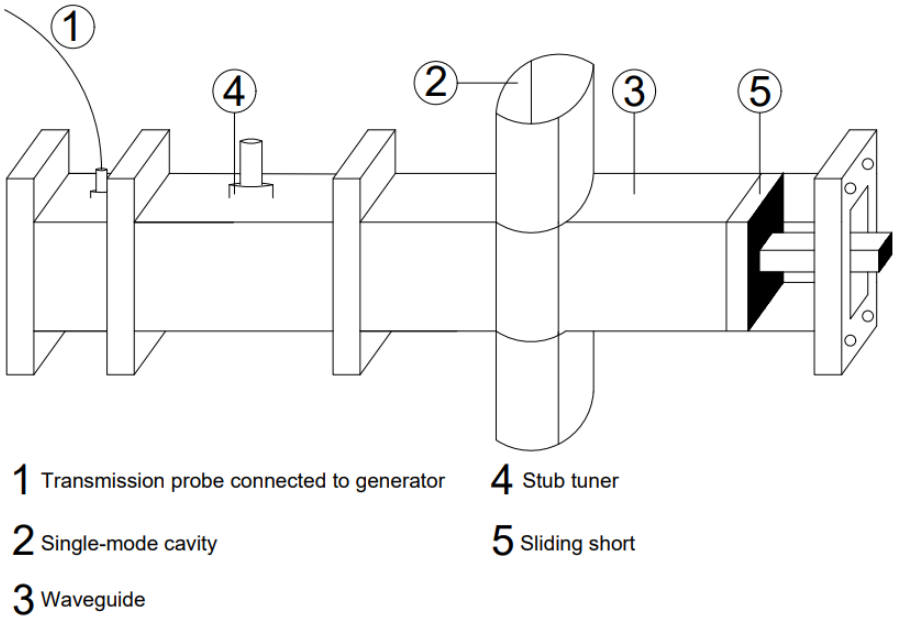


Figure 2.8 – Single-mode configuration with stub tuner and sliding short

2.1.3.4.3 Directional coupler: power detection

It is vital to measure the input and reflected powers in a microwave heating system, and this is achievable with directional couplers. These devices typically comprise a four-port junction enforcing directional bias in the power flow; hence, small quantities of the incident and reflected waves get isolated in independent ports. These waves are then used to measure the incident and reflected powers, through dedicated power meters (Meredith, 1998; Thostenson and Chou, 1999).

2.1.4 Section summary

This section discussed aspects of the microwave theory that are relevant to this thesis, including fundamental heating mechanisms, dielectric properties, heat dissipation, wave attenuation, and key components of a typical microwave heating apparatus.

Materials interact with microwaves based on their dielectric permittivity, a quantity measuring the extent to which a material polarises under the influence of electromagnetic radiation. Due to their frequency range, microwaves induce dipolar polarisation whereby dipoles exercise continuous reorientation to match the alternating electric field. However, raising the microwave frequency causes these dipoles to lag behind the increasingly fast field alterations, causing heat dissipation in the material as a substitute for the reduced effective polarisation. Another means of microwave heating is delivered through ionic conduction, where free ions embedded within a dielectric material flow under the influence of an applied electric field. This arises even with small concentrations of free ions, and occurs especially at low microwave frequencies, causing heat dissipation due to ohmic effects. Although other mechanisms like interfacial polarisation can also dissipate heat in some cases, dipolar polarisation and ionic conduction are typically regarded as the primary mechanisms for heating biomass materials like foods.

Dielectric permittivity can be defined as a complex number, whose imaginary part (dielectric loss factor; ε'') describes the ability of a material to dissipate microwave energy as heat. In fact, microwave power dissipation is proportional to the dielectric loss factor as seen in Equation (2.31), and it also depends on the properties of the wave including frequency and electric field intensity. However, heat dissipation causes the propagating microwaves to attenuate, posing a limitation to the homogeneity of heating. This is key to consider especially in large-scale processes, where a trade-off

exists between the desire for rapid heating through high dielectric properties, and the resulting amplification in microwave attenuation quantified as a reduction in the penetration depth of the material.

Microwave heating requires a generator, a waveguide to transfer the waves to the load, and an applicator where the load is subjected to radiation. Additional elements are also incorporated to support the heating setup, amongst which are circulators, stub/sliding short tuners, and directional couplers. Magnetrons are the most common type of generator, due to advantages related to cost and efficiency. Furthermore, waveguides sustain certain wave propagation modes based on their design, where these modes could either be transverse-electric (TE) or transverse-magnetic (TM). Concerning applicators, although multimode cavities are more widespread, single-mode cavities sustaining one mode of wave propagation are also fairly common. Although single-mode cavities demand detailed design/tuning and limit the allowable processing volume, they finely match the load to the field maximum, thereby maximising the imposed electric field intensity. This enhances heating compared to multimode cavities, in which the load can suffer from non-uniform heating, even though the disadvantages related to limited processing volume and detailed design/tuning are overcome.

Microwave heating is clearly a well-established field both theoretically and practically. However, as discussed earlier there remain some key challenges limiting the ability to employ microwave heating in large-scale biomass processing. Hence, this thesis attempts to utilise the available knowledge of the microwave theory to better understand microwave heating trends of biomass-solvent systems, and whether it can induce unique extraction phenomena.

2.2 Biomass-solvent extraction

2.2.1 Introduction

Biomass extraction is a physio-chemical process involving the recovery of certain components from biomass materials. Many of these components are of high added-value (Rodrigues et al., 2018), and they can serve as renewable chemical feedstocks substituting fossil-based compounds (Tsubaki, Sakamoto and Azuma, 2010), but also in the food, pharmaceutical, and cosmetic industries (Flórez, Conde and Domínguez, 2015), and in other applications. Therefore, biomass extraction is well suited to the bio-refinery concept, an idea concerned with developing processes enabling efficient

conversion of biomass feedstocks into numerous value-added products and biofuels (Herrero and Ibañez, 2018).

This thesis is concerned with extraction in biomass-solvent systems, which comprise plant-based biomass immersed in a body of solvent. Extraction entails the liberation of biomass components into the solvent phase, and such a process involves (i) penetration of the solvent into the biomass; (ii) solubilisation of the solute into the solvent; (iii) diffusion of the dissolved solute into the biomass-solvent boundary and then into the bulk solvent (Flórez, Conde and Domínguez, 2015; Mao, Robinson and Binner, 2021).

It is aimed in this section to review relevant background information on biomass-solvent systems, including structure, solvents, and mechanical expansion of cells. The general perception that microwaves enhance extraction compared with conventional heating will also be highlighted, with an emphasis on the general lack of mechanistic understanding as to why such enhancement is observed.

2.2.2 Biomass-solvent systems

2.2.2.1 Biomass

2.2.2.1.1 General description

The microstructure of plant-based biomass consists of cells, cell walls, and middle lamellae. Plant cells are eukaryotic (i.e., with fully developed nuclei) and they incorporate various organelles performing different functions. Each cell is contained within its respective cell membrane, consisting of a phospholipid bilayer that defines the cell boundary and regulates inward and outward diffusion of components (Williams, 2000). The intracellular area consisting of nucleus, cytoplasm, and other organelles, is collectively termed the protoplast, and it is well adapted to host cellular functions and processes. On the other hand, the external area running between cells is occupied by cell wall components (Devlin and Witham, 1983). Cell walls surround cells and adjoin them, providing mechanical support and uniformity to the biomass. For example, the tendency of cells to expand upon water uptake is resisted by the surrounding cell walls, inducing high intracellular pressures and, thereby, contributing towards structural stability (Williams, 2000). High biomass pressures can also improve extraction by forcing components outwards, or even by damaging cells in some extreme cases. The ability of microwave heating to induce/enhance such mechanisms is a key subject of study in this thesis, from Chapter 5 onwards.

The main constituent of a cell wall fragment is cellulose, while other key components also exist including hemicelluloses, pectic polysaccharides, lignin, suberin, and some enzymes and proteins (Devlin and Witham, 1983). However, the compositions of the various biomass constituents are very much case-specific, often depending on factors related to geography, age, type, etc (Carpenter et al., 2014; Jawaid, Paridah and Saba, 2017). It is, therefore, unsurprising that biomass materials are very heterogeneous in their chemical makeup and physical traits.

Nevertheless, cell walls are typically distinguishable into primary and secondary walls, together with a segment known as the "middle lamella" (Figure 2.9). The latter is the first to form upon biomass growth, as pectic polysaccharides get deposited into the exterior of growing/dividing cells thus cementing these together. As cells grow further, they produce and deposit cellulose, hemicelluloses, and some glycoproteins, forming a $1-3\ \mu m$ layer between the cell boundary and middle lamella known as the primary wall. In addition to this, some cells also deposit an inner-most secondary wall whose thickness is typically $5-10\ \mu m$. The chief constituent of secondary walls is lignin, whose presence enhances the structure's rigidity and can even restrict any further growth of the biomass (Devlin and Witham, 1983).

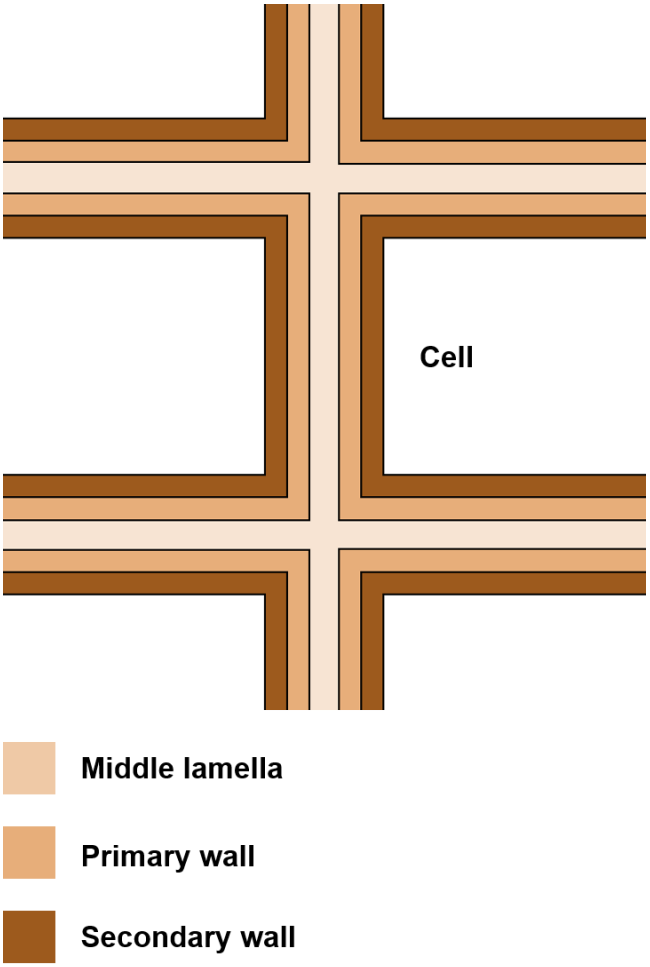


Figure 2.9 – Biomass microstructure

The primary walls are distinguishable by their unique architecture, consisting of many long cellulose-based fibres known as microfibrils (Devlin and Witham, 1983). It is commonly accepted that these microfibrils are held together with xyloglucan crosslinks; however, this remains open to experimental scrutiny (Cosgrove, 2014, 2016; Park and Cosgrove, 2012b), indicating that the exact cell wall structure is yet to be firmly established. In any case, for mechanical characterisation the primary wall can be envisaged as an amorphous matrix reinforced with cellulose microfibrils (Cosgrove, 2016; Salmén, 2004; Wu et al., 1985), resulting in a structure whose strength is comparable even to some building materials (Chaplain, 1993). Nevertheless, the primary walls remain tensile in nature, allowing them to play a key role in dictating cell growth (Bashline et al., 2014). In fact, it is often vital to characterise the structure of primary walls to understand cell properties related to growth, mechanical aspects, and water-related characteristics (Park and Cosgrove, 2012a). In this regard, a common hypothesis describing the formation and orientation

of microfibrils and how these complement the intended growth pattern, is the Multinet-Growth hypothesis (Roelofsen and Houwink, 1953). This hypothesis suggests that newly formed microfibrils get deposited onto the inner-most layer of the primary wall, in an orientation that is orthogonal to the growth axis of the cell. Therefore, the cell expands primarily in a given direction, and grows to assume a certain shape. However, as new microfibril layers form, the older ones see a gradual reorientation towards the growth axis as they are pushed outwards, resulting in an outermost layer whose microfibrils are parallel to the growth axis, and intermediate layers with microfibrils oriented in an oblique fashion (Figure 2.10). This passive reorientation of microfibrils gradually enhances the resistance to expansion in the growth axis, eventually stopping further cell growth upon maturity. This hypothesis attempts to explain why cells grow to occupy certain shapes (i.e., incorporating major and minor growth axes), and it has generally been supported by some experimental findings (Anderson et al., 2010; Green, 1960). Furthermore, this hypothesis allows the assumption that, for practical purposes, fully grown cells only expand in one direction upon experiencing high pressure/stress. This is a useful simplification employed in cell expansion analysis in the current thesis (Chapters 5 and 7), as it makes possible a meaningful and practical method to quantify cell expansion. However, it should be noted that the Multinet-Growth hypothesis does not necessarily apply in every situation. For instance, in many plants where cells exhibit variable shapes and assume a wide range of growth dynamics, it may be that the organism undergoes mechanisms to actively remodel growth, instead of depending solely on the reorientation of microfibrils (Baskin, 2005). Hence, the mechanical aspects of cell growth are likely to follow complex phenomena, and the reorientation of microfibrils may be one of the contributing factors. Nonetheless, the concept of microfibril reorientation offers a useful and meaningful simplification to quantifying cellular mechanics.

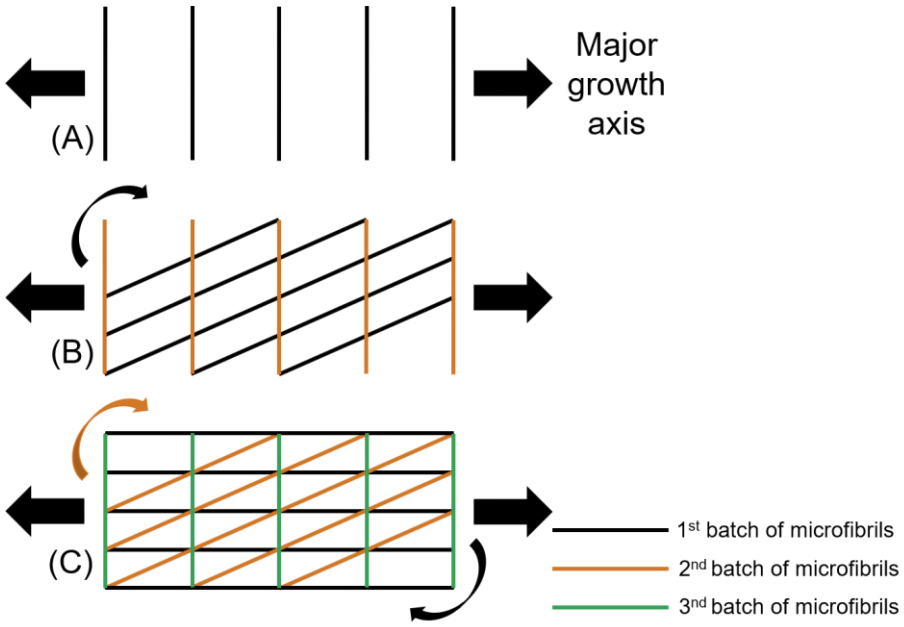


Figure 2.10 – Graphical representation of the Multinet-Growth hypothesis. Concept inspired by the description of the hypothesis (Roelofsen and Houwink, 1953)**. (A) microfibrils (black) are deposited orthogonal to the main growth axis; (B) a second layer of microfibrils (orange) is deposited while the former layer (black) gets pushed into the page and readjusted to an oblique orientation; (C) a third layer (green) is deposited while the former two layers are further pushed into the page, where the black microfibrils become tangential to the major growth axis and the orange microfibrils assume an oblique orientation**

The structural features of biomass do not cease to alter on achieving maturity, but rather they continue to change/remodel based on the various conditions/needs of the material throughout its lifecycle. Such changes do not necessarily incorporate adding strength/complexity to the structure, but instead they could entail loosening of the cell walls by enzymatic and non-enzymatic processes, which are triggered to aid various biomass functions (Fry, 1998). For example, some cells undergo programmed death, which could result in structural alterations to the extracellular matrix (Jones, 2001), including cell wall components like cellulose, hemicelluloses, pectic polysaccharides, and others (Gunawardena, Greenwood and Dengler, 2007). This process is advantageous in the growth and shaping of some biomasses, but it also aids in other functions such as in reproduction and resisting pathogenic attacks (Greenberg, 1996; Gunawardena, Greenwood and Dengler, 2004; Jones, 2001). Another example entailing structural alterations in biomass is fruit ripening, which is a key mechanism known to occur widely. Although the nature and extent of ripening processes are variable amongst different fruits, such processes generally incorporate an overall

loosening of the fruit material due to modifications to the cell wall structure and composition (Bartley and Knee, 1982; Prasanna, Prabha and Tharanathan, 2007). Degradation of cell wall constituents including cellulose, hemicelluloses, pectic polysaccharides, and others, is key in fruit ripening as it softens the texture of the biomass (Prasanna, Prabha and Tharanathan, 2007). The cell wall constituents may experience hydrolysis, solubilisation, depolymerisation, de-esterification, and other enzymatic/non-enzymatic processes (Prasanna, Prabha and Tharanathan, 2007). These examples highlight the tendency of biomasses to show different structural and mechanical features based on their shelf-lives, which is important to consider when processing these materials. Weakened cell walls enable cell rupture to be achieved more readily, which is advantageous as it can enhance extraction from biomass materials (Chapter 5). However, where rupture is not required to enhance extraction, cell wall weakening could deliver the opposite outcome, as it lowers the turgor pressures attainable in the material, thereby suppressing the driving force for solute extraction (Chapter 7). On the other hand, structural alterations in biomass may alter the amounts of extractables present within the material. For example, the quantities of phenolics, flavonoids, and antioxidants available in fruit peels, are generally reduced with fruit ripening (Vu, Scarlett and Vuong, 2019). As such, understanding the lifecycles of biomasses is necessary to predict extraction, as this influences the availability of extractables as well as the mechanical features of the containing materials.

As opposed to the elasticity of primary walls and their significant contribution towards dictating cell growth and in various other functions, the secondary walls do not offer such flexibility, and they bring about loss in the elasticity of the biomass. With lignin as their main constituent, the secondary walls inhibit cell elongation/extension and can even cause death to the intracellular organelles (Devlin and Witham, 1983). This is useful for some plant tissues like in the stem, as it aids such tissues in their water transport function through providing additional strength, and creating hollow tubes as the respective cells die (Williams, 2000). Lignocellulosic biomasses are often described as complex and recalcitrant, requiring additional pre-treatment steps before they can be effectively processed (Dotsenko et al., 2018; Mulakhudair, Hanotu and Zimmerman, 2016). Hence, this thesis will concentrate on non-lignified biomass, i.e., where the secondary wall has not formed and, therefore,

cells retain their elasticity. Lignified materials are the subject of future work, as they probably demand special mechanical treatment and extreme processing conditions compared to those intended in this work.

2.2.2.1.2 Efforts to quantify cell expansion

This thesis attempts to characterise the effect of biomass pressure on extraction; therefore, it is important to understand how the mechanical properties of primary cell walls dictate expansion and pressure build-up in cells. This section reviews some of the attempts to attain data and understanding of cell expansion and mechanical properties of the primary wall.

Although there is a general lack in the available methodologies for quantifying cellular mechanical properties, atomic-force microscopy is a notable advancement in the field enabling such quantifications to be made (Guo et al., 2012). This technique has allowed measuring stress-strain data for some cell wall fragments (Zamil et al., 2013; Zamil, Yi and Puri, 2014, 2015), and such data can be quite useful in assessing existing models and hypotheses, and in guiding future ones. For example, wall fragments tangential to the cell's main growth axis were found in some cases to be weaker than fragments obtained from elsewhere in the cell (Zamil et al., 2013). This could lay the basis for future studies aiming to support the Multinet-Growth hypothesis (section 2.2.2.1.1) with quantitative evidence, thereby generating more sophisticated models for cell growth.

However, efforts to understand and model cell expansion have long existed, even before introducing sophisticated experimental techniques like atomic-force microscopy which, as explained, could greatly aid any future attempts. Many existing cell expansion models are centred around establishing a cell pressure-volume relationship, where if the cell volume is known its pressure can be quantified, and vice versa. Early on, cell expansion modelling was attempted analytically, which is understandable given the limited numerical modelling tools that would have been available. Yet, analytical solutions often require simplifications when attempting complex mathematical problems, and in the case of cell expansion, one of these has been to assume a linear cell elastic modulus and, thereby, a linear cell pressure-volume relationship (Philip, 1958). Nevertheless, this assumption was disregarded in some later studies, where the cell pressure-volume relationship was attempted with nonlinear mechanics (Chaplain, 1993; Wu et al., 1985; Wu, Spence and Sharpe, 1988).

Additionally, some models even differentiated the mechanical responses of cellulose microfibrils from those of the wall matrix, thus demonstrating matrix-regulated and microfibril-regulated phases in the extensibility of cell walls (Chaplain, 1993; Wu, Spence and Sharpe, 1988). These advances were highly notable, especially given that they were mainly attempted analytically. However, due to the reliance on analytical frameworks, further assumptions persisted such as simplified cell geometry and regular arrangement of microfibrils.

Recent models have utilised technological advances to improve the microscale mechanical characterisation of plant-based biomass. For instance, coupling microscopic imaging with computational/numerical techniques has not only enabled a more accurate representation of the cell geometry, but has also widened the analysis framework to incorporate tissues instead of single cells (Pieczywek and Zdunek, 2014). Elsewhere, it has even been attempted to represent cell walls with more detailed three-dimensional features, and to distinguish the middle lamella mechanically from the rest of the fragment, thus investigating its effect on the overall mechanical response (Zamil, Yi and Puri, 2017). Backed by evolving technologies, efforts to better understand the mechanical behaviour of biomass are clearly growing, which indicates a promising prospect for this field. It will be attempted in this thesis to characterise biomass mechanics with relevant pressure-volume relationships (Chapters 5 and 7). The intended framework will incorporate reasonable levels of complexity, delivering meaningful results but also enabling smooth integration into the overall biomass-solvent extraction model.

2.2.2.2 Solvent

Appropriate solvent selection is of utmost importance in extraction, and it normally follows an understanding of the relevant mass transfer patterns entailing how well the solvent penetrates into the biomass, and whether it effectively dissolves the desired extractables (Spigno and De Faveri, 2009; Veggi, Martinez and Meireles, 2013). Extraction employs a wide range of solvents, where some examples include using methanol and acetone in the extraction of flavonoids (Routray and Orsat, 2012); using water-ethanol mixtures in the extraction of coffee-based antioxidants (Pavlović et al., 2013); and using acidic/alkaline solutions in the extraction of pectic polysaccharides (Mao et al., 2019). Even non-polar solvents such as hexane are used in some cases (Veggi, Martinez and Meireles, 2013).

In addition to practical aspects, it is vital when selecting a solvent to consider the implications on sustainability, including the relevant economic, environmental, societal, and other impacts (Soh and Eckelman, 2016). In this context, water is arguably the most desirable extraction solvent, due to its obvious sustainability-related advantages. However, as detailed above, numerous other solvents are still being used, to accommodate for case-specific extraction requirements (Flórez, Conde and Domínguez, 2015). Nevertheless, according to literature microwave heating offers its own enhancement to extraction (Adetunji et al., 2017; Zheng et al., 2013); moreover, water is a good absorber of microwave radiation in extraction settings (Proestos and Komaitis, 2008). This, among other reasons, has prompted numerous microwave-extraction experiments to be conducted in water (González-Nuñez and Cañizares-Macías, 2011; Tan et al., 2011; Tanongkankit et al., 2013), in an attempt to develop clean and efficient water-based extraction processes. Should microwave heating enable a more effective use of water as an extraction solvent, this technology will deliver enormous benefits compared to other extraction techniques. However, achieving such a goal demands an understanding to be formulated around the relevant microwave-induced phenomena responsible for enhanced extraction in biomass-solvent systems. This is the main goal of the current thesis; therefore, water will be used as the extraction solvent (Chapter 3 onwards).

2.2.3 Thermal extraction in biomass-solvent systems

2.2.3.1 Microwave versus conventional extraction

Biomass-solvent extraction is classically conducted with heating and/or agitation (Lee et al., 2015), where heat is delivered conventionally by providing energy to the solvent which, in turn, passes it on to the biomass (Figure 2.11). Conventional extraction has been used for a long time and is implemented in various forms, such as Soxhlet extraction, hydro-distillation, and maceration (Wang and Weller, 2006). Extraction can yield various components spanning a wide range of categories, including lipids, polysaccharides, proteins, phenolics, vitamins, pigments, aromas, antioxidants, and others (Flórez, Conde and Domínguez, 2015; Li et al., 2013). Some of these extractables exist in cells and may require cell disruption to be liberated (Lee et al., 2016), while others originate from the cell walls (e.g., pectic polysaccharides and hemicelluloses). Heating logically improves extraction as it generally accelerates diffusion, reduces liquid viscosity, and improves solute solubility.

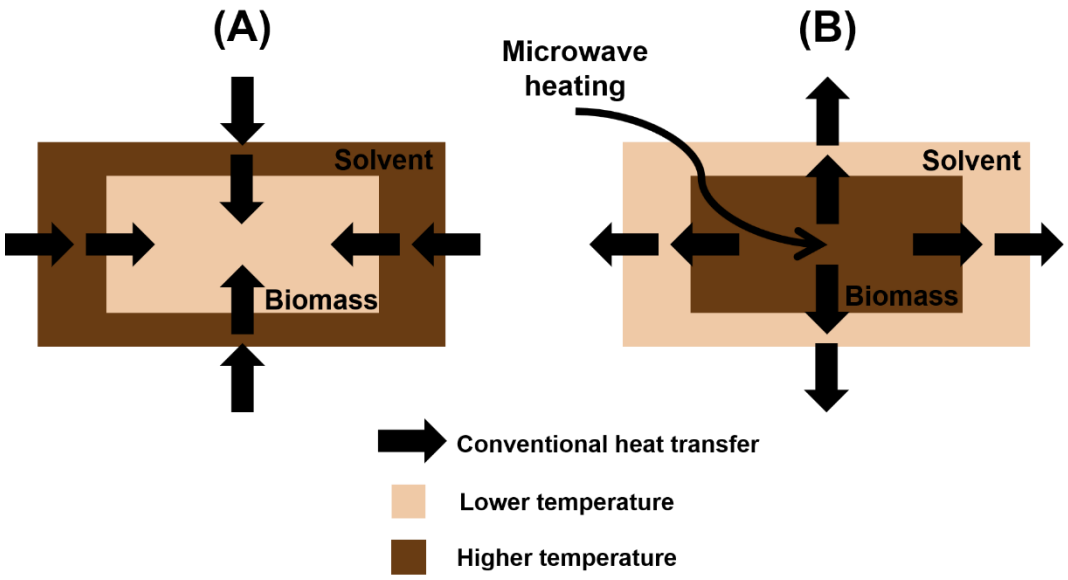


Figure 2.11 – Difference between microwave and conventional heating sources in terms of energy delivery to the biomass. (A) Conventional heat transfer incorporates the solvent as an intermediary phase, hence solvent temperature is higher than that of the biomass. (B) Microwaves deliver energy directly to the biomass, bypassing the solvent and constituting heat transfer in the opposite direction

Despite their availability, conventional extraction techniques reportedly suffer from low yields, long processing times, high energy demand, and significant solvent consumption (Rombaut et al., 2014; Wang and Weller, 2006). As such, there is an increasing need to adopt novel technologies offering higher efficiency and better environmental considerations (de Castro and García-Ayuso, 1998; Wang and Weller, 2006). Microwave-assisted extraction has attained a multitude of research interest as a novel, more efficient alternative to conventional extraction techniques (Chan et al., 2011). Several advantages have been attributed to microwave heating in various reports and experimental studies, including faster extraction, higher yields, reduced solvent consumption, and improved product quality/selectivity (Bagherian et al., 2011; Pan, Niu and Liu, 2003; Pandey and Shrivastava, 2018; Xiao, Han and Shi, 2008).

Although microwave heating is widely reported to improve extraction, the mechanistic underpinnings of such improvement are yet to be thoroughly understood. Much of the currently available explanations are qualitative, describing the envisaged mechanisms of microwave action rather than attempting to quantify them. Enhanced extraction is often attributed to the ability of microwaves to heat the biomass rapidly through direct radiation (Figure 2.11), which is then used to qualitatively describe how

improved yields could be attained. Some of these descriptions include thermal disintegration of the wall matrix, thus improving extraction (Flórez, Conde and Domínguez, 2015; Leão et al., 2018; Maran and Prakash, 2015); and, vaporisation of the intracellular moisture, thereby inducing high pressures and causing cell rupture (Chan et al., 2011; Kala et al., 2016; Letellier and Budzinski, 1999). These descriptions may match the theoretical characteristics of microwave heating (section 2.1.2), but as they stand, they do not offer any quantitative explanations as to how microwaves interfere with mass transfer patterns in biomass-solvent systems, bringing about enhanced extraction. The lack of such mechanistic understanding significantly hinders the efforts towards an efficient industrial utilisation of the process (Kostas, Beneroso and Robinson, 2017), because it limits the ability to predict extraction outcomes given a range of conditions, which poses challenges onto process design, optimisation, and scale-up.

2.2.3.2 Attempts to model microwave extraction

As discussed previously, the ability to understand microwave extraction and predict its outcomes, is key for a successful large-scale implementation of the technique. To this end, numerous experimental studies have been conducted to compare microwave-assisted extraction to its conventional counterpart (section 2.2.3.1). However, due to a lack of quantitative reasoning as to why microwaves enhance extraction, the technique struggles to advance towards large-scale implementation.

This challenge can be overcome through mathematical modelling which, if developed with an understanding of the relevant physical underpinnings of the process, may reduce the demand on experimental studies and improve outcome predictability. Some of the currently available models are summarised in Table 2.2, where numerous examples can be seen to have implemented empirical approaches. Such approaches are heavily reliant on experimental data, as their goal is to correlate process inputs and outputs through prior trends obtained experimentally. Although such models enable predicting additional processing outcomes through interpolation (hence, without further experimentation), they are still not constructed upon an understanding of the fundamental phenomena underpinning the process. This poses a major disadvantage to these models, because any outcomes relying on experimental data are only applicable to the specific experiments and scales in question, meaning they cannot be extended to further situations (Chan et al., 2016). This is due to the

heterogeneity and complexity of biomass materials (section 2.2.2), which constitutes a wide range of variables influencing any extraction processes.

Nevertheless, the challenges associated with empirical modelling have been identified, and further modelling efforts have attempted to reduce the dependence on prior experimental knowledge. As shown in Table 2.2, some of the proposed models aim to reduce the reliance on experimental data input (although remaining empirical in nature), while others adopt more mechanistic approaches entailing heat/mass transfer and other relevant concepts. However, despite the advances in driving away from empirical models and instead adopting mechanistic ones, there is still a need to develop comprehensive frameworks incorporating all relevant concepts, such as microwave heating, heat/mass transfer, expansion mechanics, and biomass microstructural features. Developing such a model will provide a clear quantitative insight based on theoretical reasons, as to why microwaves enhance extraction. This will be a key step towards extending the predictability of extraction trends to cover a wide variety of systems, while incorporating multiple conditions and scales. This will, undoubtedly, tackle much of the present challenges that prevent industrial implementation of microwave extraction.

On the other hand, despite the present challenges there have been notable improvements in the efforts to understand/model microwave extraction from a fundamental basis. For example, a fist-principles' model has been developed to quantify cell pressure under microwave heating (Chan et al., 2016), and a novel mechanism has been proposed for the effect of microwave heating on cellular scale diffusion (Lee et al., 2016). These concepts will be discussed and assessed in Chapter 5, using the model intended in this thesis.

Reference	Some features	Some drawbacks
(Kumar, Sivakumar and Ruckmani, 2016; Sinha, Saha and Datta, 2012; Sinha et al., 2013; Tran et al., 2018)	Models constructed to optimise microwave extraction of certain components from specific biomass materials, using computational techniques like response surface methodology, and artificial neural network.	Empirical frameworks aiming to correlate input and output parameters through fitting with prior experimental data. Hence: • Lack of fundamental mechanistic understanding of the process. • Framework inapplicable to situations and scales other than the experiment in question.
(Amarni and Kadi, 2010)	Implements a previous empirical extraction kinetics model, to predict microwave extraction for a given system.	• Empirical framework relying on experimental data input. • Framework does not incorporate heat transfer, biomass microstructure, or expansion mechanics.
(Gujar, Wagh and Gaikar, 2010)	Implements a previous diffusion model based on Fick's law, to determine the diffusion coefficient of a component under microwave heating.	• The relationship between microwave heating and mass transfer is still unclear. • Framework does not incorporate heat transfer, biomass microstructure, or expansion mechanics.
(Xiao et al., 2012)	Model proposing a chemical kinetics approach to quantify extraction in a system.	• Model still relies on prior experimental data. • Model does not incorporate heat/mass transfer, biomass microstructure, or expansion mechanics.
(Chan, Yusoff and Ngoh, 2013; Chan et al., 2015; Chan, Yusoff and Ngoh, 2015)	Model constructed to simulate microwave extraction based the microwave energy absorbed by the system. This approach is better suited for process scale-up, as it can	• Model still does not explain the phenomena responsible for enhanced extraction under microwave heating. • Model still relies on some experimental

	accommodate a range of processing conditions, as well as demanding less experimental data input.	data input, due to its empirical nature.
(Chumnanpaisont, Niamnuy and Devahastin, 2014)	Model constructed to simulate the distribution of temperature and solute concentration in an extraction sample, using Maxwell's equations and heat/mass transport expressions (hence, the model can run independently of experimental data input).	Modelling conducted at the experimental scale; hence: • Microstructural details of biomass cells/cell walls are absent, thus limiting the attainable understanding. • Biomass pressure was not considered, even though it can affect solute concentration. The absence of microstructural details inhibits quantifying biomass pressure. • Also due to the lack of microstructural details, any unique microwave effects felt at the cellular scale, are unlikely to be demonstratable in this model.

Table 2.2 – Examples of available microwave-assisted extraction models

2.2.4 Section summary

For the purposes of this thesis, biomass-solvent systems comprise a plant-based biomass material immersed in a body of solvent. Biomass consists of cells surrounded by cell walls, which can be distinguished into middle lamellae, and primary/secondary walls. The middle lamella mainly consists of pectic polysaccharides, whereas the primary wall is constructed of numerous cellulose microfibrils embedded in an amorphous matrix. Due to their remarkable strength but also elasticity, primary walls play an important role in dictating cell mechanics and growth, as newly developed microfibrils are thought to get deposited so as to enhance the structure's rigidity in certain directions but not in others. This promotes cell elongation in preferential outlooks, allowing cells to grow into specific shapes, but also to show certain mechanical characteristics. One way to describe this process of microfibril deposition/reorientation is through the Multinet-Growth hypothesis, which can also be used to assume that fully grown cells only expand in one direction when experiencing pressure/stress. This simplification will be employed in Chapters 5 and 7 of this thesis, where cell/cell wall expansion frameworks will be attempted. Cell mechanics have been the subject of numerous modelling efforts, aiming to understand how cells expand in response to force, through knowledge of the mechanical properties of the primary walls. Backed by recent technological advances, these models have become increasingly more sophisticated, and further experimental studies have been conducted to directly acquire certain mechanical data of some cell walls.

The current thesis will be focussed upon non-lignocellulosic biomass, i.e., where the secondary walls have not formed. The main constituent of secondary walls is lignin, which adds significant rigidity to cells and recalcitrance to the biomass. Lignocellulosic materials probably require special mechanical treatment and extreme processing conditions; therefore, they are a subject of future work. Regarding solvent selection, this should follow sustainability considerations as well as practical aspects, which is why water is arguably the most desired solvent to use. However, while other solvents are still utilised to meet specific process requirements, this thesis will focus on water given that it is a good microwave absorber, and that microwave heating can offer its own enhancement to extraction. Attempting to develop an efficient water-based extraction process will be a very useful endeavour in the biomass extraction field.

Biomass-solvent extraction is often conducted with heating; however, conventional heating techniques incorporate practical disadvantages that have necessitated searching for novel extraction methods. Among these methods is microwave extraction, which has been widely reported to accelerate the process, increase the yield, and lower solvent consumption. Nevertheless, upscaling this technology has been hindered by a lack in fundamental understanding of how microwaves enhance extraction. Without such understanding, it is not possible to predict extraction outcomes given a range of systems, conditions, and scales, which, in turn, does not allow process design, optimisation, and scale-up. This gap is evident given the various available microwave extraction models which, in many cases, are based upon empirical approaches relying on prior experimental trends. There is a need to develop comprehensive mechanistic models based on fundamental physical principles, incorporating microwave heating, heat/mass transport, microscale geometrical aspects, and mechanical responses of cells/cell walls. The key intention of this thesis is to develop such a model to propose an explanation as to how microwave heating enhances extraction.

2.3 Nomenclature

Symbols

$\vec{E}$	Vm^{-1}	Electric field vector
$\vec{H}$	Am^{-1}	Magnetic field vector
$\vec{D}$	Cm^{-1}	Electric displacement vector
$\vec{I}$	Am^{-2}	Electric current vector
$\tilde{E}$	Vm^{-1}	Peak electric field intensity
$\tilde{H}$	Am^{-1}	Peak magnetic field intensity
$\|E\|$	Vm^{-1}	Root-mean-squared (average) electric field intensity
ε	Fm^{-1}	Dielectric permittivity
ε'	$-$	Relative permittivity/dielectric constant
ε''	$-$	Dielectric loss factor
ε_0	Fm^{-1}	Permittivity of free space
$\hat{\varepsilon}$	$-$	Complex dielectric permittivity
ε_{dc}	$-$	Permittivity at static frequency
ε_∞	$-$	Permittivity at very high frequencies
b	Hm^{-1}	Magnetic permeability
α	m^{-1}	Wave attenuation factor
β	m^{-1}	Displacement factor along the direction of wave propagation
ω	$rad\ s^{-1}$	Angular velocity
t	s	Time
$\ddot{t}$	s	Relaxation time
$\bar{\bar{t}}$	s	Wave periodic time
p	m	Direction of wave propagation
e	m	Direction of electric field polarisation
h	m	Direction of magnetic field polarisation
$\vec{e}$	$-$	Unit vector in the electric field direction
$\vec{h}$	$-$	Unit vector in the magnetic field direction
$Re\{\}$	$-$	Real part of a complex number
k_α	$msF^{-1}rad^{-1}$	Factor representing ohmic losses in a material
k_β	$msF^{-1}rad^{-1}$	Factor representing polarisation losses in a material
$\vec{Q}_{At}$	$Wm^{-2}s^{-1}$	Poynting vector
$\vec{Q}_A$	Wm^{-2}	Time-averaged microwave power dissipation
Q_M	W	Total microwave power dissipation
$\dot{Q_M}$	Wm^{-3}	Microwave power density
A	m^2	Surface area
V	m^3	Volume
$\vec{a}$	m^2	Infinitesimal surface area vector
v	m^3	Infinitesimal volume
δ_p	m	Penetration depth

c	$\boldsymbol{ms^{-1}}$	Speed of light in vacuum

Subscripts and superscripts

$()_0$	Incident/initial value
$()^*$	Complex conjugate of a complex number/vector

Note: symbols denoting vector quantities are written in bold and supplemented with an arrow above them (e.g., $\vec{\boldsymbol{E}}$).

3 MICROWAVE HEAT TRANSFER IN BIOMASS-SOLVENT SYSTEMS

The aim of this chapter is to present the steps and methods applied in the construction of a microwave heat transfer model dedicated to biomass-solvent systems at the cellular scale. This model will subsequently be used to provide quantitative understanding of the thermal patterns in biomass-solvent systems.

This chapter has contributed towards publishing Taqi et al. (Taqi et al., 2020). The format of this chapter is as follows:

3.1 Introduction 57
3.2 Methodology 58
3.2.1 System geometry 58
3.2.2 The heat equation 59
3.2.3 Numerical solution to the heat equation 62
3.2.3.1 Initial and boundary conditions 62
3.2.3.2 Model discretisation 63
3.2.3.3 Taylor series approximation 64
3.2.3.4 Solution framework 66
3.3 Predicted temperature distribution 67
3.3.1 System-related parameters 70
3.3.1.1 Effect of dielectric loss factor (ε'') 70
3.3.1.2 Effect of penetration depth (δ_p) 73
3.3.1.3 Effect of thermal conductivity (k) 75
3.3.1.4 Effect of specific heat capacity (C_p) 77
3.3.1.5 Effect of solvent-to-solid ratio (S_R) 78
3.3.1.6 Effect of density (ρ_L) 79
3.3.1.7 Effect of cell dimensions 79
3.3.2 Heating-related parameters 80
3.3.2.1 Effect of microwave frequency (F) 80
3.3.2.2 Effect of incident electric field intensity ($|E|_0$) 81
3.3.3 Temperature-time plots for selected heating parameters 83
3.4 Summary 84
3.5 Thesis recap 86
3.6 Nomenclature 87

3.1 Introduction

As discussed in Chapter 2 (section 2.1), the extent to which microwave energy gets converted to heat upon interacting with a material, depends on the material's dielectric properties. Conversion into heat is a function of the imaginary part of the permittivity value, which is otherwise known as the dielectric loss factor of the material (ε'') (Metaxas and Meredith, 1983). The dissipation of power in a material (per unit volume) is described in Equation (2.31).

Given that permittivity is a material property, different heating rates are to be expected in different materials, as they absorb microwaves up to variable extents. Furthermore, irregular heating is also to be expected in heterogeneous materials (i.e., with multiple constituents), where this heterogeneity leads to variable dielectric properties across a material's matrix. In such a case, different parts of the heated material experience different heating rates, which is commonly referred to as selective heating (Kappe, Stadler and Dallinger, 2012).

The variability in heating rates within a material experiencing selective heating, can induce non-uniform temperature distribution. As such, it has been hypothesised that temperature distribution in a microwave-heated biomass-solvent system is proportional to the distribution of dielectric properties within the system (Lee et al., 2016; Galan et al., 2017). This means that, if the biomass possesses a higher dielectric loss factor than the solvent its temperature will be higher, and vice versa. However, the quantitative basis upon which this link has been established is unclear, due to the lack of heat transfer modelling in this regard. Heat transfer is logically expected to demonstrate profound influence on temperature distribution, regardless of the method of heating. Elsewhere yet more commonly in literature, even the role of dielectric properties and the concept of temperature distribution have been neglected, and instead microwave heating is only highlighted for its ability to induce direct and rapid heating. This is then employed qualitatively to explain the enhanced extraction observed under microwave heating (Chan et al., 2011; Flórez, Conde and Domínguez, 2015; Leão et al., 2018).

There is a clear lack of quantitative understanding of microwave heating in biomass-solvent systems. A prior step to understanding extraction is to characterise how these systems heat up with microwaves, which is the aim of this chapter.

3.2 Methodology

3.2.1 System geometry

The system under investigation incorporates a biomass material immersed in a body of solvent (Figure 3.1).

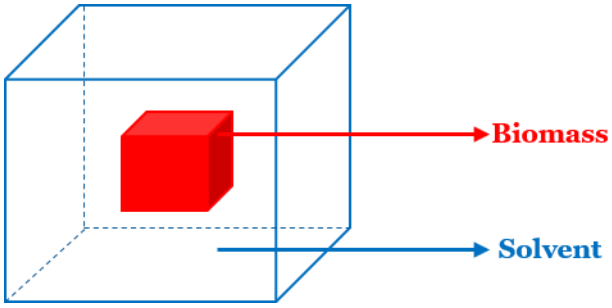


Figure 3.1 - General model structure

In defining the constituents of biomass, it was aimed to replicate the structure of some real-world materials as far as was reasonably practical. As discussed in Chapter 2 (section 2.2), biomass incorporates cells and a network of adjoined cell wall fragments. Cells were estimated here as cuboids, thus approximating biomass cell types such as onion epidermal cells, which are well characterised in terms of their mechanical behaviour (Zamil et al., 2013). Such an approximation also enables thermal characterisation to be conducted with Cartesian coordinates. On the other hand, cells were also assumed to have an identical geometry to each other and a regular arrangement, entailing adjacent cells within the matrix that possess the same length, width, height, and wall thickness.

While the size of the biomass is specified with the number and size of its cells and the thickness of its cell walls, the amount of solvent is defined by its volume. The solvent-to-solid ratio (S_R, in mLg^{-1}) is a user-input parameter defining the volume of the solvent based on the mass of the biomass.

Figure 3.2 shows a single cell constructed with the geometry specified above, while Figure 3.3 shows a 2-dimensional representation of a multicellular biomass geometry.

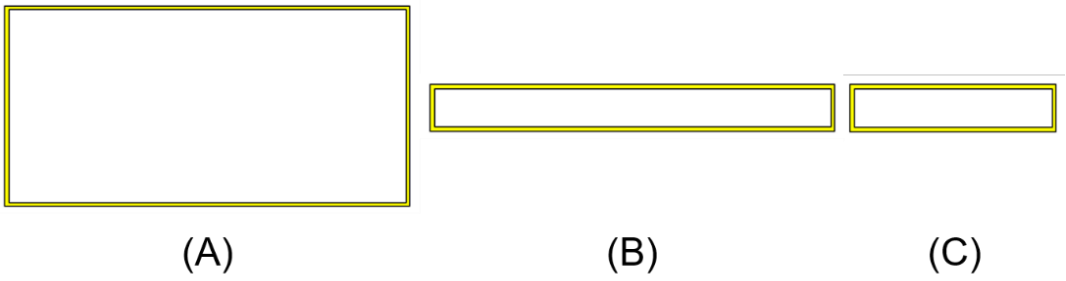


Figure 3.2 - The geometry of a single cell; (A) XY cross-section; (B) XZ cross-section; (C) YZ cross-section

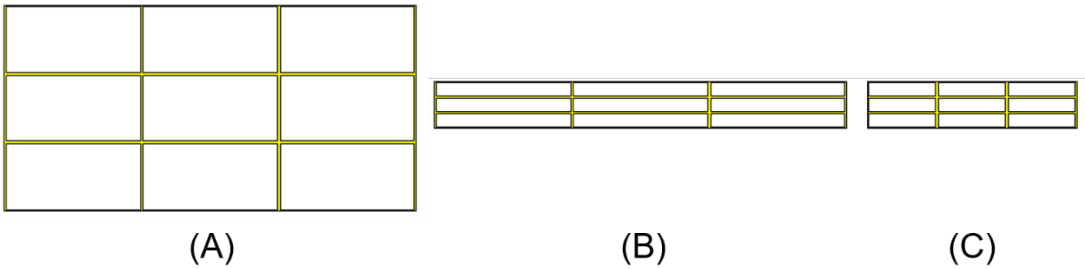


Figure 3.3 - The geometry of a multicellular biomass cluster; (A) XY cross-section; (B) XZ cross-section; (C) YZ cross-section

3.2.2 The heat equation

Temperature distribution in the biomass-solvent system is influenced by microwave radiation and conventional heat transfer. A heat equation was derived to quantify temperature within the system, as follows.

Consider an infinitesimal unit in space, whose bottom-left-front corner is located at Cartesian coordinates *(x, y, z)*, and whose top-right-back corner is located at *(x+δx, y+δy, z+δz)* (Figure 3.4). Energy is delivered into the unit in the *x-direction*, *y-direction*, and *z-direction* at flux rates Q_{x-in}, Q_{y-in}, and Q_{z-in}, respectively, and energy is removed at flux rates Q_{x-out}, Q_{y-out}, and Q_{z-out} through the respective directions. The unit is also being heated volumetrically through microwave radiation at a per-volume rate $\dot{Q_M}$.

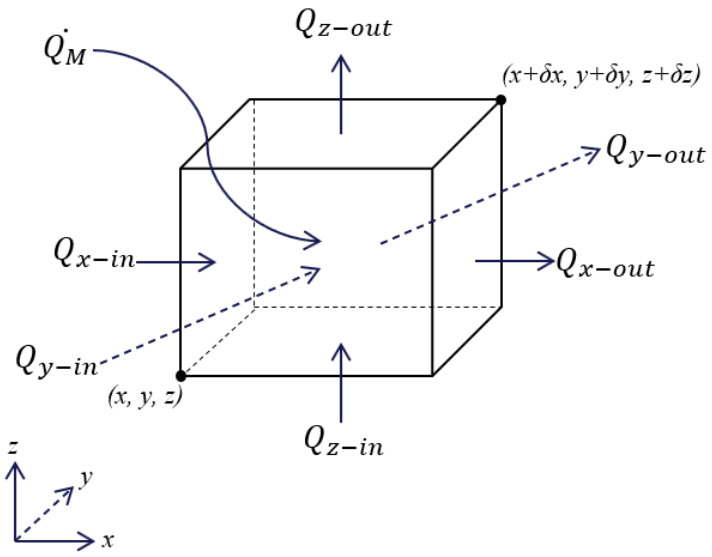


Figure 3.4 - Differential heat transfer element. Directions of heat flow are arbitrary and used for demonstration purposes

The energy conservation principle dictates the following:

$$Energy\ accumulated = Energy\ input - Energy\ output \tag{3.1}$$

The output energies can be expressed in terms of the input energies (excluding the input microwave heating term; $\dot{Q_M}$). By considering the *x-direction* only, the following can be written:

$$Q_{x-out}\delta y\delta z = \left(Q_{x-in} + \frac{\partial Q_{x-in}}{\partial x}\delta x\right)\delta y\delta z \tag{3.2}$$

Therefore, the input and output energies (excluding microwave heating) can be expressed collectively as follows:

$$Q_{x-in}\delta y\delta z - Q_{x-out}\delta y\delta z = -\frac{\partial Q_{x-in}}{\partial x}\delta x\delta y\delta z \tag{3.3}$$

Fourier's law of heat transfer (Coulson et al., 1999) can be used to write the input and output energies as follows:

$$Q_{x-in}\delta y\delta z - Q_{x-out}\delta y\delta z = k_x\frac{\partial^2 T}{\partial x^2}\delta x\delta y\delta z \tag{3.4}$$

Summation over all input and output energies in the 3 directions yields the following:

$$Energy\ input - Energy\ output = \left[k_x \frac{\partial^2 T}{\partial x^2} + k_y \frac{\partial^2 T}{\partial y^2} + k_z \frac{\partial^2 T}{\partial z^2}\right] \delta x \delta y \delta z \qquad \textbf{(3.5)}$$

By assuming thermal conductivity is equal throughout the unit ($k = k_x = k_y = k_z$), and with reintroducing the microwave heating term, the expression can be rewritten as follows:

$$Energy\ input - Energy\ output = k\nabla^2 T \delta x \delta y \delta z + \dot{Q_M} \delta x \delta y \delta z \qquad \textbf{(3.6)}$$

Energy accumulated in the unit is proportional to the temporal derivative of temperature, as follows:

$$Energy\ accumulated = \rho_L C_p \frac{\partial T}{\partial t} \delta x \delta y \delta z \qquad \textbf{(3.7)}$$

Substituting Equations (3.6) - (3.7) into the initial energy conservation expression (Equation (3.1)) yields the following:

$$\frac{\partial T}{\partial t} = \beta \nabla^2 T + \frac{\beta}{k} 2\pi F \varepsilon_0 \varepsilon'' |E|^2 \qquad \textbf{(3.8)}$$

$\beta = k/\rho_L C_p$ is the heat transfer coefficient.

Equation (3.8) is the heat equation describing temperature in the biomass-solvent system at any given location and time. It is a partial-differential equation (PDE) which should be solved to yield the desired temperature distribution. Numerical solution to the heat equation is described in section 3.2.3.

In addition to the heat equation, microwave attenuation (see Chapter 2, section 2.1) was also considered using Lambert's law (Ayappa et al., 1991). As shown in Equation (3.9), the square of the electric field intensity, which is proportional to the input microwave power, decays exponentially as the wave propagates through the system.

For simplicity, and due to the small scale of the model, it was assumed that microwaves propagate through the system parallel to the *x-direction* only.

$$|E|^2 = |E|_0{}^2 \, exp\left(-x/\delta_p\right) \quad \textbf{(3.9)}$$

3.2.3 Numerical solution to the heat equation

This work employs a finite-difference time-domain (FDTD) technique, known as the method of lines, to solve the partial-differential heat equation (Equation (3.8)). While finite-difference methods are undemanding to understand and implement, they are also well-adapted for regular geometries. These features make finite-difference methods more attractive to newly developed models compared with other alternatives, especially where complex geometrical characteristics are absent. As such, it has been reported that FDTD methods are amongst the most widely used numerical techniques in microwave heating models (Yakovlev, 2006).

Applying the method of lines to Equation (3.8) incorporates approximating the spatial second derivatives of temperature as finite values. This allows the partial-differential equation (PDE) to be estimated as an ordinary-differential equation (ODE) with a single time domain, which can then be solved numerically. Approximating the spatial second derivatives of temperature was achieved through dividing the geometrical domain of the model into discrete points, and subsequently applying a second-order Taylor series expansion (sections 3.2.3.2 and 3.2.3.3).

3.2.3.1 Initial and boundary conditions

The initial temperature of the system ($T_{initial}$) is a user input. A saturation temperature ($T_{saturation}$) should also be defined, and this is recognised by the model as the maximum temperature achievable in the solvent.

Due to the small scale of the model, the boundary condition was set to reflect perfect insulation from the surroundings. This assumption does not affect the system's temperature distribution at steady state, because in such a case the solvent acts as a heat sink (i.e., it maintains $T_{saturation}$ regardless of any further heating); hence, the biomass will also have to maintain a specific temperature distribution regardless of whether heat is lost from solvent to the surroundings. Therefore, the effects of negligible heat loss can be summarised in two points: firstly, the predicted time needed to increase the temperature from $T_{initial}$ to $T_{saturation}$ could be smaller than it is in

reality; secondly, with negligible heat loss all energy delivered to the solvent after achieving $T_{saturation}$ would be used in boiling which, in any case, is not considered in this work.

3.2.3.2 Model discretisation

Dividing the model into discrete points means to assume that each cell and cell wall fragment is a distinct phase, represented by a discrete finite point (Figure 3.5). The properties of any given phase (such as temperature) are assumed to be homogeneous throughout the phase and equal to the properties computed at the location of the discrete point. Also, the displacement between any two adjacent phases is assumed equal to the separation between their respective discrete points. Due to the cuboid shape of cells and the regular geometry assumed previously (section 3.2.1), the mesh of discrete numerical points within the biomass can be represented using a Cartesian system of coordinates.

The solvent was assumed as one homogeneous phase described by a single numerical point. This avoids the need for complex analysis of the solvent phase which firstly is a fluid, and secondly is likely to possess homogeneous temperature at thermal steady state (section 3.3.1.1). The homogeneous solvent phase surrounds the biomass; hence, the various cell wall phases at the edge of the biomass are in direct contact with the solvent. Therefore, the numerical point describing the solvent cannot be denoted a fixed location, but rather it should "move" continuously alongside the biomass-solvent boundary, so that all biomass phases at the edge are in the same proximity to the solvent phase (Figure 3.5). With this in place, the method of lines adopted here to solve the heat equation still applies to biomass phases adjacent to the solvent, even though the solvent is homogeneous and represented by a single numerical point. However, solvent temperature cannot be determined by the same method, due to the absence of discretisation as carried out with the biomass. Instead, solvent temperature was computed here through applying a heat balance with all the adjacent biomass phases (section 3.2.3.3).

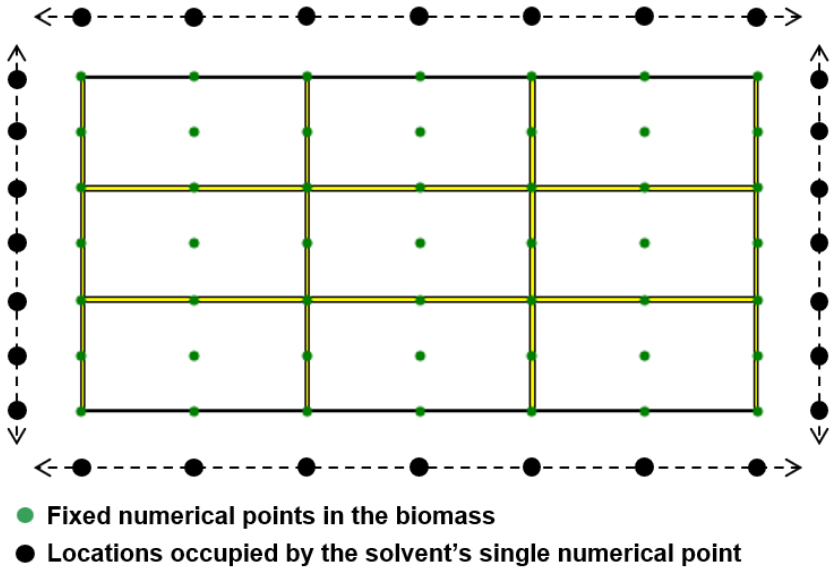


Figure 3.5 – 2-dimensional representation of model discretisation for heat transfer. Biomass phases are discretised with the method of lines, while the solvent is denoted a single mobile numerical point

3.2.3.3 Taylor series approximation

Discretisation of the model's geometry (specifically biomass) enables approximating the spatial second derivatives of temperature in Equation (3.8) as finite values. The following steps demonstrate the method by which the Taylor series expansion was applied to estimate these derivatives.

Consider three adjacent points in space (Figure 3.6), whose unidimensional distances from the origin point are x_{i-1}, x_i, and x_{i+1}, and whose temperatures are T_{i-1}, T_i, and T_{i+1}, respectively. The points are separated by a displacement equivalent to δx.

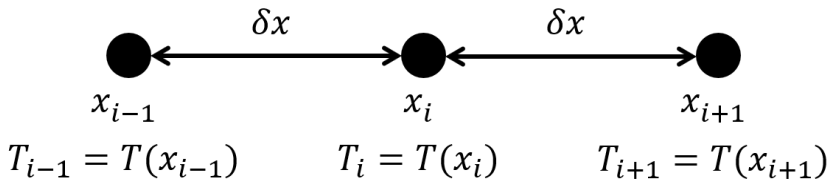


Figure 3.6 – Taylor expansion framework for 3 unidimensional points

It is required to estimate the second derivative of a function $T(x)$ at the point $x = x_i$. Since the exact expression of $T(x)$ is unknown, the function can instead be expressed using Taylor series expansion about the point $x = x_i$, as follows:

$$T(x)|_{x=x_i} = \sum_{n=0}^{\infty} \frac{[x - x_i]^n}{n!} \frac{d^n}{dx^n}[T(x_i)] \quad \textbf{(3.10)}$$

Equation (3.10) gives temperature in terms of location; hence, it can be used to estimate temperatures T_{i-1}, T_i, and T_{i+1}, which are shown in Figure 3.6. When $x = x_i$, the high order terms are eliminated and Equation (3.10) gets reduced to the following:

$$T_i \equiv T(x_i)|_{x=x_i} = T(x_i) \quad \textbf{(3.11)}$$

When $x = x_{i-1}$, the following can be written:

$$T_{i-1} \equiv T(x_{i-1})|_{x=x_i} = \sum_{n=0}^{\infty} \frac{[-\delta x]^n}{n!} \frac{d^n}{dx^n}[T(x_i)] \quad \textbf{(3.12)}$$

Similarly, when $x = x_{i+1}$, the following can be written:

$$T_{i+1} \equiv T(x_{i+1})|_{x=x_i} = \sum_{n=0}^{\infty} \frac{[\delta x]^n}{n!} \frac{d^n}{dx^n}[T(x_i)] \quad \textbf{(3.13)}$$

Observing Equations (3.11) – (3.13), the second derivative at the point $x = x_i$ is obtained upon adding up T_{i+1} and T_{i-1} and subtracting $2T_i$, thus eliminating the zeroth-order term together with all odd-order terms. Due to the small scale of the model, all terms beyond the second-order term can be considered as truncation, and an expression for the second derivative can be written as follows:

$$\frac{d^2}{dx^2}[T(x_i)] = \frac{T_{i+1} + T_{i-1} - 2T_i}{\delta x^2} + O(\delta x^4) \quad \textbf{(3.14)}$$

Equation (3.14) can be generalised into the three dimensions, thus approximating the heat equation (Equation (3.8)) as a time-domain ODE shown in Equation (3.15). Numerical points arranged in the *x-direction*, *y-direction*, and *z-direction* are denoted the letters *i*, *j*, and *k*, respectively.

$$\left.\frac{dT}{dt}\right|_{ijk} \approx \beta\left[\frac{T_{(i+1)jk}+T_{(i-1)jk}-2T_{ijk}}{\delta x^2}+\frac{T_{i(j+1)k}+T_{i(j-1)k}-2T_{ijk}}{\delta y^2}+\frac{T_{ij(k+1)}+T_{ij(k-1)}-2T_{ijk}}{\delta z^2}\right]+\frac{\beta}{k}2\pi F\varepsilon_0\varepsilon''|E|^2 \quad \textbf{(3.15)}$$

The heat equation has been approximated using the method of lines. The spatial second derivatives of temperature at any discrete point can be approximated using Equation (3.15), which requires knowledge of the temperatures of the current, previous, and next points in space. The displacements between points should also be known. As explained in section 3.2.3.2, this is applicable to all numerical points within the biomass including those adjacent to the solvent phase; however, Equation (3.15) cannot be used to determine solvent temperature due to the mobile nature of the numerical point representing this phase. Instead, solvent temperature can be obtained through a heat balance applied between the solvent and all adjacent biomass phases (Equation (3.16)).

$$\left.\frac{dT}{dt}\right|_{solvent} = -\frac{1}{N_{solvent}C_p}\sum_{ijk} Q_{ijk-solvent} \quad \textbf{(3.16)}$$

$Q_{ijk-solvent}$ is the heat exchanged between a boundary phase *ijk* and the solvent.

3.2.3.4 *Solution framework*

Equation (3.15) was generated using the method of lines to approximate the heat equation as an ODE. From there, the ODE was then solved numerically over a predefined domain of discrete time values, separated by a finite step (δt). For example, solving over $100\ s$ with $\delta t = 1\ s$, is analogous to solving in a stepwise manner over a time domain of $0, 1, 2, \ldots, 100\ s$. The smaller the time-step (δt) the more accurate the result, but also the more computationally intensive the simulation. Moreover, too large δt values cause instability to the computation and can lead the results to diverge towards infinity. Hence, the chosen δt should neither be too small nor too large.

At first, a set of input geometrical and heating parameters must be chosen, including the initial and saturation temperatures ($T_{initial}$ and $T_{saturation}$). As shown in Figure 3.7, Equation (3.15) was solved at every spatial numerical point in the biomass in a stepwise manner, to yield a temperature distribution for every consecutive value in the

time domain. Solvent temperature was also computed at every consecutive time value using Equation (3.16). Key model validation steps are presented in APPENDIX A.

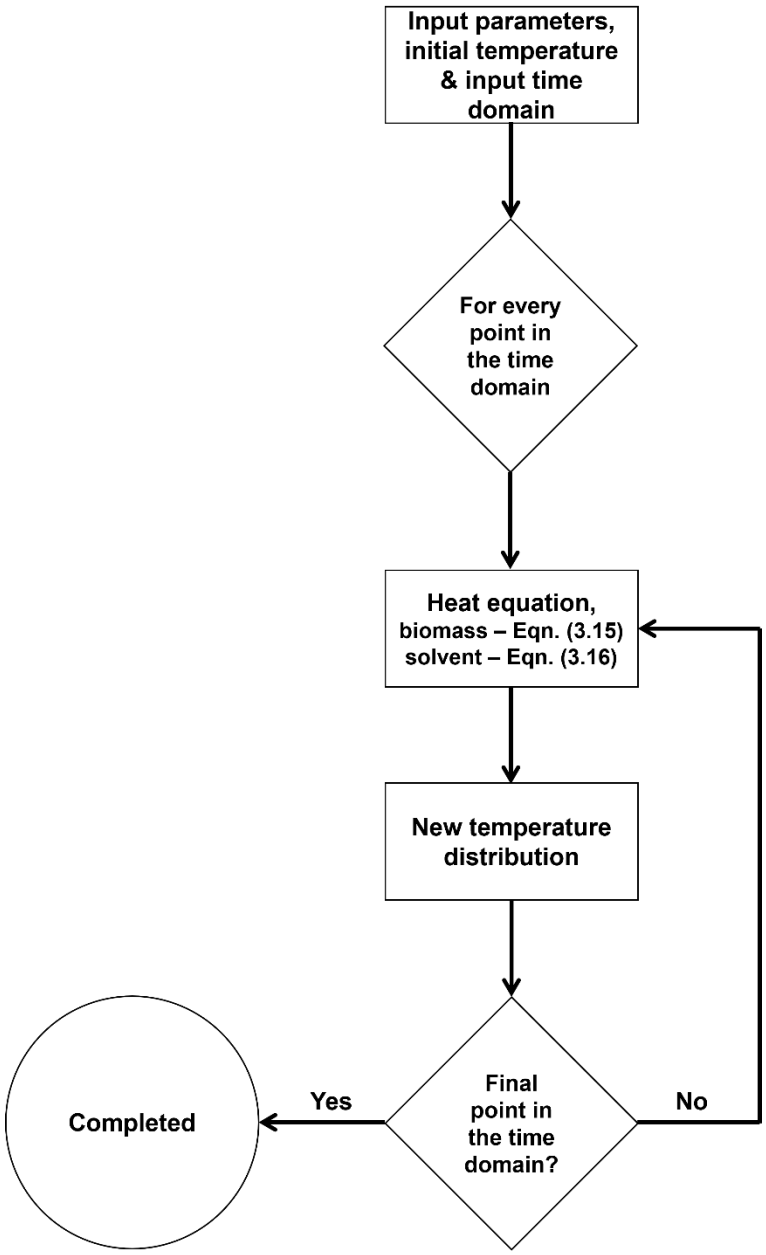


Figure 3.7 – Numerical framework for the heat model

3.3 Predicted temperature distribution

The heat equation was solved for a range of input parameters, thus yielding a series of temperature-time relationships. To characterise the unique effects of the different microwave heating parameters, a single independent parameter was varied for each analysis, while all other parameters were kept constant. Outputs are presented according to the key independent parameters varied.

The investigated parameters were classified as either system-related (describing system properties) or heating-related (describing manipulatable heating parameters). Table 3.1 summarises the typical value ranges and selected baseline values for all parameters. Results are shown in the following subsections.

Parameter & value range	$\varepsilon''_{biomass} = 0 - 30$	$\varepsilon''_{solvent} = 0 - 10$	$\delta_p = 1 - 10$ cm	$k = 0.1 - 1$ $Wm^{-1}K^{-1}$	$C_p = 4$ JgK^{-1}	$S_R = 5 - 30$ mLg^{-1}	$\rho_L = 1000$ kgm^{-3}	Cell dimensions = $25 - 200$ μm	Cell wall thickness = $1 - 10$ μm
Justification	Fair for edibles at 2.45 GHz (Sipahioglu and Barringer, 2003)	Fair for water at 2.45 GHz (Datta, Sumnu and Raghavan, 2005)	Typical order for water (Pueschner, 2015)	Reasonable order for water (Engineering Toolbox, 2003)	Typical for water (Rogers and Mayhew, 1995)	Used empirically (Galan et al., 2017)	Typical for water (NIST, 2017)	Fair with imaging and models (Zamil et al., 2013; Zamil, Yi and Puri, 2017)	Fair (Devlin and Witham, 1983; Pieczywek and Zdunek, 2014)
Selected base value	10	5	1 cm	0.6 $Wm^{-1}K^{-1}$	4 JgK^{-1}	100 mLg^{-1} (See point 1)	1000 kgm^{-3}	Length = 100 μm Width = 50 μm Height = 10 μm	1 μm
Sensitivity analysis in…	Section 3.3.1.1		Section 3.3.1.2	Section 3.3.1.3	Section 3.3.1.4	Section 3.3.1.5	Section 3.3.1.6	Section 3.3.1.7	–

Parameter & value range	$F = 2.45$ GHz	$\lvert E\rvert_0 = 0 - 10^4$ Vm^{-1}	Cell cluster size = 1 cell onwards	$\varepsilon_0 = 8.854 \times 10^{-12} Fm^{-1}$	$T_{initial} = 20$ °C	$T_{saturation} = 100$ °C
Justification	Typical frequency value	Fair for single-mode cavities (Robinson et al., 2010)	–	–	–	Water's normal boiling point
Selected base value	2.45 GHz	10^4 Vm^{-1}	$1 - 1000$ $cells$	8.854×10^{-12} Fm^{-1}	20 °C	100 °C
Sensitivity analysis in…	Section 3.3.2.1	Section 3.3.2.2	All analyses	–	–	–

1- The selected value is intended to provide consistency with the work in Chapter 5.

Table 3.1 – Typical value ranges and selected baseline values for the various model parameters

3.3.1 System-related parameters

3.3.1.1 Effect of dielectric loss factor (ε'')

Initially, a single-cell system was considered where $\varepsilon''_{biomass}$ was fixed at 25, and $\varepsilon''_{solvent}$ was varied from 0 ($\Delta\varepsilon'' = 25$) to 50 ($\Delta\varepsilon'' = -25$). This is not intended to represent a particular physical condition, but it will span the full range from a microwave transparent solvent to one that absorbs much more strongly than the biomass itself. Figure 3.8 shows the temperature increase with time for both the single cell and the solvent for the two extreme cases of $\Delta\varepsilon''$.

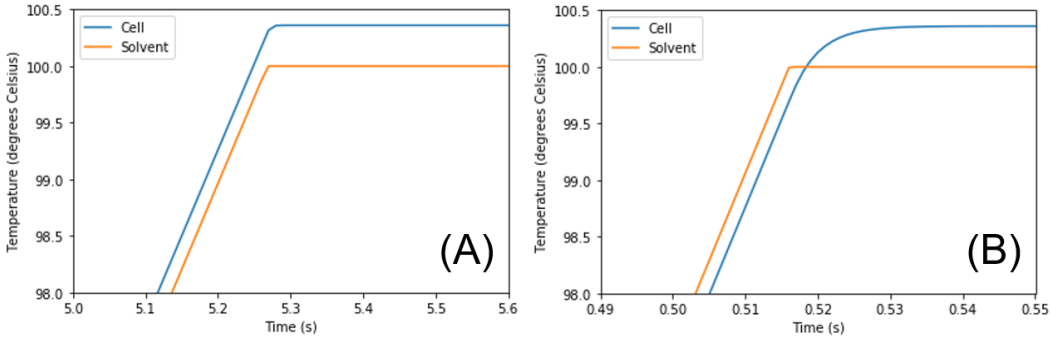


Figure 3.8 – Temperature-time profile for a single-cell biomass-solvent system; (A) $\Delta\varepsilon'' = 25$; (B) (A) $\Delta\varepsilon'' = -25$

Figure 3.8A shows that the cell is at a higher temperature than the solvent during the heat-up period, which is to be expected given that the solvent is microwave-transparent, and only heats indirectly due to heat transfer from the cell. The solvent temperature plateaus at the boiling point ($T_{saturation}$) of 100 ℃ and the cell temperature continues to increase. The cell temperature plateaus shortly after the solvent temperature, when equilibrium is established between the input energy due to microwave heating and the output energy due to conventional heat transfer to the surrounding solvent. Under the conditions applied here, a cell temperature of around 100.4 ℃ is required to obtain a balance between the input and output energies, thus achieving a comprehensive thermal steady state in the cell-solvent system.

For the microwave-absorbent solvent, Figure 3.8B shows that the solvent temperature is higher than the cell temperature during the heat-up period, which is to be expected since the solvent absorbs more microwave energy than the cell. The solvent attains its $T_{saturation}$ in around 0.5 s in this case, compared to 5 s for the case incorporating a microwave-transparent solvent. However, the cell temperature continues to rise beyond 100 ℃ in Figure 3.8B, even though it absorbs less microwave

energy than the solvent here. In fact, the cell temperature at steady state is higher in this case than that of the solvent, despite the fact it had been lower during the heat-up phase. Interestingly, the steady state cell temperatures in Figure 3.8A-B are the same (around 100.4 ℃), which could be illogical initially, but it results from a constant $\varepsilon''_{biomass}$, which, in turn, yields the same input microwave energy to the cell in both cases. It is, therefore, seen that the temperature distribution at thermal steady state and given input power, is only a function of $\varepsilon''_{biomass}$ but not of $\varepsilon''_{solvent}$.

This observation was further validated through analysing multicellular biomass. When multiple cells are considered, there is a gradient in temperature with a maximum around the centre of the cluster and a minimum at the biomass-solvent boundary. The maximum temperature does not occur exactly at the centre due to microwave attenuation (section 3.2.2), but nonetheless it is very close in this case. Figure 3.9 shows an example of temperature distribution at steady state for a biomass system consisting of 1000 cells, with $\varepsilon''_{biomass} = 20$ and $\varepsilon''_{solvent} = 5$. In this case, the temperature difference between the centre of the cell cluster and the surrounding solvent is around 1 ℃.

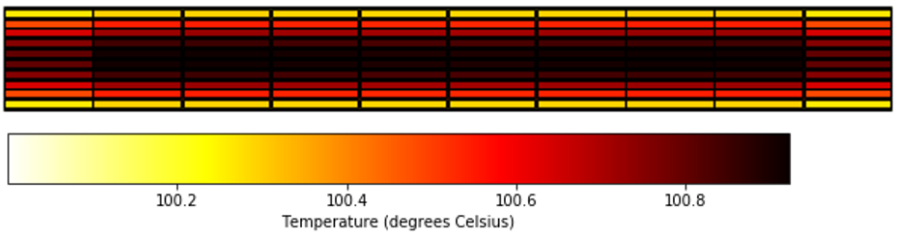


Figure 3.9 – Steady state temperature distribution of an XZ cross-section of 1000-cell biomass-solvent system. Dielectric loss factors of biomass and solvent are 20 and 5, respectively

Table 3.2 summarises the maximum temperature difference between the biomass and the solvent at thermal steady state (ΔT_{max}), for different-sized biomass cell clusters and different values of $\varepsilon''_{biomass}$ and $\varepsilon''_{solvent}$. Table 3.2 also presents the time required in each case, to achieve 95% of the steady state temperature distribution (t_{95-T}). All other parameters are fixed as shown in Table 3.1.

	Number of cells		
$\boldsymbol{\varepsilon''_{biomass}}$	**1 cell**	**125 cells**	**1000 cells**
0	0.000 / 0.000;	0.000 / 0.000;	0.000 / 0.000;

	5.725 / 1.432	5.742 / 1.452	5.828 / 1.525
10	0.012 / 0.012; 3.990 / 1.292	0.138 / 0.138; 4.033 / 1.315	0.461 / 0.461; 4.111 / 1.388
20	0.024 / 0.024; 3.062 / 1.176	0.276 / 0.276; 3.110 / 1.202	0.922 / 0.922; 3.185 / 1.276
25	0.030 / 0.030; 2.743 / 1.126	0.345 / 0.345; 2.792 / 1.152	1.153 / 1.153; 2.867 / 1.226
	ΔT_{max} (°C); t_{95-T} (s) $(\varepsilon''_{solvent} = 5$ / $\varepsilon''_{solvent} = 20)$		

Table 3.2 – Maximum temperature difference between biomass and solvent at thermal steady state, and time required to achieve 95% of steady state, for variable dielectric loss factors and cell cluster size

It is clear from Table 3.2 that, ΔT_{max} only increases with the cluster size and with $\varepsilon''_{biomass}$, but it is independent of $\varepsilon''_{solvent}$. In this analysis, the largest ΔT_{max} was just below 1.2 ℃ for a 1000-cell cluster and $\varepsilon''_{biomass}$ of 25. At steady state and regardless of $\varepsilon''_{solvent}$, the biomass temperature will be higher than that of the solvent given that $\varepsilon''_{biomass}$ is larger than zero, and that the biomass saturation temperature is higher than $T_{saturation}$. The saturation temperature of the biomass is likely to be higher than $T_{saturation}$, which is due to the presence of solutes, but also the tendency of biomasses to resist any expansion due to internal boiling, thereby inducing high pressures within their structures (Chapter 5). On the other hand, ΔT_{max} increases with cell cluster size due to the decrease in surface area-to-volume ratio of the biomass, which limits its contact with the solvent, and introduces further resistance to heat transfer that can only be overcome through raising the temperature gradient.

On the other hand, t_{95-T} is also influenced by the different parameters, as it increases with the cell cluster size and decreases with raising $\varepsilon''_{biomass}$ and $\varepsilon''_{solvent}$. A larger cell cluster indicates larger and heavier biomass material immersed in a solvent of a larger volume (due to constant solvent-to-solid ratio); hence, it is intuitive that t_{95-T} should increase with the cell cluster size. On the other hand, increasing $\varepsilon''_{biomass}$ and $\varepsilon''_{solvent}$ indicates an increase in the extent of microwave volumetric heating in the system; therefore, the system approaches steady state much faster. Nevertheless, t_{95-T} remains within the order of seconds for all investigated conditions, which is well within the frame of empirical studies using an input microwave power

corresponding to $|E|_0 = 10^4\ Vm^{-1}$ (Adam et al., 2017; Beneroso et al., 2017; Shepherd et al., 2018) (see section 3.3.2.2).

The observations made here question the link established in literature between dielectric properties and temperature distribution, where it is proposed that microwaves always induce higher temperature in the phase possessing higher dielectric loss factor (ε''). It is shown here that, the temperature distribution is only proportional to the distribution of dielectric loss factor (ε'') during the heat-up phase. However, when the system is at thermal steady state, the biomass attains a higher temperature than the solvent provided $\varepsilon''_{biomass} > 0$. As such, the influence of dielectric property distribution (i.e., whether $\varepsilon''_{biomass} > \varepsilon''_{solvent}$) on the temperature distribution during an extraction process, depends on how fast thermal steady state can be achieved compared with the diffusion rate in the system. If the heating and diffusion rates are comparable as with some empirical studies (Amarni and Kadi, 2010; Calinescu et al., 2017), then temperature distribution during extraction will depend on the distribution of dielectric properties. However, if thermal steady state is achieved much faster than the time needed for diffusion (Mao et al., 2019; Nkhili et al., 2009), then the biomass is likely to possess a higher temperature than the solvent for most of the extraction process, even if $\varepsilon''_{biomass} < \varepsilon''_{solvent}$. This leads to an important conclusion, which is that enhanced extraction under microwave heating when thermal steady state is achieved rapidly, is unlikely to be caused by the distribution of dielectric properties as suggested by some studies (Galan et al., 2017; Lee et al., 2016). According to these studies, microwaves enhance biomass extraction when the condition $\varepsilon''_{biomass} > \varepsilon''_{solvent}$ is satisfied, and this would typically occur beyond some threshold extraction temperature. As demonstrated here, this is a reasonable hypothesis when the heating and diffusion rates are comparable, but if heating is much faster, then the biomass will likely possess higher temperatures even if $\varepsilon''_{biomass} < \varepsilon''_{solvent}$ (provided $\varepsilon''_{biomass} > 0$). Therefore, future empirical studies should investigate the effect of dielectric property distribution on extraction at variable input microwave powers. This has not been addressed sufficiently in literature.

3.3.1.2 <u>Effect of penetration depth (δ_p)</u>

Microwave penetration depth (δ_p) was varied to understand its effect on the magnitude and distribution of temperature in biomass-solvent systems. Table 3.3

presents ΔT_{max} and t_{95-T} for different-sized biomass cell clusters and different δ_p values. All other parameters are fixed as shown in Table 3.1.

	Number of cells		
$\boldsymbol{D_p\ (cm)}$	**1 cell**	**125 cells**	**1000 cells**
0.1	0.011; 4.074	0.110; 4.323	0.297; 4.647
1	0.012; 3.990	0.138; 4.033	0.461; 4.111
5	0.012; 3.983	0.142; 4.005	0.483; 4.055
	$\Delta \boldsymbol{T_{max}}$ (°C); $\boldsymbol{t_{95-T}\ (s)}$		

Table 3.3 – Maximum temperature difference between biomass and solvent at thermal steady state, and time required to achieve 95% of steady state, for variable microwave penetration depths and cell cluster size

ΔT_{max} decreases and t_{95-T} increases as δ_p is decreased. Smaller penetration depths indicate reduced ability of microwaves to penetrate the system and induce volumetric heating; hence, smaller biomass temperatures and a delayed approach to steady state are observed. This effect is more pronounced with larger cell clusters, due to the increased size of the biomass-solvent system which the microwaves need to penetrate. Nevertheless, t_{95-T} remains well within the timeframes reported in empirical studies (section 3.3.2.2).

In addition to its effect on ΔT_{max}, altering δ_p also affects the steady state temperature distribution in the biomass. Figure 3.10 shows that, lowering δ_p decreases ΔT_{max} (as also shown in Table 3.3), but it also dislocates this maximum temperature towards regions closer to the biomass-solvent boundary.

The effects exercised by δ_p are more important to consider in large biomass-solvent systems; however, the effect of δ_p is small here given the scale of the current model, especially given that δ_p of water is typically within the order of 1 cm (Pueschner, 2015).

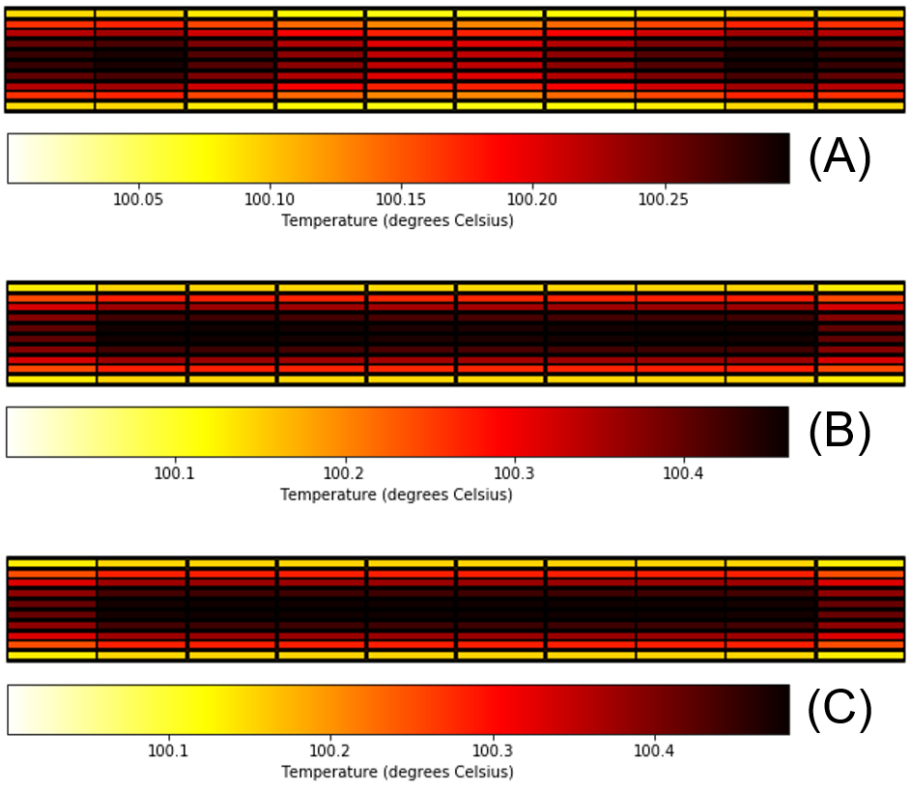


Figure 3.10 - Steady state temperature distribution of an XZ cross-section of 1000-cell biomass-solvent system; penetration depth = (A) 0.1 cm; (B) 1 cm; (C) 5 cm

3.3.1.3 Effect of thermal conductivity (k)

Table 3.4 summarises ΔT_{max} and t_{95-T} for variable thermal conductivity (k) and different-sized biomass cell clusters. All other parameters are fixed as shown in Table 3.1.

	Number of cells		
$\boldsymbol{k}$ $(\boldsymbol{Wm^{-1}K^{-1}})$	**1 cell**	**125 cells**	**1000 cells**
0.050	0.144; 4.009	1.656; 4.338	5.533; 5.294
0.075	0.096; 4.002	1.104; 4.219	3.689; 4.838
0.100	0.072; 3.998	0.828; 4.162	2.766; 4.618
0.200	0.036; 3.993	0.414; 4.081	1.383; 4.302
0.300	0.024;	0.276;	0.922;

	3.991	4.056	4.203
0.400	0.018; 3.991	0.207; 4.044	0.692; 4.156
0.600	0.012; 3.990	0.138; 4.033	0.461; 4.111
1.000	0.007; 3.990	0.083; 4.024	0.277; 4.076
	ΔT_{max} (°C); t_{95-T} (s)		

Table 3.4 – Maximum temperature difference between biomass and solvent at thermal steady state, and time required to achieve 95% of steady state, for variable thermal conductivity and cell cluster size

t_{95-T} increases with smaller k values and with larger biomass cell clusters, due to the increased resistance to heat transfer that the changes in these two parameters bring about to the system. Once again, t_{95-T} remains in the order of seconds, well within the timeframes reported in empirical studies (section 3.3.2.2).

However, it is evident from the results that, ΔT_{max} is also influenced by changes in k, although thermal conductivity is typically only concerned with the rates of/ resistance to heat flow. Therefore, to validate this outcome shown in Table 3.4, the heat equation (Equation (3.8)) was written to represent the steady state condition, as follows:

$$\nabla^2 T + \frac{1}{k}\dot{Q_M} = 0 \qquad \textbf{(3.17)}$$

At steady state, the microwave volumetric heating term in Equation (3.17) depends on thermal conductivity, as it gets larger with lower k and smaller with higher k. A larger microwave volumetric heating term requires larger temperature gradients to balance the expression as needed. Furthermore, if the biomass-solvent system is heated conventionally but not with microwaves (i.e., $\dot{Q_M} = 0$), then k is dropped from Equation (3.17), and the expression would, thereby, represent a classical steady state condition independent of thermal conductivity. Therefore, unlike the case with conventional heating, k affects the steady state temperature under microwave heating.

In Table 3.4, for a 1000-cell cluster a ΔT_{max} of over 5.5 ℃ is apparent when $k = 0.05\ Wm^{-1}K^{-1}$, compared to just 0.28 ℃ when $k = 1.00\ Wm^{-1}K^{-1}$. ΔT_{max}

increases nonlinearly as k is decreased, with the effect being more pronounced for larger cell clusters, due to the increased thermal insulation brought about by the larger number of cells, but also the reduced contact area between the biomass and the solvent. When k is low, volumetric heating occurs much faster than conventional heat transfer; in other words, each phase in the system tends to heat volumetrically in a more intense fashion than the rate at which it loses heat to the adjacent phases. Therefore, energy distribution becomes less even in the system, eventually leading to larger temperature gradients at thermal steady state.

Compared to the effects of dielectric loss factor (ε'') shown in Table 3.2, the magnitudes of ΔT_{max} in the current analysis are much higher as they increase nonlinearly with decreasing k. This shows that k possesses a strong effect on the temperature gradients in biomass-solvent systems. This effect is likely more important to consider than that of ε'', due to the already large differences in ΔT_{max} observed at the current cellular scale. However, the effects of k on temperature distribution and, thereby, on microwave extraction in biomass-solvent systems, have not been discussed widely in literature. Instead, focus has been drawn exclusively on parameters such as dielectric properties and penetration depth, both in theory and in experiments/modelling (Chan et al., 2016; Kostas, Beneroso and Robinson, 2017; Lee et al., 2016; Meredith, 1998). This reaffirms the lack of understanding of thermal patterns induced in biomass-solvent systems with microwave heating. Future studies in this field should consider thermal conductivity as a key parameter with significant potential impacts.

3.3.1.4 Effect of specific heat capacity (C_p)

Table 3.5 summarises ΔT_{max} and t_{95-T} for variable specific heat capacity (C_p) and different-sized biomass cell clusters. All other parameters are fixed as shown in Table 3.1.

	Number of cells		
C_p $(Jg^{-1}K^{-1})$	**1 cell**	**125 cells**	**1000 cells**
2	0.012; 1.995	0.138; 2.016	0.461; 2.055
4	0.012; 3.990	0.138; 4.033	0.461; 4.111

6	0.012; 5.985	0.138; 6.049	0.461; 6.166
	ΔT_{max} (°C); t_{95-T} (s)		

Table 3.5 – Maximum temperature difference between biomass and solvent at thermal steady state, and time required to achieve 95% of steady state, for variable specific heat capacity and cell cluster size

As seen in Table 3.5, only t_{95-T} is affected by C_p while ΔT_{max} remains independent of this parameter. C_p is concerned with the amount of energy needed by the system to achieve its steady state temperature. The higher the energy required by the system at a fixed input power, the longer the system would take to approach steady state, although its steady state temperature remains unchanged. This analogy is consistent with the results seen in Table 3.5, but nonetheless it should be noted that t_{95-T} remains within the timeframes reported in empirical studies for all investigated conditions (section 3.3.2.2).

3.3.1.5 Effect of solvent-to-solid ratio (S_R)

Table 3.6 summarises ΔT_{max} and t_{95-T} for variable solvent-to-solid ratio (S_R) and different-sized biomass cell clusters. All other parameters are fixed as shown in Table 3.1.

	Number of cells		
S_R $(mL g^{-1})$	**1 cell**	**125 cells**	**1000 cells**
50	0.012; 3.610	0.139; 3.651	0.469; 3.726
100	0.012; 3.990	0.138; 4.033	0.461; 4.111
200	0.012; 4.282	0.136; 4.321	0.451; 4.399
	ΔT_{max} (°C); t_{95-T} (s)		

Table 3.6 – Maximum temperature difference between biomass and solvent at thermal steady state, and time required to achieve 95% of steady state, for variable solvent-to-solid ratio and cell cluster size

S_R dictates the volume of solvent surrounding the biomass; hence, with larger S_R the biomass-solvent system is larger, and vice versa. Therefore, the results shown in Table 3.6 are to be expected for both ΔT_{max} and t_{95-T}. With larger S_R, ΔT_{max} decreases slightly due to an increase in microwave attenuation, as the size of the

system increases. Also, with larger S_R the system takes longer to approach steady state due to its larger volume. Nevertheless, all t_{95-T} values reported here remain within the timeframes reported in empirical studies (section 3.3.2.2).

3.3.1.6 Effect of density (ρ_L)

Table 3.7 summarises ΔT_{max} and t_{95-T} for variable density (ρ_L) and different-sized biomass cell clusters. All other parameters are fixed as shown in Table 3.1.

	Number of cells		
$\boldsymbol{\rho_L}$ $\boldsymbol{(kgm^{-3})}$	**1 cell**	**125 cells**	**1000 cells**
500	0.012; 1.805	0.139; 1.825	0.469; 1.863
1000	0.012; 3.990	0.138; 4.033	0.461; 4.111
2000	0.012; 8.564	0.136; 8.643	0.451; 8.798
	$\Delta \boldsymbol{T_{max}}$ (°C); $\boldsymbol{t_{95-T}}$ $\boldsymbol{(s)}$		

Table 3.7 – Maximum temperature difference between biomass and solvent at thermal steady state, and time required to achieve 95% of steady state, for variable density and cell cluster size

Increasing ρ_L signifies an increase in the masses of the biomass and the solvent, and a further increase in the volume of solvent due to the constant solvent-to-solid ratio (S_R) imposed on the system. Therefore, as seen in Table 3.7 ΔT_{max} decreases slightly at larger ρ_L, due to an increase in microwave attenuation, as the size of the system increases. Furthermore, t_{95-T} increases with ρ_L due to the larger volume of the system, but it remains within the timeframes reported in empirical studies (section 3.3.2.2).

3.3.1.7 Effect of cell dimensions

Table 3.8 summarises ΔT_{max} and t_{95-T} for variable cell dimensions and different-sized biomass cell clusters. All other parameters are fixed as shown in Table 3.1.

	Number of cells		
Cell length; width; height (μm)	**1 cell**	**125 cells**	**1000 cells**

50; 25; 5	0.004; 4.129	0.048; 4.165	0.161; 4.187
100; 50; 10	0.012; 3.990	0.138; 4.033	0.461; 4.111
200; 100; 20	0.040; 3.750	0.452; 3.873	1.473; 4.173
	ΔT_{max} (°C); t_{95-T} (s)		

Table 3.8 – Maximum temperature difference between biomass and solvent at thermal steady state, and time required to achieve 95% of steady state, for variable cell dimensions and cell cluster size

ΔT_{max} increases with cell volume, which occurs due to an increase in the cell cluster size and a decrease in its surface-area-to-volume ratio. This suppresses heat transfer between the biomass and the solvent; hence, larger temperature gradients are required between the various phases, to balance the input microwave power with conventional heat transfer, thereby achieving thermal steady state.

On the other hand, t_{95-T} generally decreases with increasing cell volume, due to the larger temperature gradients induced which accelerate conventional heat transfer, allowing a faster approach to steady state. However, this trend does not always hold in larger biomass cell clusters, where significantly high ΔT_{max} values are required, which may take long to be achieved. This could result in t_{95-T} increasing with the cell volume, even though increasing the volume is normally expected to accelerate conventional heat transfer, thereby allowing steady state to be achieved faster. An example of this from Table 3.8, is where cells in a 1000-cell cluster see an increase in their length from 100 μm to 200 μm. Here, t_{95-T} increases from 4.111 s to 4.173 s, unlike all other cases presented, where t_{95-T} decreases with increasing the cell volume.

Nevertheless, all t_{95-T} values reported here remain within the timeframes reported in empirical studies (section 3.3.2.2).

3.3.2 Heating-related parameters

3.3.2.1 Effect of microwave frequency (F)

Table 3.9 summarises ΔT_{max} and t_{95-T} for variable microwave frequency (F) and different-sized biomass cell clusters. All other parameters are fixed as shown in Table 3.1.

	Number of cells		
$\boldsymbol{F}$ $\boldsymbol{(GHz)}$	**1 cell**	**125 cells**	**1000 cells**
1.45	0.007; 6.741	0.082; 6.799	0.273; 6.887
2.45	0.012; 3.990	0.138; 4.033	0.461; 4.111
3.45	0.017; 2.834	0.194; 2.870	0.649; 2.945
	$\Delta \boldsymbol{T_{max}}$ (°C); $\boldsymbol{t_{95-T}}$ $\boldsymbol{(s)}$		

Table 3.9 – Maximum temperature difference between biomass and solvent at thermal steady state, and time required to achieve 95% of steady state, for variable microwave frequency and cell cluster size

The input microwave power density ($\dot{Q}_M$) is proportional to F (Equation (2.32)); hence, as seen in Table 3.9, ΔT_{max} increases and t_{95-T} decreases as F is increased. All t_{95-T} values reported here remain within the timeframes reported in empirical studies (section 3.3.2.2).

Although the input microwave power can be adjusted by changing F, this is not usually a preferred method in real-world situations. There are several reasons for this (Metaxas and Meredith, 1983), including the dependence of ε'' on F, which dictates the need to select a value for F to maximise ε''; the inability of microwave generators and applicators/cavities to support wide ranges of F values; the limitation on F values allowed for industrial, scientific, and medical (ISM) use, to avoid interference with frequencies used in other applications. Due to this, the input microwave power is commonly characterised with the electric field intensity ($|E|_0$) instead of F. $|E|_0$ is investigated in the next section.

3.3.2.2 Effect of incident electric field intensity ($|E|_0$)

Table 3.10 summarises ΔT_{max} and t_{95-T} for variable incident electric field intensity ($|E|_0$) and different-sized biomass cell clusters. All other parameters are fixed as shown in Table 3.1.

	Number of cells		
$\boldsymbol{\|E\|_0}$ $\boldsymbol{(Vm^{-1})}$	**1 cell**	**125 cells**	**1000 cells**
0	0.000	0.000;	0.000;

	N/A	N/A	N/A
2000	0.000; 99.741	0.006; 100.364	0.018; 100.886
6000	0.004; 11.083	0.050; 11.166	0.166; 11.270
10000	0.012; 3.990	0.138; 4.033	0.461; 4.111
	ΔT_{max} (°C); t_{95-T} (s)		

Table 3.10 – Maximum temperature difference between biomass and solvent at thermal steady state, and time required to achieve 95% of steady state, for variable electric field intensity and cell cluster size

$|E|_0$ is the primary parameter representing the input microwave power (Equation (2.31)). Therefore, it is intuitive that ΔT_{max} increases with $|E|_0$ as seen in Table 3.10, because more microwave energy dissipation within the biomass requires higher temperature gradients with the solvent phase, to increase heat transfer and achieve thermal steady state. In fact, the relationship observed between ΔT_{max} and $|E|_0$ is nearly quadratic, due to the proportionality between power density ($\dot{Q_M}$) and $|E|^2$ in the microwave power density expression (Equation (2.31)).

On the other hand, t_{95-T} is clearly much more sensitive to $|E|_0$ than it is to cell cluster size, $\varepsilon''_{biomass}$, k, and other parameters investigated. As seen in Table 3.10 t_{95-T} varies in multiple orders of magnitude within $0 \leq |E|_0 \leq 10^4$, which is the likely range for single-mode microwave cavities (Robinson et al., 2010). As $|E|_0$ increases from $0\ Vm^{-1}$ to $2 \times 10^3\ Vm^{-1}$ and onwards to $10^4\ Vm^{-1}$, t_{95-T} falls dramatically from infinity to an order of $100\ s$, and then to an order of $1\ s$. This shows that $|E|_0$ is the primary parameter representing microwave power input and the heating rate.

Despite the wide range of t_{95-T} values reported here, a key observation made is that these values match those reported in literature. $\dot{Q_M}$ in microwave extraction studies is typically maintained at low values, usually within the order of $10^6\ Wm^{-3}$. However, other biomass processing techniques such as pyrolysis require much higher $\dot{Q_M}$ values, probably as high as $10^7\ Wm^{-3}$. With $\dot{Q_M} = 10^6\ Wm^{-3}$ and $\dot{Q_M} = 10^7\ Wm^{-3}$, $|E|_0$ is quantifiable at $2 \times 10^3\ Vm^{-1}$ and $10^4\ Vm^{-1}$, respectively, for a dielectric loss factor (ε'') of 5, and this nearly spans the full range of $|E|_0$ values

investigated in Table 3.10. The 100 s order of magnitude reported here for $|E|_0 = 2 \times 10^3\ Vm^{-1}$ and $\dot{Q_M} = 10^6\ Wm^{-3}$, agrees entirely with microwave extraction studies using similar $\dot{Q_M}$ values (Galan et al., 2017; Mao et al., 2019). Furthermore, the 1 s order of magnitude reported for $|E|_0 = 10^4\ Vm^{-1}$ and $\dot{Q_M} = 10^7\ Wm^{-3}$, is also in close agreement with pyrolysis studies using similar $\dot{Q_M}$ values (Adam et al., 2017; Beneroso et al., 2017; Shepherd et al., 2018). This key observation shows that, the predictive capability of the current model extends beyond microwave extraction studies to cover many other applications. This is especially important given the recent advances in biomass processing within solvent media, such as microwave-assisted liquid pyrolysis (Shepherd et al., 2018). According to the author's knowledge, this is the first biomass-solvent model to predict microwave heating and temperature distribution within the full range of physically realistic $|E|_0$ values for single-mode cavities.

3.3.3 Temperature-time plots for selected heating parameters

This section presents a series of temperature-time plots for generated with varying 3 key microwave heating parameters, namely $\varepsilon''_{biomass}$, k, and $|E|_0$. All other parameters are fixed as shown in Table 3.1, and the biomass cell cluster consists of 125 ($5 \times 5 \times 5$) cells. Plots with variable $\varepsilon''_{biomass}$, k, and $|E|_0$ are shown in Figure 3.11, Figure 3.12, and Figure 3.13, respectively.

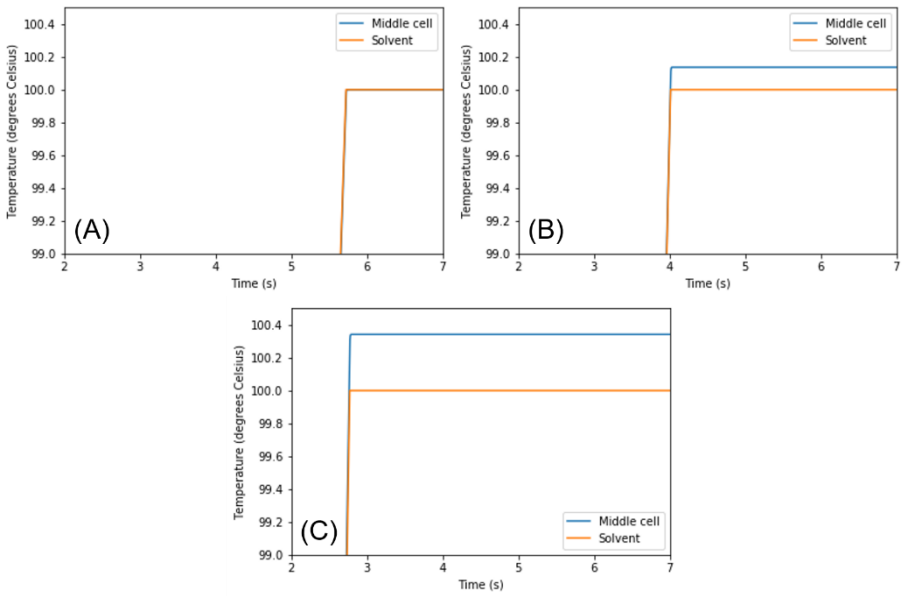


Figure 3.11 – Temperature-time plots for a 125-cell biomass-solvent system with variable biomass dielectric loss factor. Temperatures are shown for the solvent

and a cell located at the middle of the cluster. Dielectric loss factor = (A) 0; (B) 10; (C) 25

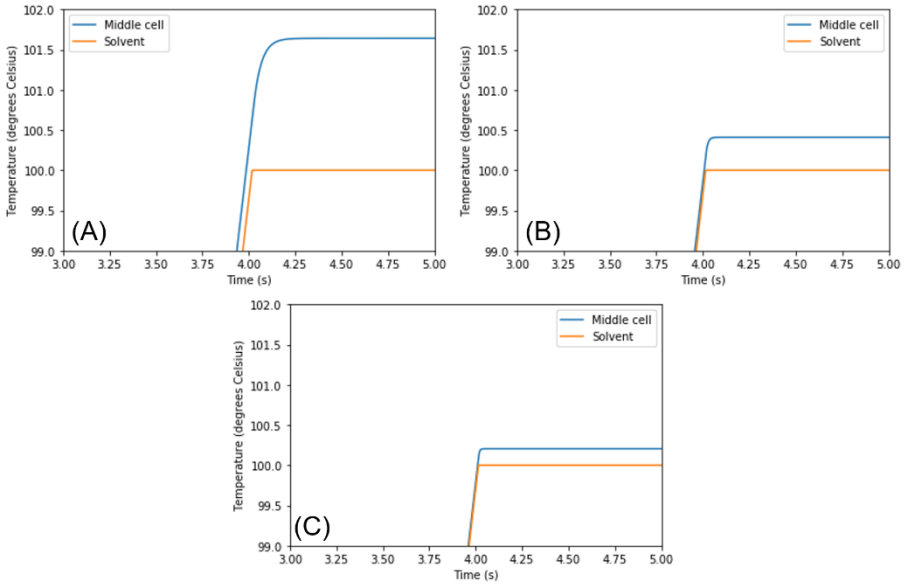


Figure 3.12 – Temperature-time plots for a 125-cell biomass-solvent system with variable thermal conductivity. Temperatures are shown for the solvent and a cell located at the middle of the cluster. Thermal conductivity = (A) 0.05 $Wm^{-1}K^{-1}$; (B) 0.2 $Wm^{-1}K^{-1}$; (C) 0.4 $Wm^{-1}K^{-1}$

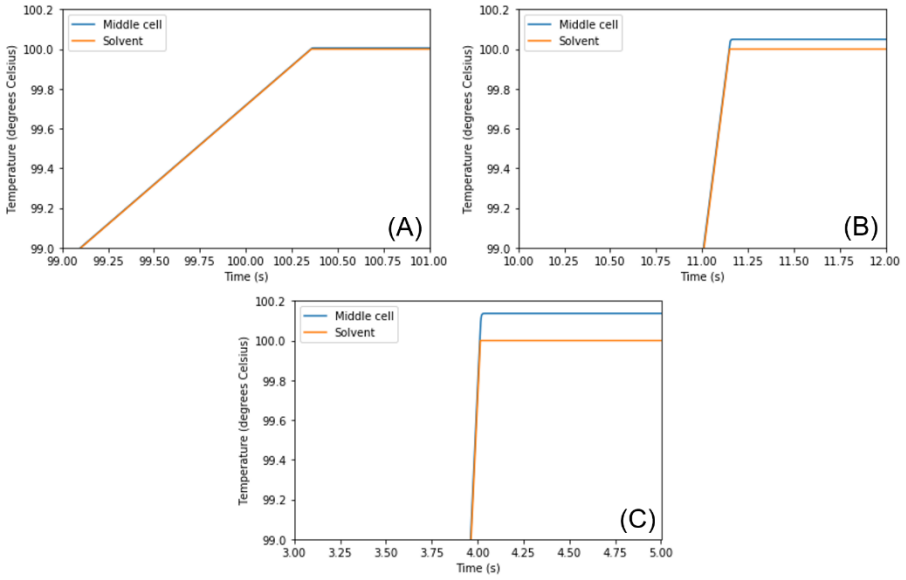


Figure 3.13 – Temperature-time plots for a 125-cell biomass-solvent system with variable incident electric field intensity. Temperatures are shown for the solvent and a cell located at the middle of the cluster. Electric field intensity = (A) 2000 Vm^{-1}; (B) 6000 Vm^{-1}; (C) 10000 Vm^{-1}

3.4 Summary

In this chapter, a new model was developed to describe microwave heating and heat transfer in biomass-solvent systems at the cellular scale. The model explains

quantitatively how temperature gradients arise within clusters of biomass cells, due to competing effects of microwave volumetric heating and conventional heat transfer.

At thermal steady state, a temperature gradient is established in the biomass with a maximum around the centre and a minimum at the biomass-solvent boundary. Different parameters were found to affect the magnitudes of these gradients and the timeframes required to achieve thermal steady state. These parameters include $\varepsilon''_{biomass}$, $\varepsilon''_{solvent}$, δ_p, k, C_p, S_R, ρ_L, cell dimensions, cell cluster size, F, and $|E|_0$. This is the first model dedicated to microwave extraction in biomass-solvent systems at the cellular scale, which incorporates heat transfer alongside microwave heating, but also enables a wide variety of heating parameters to be manipulated.

It has been shown that, regardless of whether $\varepsilon''_{biomass}$ is larger or smaller than $\varepsilon''_{solvent}$, the biomass temperature will be larger than that of the solvent at thermal steady state. This is always true given that the biomass absorbs microwaves, and that its saturation temperature is higher than that of the solvent. Therefore, during an extraction process, the distribution of dielectric properties (i.e., whether $\varepsilon''_{biomass} > \varepsilon''_{solvent}$) does not affect whether the biomass possesses higher temperature than the solvent, unless the rates of heat and mass transfer are comparable (Chapter 7). On the other hand, k has been shown to significantly affect the temperature gradient magnitudes at thermal steady state, perhaps even more significantly than $\varepsilon''_{biomass}$. This is a key conclusion given that, under conventional heating k only affects the heat transfer rate rather than the steady state temperature magnitudes; hence, k has rarely (if at all) been considered in microwave extraction studies. Furthermore, while $|E|_0$ also affects the temperature gradient magnitudes, its effect on the time required to achieve steady state is more significant than any other parameter. This is because, $|E|_0$ describes the input microwave power which, in turn, dictates the heating rate in the system. Although the timeframes required for thermal steady state vary in orders of magnitude with $|E|_0$, it has been shown that these timeframes match those reported in literature, both when $|E|_0$ is low as it is in microwave extraction studies, and when $|E|_0$ is high as it is in microwave pyrolysis studies. This agreement in the wide range of timeframes predicted here and reported in empirical studies, shows that the model can be used in many applications where biomass-solvent systems are processed with microwaves.

This model will be used/further developed in the rest of this thesis to further study microwave extraction in biomass-solvent systems.

3.5 Thesis recap

Chapter 2 discussed the need to develop a first principles' model to conceptualise biomass-solvent extraction, combining various physical elements like heat/mass transfer and cell expansion mechanics.

In the current chapter, a microwave heat transfer model was developed at the cellular scale, which was used to understand temperature distributions in biomass-solvent systems heated with microwaves.

3.6 Nomenclature

Symbols

$\dot{Q_M}$	$\boldsymbol{Wm^{-3}}$	Microwave power density
$Q_{ijk-solvent}$	$\boldsymbol{W}$	Heat exchanged between the solvent and an adjacent phase *ijk*
F	$\boldsymbol{Hz}$	Microwave frequency
ε_0	$\boldsymbol{Fm^{-1}}$	Permittivity of free space
ε''	$-$	Dielectric loss factor
$\Delta\varepsilon''$	$-$	$\varepsilon''_{biomass} - \varepsilon''_{solvent}$
$\lvert E \rvert$	$\boldsymbol{Vm^{-1}}$	Electric field intensity
k	$\boldsymbol{Wm^{-1}K^{-1}}$	Thermal conductivity
T	$\boldsymbol{K}$	Temperature
$T_{initial}$	$\boldsymbol{K}$	Initial temperature
$T_{saturation}$	$\boldsymbol{K}$	Saturation temperature of the solvent
ΔT_{max}	$\boldsymbol{K}$	Maximum temperature difference at steady state
t	$\boldsymbol{s}$	Time
t_{95-T}	$\boldsymbol{s}$	Time required to achieve 95% of thermal steady state
δt	$\boldsymbol{s}$	Time-step for the numerical heat analysis
ρ_L	$\boldsymbol{kgm^{-3}}$	Density
C_p	$\boldsymbol{Jg^{-1}K^{-1}}$	Specific heat capacity
β	$\boldsymbol{m^2s^{-1}}$	Thermal diffusivity/heat transfer coefficient; $\beta = k/\rho_L C_p$
δ_p	$\boldsymbol{m}$	Penetration depth
N	$\boldsymbol{mol}$	Molar quantity
S_R	$\boldsymbol{mLg^{-1}}$	Solvent-to-solid ratio

Subscripts

$()_{biomass}$	Biomass property
$()_{solvent}$	Solvent property
$()_0$	Incident/initial value
$()_x$	Applicable parallel to the *x-direction*
$()_y$	Applicable parallel to the *y-direction*
$()_z$	Applicable parallel to the z-*direction*
$()_{ijk}$	Property of the spatial numerical point ijk, i in the *x-direction;* j in the y-*direction;* k in the z-*direction*

4 MASS TRANSFER UNDER TEMPERATURE GRADIENT

The aim of this chapter is to characterise the effect of temperature on mass transfer, specifically how temperature gradient affects the equilibrium condition. This is a key step towards understanding how microwave heating influences extraction patterns in biomass-solvent systems compared with conventional heating. This chapter will utilise relevant concepts of statistical mechanics and thermodynamics to characterise mass equilibrium, offering a novel approach in the biomass extraction and processing fields. Furthermore, chemical potential will be expressed mathematically so it can be implemented later in kinetic mass transfer analyses.

This chapter has contributed towards publishing Robinson et al. (Robinson et al., 2019). The format of this chapter is as follows:

4.1 Introduction 89
4.2 Review: statistical interpretation of thermodynamic systems 91
4.2.1 Basic concepts and assumptions 91
4.2.2 Microstates and macrostates 91
4.2.3 Equilibrium from a statistical viewpoint 94
4.2.3.1 The microcanonical ensemble 94
4.2.3.2 The condition at equilibrium 95
4.2.4 Validation against classical thermodynamics 99
4.3 Equilibrium under a temperature gradient 101
4.3.1 Modified microcanonical ensemble 101
4.3.2 Temperature-induced volume and mass transfer 105
4.3.3 How transfer phenomena increase entropy 111
4.4 Chemical potential 114
4.4.1 The Gibbs-Duhem argument 115
4.4.2 Derivation for impure components 115
4.5 Summary 119
4.6 Thesis recap 120
4.7 Nomenclature 121

4.1 Introduction

It has been shown in Chapter 3 that, in biomass-solvent systems heated with microwaves, a thermal steady state condition comprises temperature gradients between the biomass and the solvent. This is due to the unique microwave heating patterns with which energy is delivered directly to the biomass through radiation, bypassing the solvent phase. As a result, the balance constituted between microwave volumetric heating and conventional heat transfer brings about a constant, but not necessarily uniform, temperature distribution in the system (i.e., temperature gradients).

As discussed in section 3.1, although enhanced extraction observed under microwave heating is commonly attributed to the unique heating patterns, this is rarely done quantitatively, and so the physical mechanisms underpinning these observations are poorly understood. Chapter 3 has presented, for the first time, a detailed quantitative insight of microwave heating in biomass-solvent systems at the cellular scale. However, to establish the link between thermal patterns and extraction, there is still a need to understand an underlying link between temperature and mass transfer. The aim of this chapter is to characterise such a link which, if understood at equilibrium, can then be used in kinetic mass transfer analysis, to characterise the differences between microwave and conventional heating techniques on extraction patterns. Such a link can be envisaged from concepts like the Ludwig-Soret effect, a widely discussed mechanism in which temperature gradients are deemed responsible for inducing diffusion in convection-free settings, thereby separating mixtures as lighter components migrate more readily towards higher temperature regions (Kishikawa et al., 2012; Koyama and Tsukada, 2021; Rahman and Saghir, 2014). Furthermore, the link between temperature and mass transfer has also been attempted in some biomass-solvent extraction studies. A notable example is the attempt to establish such a link through a thermodynamic parameter known as the chemical potential (μ) (Lee et al., 2016). This is arguably the most fundamental approach to explaining mass transfer, given that the chemical potential (μ) adjoins different diffusion drivers (i.e., gradients in activity, pressure, and temperature) into a single mathematical expression (Wijmans and Baker, 1995). It follows that, concepts like Fick's Law, osmotic pressure, and the Ludwig-Soret effect, merely represent special cases in mass transfer obtainable from a principal chemical potential (μ) expression

(see Chapter 5, section 5.3.1.1.1). Despite the work by Lee et al. (Lee et al., 2016), other attempts to describe a link between temperature and diffusion using the chemical potential (μ) are rare generally, but more importantly, they are very scarce (if any exist) in the biomass processing and biomass-solvent extraction fields. Therefore, this work attempts to characterise the relationship between temperature gradients and mass transfer from a fundamental perspective, using principles of statistical mechanics and thermodynamics. This will be attempted here with specific emphasis on biomass-solvent extraction, where the need is imminent to understand diffusion under microwave heating, but such understanding is yet to be formulated. As explained in Chapter 2 (section 2.2), developing such understanding is vital to attain the ability to predict the performance of microwaves, which would then enable effective process industrialisation. Nonetheless, it is also hoped that this work will benefit numerous other fields, which also may require to formulate an understanding of the fundamental link between temperature and mass transfer.

Statistical mechanics is arguably the most fundamental study in classical physics concerned with particle dynamics; therefore, using this to achieve the required understanding does not only enable validating the existing attempts in literature (e.g., (Lee et al., 2016)), but it also provides a logical inference of the underpinning processes beyond mere mathematical derivation. Furthermore, should such basic understanding be thoroughly described for mass transfer, it might then be possible to predict various diffusion scenarios beyond those that are currently known (e.g., Fick's law and osmotic pressure), which would undoubtedly be of huge benefit to many scientific fields. As discussed above, the field of biomass-solvent extraction still lacks basic characterisation of mass transfer mechanisms, which adds to the importance of the current work as a first endeavour, attempting to introduce systematic understanding of mass transfer under temperature gradients, induced by microwave heating.

This chapter is divided into three sections: section 4.2 introduces/summarises basic concepts of statistical mechanics used in this work; section 4.3 discusses the likely condition for mass equilibrium under temperature gradient; section 4.4 derives an expression for the chemical potential quantity (μ).

4.2 Review: statistical interpretation of thermodynamic systems

This section summarises basic concepts of statistical mechanics relevant to this work. These concepts include the fundamental assumptions; the idea of microstates and macrostates; a description of equilibrium as depicted in the microcanonical ensemble; and finally, a mathematical validation of the arguments presented against classical thermodynamics.

4.2.1 Basic concepts and assumptions

Consider a thermodynamic system completely isolated from its surroundings. The system is large enough for individual particles to be observed and counted, and for a finite total number of particles to be identified (Reif, 1965). Furthermore, the total energy of the system can be made equal to the summation of the energies of any envisaged subsystems; in other words, non-ideal behaviour or any interactive energies (e.g., potential energies) can be neglected (Chandler, 1987; Reif, 1965).

From the two assumptions above, the system contains numerous particles collectively incorporating a given total energy. An average energy can be described for the system, but this value does not apply to each individual particle. Instead, this value represents a collection of particles at a macroscopic scale, while individual particles may still occupy different energy levels and exhibit variable momenta. To understand why certain average values are observed macroscopically at given conditions, particles should be treated statistically to characterise the probability distributions of the different possible states of the system. This is the fundamental purpose of statistical mechanics.

This work will investigate probability distributions at thermodynamic equilibrium, which is a condition of the system where all macroscopic parameters are independent of time (Bowley and Sanchez, 1999). Such parameters include average kinetic energy, temperature, pressure, average momentum, etc, but not necessarily the states occupied by individual particles. When the average macroscopic parameters are constant, it is intuitive that the probability distribution functions describing the system are also independent of time.

4.2.2 Microstates and macrostates

Any given thermodynamic system has a range of accessible states, meaning that there exists a finite number of ways in which the constituents can be arranged. For instance, if the total energy is a finite value, all individual particles are bound by this

upper limit, as none can possess a higher energy than the total. Also, if the total volume is a given value, no individual particle is permitted to occupy a volume larger than the limit imposed onto the system.

The accessible states of a system are described by its microstates and macrostates. As discussed in literature (Bowley and Sanchez, 1999), a microstate is a measure of the different possible outcomes (for instance, energy distribution amongst particles) while accounting for the alternative ways/arrangements in which each outcome can be achieved (i.e., permutations). On the other hand, while a macrostate is also a measure of the different possible outcomes, it disregards the alternative ways in which each outcome can be achieved (i.e., combinations). For example, consider an exercise where a fair coin is tossed twice, and the outcomes are observed. Denoting a heads' outcome as "H" and a tails' outcome as "T", the four possible outcomes of this exercise are HH, HT, TH, and TT. These four outcomes are microstates where not only the overall result is observed, but also the arrangement in which H and T appear is considered. On the other hand, the macrostates of the exercise are either two H's, two T's, or one H and one T, disregarding the ways in which the outcomes can be arranged. Given that both coin tosses are independent events, all microstates are equally probable, yet the macrostate with one H and one T is more probable than the other two macrostates, because it incorporates two contributing microstates rather than one. This is analogous to a fundamental postulate of statistical mechanics, which states that all microstates accessible to a system are equally probable at thermodynamic equilibrium, yet the most probable macrostate is that which incorporates the largest number of contributing microstates (Bowley and Sanchez, 1999).

Consider N particles in a system, each of which can occupy energy states within a range of discrete integer values from 1 to ε. The number of particles occupying a given energy state e (i.e., $1 \leq e \leq \varepsilon$) is N_e, while all other particles occupy energy states other than e. The total number of accessible microstates of the system is, therefore, equal to ε^N, and given that all microstates are equally likely, the probability of any given microstate is ε^{-N}. Since it is assumed that occupying a state is independent of all other possible outcomes, the probability of any given macrostate follows a binomial distribution function, shown in Equation (4.1) (Eastman, 2019; Reif, 1965). In this expression, the macrostate probability in question describes the likelihood of achieving N_e particles in the system each occupying energy state e, where it does not

matter which particles exactly occupy this energy state (i.e., arrangement is indifferent to the observer). This probability ($p(N_e)$) is a function of the probability of achieving any given microstate incorporating N_e particles (i.e., ε^{-N}), but also the probability of obtaining $N - N_e$ particles with any energy state other than e. This is then multiplied by a binomial factor (${}^{N}C_{N_e}$) representing the number of combinations in which this microstate can be repeated in different arrangements.

$$p(N_e) = {}^{N}C_{N_e}\left(\frac{1}{\varepsilon}\right)^{N_e}\left(1-\frac{1}{\varepsilon}\right)^{N-N_e} \quad \textbf{(4.1)}$$

The binomial factor ${}^{N}C_{N_e}$ can be expressed as shown in Equation (4.2), and for large values of N and N_e, Stirling's approximation can be used to estimate the factorials in N and N_e (Bowley and Sanchez, 1999), although this has not been applied here.

$${}^{N}C_{N_e} = \frac{N!}{N_e!\,(N-N_e)!} \quad \textbf{(4.2)}$$

Figure 4.1 shows the probability distribution of N_e where $0 \leq N_e \leq N$, for variable ε and N. In all cases presented, the most probable macrostate depends on the value of ε; when $\varepsilon = 2$, 50% of all particles occupy the energy state e (i.e., $N_e = 0.5N$), which is to be expected since there are two accessible energy states per particle. Similarly, with $\varepsilon = 3$ the most probable macrostate comprises $N_e = 0.33N$, whereas with $\varepsilon = 1.5$ the most probable macrostate is where $N_e = 0.67N$. However, as seen in Figure 4.1, it is possible to attain macrostates other than the most probable one, but this deviation from the most probable macrostate (the mean) shrinks considerably as N increases from 50 to 10000. Therefore, at large scales where the number of particles is at least of the order of Avogadro's constant, variations about the mean are extremely small and the most probable macrostate is overwhelmingly more probable than any other macrostate. Hence, at experimental scales the measurable average quantities describing the system are reproducible, explaining why the laws of classical thermodynamics hold true in real-world situations.

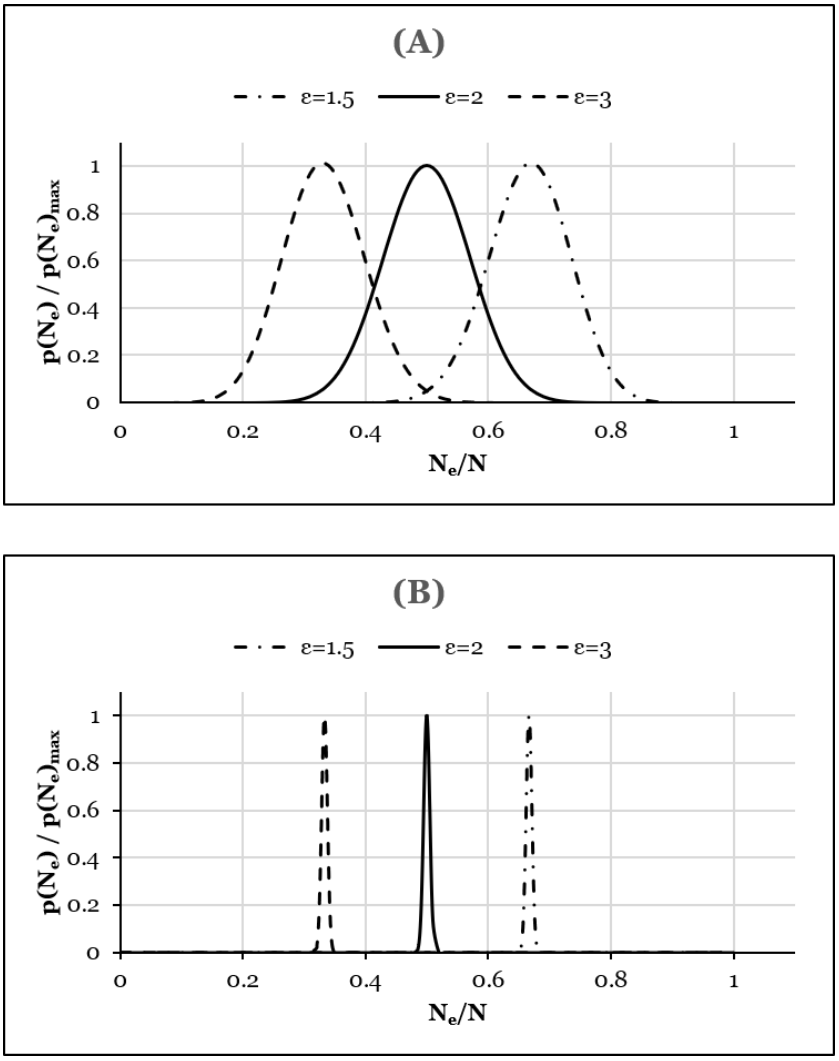


Figure 4.1 – Binomial distribution for variable ε where (A) N = 50; (B) N = 10000. Concept inspired by Eastman and Reif (Eastman, 2019; Reif, 1965)

4.2.3 Equilibrium from a statistical viewpoint

4.2.3.1 The microcanonical ensemble

An ensemble is a collection of thermodynamic systems designed to be identical in certain respects. Microcanonical ensemble (following conventional nomenclature) denotes a collection of systems that together maintain constant total energy, volume, and number of particles (Chandler, 1987). However, since these properties can still be different from one system to another, the accessible states and probability distributions remain variable in the individual systems. Therefore, the microcanonical ensemble aims to identify the most probable macrostate governing the overall collection of systems at thermodynamic equilibrium.

Consider two thermodynamic systems (A and B) separated by a boundary (Figure 4.2). The two systems interact according to the microcanonical ensemble, as their total

energy (E_T), volume (V_T), and number of particles (N_T) remain fixed. Moreover, these total quantities are assumed to be equivalent to the summations of the respective properties in the two subsystems (Chandler, 1987; Reif, 1965).

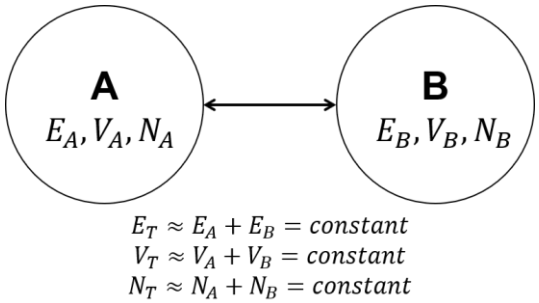


Figure 4.2 – Microcanonical ensemble

Since all microstates accessible to the ensemble are equally probable at thermodynamic equilibrium, the probability of system A being at E_A, V_A, and N_A is equal to the number of microstates accessible to the ensemble such that system A is at the desired values ($\Omega_T(E_A, V_A, N_A)$), divided by the total number of microstates accessible to the ensemble ($\Omega_T(E_T, V_T, N_T)$) (Reif, 1965). This is shown in Equation (4.3).

$$p(E_A, V_A, N_A) = \frac{\Omega_T(E_A, V_A, N_A)}{\Omega_T(E_T, V_T, N_T)} \quad \textbf{(4.3)}$$

Moreover, since achieving a given microstate is an independent event, the parameter $\Omega_T(E_A, V_A, N_A)$ is equal to the number of microstates in system A corresponding to E_A, V_A, and N_A ($\Omega_A(E_A, V_A, N_A)$), multiplied by the number of microstates in system B not corresponding to E_A, V_A, and N_A ($\Omega_B([E_T - E_A], [V_T - V_A], [N_T - N_A])$) (Chandler, 1987). As E_T, V_T, and N_T are assumed equivalent to the summations of the respective properties in the two phases, Ω_B can be defined as $\Omega_B(E_B, V_B, N_B)$. Equation (4.3) is, therefore, rewritten as follows:

$$p(E_A, V_A, N_A) = \frac{\Omega_A(E_A, V_A, N_A)\, \Omega_B(E_B, V_B, N_B)}{\Omega_T(E_T, V_T, N_T)} \quad \textbf{(4.4)}$$

4.2.3.2 The condition at equilibrium

Consider the dual system described in section 4.2.3.1, whose probability distribution function is characterised by Equation (4.4). At thermodynamic

equilibrium, the most probable macrostate must satisfy the conditions described in Equations (4.5) – (4.7), because this state is represented by a maximum point in the probability distribution function (Reif, 1965).

$$\left.\frac{\partial p(E_A, V_A, N_A)}{\partial E_A}\right|_{V_A,N_A} = 0 \tag{4.5}$$

$$\left.\frac{\partial p(E_A, V_A, N_A)}{\partial V_A}\right|_{E_A,N_A} = 0 \tag{4.6}$$

$$\left.\frac{\partial p(E_A, V_A, N_A)}{\partial N_A}\right|_{E_A,V_A} = 0 \tag{4.7}$$

It follows that Equations (4.8) – (4.10) also hold true for the most probable macrostate.

$$\left.\frac{\partial [ln\ p(E_A, V_A, N_A)]}{\partial E_A}\right|_{V_A,N_A} = 0 \tag{4.8}$$

$$\left.\frac{\partial [ln\ p(E_A, V_A, N_A)]}{\partial V_A}\right|_{E_A,N_A} = 0 \tag{4.9}$$

$$\left.\frac{\partial [ln\ p(E_A, V_A, N_A)]}{\partial N_A}\right|_{E_A,V_A} = 0 \tag{4.10}$$

In Equation (4.4) the total number of microstates accessible to the ensemble ($\Omega_T(E_T, V_T, N_T)$) is a constant, because E_T, V_T, and N_T are constants. Therefore, upon substituting Equation (4.4) into Equations (4.8) – (4.10), the following can be written:

$$\left.\frac{\partial [ln\ \Omega_A]}{\partial E_A}\right|_{V_A,N_A} + \left.\frac{\partial [ln\ \Omega_B]}{\partial E_A}\right|_{V_A,N_A} = 0 \tag{4.11}$$

$$\left.\frac{\partial[ln\,\Omega_A]}{\partial V_A}\right|_{E_A,N_A} + \left.\frac{\partial[ln\,\Omega_B]}{\partial V_A}\right|_{E_A,N_A} = 0 \quad \textbf{(4.12)}$$

$$\left.\frac{\partial[ln\,\Omega_A]}{\partial N_A}\right|_{E_A,V_A} + \left.\frac{\partial[ln\,\Omega_B]}{\partial N_A}\right|_{E_A,V_A} = 0 \quad \textbf{(4.13)}$$

Given that $E_A = E_T - E_B$, $V_A = V_T - V_B$, and $N_A = N_T - N_B$, it then follows that $dE_A = -dE_B$, $dV_A = -dV_B$, and $dN_A = -dN_B$. Therefore, Equations (4.11) - (4.13) can be rewritten as follows (Reif, 1965):

$$\left.\frac{\partial[ln\,\Omega_A]}{\partial E_A}\right|_{V_A,N_A} = \left.\frac{\partial[ln\,\Omega_B]}{\partial E_B}\right|_{V_B,N_B} \quad \textbf{(4.14)}$$

$$\left.\frac{\partial[ln\,\Omega_A]}{\partial V_A}\right|_{E_A,N_A} = \left.\frac{\partial[ln\,\Omega_B]}{\partial V_B}\right|_{E_B,N_B} \quad \textbf{(4.15)}$$

$$\left.\frac{\partial[ln\,\Omega_A]}{\partial N_A}\right|_{E_A,V_A} = \left.\frac{\partial[ln\,\Omega_B]}{\partial N_B}\right|_{E_B,V_B} \quad \textbf{(4.16)}$$

Equations (4.14) – (4.16) demonstrate the most probable macrostate at thermodynamic equilibrium. The differentials of $ln\,\Omega$ (natural logarithm of the number of microstates) with respect to E, V, and N are the same in both systems. These differentials can be further defined as follows (Eastman, 2019) (to be validated in section 4.2.4):

$$\left.\frac{\partial[ln\,\Omega]}{\partial E}\right|_{V,N} = \frac{1}{k_B T} \quad \textbf{(4.17)}$$

$$\left.\frac{\partial[ln\,\Omega]}{\partial V}\right|_{E,N} = \frac{P}{k_B T} \quad \textbf{(4.18)}$$

$$\left.\frac{\partial[ln\ \Omega]}{\partial N}\right|_{E,V} = -\frac{\mu}{k_B T} \tag{4.19}$$

k_B is Boltzmann's constant, a universal value acting here as a conversion factor from units of energy to units of temperature.

Equations (4.17) – (4.19) define temperature (T), pressure (P), and chemical potential (μ), a set of parameters that are merely descriptive of how the number of microstates (Ω) varies when changing energy, volume, and number of particles in the system, respectively. At equilibrium, the most probable macrostate comprises equal rates of change in the two systems, and this equivalence is not compromised by any exchange of energy, volume, or particles between the two systems.

Although the definitions of T, P, and μ are yet to be validated against classical thermodynamics, substituting Equations (4.17) – (4.19) into Equations (4.14) – (4.16) yields the following outcomes:

$$T_A = T_B \tag{4.20}$$

$$\frac{P_A}{T_A} = \frac{P_B}{T_B} \tag{4.21}$$

$$\frac{\mu_A}{T_A} = \frac{\mu_B}{T_B} \tag{4.22}$$

Equations (4.20) – (4.22) set out the most probable conditions defining thermal, mechanical, and mass equilibria, in terms of temperature, pressure, and chemical potential, respectively. As expected, the most probable condition at thermal equilibrium between two systems, is such that they exhibit equal temperatures. Interestingly, however, mechanical equilibrium and mass equilibrium are not characterised by equal pressures and chemical potentials amongst the two systems, but rather they are characterised by equal ratios of these parameters to temperature. This demonstrates that temperature does not only drive heat transfer, but it is also influential on diffusion and pressure-volume relationships. Nevertheless, this effect of

temperature is unlikely to be observed many real-world situations, because in most cases, conventional heating is employed with which temperature gradients are not sustained. If two phases possess equal temperatures, their pressures and chemical potentials must also be equal at equilibrium.

Since mass equilibrium is characterised by equal μ/T, it can be summarised that that mass transfer is proportional to spatial gradients in μ/T. This is the most fundamental relationship between temperature and mass transfer, but it is usually investigated under constant temperature, thus eliminating T from the picture. As seen in Chapter 3, microwaves induce temperature gradients in biomass-solvent systems, indicating the importance of characterising mass and mechanical equilibria under non-uniform temperature, and this will be carried out in section 4.3.

4.2.4 Validation against classical thermodynamics

Equations (4.20) – (4.22) define temperature, pressure, and chemical potential as mere derivatives of the logarithmic number of microstates ($ln\ \Omega$), with respect to other extensive properties of a thermodynamic system such as energy, volume, and number of particles. This definition is to be validated here against classical thermodynamics, thus bridging the gap.

The first law of thermodynamics is a statement of energy conservation. The general form of this law is shown in Equation (4.23), where the energy supplied to a system (δQ) is either stored as internal energy (dE) or lost to the surroundings as a result of mechanical work, mass transfer, etc (i.e., $\sum_i A_i dx_i$, where A is a generalised force variable like pressure, and dx_i is a generalised field variable like volume (Chandler, 1987)).

$$dE = \delta Q - \sum_i A_i dx_i \qquad \textbf{(4.23)}$$

E in this case is analogous to the average energy of a system as described in the previous sections.

Assuming that the system undergoes quasi-static and reversible processes, δQ is, by virtue of the second law of thermodynamics, equivalent to TdS (Huang, 1963; Reif, 1965). On the other hand, the forms of energy exchange with the surroundings

($\sum_i A_i dx_i$) are confined here to mechanical work and mass transfer. Therefore, Equation (4.23) can be rewritten as follows:

$$dE = TdS - PdV + \mu dN \tag{4.24}$$

S denotes the system's entropy.

Rearranging Equation (4.24) to make dS the subject, yields the following:

$$dS = \frac{1}{T}dE + \frac{P}{T}dV - \frac{\mu}{T}dN \tag{4.25}$$

It follows from Equation (4.25):

$$\left.\frac{\partial S}{\partial E}\right|_{V,N} = \frac{1}{T} \tag{4.26}$$

$$\left.\frac{\partial S}{\partial V}\right|_{E,N} = \frac{P}{T} \tag{4.27}$$

$$\left.\frac{\partial S}{\partial N}\right|_{E,V} = -\frac{\mu}{T} \tag{4.28}$$

Equations (4.26) – (4.28) are analogous to Equations (4.17) – (4.19), and since k_B is a universal constant, entropy (S) and the number of microstates (Ω) can be related as shown below:

$$S = k_B ln(\Omega) \tag{4.29}$$

Equation (4.29) is Boltzmann's definition of entropy (Bowley and Sanchez, 1999; Chandler, 1987; Huang, 1963; Reif, 1965), which argues that this parameter is merely a statistical concept providing a measure for the number of microstates accessible to a system. This expression demonstrates that the earlier definitions of T, P, and μ are analogous to classical thermodynamics and adherent to the laws thereof; hence, the

underpinning statistical arguments and concepts are also reliable means of investigation. These arguments will, therefore, be used in section 4.3 to understand equilibrium under a temperature gradient.

4.3 Equilibrium under a temperature gradient

The classical two-system microcanonical ensemble discussed in section 4.2.3 comprises fixed total energy (E_T), volume (V_T), and number of particles (N_T). The aim of this isolated ensemble is to determine the most probable equilibrium distribution of energy, volume, and particles amongst the two systems it contains. The most probable equilibrium distribution was shown to satisfy the known conditions for thermal, mechanical, and mass equilibria, comprising equal temperatures, pressures, and chemical potentials, respectively, amongst the two systems (Equations (4.20) – (4.22)).

4.3.1 Modified microcanonical ensemble

The classical two-system ensemble is compatible with biomass-solvent systems heated conventionally; firstly, such systems constitute a batch setting (i.e., V_T and N_T can be assumed constant), and secondly, beyond the heat-up phase E_T is also likely to be conserved (assuming negligible heat loss or rapid replacement of any lost energy). In other words, biomass-solvent systems only attain energy as they are heated, but once the desired temperature is achieved, no further energy gets introduced deliberately to these systems except to account for lost energy; therefore, E_T is conserved beyond the heat-up phase. However, this analogy is not necessarily applicable under microwave heating where, for instance, energy can be delivered directly from the environment to the biomass through microwave radiation, but the biomass does not deliver energy except to the surrounding solvent, which, in turn, loses energy back to the environment. As shown in Figure 4.3, this constitutes a cycle whereby energy delivery to the biomass bypasses the solvent phase, but energy removal from the biomass still requires the solvent medium. This cycle essentially means that, unlike V_T and N_T, E_T is not conserved within the biomass-solvent system; therefore, the system only exhibits batch setting characteristics partially (i.e., with respect to V_T and N_T, but not E_T).

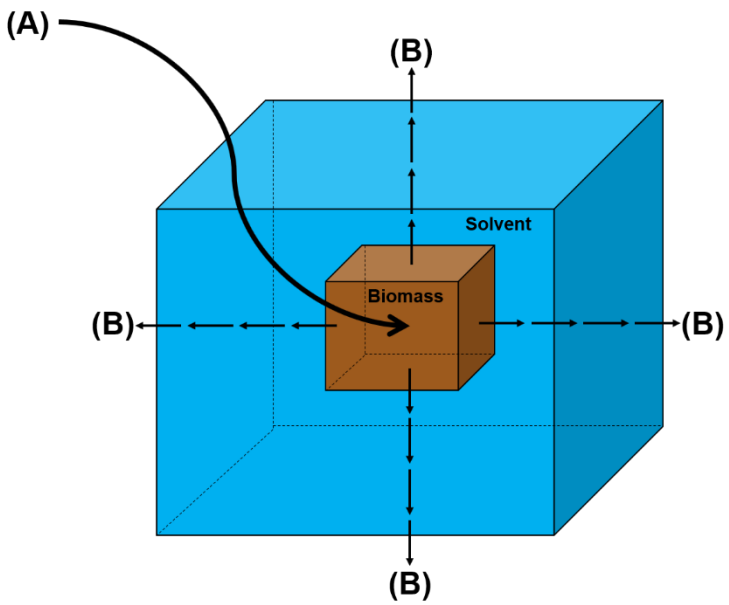


Figure 4.3 – Biomass solvent system under microwave heating. Energy cycle is induced where (A) biomass is heated directly with microwave radiation, and (B) energy is lost conventionally from biomass to solvent and then back to the environment

This unique situation is arguably only achievable with unconventional heating methods such as microwave heating, due to the unique heating patterns induced. The present situation requires a novel statistical treatment to account for the fact that, batch characteristics are only exhibited partially in the biomass-solvent system (i.e., V_T and N_T are conserved but E_T is not). This unique heating situation is important to analyse, because as shown in Chapter 3, it could result in unequal temperatures within the biomass-solvent system, possibly altering the conditions for mechanical and mass equilibria (section 4.2.3.2). To statistically understand whether temperature gradients can be established in biomass-solvent systems heated with microwaves, consider a modified ensemble comprising three thermodynamic systems (Figure 4.4).

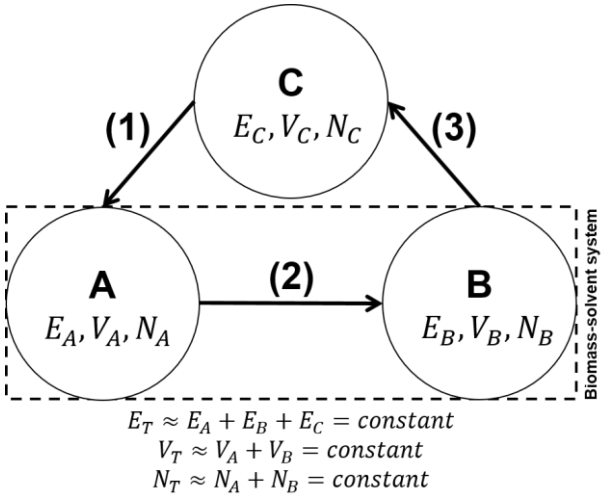


Figure 4.4 – Three-way microcanonical ensemble comprising energy cycle. (1) direct energy delivery from C to A by microwave radiation; (2) conventional heat transfer from A to B; (3) energy removal from B back to C either by conventional heat transfer or through reflux (i.e., evaporation and condensation)

In Figure 4.4, systems A and B can be envisaged as biomass and solvent, respectively, whereas system C is the surrounding environment. Systems A and B are much smaller than system C, but all still incorporate large degrees of freedom such that T, P, and μ can be defined for each (these will be hypothetical in system C due to the very complex nature of the environment). As seen in Figure 4.4, energy flows in cycle from A to B then C, and then back to A; therefore, this setting is compatible with biomass-solvent systems heated with microwaves (Figure 4.3). As volume and particles are contained within the biomass-solvent system, V_T and N_T are conserved within systems A and B. However, E_T can only be conserved within the full ensemble comprising all systems A, B, and C, signifying a conservation in energy within the combined system-environment entity. This distinctiveness in defining the energy conservation boundary is what makes this ensemble compatible with microwave heating scenarios, and to express this mathematically, the probability distribution function in energy (Equation (4.4)) has been modified to include system C. Assuming that all microstates are independent, such a modification can be expressed as shown in Equation (4.30). Note that V and N have been dropped from Equation (4.30) to draw focus on E.

$$p(E_A) = \frac{\Omega_A(E_A)\,\Omega_B(E_B)\,\Omega_C(E_C)}{\Omega_T(E_T)} \tag{4.30}$$

Equation (4.8) holds at equilibrium, and the following is obtained on substituting Equation (4.30):

$$\frac{\partial[ln\,\Omega_A]}{\partial E_A}+\frac{\partial[ln\,\Omega_B]}{\partial E_A}+\frac{\partial[ln\,\Omega_C]}{\partial E_A}=0 \qquad \textbf{(4.31)}$$

Since $E_A + E_B + E_C = E_T = constant$, the following can be written:

$$\frac{dE_B}{dE_A}+\frac{dE_C}{dE_A}+1=0 \qquad \textbf{(4.32)}$$

Substituting Equation (4.32) into Equation (4.31) yields the following:

$$\frac{\partial[ln\,\Omega_A]}{\partial E_A}=\frac{\partial[ln\,\Omega_B]}{\partial E_B}+\left(\frac{\partial[ln\,\Omega_B]}{\partial E_B}-\frac{\partial[ln\,\Omega_C]}{\partial E_C}\right)\frac{dE_C}{dE_A} \qquad \textbf{(4.33)}$$

Equation (4.33) describes the most probable condition for thermal equilibrium in the three-way ensemble (Figure 4.4). As shown in Equation (4.17), $\partial[ln\,\Omega_A]/\partial E_A$ and $\partial[ln\,\Omega_B]/\partial E_B$ directly represent temperatures T_A and T_B, respectively. However, defining $\partial[ln\,\Omega_C]/\partial E_C$ is non-trivial since system C (i.e., the environment) is a complex entity. As such, there are many possible equilibrium conditions that satisfy Equation (4.33), depending on the characteristics of system C. While system C delivers energy to system A, it also extracts energy from system B to maintain thermal equilibrium. This indicates numerous phenomena taking place in system C, enabling the energy flow cycle of to be completed from the point of extracting energy from B to the point of resupplying energy back to A. Although system C cannot be fully understood in this context, useful deductions can still be made from Equation (4.33), to draw conclusive insight on the most likely equilibrium temperature distribution in systems A and B, as follows:

1- Under conventional heating, thermal steady state comprises $\partial[ln\,\Omega_B]/\partial E_B = \partial[ln\,\Omega_C]/\partial E_C$, meaning that Equation (4.33) gets reduced to the form shown in Equation (4.14). This essentially reduces the ensemble to the original two-way system isolated from its surroundings (Figure 4.2), where the most probable macrostate comprises the condition $T_A = T_B$.

2- Under microwave heating (Figure 4.4), given that system B loses energy to its immediate surrounding environment, it must follow that $T_B > T_C$ which, in turn, means that $\partial[ln\ \Omega_B]/\partial E_B < \partial[ln\ \Omega_C]/\partial E_C$. Furthermore, $dE_C/dE_A = 1$ here because any energy delivered directly to system A through microwave heating, is eventually deposited back to system C. Therefore, it is clear that $\partial[ln\ \Omega_A]/\partial E_A < \partial[ln\ \Omega_B]/\partial E_B$, in other words $T_A > T_B$.

It can be summarised from the deductions above that, under microwave heating, the most probable equilibrium temperature distribution amongst systems A and B should satisfy the inequality $T_A > T_B$. The magnitude of this temperature difference depends on the characteristics of system C, including the input microwave power, the rate of energy removal from system B, etc. This is in total agreement with the findings made in Chapter 3, and the implication is that mass transfer in biomass-solvent systems is likely to exhibit different trends under microwave heating than it does conventionally. To characterise these trends quantitatively, it should be understood how μ and μ/T change with T, which will be expanded upon in the following sections.

4.3.2 Temperature-induced volume and mass transfer

Recall that, unlike E_T, V_T and N_T are conserved within systems A and B only (Figure 4.4), which means that mechanical and mass equilibria are still characterised by equal P/T and μ/T amongst the two systems (Equations (4.21) and (4.22)). However, since $T_A \neq T_B$ (section 4.3.1), an interplay is generated between temperature and other parameters, which fundamentally alters the most probable equilibrium distribution of volume and number of particles amongst systems A and B. For instance, although P_A/T_A should equal P_B/T_B at equilibrium, P_A and P_B may not be equal to each other (because $T_A \neq T_B$), and this affects the most probable distribution of volume. The same can be said regarding the most probable distribution of particles, which would also be affected by unequal temperatures and chemical potentials.

To characterise the effect of temperature gradient, consider a system in space (denoted the letter "i") capable of expanding freely, but cannot exchange particles with its surroundings (denoted the letter "j"). If the system is heated with microwaves, its temperature (T_i) gets higher than that of the surrounding environment (T_j) (i.e., $T_i > T_j$). As the system (denoted the letter "i") gets heated selectively, and it simultaneously

attempts to achieve mechanical equilibrium with its surroundings (denoted the letter "j"), one of the three scenarios summarised in Table 4.1 would take place.

Scenario	P_i/T_i	**Direction of volume transfer**	**Example of occurrence in nature**
As T_i is raised beyond T_j, P_i increases to a much **higher** extent than T_i (disproportionately)	Increases	From surroundings "j" to system "i" (i.e., "i" expands)	Most fluids (if not all) expand when heated
As T_i is raised beyond T_j, P_i increases to a much **lower** extent than T_i (disproportionately)	Decreases	From system "i" to surroundings "j" (i.e., "i" contracts)	Water below 4 ℃ (atmospheric pressure) contracts when heated
P_i increases **proportionally** with T_i	Remains constant	No volume transfer	Water at 4 ℃ (atmospheric pressure), since it is at the boundary between the two scenarios above

Table 4.1 – Volume transfer scenarios when a system "i" possesses higher temperature than its surroundings "j"

The three qualitative scenarios in Table 4.1 also apply to mass transfer situations, where P is replaced with μ and volume with number of particles. For example, taking the first scenario: as T_i increases beyond T_j, the chemical potential magnitude $|\mu_i|$ increases to a much higher extent than T_i (disproportionately), prompting mass transfer from surroundings "j" (lower temperature and potential magnitude) to system "i" (higher temperature and potential magnitude), so as to lower the surplus $|\mu_i|$ and achieve the required μ_i/T_i ratio. Note that unlike P, μ is conventionally defined as a negative quantity (Equations (4.19) and (4.28)); hence, mass transfer is strictly analogous to volume transfer only when considering magnitudes in μ rather than the absolute values (i.e., $|\mu|$ instead of μ).

All three in Table 4.1 above are possible, yet from an observatory perspective, the first scenario occurs more widely. In real-world situations, fluid systems are known to expand upon heating due to an increase in their pressures, and this is explicable through the first scenario in Table 4.1. Expansion is essentially a process of volume transfer whereby a system receiving volume ends up occupying a larger portion of the available space. This is a commonly observable phenomenon, and while an analogous

mechanism for mass transfer could also be inferred, this is usually less understood. In mass transfer, particles could also diffuse under the influence of temperature gradient from high potential areas (i.e., low $|\mu|$) to low potential areas (i.e., high $|\mu|$). This would take place due to a disproportionate increase in $|\mu|$ compared with increasing T, just as P increases disproportionately with T in the first scenario of Table 4.1.

To characterise the most likely scenario in Table 4.1 from the viewpoint of statistical mechanics, it should be roughly understood how $ln\,\Omega$ changes with E, V, and N. This will provide an insight on how P and μ are related to T in an ideal situation (e.g., where no intermolecular forces exist between the particles). The following analysis is divided into two parts, the first of which estimates $ln\,\Omega$ as a function of E and N, while the second estimates $ln\,\Omega$ in terms of E and V. These estimations will then be used to approximate $\partial[ln\,\Omega]/\partial N$ and $\partial[ln\,\Omega]/\partial V$ for ideal situations.

For the first part, consider a system comprising a fixed total number of particles, N, where each can occupy discrete energy states up to a maximum of ε. For the purposes of this analysis, it can be assumed that the total energy of the system (E) is shared equally amongst all particles, which is reasonable for sufficiently large systems. Therefore, E can be estimated as $N\varepsilon$, and this establishes a simplistic yet satisfactory link between molecular-level energy states, ε, and the total energy imposed upon the system, E. An increase in E raises the value of ε, indicating that the molecules may access higher energy levels. The total number of microstates in the system (Ω) is equivalent to ε^N; however, based on the assumption established here, this can be estimated as $(E/N)^N$. Therefore, the parameters $ln\,\Omega$, $\partial[ln\,\Omega]/\partial E$, and $\partial[ln\,\Omega]/\partial N$ can be approximated in terms of E and N as show in Equations (4.34) – (4.36). These are approximations rather than exact expressions; therefore, the relationships use "~" instead of "=" to indicate approximated equivalence.

$$ln\,\Omega \sim N(ln\,E - ln\,N) \tag{4.34}$$

$$\frac{\partial ln\,\Omega}{\partial E} \sim \frac{N}{E} \tag{4.35}$$

$$\frac{\partial ln\,\Omega}{\partial N} \sim ln\,E - (ln\,N + 1) \tag{4.36}$$

For the second part of this analysis, envisage that the system described in the first part occupies a space of volume V. Each particle can occupy discrete volume quantities up to a maximum of $\bar{v}$; however, similar to energy, it is assumed here that the total volume of the system (V) is shared equally amongst all particles, which is reasonable for sufficiently large systems. Hence, V can be estimated as $N\bar{v}$, thereby establishing a simplistic yet satisfactory link between molecular-level volumes, $\bar{v}$, and the total volume imposed upon the system, V. Based on this, the total number of accessible microstates (Ω) can be rewritten as $(E\bar{v}/V)^{V/\bar{v}}$, and the parameters $ln\,\Omega$, $\partial[ln\,\Omega]/\partial E$, and $\partial[ln\,\Omega]/\partial V$ can be approximated in terms of E, N, and V as shown in Equations (4.37) – (4.39).

$$ln\,\Omega \sim \frac{V}{\bar{v}}\left(ln\,E - ln\,\frac{V}{\bar{v}}\right) \equiv N(ln\,E - ln\,N) \tag{4.37}$$

$$\frac{\partial ln\,\Omega}{\partial E} \sim \frac{V}{\bar{v}E} \equiv \frac{N}{E} \tag{4.38}$$

$$\frac{\partial ln\,\Omega}{\partial V} \sim \frac{1}{\bar{v}}\left[ln\,E - (ln\,\frac{V}{\bar{v}} + 1)\right] \equiv \frac{1}{\bar{v}}[ln\,E - (ln\,N + 1)] \tag{4.39}$$

Equations (4.37) and (4.38) for estimating $ln\,\Omega$ and $\partial[ln\,\Omega]/\partial E$ are identical to Equations (4.34) and (4.35), respectively. Also, Equations (4.36) and (4.39) show that $\partial[ln\,\Omega]/\partial V$ and $\partial[ln\,\Omega]/\partial N$ are interrelated through the parameter $\bar{v}$, which is a molecular density parameter describing the volume occupied by each particle. This is an expected outcome since, energy distribution in space depends on how particles are distributed, because particles constitute the medium that carries energy in space. Varying $\bar{v}$ results in a change in the number of ways for distributing particles in space, which, in turn, alters the permutations of energy distribution. In real-world situations, ε and $\bar{v}$ are complex functions of E, N, and V; however, these were assumed constant and uniform here to preserve the simplicity of the current analysis. This is a reasonable assumption for sufficiently large thermodynamic systems. Moreover, constant $\bar{v}$ has

also been used in literature to derive the ideal gas equation (Bowley and Sanchez, 1999), which essentially describes the macroscopic behaviour of any ideal system. Nevertheless, further analysis on $\bar{v}$ is a subject of future work.

The outcomes of this analysis are shown in Equations (4.53), (4.54), and (4.55), and in Figure 4.5, which roughly summarise the likely trends of $\partial ln\,\Omega/\partial E$, $\partial[ln\,\Omega]/\partial N$, and $\partial[ln\,\Omega]/\partial V$ with changing E.

$$\left.\frac{\partial ln\,\Omega}{\partial E}\right|_{N,V} \sim \frac{1}{E} \tag{4.40}$$

$$\left.\frac{\partial ln\,\Omega}{\partial N}\right|_{E,V} \sim ln\,E \tag{4.41}$$

$$\left.\frac{\partial ln\,\Omega}{\partial V}\right|_{E,N} \sim ln\,E \tag{4.42}$$

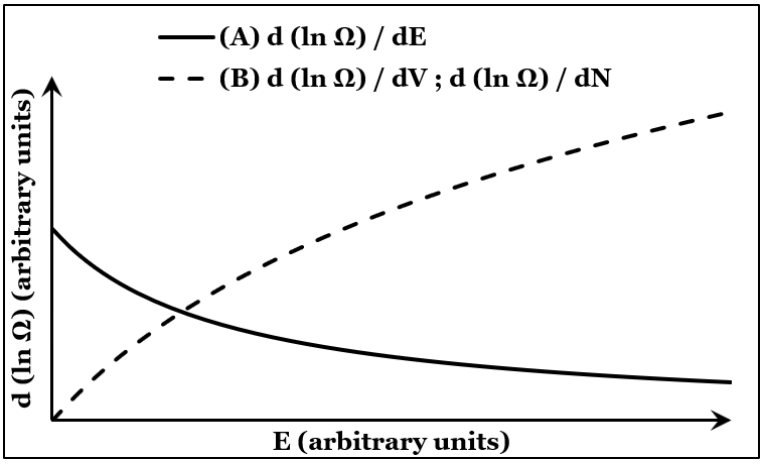


Figure 4.5 – Rough representation of $\partial[ln\,\Omega]/\partial E$, $\partial[ln\,\Omega]/\partial V$, and $\partial[ln\,\Omega]/\partial N$ as functions of E. (A) $\partial[ln\,\Omega]/\partial E \sim 1/E$; (B) $\partial[ln\,\Omega]/\partial V$ and $\partial[ln\,\Omega]/\partial N \sim ln\,E$

As expected, $\partial[ln\,\Omega]/\partial E$ decreases with E; hence, temperature T increases as energy is introduced to a system (Equation (4.17)). On the other hand, both $\partial[ln\,\Omega]/\partial V$ and $\partial[ln\,\Omega]/\partial N$ increase with E, meaning that as energy is introduced to a system, both P/T and $|\mu|/T$ increase (Equations (4.18) and (4.19)). Given that T, P/T, and $|\mu|/T$ are all likely to increase with E, it must follow that P and $|\mu|$ increase

more significantly than T in response to any increase in E, otherwise $\partial[ln\ \Omega]/\partial V$ and $\partial[ln\ \Omega]/\partial N$ cannot be increasing functions of E.

As can be seen, the first scenario in Table 4.1 comprising P/T increasing with T, is most likely in near-ideal situations, which explains why many fluids expand when heated. However, in other situations, factors governing the deviation from ideal behaviour should be considered. Such factors may hinder the particles from behaving independently of each other, which demands redefinition of the number of microstates (Ω). For example, water molecules exhibit significant hydrogen bonds; hence, below 4 ℃ any heating could increase the pressure, but the supplied energy would also be used to overcome the intermolecular forces. The overall result would, therefore, entail a contraction of water as it gets heated.

Like P, $|\mu|$ also rises disproportionately with increasing T (Figure 4.5), and if T in a system approaches higher values than in the surroundings, mass transfer would then be induced against the established temperature gradient, to lower the surplus $|\mu|$ and achieve mass equilibrium by retaining the required $|\mu|/T$ ratio. This mass transfer scenario is likely to arise in batch settings being heated unconventionally. A prime example of this is a biomass-solvent system under microwave heating, where mass and volume are largely contained within the system, but energy is continuously exchanged with the environment in the form of a cycle.

$P-V-T$ relationships are well-established, but the existence of an analogous set of $|\mu|-N-T$ relationships clearly has not yet been investigated thoroughly. Mass transfer is more challenging to observe compared with volume transfer. Even though diffusion under the influence of temperature gradients has been observed (i.e., the Ludwig-Soret effect) (Kishikawa et al., 2012; Koyama and Tsukada, 2021; Rahman and Saghir, 2014), volume transfer is still more commonly observed. Furthermore, μ is not directly measurable, unlike P which is well known in various applications and is measured with its own set of units. This poses a challenge in the current work for two reasons; firstly, μ must be known if any further mass transfer analyses are to be conducted; secondly, given that μ, P, and T are all measures of the same underpinning property (number of microstates; Ω), they are interrelated and cannot be treated in isolation. This means that, unlike the examples presented here where, for instance, expansion is permitted but diffusion is not, in real-world situations all transfer

phenomena take place simultaneously, and ultimately μ, P, and T all affect these phenomena collectively. For example, if water diffuses into a system, it does not only alter the chemical potential of the system, but it can also induce pressure which, in turn, causes expansion. This demonstrates the need to express μ in terms of other measurable parameters, namely P and T, and this will be carried out in section 4.4.

It is summarised from this section that $|\mu|$ may rise disproportionately with T, making $|\mu|/T$ an increasing function of T, and meaning that diffusion should take place against a temperature gradient to achieve mass equilibrium. The relationship underpinning temperature and mass transfer has now been described, but μ is yet to be expressed in terms of P and T to enable full quantification of mass transfer.

4.3.3 How transfer phenomena increase entropy

This section summarises how mass and volume transfer against a temperature gradient (section 4.3.2) match the second law of thermodynamics. The work presented here is confined to the principles of classical thermodynamics.

In addition to Equation (4.24) describing energy gains and losses in a thermodynamic system, it is further assumed that that the absolute average energy (E) is a homogeneous first-order function of the other extensive properties including volume (V), number of particles (N), and entropy (S). Therefore, E can be expressed using Euler's formula (Chandler, 1987), as follows:

$$E = S\frac{\partial E}{\partial S}\Big|_{V,N} + V\frac{\partial E}{\partial V}\Big|_{S,N} + N\frac{\partial E}{\partial N}\Big|_{S,V} \quad \textbf{(4.43)}$$

Based on the definitions of the three derivatives in Equation (4.43) presented in the previous sections, the expression can be rewritten as follows (Chandler, 1987):

$$E = TS - PV + \mu N \quad \textbf{(4.44)}$$

Equation (4.44) is the basic expression from which all thermodynamic potentials are derived, including enthalpy ($H \equiv E + PV = TS + \mu N$), Gibbs' free energy ($G \equiv E + PV - TS = \mu N$), and Helmholtz free energy ($F \equiv E - TS = \mu N - PV$).

Enthalpy (H) can be used to determine how chemical potential (μ) changes with T and P. At constant moles, the differential entropy (dS) can be written as follows:

$$dS = \frac{1}{T} dH - \frac{V}{T} dP \quad \textbf{(4.45)}$$

The differential enthalpy (dH) can be expressed in terms of temperature using specific heat capacity at constant pressure (C_p), as follows:

$$dS = \frac{NC_p}{T} dT - \frac{V}{T} dP \quad \textbf{(4.46)}$$

As can be seen, entropy (S) increases with increasing temperature (T) and decreases with increasing pressure (P).

Similarly, a free energy parameter analogous to H can be defined for chemical potential (μ), as follows:

$$B \equiv E - \mu N = TS - PV \quad \textbf{(4.47)}$$

From this, the differential entropy (dS) can be written at constant volume as follows:

$$dS = \frac{1}{T} dB + \frac{N}{T} d\mu \quad \textbf{(4.48)}$$

The differential B-free energy (dB) can be expressed in terms of temperature using specific heat capacity at constant chemical potential (C_μ), as follows:

$$dS = \frac{VC_\mu}{T} dT + \frac{N}{T} d\mu \quad \textbf{(4.49)}$$

In this case, entropy (S) increases with increasing both temperature (T) and chemical potential (μ). However, since chemical potential is by convention a negative quantity, entropy (S) can be seen to decrease with increasing the chemical potential magnitude ($|\mu|$).

Furthermore, the differentials $\partial S/\partial E\big|_{N,V}$, $\partial S/\partial V\big|_{E,N}$, and $\partial S/\partial N\big|_{E,V}$ vary with T, P, and $|\mu|$ as shown in Equations (4.26) – (4.28). An increase in these differentials signifies a more pronounced increase in entropy (S) as E, V, or N are raised. This results in a framework for heat, mass, and volume transfer summarised in Table 4.2. As can be seen, all transfer phenomena occur such that the entropy increases in accordance with the second law of thermodynamics. The occurrence of mass/volume transfer against a temperature gradient are not an exception, as they are also justified by the need to increase the overall entropy. At this level of analysis, the most fundamental condition for heat/mass/volume transfer is that these should occur from a system "i" comprising high entropy, to a system "j" comprising low entropy, since this ensures the overall entropy is increased. In other words, transfer phenomena take place down an entropy gradient.

		How T changes (applicable to P and $\|\mu\|$)		
		increases non proportionally to a lesser extent than parameter	**increases proportionally with parameter**	**increases non proportionally to a higher extent than parameter**
P increases (no heat/mass transfer)	S	Decreases	Unchanged	Increases
	$\partial S/\partial V\|_{E,N}$	Increases	Unchanged	Decreases
	Direction of volume transfer	Towards the system	None	Away from the system
	Justification	Volume flows towards the area where it generates most entropy, i.e., down an entropy gradient		
	Impact	Flow against a temperature gradient; system expands	No flow; system unchanged	Flow down a temperature gradient; system contracts
$\|\mu\|$ increases (no heat/volume transfer)	S	Decreases	Unchanged	Increases
	$\partial S/\partial N\|_{E,V}$	Increases	Unchanged	Decreases
	Direction of mass transfer	Towards the system	None	Away from the system
	Justification	Particles flow towards the area where their presence generates most entropy, i.e., down an entropy gradient		
	Impact	Flow against a temperature gradient	No mass transfer as equilibrium is unaffected	Flow down a temperature gradient
T increases (no mass/volume transfer)	S	Increases		
	$\partial S/\partial E\|_{N,V}$	Decreases		
	Direction of heat transfer	Away from the system		
	Justification	Heat flows towards the area where its presence generates most entropy, i.e., down an entropy gradient		
	Impact	Heat transfer down a temperature gradient		

Table 4.2 – Summary of the framework for transfer phenomena (ideal system where $C_V = 0\ JK^{-1}mol^{-1}$ and $C_N = 0\ JK^{-1}m^{-3}$)

4.4 Chemical potential

Unlike P and T, μ cannot be measured directly; hence, an expression is required to infer μ from other measurable parameters, and the aim of this section is to derive such an expression. The work presented here is confined to the principles of classical thermodynamics.

4.4.1 The Gibbs-Duhem argument

Differentiating the energy equation (Equation (4.44)) yields the following:

$$dE = TdS + SdT - PdV - VdP + \mu dN + Nd\mu \quad \textbf{(4.50)}$$

On comparing Equations (4.50) and (4.24), it is clear that $SdT - VdP + Nd\mu$ equals zero. Therefore, $d\mu$ can be expressed as follows:

$$d\mu = -\frac{S}{N}dT + \frac{V}{N}dP \equiv -sdT + vdP \quad \textbf{(4.51)}$$

s and v are the specific entropy and volume of the system, respectively.

Equation (4.51) describes the differential chemical potential of a pure component. This expression is a direct result of the initial assumption that E is a homogeneous first-order function of the extensive properties V, S, and N (Equation (4.43)). This assumption has led to the notion that, the sum of all thermodynamic conjugate pairs or derivatives thereof not described in the first law of thermodynamics, is equal to zero. Here, such terms include SdT, VdP, and $Nd\mu$. This mathematical treatment is otherwise known as the Gibbs-Duhem argument (Chandler, 1987), and it provides a pathway to defining μ in terms of other measurable parameters.

To emphasise that Equation (4.51) describes a pure component, it is rewritten below using a "hat" notation:

$$d\hat{\mu}_\iota = -\hat{s}_\iota dT + \hat{v}_\iota dP \quad \textbf{(4.52)}$$

4.4.2 Derivation for impure components

Equation (4.52) describes chemical potential of a pure component. The specific volume ($\hat{v}_\iota$) can be expressed using the ideal gas law, but instead of pressure (P) the term liquid fugacity (f) is used, indicating that the ideal gas law is used here to describe solutions (potentially behaving non-ideally) instead of gas. The following can be written:

$$d\hat{\mu}_\iota = -\hat{s}_\iota dT + RT\frac{d\hat{f}_\iota}{\hat{f}_\iota} = -\hat{s}_\iota dT + RTd\left[ln(\hat{f}_\iota)\right] \quad \textbf{(4.53)}$$

It is clear from the Gibbs-Duhem argument that, when a system with more than one component is considered, the chemical potential of a given component is a function of the chemical potentials of all other components; hence, the degrees of freedom do not allow quantifying the chemical potential of a single desired component within a mixture. Therefore, an alternative approach was considered where Equation (4.53) for a pure component was still used, but with some modification introduced to the fugacity term to reflect that "i" does not exist in pure form in the system. Such modification can be achieved by considering a form of Raoult's law adapted for non-ideal behaviour (Equation (4.54)). Raoult's law relates the vapour pressure of a component in a mixture to the vapour pressure of the same component if it were pure, using mole fraction (Sahin and Sumnu, 2006). The same is done in Equation (4.54), but while replacing pressure with fugacity (f) and mole fraction with activity (α), to account for non-ideal behaviour. Activity (α) is a modified mole fraction used to account for non-ideal behaviour in mixtures arising due to intermolecular forces.

$$f_i = \alpha_i \widehat{f_i} \tag{4.54}$$

Substituting Equation (4.54) into Equation (4.53) yields the following:

$$d\mu_i = RTd\left[ln(\widehat{f_i})\right] - s_i dT + RTd[ln(\alpha_i)] \tag{4.55}$$

A general differential expression has been derived for the chemical potential of a component in a mixture (Equation (4.55)). This expression should be integrated to give the absolute value of the chemical potential quantity.

Chemical potential of a component "i" is to be determined at temperature T, pure component fugacity $\widehat{f_i}$, and activity α_i. If a reference/datum value of the chemical potential is known at a set of reference conditions (T_0; $\widehat{f_{i0}}$; α_{i0}), then integration can be done in a stepwise manner to account for change in every parameter separately, until the set of desired conditions (T; $\widehat{f_i}$; α_i) is approached (Equation (4.56)).

$$\mu_i|_{T,\widehat{f_i},\alpha_i} = \mu_{i0}|_{T_0,\widehat{f_{i0}},\alpha_{i0}} + \int_{\widehat{f_{i0}}}^{\widehat{f_i}} RTd\left[ln(\widehat{f_i})\right]\Bigg|_{T_0,\alpha_{i0}} \tag{4.56}$$

$$-\int_{T_0}^{T} s_i dT\Big|_{\hat{f}_i,\alpha_{i0}} + \int_{\alpha_{i0}}^{\alpha_i} RTd[ln(\alpha_i)]\Big|_{T,\hat{f}_i}$$

The activity term in Equation (4.56) gives the following:

$$\int_{\alpha_{i0}}^{\alpha_i} RTd[ln(\alpha_i)]\Big|_{T,\hat{f}_i} = RTln\left(\frac{\alpha_i}{\alpha_{i0}}\right) \quad \textbf{(4.57)}$$

The temperature term in Equation (4.56) can be expanded based on entropy as a function of temperature (i.e. $dS = dE/T$ from Equation (4.26), so $ds = C_p\, dT/T$). The following can be expressed for small changes in temperature:

$$\begin{aligned}\int_{T_0}^{T} s_i dT\Big|_{\hat{f}_i,\alpha_{i0}} &= s_{i(T_0)}\int_{T_0}^{T} dT + C_p\iint_{T_0}^{T}\frac{dT^2}{T} \\ &= s_{i(T_0)}(T-T_0) - C_p\left[(T-T_0) - Tln\left(\frac{T}{T_0}\right)\right]\end{aligned} \quad \textbf{(4.58)}$$

The fugacity term in Equation (4.56) gives the following:

$$\int_{\widehat{f_{i0}}}^{\hat{f}_i} RTd\left[ln(\hat{f}_i)\right]\Big|_{T_0,\alpha_{i0}} = RT_0 ln\left(\frac{\hat{f}_i}{\widehat{f_{i0}}}\right) \quad \textbf{(4.59)}$$

For liquids, fugacity can be related to the value at saturation and the pressure of the condensed phase (Lee et al., 2016):

$$ln\,\hat{f}_i = ln\,\widehat{f_i^*} + \frac{v_L}{RT}(P_L - P_i^*) \quad \textbf{(4.60)}$$

Hence, the fugacity term can be rewritten as follows:

$$RT_0 ln\left(\frac{\widehat{f_i}}{\widehat{f_{i0}}}\right) = RT_0 ln\left(\frac{\widehat{f_{i(T_0)}}^*}{\widehat{f_{i0}}}\right) + v_{L(T_0)}(P_L - {P_{i(T_0)}}^*) \quad \textbf{(4.61)}$$

If the reference fugacity $\widehat{f_{i0}}$ is taken as equal to the saturation fugacity at temperature T_0 (i.e. $\widehat{f_{i0}} = \widehat{f_{i(T_0)}}^*$), the fugacity term drops altogether and Equation (4.61) can be rewritten as follows:

$$RT_0 ln\left(\frac{\widehat{f_i}}{\widehat{f_{i0}}}\right) = v_{L(T_0)}(P_L - {P_{i(T_0)}}^*) \quad \textbf{(4.62)}$$

Therefore, an expression for the absolute value of chemical potential has been developed as shown in Equation (4.63).

$$\mu_i = \mu_{i0} + v_{L(T_0)}\left(P_L - {P_{i(T_0)}}^*\right) - s_{i(T_0)}(T - T_0) + C_p\left[(T - T_0) - Tln\left(\frac{T}{T_0}\right)\right] + RTln\left(\frac{\alpha_i}{\alpha_{i0}}\right) \quad \textbf{(4.63)}$$

It is worthwhile to note here that, $(T - T_0) \approx Tln\left(\frac{T}{T_0}\right)$ for a large domain of temperatures. Therefore, a simplified version of Equation (4.63) can be devised where μ and T are linearly related (Equation (4.64)). Such an assumption has been reported in literature (Job and Herrmann, 2006).

$$\mu_i = \mu_{i0} + v_{L(T_0)}\left(P_L - {P_{i(T_0)}}^*\right) - s_{i(T_0)}(T - T_0) + RTln\left(\frac{\alpha_i}{\alpha_{i0}}\right) \quad \textbf{(4.64)}$$

Furthermore, it can be shown from Equation (4.63) that μ_i/T is an increasing function of T, which matches the analysis and arguments presented in section 4.3.2. Since mass equilibrium is characterised with equal μ/T amongst two systems, it can be inferred that diffusion is proportional to spatial gradients in μ/T. However, in cases where the two systems possess equal temperatures, or where the temperature gradients are small, mass equilibrium will then be characterised with equal μ amongst the two systems, and diffusion will be proportional to spatial gradients in μ. In the subsequent chapters analysing mass transfer under temperature gradient, diffusion will be made

proportional to gradients in μ/T to maintain consistency and precision. Nevertheless, since diffusion patterns in this work can be altered greatly even with small temperature gradients (see Chapters 5 and 7), it would be indifferent whether diffusion is proportional to μ/T or μ.

4.5 Summary

In this chapter, it was aimed to understand the underpinning link between temperature gradients and mass transfer. This is the first endeavour in the biomass processing and extraction fields, attempting to characterise such a link using relevant principles of statistical mechanics and thermodynamics. Furthermore, this is one of the very few attempts to attain logical inference beyond mere mathematical derivation, of the relationships between diffusion and temperature which have recently been proposed in literature.

Initially, it was shown that the most probable equilibrium state of an isolated two-system ensemble, is one where the two systems possess equal temperatures, pressures, and chemical potentials. Nevertheless, it was also demonstrated that if temperature gradient were to arise between the two systems, a more precise equilibrium condition would then comprise equal pressure-to-temperature ratios (P/T) for mechanical equilibrium, and equal chemical potential-to-temperature ratios (μ/T) for mass equilibrium. This means that, mass transfer between two phases possessing unequal temperatures, would be driven by spatial gradients in μ/T. While it is not very common to observe scenarios comprising non-uniform temperatures, such condition has been shown to be achievable in biomass-solvent systems heated with microwaves. This is because, these systems exhibit batch characteristics partially, where only mass and volume are conserved but energy flows in cycle from the environment into the system and back to the environment. The continuous motion of energy was shown to alter the condition of thermal equilibrium, where instead of having equal temperatures, the inner phase (biomass) would possess higher temperatures than the outer phase (solvent). This fully matches the findings made earlier in Chapter 3 through heat transfer modelling.

The effect of temperature gradient on mechanical and mass equilibria was studied. It was shown that, for a unit increase in temperature (due to increasing energy) a system's pressure and chemical potential may increase disproportionately, causing a distortion in the equilibrium state. If a temperature gradient existed between the system

and its surroundings, volume transfer and mass transfer would take place against this gradient (i.e., towards the system) to lower the surplus P and $|\mu|$, respectively, and re-establish mechanical and mass equilibria. While this matches common intuition in the case of $P-V-T$ relationships, it is a highly non-trivial description of mass transfer and the analogous $|\mu|-N-T$ relationships, and this should be further investigated in literature and empirical studies.

Due to the inability to directly measure chemical potential, this parameter was expressed in terms of other measurable parameters (including P and T), and in doing so it was shown again that $|\mu|$ increases disproportionately with T. Moreover, expressing μ in terms of P and T enables depicting real-world situations where μ, P, and T are interrelated, and they collectively represent all transfer phenomena taking place simultaneously.

This chapter has achieved the link between temperature and diffusion needed to quantify mass transfer in biomass-solvent systems under microwave heating (Chapter 5 onwards). Cellular-scale diffusion in such systems is mostly described qualitatively in literature, indicating the lack of appreciation of mass transfer in the biomass processing field, but also emphasising the importance of the current work. Very few attempts have been made in the biomass-solvent extraction field to characterise mass transfer under temperature gradient (e.g., (Lee et al., 2016)). Nonetheless, the current work proceeds beyond any other in the field, in adopting a first principles' approach to understanding how microwave-induced temperature gradients can alter diffusion, thereby extraction patterns. The fundamental description offered here for mass transfer can benefit numerous fields beyond biomass-solvent extraction, as it lays a foundation for predicting various diffusion scenarios beyond those that are currently known (e.g., Fick's law, osmotic pressure, and the Ludwig-Soret effect). This contribution can, therefore, be of huge significance.

4.6 Thesis recap

To address the gap in knowledge discussed in Chapter 2, a model was developed in Chapter 3 to simulated microwave heat transfer in biomass-solvent systems at the cellular scale. To further expand the model to incorporate mass transfer, it was vital to understand the fundamental link between temperature and diffusion, and this was conducted in the current chapter.

4.7 Nomenclature

Symbols

ε	$-$	Number of accessible energy states per particle
e	$\boldsymbol{J}$	A given energy state of a particle
E	$\boldsymbol{J}$	Energy
N	$-$	Number of particles
N_e	$-$	Number of particles occupying energy state e
V	$\boldsymbol{m^3}$	Volume
v	$\boldsymbol{m^3}$	Specific volume
$\bar{v}$	$\boldsymbol{m^3}$	Volume occupied by individual particles
p	$-$	Probability
C	$-$	Binomial factor describing combinations of events
Ω	$-$	Number of accessible microstates
S	$\boldsymbol{JK^{-1}}$	Entropy
s	$\boldsymbol{Jmol^{-1}K^{-1}}$	Specific entropy
k_B	$\boldsymbol{JK^{-1}}$	Boltzmann's constant
R	$\boldsymbol{Jmol^{-1}K^{-1}}$	Universal gas constant
T	$\boldsymbol{K}$	Temperature
P	$\boldsymbol{bar}$	Pressure
μ	$\boldsymbol{Jmol^{-1}}$	Chemical potential
δQ	$\boldsymbol{J}$	Energy delivered to a thermodynamic system
A	$-$	Generalised force (intensive property) of a thermodynamic system
x	$-$	Generalised field (extensive property) of a thermodynamic system
H	$\boldsymbol{J}$	Enthalpy
G	$\boldsymbol{J}$	Gibbs' free energy
F	$\boldsymbol{J}$	Helmholtz free energy
B	$\boldsymbol{J}$	$E - \mu N$
f	$\boldsymbol{bar}$	Fugacity
α	$-$	Activity
C_p	$\boldsymbol{Jmol^{-1}K^{-1}}$	Specific heat capacity at constant pressure
C_V	$\boldsymbol{Jmol^{-1}K^{-1}}$	Specific heat capacity at constant volume
C_μ	$\boldsymbol{Jm^{-3}K^{-1}}$	Specific heat capacity at constant chemical potential
C_N	$\boldsymbol{Jm^{-3}K^{-1}}$	Specific heat capacity at constant molar quantity

Subscripts and superscripts

$()_{A/B/C}$	Property of system A, B, or C
$()_T$	Total value over all systems
$()_i$	Property of a component "i"
$\widehat{()}$	Property of a pure component
$()_0$	Baseline value

$()_L$	Property of a condensed state
$()^*$	Property of a saturated vapour associated with the system
$()_{()}$	Property at a given condition, e.g., $v_{(T)}$ is specific volume at temperature *T*

5 TWO COMPETING HYPOTHESES TO EXPLAIN CELL RUPTURE

The aim of this chapter is to validate and compare the two most popular hypotheses attempting to explain why microwave heating improves cell rupture and extraction in biomass-solvent systems. In validating one of the two hypotheses, the steps and methods applied in including mass transfer and cell pressure build-up to the model developed in Chapter 3, will be presented.

This chapter has contributed towards publishing Taqi et al. (Taqi et al., 2020). The format of this chapter is as follows:

5.1 Introduction 124
5.2 Assessment of Steam-Rupturing hypothesis 128
5.2.1 Background and methodology 128
5.2.2 Results and discussion 130
5.3 Assessment of Temperature-Induced Diffusion hypothesis 133
5.3.1 Methodology 133
5.3.1.1 The mass equation 133
5.3.1.1.1 Link between mass transfer and chemical potential 133
5.3.1.1.2 Equation derivation 135
5.3.1.1.3 Assumptions on mass transfer 138
5.3.1.1.4 Assumptions on mass transfer coefficient 139
5.3.1.2 Cell expansion 139
5.3.1.3 Numerical solution to the mass equation 144
5.3.1.4.1 Initial and boundary conditions 145
5.3.1.4.2 Model discretisation and Taylor series approximation 145
5.3.1.4.3 Solution framework 147
5.3.2 Predicted pressure distribution 151
5.3.2.1 Heating-related parameters 154
5.3.2.1.1 Effect of dielectric loss factor (ε'') 154
5.3.2.1.2 Effect of thermal conductivity (k) 157
5.3.2.1.3 Effect of incident electric field intensity ($|E|_0$) 159
5.3.2.2 Other parameters 160
5.3.3 Threshold parameters needed for cell rupture 163
5.4 Summary 164
5.5 Thesis recap 166
5.6 Nomenclature 168

5.1 Introduction

In biomass-solvent systems, the extraction of solutes is usually characterised as a mass transfer process entailing the following: (i) penetration of the solvent into the biomass; (ii) solubilisation of the solute into the solvent; (iii) diffusion of the dissolved solute into the biomass-solvent boundary and then into the bulk solvent (Flórez, Conde and Domínguez, 2015; Mao, Robinson and Binner, 2021). As shown in Chapter 3, microwave heating induces unique heating patterns in biomass-solvent systems; moreover, it is believed that these patterns promote rapid loosening of the cell wall matrix and cause cell rupture (Maran and Prakash, 2015; Mandal, Mandal and Das, 2015; Osaili, 2012). In other words, the prevailing trend in literature accepts cell rupture as the rate-limiting step to extraction, where such an event is thought to improve the three mass transfer steps highlighted above, allowing for enhanced solvent penetration into the biomass; better solute exposure inducing more rapid solubilisation; and improved diffusion of the dissolved solute to the bulk solvent. Although this idea of cell rupture has been discussed widely in literature, and some authors have illustrated structural changes in biomasses treated with microwaves using microscopic imaging (Ferhat et al., 2006; Kratchanova, Pavlova and Panchev, 2004; Rodriguez-Jasso et al., 2011; Yanık, 2017; Zhongdong et al., 2006), almost all discussions are qualitative. As such, there is still no clear quantitative evidence of how microwave heating causes to structural modifications in the biomass, thereby leading to enhanced extraction. Nevertheless, there have recently been two attempts to relate microstructural modifications to microwave heating quantitatively and from a fundamental perspective, and these are discussed below.

The first attempt relates to the common hypothesis that rapid and internal heating under microwaves induces vaporisation within cellular structures, thereby quickly increasing their internal pressures and causing them to rupture (Chan et al., 2011; Chan, Yusoff and Ngoh, 2014; Kala et al., 2016; Letellier and Budzinski, 1999; Yan et al., 2010; Yeoh, Shi and Langrish, 2008). This will be referred to in this work as the Steam-Rupturing hypothesis. A quantitative model has been proposed by Chan et al. (Chan et al., 2016) to link microwave heating with cell pressure through the idea of intracellular steam generation. It is the first model of its kind, in that it couples thermodynamic heating/vaporisation of intracellular moisture and the resulting pressure build-up, with the mechanical properties of the cell wall to predict the time

required for cell rupture. While this model appreciates microwave heating principles through considering dielectric properties and microwave attenuation, it disregards heat transfer and its effect on temperature patterns. This key limitation makes steam rupture possible with any input microwave power since there is no other mechanism for energy transfer within/from the biomass. The key features, strengths, and limitations of Chan's model are summarised in Table 5.1.

The second attempt to relate microwave heating to cell rupture has been proposed by Lee et al. (Lee et al., 2016), through their Temperature-Induced Diffusion hypothesis. This work proposes that the unique temperature gradients induced with microwaves, could alter mass transfer patterns in biomass-solvent systems and, thereby, cause cell rupture. At constant temperature, water flows between a biomass cell and the solvent down its chemical potential gradient (Chapter 4), a quantity which fundamentally depends on gradients in activity and pressure between the two phases (Wijmans and Baker, 1995). It has been proposed by Lee et al. that, if the cell temperature is higher than that of the solvent, then additional water diffuses into the cell (i.e., Temperature-Induced Diffusion), which generates higher cell pressures and increases the likelihood of cell rupture compared with the conventional heating case. This matches the outcomes of Chapter 4, where it has been shown that, mass transfer can occur against a temperature gradient between two phases within a closed system, if such system is, for instance, heated with microwaves. Lee et al. demonstrated that, in theory, even a temperature difference of 1 ℃ could raise the cell pressure up to values large enough to infer cell rupture. However, this concept of Temperature-Induced Diffusion has only been theorised within a hypothetical steady-state paradigm, independent of kinetic aspects underpinning heat/mass transfer, cell expansion, or system geometry/microstructural characteristics. Hence, it cannot be understood whether cell rupture is possible within a realistic timeframe when using a realistic set of input parameters. Another limitation of this hypothesis is the assumption that diffusion is proportional to gradients in chemical potential rather than chemical potential-to-temperature ratios. Although this is reasonable for small temperature gradients, it does not allow expanding the scale of the system or applying large input powers, because such aspects would likely raise the temperature gradients beyond the order of 1 ℃. These key limitations constitute the need for further detailed analysis of the hypothesis, using a framework that incorporates kinetic aspects and

other system characteristics. The key features, strengths, and limitations of Lee's hypothesis are summarised in Table 5.1.

Therefore, the aim of this chapter is to use and further develop the heat transfer model from Chapter 3, to assess both the Steam-Rupturing hypothesis and the Temperature-Induced Diffusion hypothesis, in terms of their ability to explain cell rupture under microwave heating.

Existing hypothesis	Strengths	Limitations
Steam-Rupturing hypothesis; Chan model (Chan et al., 2016) **Key features:** • Pressure-volume relationship based on mechanical properties of the parenchyma cell wall. • Average radiative heating power of intracellular water.	• Accounts for some microstructural features. • Accounts for dielectric properties. • Incorporates simplified distribution of particles and solvent within a reaction vessel. • Models power dissipation using Lamberts law. • Couples heating with pressure build-up. • Model can be applied to different systems using variable input power.	• Assumes all moisture is concentrated in one part of the plant cell. • No heat transfer (except microwave heating) and no mass transfer. • Predicted rupture time does not correlate with the experimentally measured extraction rate (~70% yield attained after 1 min; ~100% achieved after 4 minutes; however, rupture predicted at 5.4 minutes). • Applicable to low solvent-to-solid ratios only.
Temperature-Induced Diffusion hypothesis (Lee et al., 2016) **Key features:** • Mass transfer occurs due to chemical potential gradients. • Temperature gradients induced by microwaves, raise the gradients in chemical potential and increase cell pressure, making cell rupture more likely.	• Identifies temperature as a driving force for mass transfer. • Correlates dielectric properties with temperature gradients and, in turn, cell pressure build-up. • States that cell rupture could be achieved with a temperature gradient of as low as 1 °C.	• Microstructural features of the biomass-solvent system not included. • Equilibrium processes only; no kinetic processes. • The effects of microwave power dissipation due to heat transfer not investigated. • Diffusion assumed proportional to chemical potential rather than the ratio with temperature. • Hence, this hypothesis is a proof-of-concept only.

Table 5.1 – Key features, strengths, and limitations of the existing microwave cell rupture hypotheses

5.2 Assessment of Steam-Rupturing hypothesis

5.2.1 Background and methodology

Under this hypothesis, cell rupture occurs when steam is raised at sufficiently high pressures to overcome the mechanical resistance of cells, thus causing structural damage and rupture. Unlike what had been described in Chan's Steam-Rupturing model (Chan et al., 2016), steam generated within a cell is likely to be saturated rather than superheated. This is because, as steam expands within the cell it eventually experiences a resistant compressive force from the surrounding cell walls, causing it to maintain its saturation state even as temperature increases. To overcome this resistance, temperature should be increased to a value corresponding to the minimum saturation pressure required for inducing rupture within the cell structure (Figure 5.1). Therefore, validating the Steam-Rupturing hypothesis can be achieved through heat transfer analysis of the biomass-solvent system, using the model developed in Chapter 3.

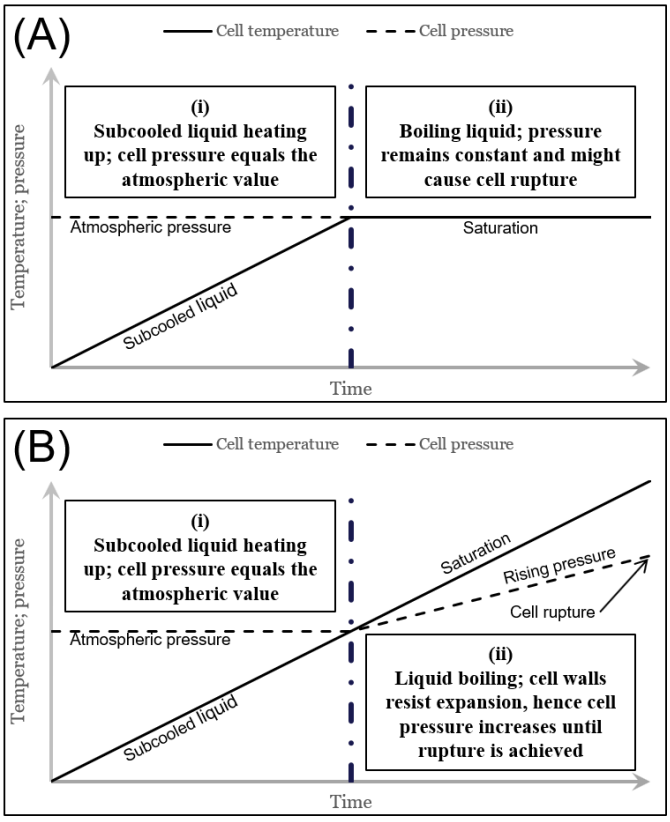


Figure 5.1 – Demonstration of how cell pressure rises due to vaporisation when (A) there is no cell wall; (B) there is a cell wall. In (A), boiling occurs at atmospheric pressure, which might or might not be sufficient for cell rupture. In (B), boiling is resisted by the surrounding cell walls, inducing pressure within the cell. This pressure increases together with temperature as the saturation condition, until cell rupture is achieved

With incorporating a cellular-scale heat transfer element, and allowing a more comprehensive set of heating parameters to be manipulated, the model developed in Chapter 3 overcomes a key limitation in the Steam-Rupturing model available in literature (Chan et al., 2016). A similar analysis approach to that shown in Chapter 3 was applied to this analysis, where a single independent heating parameter was varied at a time while keeping all other parameters constant. A range of key parameters were studied, including dielectric loss factor of biomass ($\varepsilon''_{biomass}$), thermal conductivity (k), and incident electric field intensity ($|E|_0$).

It was intended here to investigate whether biomass cell temperatures sufficient for steam-rupturing can be achieved with a realistic set of input heating parameters. Hence, the physical limits of $\varepsilon''_{biomass}$, k, and $|E|_0$ were considered to account for the most extreme heating scenario. $|E|_0$ was fixed at a value of $10^4\ Vm^{-1}$ which is the limit for single-mode microwave cavities (Robinson et al., 2010). Moreover, the upper limit for $\varepsilon''_{biomass}$ was set at 35, since the largest reported value for some edible materials between 0 ℃ and 100 ℃, at a microwave frequency of $2.45\ GHz$, is around 30 (Sipahioglu and Barringer, 2003). Also, the lower limit for k was set at $0.1\ Wm^{-1}K^{-1}$ since values as low as 0.2 have been reported for fruits and vegetables with 80% moisture, and k is known to increase with higher moisture levels (Nesvadba, 2005). Furthermore, the biomass geometry has been modified in this analysis, as the number of cells in each dimension was defined to constitute a cubic cell cluster with dimensions ranging from 0.1 to 0.5 mm (Figure 5.2). On one hand this better resembles experimental situations, and on the other hand, the cubic shape decreases the surface area-to-volume ratio of the biomass, compared to the previous cluster size definition (equal number of cells in each dimension). This minimisation of the surface area-to-volume ratio further increases the steady state temperature gradient, thereby ensuring the most extreme of cases is being accounted for.

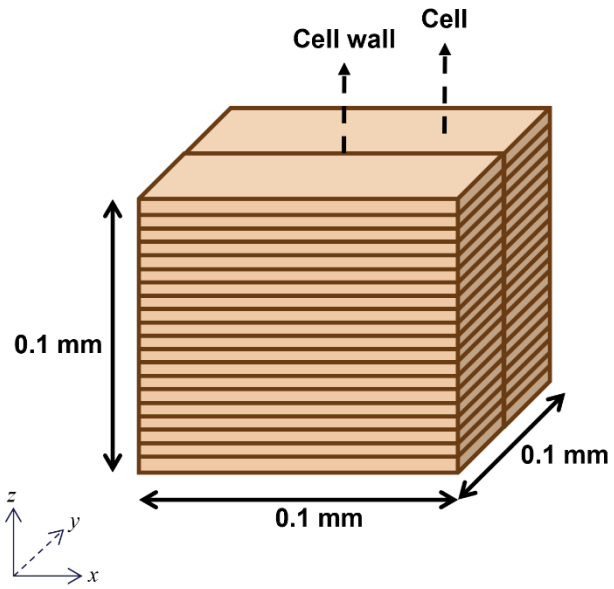


Figure 5.2 – A cubic biomass cluster with 1x2x10 cells and particle size of 0.1 mm

Table 5.2 summarises the variables and constants for the current analysis, while all other parameters were kept constant as shown in Table 5.5.

Figure/Table	$\varepsilon''_{biomass}$	$\lvert E\rvert_0$ (Vm^{-1})	k $(Wm^{-1}K^{-1})$
Table 5.3A	35	10000	0.1, 0.2, 0.4
Table 5.3B	5, 20, 35	10000	0.2

Table 5.2 - Input variables and constants for the Steam-Rupturing analysis

5.2.2 Results and discussion

Table 5.3 shows the maximum temperature difference between biomass and solvent at thermal steady state (ΔT_{max}), and the time required to achieve 95% of the steady state temperature (t_{95-T}), for variable thermal conductivity (k) and dielectric loss factor of biomass ($\varepsilon''_{biomass}$), and different-sized biomass particles.

	(A) $\varepsilon''_{biomass} = 35$ Variable k $(Wm^{-1}K^{-1})$			**(B)** $k = 0.2\ Wm^{-1}K^{-1}$ Variable $\varepsilon''_{biomass}$		
Particle size (mm)	**0.1**	**0.2**	**0.4**	**5**	**20**	**35**
0.1	5.374; 1.790	2.687; 1.635	1.344; 1.563	0.384; 4.841	1.535; 2.405	2.687; 1.635
0.3	34.397;	17.198;	8.599;	2.457;	9.828;	17.198;

	3.670	2.534	1.995	5.674	3.276	2.534
0.5	83.801; 7.292	41.901; 4.277	20.950; 2.838	5.986; 7.268	23.943; 4.971	41.901; 4.277
	ΔT_{max} (°C); t_{95-T} (s)					

Table 5.3 – Maximum temperature difference between biomass and solvent at thermal steady state, and time required to achieve 95% of steady state, for variable cell cluster size and (A) thermal conductivity; (B) dielectric loss factor of biomass

The heating trends observed here match those obtained in Chapter 3, where at thermal steady state a temperature gradient is established in the biomass, with a maximum temperature around the centre of the cluster and a minimum at the biomass-solvent boundary (Figure 5.3). As seen in Table 5.3 ΔT_{max} is always positive given $\varepsilon''_{biomass} > 0$, and it increases in magnitude as $\varepsilon''_{biomass}$ and particle size are increased, and when k is decreased. On the other hand, t_{95-T} remains in the order of seconds for all conditions investigated, which is well within the timeframes reported in empirical studies applying similar input microwave powers (Beneroso et al., 2017; Adam et al., 2017; Shepherd et al., 2018) Nevertheless, as observed in Chapter 3, t_{95-T} increases when particle size is increased, and when $\varepsilon''_{biomass}$ and k are decreased.

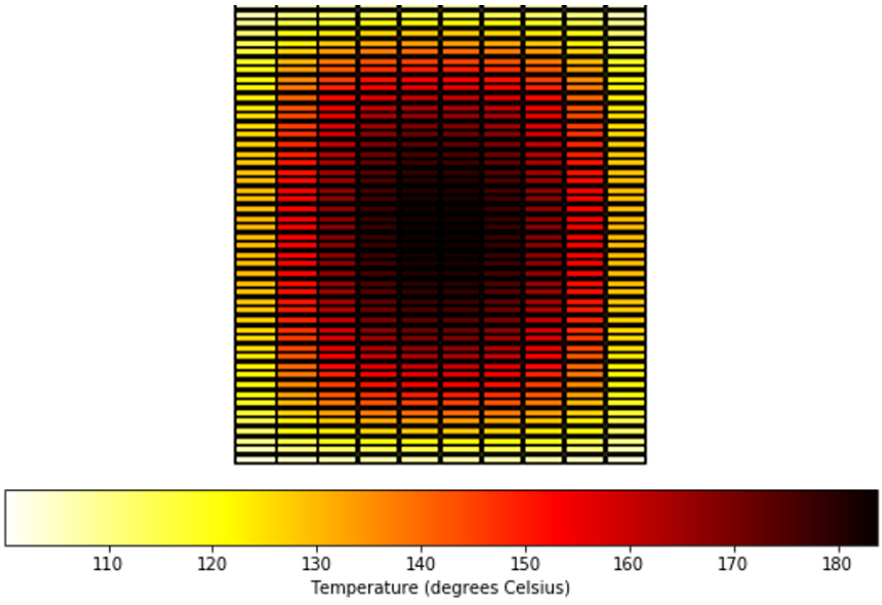


Figure 5.3 – Steady state temperature distribution of a YZ cross-section of a 0.5 mm cubic biomass within a biomass-solvent system. Dielectric loss factor of biomass = 35; thermal conductivity = 0.1 $Wm^{-1}K^{-1}$; incident electric field intensity = 10000 Vm^{-1}

The largest ΔT_{max} in Table 5.3 is around 84 ℃, and it corresponds to the most extreme values of $\varepsilon''_{biomass}$, k, $|E|_0$, and particle size. Under more realistic conditions, it is likely that a temperature difference of just $10 - 20$ ℃ is achieved which, as mentioned above, will only occur near the centre of the biomass, as lower temperatures are expected closer to the edge of the material (Figure 5.3). As discussed in section 5.2.1, if cell rupture is achieved through intracellular steam generation, then the generated steam must exhibit the minimum pressure required to overcome mechanical resistance of the cell walls surrounding the cell. Steam is highly unlikely to be superheated within an intact cell due to the compressive force applied by the elastic cell walls, which maintains the saturation condition as the cell temperature increases. Therefore, cell rupture can only be achieved if the cell temperature is raised to a value corresponding to a saturation vapour pressure, equal to the minimum pressure needed for plastic deformation of the cell walls. As seen in Table 5.3, under the most extreme heating conditions, the maximum temperature obtainable within the biomass during an ambient-pressure extraction process is 184 ℃ (i.e., the solvent temperature of 100 ℃, plus a temperature difference of 84 ℃). At 184 ℃ the saturation steam pressure equals $10\ bar$ (Rogers and Mayhew, 1995), which is sufficient to cause rupture within some types of cell. However, for other cell types the required pressure could be much higher, constituting the need for even higher temperatures. For example, the rupture pressure of epidermal cells has been estimated around $70\ bar$ (Lee et al., 2016); hence, a temperature around 280 ℃ would be needed to achieve cell rupture through intracellular steam (Rogers and Mayhew, 1995). Such unrealistically high temperatures are more likely to bring about thermochemical degradation in biomass materials (e.g., cellulose decomposition), rather than causing physical phenomena like cell rupture (Budarin et al., 2010). Furthermore, even if such high temperatures are achievable in biomass without inducing thermochemical degradation, these will be confined to the centre of the biomass cluster rather than being evenly distributed. Therefore, away from the centre of the biomass and under realistic physical and experimental conditions, the temperature and pressure within the biomass cluster are expected to be much lower, equating to values that are insufficient to underpin the steam-rupturing concept. Nevertheless, enhanced extraction has been observed under microwave heating, in studies investigating biomasses sized less than a millimetre (like Table 5.3) (Bagherian

et al., 2011; Galan et al., 2017). This indicates that cell rupture is underpinned by an alternative mechanism.

In summary, steam-rupturing of cells could occur at the extreme fringes of physical and experimental conditions, but the physics of heat transfer at the cellular scale mean that it is highly unlikely to be as widespread as previously proposed. Therefore, if cell rupture does readily occur during microwave heating, then clearly an alternative mechanism is responsible for this effect.

5.3 Assessment of Temperature-Induced Diffusion hypothesis

Under this hypothesis, cell pressure varies as water diffuses in and out of cells, and this diffusion takes place in accordance with chemical potential gradients and resistance to mass transfer. Therefore, to assess and validate the Temperature-Induced Diffusion hypothesis, the heat transfer model developed in Chapter 3 must be extended to include mass transfer and cell expansion, and section 5.3.1 below presents the steps and methods applied for this purpose. The extended model is subsequently used in section 5.3.2 to assess the Temperature-Induced Diffusion hypothesis with a set of physical parameters.

5.3.1 Methodology

5.3.1.1 The mass equation

5.3.1.1.1 Link between mass transfer and chemical potential

Mass equilibrium between two phases is characterised by an equal chemical potential-to-temperature ratio amongst them (Chapter 4). Therefore, it follows that matter flows down a spatial gradient in μ/T, which is analogous to Fourier's law of heat transfer where heat flows down a spatial gradient in temperature. Considering a unidimensional case (i.e., the *x-direction* only), the molar flux of a species can be expressed as follows:

$$J_i = -L_i \frac{d}{dx}\left(\frac{\mu_i}{T}\right) \qquad \textbf{(5.1)}$$

J_i and L_i are the mass flux and mass transfer coefficient of a component in phase "i", respectively.

Assuming uniform temperature, Equation (5.1) reverts to the form shown in Equation (5.2), which is analogous to the classical conception that diffusion is proportional to spatial gradients in chemical potential (Wijmans and Baker, 1995).

$$J_i = -\frac{L_i}{T}\frac{d\mu_i}{dx} = -\bar{L_\iota}\frac{d\mu_i}{dx} \quad \textbf{(5.2)}$$

$\bar{L_\iota}$ is the mass transfer coefficient per unit temperature.

If pressure is also assumed uniform, chemical potential (Equation (4.63)) can be written as follows:

$$\mu_i = \mu_{i0} + RTln\left(\frac{\alpha_i}{\alpha_{i0}}\right) \quad \textbf{(5.3)}$$

Substituting Equation (5.3) into Equation (5.2) yields the following:

$$J_i = -\frac{L_i R}{\alpha_i}\frac{\partial \alpha_i}{\partial x} = -\frac{\bar{L_\iota} RT}{\alpha_i}\frac{\partial \alpha_i}{\partial x} \quad \textbf{(5.4)}$$

Equation (5.4) is analogous to Fick's law of diffusion, but it uses activity instead of molar concentration. Therefore, Fick's law describes a special case in mass transfer, where both temperature and pressure are held constant. On the other hand, if temperature is uniform but pressure is variable, chemical potential (Equation (4.63)) reverts to a form analogous to the van't Hoff osmotic pressure expression. This is shown in Equation (5.5), where the osmotic pressure of a phase "i" can be obtained by equating the chemical potentials of phases "i" and "j", assuming they are separated by a semi-permeable membrane, and that pressure can only rise in phase "i". Applying further assumptions on the purity and ideal nature of the mixtures involved, Equation (5.5) can be transformed to the exact van't Hoff expression.

$$\pi_i = \frac{RT}{v_{L(T)}} ln\left(\frac{\alpha_j}{\alpha_i}\right) \quad \textbf{(5.5)}$$

π_i is the osmotic pressure of phase "i".

A third example can also be demonstrated on assuming uniform pressure but allowing activity and temperature to vary. In this case, Equation (5.1) can be expressed as follows (assuming small variation in temperature):

$$J_i = -\left[\frac{L_i R}{\alpha_i}\right]\frac{\partial \alpha_i}{\partial x} - \left[\frac{L_i}{{T_i}^2}\left(s_{i(T_0)}\left[T_0(T_i - 1) - {T_i}^2\right] - \mu_{i0} - v_{L(T_0)}\left[P_L - {P_{i(T_0)}}^*\right]\right)\right]\frac{\partial T_i}{\partial x} \quad \textbf{(5.6)}$$

Equation (4.6) is analogous to a unidimensional case of the Ludwig-Soret effect, a mechanism in which temperature gradients are deemed responsible for inducing mass diffusion in convection-free settings, causing mixture separation as lighter particles tend to migrate to the hotter region more readily. The Ludwig-Soret expression is a two-term equation, where one term describes diffusion under activity/concentration gradients, and the other describes diffusion under temperature gradients. Mass equilibrium is, therefore, constituted through a balance between the two gradients (Kishikawa et al., 2012; Koyama and Tsukada, 2021; Rahman and Saghir, 2014).

From the examples shown here, it is clear that the chemical potential expression derived in Chapter 4 (Equation (4.63)) is in full agreement with the previously proposed laws and arguments on mass transfer. In fact, this expression underpins the other mass transfer laws, as these can be derived from the chemical potential expression on applying certain assumptions.

As discussed in section 4.4.2, although diffusion is proportional to gradients in μ/T (Equation (5.1)), the same modelling outcomes can still be drawn if diffusion was instead made proportional to gradients in μ (as carried out in literature (Lee et al., 2016)). As will be seen, even temperature gradients as small as 1 ℃ can cause significant changes to diffusion, but with such small temperature gradients it can be assumed for all practical purposes, that the biomass-solvent system possesses a uniform temperature. Therefore, mass transfer can be reduced to Equation (5.2), where diffusion is proportional to gradients in μ instead of μ/T. In the current work, μ/T is used to maintain consistency and precision.

5.3.1.1.2 Equation derivation

The steps presented below for deriving the mass equation are analogous to those shown in section 3.2.2 for deriving the heat equation.

Consider an infinitesimal unit in space, whose bottom-left-front corner is located at Cartesian coordinates *(x, y, z)*, and whose top-right-back corner is located at *(x+δx,*

y+δy, z+δz) (Figure 5.4). Some matter is being delivered into the unit in the *x-direction*, *y-direction* and *z-direction* at flux rates J_{x-in}, J_{y-in}, and J_{z-in}, respectively, and some matter is being removed at flux rates J_{x-out}, J_{y-out}, and J_{z-out} through the respective directions.

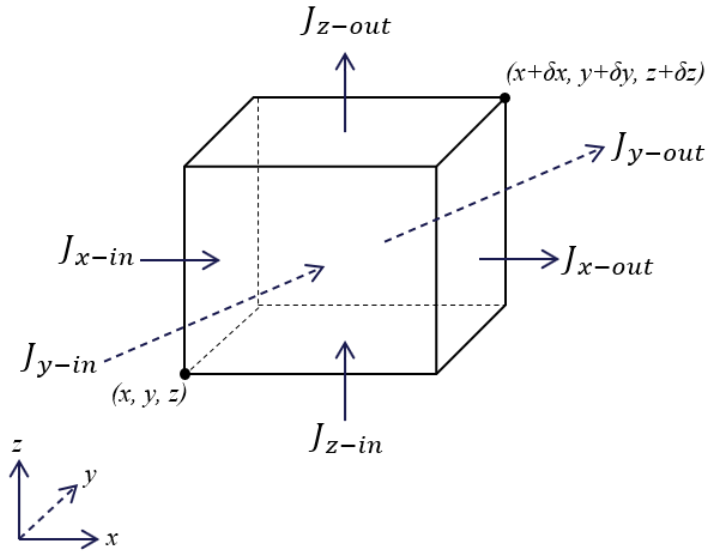


Figure 5.4 – Differential mass transfer element. Directions of mass flow are arbitrary and used for demonstration purposes

The matter conservation principle dictates the following (assuming no chemical reactions take place):

$$Moles\ accumulated = Moles\ input - Moles\ output \tag{5.7}$$

The output moles can be expressed in terms of the input moles. By considering the *x-direction* only, the following can be written:

$$J_{x-out}\delta y\delta z = \left(J_{x-in} + \frac{\partial J_{x-in}}{\partial x}\delta x\right)\delta y\delta z \tag{5.8}$$

Therefore, the input and output moles can be expressed collectively as follows:

$$J_{x-in}\delta y\delta z - J_{x-out}\delta y\delta z = -\frac{\partial J_{x-in}}{\partial x}\delta x\delta y\delta z \tag{5.9}$$

Substituting the chemical potential-diffusion relationship (Equation (5.1)) into Equation (5.9) yields the following:

$$J_{x-in}\delta y\delta z - J_{x-out}\delta y\delta z = L_x \frac{\partial^2}{\partial x^2}\left(\frac{\mu}{T}\right)\delta x\delta y\delta z \quad \textbf{(5.10)}$$

Summation over all input and output moles in the 3 directions yields the following:

$$Moles\ input - Moles\ output = \left[L_x \frac{\partial^2}{\partial x^2}\left(\frac{\mu}{T}\right) + L_y \frac{\partial^2}{\partial y^2}\left(\frac{\mu}{T}\right) + L_z \frac{\partial^2}{\partial z^2}\left(\frac{\mu}{T}\right)\right]\delta x\delta y\delta z \quad \textbf{(5.11)}$$

By assuming the mass transfer coefficient is equal throughout the unit ($L = L_x = L_y = L_z$), the expression can be rewritten as follows:

$$Moles\ input - Moles\ output = L\delta x\delta y\delta z\nabla^2\left(\frac{\mu}{T}\right) = L\delta V\nabla^2\left(\frac{\mu}{T}\right) \quad \textbf{(5.12)}$$

$\delta V = \delta x\delta y\delta z$ is the infinitesimal volume of the differential mass transfer element.

Matter accumulated in the unit is simply equivalent to the temporal rate of change of the molar quantity, as shown below:

$$Moles\ accumulated = \frac{\partial N}{\partial t} \quad \textbf{(5.13)}$$

Substituting Equations (5.12) - (5.13) into the initial matter conservation expression (Equation (5.7)) yields the following:

$$\frac{\partial N}{\partial t} = L\delta V\nabla^2\left(\frac{\mu}{T}\right) \quad \textbf{(5.14)}$$

Equation (5.14) is the mass equation describing molar quantity of any given species in the biomass-solvent system in any given location at any given time. Like the heat equation (Equation (3.8)), it is a partial-differential equation (PDE) that should be solved to result in the desired molar distribution. Numerical solution to the mass equation is described in section 5.3.1.3.

5.3.1.1.3 Assumptions on mass transfer

In this work, the biomass-solvent system incorporates two species, namely water and solute. The solvent phase comprises pure water while cells contain both water and small amounts of solute (cell water activity, $\alpha_W > 0.95$). Water activity (α_W) was taken as equal to the mole fraction because it is always very close to unity.

This model evaluates cell rupture as a rate-limiting step to enhancing extraction, which is a widely adopted and discussed assumption (section 5.1). Based on this, two key assumptions were made here to remove unnecessary complexity from the mass transfer framework, which are detailed below.

Firstly, it was assumed that only water is capable of diffusing between cells and the solvent, which is because water is the constituent regulating cell pressure and dictating the likelihood of rupture. Solutes get liberated upon cell rupture, but the physics of rupture itself and the subsequent events were not included in the model, as they are immaterial to this work. It was only intended here to infer the likelihood of cell rupture through quantifying cell pressure, thereby maintaining the literature assumption that a cell rupture event is required to enhance extraction. Therefore, this model is not expected to apply in cases where mass transfer occurs readily at room temperature, or at any other condition where cell rupture is not applicable. Nevertheless, this assumption will be readdressed in Chapter 7, where both water and solute diffusion are to be modelled independently of cell rupture.

Secondly, since cell rupture is the rate-limiting step here, it was assumed that the most significant resistance to water flow within the biomass, is experienced across cell boundaries (i.e., membranes). Hence, the time required to achieve cell rupture (if such an event is possible) depends predominantly on how rapidly water flows through the cell boundary and accumulates in the cell. Due to this, water diffusion through the cell walls was ignored in this model, as this process was considered to take place much faster than water diffusion into cells, which is supposed to dictate whether cell rupture can occur fast enough. Considering this, the cell walls were treated in this model as part of the solvent phase (section 5.3.1.4.2).

Both assumptions discussed above are to be readdressed in Chapter 7. Nevertheless, for the current analysis addressing cell rupture as the rate-limiting step, only water diffuses in the system, and it does so directly between cells and the solvent phase.

5.3.1.1.4 Assumptions on mass transfer coefficient

The mass equation requires knowledge of the value of L, which describes the resistance to mass transfer. However, this parameter is not commonly available in literature; hence, an alternative means should be considered, such as expressing L in terms of other known parameters. Given that Equation (5.4) is analogous to Fick's law of diffusion (Equation (5.15)), the mass transfer coefficient (L) can be related to diffusivity (D) as shown in Equation (5.16).

$$J_i = -D_i \frac{\partial c_i}{\partial x} \tag{5.15}$$

$$L_i = \bar{L}_i T = \frac{D_i c_i}{R} \tag{5.16}$$

Diffusivity (D) is more widely available in literature than the parameter L. However, Equation (5.16) only holds true at uniform temperature and pressure since Equation (5.4) (analogous to Fick's law) has been derived on this basis. This means that L should be defined separately for each phase in the system, and then, considering diffusion between two phases "i" and "j", the effective L can be assumed as the mean average of L_i and L_j, due to the very small scale of the system.

5.3.1.2 Cell expansion

Mass transfer and pressure distribution are interdependent; on one hand mass transfer is driven by pressure gradients, but on the other hand pressure build-up is influenced by the quantity of matter accumulated due to diffusion (Equations (4.63) and (5.1)). For instance, a biomass cell tends to expand upon receiving an influx of incompressible liquid such as water, but this expansion is resisted by the surrounding cell walls, inducing pressure within the cell structure which resists further inward diffusion. In accordance with the principles underpinning osmosis (Devlin and Witham, 1983), cell pressure is expected to increase with liquid influx until it is high enough to completely resist inward diffusion (i.e. cell turgor pressure equals the osmotic pressure). This series of events is demonstrated in Figure 5.5.

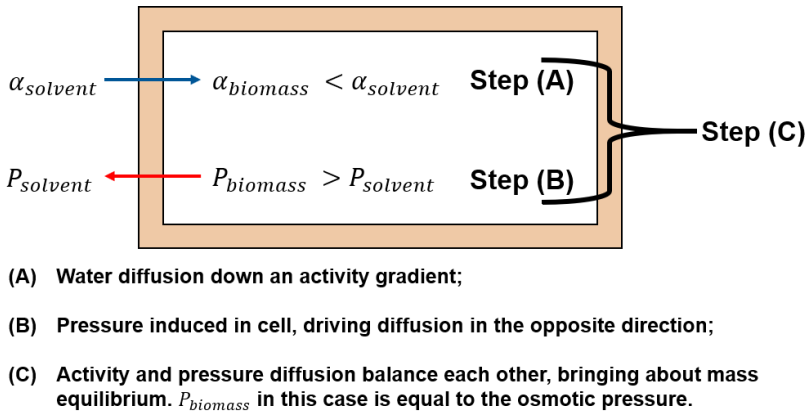


Figure 5.5 – Schematic demonstrating the interdependence between pressure and diffusion, where water influx to cells induces pressure, which then drives water to diffuse out of the cell

A quantitative expression for how pressure distribution affects mass transfer is available through the chemical potential expression (Equation (4.63)). However, to complete the cycle an expression is needed to define how the quantity of accumulated matter affects cell pressure build-up. This section attempts to estimate a pressure-volume relationship for biomass cells such that, under the geometrical constraints set in section 3.2.1, the pressure of a cell is quantifiable given that its volume (hence, molar quantity) is known. The methods and assumptions applied to achieve such cell pressure-volume relationship are presented below.

As discussed in Chapter 2 (section 2.2), a primary cell wall fragment can be envisaged as a polymer constituted of cellulose microfibrils embedded within an amorphous matrix (Wu et al., 1985). Hence, cell walls exhibit mechanical behaviour akin to reinforced rubber, and such behaviour has been demonstrated experimentally for some types of hydrated cell wall (Zamil, Yi and Puri, 2015). The typical stress-strain curve of rubber-like materials can be represented mathematically, and an adequate example of this is the "MRS equation" (Wood, 1977) which has been further developed for this work by introducing the parameter "Z" (Equation (5.17)).

$$\sigma/_{W} = ((1 + Z\epsilon)^{-1} - (1 + Z\epsilon)^{-2})\, exp\, 0.38((1 + Z\epsilon) - (1 + Z\epsilon)^{-1}) \qquad \textbf{(5.17)}$$

Equation (5.17) gives stress (σ) as a function of strain (ϵ) for rubber-like materials. W and Z are manipulated to dictate the strength of a cell wall fragment, as the product of these two parameters is equal to the elastic modulus of the fragment at zero strain

(Y_0). For example, fixing Y_0 at a value of $800\,MPa$ generates Figure 5.6, which matches experimental stress-strain curves attained for some types of hydrated cell wall (Zamil, Yi and Puri, 2015). This demonstrates the suitability of this framework, as it is meaningful on one hand, but also easy to incorporate within the overall extraction model intended here. Nevertheless, future developments should consider further approaches for the mechanical characterisation of cell walls, thereby improving the model's predictability and widening its applicability. Such developments may include expanding the domain of stress-strain equations used; providing specific mechanical data by conducting relevant experiments; and characterising the mechanical behaviour of secondary cell walls.

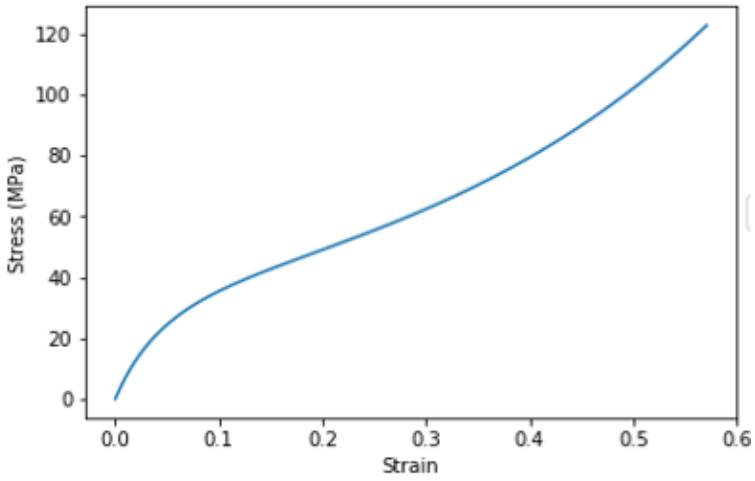


Figure 5.6 – Computational stress-strain behaviour with Y_0 = 800 MPa (Equation (5.17))

When mechanical equilibrium exists between the forces acting on the cell and those acting on the surrounding cell wall fragments, the cell pressure (P_L) can be expressed in terms of the cell wall stress (σ). Quantifying such a balance requires understanding the stress distribution in cell wall fragments and setting some simplifying assumptions.

Figure 5.7 demonstrates an example of the 3-dimentional stress distribution in a cell wall fragment aligned parallel to the *x-direction*. Axial stress components are denoted the letter sigma (σ) while shear stress components are denoted the letter tau (τ). The subscripts indicate the orientation of the surface upon which the stress component is acting, together with the direction of the component. For instance, τ_{xy} is a shear stress component directed towards the *y-direction* and acting upon the surface normal to the *x-direction*.

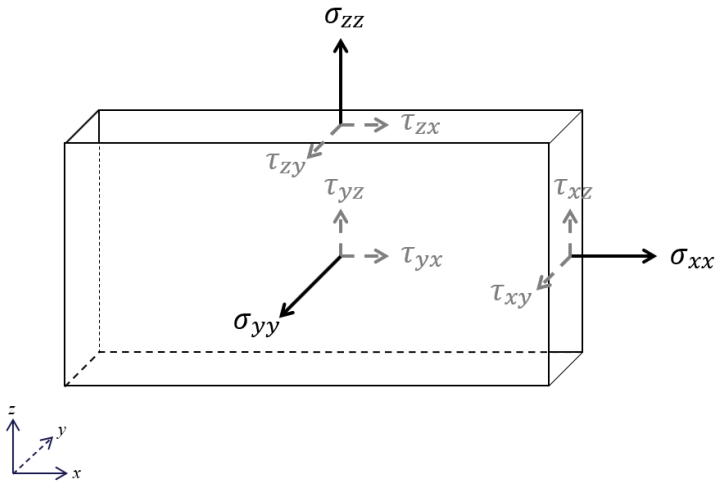


Figure 5.7 – Stress components acting on a cell wall fragment

Two assumptions have been made here to simplify the analysis. Firstly, the cell wall is a single, rubber-like fragment with no mechanical distinction between the different layers such as the primary wall and the middle lamella (Chaplain, 1993; Pieczywek and Zdunek, 2014; Wu, Spence and Sharpe, 1988). Therefore, the shear stress components can be ignored since cell walls stretch unidirectionally and elastically.

Secondly, cell wall fragments can only expand in one direction, namely, the *x-direction*. This is because cells have grown to occupy their cuboid shape, and for this to take place, the stiffness in the *x-direction* must be smaller than those applicable in other directions. This analogy is based on the Multinet-Growth hypothesis (Roelofsen and Houwink, 1953), which has been discussed in Chapter 2 (section 2.2). Based on the assumption made here, all axial stress components other than σ_{xx} can be ignored.

As a cell expands, its pressure is balanced by the axial stress (σ_{xx}) developed in its cell wall (Figure 5.8). The force balance constitutes the relationship shown in Equation (5.18) between stress (σ_{xx}) and cell pressure (P_L).

$$P_L yz = 2t_{CW}\sigma_{xx}(y + z + 2t_{CW}) \quad \textbf{(5.18)}$$

y and z denote the cell's width and height, respectively. Also, t_{CW} is the cell wall thickness.

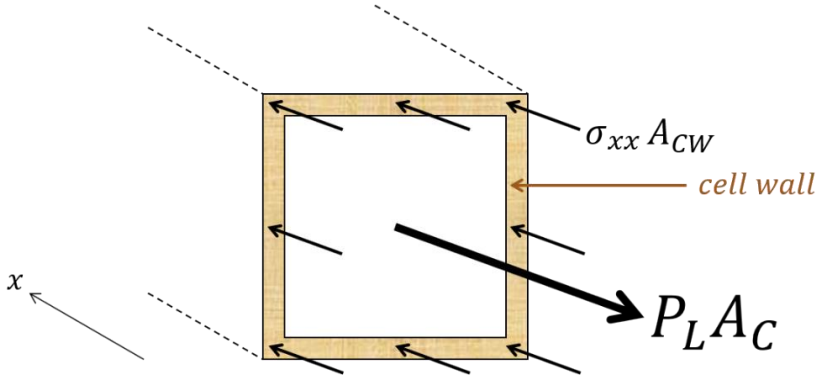


Figure 5.8 – Force balance between a cell and its surrounding cell wall. A_C and A_{CW} are the cross-sectional areas of the cell and surrounding cell wall, respectively, along the *x-direction*

Cell pressure can be expressed in terms of cell volume by solving Equations (5.17) – (5.18) simultaneously. However, it should be noted that the cell wall thickness (t_{CW}) is not constant, but rather it shrinks as the fragment elongates. It has been suggested that this shrinkage occurs to preserve the volume of the wall fragment as its length increases (i.e., the cell wall fragment is incompressible) (Chaplain, 1993). This assumption has also been made in the current work, and with it the cell wall thickness (t_{CW}) can be related to the strain (ϵ_x) by Equation (5.19).

$$t_{CW} = \frac{t_{CW_0}}{1 + \epsilon_x} \tag{5.19}$$

t_{CW_0} is the resting/unstretched cell wall thickness.

While a pressure-volume relationship can be derived analytically with Equations (5.17) – (5.19), a numerical approach has been adopted instead, to set a foundation upon which further complexity can be introduced beyond the scope of this thesis. Such complexity might be necessary for more complex geometry, but it would likely complicate any attempts to solve the problem analytically.

Figure 5.9 describes the numerical framework. The required inputs are a set of geometrical values (i.e., cell length, width, height, and wall thickness) and an input array of discrete pressure values separated by a finite step (δP). For every pressure value in the predefined domain, the stress (σ_{xx}) and strain (ϵ_x) are computed using Equations (5.18) and (5.17), respectively. The strain (ϵ_x) is then used to compute new values for the cell volume, length, and wall thickness, which are subsequently used

for the next pressure value in the array. The cycle is repeated for every consecutive pressure value in the predefined domain.

The numerical framework computes a cell volume corresponding to every input pressure value. Hence, a cell pressure-volume relationship is generated where, if the volume is known the pressure can be interpolated, and vice versa.

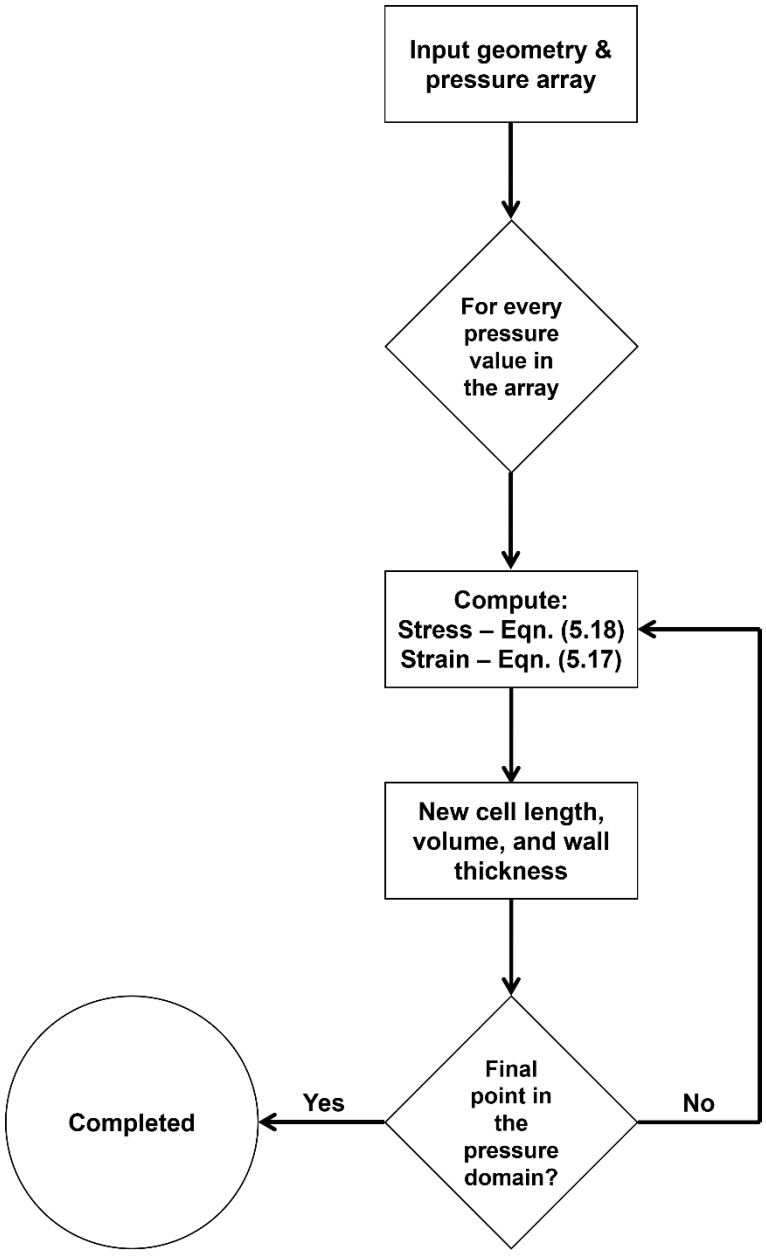


Figure 5.9 – Numerical framework for cell expansion

5.3.1.3 Numerical solution to the mass equation

Like the heat equation (Equation (3.8)), the partial-differential mass equation (Equation (5.14)) was solved using a finite-difference time-domain (FDTD) technique known as the method of lines.

5.3.1.4.1 Initial and boundary conditions

The initial distribution of μ/T in the biomass-solvent system depends on the initial temperature, pressure, and water activity. Initial temperature ($T_{initial}$) is a user input applicable throughout the system, while initial pressure ($P_{L_{initial}}$) equals the atmospheric value in all phases. Water activity in the solvent always equals unity since the solute does not diffuse in this model; however, the initial cell water activity ($\alpha_{W_{initial}}$) is a user input applicable to all biomass cells. On the other hand, initial water-molar distribution depends on the user inputs for density (ρ_L) and volume. In the solvent phase, initial volume depends on the solvent-to-solid ratio (S_R), whereas for cells a set of input dimensions (length, width, and height) defines the volume. Cells are assumed to experience zero strain initially, but this condition can be achieved in multiple ways, either by having cells that are empty, full, or partially occupied by water. Therefore, a void fraction (Φ_C) has been defined, which is a user input dictating the percentage of cell volume that is initially empty from water.

The boundary condition has been set such that water cannot escape the biomass-solvent system. In other words, the total molar quantity in the biomass-solvent system is conserved.

5.3.1.4.2 Model discretisation and Taylor series approximation

The steps employed in approximating the mass equation (Equation (5.14)) as an ODE using the method of lines, are the same are those used earlier in solving the heat equation (section 3.2.3). Firstly, the model was divided into discrete numerical points and, secondly, the spatial second derivatives in μ/T were approximated using a second-order Taylor series expansion. See section 3.2.3 for a detailed discussion of the steps and methods applied here.

As previously done in section 3.2.3.2 for heat transfer, the biomass was discretised into many finite numerical points, and the solvent was assumed as one homogeneous phase described by a single numerical point. However, in accordance with defining cell rupture as the rate-limiting step to enhancing extraction, water diffusion through the cell walls had been ignored in the current model (section 5.3.1.1.3). Therefore, and unlike the case presented in section 3.2.3.2 for the heat transfer analysis, the cell wall fragments were taken here as part of the solvent phase. This means that, within the biomass, only cells are distinct phases represented by discrete numerical points (Figure 5.10), whereas the cell walls are described by the numerical point representing the

solvent. Like section 3.2.3.2, the numerical point describing the solvent (and cell wall fragments) cannot be denoted a fixed location, but rather, it should "move" continuously so that it is in the same proximity to all biomass phases. However, since the cell walls are part of the solvent phase here, the discrete point representing the solvent is not displaced alongside the biomass-solvent boundary, but instead, it moves across the biomass to surround cells and enable direct mass transfer between the solvent phase and each cell (Figure 5.10). As discussed in section 5.3.1.1.3, incorporating cell walls as part of the solvent phase is an assumption intended to remove complexity beyond the fundamental perception that cell rupture is the rate-limiting step to enhancing extraction. This perception follows arguments in literature (section 5.1) and, thereby, enables assessing these quantitatively.

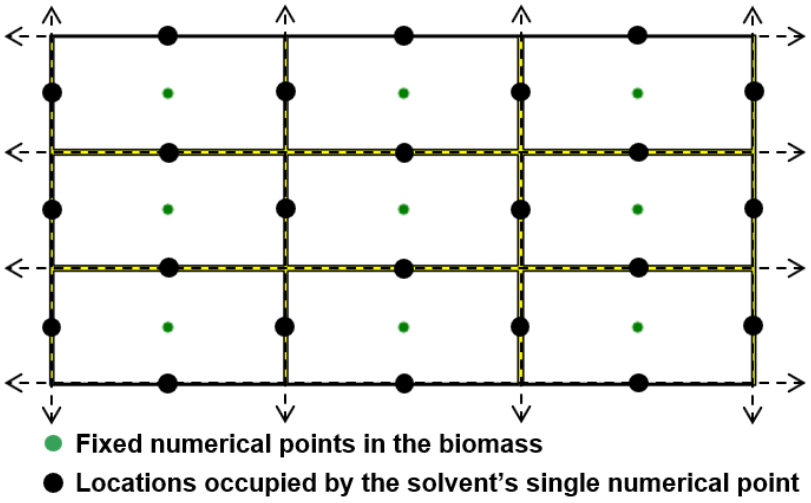


Figure 5.10 – 2-dimensional representation of model discretisation for mass transfer. Biomass cells are discretised with the method of lines, while the solvent and cell walls are denoted a single mobile numerical point

Following model discretisation, the mass equation (Equation (5.14)) was approximated as an ODE using Taylor series expansion. The resulting expression is shown in Equation (5.20), where numerical points arranged in the *x-direction*, *y-direction*, and *z-direction* are denoted the letters *i*, *j*, and *k*, respectively. L_{ave} is a mean average describing L values in the solvent and any given cell (Equation (5.21)).

$$\left.\frac{dN}{dt}\right|_{ijk} \approx L_{ave}\left[\frac{(\mu/T)_{(i+1)jk} + (\mu/T)_{(i-1)jk} - 2(\mu/T)_{ijk}}{\delta x^2} + \frac{(\mu/T)_{i(j+1)k} + (\mu/T)_{i(j-1)k} - 2(\mu/T)_{ijk}}{\delta y^2} + \frac{(\mu/T)_{ij(k+1)} + (\mu/T)_{ij(k-1)} - 2(\mu/T)_{ijk}}{\delta z^2}\right]\delta V_{ijk} \quad \textbf{(5.20)}$$

$$L_{ave} = \frac{1}{2}\left(L_{solvent} + L_{ijk}\right) \quad \textbf{(5.21)}$$

ijk denotes a discrete numerical point representing a cell.

The mass equation has been approximated using the method of lines. The spatial second derivatives of μ/T at any discrete point can be approximated using Equation (5.20), which requires knowledge of the current cell phase and the solvent phase surrounding the cell (solvent represents both the previous and next numerical points; Figure 5.10). The displacements between the points should also be known. This framework is applicable to all numerical points representing cells, but Equation (5.20) cannot be used to solve for molar quantity in the solvent, due to the mobile nature of the numerical point representing this phase. Instead, molar quantity in the solvent phase can be obtained through a mass balance applied between the solvent and all biomass cells (Equation (5.22)).

$$\left.\frac{dN}{dt}\right|_{solvent} = -\sum_{ijk}\left.\frac{dN}{dt}\right|_{ijk} \quad \textbf{(5.22)}$$

ijk denotes a discrete numerical point representing a cell.

5.3.1.4.3 <u>*Solution framework*</u>

The heat transfer model from Chapter 3 has now been further developed to incorporate mass transfer and cell expansion mechanics. The heat and mass equations (Equations (3.8) and (5.14)) can both be solved in one simulation run using the same input geometry and parameters, and through the same system of discrete numerical points (although the cell walls are ignored for mass transfer). Chemical potential (Equation (4.63)) is a single expression combining the various driving forces of diffusion, which are gradients in activity, pressure, and temperature (Wijmans and Baker, 1995). Furthermore, the cell pressure-volume relationship (Equations (5.17) – (5.19)) relates the pressure of a cell to its volume (and the moles it contains), thus completing the cycle of interdependence between mass transfer and pressure distribution. The newly developed biomass-solvent extraction model is the first of its kind, as it combines microwave heating, heat transfer, mass transfer (underpinned by

the relevant thermodynamic concepts), and cell expansion mechanics; all these are implemented at the cellular scale of biomass-solvent systems.

Figure 5.11 summarises the numerical framework of the model, where two stages exist in the computational process. In the first stage, the model handles heat transfer and cell expansion mechanics as described in sections 3.2.3.4 and 5.3.1.2, respectively, using a set of input geometrical, heating, and mechanical parameters. As a result, a steady state temperature distribution is achieved for the model, together with a ready-to-use cell pressure-volume relationship. These outcomes, along with the input mass transfer parameters, are used in the second stage of the simulation, in which the mass equation is solved to give temporal changes in pressure and water-molar distributions in the system.

Equations (5.20) – (5.22) were solved over a predefined domain of discrete time values, which are separated by a finite step (δt). For example, solving over $100\ s$ with a time-step $\delta t = 1\ s$, is analogous to solving in a stepwise manner over a time domain of $0, 1, 2, \dots, 100\ s$. The smaller the time-step (δt) the more accurate the result, but also the more computationally intensive the simulation. Moreover, too large δt values cause instability in the computation and can lead the results to diverge towards infinity. Hence, the chosen δt should neither be too small nor too large.

For every value in the time array, μ was computed for all spatial numerical points using water activity, pressure, and temperature. New molar quantities were then computed with the mass equation and, subsequently, new cell dimensions/volumes and pressures were also achieved. The new molar and pressure distributions and modified dimensions were then used in the next time step, and this was repeated for every consecutive value in the time domain. Key model validation steps are presented in APPENDIX B.

In the current work, it was intended to investigate the effects of microwave heating on mass transfer at thermal steady state. Hence, although this model enables heat and mass equations to be solved in a single simulation run, the two analyses are not conducted simultaneously, but rather, mass transfer is initiated after heat transfer had been completed (Figure 5.11). The heat transfer step results in a steady (but not necessarily uniform) temperature distribution in the biomass-solvent system, which is subsequently used for mass transfer. This approach matches the initial Temperature-

Induced Diffusion hypothesis (Lee et al., 2016), in which mass transfer had also been investigated at thermal steady state. Therefore, making this assumption allows a fair assessment of the hypothesis, which, if validated, can then be extended to incorporate simultaneous heat and mass transfer (Chapter 7).

However, note that the assumption discussed above limits the model's predictability to cases in which considerably high input power is used, where the extraction temperature set-point is achieved much faster compared to extraction itself (i.e., heat transfer is faster than mass transfer). Such an approach has been implemented in numerous empirical studies (Galan et al., 2017; Mao et al., 2019; Nkhili et al., 2009).

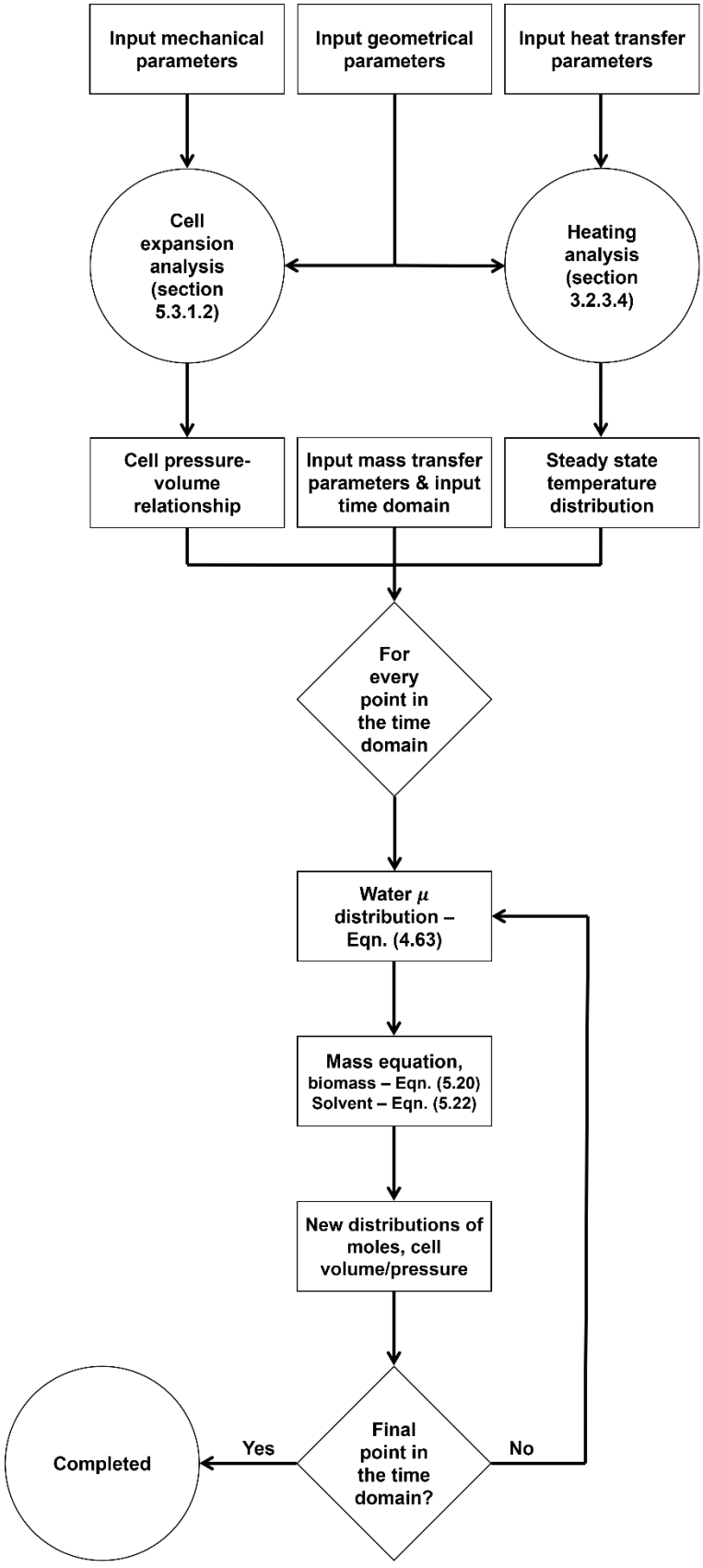


Figure 5.11 – Numerical framework for the combined heat, mass, and mechanical model

5.3.2 Predicted pressure distribution

It was aimed here to observe whether the pressure-time relationships obtained under microwave heating at thermal steady state, are consistent with the conditions needed for cell rupture, when a realistic set of input heat, mass, geometrical, and mechanical parameters are used. As such, this work shall assess the Temperature-Induced Diffusion hypothesis (Lee et al., 2016).

For cell rupture to explain enhanced extraction, it is not enough to only achieve sufficiently high cell pressures, but it is also necessary to obtain these within reasonable timeframes matching empirical findings. Therefore, two modelling outcomes will be presented and discussed in each analysis in the subsections below, which are the maximum pressure achieved at mass equilibrium ($P_{L_{max}}$), and the time required to achieve 95% of the molar and pressure distributions at mass equilibrium (t_{95-M}). Both outcomes should be of reasonable magnitude to conclude that cell rupture is responsible for enhancing extraction.

Following the estimate by Lee et al. (Lee et al., 2016) on cell rupture pressure, and the deducible rupture values from empirical stress-strain curves of some hydrated cell walls (Zamil, Yi and Puri, 2015), 50-70 bar will be considered here as a reference cell rupture pressure range. Hence, cell rupture will only be considered likely if $P_{L_{max}}$ lies within or is larger than 50-70 bar. On the other hand, considering extraction times reported in numerous studies, many of which (like this work) use biomass particles sized within or less than the order of millimetres (Bagherian et al., 2011; Karabegović et al., 2013; Liu et al., 2010; Nomanbhay, Hussain and Palanisamy, 2013; Tsubaki, Sakamoto and Azuma, 2010), a timeframe of the order of minutes will be considered here as a reference for cell pressure build-up. In other words, cell rupture will only be considered responsible for enhanced extraction if t_{95-M} lies within or is smaller than the order of minutes.

In the subsequent analyses, a single independent input parameter was varied at a time to characterise the unique effects of each parameter. The key parameters investigated are those responsible for microwave heating, including $\varepsilon''_{biomass}$, k, and $|E|_0$, while other parameters were also investigated briefly. Table 5.4 summarises the typical value ranges of the different model parameters, whereas Table 5.5 presents the selected baseline values for these parameters used in the current work.

Parameter & value range	$\varepsilon''_{biomass} = 0 - 30$	$k = 0.1 - 1$ $Wm^{-1}K^{-1}$	$\lvert E\rvert_0 = 0 - 10^4\ Vm^{-1}$	$\rho_L = 1000$ kgm^{-3}	$s_{W(T_0)} = 70$ $Jmol^{-1}K^{-1}$	$C_p = 4$ JgK^{-1}	$T_{extraction} = 100$ °C	$\alpha_{W_{initial}} = 0.95 - 1$	$\Phi_C = 0 - 1$
Justification	Fair for edibles at 2.45 GHz (Sipahioglu and Barringer, 2003)	Reasonable order for water (Engineering Toolbox, 2003)	Fair for single-mode cavities (Robinson et al., 2010)	Typical for water (NIST, 2017)	Typical for water (Engineering Toolbox, 2005)	Typical for water (Rogers and Mayhew, 1995)	–	Fair for plant-based biomass such as fruit and vegetables (Lee et al., 2016; Rizvi, 2005)	Water may occupy 0-100% of the initial cell volume
Parameter & value range	$D = 10^{-13} - 10^{-11}$ m^2s^{-1}	$S_R = 5 - 30$ mLg^{-1}	Cell cluster size = 1 cell onwards	Cell dimensions = $25 - 200\ \mu m$	$t_{CW_0} = 1 - 10$ μm	$Y_0 = 100 - 5000$ MPa	$\varepsilon''_{solvent} = 0 - 10$	$\delta_p = 1 - 10$ cm	$F = 2.45$ GHz
Justification	Water diffusing through cellulose acetate at room temperature (Saravacos, 2005)	Used empirically (Galan et al., 2017)	–	Fair with imaging and models (Zamil et al., 2013; Zamil, Yi and Puri, 2017)	Fair (Devlin and Witham, 1983; Pieczywek and Zdunek, 2014)	Fair for some hydrated/un-hydrated cell walls (Zamil, Yi and Puri, 2015)	Fair for water at 2.45 GHz (Datta, Sumnu and Raghavan, 2005)	Typical order for water (Pueschner, 2015)	Typical frequency value
Parameter & value range	$\varepsilon_0 = 8.854 \times 10^{-12} Fm^{-1}$	$Mr_W = 18$ $gmol^{-1}$	$T_{initial} = 30$ °C	$T_0 = 25$ °C	$\alpha_0 = 1$	$\mu_0 = 0$ $Jmol^{-1}$	$R = 8.314$ $Jmol^{-1}K^{-1}$		
Justification	–	–	–	–	–	–	–		

Table 5.4 – Typical value ranges for the various model parameters

Parameter & selected base value	$\varepsilon''_{biomass} = 10$	$k = 0.2$ $Wm^{-1}K^{-1}$	$\lvert E\rvert_0 = 10^4\ Vm^{-1}$	$\rho_L = 1000$ kgm^{-3}	$s_{W(T_0)} = 70$ $Jmol^{-1}K^{-1}$	$C_p = 4$ JgK^{-1}	$T_{extraction}$ = 100 °C	$\alpha_{W_{initial}}$ = 0.98	$\Phi_C = 0$
Sensitivity analysis in…	Section 5.3.2.1.1	Section 5.3.2.1.2	Section 5.3.2.1.3	Section 5.3.2.2					
Parameter & selected base value	$D = 10^{-12}$ m^2s^{-1}	$S_R = 100$ mLg^{-1}	Cell cluster size = 0.1 mm	Cell dimensions: Length = 100 μm Width = 50 μm Height = 10 μm	$t_{CW_0} = 1$ μm	$Y_0 = 800$ MPa	$\varepsilon''_{solvent}$ = 5	$\delta_p = 1$ cm	$F = 2.45$ GHz
Sensitivity analysis in…	Section 5.3.2.2	Section 5.3.2.2; See point 1	Sections 5.3.2.1.1, 5.3.2.1.2, and 5.3.2.1.3	Section 5.3.2.2			Effects discussed in Chapter 3	Effects discussed in Chapter 3	Effects discussed in Chapter 3
Parameter & selected base value	$\varepsilon_0 = 8.854 \times 10^{-12} Fm^{-1}$	$Mr_W = 18$ $gmol^{-1}$	$T_{initial} = 30$ °C	$T_0 = 25$ °C	$\alpha_0 = 1$	$\mu_0 = 0$ $Jmol^{-1}$	$R = 8.314$ $Jmol^{-1}K^{-1}$		
Sensitivity analysis in…	–	–	–	–	–	–	–		

1- This high value is chosen to ensure sufficient amounts of water exist to be absorbed by the biomass under microwave heating. As will be seen in section 5.3.2.2, this parameter does not affect the outcomes significantly in the current work, due to the absence of solute extraction. Chapter 7 is to communicate a model quantifying solute extraction, where S_R will be more relevant to consider.

Table 5.5 – Selected baseline values for the various model parameters

5.3.2.1 Heating-related parameters

5.3.2.1.1 Effect of dielectric loss factor (ε'')

An initial comparison was conducted between the effects of microwave and conventional heating for a single-cell system, where $\varepsilon''_{biomass}$ was varied between 0 (i.e., conventional heating) and 35 (i.e., microwave heating). $\varepsilon''_{solvent}$ was fixed at 5 and all other parameters were fixed as shown in Table 5.5. The resulting pressure-time relationships, and the corresponding cell and solvent temperatures, are shown in Figure 5.12.

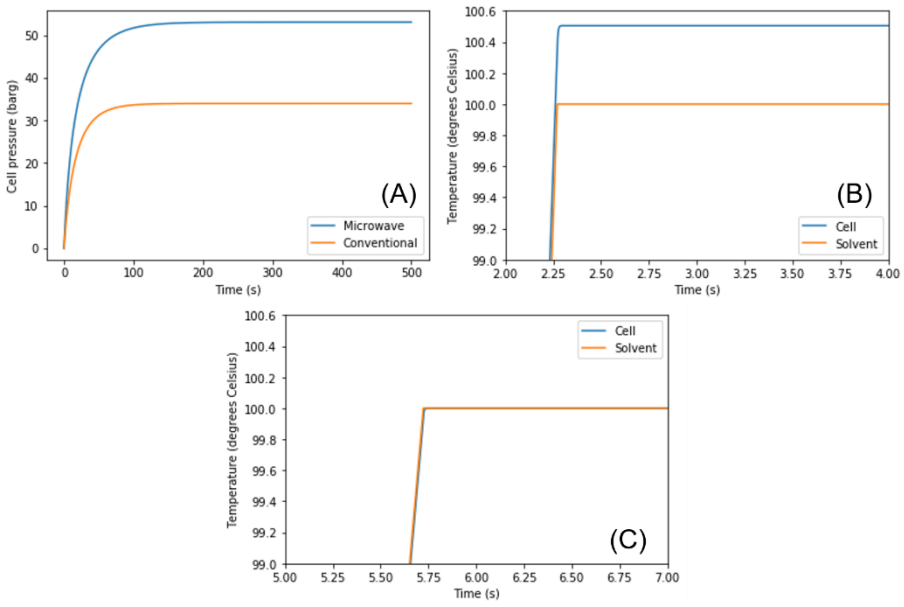


Figure 5.12 – Pressure induced in a single-cell biomass-solvent system with microwave and conventional heating. (A) Cell pressure against time; (B) temperature against time under microwave heating; (C) temperature against time under conventional heating

Observing Figure 5.12, microwave heating induces a temperature gradient between the cell and the solvent at thermal steady state, whereas the steady state temperatures of the two phases are equal under conventional heating. These observations match the outcomes of Chapter 3 and section 5.2; however, the novel observation here is the effect of temperature gradient on cell pressure, which can be seen in Figure 5.12A. It is evident that a temperature gradient of around 0.5 ℃ between the cell and the solvent under microwave heating, has raised the equilibrium cell pressure to $\sim 50\ bar$ from its original $\sim 30\ bar$ under conventional heating. Temperature gradient has provided an additional driving force for water to diffuse into the cell, resulting in a higher pressure at mass equilibrium. These observations match the original hypothesis set out by Lee et al. (Lee et al., 2016), in terms of the direction of mass flow against a

temperature gradient, as well as the extent to which pressure is raised for a given magnitude of temperature gradient.

Further to the single-cell scenario presented in Figure 5.12, it has been shown previously in Figure 3.9 and Figure 5.3 that, multicellular biomass materials heated with microwaves exhibit non-uniform temperatures at thermal steady state. Also, this work has also assumed negligible resistance to mass transfer within the cell walls, as these are considered part of the solvent phase (sections 5.3.1.1.3 and 5.3.1.4.2). Due to these two aspects, a range of pressures is to be expected for multicellular biomasses heated with microwaves, in which the maximum pressure develops around the centre where temperature is highest, and the minimum occurs at the biomass-solvent boundary where temperature is lowest. An example of such pressure distribution at mass equilibrium is presented in Figure 5.13, for a 0.5 mm biomass cluster (number of cells in each dimension matches the example of Figure 5.2). In this example, a maximum pressure just below 500 bar occurs around the centre, whilst pressures on the outer edges of the cluster are still of the order of 40 bar. Pressure distribution in this case is primarily a result of the temperature gradients established under microwave heating, which enhance mass transfer and cause an increase in the cell pressures.

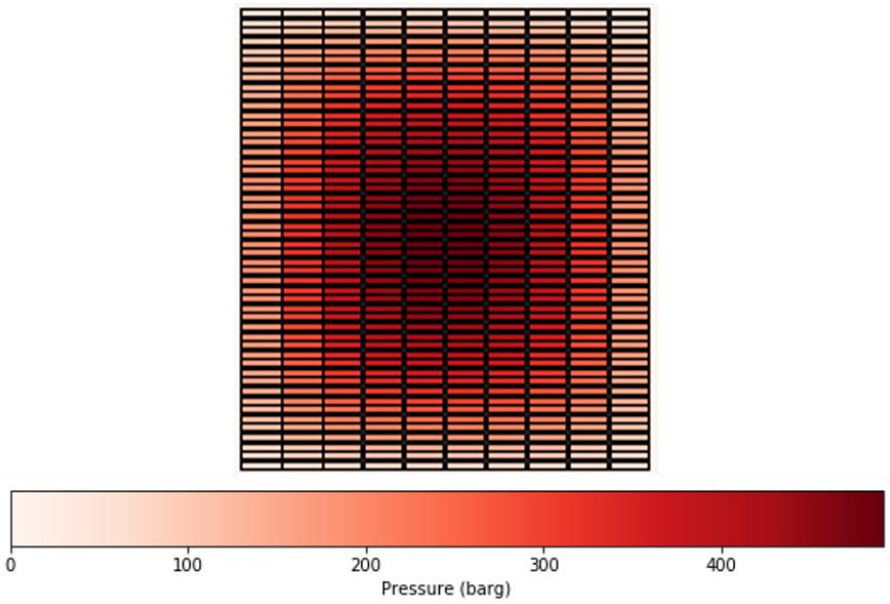


Figure 5.13 – Pressure distribution at mass equilibrium for a YZ cross-section of a 0.5 mm cubic biomass within a biomass-solvent system. Dielectric loss factor of biomass = 10; thermal conductivity = 0.2 $Wm^{-1}K^{-1}$; incident electric field intensity = 10000 Vm^{-1}

The analysis of equilibrium cell pressure was extended to cover $\varepsilon''_{biomass}$ values ranging from 5 to 20, and biomass particles sized 0.1 - 0.5 mm. Table 5.6 presents $P_{L_{max}}$ and t_{95-M} achieved with these values.

	Biomass particle size (mm)		
$\boldsymbol{\varepsilon''_{biomass}}$	**0.1**	**0.3**	**0.5**
5	47.025; 79.420	122.833; 197.920	256.114; 210.460
10	59.939; 96.130	213.085; 226.670	491.086; 153.070
20	85.289; 152.520	402.082; 164.910	976.370; 98.370
	$\boldsymbol{P_{L_{max}}\,(barg)}$; $\boldsymbol{t_{95-M}\,(s)}$		

Table 5.6 – Maximum cell pressure at mass equilibrium, and time required to achieve 95% of mass equilibrium, for variable biomass dielectric loss factor and particle size

Table 5.6 shows both $P_{L_{max}}$ and t_{95-M} to be within the magnitudes required for cell rupture, as the former is generally within or above 50-70 bar, and the latter is well within the order of minutes. Furthermore, given that the largest reported $\varepsilon''_{biomass}$ for some edible biomasses between 0 ℃ and 100 ℃, at a microwave frequency of 2.45 GHz, is around 30 (Sipahioglu and Barringer, 2003), it is clear that the $\varepsilon''_{biomass}$ values used here are physically realistic. Therefore, it can be deduced that cell rupture as depicted in the Temperature-Induced Diffusion hypothesis, is entirely possible with a realistic set of input $\varepsilon''_{biomass}$ values.

$P_{L_{max}}$ increases with $\varepsilon''_{biomass}$ and particle size, which is due to the increase in temperature gradient. At higher $\varepsilon''_{biomass}$, cell clusters experience higher microwave volumetric heating rates, thus requiring higher temperature gradients with the solvent to achieve balance between the input and output energies, bringing about thermal steady state. Furthermore, increasing the size of the biomass particle reduces its surface area-to-volume ratio, thereby limiting its contact with the solvent phase and introducing further resistance to heat transfer, which can only be overcome through raising the temperature gradient. The increase in $P_{L_{max}}$ with $\varepsilon''_{biomass}$ and particle size is significant, indicating that small temperature gradients are sufficient to induce

large equilibrium cell pressures, which matches the original hypothesis set out by Lee et al. (Lee et al., 2016). For a particle size of 0.1 mm, $P_{L_{max}}$ increases from ~45 bar at $\varepsilon''_{biomass} = 5$, to ~85 bar at $\varepsilon''_{biomass} = 20$. Also, with $\varepsilon''_{biomass} = 10$, $P_{L_{max}}$ increases significantly from ~60 bar at a particle size of 0.1 mm, to ~500 bar at a particle size of 0.5 mm.

On the other hand, t_{95-M} does not follow a single trend with $\varepsilon''_{biomass}$ and biomass particle size. While this parameter increases with $\varepsilon''_{biomass}$ at a particle size of 0.1 mm, the opposite trend can be observed as the particle grows larger. Moreover, with $\varepsilon''_{biomass} = 5$, t_{95-M} increases initially from 80 s at a particle size of 0.1 mm to 210 s at a particle size of 0.5 mm; however, with $\varepsilon''_{biomass} = 20$, t_{95-M} decreases with the same increase in size. These changing trends emerge because t_{95-M} depends on two factors: the driving force for mass transfer, and the magnitude of the equilibrium pressure being approached. In small particles, temperature gradient increases slightly as $\varepsilon''_{biomass}$ is raised, which increases the equilibrium pressure significantly but does not alter the diffusion rate; hence, it takes longer to achieve the higher $P_{L_{max}}$ values. In contrast, with large particles, temperature gradient increases more significantly with $\varepsilon''_{biomass}$, thus increasing $P_{L_{max}}$ on one hand but also enhancing the diffusion rate, which leads to shorter overall times for achieving mass equilibrium.

5.3.2.1.2 Effect of thermal conductivity (k)

Table 5.7 summarises the values of $P_{L_{max}}$ and t_{95-M} achieved under variable thermal conductivity (k) and biomass particle size. All other parameters are fixed as shown in Table 5.5.

	Biomass particle size (mm)		
$\boldsymbol{k}$ $(\boldsymbol{Wm^{-1}K^{-1}})$	**0.1**	**0.3**	**0.5**
0.1	85.289; 152.520	402.082; 164.910	976.370; 98.370
0.2	59.939; 96.130	213.085; 226.670	491.086; 153.070
0.4	47.025; 79.420	122.833; 197.920	256.114; 210.460
	$\boldsymbol{P_{L_{max}}}$ $(\boldsymbol{barg})$; $\boldsymbol{t_{95-M}}$ $(\boldsymbol{s})$		

Table 5.7 – Maximum cell pressure at mass equilibrium, and time required to achieve 95% of mass equilibrium, for variable thermal conductivity and particle size

Like $\varepsilon''_{biomass}$, cell rupture (as depicted in the Temperature-Induced Diffusion hypothesis) is entirely possible using a realistic set of input k values. As required to indicate cell rupture, Table 5.7 shows $P_{L_{max}}$ is well above $70\ bar$, and t_{95-M} is well within the order of minutes. Moreover, compared to the k values used here, values as low as 0.2 have been reported for fruits and vegetables with 80% moisture (Nesvadba, 2005), showing that the k values investigated here are physically realistic.

$P_{L_{max}}$ increases with decreasing k, due to the increased temperature gradient between biomass and solvent. As explained in section 3.3.1.3, lowering k increases resistance to heat transfer in the system, causing volumetric heating in each phase to be more pronounced than the rate of heat loss to the surroundings. Therefore, energy distribution becomes less even in the system, eventually leading to larger temperature gradients at thermal steady state, thereby larger equilibrium pressures. On the other hand, $P_{L_{max}}$ also increases with particle size (as seen in section 5.3.2.1.1) due to the reduced surface area-to-volume ratio which introduces further resistance to heat transfer. $P_{L_{max}}$ increases nonlinearly with decreasing k; at a particle size of 0.1 mm, $P_{L_{max}}$ increases from $\sim 45\ bar$ to $\sim 60\ bar$ and onwards to $\sim 85\ bar$, as k in decreased from $0.4\ \mathrm{Wm^{-1}K^{-1}}$ to $0.2\ \mathrm{Wm^{-1}K^{-1}}$, and then to $0.1\ \mathrm{Wm^{-1}K^{-1}}$. Moreover, with the same decrease in k but with a particle size of 0.5 mm, $P_{L_{max}}$ also increases from $\sim 260\ bar$ to $\sim 490\ bar$ and onwards to $\sim 980\ bar$. This nonlinear increase in $P_{L_{max}}$ is due to a similar nonlinear increase in the temperature gradient with decreasing k, which has been demonstrated in sections 3.3.1.3 and 5.2.2.

On the other hand, like section 5.3.2.1.1, t_{95-M} does not follow a single trend here with k and biomass particle size. In small particles such as those sized 0.1 mm, $P_{L_{max}}$ is achieved more slowly with smaller k, due to the slight increase in temperature gradient which raises $P_{L_{max}}$ considerably but does not cause any significant change in the diffusion rate. In contrast, with larger particles such as those sized 0.5 mm, t_{95-M} decreases with lowering k due to the significant increase in temperature gradient, which increases $P_{L_{max}}$ but also enhances the diffusion rate, allowing equilibrium to be achieved faster.

5.3.2.1.3 Effect of incident electric field intensity ($|E|_0$)

Table 5.8 summarises the values of $P_{L_{max}}$ and t_{95-M} achieved under variable incident electric field intensity ($|E|_0$) and biomass particle size. All other parameters are fixed as shown in Table 5.5.

	Biomass particle size (mm)		
$|E|_0$ (Vm^{-1})	**0.1**	**0.3**	**0.5**
2000	35.054; 68.260	41.353; 71.410;	52.039; 77.700
6000	43.390; 75.710	98.549; 146.02	192.139; 227.740
10000	59.939; 96.130	213.085; 226.670	491.086; 153.070
	$P_{L_{max}}$ $(barg)$; t_{95-M} (s)		

Table 5.8 – Maximum cell pressure at mass equilibrium, and time required to achieve 95% of mass equilibrium, for variable incident electric field intensity and particle size

$P_{L_{max}}$ increases with $|E|_0$ due to the increased temperature gradients between biomass cells and the solvent. As explained in section 3.3.2.2, the increased energy dissipation within biomass caused by higher $|E|_0$, requires larger temperature gradients within the system to achieve thermal steady state. $P_{L_{max}}$ also increases with particle size (as seen in section 5.3.2.1.1) due to the reduced surface area-to-volume ratio which introduces further resistance to heat transfer. $P_{L_{max}}$ increases nonlinearly with $|E|_0$, which is to be expected given the quadratic relationship between the absorbed microwave power density ($\dot{Q_M}$) and $|E|_0$ (Equation (2.31)), leading to a nonlinear increase in temperature gradient with $|E|_0$. At a particle size of 0.1 mm, $P_{L_{max}}$ increases from $\sim 35\ bar$ to $\sim 43\ bar$ and onwards to $\sim 60\ bar$, as $|E|_0$ increases from $2 \times 10^3\ Vm^{-1}$ to $6 \times 10^3\ Vm^{-1}$, and then to $10^4\ Vm^{-1}$. Also, for the same increase in $|E|_0$ but with a particle size of 0.5 mm, $P_{L_{max}}$ increases from $\sim 52\ bar$ to $\sim 192\ bar$ and onwards to $\sim 491\ bar$.

On the other hand, like section 5.3.2.1.1, t_{95-M} does not follow a single trend with $|E|_0$ and biomass particle size. In small particles such as those sized 0.1 mm, $P_{L_{max}}$ is achieved slower with higher $|E|_0$ values, due to the slight increase in temperature

gradient which raises the equilibrium pressure considerably but does not alter the diffusion rate considerably. In contrast, with a particle sized 0.5 mm, t_{95-M} increases initially with $|E|_0$, but it then decreases as $|E|_0$ rises further. This is because larger particles exhibit a significant increase in temperature gradient as $|E|_0$ is raised, which increases $P_{L_{max}}$ but also enhances the diffusion rate, allowing equilibrium to be achieved faster overall.

Observing the $P_{L_{max}}$ and t_{95-M} values in Table 5.8, it is clear that cell rupture is entirely possible if $|E|_0$ is sufficiently large ($\geq 6 \times 10^3\ Vm^{-1}$ in this case). This is a key observation, as it indicates the existence of a threshold $|E|_0$ value (thereby, threshold input microwave power) required to achieve cell rupture. This threshold is likely to be case-specific, as it also depends on parameters such as $\varepsilon''_{biomass}$, k, biomass particle size, etc (e.g., the required $|E|_0$ decreases with increasing particle size; Table 5.8). However, observing sections 5.3.2.1.1 and 5.3.2.1.2, $|E|_0$ evidently remains the most influential parameter in dictating whether widespread cell rupture is possible.

In laboratory-scale studies, achieving the required threshold in $|E|_0$ and the subsequent enhancement in extraction, are more likely in single-mode microwave cavities than they are in multimode applicators (e.g., many domestic ovens). With their likely maximum intensity of $10^4\ Vm^{-1}$ (Robinson et al., 2010), single-model cavities support higher $|E|_0$ than their multimode counterparts for the same input power (Metaxas and Meredith, 1983). This is due to the careful design and tuning of these cavities, which aim to expose the heated sample to the peak intensity, thereby optimising the heating process (section 2.1.3.3). As such, given the large $|E|_0$ required for cell rupture in small-sized particles (Table 5.8), enhanced extraction might not be observable in every experimental setup, especially where common multimode applicators are used.

5.3.2.2 <u>Other parameters</u>

This section investigates a set of secondary parameters for their effect on the likelihood of cell rupture. Table 5.9 summarises $P_{L_{max}}$ and t_{95-M} achieved under variable ρ_L, $s_{W(T_0)}$, C_p, $T_{extraction}$, $\alpha_{W_{initial}}$, Φ_C, D, S_R, cell dimensions, t_{CW_0}, and Y_0. All baseline parameters are as shown in Table 5.5.

		$P_{L_{max}}\ (barg)$	$t_{95-M}\ (s)$
Base case		59.939	96.130
ρ_L (kgm^{-3})	**500**	30.575	31.450
	2000	111.438	430.240
$s_{W(T_0)}$ $(Jmol^{-1}K^{-1})$	**0**	39.444	72.130
	140	80.044	137.700
C_p $(Jg^{-1}K^{-1})$	**2**	57.292	92.210
	6	62.579	100.360
$T_{extraction}$ (K)	**80**	58.212	88.340
	120	61.651	104.340
$\alpha_{W_{initial}}$	**0.97**	75.323	128.790
	0.99	43.658	73.070
Φ_C	**0.25**	49.058	201.460
	0.5	34.386	536.800
D (m^2s^{-1})	10^{-13}	59.939	961.300
	10^{-11}	59.939	9.613
S_R (mLg^{-1})	**50**	60.061	96.320
	200	59.785	95.900
Cell length; width; height (μm)	**25; 12.5; 2.5**	62.568	1.570
	50; 25; 5	58.826	9.760
t_{CW_0} (μm)	**0.5**	53.659	361.860
	2	65.654	41.410
Y_0 (MPa)	**250**	51.684	650.830
	5000	61.525	7.980

Table 5.9 – Maximum cell pressure at mass equilibrium, and time required to achieve 95% of mass equilibrium, for a collection of secondary input parameters. Particle size = 0.1 mm

$P_{L_{max}}$ and t_{95-M} increase with ρ_L, $s_{W(T_0)}$, C_p, and $T_{extraction}$, and this is deducible from the chemical potential expression (Equation (4.63)). ρ_L is inversely proportional to $v_{L_{(T_0)}}$ whose decrease raises $P_{L_{max}}$, while s_{W_0} and C_p both magnify the temperature gradient effect thereby raising $P_{L_{max}}$, and $T_{extraction}$ raises $P_{L_{max}}$ in accordance with the van't Hoff osmotic pressure analogy (Equation (5.5)). The typical values of ρ_L,

$s_{W(T_0)}$, and C_p for water are 1000 kgm^{-3} (NIST, 2017), 70 $Jmol^{-1}K^{-1}$ (Engineering Toolbox, 2005), and 4 $Jg^{-1}K^{-1}$ (Rogers and Mayhew, 1995), respectively, which reaffirms that cell rupture is physically possible within the ranges investigated.

As expected, $P_{L_{max}}$ and t_{95-M} increase with decreasing $\alpha_{W_{initial}}$, which is to be expected since larger activity gradients are only balanced with larger equilibrium cell pressures (osmotic pressure analogy; Equation (5.5)). Furthermore, $P_{L_{max}}$ decreases with increasing Φ_C due to the delayed increase in cell pressure, i.e., since cells are not turgid initially, water should accumulate within before pressure can increase. Therefore, as the cells eventually become turgid and pressure starts to increase, significant quantities of water will have already diffused in, leading to smaller activity gradient with the solvent and, thereby, resulting in smaller $P_{L_{max}}$ values at equilibrium. On the other hand, t_{95-M} increases with Φ_C due to the delayed cell pressure build-up, which is due to the larger cell capacity for water uptake.

As it describes resistance to mass transfer, D has no effect on $P_{L_{max}}$ but it significantly influences t_{95-M}, which varies 100-fold within the investigated range. Nevertheless, cell rupture remains possible here even with this significant change in t_{95-M}, reaffirming robustness of the predictions made in this work. On the other hand, S_R is practically ineffective on $P_{L_{max}}$ and t_{95-M}, because it does not alter the activity gradients between biomass cells and the solvent. The very small decrease in $P_{L_{max}}$ and t_{95-M} with increasing S_R, is due to the slight drop in temperature gradient caused by increased microwave attenuation, since the system volume increases with S_R (see section 3.3.1.2 for microwave attenuation).

$P_{L_{max}}$ varies slightly with changes in cell volume and t_{CW_0}, which is due to the slight disparity in particle size arising from changes in cell dimensions/wall thickness, as this leads to variations in temperature gradient. Nevertheless, geometry possesses a clearer and more systematic effect on t_{95-M}, as this parameter increases noticeably with cell volume and decreases dramatically with increasing t_{CW_0}. Both these cases entail increasing the cell-to-cell wall volume ratio within the biomass, which suppresses the overall ability of cell walls to resist cell expansion. This means that, more cell expansion is required to raise the cell pressure, and this demands more water uptake. The increased demand for water by cells results in higher t_{95-M} values.

$P_{L_{max}}$ increases slightly with Y_0, because at low Y_0 values, cells tend to expand more readily upon water uptake, which increases cell water activity but limits cell pressure build-up. Hence, mass equilibrium is established with lower activity gradients between biomass cells and the solvent, indicating lower cell pressures required to balance these gradients (i.e., osmotic pressure analogy; Equation (5.5)). In contrast, at high Y_0 values the cell walls are much stiffer, and so less water uptake is needed to increase cell pressure. This results in an equilibrium position consisting of high cell pressures, but also lower cell water activities to balance these pressures. On the other hand, stiffer cell walls also decrease t_{95-M} significantly, because with larger Y_0, cell pressure tends to increase rapidly with small water uptake, and so mass equilibrium is approached much faster. The wide range of Y_0 values investigated reaffirms that the predictions made in this work are robust and applicable to different biomass materials.

It is concluded here that cell rupture is entirely possible with most cases shown in Table 5.9, despite the broad range and wide variety of data investigated. This is evident given that the largest t_{95-M} recorded (i.e., 960 s) is still within the order of minutes, and the vast majority of $P_{L_{max}}$ values are within the 50-70 bar threshold required for cell rupture. Furthermore, these data have been obtained for a biomass particle size of 0.1 mm; hence, $P_{L_{max}}$ is likely to be even higher for larger particles (as shown in section 5.3.2.1). Therefore, findings and predictions made in section 5.3.2.1 on the effects of key microwave heating parameters on cell rupture, are applicable to a wide range of biomass materials.

5.3.3 Threshold parameters needed for cell rupture

It was demonstrated in section 5.3.2 that, cell rupture is fully explicable with the Temperature-Induced Diffusion hypothesis, yet a threshold set of input heating parameters is required to trigger cell rupture by inducing sufficiently high temperature gradients. Amongst the heating parameters, $|E|_0$ is of special importance due to its large influence, but also since it is directly manipulatable in real-world situations, e.g., by adjusting the input power; through using larger microwave generators with higher upper power limits; or by selecting suitable microwave applicators/cavities. Therefore, this section presents a range of predicted threshold $|E|_0$ values that are likely to induce widespread cell rupture, for different $\varepsilon''_{biomass}$, k, and biomass particle sizes. This matrix of data (Table 5.10) can be used as a basis for further empirical studies.

Although it had been estimated that 50-70 bar achieved within minutes is likely sufficient to explain enhanced extraction with cell rupture, Table 5.10 presents $|E|_0$ values needed for $P_{L_{max}}$ to be around 70 bar achieved within 5 minutes at most. This additional constraint is to ensure the conditions required for widespread cell rupture are met.

		$\varepsilon''_{biomass}$		
		5	**10**	**20**
$\boldsymbol{k}$ $(\boldsymbol{Wm^{-1}K^{-1}})$	**0.1**	Unachievable; 6500; 4500	8000; 5000; 3000	6000; 3500; 2000
	0.2	Unachievable; 9000; 6000	Unachievable; 6500; 4500	8000; 5000; 3000
	0.4	Unachievable; Unachievable; 8500	Unachievable; 9000; 6000	Unachievable; 6500; 4500
		$\boldsymbol{\|E\|_0}$ $\boldsymbol{(Vm^{-1})}$ **for particle size = 0.1; 0.2; 0.3 mm**		

Table 5.10 – Threshold electric field intensities needed for cell rupture, for variable biomass dielectric loss factor, thermal conductivity, and biomass particle size. The condition for rupture is attaining a maximum equilibrium cell pressure of at least 70 bar within 5 minutes at most. Field intensity values are quoted to the nearest 500 $\mathbf{Vm^{-1}}$. Cell rupture is deemed unachievable if a field intensity larger than $\mathbf{10^4}$ $\mathbf{Vm^{-1}}$ is required, as this is the likely maximum under single-mode cavities (Robinson et al., 2010)

5.4 Summary

In this chapter, two hypotheses attempted at explaining biomass cell rupture as a means of enhancing extraction under microwave heating, were investigated. The popular Steam-Rupturing hypothesis claims that microwaves generate intracellular steam, thereby rapidly increasing cell pressure and causing rupture. This hypothesis was assessed using the heat transfer model from Chapter 3, by attempting to understand whether temperatures required for steam-rupturing are achievable in the biomass under a realistic set of input microwave parameters. It was shown that, in all but the most extreme of cases, the temperature gradients obtained under microwave heating were less than 30 ℃, which are not sufficient to underpin the Steam-Rupturing hypothesis. The multitude of empirical observations of cell rupture during microwave heating are, therefore, caused by another mechanism.

The model was applied to the alternative Temperature-Induced Diffusion hypothesis, through the inclusion of elements describing mass transfer and cell expansion mechanics. A partial-differential mass equation was derived to quantify mass transfer based on chemical potential, thereby introducing water diffusion between biomass cells and the solvent, driven by gradients in activity, pressure, and temperature. Furthermore, a mechanical analysis framework was incorporated to quantify cell pressure as a function of cell volume and water quantity, thus completing the cycle of interdependence between mass transfer and pressure build-up. As a result, the model can now simulate water diffusion between biomass cells and the solvent, in addition to predicting heat transfer and temperature distribution. Water diffuses down its activity gradient from the solvent to biomass cells; hence, these cells expand, but in doing so they encounter resistance from the surrounding cell walls, causing intracellular pressure build-up. Under microwave heating, temperature gradients are induced where cells are warmer than the solvent. This introduces an additional driving force for water diffusion into cells, causing higher in cell pressures and increasing the likelihood of cell rupture compared with conventional heating cases.

The new model was used to show that, cell pressures within and above the estimated rupture threshold of 50-70 bar can occur readily, and these pressures are achievable within reasonable timeframes matching those reported in empirical microwave extraction studies. It was found that, cell rupture is entirely possible with a realistic range of key input microwave parameters (i.e., $\varepsilon''_{biomass}$, k, and $|E|_0$), when using biomass particles sizes that match empirical studies. Furthermore, this finding holds true for a broad range and wide variety of secondary parameters, including ρ_L, $s_{W(T_0)}$, C_p, $T_{extraction}$, $\alpha_{W_{initial}}$, Φ_C, D, S_R, cell dimensions, t_{CW_0}, and Y_0, showing that the outcomes of this work are applicable to different types of biomass-solvent systems. Therefore, if cell rupture is the governing mechanism for enhanced extraction under microwave heating, then it can be concluded that Temperature-Induced Diffusion is the underpinning cause of this rupture, rather than the Steam-Rupturing hypothesis.

Achieving widespread cell rupture, thereby enhanced extraction, only occurs beyond a set of threshold microwave parameters, which induce the required temperature gradients to cause the needed widespread rupture within biomass. Amongst the microwave parameters, $|E|_0$ is of special importance since it is directly

manipulatable in real-world situations. In experimental settings, $|E|_0$ can be increased either by raising the input power, using larger microwave generators with higher upper power limits, or selecting suitable microwave applicators/cavities. Single-mode cavities maximise $|E|_0$ for a given input power compared to multimode applicators and domestic ovens, meaning that cell rupture and enhanced extraction are more likely when single-mode cavities are used. A range of threshold $|E|_0$ required for widespread cell rupture and enhanced extraction, have been presented in Table 5.10.

This model is the first of its kind, as it combines microwave heating, heat/mass transfer, and cell expansion into a single framework assessing cell rupture in biomass-solvent systems. As such, this work provides a significant advancement in the mechanistic understanding of microwave heating and mass transfer within biomasses, and for the first time, it allows cell rupture to be rationalised with wide and realistic sets of physical parameters. Unlike many other models in literature, this model is based upon fundamental principles; hence, it is well-suited for further improvements and utilisation not only in the biomass extraction field, but also in other related fields such as biomass pyrolysis. For this purpose, additional elements such as solute diffusion or chemical reactions can be introduced with ease, just like how mass transfer and cell expansion have been introduced here to investigate Temperature-Induced Diffusion.

Nevertheless, from the viewpoint of this thesis, the model can still be improved further by readdressing its assumptions, such as disregarding solute diffusion; neglecting mass transfer within the cell walls; assuming thermal steady state during the diffusion process; and others, but above all making the fundamental assumption that cell rupture is the only rate-limiting step in extraction. In Chapter 7, the model will be improved, and its key assumptions will be readdressed. In Chapter 6, on the other hand, a brief empirical analysis will be conducted to screen for evidence that enhanced extraction is underpinned by cell rupture.

5.5 Thesis recap

In Chapter 3, a microwave heat transfer model was developed at the cellular scale to understand thermal patterns emerging in biomass-solvent systems heated with microwaves. It was shown that microwaves sustain temperature gradients in the system at thermal steady state, which prompted the need to investigate and establish the fundamental link between diffusion and temperature. This effort was conducted in Chapter 4.

In the current chapter, the model was expanded to incorporate mass transfer and cell expansion, which were integrated together with microwave heat transfer into a single computational framework. The model predicts cell pressure build-up and distribution within biomasses during microwave heating, and it was used here to investigate the conditions necessary to achieve widespread cell rupture within biomasses. It was demonstrated that, the popular Steam Rupturing hypothesis whereby cell rupture is caused through rapid vaporisation of intracellular moisture, is unlikely to underpin enhanced extraction as widely as previously proposed. Instead, the novel Temperature-Induced Diffusion hypothesis is a more suitable alternative entirely capable of underpinning enhanced extraction through cell rupture given a realistic set of input physical parameters. As such, if enhanced extraction is caused by cell rupture, then Temperature-Induced Diffusion is a viable mechanism to explain how widespread cell rupture can be achieved.

5.6 Nomenclature

Symbols

ε''	$-$	Dielectric loss factor
ε_0	$\boldsymbol{Fm^{-1}}$	Permittivity of free space
k	$\boldsymbol{Wm^{-1}K^{-1}}$	Thermal conductivity
$\|E\|$	$\boldsymbol{Vm^{-1}}$	Electric field intensity
T	$\boldsymbol{K}$	Temperature
ΔT_{max}	$\boldsymbol{K}$	Maximum temperature difference at steady state
$T_{extraction}$	$\boldsymbol{K}$	Extraction temperature set-point; analogous to $T_{saturation}$
t	$\boldsymbol{s}$	Time
t_{95-T}	$\boldsymbol{s}$	Time required to achieve 95% of thermal steady state
t_{95-M}	$\boldsymbol{s}$	Time required to achieve 95% of mass equilibrium
δt	$\boldsymbol{s}$	Time-step for the numerical mass analysis
P	$\boldsymbol{bar}$	Pressure
$P_{L_{max}}$	$\boldsymbol{bar}$	Maximum cell pressure at mass equilibrium
δP	$\boldsymbol{bar}$	Pressure-step for the numerical mechanical analysis
N	$\boldsymbol{mol}$	Number of particles/molar quantity
S	$\boldsymbol{JK^{-1}}$	Entropy
s	$\boldsymbol{Jmol^{-1}K^{-1}}$	Specific entropy
V	$\boldsymbol{m^3}$	Volume
v	$\boldsymbol{m^3mol^{-1}}$	Specific volume
δV	$\boldsymbol{m^3}$	Volume of a phase
μ	$\boldsymbol{Jmol^{-1}}$	Chemical potential
α	$-$	Activity
R	$\boldsymbol{Jmol^{-1}K^{-1}}$	Universal gas constant (Avogadro's const. times Boltzmann's const.)
C_p	$\boldsymbol{Jg^{-1}K^{-1}}$	Specific heat capacity
ρ	$\boldsymbol{kgm^{-3}}$	Density
Mr	$\boldsymbol{gmol^{-1}}$	Molecular weight
J	$\boldsymbol{mols^{-1}m^{-2}}$	Molar flux
L	$\boldsymbol{mol^2KJ^{-1}m^{-1}s^{-1}}$	Mass transfer/diffusion coefficient
$\bar{L}$	$\boldsymbol{mol^2J^{-1}m^{-1}s^{-1}}$	Mass transfer/diffusion coefficient per unit temperature
c	$\boldsymbol{molm^{-3}}$	Molar concentration
D	$\boldsymbol{m^2s^{-1}}$	Diffusivity
π	$\boldsymbol{bar}$	van't Hoff's osmotic pressure
σ	$\boldsymbol{MPa}$	Axial/normal stress
τ	$\boldsymbol{MPa}$	Shear stress
ϵ	$-$	Strain
Y_0	$\boldsymbol{MPa}$	Elastic modulus at zero strain
y	$\boldsymbol{m}$	Width (only in Equation (5.18))
z	$\boldsymbol{m}$	Height (only in Equation (5.18))
t_{CW}	$\boldsymbol{m}$	Cell wall thickness

A	$\boldsymbol{m^2}$	Cross-sectional area
Φ_C	$-$	Initial cell void fraction
S_R	$\boldsymbol{mLg^{-1}}$	Solvent-to-solid ratio
F	$\boldsymbol{Hz}$	Microwave frequency
δ_p	$\boldsymbol{m}$	Penetration depth

Subscripts and superscripts

$()_{biomass}$	Biomass property
$()_{solvent}$	Solvent property
$()_0$	Incident/baseline value
$()_{initial}$	Initial value
$()_L$	Property of a condensed state
$()_W$	Property of water
$()_{i/j}$	Property of a phase "i" or "j"
$()_{()}$	Property at a given condition, e.g., $v_{(T)}$ is specific volume at temperature *T*
$()_x$	Applicable parallel to the *x-direction*
$()_y$	Applicable parallel to the *y-direction*
$()_z$	Applicable parallel to the z-*direction*
$()_{ijk}$	Property of the spatial numerical point *ijk*, *i* in the *x-direction; j* in the y-*direction; k* in the z-*direction*

6 EVIDENCE FOR CELL RUPTURE – EMPIRICAL ANALYSIS

The aim of this chapter is to investigate empirically whether, as discussed in Chapter 5, enhanced extraction is underpinned by cell rupture. This requires implementing a setup where constant input microwave power can be applied continuously, thus better resembling the conditions prescribed in Chapter 5.

I would like to acknowledge Dr. Fátima Arrutia Rodriguez, affiliated to the Faculty of Engineering, University of Nottingham during her contribution, for her valuable collaboration in the development and initial tests of the experimental setup. I would also like to acknowledge Dr. Yujie Mao, affiliated to the Faculty of Engineering, University of Nottingham during her contribution, for her valuable collaboration in the post-processing of some samples during the restrictive COVID-19 pandemic lockdown.

The format of this chapter is as follows:

6.1 Introduction 171
6.2 Methodology 176
6.2.1 Setup design and formulation 176
6.2.2 Experimental procedures 178
6.2.2.1 Materials 178
6.2.2.2 Sample preparation 179
6.2.2.3 Extraction experiments 179
6.2.2.3.1 Continuous microwave heating experiments 179
6.2.2.3.2 Ramp microwave heating experiments 179
6.2.2.3.3 Room temperature extraction 180
6.2.2.4 Post-processing and yield measurement 180
6.3 Results and discussion 181
6.3.1 Heating profiles 181
6.3.2 Microwave extraction 183
6.3.3 Room temperature extraction 186
6.4 Summary 187
6.5 Thesis recap 188
6.6 Nomenclature 190

6.1 Introduction

Extraction in biomass-solvent systems is thought to be enhanced through cell rupture, which, in turn, is considered more easily achievable under microwave heating than it is under conventional heating (Maran and Prakash, 2015; Mandal, Mandal and Das, 2015; Osaili, 2012). In Chapter 5, two hypotheses were discussed summarising how microwave heating is thought to bring about cell rupture. Of these two hypotheses, Temperature-Induced Diffusion first proposed by Lee et al. (Lee et al., 2016), was shown to be the most suitable alternative to underpin microwave-induced cell rupture, within the fringes of physically realistic conditions.

Temperature-Induced Diffusion is a mechanism with which diffusion occurs against a temperature gradient, from an area of low temperature to an area of high temperature. Under microwave heating, the biomass temperature can rise beyond that of the bulk system (i.e., $T_{extraction}$ or solvent temperature), thereby enhancing water influx to cells, increasing cell pressure, and improving the likelihood of cell rupture. It has been shown in section 3.3.1.1 that, under microwave heating, the biomass is likely to always attain higher temperatures than the solvent at thermal steady state, provided that $\varepsilon''_{biomass} > 0$. Therefore, the higher the input microwave power applied at thermal steady state, the larger the temperature gradient between biomass and solvent, the more likely it becomes to achieve cell rupture. This was thoroughly demonstrated in Chapter 5, where cell pressure was shown to increase with $|E|_0$ which directly represents the input microwave power, and with other system-specific properties like higher $\varepsilon''_{biomass}$ and lower k.

Although extraction under microwave and conventional heating has been compared widely, it is often challenging to establish a fair basis of comparison due to the different characteristics of the two heating methods. For example, microwave extraction at given input power is sometimes compared with conventional extraction at given temperature (Bagherian et al., 2011; Dahmoune et al., 2015; Pandey and Shrivastava, 2018; Zhang et al., 2018). This limits the ability to evaluate computational predictions presented in this thesis, for which more comprehensive sets of data are required including temperature, input power, system-specific properties like $\varepsilon''_{biomass}$ and k, etc. Recently, comparing the two heating methods has been attempted more fairly, through applying the same heating rate (i.e., rate of temperature increase) and steady state extraction temperature (Galan et al., 2017; Mao et al., 2019;

Mao, Robinson and Binner, 2021). This means that the total energy delivered to the system is similar in both cases, allowing any differences in extraction to be attributed to the distinctive heating patterns between the two methods (e.g., microwave-induced temperature gradients). On imposing the same heating rate and steady state temperature, it was found in some studies that microwave heating did not return any advantages over conventional heating (Mao et al., 2019), while in others microwave heating yielded slightly larger amounts of extract, especially at the higher end of investigated extraction temperatures (Galan et al., 2017). Unlike many previous studies, these outcomes show much smaller differences between microwave and conventional heating, and they indicate that these differences are only applicable to specific types of biomasses. In other words, if the biomass is "naturally suitable" for microwave heating (e.g., high $\varepsilon''_{biomass}$ or low k), then microwaves deliver small additional energy directly to the material through radiation, inducing temperature gradients in the system and enhancing extraction accordingly (Mao, Robinson and Binner, 2021). However, in other circumstances the magnitudes of any induced temperature gradients would not be sufficiently high to enable enhanced extraction under microwave heating.

Therefore, in studies comparing microwave and conventional heating under the same temperature and heating rate, the question of whether microwave heating is advantageous depends primarily on the specific properties of the biomass-solvent system (e.g., $\varepsilon''_{biomass}$ and k), more so than it depends on universally applicable heating parameters like $|E|_0$ or the input microwave power. While this argument is true to a certain extent, the emphasis drawn here on system-specific properties is seen to be the result of a key practical limitation, arising from an inability to sustain sufficiently high temperature gradients during heating. It has been shown in Chapters 3 and 5 that, in a biomass-solvent system at thermal steady state, temperature gradients increase with the input microwave power (through $|E|_0$), which, in turn, raises the likelihood of cell rupture. However, in real-world situations it is not possible to manipulate the input power while also maintaining a fixed sub-saturation temperature. Under microwave heating, to avoid further temperature increase the input power must be lowered to near-zero values once the desired operating temperature is approached (e.g., Figure 6.1). Therefore, the input power is essentially only applied during the heat-up phase, signifying that any unique microwave effects are only sustained for a

limited period. The near-zero input powers indicate inherently low temperature gradients between the biomass and the solvent at thermal steady state, and these low gradients can only be raised through altering system-specific properties like $\varepsilon''_{biomass}$ and k. Therefore, enhanced microwave extraction becomes excessively dependent upon system-specific properties, due to the low input powers restricting temperature gradient magnitudes at thermal steady state.

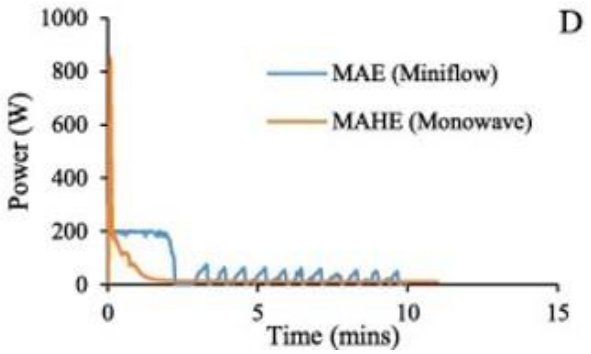


Figure 6.1 – Example from Mao et al. (Mao et al., 2019) **to demonstrate the dramatic drop in the input microwave power on approaching a desired temperature set-point. Figure from Mao et al.** (Mao et al., 2019)**, cropped from a larger figure comprising four plots, but unmodified otherwise (© 2019 The Authors. Published by Elsevier Ltd.), available under CC BY 4.0 license (https://creativecommons.org/licenses/by/4.0/) when obtained. Further use of this item is governed by the said license unless otherwise indicated by the copyright holders**

Microwave and conventional extraction must be compared fairly using the same input power and $T_{extraction}$; however, these two parameters should be decoupled from each other so that power can still be applied while maintaining constant $T_{extraction}$. Microwaves are unique because, unlike conventional heating, they continue to heat the biomass even at thermal steady state, by delivering energy directly through radiation. This induces temperature gradients which, according to Temperature-Induced Diffusion, enhance the likelihood of cell rupture. Therefore, microwave and conventional heating could show different outcomes even if the same input power is applied, but for this to occur, the input power must be decoupled from $T_{extraction}$ and applied continuously. This decoupling can be achieved through conducting extraction under reflux at the solvent's boiling point, which is the maximum achievable solvent temperature. In such a case, $T_{extraction}$ will not exceed the solvent's boiling point regardless of the power applied; hence, input microwave power and temperature are decoupled. For example, consider an extraction process where the desired $T_{extraction}$

is 80 ℃. If this temperature equals the solvent's boiling point, then microwave power can be applied continuously, thereby inducing a temperature gradient at thermal steady state due to direct energy dissipation into the biomass (Figure 6.2A). However, if 80 ℃ is a sub-saturation temperature, then the microwave power cannot be maintained when $T_{extraction}$ is approached, meaning that no temperature gradient can be induced at thermal steady state except in very small magnitudes (Figure 6.2B). In this work, extraction cases comprising continuous heating with a constant input power for the full processing duration, shall be denoted the term "continuous microwave heating." On the other hand, extraction cases where the input power is only maintained during heat-up, but beyond that heating is either stopped or significantly suppressed, shall be defined as "ramp microwave heating." This heating mode occurs when a sub-saturated temperature set-point is to be maintained, or when heating is stopped altogether on approaching a target temperature.

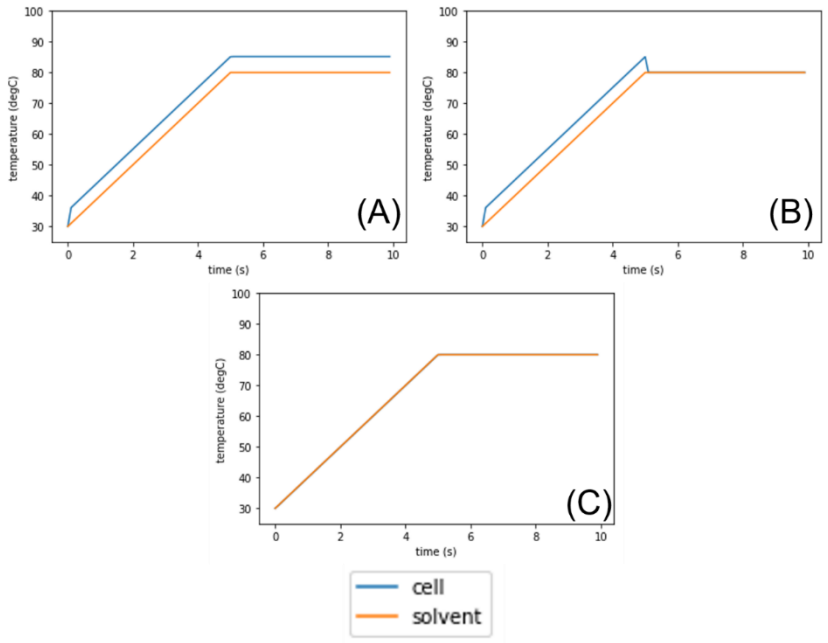


Figure 6.2 – Single-cell biomass-solvent system being heated up to $T_{extraction}$ = 80 ℃. (A) Solvent boiling point equals $T_{extraction}$ (i.e., continuous microwave heating); (B) $T_{extraction}$ is lower than solvent boiling point (i.e., ramp microwave heating); (C) conventional heating

Continuous microwave heating is not a new concept; it has been implemented in a variety of fields such as organic synthesis reactions, where this heating mode was investigated for its effect on conversion (Kappe, Pieber and Dallinger, 2013; Rosana et al., 2012). This concept has also been used in biomass-solvent extraction, where fixed input microwave power was applied either continuously or in intervals under

some form of reflux (Dahmoune et al., 2014; Dang, Zhang and Xiu, 2014; Švarc-Gajić et al., 2013).

Given the description above, continuous and ramp microwave heating are likely to result in different extraction trends, because they differ in their heat delivery to the extraction system. It is, therefore, necessary to evaluate extraction under both heating modes, as it might not be sufficient otherwise to draw any meaningful conclusions on cell rupture. As such, unlike the previous chapters, the current work does not accept cell rupture as a rate-limiting step in extraction, but rather, it aims to re-examine this concept experimentally to understand its suitability in explaining extraction trends. The intended comparison between continuous and ramp microwave heating constitutes a critical experiment to understand whether the rate-limiting step in extraction is cell rupture as proposed in literature and accepted in Chapter 5. If a step change in extraction is observed under both heating modes only beyond a threshold input power, then enhanced extraction can be attributed to cell rupture. However, if the two outcomes differ then extraction should be reconceptualised, and the model developed in Chapter 5 should be modified accordingly.

To adhere to the aim of this chapter, the analyses intended here will be specifically focussed on certain aspects which could hint towards the need to further develop the model from Chapter 5. These include the nature of any step-change events observable in the yield trends, and whether certain enhancements in extraction are not necessarily attributable to a step-change-inducing event like cell rupture. While this work is not exhaustive, it lays the foundation for future endeavours aiming to assess the Temperature-Induced Diffusion hypothesis more comprehensively using continuous microwave heating. As discussed above, this heating mode should make enhanced extraction more dependent on $|E|_0$ and the input power, and less dependent upon system-specific properties like $\varepsilon''_{biomass}$ and k. As such, it could be demonstrated that microwave heating is advantageous in more biomass-solvent systems than previously thought.

This work uses onion peels as the biomass material, since the cellular structure and measurable stress-strain data of this material match the model's geometrical traits (section 3.2.1) and mechanical features (section 5.3.1.2) (Zamil et al., 2013; Zamil, Yi and Puri, 2014, 2015). Furthermore, of the various components present, pectin was

selected as the extract to be measured, as it reasonably complements the intentions of this work due to the following: (i) pectin is polymeric and well-attached to the cell wall, so its extraction is thought to be enhanced on achieving structural modifications/cell rupture (Bagherian et al., 2011; Kratchanova, Pavlova and Panchev, 2004); (ii) pectin dissolves in water, unlike other solutes which may require other types of solvent; (iii) pectin has also been the extract of interest in various microwave extraction studies which can be compared with the current work (Mao et al., 2019; Mao, Robinson and Binner, 2021).

6.2 Methodology

6.2.1 Setup design and formulation

Figure 6.3 demonstrates the extraction setup enabling continuous microwave heating, while Table 6.1 provides description of the different parts.

Since $T_{extraction}$ equals solvent's boiling point, the choice of temperature gets restricted to precisely one value (e.g., 100 ℃ for pure water). This significantly limits the capabilities of the system, as it imposes restriction on conducting and comparing extraction at different temperatures. To overcome this challenge, a vacuum pump was introduced to control the operating pressure of the system (Figure 6.3). The saturation temperature of the solvent decreases when the operating pressure is reduced, meaning that the boiling point can be readjusted to match the desired $T_{extraction}$ through pressure manipulation. As such, the intended system can operate at any $T_{extraction}$ below the solvent's normal boiling point, while also ensuring that $T_{extraction}$ is equivalent to the solvent's saturation temperature. This widens the opportunities to conduct more analyses and future investigations.

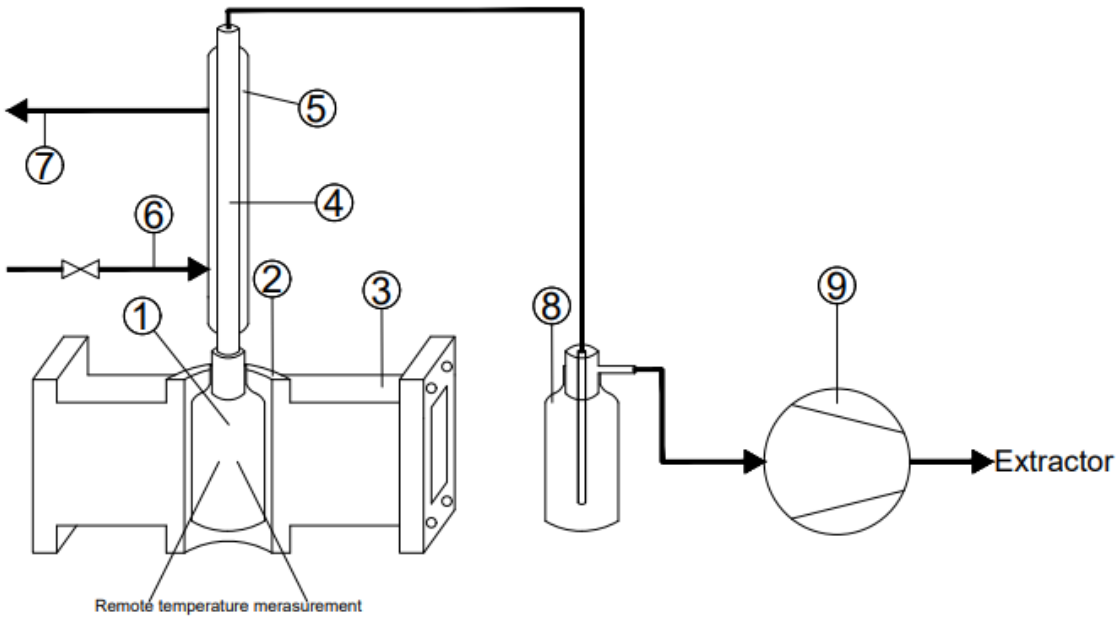


Figure 6.3 – Microwave extraction system enabling continuous power input. See Table 6.1 for description

I.D. in Figure 6.3	Description
1	Reaction vessel containing the biomass-solvent sample.
2	Single-mode cavity.
3	Microwave waveguide.
4	Condensation column (process side – sample vapour).
5	Condensation column (service side – cooling water).
6	Cooling water input.
7	Cooling water output.
8	Buffer vial protecting the vacuum pump by collecting any liquid escaping the condensation column.
9	Vacuum pump whose output is connected to an extractor/ventilator.

Table 6.1 – Description of the parts incorporated in the microwave extraction system enabling continuous power input (Figure 6.3). Setup materials should withstand pressure gradients and be compatible with microwave heating

6.2.2 Experimental procedures

The setup demonstrated in Figure 6.3 was used to conduct two sets of microwave extraction experiments. The following points describe common attributes of all heating experiments:

- All heating experiments were conducted using Miniflow 200SS (Sairem, France) as the microwave generator/cavity, and a microwave frequency of 2.45 GHz was applied throughout.
- All heating experiments were carried out at $T_{extraction}$ equivalent to the normal boiling point of deionised water (i.e., vacuum pump not operating).
- The input microwave powers used were either 45W, 90W, or 135W.
- Sample surface temperature was measured non-intrusively using an infrared thermal camera, and temperature measurements were taken and recorded manually.
- Microwave leakage detection was conducted regularly, especially during the solvent boiling phase. No experimental run would be continued should a leakage be detected.
- Every experiment was monitored closely to ensure liquid did not accumulate in the buffer vial (number 8 in Figure 6.3), otherwise the respective experiment would be stopped and repeated.

Additionally, a third set of experiments was conducted at room temperature to provide a better insight into the results obtained.

All samples were of the same type and prepared/post-processed in the same way. The following subsections summarise the experimental procedures.

6.2.2.1 Materials

Red onions were obtained from a local supermarket (Nottingham, UK), and were peeled manually while maintaining random size distributions. This method was preferred to best resemble unprocessed raw waste materials. Deionised water was used as the extraction solvent, and isopropanol obtained from Sigma Aldrich (Dorset, UK) was used in post-processing.

6.2.2.2 Sample preparation

Since all experiments involving heating were conducted using Miniflow 200SS (Sairem, France), all samples were prepared in identical reaction vessels whose size matches the maximum allowed under this cavity. Each extraction sample was prepared by placing $1.5000 \pm 0.0100\ g$ of onion peels into a reaction vessel, and then pouring $50\ mL$ deionised water at $13 - 18$ ℃ (thus maintaining constant solvent-to-solid ratio for all samples). Deionised water was added just before starting an experiment, to avoid any prior extraction taking place in the system.

6.2.2.3 Extraction experiments

Three sets of experiments were conducted in total, two of which incorporated microwave extraction while the third comprised extraction at room temperature. These experiments are detailed below.

6.2.2.3.1 Continuous microwave heating experiments

Continuous heating was achieved through irradiating the samples at fixed input microwave powers for given durations. The input powers used were 45W, 90W, and 135W, and different samples were heated for variable time intervals from 1 to 60 minutes. Prior to every experimental run, the reflected power was minimised through adjusting the stub tuner and sliding short. However, as boiling was achieved in the solvent the reflected power increased, and the values ranged between 0-5W, 2-7W, and 5-12W under input powers of 45W, 90W, and 135W, respectively. Each experimental run was repeated at least once additionally, and for each run, the sample surface temperatures measured non-intrusively were recorded every 1 minute.

6.2.2.3.2 Ramp microwave heating experiments

Ramp heating was achieved through irradiating the samples at fixed input microwave powers only for the durations required to achieve solvent boiling (as a maximum). However, to allow comparison with continuous heating experiments (section 6.2.2.3.1), the total processing times were still maintained at 1 to 60 minutes. In that, samples being processed for times longer than those needed to achieve solvent boiling, were left out at room temperature (around $13 - 18$℃) for the additional time required to complete the full duration of the experimental run. The input powers used here were 45W, 90W, and 135W, and each experimental run was repeated at least once additionally. For each run, the sample surface temperatures were measured non-intrusively and recorded every 1 minute while samples were being heated. Also, prior

to every experimental run, the reflected power was minimised through adjusting the stub tuner and sliding short.

For cell rupture to occur, a temperature gradient is required between the biomass and the solvent (Chapter 5); however, ramp microwave heating only sustains such gradient during the time-limited heat-up phase (Figure 6.2). Hence, if cell rupture is the underpinning cause of enhanced extraction under ramp microwave heating (Galan et al., 2017; Mao, Robinson and Binner, 2021), it should mostly occur during the heat-up phase. As such, it should be indifferent to the process beyond achieving solvent boiling, whether the sample is quenched, left out, or heated slightly to maintain temperature, since all these options practically entail no temperature gradient. This study allowed samples to be left out at room temperature post heating, in cases where the duration of a run was longer than the time needed to achieve boiling. Hence, the results obtained here can be compared with other ramp heating studies, where the extraction temperature was maintained beyond the heat-up phase (Galan et al., 2017; Mao, Robinson and Binner, 2021). Furthermore, by comparing the results of the current experiments with those from continuous microwave heating (section 6.2.2.3.1), it can be understood whether enhanced extraction requires high temperatures and sustained temperature gradients, or whether it occurs on inducing temperature gradients for short durations.

6.2.2.3.3 Room temperature extraction

Samples were left at room temperature for durations between 1 hour and 6 days to investigate no-heating extraction. These experiments were conducted at room temperatures of $13-18\,℃$. Each experimental run was repeated at least once additionally.

6.2.2.4 Post-processing and yield measurement

As discussed in section 6.1, this work is focussed on extracting pectic polysaccharides. Therefore, the post-processing stage was based on a technique previously used in literature, in which the interest had also been to characterise pectin extracts (Mao et al., 2019). The methodology was adapted/modified here to match the requirements of the current work.

After processing, samples were filtered under vacuum immediately, as the immediate separation of biomass from solvent ensured no further extraction took place. Appropriate means were incorporated to safely handle high-temperature

samples. Subsequently, isopropanol was added to the solvent in a 1:1 volume ratio and mixed thoroughly, and the samples were refrigerated for at least 2-3 days until an alcohol-insoluble solid (AIS) became visible. Plant polysaccharides precipitate out of solution under the influence of alcohol (Moyer and Holgate, 1948), and AIS obtained with isopropanol mainly comprises pectin (Mao, Robinson and Binner, 2021). After refrigeration, the samples were centrifuged at 4 ℃ under 3900 RPM for at least 5 hours, ensuring that the AIS firmly deposited at the bottom of the tube. The liquid fraction was then decanted and disposed of appropriately, and $10\,mL$ of deionised water was added to the remaining solid samples prior to freezing them. Freezing was key to conducting the subsequent freeze-drying step, and adding deionised water was essential to ensuring proper freezing. Samples were left to freeze overnight, and then they were freeze-dried for 3-5 days.

Dried AIS weights were measured and recorded, and percentage yields were calculated as shown in Equation (6.1).

$$\%\ yield = \frac{Weight\ of\ dry\ AIS\ solid\ precipitate}{Initial\ weight\ of\ onion\ peel} \times 100 \qquad \textbf{(6.1)}$$

6.3 Results and discussion

6.3.1 Heating profiles

Figure 6.4 shows an average temperature-time profile during the heat-up phase, where Figure 6.4A presents a plot for the continuous heating experiments, and Figure 6.4B presents a plot for the ramp heating experiments. The plots were constructed using data from all microwave experiments collectively, e.g., the temperature after 1 minute of heating with a given power, is the mean ± 1 standard deviation of all temperature readings at 1 minute, recorded in the various experimental runs whose total durations were 1 minute or more. As such, every datapoint in Figure 6.4 describes a mean ± 1 standard deviation of at least 10 readings.

As can be seen, the temperature in all cases rises to around 100 ℃ and ceases to increase thereafter regardless of the input power, which indicates that the solvent has approached saturation as per initially required in the design (section 6.2.1). Moreover, despite the large number of experimental runs represented in Figure 6.4, both plots show regular heating trends with negligible inconsistency. In other words, the standard deviations remain small for all datapoints, indicating firmly maintained experimental

conditions which include identical samples, minimal disparity in the power absorbed, and same environmental conditions. Furthermore, Figure 6.4 clearly demonstrates a direct proportionality between the input power and the rate of temperature increase, further indicating robustness of the system design. While 10 min are required to approach 100 ℃ under 45W, this duration drops to 5 min with 90W (i.e., heating rate doubled) and 3.5 min with 135W (i.e., heating rate tripled).

Note that, the measured steady temperatures are not exactly 100 ℃, which is because measurements were conducted manually and non-intrusively. Nevertheless, the fact that temperature ceases to increase on approaching 100 ℃, and that the heating rate is proportional to the input power, are sufficient to confirm that the system operates as expected.

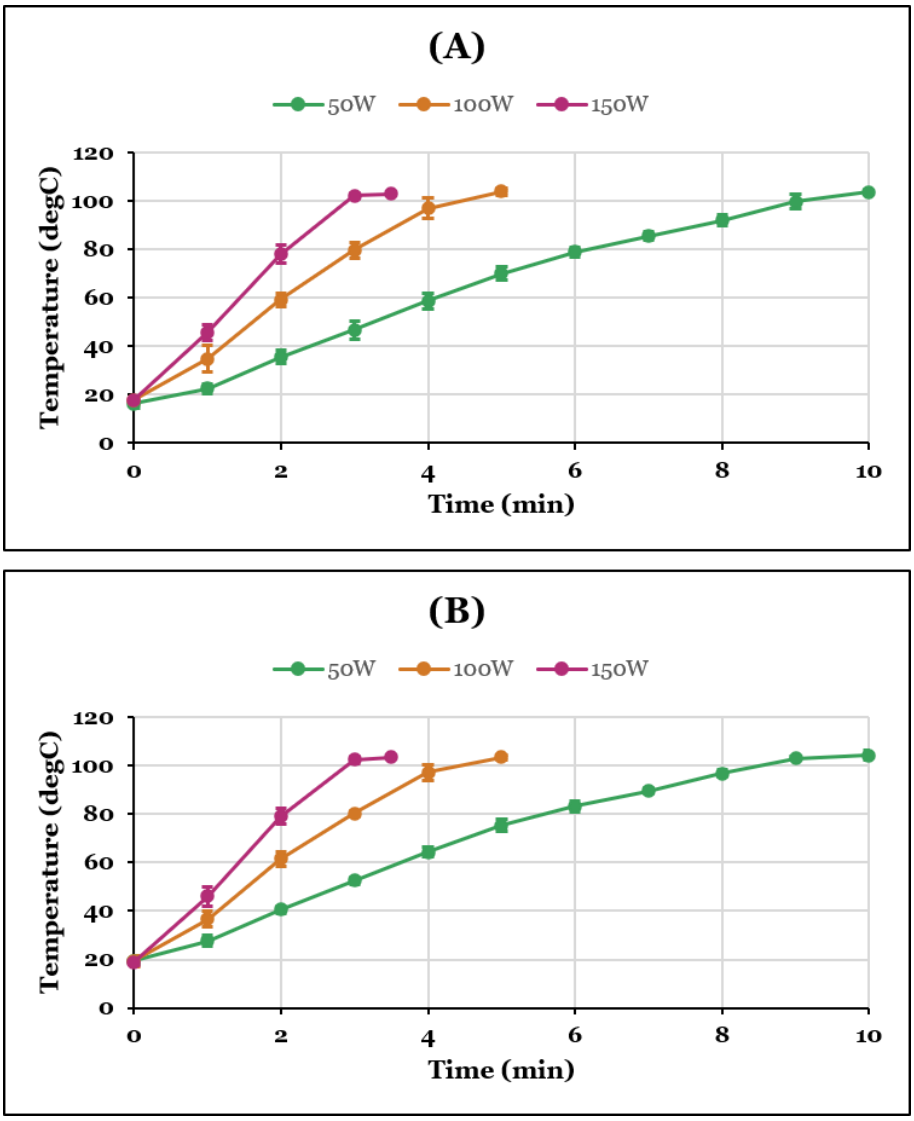


Figure 6.4 – Average temperature-time profiles for different microwave extraction runs; (A) continuous heating experiments; (B) ramp heating experiments

6.3.2 Microwave extraction

Results are presented in Figure 6.5, where the outcomes of continuous microwave heating are shown in Figure 6.5A, and those of ramp microwave heating are summarised in Figure 6.5B. The results are reported as the mean ± 1 standard deviation.

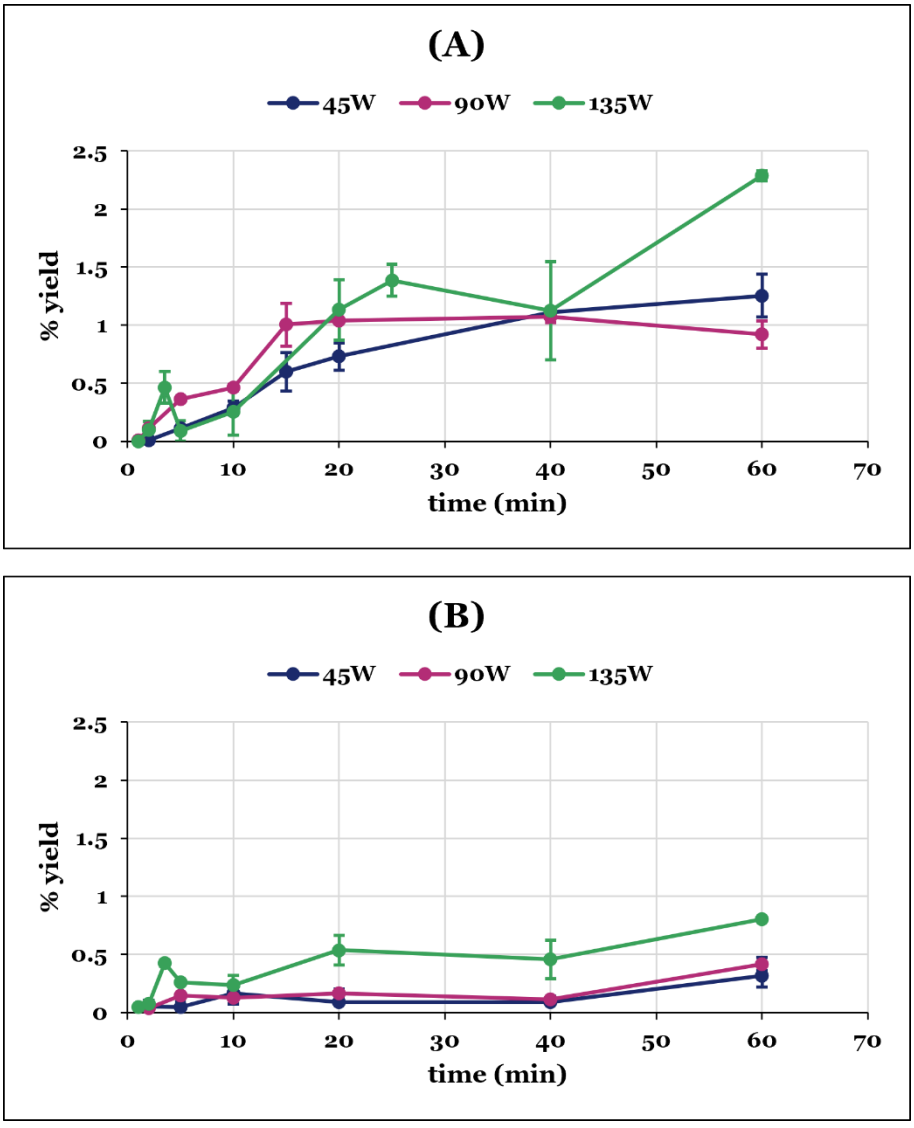


Figure 6.5 – Results for the (A) continuous heating experiments; (B) ramp heating experiments

The pectin content of red onion peels has been measured at ~7% on a dry weight basis (Alexander and Sulebele, 1973). Given that onion peels can acquire moisture contents up to 40% at very humid conditions (i.e., relative humidity > 95%) (Hole,

Drew and Gray, 2000), such extreme state would stipulate a pectin content of ~4% on a wet basis. Hence, the pectin content under normal environmental conditions can be estimated at $\sim 4 - 7\%$ on a wet basis, and as can be seen, all outcomes in Figure 6.5 are compliant with this upper limit.

On the other hand, the yields attained with continuous microwave heating (Figure 6.5A) are generally higher than those achieved under ramp microwave heating (Figure 6.5B), which is logical given the higher extraction temperatures being maintained in the former case (Chew et al., 2011; Spigno, Tramelli and De Faveri, 2007).

The ramp microwave heating results (Figure 6.5B) indicate a rate-limiting step underpinning extraction. This is evident as the yields achieved with 45W and 90W are the same throughout, but they exhibit a step-increase when 135W is applied. This outcome matches Chapter 5, where a threshold input power was deemed necessary to induce widespread cell rupture in the biomass, thereby enhancing extraction. This outcome also matches literature studies, where extraction under ramp heating was only found to accelerate on applying a threshold input power (Mao, Robinson and Binner, 2021). Hence, when discussed alone, the ramp microwave heating results (Figure 6.5B) are sufficient to conclude that enhanced extraction is underpinned by a rate-limiting step such as cell rupture.

However, the continuous microwave heating results (Figure 6.5A) do not fully complement the aforementioned view on cell rupture and extraction. Under continuous heating, extraction clearly accelerates on raising the input power from 45W to 90W, as the yields at 90W are higher at every timestep up to 40 minutes, compared to the corresponding cases under 45W. This is unlikely to be caused by cell rupture, since the acceleration in Figure 6.5A is initiated right from the beginning of the process, when the temperature gradients would still exist under ramp heating as well as continuous heating. As such, any cell rupture should have also occurred under ramp heating, causing the yields at 45W and 90W to be different in Figure 6.5B; however, this is clearly not the case here. Moreover, increasing the power under continuous heating (Figure 6.5A) to 135W further speeds up extraction, indicating that the acceleration seen here occurs gradually as the input power is raised. Relating such gradual acceleration with a step-change-inducing phenomenon like cell rupture, would demand an unrealistically complex physical mechanism. Instead, it is much more

realistic to substitute this with an alternative mechanism capable of explaining all results being observed here, under both continuous and ramp heating (Chapter 7).

It should be highlighted here that the yields at 135W continuous heating (Figure 6.5A) tend to fluctuate, unlike the cases observed at lower powers or those seen with ramp heating (Figure 6.5B). Initially, the yield increases to 0.5% in 3.5 minutes, showing an acceleration in extraction from the case of 90W. However, the yield decreases to nearly 0% between 3.5 minutes and 5 minutes, before increasing once again as it approaches 1.4% at 25 minutes. This fluctuation could be attributed to a thermal degradation of the extract, which is thought to occur more readily with intense/prolonged heating (Arrutia et al., 2020), and pectin yields have been shown to decrease at high microwave powers (Maran and Prakash, 2015; Wang et al., 2007). Degraded extracts may escape being measured as part of the yield, due to an increase in their solubility which hinders them from precipitating out of solution on adding isopropanol in the post-processing stage (section 6.2.2.4) (El-Nawawi and Shehata, 1987). Increased solubility also favours reabsorption of extracted solutes back into the biomass (Chapter 7).

On the other hand, a unique observation is made at 135W continuous heating (Figure 6.5A), entailing a sharp second increase in the yield starting at 40 minutes, reaching to a value as high as 2.3% at 60 minutes. This could be classified as a step-increase in extraction, but the analysis should be extended to beyond 60 minutes before such a conclusion can be made. On expanding the analysis, if the second increase in yield remains attainable only at 135W or higher powers, then it could be attributed to a rate-limiting step like cell rupture. However, if this observation is made under all input powers, even those less than 135W, then the effect in question should be explained by an alternative mechanism not incorporating any step-change-inducing events. Nevertheless, it could still be argued that 135W causes a step-change in extraction here through cell rupture, due to the fact that this power also enhances extraction under ramp heating (Figure 6.5B). However, it is unlikely that both observations are caused by a single cell rupture event, as these do not take place during the same timeframes. The step-change under ramp heating occurs right from the beginning of the process, and it remains evident even after heating has been stopped (Figure 6.5B). In contrast, the yield surplus under continuous heating takes place later in the process (after 40 minutes in this case), even though heating is applied for the

full duration (Figure 6.5A). If the continuous heating step-change is caused by cell rupture, then the ramp heating step-change occurring much earlier must be attributed to another cause. Similarly, if the ramp heating step-change is due to cell rupture, then the continuous heating step-change occurring much later cannot be attributed to the same cell rupture which would have already occurred at the beginning of the process.

Furthermore, it could also be argued that the yield enhancement under 135W continuous heating is due to the vigorous boiling in this case, which could lead to structural deformations in the biomass regardless of the heating method. However, this is unlikely due to the following: (i) such deformations would probably have also been evident at lower input powers albeit to lesser extents, as these powers also induce boiling at the same solvent temperature; (ii) it has been reported that, cell wall deformation under conventional boiling principally entails pectin leaching (Renard, 2005), which is arguably just a mass transfer process that could be enhanced with microwaves; (iii) textural softening induced during conventional boiling has been reported to preserve the cell walls of some biomasses against fracture, as instead it leads to cell-cell separation (Ng and Waldron, 1997); (iv) biomass cells are likely to withstand high pressures induced during boiling, as discussed in Chapter 5 (section 5.2). Therefore, the yield enhancement under 135W continuous heating is more likely a microwave-induced phenomenon altering diffusion patterns.

The results presented here suggest that cell rupture can only be a fully viable explanation for enhanced extraction when considering ramp microwave heating (Figure 6.5B). However, the trends attained with continuous microwave heating hint towards an alternative mechanism for microwave extraction. Such mechanism should be able to explain both the step-changes observed at high input powers, and the gradual acceleration in extraction seen under continuous microwave heating. If such mechanism can be proposed independently of any structural modifications, then the idea of cell rupture being a rate-limiting step in extraction will be challenged.

6.3.3 Room temperature extraction

Results are shown in Figure 6.6 as a yield-time plot, where the outcomes are reported as the mean ± 1 standard deviation. It can be seen that the yield increases very slowly over a period of 6 days. This confirms that extraction occurs at room temperature without the need for any cell rupture, but rather, it is accelerated/enhanced when heating is applied.

This outcome confirms that, proposing an alternative mechanism for microwave extraction away from cell rupture would not violate the fundamental principles governing extraction. Unlike what had been suggested, that polymers like pectin require structural modifications as a prerequisite for their extraction (Bagherian et al., 2011; Kratchanova, Pavlova and Panchev, 2004), it is shown here such polymers can diffuse normally even in the absence of heating, albeit very slowly.

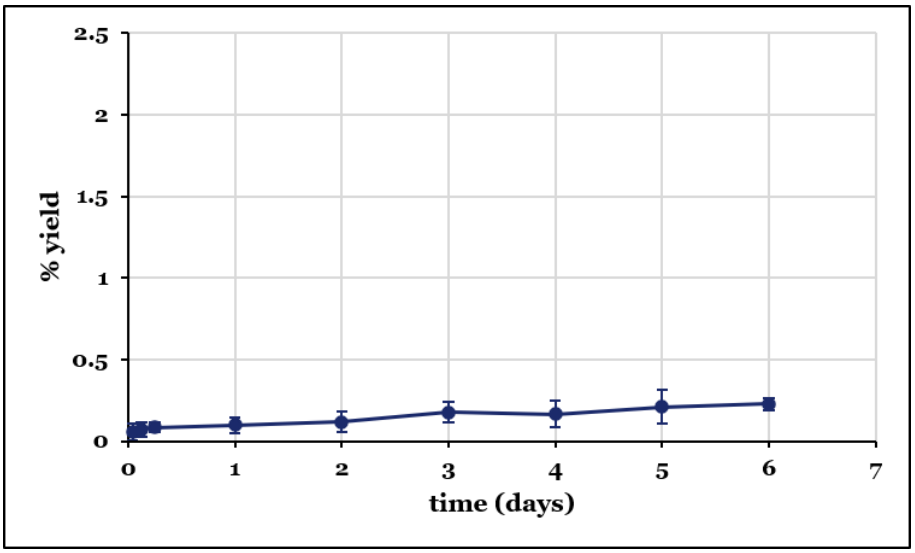


Figure 6.6 – Results for the room temperature experiments

6.4 Summary

This chapter investigated the extraction of pectin from onion peels under two microwave heating modes: continuous microwave heating and ramp microwave heating. The aim was to infer whether the idea of cell rupture is sufficient to underpin enhanced extraction under microwave heating, or whether the model developed in Chapter 5 should be re-evaluated. Continuous microwave heating denotes a non-stop heating of the sample with microwaves at a given input power, for the full processing duration. In contrast, ramp microwave heating signifies maintaining a constant input power only as long as the sample's temperature is increasing, but once a target temperature is achieved, heating would be stopped or significantly suppressed. Although ramp microwave heating has been used widely in literature, it does not sustain any microwave-induced temperature gradients throughout the extraction process, which limits the potential for microwaves to enhance extraction. Therefore, it was necessary here to study extraction under both microwave heating modes, in order to understand whether all observable outcomes can be attributed to a rate-limiting step such as cell rupture.

The extraction trends observed under ramp microwave heating were fully explicable with cell rupture, as a step-increase in the yield was observed on increasing the input power to a threshold value of 135W. This matches the predictions made in Chapter 5, as well as some findings in literature where ramp microwave heating had also been implemented. However, the results attained with continuous microwave heating do not fully complement the idea of cell rupture. Firstly, under this heating mode extraction accelerates gradually on raising the input power. This occurs right from the beginning of the process; hence, if it is caused by cell rupture then it should also be observed under ramp heating, but this is not the case in the current results. Secondly, although 135W continuous heating induces a unique increase in the yield, the cause of this effect is unclear as it cannot be matched with the step-change observed at the same power under ramp heating.

The room temperature experiments confirmed that extraction is possible without cell rupture or heating, even though the rate of such extraction is very slow. Unlike what had been suggested in literature, this outcome indicates that structural modifications in the biomass are not a necessary prerequisite for achieving reasonable yields of water-soluble polymers like pectin. As such, proposing an alternative mechanism for microwave extraction away from cell rupture, would not violate the fundamental principles governing extraction.

These results are sufficient to highlight the need to expand the model from Chapter 5, and further its underpinning extraction mechanism which currently entails cell rupture. The improved mechanism should explain both the step-changes observed at high input powers, and the gradual extraction acceleration under continuous microwave heating. If such mechanism can be proposed independently of any structural modifications, then the idea of cell rupture being a rate-limiting step in extraction will be challenged. An alternative mechanism will be proposed in Chapter 7, where it will be shown that rupture may affect diffusion, but it does not constitute a rate-limiting step in the process as previously perceived.

6.5 Thesis recap

In Chapter 5, a biomass-solvent extraction model was developed, which can be used to predict whether widespread cell rupture within biomasses is achievable given a set of input physical conditions. The model is the first of its kind as it integrates microwave heat transfer, mass transfer, and cellular expansion mechanics. The model

also demonstrates that the novel Temperature-Induced Diffusion hypothesis is a more suitable alternative than the popular Steam-Rupturing hypothesis to underpin cell rupture. This alternative hypothesis also demonstrated that enhanced cell rupture under microwave heating can only be achieved beyond some threshold input power.

In the current chapter, a critical experiment was conducted to assess the viability of the model and the wider conception that cell rupture is the rate-limiting step of extraction. The experiment entailed conducting biomass-solvent extraction under two microwave heating modes, namely "continuous heating" where constant input power was maintained throughout the process; and "ramp heating" where the power was only maintained for limited periods. While ramp heating showed a step-increase in yield beyond a threshold input power (as predicted in Chapter 5), continuous heating demonstrated gradual extraction acceleration with increasing power, and a unique steep increase in yield late in the process at high powers. These differing outcomes cannot both be attributed to a single cell rupture event; hence, a more suitable mechanism underpinning both extraction regimes should be conceptualised.

6.6 Nomenclature

Symbols

$\|E\|_0$	$\boldsymbol{Vm^{-1}}$	Electric field intensity
$\varepsilon''_{biomass}$	$-$	Dielectric loss factor of biomass
k	$\boldsymbol{Wm^{-1}K^{-1}}$	Thermal conductivity
$T_{extraction}$	$\boldsymbol{K}$	Extraction temperature set-point; equivalent to solvent temperature

7 MICROWAVES IMPROVE EXTRACTION WITHOUT RUPTURE

The aim of this chapter is to propose a novel framework for understanding microwave extraction in biomass-solvent systems away from cell rupture. This alternative framework shall be focussed on investigating the effects of different heating methods/modes and mass transfer parameters on extraction trends, thereby presenting a new perspective on how extraction takes place both at room temperature and under heating. In conducting the above, this work shall improve on the model developed in Chapter 5 by addressing its key limitations.

The format of this chapter is as follows:

7.1 Introduction 193
7.2 Methodology 198
7.2.1 System geometry 198
7.2.2 Mass transfer 198
7.2.2.1 The mass equation 198
7.2.2.1.1 A system of equations 198
7.2.2.1.2 Adhering to physical limits 199
7.2.2.2 Chemical potential and activity 202
7.2.2.3 Solubility and mole fraction 204
7.2.2.4 Diffusivity and mass transfer coefficient 206
7.2.3 Heat transfer 206
7.2.3.1 Heating biomass 206
7.2.3.2 Heating the solvent 207
7.2.4 Cell wall expansion 208
7.2.4.1 Expansion mechanics and assumptions 208
7.2.4.2 Rupture 211
7.2.5 Numerical solution 212
7.2.5.1 Initial and boundary conditions 213
7.2.5.2 Model discretisation 214
7.2.5.3 Approximating the mass and heat equations 214
7.2.5.4 Solution framework 215
7.3 Predicted extraction trends at room temperature 218
7.3.1 Base case 218
7.3.2 Effect of solubility (S_s) 230
7.3.3 Effect of diffusivity (D) 231
7.3.3.1 Equal solute diffusivities ($D_{s1}=D_{s2}$) 231
7.3.3.2 Unequal solute diffusivities ($D_{s1}\neq D_{s2}$) 233
7.3.4 Effect of solvent-to-solid ratio (S_R) 237
7.3.5 Effect of biomass particle size 238
7.3.6 Effect of solute activity-mole fraction relationship (n) 239

7.3.7 Effect of initial solvent purity ($\%_{s\text{-}S}$) 240
7.3.8 Effect of initial solute quantity in cell wall ($\%_{s\text{-}CW}$) 241
7.4 Predicted extraction trends with heating 244
7.4.1 Base case 244
7.4.2 Effects of microwave heating parameters 250
7.4.3 Effect of dielectric loss distribution (whether $\varepsilon''_{biomass} > \varepsilon''_{solvent}$) 252
7.4.4 Extraction scenarios under variable solubility/diffusivity/heating 258
7.4.4.1 Selected extraction scenarios 258
7.4.4.1.1 Continuous heating vs ramp heating 258
7.4.4.1.2 Ramp heating at variable heating rates (no rupture effect) 259
7.4.4.1.3 Ramp heating at variable heating rates (with rupture effect) 262
7.4.4.1.4 Extracting highly soluble components (equal diffusivities) 263
7.4.4.1.5 Extracting highly soluble components (unequal diffusivities) 264
7.4.4.2 Further/general extraction scenarios 266
7.4.4.2.1 Scenario 1: low S_s; $D_{s1}=D_{s2}$ 266
7.4.4.2.2 Scenario 2: high S_s; $D_{s1}=D_{s2}$ 267
7.4.4.2.3 Scenario 3: low S_s; $D_{s1}\neq D_{s2}$ 268
7.4.4.2.4 Scenario 4: high S_s; $D_{s1}\neq D_{s2}$ 269
7.4.4.2.5 Scenario 5: low S_s; $D_{s1}=D_{s2}$ & both increase with rupture 271
7.4.4.2.6 Scenario 6: high S_s; $D_{s1}=D_{s2}$ & both increase with rupture 272
7.4.4.2.7 Scenario 7: low S_s; $D_{s1}\neq D_{s2}$ & values swap with rupture 273
7.4.4.2.8 Scenario 8: high S_s; $D_{s1}\neq D_{s2}$ & values swap with rupture 274
7.5 Summary 276
7.6 Thesis recap 280
7.7 Nomenclature 283

7.1 Introduction

In Chapter 5, a model was developed to investigate extraction in biomass-solvent systems at the cellular scale. This model incorporated elements of microwave heating, heat transfer, mass transfer, and cell expansion mechanics, making it the first of its kind in the biomass-solvent extraction field. The model was based on a fundamental assumption that achieving cell rupture is the primary mechanism causing enhanced extraction under microwave heating. This matches general assumptions and trends in literature, but unlike most publications, this model showed that cell rupture is inexplicable with the popular Steam-Rupturing hypothesis. Instead, it was demonstrated that the Temperature-Induced Diffusion hypothesis is a more suitable alternative, as it is entirely capable of underpinning microwave-induced cell rupture using a realistic set of input parameters. Furthermore, the model predicted the existence of a threshold microwave power, which must be applied to achieve widespread cell rupture and, thereby, observe enhanced extraction.

The outcomes from Chapter 5 were assessed empirically in Chapter 6, where a critical experiment was conducted to observe whether cell rupture is the rate-limiting step of extraction as proposed in literature. The analysis was conducted under two modes of microwave heating, namely “continuous microwave heating,” and “ramp microwave heating.” Continuous microwave heating denotes non-stop heating with a constant input power for the full extraction duration. In contrast, ramp microwave heating signifies maintaining a constant input power only as long as the sample’s temperature is increasing, but once a target temperature is achieved, heating would be stopped or significantly suppressed. The extraction trends attained with ramp microwave heating were fully explicable with cell rupture, as they showed a step-increase in the yield on applying a threshold power. These results match the predictions made in Chapter 5, together with some other extraction studies also implementing ramp microwave heating (Mao, Robinson and Binner, 2021). Despite this, continuous and ramp microwave heating differ in their energy delivery to biomass-solvent systems; hence, it is insufficient to draw conclusions from investigating just one of the two modes. For instance, the results achieved in Chapter 6 under continuous microwave heating are not fully explicable with cell rupture, as the evidence attained hints towards the need to re-evaluate the model from Chapter 5,

preferably proposing an alternative extraction mechanism independently of cell rupture.

Recently, the challenges associated with attributing enhanced extraction to cell rupture have been highlighted, including in a study implementing ramp microwave heating and observing step-changes in extraction (Mao, Robinson and Binner, 2021). Instead of cell rupture, this study attributes the step-increase in yield to changes in some mass transfer parameters, which are thought to occur due to microwave-induced temperature gradients. This means that temperature gradients interfere with diffusion directly, causing step-changes in extraction without the need for cell rupture (Figure 7.1). These matching conclusions from Chapter 6 and recent literature findings (Mao, Robinson and Binner, 2021) challenge the prevailing assumption that cell rupture is the primary cause of enhanced extraction under microwave heating. Instead, an alternative mechanism is required to explain microwave extraction in biomass-solvent systems, where focus is to be drawn on diffusion trends instead of cell rupture only. Developing such mechanism is the aim of the current chapter.

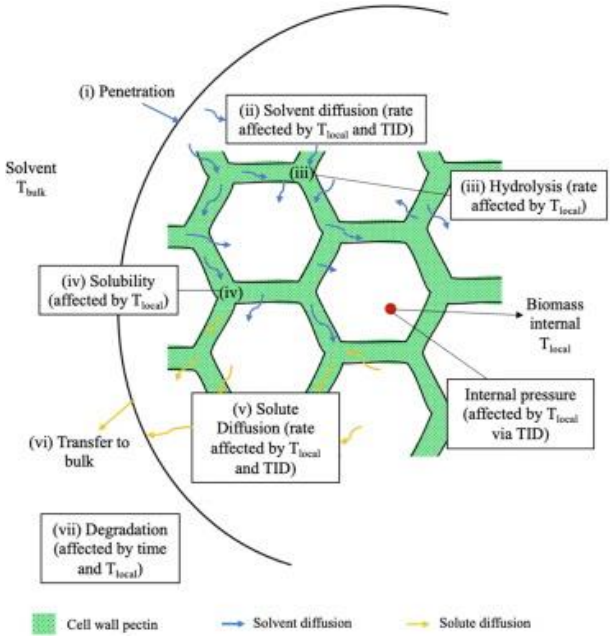


Figure 7.1 – Visual demonstration by Mao et al. (Mao, Robinson and Binner, 2021) **of how extraction could be enhanced with temperature gradients without the need for cell rupture. Localised temperature gradients are thought to improve diffusion, solubilisation, hydrolysis, and pressure build-up, resulting in enhanced extraction of pectin in this case. Figure unmodified from Mao et al.** (Mao, Robinson and Binner, 2021) **(© 2021 The Authors. Published by Elsevier Ltd.), available under CC BY 4.0 license (https://creativecommons.org/licenses/by/4.0/) when obtained. Further use of**

this item is governed by the said license unless otherwise indicated by the copyright holders

As it deviates from the prevailing literature trends (with support from recent empirical findings), this chapter provides a major advancement in the biomass-solvent extraction field. The intended work offers a novel perspective on extraction through defining diffusion-related limiting parameters rarely discussed previously, and then it shows how microwave heating can overcome these limitations through altering diffusion patterns. Again, this demonstrates the lack of understanding of mass transfer in the field, highlighting the importance of the current work.

The intended framework will be based on the already existing model from Chapter 5, where limitations are to be readdressed and new elements are to be introduced. Key limitations include disregarding solute diffusion and neglecting mass transfer through cell wall fragments. Both these assumptions were made as the model exclusively investigated cell pressure build-up and rupture due to water diffusion; however, in the current chapter these limitations should be readdressed to enable assessing extraction away from cell rupture. Furthermore, it was assumed in Chapter 5 that extraction occurs at thermal steady state, but this assumption should also be revisited here to attain more accurate understanding of the effect of heating on diffusion trends. Table 7.1 summarises the existing limitations, their implications, and how they will be readdressed in this chapter.

Limitation	Implications	Methods to readdress
Cell rupture assumed to be the primary rate-limiting step for enhancing extraction.	Model predictability limited to cases where cell rupture carries such an effect.	This is the underlying assumption/limitation; it will be readdressed through all points below.
Solute diffusion disregarded as only water is permitted to flow.	• Model does not quantify extraction/yield, but rather it only computes cell pressure. • Therefore, model predictions cannot be benchmarked quantitatively with empirical data. • Also, this does not allow understanding diffusion trends as required in this chapter.	Elements of solute diffusion to be introduced by revisiting mass transfer (section 7.2.2).
Mass transfer within cell walls neglected as these are assumed part of the solvent phase.	• Diffusion pathways and resistance to mass transfer not represented as accurately as possible. • Extractable solutes might originate from cell walls, and in such a case, these will not be covered by the model.	Diffusion through cell walls permitted as each fragment is to be considered a distinct phase (section 7.2.5.2).
Mass transfer assumed to occur at thermal steady state.	• With heat and mass transfer decoupled, the effect of heating on diffusion cannot be depicted accurately. • For instance, the effect of heating rate cannot be understood. • Furthermore, dielectric loss distribution (i.e., whether $\varepsilon''_{biomass} > \varepsilon''_{solvent}$) cannot be investigated for its effect on whether temperature gradient is established as required (see section 3.3.1.1).	Heat and mass transfer to be computed simultaneously, i.e., mass transfer is not to be assumed to occur at thermal steady state (section 7.2.5.4).
Heating rate defined indirectly via the heating parameters such as dielectric properties and electric field intensity.	• Although this enabled straightforward analyses to understand the effect of each heating parameter separately, in this chapter this will not enable a fair comparison between microwave and conventional heating. • With such a comparison absent, the effects of specific heating modes cannot be understood.	Heating to be defined with a user input parameter which allows a fair comparison between microwave and conventional heating (section 7.2.3).
Diffusivity and thermal conductivity assumed homogeneous throughout the system.	• Phase-specific conditions affecting these parameters not taken into consideration.	• Mathematical representation of the heat and mass equations to be modified to allow phase-

	• Such conditions might include variable concentrations and temperatures, and whether the specific phase has been ruptured. • Also, thermal conductivity should be linked to water activity for the purposes of future investigation (beyond this thesis).	specific values (sections 7.2.2 and 7.2.3). • Thermal conductivity to be made a function of water activity (although this feature has not been used in the current work).
Only cells are considered to have internal pressure, but not cell walls.	• Given that diffusion is to be considered through cell walls, pressure must be quantifiable in these fragments for the chemical potential expression to be employed. • Moreover, the absence of cell wall pressure means any possible rupture/structural alteration in these structures cannot be included in the model.	A framework for pressure build-up and expansion in cell wall fragments to be included (section 7.2.4).
Both water and solutes assumed to behave ideally in solution.	• Model restricted to situations where this holds true. • The wide variety of solutes within biomass demand a more flexible approach allowing non-ideal behaviour.	Activity-mole fraction relationship redefined (section 7.2.2.2).
Initial condition only incorporates pure water as a solvent phase.	• This does not represent real-world situations as accurately as possible. • Empirical studies employing impure water as a solvent are not covered in this model.	Initial condition redefined to allow impure water (section 7.2.5.1).
Initial water activity values defined directly through user inputs.	• This does not match empirical data as these rarely refer to activity gradients. • Therefore, model results cannot be fully benchmarked against empirical data.	Activity and mole fraction defined in terms of solubility, which is readily available and frequently referred to (section 7.2.2.3).

Table 7.1 – Existing limitations in the model from Chapter 5, along with the implications and methods to readdress

7.2 Methodology

7.2.1 System geometry

The geometry applied here is the same as that used in Chapters 3 and 5, which has been discussed in section 3.2.1. The model incorporates a cluster of biomass cells surrounded by solvent (Figure 3.1), where cells occupy a cuboid shape and are assembled regularly (Figure 3.2 and Figure 3.3). Cell dimensions (length, width, and height), cell wall thickness (t_{CW}), and solvent-to-solid ratio (S_R) prescribed as input parameters, are used to define the shape of the biomass and the volume of the surrounding solvent.

7.2.2 Mass transfer

The innovations intended for the model in this chapter, which have been discussed in section 7.1, demand re-conceptualising some of the elements of mass transfer, and this task was conducted as shown below.

7.2.2.1 The mass equation

7.2.2.1.1 A system of equations

A standard form of the mass equation had been derived in section 5.3.1.1.2 and used throughout Chapter 5. This expression (Equation (5.14)) is a partial-differential equation (PDE) accounting for mass transfer between a given point and all adjacent points (i.e., it accounts for diffusion in all directions). However, as seen in section 5.3.1.1.2, a key assumption in deriving Equation (5.14) is that the diffusion coefficient remains uniform in the *x-direction*, *y-direction*, and *z-direction* (i.e., $L = L_x = L_y = L_z$). This poses a limitation to the current work, as it was aimed here to enable variation in L based on local properties, and on whether physical rupture has been achieved in a phase. Therefore, mass transfer has been redefined mathematically, as shown below.

Water and solutes diffuse down spatial gradients in their chemical potential-to-temperature ratios (μ/T), as shown in Equation (5.1) for a unidimensional case. Note, however, that it is indifferent to this work whether diffusion occurs down gradients in μ/T or μ (see sections 4.4.2 and 5.3.1.1.1). Although the former is more precise, the latter will not change the outcomes of this work significantly, because temperature gradients are low here (1 ℃ can cause significant changes to extraction). This work uses μ/T solely to maintain consistency and precision.

For a given infinitesimal domain/cuboid *xyz* located within the system, diffusion takes place with the adjacent phases that are above and below; right and left; ahead

and behind (Figure 7.2). Consequently, summation of all mass transfer gives the rate of change of molar quantity in the current point *xyz* (Equation (7.1)).

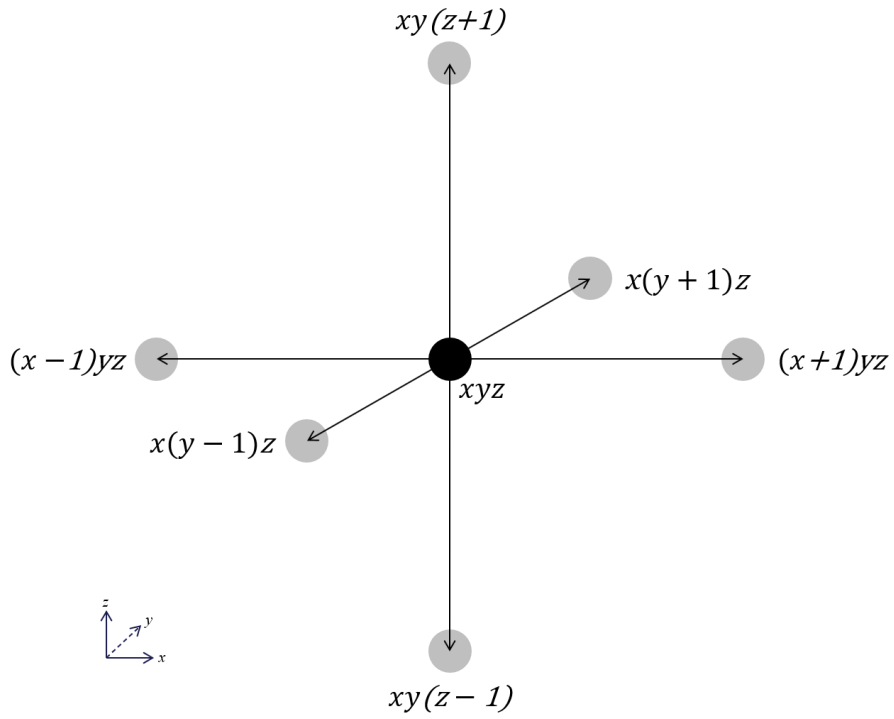


Figure 7.2 – Infinitesimal domain/cuboid and its 6 adjacent phases of direct interaction

$$\frac{\partial N_i}{\partial t} = \sum_j J_{i-j} = -\sum_j L_{i-j} A_{i-j} \frac{\partial}{\partial x}\left(\frac{\mu_{i-j}}{T_{i-j}}\right) \tag{7.1}$$

Phase "i" in Equation (7.1) is the infinitesimal phase *xyz*, while "j" represents the adjacent points. J_{i-j}, L_{i-j}, and A_{i-j} are the molar flow rate, diffusion coefficient, and cross-sectional area between phases "i" and "j", respectively.

Mass transfer has now been defined with a system of differential equations, each representing diffusion with one of the six adjacent phases. The temporal rate of change of molar quantity is obtained with summing up the six equations.

7.2.2.1.2 *Adhering to physical limits*

Unlike temperature (an intensive property), molar quantities in this work are very small in magnitude due to the small scale of the model. This poses a risk of encountering negative quantities due to numerical error or otherwise. However, in Chapter 5 only water had been permitted to diffuse, and this diffusion had occurred

normally in one direction, namely going from the solvent phase (which was abundant in water) directly into cells. Under this regular flow pattern, it was highly unlikely to observe any negative water quantities; hence, no further modification had been introduced to the mass equation at that stage. However, the current work incorporates water and solutes, and it accounts for diffusion within cell wall fragments in addition to cells and solvent. Hence, diffusion patterns are not necessarily regular (i.e., following a single path), which poses a risk of obtaining physically meaningless negative molar quantities.

Therefore, it was vital here to introduce a parameter into Equation (7.1) that defines the physical limits of mass transfer. Considering phases *xyz* and *(x+1)yz* in Figure 7.2 as an example, these limits can be summarised as follows:

- if phase *xyz* has zero mass yet Equation (7.1) indicates a flow from *xyz* to *(x+1)yz*, then flow should be readjusted to zero; and
- if phase *(x+1)yz* has zero mass yet Equation (7.1) indicates a flow from *(x+1)yz* to *xyz*, then flow should also be readjusted to zero.

Adhering to these limits was achieved by introducing a parameter $\widehat{\mathcal{H}}$ (Equation (7.2)), which is a collection of Heaviside functions that equals zero when the physical limits are not adhered to, but it equals unity otherwise. $\widehat{\mathcal{H}}$ is defined in Equation (7.3).

$$\frac{\partial N_i}{\partial t} = \sum_j \widehat{\mathcal{H}_{i-j}} J_{i-j} = -\sum_j \widehat{\mathcal{H}_{i-j}} L_{i-j} A_{i-j} \frac{\partial}{\partial x}\left(\frac{\mu_{i-j}}{T_{i-j}}\right) \tag{7.2}$$

$$\widehat{\mathcal{H}_{i-j}} = \left[\mathcal{H}(N_i) + \mathcal{H}\left(J_{i-j}\right) - \mathcal{H}(N_i)\mathcal{H}\left(J_{i-j}\right)\right] \left[\mathcal{H}\left(N_j\right) + \left(1 - \mathcal{H}\left(J_{i-j}\right)\right) - \mathcal{H}\left(N_j\right)\left(1 - \mathcal{H}\left(J_{i-j}\right)\right)\right] \tag{7.3}$$

N_i in Equations (7.2) and (7.3) is the molar quantity in phase *xyz*; N_j is the molar quantity in the respective adjacent phase; J_{i-j} is the molar flow rate between the two phases; A_{i-j} is the cross-sectional area between the two phases; and L_{i-j} is the diffusion coefficient governing mass transfer between the two phases. In addition, $\mathcal{H}$ represents a Heaviside function.

The different possible outcomes of Equation (7.3) are summarised in Table 7.2 where, $\widehat{\mathcal{H}_{i-j}}$ equals zero if mass transfer is not possible physically, but otherwise it equals unity. The need to introduce $\widehat{\mathcal{H}_{i-j}}$ into Equation (7.2) arises from the fact that, chemical potential (μ) does not depend on the absolute molar quantities of the different components. Rather, μ depends on mole fractions dictating the activity (α) of components in a phase, together with the pressure and temperature of that phase. As such, from a mathematical viewpoint mass transfer is possible even with zero or negative molar quantities; in other words, a diffusion driving force from "i" to "j" may exist even if the mass in "i" is zero. Therefore, what stops diffusion from "i" to "j" in such case is not a mathematical limit in the driving force, but rather a physical constraint entailing depletion in the mass available in "i". This necessitates the introduction of $\widehat{\mathcal{H}_{i-j}}$, which reflects the zero-mass physical constraint and, thereby, avoids computing negative molar quantities in the model.

Physical condition	$\boldsymbol{\mathcal{H}(N_i)}$; $\boldsymbol{\mathcal{H}(N_j)}$; $\boldsymbol{\mathcal{H}(J_{i-j})}$	$\boldsymbol{\widehat{\mathcal{H}_{i-j}}}$
• positive molar quantities in both phases; • spatial gradient allows flow from "j" to "i".	1; 1; 1	1
• positive molar quantities in both phases; • spatial gradient allows flow from "i" to "j".	1; 1; 0	1
• positive moles in "i" and zero moles in "j"; • spatial gradient allows flow from "j" to "i".	1; 0; 1	0
• zero moles in "i" and positive moles in "j"; • spatial gradient allows flow from "j" to "i".	0; 1; 1	1
• positive moles in "i" and zero moles in "j"; • spatial gradient allows flow from "i" to "j".	1; 0; 0	1
• zero moles in "i" and positive moles in "j"; • spatial gradient allows flow from "i" to "j".	0; 1; 0	0
• zero molar quantities in both phases;	0; 0; 1	0

• spatial gradient allows flow from "j" to "i".		
• zero molar quantities in both phases; • spatial gradient allows flow from "i" to "j".	0; 0; 0	0

Table 7.2 – $\widehat{\mathcal{H}_{\iota-J}}$ values corresponding to the different physical conditions governing mass transfer between two phases "i" and "j"

Equation (7.2) can be used to describe mass transfer of any species, including both water and solutes. The current model is capable of incorporating an infinite number of solutes, all of which diffusing in accordance with Equation (7.2). The desired number of solutes is set out by the user; however, more solutes require larger computational power to be simulated. Hence, the analyses presented in the current chapter are restricted to two solutes plus water (sections 7.3 and 7.4).

7.2.2.2 Chemical potential and activity

Chemical potential (μ) is defined in Equation (4.63).

Regarding activity (α), this is generally related to the mole fraction (X) through a parameter known as the activity coefficient (γ) (Equation (7.4)). When α equals X (i.e., $\gamma = 1$), the substance is said to behave ideally in solution. Furthermore, it is generally accepted that γ tends to unity as X tends to the same, meaning that a pure substance always behaves ideally (i.e., $X = \alpha = \gamma = 1$ for a pure substance).

$$\alpha = \gamma X$$
$$\gamma \to 1 \; as \; X \to 1 \qquad \textbf{(7.4)}$$

In this work, activity was expressed in terms of mole fraction as shown thus:

$$\alpha = X^n \qquad \textbf{(7.5)}$$

Equation (7.5) is a simple activity model capable of capturing both ideal and non-ideal behaviour in solutions. This is shown in Figure 7.3 where, if $n = 1$ ideal behaviour is obtained as activity (α) equals mole fraction (X) throughout. However, if $n > 1$ a negative deviation from ideal behaviour is observed, since α is generally smaller than X, and γ is generally smaller than 1. On the other hand, with $n < 1$ a positive deviation is seen as $\alpha > X$ and $\gamma > 1$. In all cases, γ tends to unity as X tends

to the same, which matches the fundamental definitions of activity (α) and activity coefficient (γ) shown in Equation (7.4). Hence, Equation (7.5) offers a straightforward yet efficient tool to describe activity-mole fraction relationships, waiving the need to investigate complex relationships found in literature.

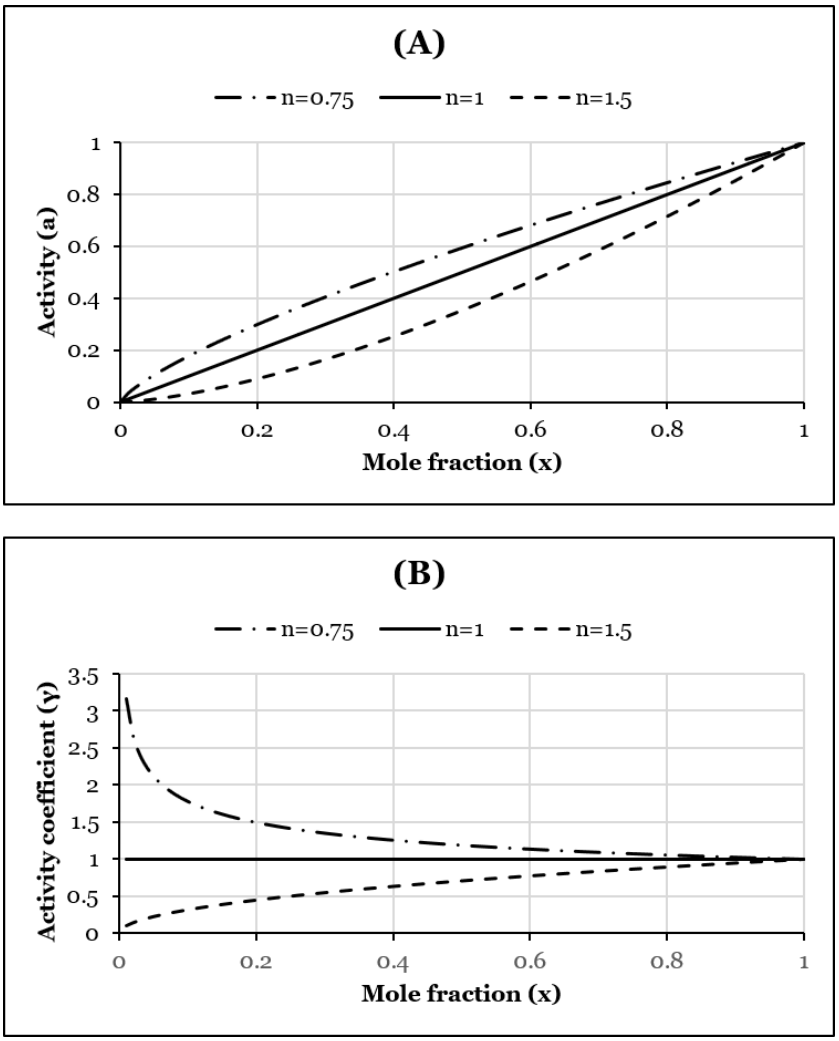


Figure 7.3 – Activity-mole fraction relationship described in Equation (7.5); (A) Plot of activity against mole fraction for different values of n; (B) Plot of activity coefficient against mole fraction for different values of n

On the other hand, although the current model enables an infinite number of solute types in the biomass, it should be noted that all solutes are assumed to possess a single collective activity (α_s) and, thereby, chemical potential (μ_s). This signifies that all solutes are assumed to behave similarly at the molecular level, demonstrating similar solute-water interactions due to their comparable chemical makeup and physical characteristics. Hence, all solutes flow down a unified spatial gradient, but they are still permitted to differ in their diffusion rates (i.e., mass transfer coefficient, L). Given

the wide variety of components contained within a biomass material, this is a reasonable assumption which allows investigating solutes behaving similarly. Such solutes might originate from the same polymeric source in the biomass (decomposed due to natural or external processes), or they might exist in certain locations within the biomass matrix and have comparable functions, thus exhibiting similar structure and behaviour. This work is a novel first step upon which the domain of solutes can be widened in future iterations. Future developments could include groups of solutes that behave uniquely, while each group consists of solutes behaving similarly.

7.2.2.3 Solubility and mole fraction

Mole fraction is conventionally defined based on the compositions of different components in solution. However, although biomass materials contain significant amounts of solute (which are to be extracted), many of these solutes originate from sources that are typically not very soluble in water. For instance, solubilities as low as the order of $10^{-5}\ g_s g_W{}^{-1}$ have been reported for cellulose (Strachan, 1938).

The presence of negligibly soluble components within biomass indicates that the mole fractions of water are high in solution, even if the solutes are present in larger amounts. This is because, not all solutes will be able to dissolve in the available water/moisture within the respective biomass phases, thus granting high water mole fractions in solution. Therefore, mole fractions of water and solute are dictated by the solubility of solutes in water (S_s); the higher the value of S_s, the more solutes dissolve in the available water, the larger the mole fraction of these solutes in solution. This could explain why water activity generally approaches unity in biomass materials such as fruits and vegetables (between 0.95 and 1 (Rizvi, 2005)).

It can be inferred from this analogy that, based on the solute's solubility in water (S_s) there is maximum mole fraction that solutes can have in solution, and, in turn, there is a minimum mole fraction that water can have. If the water available in a phase is not enough to dissolve all solutes, then the mole fractions in solution will remain constant even as mass transfer takes place. This is because, undissolved solutes will replace any dissolved solutes diffusing away, and any new solutes introduced beyond water's capacity to dissolve, will simply precipitate out of solution (Figure 7.4). However, if all solutes in a phase are dissolved, then the mole fractions in solution will be subject to change with mass transfer as expected normally, but the solute mole

fraction will always be lower than the maximum allowed by solubility, and the water mole fraction will always be higher than the minimum allowed.

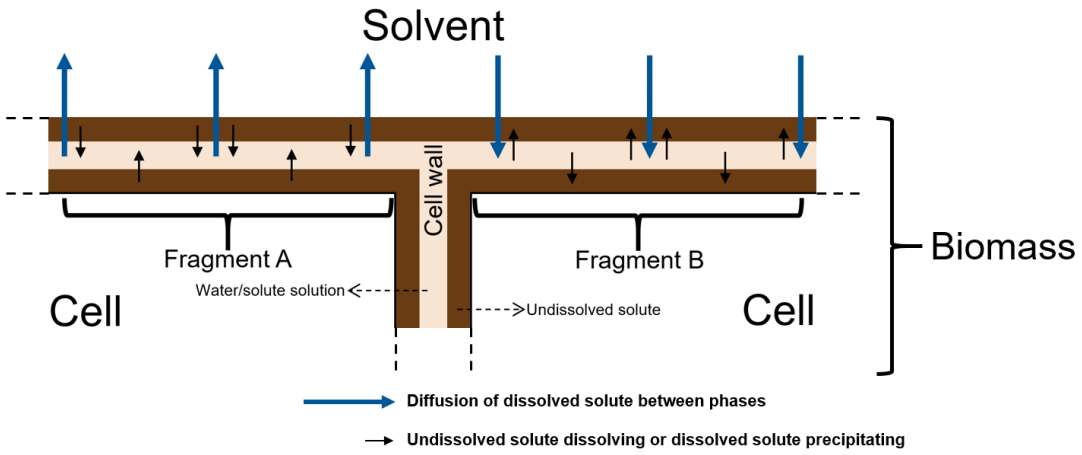


Figure 7.4 – Demonstration of how the presence of undissolved solutes inhibits changes in mole fraction as mass transfer takes place. Cell wall fragment A: solute diffusing to the solvent is substituted by surplus dissolving solute. Cell wall fragment B: solute diffusing from the solvent precipitates out of solution

Based on this, an expression can be derived where, if the compositions of water and total solutes (dissolved and otherwise) are known, then the mole fractions in solution can be determined through knowledge of solubility (S_s). This expression (Equation (7.6)), which uses a Heaviside function, works such that if the water mixture fraction/composition ($\bar{X}_W$) is smaller than the minimum mole fraction in solution dictated by solubility ($X_W{}^*$), then the mole fraction is constant and equal to $X_W{}^*$. It is only when $\bar{X}_W$ is larger than $X_W{}^*$ that the mole fraction becomes a function of the composition of water present in the phase (Figure 7.5). The relationship between solubility (S_s) and the minimum water mole fraction in solution dictated by solubility ($X_W{}^*$), is summarised in Equation (7.7).

Unlike cell wall fragments consisting of solidified polymeric structures, this model assumes all cells not to have any undissolved solutes initially, which is because cells largely consist of liquid solutions. Nevertheless, all phases in the biomass-solvent system are governed by Equation (7.6), meaning that solutes will precipitate out of solution within cells if their molar quantity exceeds water's capacity to dissolve.

$$X_W = X_W{}^* + (\bar{X}_W - X_W{}^*)\mathcal{H}(\bar{X}_W - X_W{}^*) \quad \textbf{(7.6)}$$

$$X_W{}^* = \frac{1}{S_s + 1} \tag{7.7}$$

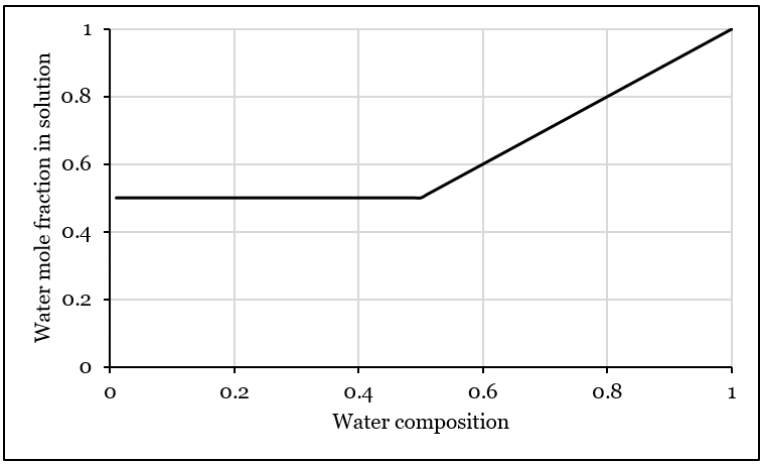


Figure 7.5 – Mole fraction as a function of mixture fraction/composition (Equation (7.6)). $X_W{}^* = 0.5$

7.2.2.4 Diffusivity and mass transfer coefficient

Diffusivity (D) is preferable to use over mass transfer coefficient (L) since the former is more widely available in literature. As demonstrated in section 5.3.1.1.4, L is related to D through Equation (5.16), but L should be defined separately for each phase comprising a given homogeneous temperature and molar concentration. Therefore, the effective mass transfer coefficient applicable between phases "i" and "j" (L_{i-j} in Equation (7.2)), can be estimated as the mean average of L_i and L_j, due to the very small scale of the system (Equation (7.8)).

$$L_{i-j} = \frac{1}{2}\left(L_i + L_j\right) \tag{7.8}$$

Phase "i" in Equation (7.8) is the infinitesimal point *xyz*, while "j" represents the respective adjacent point.

7.2.3 Heat transfer

7.2.3.1 Heating biomass

Like mass transfer, heat transfer is conducted through interaction between an infinitesimal domain/cuboid and its 6 adjacent phases of direct interaction (Figure 7.2). However, the standard form of the heat equation derived in section 3.2.2 and used throughout Chapters 3 and 5 (i.e., Equation (3.8)), cannot be used here. This is because, Equation (3.8) had been derived on the basis that thermal conductivity (k)

remains the same for heat transfer in the *x-direction*, *y-direction*, and *z-direction* (i.e., $k = k_x = k_y = k_z$). Although k is held uniform throughout the system in the current work, the model is still capable of handling phase-specific k values, thus enabling further investigations and analyses to be conducted beyond this thesis. Therefore, as shown in section 7.2.2.1.1 for mass transfer, heat transfer in the current work was also redefined mathematically.

Equation (7.9) describes unidimensional heat transfer in biomass, consisting of conventional heat transfer (i.e., Fourier's law) and volumetric heating through microwave radiation. Microwave attenuation is accounted for using the principles of Lambert's law, as discussed in section 3.2.2 and shown in Equation (3.9).

$$Q = 2\pi F \varepsilon_0 \varepsilon'' |E|^2 - kA\frac{dT}{dx} \tag{7.9}$$

Like with the case of mass transfer, heat transfer takes place with the adjacent phases that are above and below; right and left; ahead and behind (Figure 7.2). Subsequently, summation of all heat transfer gives the rate of change of temperature in the current phase *xyz* (Equation (7.10)).

$$\frac{\partial T_i}{\partial t} = \frac{1}{N_i C_p}\left[2\pi F \varepsilon_0 \varepsilon''_i |E|_i^{\,2} - \sum_j k_{i-j} A_{i-j} \frac{\partial T_{i-j}}{\partial x}\right] \tag{7.10}$$

Phase "i" in Equation (7.10) is the infinitesimal phase *xyz*, while "j" represents the adjacent phases.

7.2.3.2 <u>Heating the solvent</u>

In Chapters 3 and 5, microwave power applied to the biomass and the solvent had been defined indirectly, using input parameters such as incident electric field intensity ($|E|_0$), dielectric loss factor (ε''), etc. This approach was sufficient, since it had been aimed to study the effects of individual microwave heating parameters on the induced temperature gradient magnitudes, and the subsequent rise in cell pressure due to enhanced water influx. Effectively, thereby, it had been accepted that enhanced extraction is brought about exclusively by cell rupture, which only demands characterising water diffusion (this matches the assumptions in literature). However,

the current work deviates from the assumption on cell rupture, and instead it aims to characterise water and solute diffusion simultaneously, and to understand how these diffusion trends are influenced by microwave and conventional heating.

Microwave and conventional heating must be compared fairly, and such fairness is benchmarked empirically through equating the heating rates applied with the two heating methods (Galan et al., 2017). In other words, for a fair comparison both heating methods should heat up the system at the same rate, specifically this should be the case in the solvent phase from which temperature measurements are normally taken in empirical studies (i.e., a probe cannot be inserted into biomass). Therefore, in this work heating was defined in the solvent phase with a user-input rate of temperature increase (Q_s, in Ks^{-1}), which is applicable regardless of whether microwave or conventional heating are used. This ensures that the exact same temperature ramp profile is observed in the solvent phase, thus allowing a fair test to be conducted between the two heating methods. If microwave heating is imposed upon the system, the model infers the value of $|E|_0$ from the input parameters Q_s and the dielectric loss factor of solvent ($\varepsilon''_{solvent}$). $|E|_0$ is then used, together with the other input microwave heating parameters, to quantify heating in the biomass (Equation (7.10)).

The solvent is heated up to a set-point temperature $T_{extraction}$, beyond which it behaves as a heat sink at thermal steady state.

7.2.4 Cell wall expansion

7.2.4.1 Expansion mechanics and assumptions

Cell mechanics and pressure-volume relationship are the same as outlined in section 5.3.1.2. The novel aspect of the current work is the inclusion of a pressure-volume relationship for cell wall fragments, which is to be expanded upon in this section.

Like cells, stress-strain behaviour in cell wall fragments was assumed to follow a rubber-like behaviour (Equation (5.17)). Moreover, as outlined in section 5.3.1.2, it was also assumed that cell wall fragments do not experience shear strains, and that they only expand in one direction, namely, the *x-direction*. However, unlike the case shown in section 5.3.1.2 for cells, the voids in cell wall fragments are not uniform, i.e., they are distributed based on the specific structure, in contrast to cells which are

uniform and surrounded by a wall boundary (Figure 5.8). Therefore, to simplify this it was assumed that voids are concentrated in the middle of a cell wall fragment, creating a hollow-shaped fragment with a square cross-section. As shown in Figure 7.6, cell wall voids were assumed to run along the *x-direction*, yet mass transfer can still take place between the voids in all directions. Axial stress within cell wall fragments (σ_{xx}) was assumed to apply only to the area immediately adjacent to the voids, as shown in Figure 7.6. This area, together with the void it frames, constitutes a square segment of length t_{CW} (i.e., equal to the cell wall thickness); stress (σ_{xx}) applies to the frame while pressure (P_L) is applicable within the void itself.

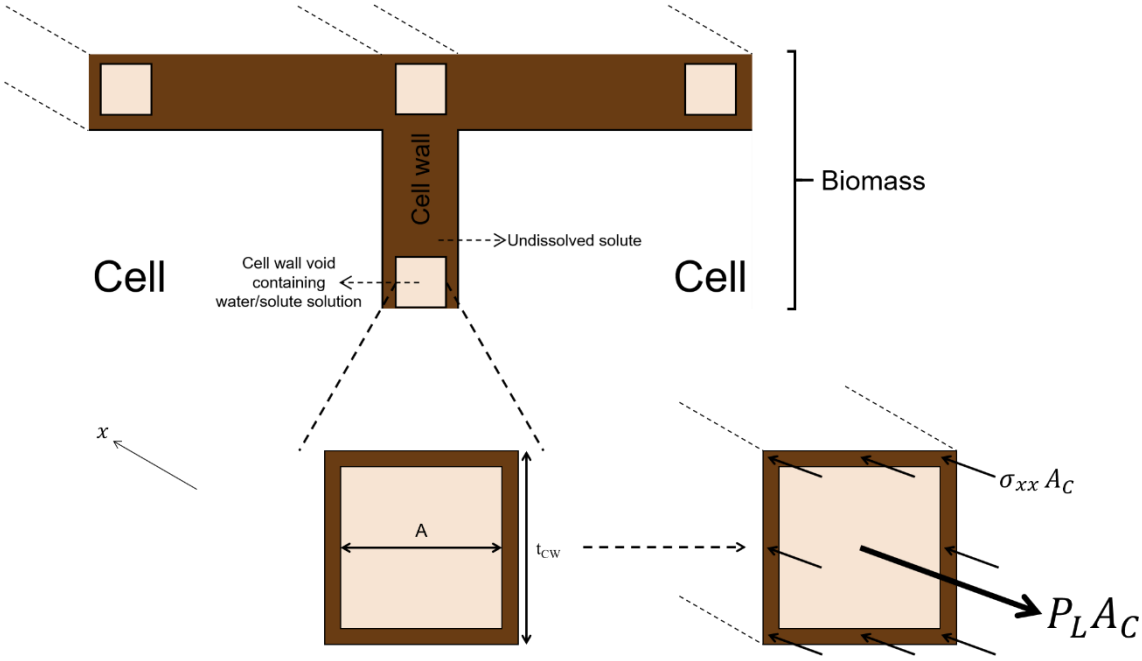


Figure 7.6 – Demonstration of the shape that cell wall voids are assumed to take. Each cell wall fragment has a square-shaped concentration of voids running through the *x-direction* (into the page). Axial stress is applicable along the *x-direction* and is limited to areas adjacent to voids, so as to maintain a square-shaped area of mechanical influence

Assuming the dimensions described in Figure 7.6 remain constant (a simplification), stress (σ_{xx}) and pressure (P_L) can be related as shown below (for a unit depth along the *x-direction*):

$$P_L A^2 = \sigma_{xx}\left[4A\left(\frac{t_{CW}-A}{2}\right)+4\left(\frac{t_{CW}-A}{2}\right)^2\right] \quad \textbf{(7.11)}$$

Equation (7.11) can be simplified into the following form:

$$P_L A^2 = \sigma_{xx}[{t_{CW}}^2 - A^2] \quad \textbf{(7.12)}$$

On the other hand, the volume of voids relative to the total volume of a cell wall fragment, can be described with a cell wall void fraction (Φ_{CW}). For a unit depth along the *x-direction*, the following holds true:

$$A^2 = \Phi_{CW}{t_{CW}}^2 \quad \textbf{(7.13)}$$

Substituting Equation (7.13) into Equation (7.12) yields the following expression:

$$\sigma_{xx} = P_L \frac{\Phi_{CW}}{1 - \Phi_{CW}} \quad \textbf{(7.14)}$$

Equation (7.14) relates σ_{xx} with P_L for cell wall fragments using the parameter Φ_{CW}. This relationship constitutes a rough estimate based on simplifying assumptions applied to the dimensions of voids and the area in which stress is applicable, together with the presuppositions of rubber-like behaviour, unidirectional axial stress, and negligible shear stress. The estimate used here is sufficient for this work; a relationship between pressure and stress is developed from a reasonable basis, and it can be incorporated within the intended numerical framework.

As shown in section 5.3.1.2 for cells, a numerical approach has been adopted here to construct a pressure-volume relationship for cell wall fragments (Figure 7.7). The required inputs are Φ_{CW}, cell wall stiffness at zero strain (Y_{0-CW}), and an input array of discrete pressure values separated by a finite step (δP). For every pressure value in the predefined domain, the stress (σ_{xx}) and strain (ϵ_x) are computed using Equations (7.14) and (5.17), respectively; hence, the corresponding volumetric strain of the fragment is calculated. However, since Φ_{CW} is assumed to remain constant (because stress/strain are applicable in the *x-direction*, and the voids maintain a square cross-section), the new dimensions computed at each finite step (δP) do not alter the relationship between σ_{xx} and P_L (Equation (7.14)) for the next step. This is as opposed to the cell pressure-volume relationship where, the regular shrinkage in t_{CW} alters the relationship between σ_{xx} and P_L continuously (Figure 5.9 and Equation (5.18)).

Nevertheless, note that this shrinkage in t_{CW} is still assumed not to affect the shape of the cell wall voids.

The numerical framework computes a cell wall volumetric strain corresponding to every input pressure value. Hence, a cell wall pressure-volume relationship is generated where, if the volume of solution in voids is known, the pressure can be interpolated, and vice versa.

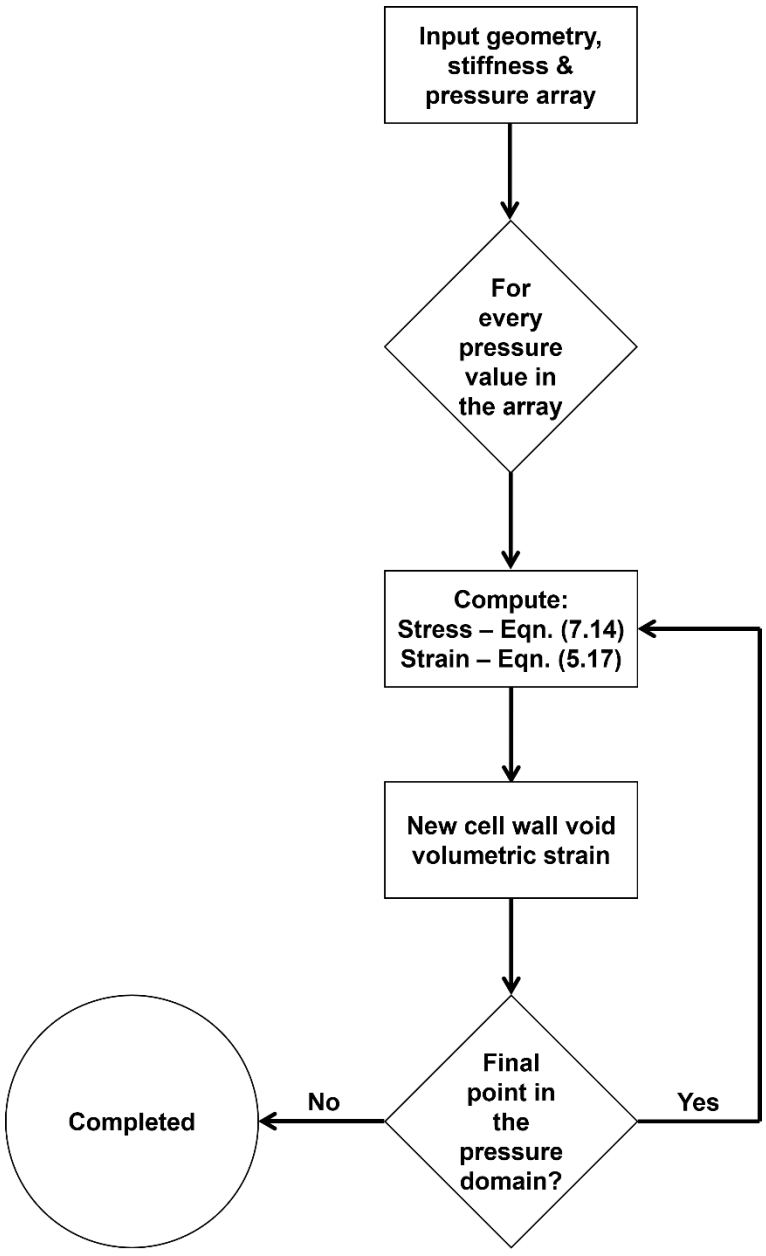


Figure 7.7 – Numerical framework for cell wall expansion

7.2.4.2 Rupture

In Chapter 5, cell rupture could be inferred on approaching certain threshold cell pressure values; however, the rupture event itself had not been incorporated in the

model. In the current work, it was intended to incorporate a more meaningful definition of rupture, specifically to envisage a possibility as to how such an event might alter mass transfer. In previous microwave extraction models (e.g., Chapter 5 and Chan et al. (Chan et al., 2016)) it had been assumed that cell rupture is primarily responsible for enhancing extraction; hence, it was seen irrelevant to quantitatively understand the events occurring after rupture had been achieved (section 7.1). In other words, all that mattered was to investigate whether rupture can be achieved under specific conditions. However, the current work is aimed at redefining the underpinnings of extraction away from rupture as a rate-limiting step. Therefore, it becomes imperative to incorporate a quantitative definition for rupture (albeit simplistic), to investigate any effects it may have on mass transfer and the overall extraction mechanism. Such an attempt is novel due to its absence from literature.

In this work, the possibility of rupture was extended to include all cell wall fragments (each individually) in addition to cells. Rupture takes place once a threshold pressure is achieved in any given biomass phase, and it results in a change in the diffusivity of solutes. Therefore, the model demands two sets of input solute diffusivity values, one for unruptured phases (D_s) and another for ruptured phases ($D^R{}_s$). The threshold rupture pressures are $P^R{}_C$ and $P^R{}_{CW}$ for cells and cell wall fragments, respectively.

A simplistic definition for rupture is maintained in this work, due to its novelty. Rupture takes place in a biomass phase when a threshold pressure is achieved, and thereafter, the resulting structural modifications alter diffusivity and mass transfer coefficient of solutes in that phase. However, following a rupture event the respective phases maintain their shape, and they continue to obey the mass transfer law described in Equation (7.2).

7.2.5 Numerical solution

Equations (7.2) and (7.10) describing mass and heat transfer, respectively, were solved using a finite-difference time-domain (FDTD) technique known as the method of lines.

7.2.5.1 Initial and boundary conditions

Initial temperature ($T_{initial}$) is a user input applicable throughout the system, while the thermal boundary condition has been set for achieving zero heat loss from the system, due to the very small scale of the model.

Initial molar quantities of solutes are set based on the biomass phase concerned (i.e., cell or cell wall fragment). In cells, a user-input volume fraction ($\%_{s-C}$) is used to set the initial moles of each solute, while in cell walls the moles of solutes are dictated with several user inputs including cell wall void fraction (Φ_{CW}); initial mass percentages of the different solutes relative to the total dry mass ($\%_{s-CW}$); collective density (ρ_s) and molecular weight (Mr_s) of solutes; and volumes of the individual cell wall fragments (the total solute moles are divided amongst the fragments, based on their volume as a fraction of the total cell wall volume). Initial solute moles in the solvent phase are dictated by a user-input initial percentage mass of solutes ($\%_{s-S}$).

Initial water moles in cell walls are set as a percentage of the total moles of dry material ($\%_{W-S}$), which is added as a surplus amount to the total cell wall moles already present, and then divided amongst fragments according to the volumes they occupy. On the other hand, initial water moles in cells are calculated assuming that the initial water and solute activities are equal to those in the cell walls. In other words, activity values are equal throughout the biomass initially, and so the biomass is in equilibrium with itself. Therefore, the minimum amount of water needed to constitute a saturated solution in cells, with the same activities as in the cell walls, is calculated and applied.

In real-world situations, an equilibrium state within a biomass comprises equal chemical potential values in the different cell/cell wall phases. Such equivalence may be achieved with various pressure/activity combinations in the system, meaning that these two parameters may not necessarily be uniform throughout the material at the initial state. However, to avoid complexity in the current work, the initial state was assumed to comprise uniform activity values in biomass (as stated above), and, therefore, uniform pressures. This is perhaps the easiest pressure/activity combination to implement at the initial state, as it does not necessitate balancing pressures and activities to equalise the chemical potential values, nor does it demand additional input parameters describing the initial pressure distribution in the biomass. In this work, the initial pressure was set equal to the atmospheric value in all biomass phases and in the

solvent. This eliminates any pressure-driven diffusion at the initial state, thereby avoiding possible interferences with the effects of any pressures arising in the model as heating is introduced. Future efforts may allow non-uniform initial activities, pressures, and even temperatures in the biomass, which will further widen the scenarios that can be studied using this model.

For all components (water and solutes), the boundary condition is set such that no mass escapes the biomass-solvent system.

7.2.5.2 Model discretisation

In this work, model discretisation follows the example of section 3.2.3.2 for heat transfer, where each cell and cell wall fragment were denoted a discrete numerical point. Dividing the model into discrete points means to assume that each cell and cell wall fragment is a distinct phase, represented by a discrete finite point (Figure 3.5). The properties of any given phase (such as temperature) are assumed to be homogeneous throughout the phase and equal to the properties computed at the location of the discrete point. Also, the displacement between any two adjacent phases is assumed equal to the separation between their respective discrete points.

As discussed in section 3.2.3.2, the solvent was assumed as one homogeneous phase described by a single numerical point. Since this homogeneous solvent phase surrounds the biomass, it cannot be denoted a fixed numerical point, but rather this point should "move" continuously alongside the biomass-solvent boundary, so that all biomass phases at the edge are at the same proximity to the solvent phase (Figure 3.5). It is assumed here that the rate-limiting step to enhancing extraction lies within the biomass rather than the solvent phase. It is, therefore, reasonable to represent the solvent with a single numerical point, and to allow this point to be in direct contact with all biomass phases at the biomass-solvent boundary.

7.2.5.3 Approximating the mass and heat equations

The mass and heat equations (Equations (7.2) and (7.10)) were approximated by assuming that the spatial gradients in μ/T (for mass transfer) and T (for heat transfer), are linear between any two discrete numerical points concerned. This renders the expressions to those shown below in Equations (7.15) and (7.16), constituting a system of ordinary-differential equations (ODE) that can be solved numerically.

$$\frac{dN_i}{dt} = -\sum_j \widehat{\mathcal{H}_{i-j}} L_{i-j} A_{i-j} \frac{{\mu_i}/{T_i} - {\mu_j}/{T_j}}{\delta x} \quad \textbf{(7.15)}$$

$$\frac{dT_i}{dt} = \frac{1}{N_i C_p}\left[2\pi F \varepsilon_0 \varepsilon''_i |E|_i^{\,2} - \sum_j k_{i-j} A_{i-j} \frac{T_i - T_j}{\delta x}\right] \quad \textbf{(7.16)}$$

Due to the mobile nature of the numerical point representing the solvent phase (section 7.2.5.2), Equations (7.15) and (7.16) cannot be used to solve for temperature and molar quantities in this phase. Instead, molar quantities in the solvent can be obtained through a mass balance applied with all adjacent biomass phases (Equation (7.17)). Also, the solvent temperature remains directly computable from the heating rate of the solvent (Q_s), which is a user input.

$$\left.\frac{dN}{dt}\right|_{solvent} = -\sum_{ijk} \left.\frac{dN}{dt}\right|_{ijk} \quad \textbf{(7.17)}$$

Phase *ijk* in Equation (7.17) is a biomass-solvent boundary/edge phase.

7.2.5.4 Solution framework

This work has overcome some key limitations of the previous model presented in Chapter 5, allowing extraction in biomass-solvent systems to be investigated independently of cell rupture (see section 7.1). Cell wall fragments have been included in this work (together with a cell wall pressure-volume relationship), and mass transfer of solutes has also been incorporated where each solute has its own diffusivity (D). Mole fraction has been characterised based on solubility (S_s), which is a more realistic approach for the intended definition. Also, non-ideal solution behaviour has been enabled through utilising a simplistic activity-mole fraction relationship that adheres to the fundamental principles that define activity (α) and activity coefficient (γ).

Figure 7.8 summarises the numerical framework of the model where, Equations (7.15) and (7.16) were solved over a predefined domain of discrete time values separated by a finite step (δt). For example, solving over $100\ s$ with a time-step $\delta t = 1\ s$, is analogous to solving in a stepwise manner over a time domain of

$0, 1, 2, \ldots, 100\ s$. The smaller the time-step (δt) the more accurate the result, but also the more computationally intensive the simulation. Moreover, too large δt values cause instability to the computation and can lead the results to diverge towards infinity. Hence, the chosen δt should neither be too small nor too large.

Starting from the input geometrical, heat, and mass parameters, and the pressure-volume relationships, μ and T were computed for all spatial numerical points in the biomass-solvent system. Following this, new temperatures and molar quantities were computed and, subsequently, new pressures were also obtained using the relevant pressure-volume relationships. The new values were then used in the next time step, and this was repeated for every consecutive value in the time domain. Key model validation steps are presented in APPENDIX C.

As shown in Figure 7.8, this work does not only enable mass and heat transfer to be conducted in a single simulation run, but unlike Chapter 5 these two analyses are also conducted simultaneously over a single time domain. This is a key advancement signifying that extraction does not necessarily take place at thermal steady state, but rather, both mass and heat transfer occur simultaneously at the same time. In comparison, the previous model (Chapter 5) had exclusively focussed on extraction at steady state temperature distribution; hence, heat transfer had been assumed to occur before any mass transfer was initiated (section 5.3.1.4.3). The previous model was, therefore, limited to cases with rapid heating where thermal steady state is achieved much faster than extraction itself, whereas the current work can be applied to a much wider range of extraction scenarios.

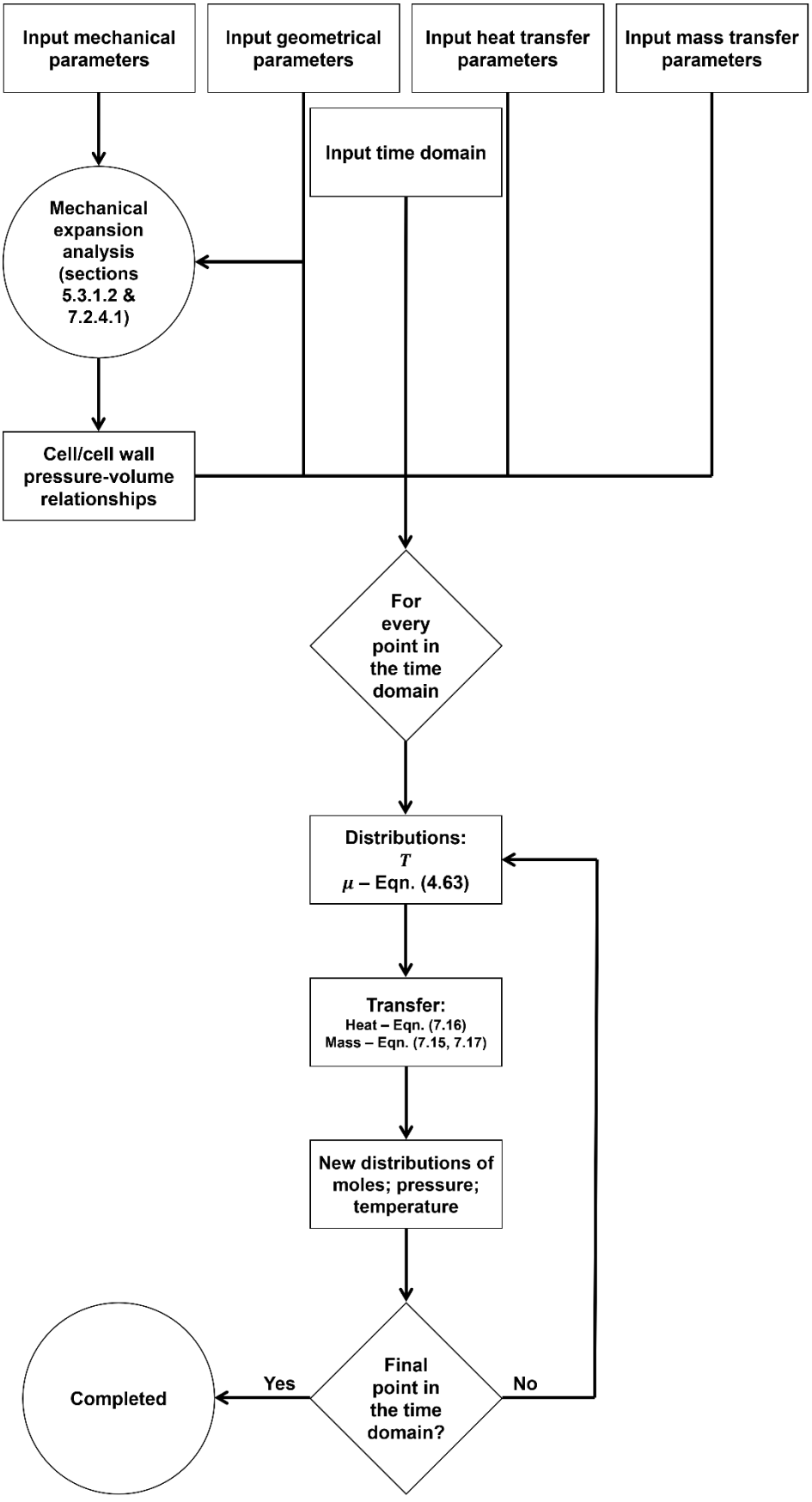


Figure 7.8 – Numerical framework for the comprehensive extraction model

7.3 Predicted extraction trends at room temperature

Initially, extraction was investigated at room temperature to understand the underlying effects of the mass transfer parameters including solubility (S_s), diffusivity (D), solvent-to-solid ratio (S_R), biomass particle size, non-ideal behaviour of solutions, solvent purity, and solute distribution amongst cells and cell walls. Typical value ranges for the different parameters of the model are shown in Table 7.3.

7.3.1 Base case

This case comprises the smallest possible cubic-shaped biomass cluster (1x2x2 cells; particle size = 0.1 mm; Figure 7.9), surrounded by a solvent with $S_R = 10\ mLg^{-1}$. The biomass incorporates two solutes, where the initial mass percentage of each solute in cell wall fragments ($\%_{s-CW}$) was fixed at 25%, and the initial volume fraction in cells ($\%_{s-C}$), representing both solutes collectively, was assigned a value of 0.025%. This means that the intended extracts mainly originate from the cell walls, but nonetheless, the effect of redistributing solutes into cells has been studied in section 7.3.8. On the other hand, solubility (S_s) was assigned a value of 0.01 $g_S{g_W}^{-1}$, and this is justified given that even smaller figures have been reported for cellulose (Strachan, 1938), which is a key component in the structure of cell wall materials (Chapter 2; section 2.2). Moreover, water diffusivity (D_W) was fixed at $10^{-9}\ m^2s^{-1}$, and both solutes were assigned a diffusivity value of $10^{-10}\ m^2s^{-1}$. Table 7.4 summarises the baseline values assigned to the different model parameters.

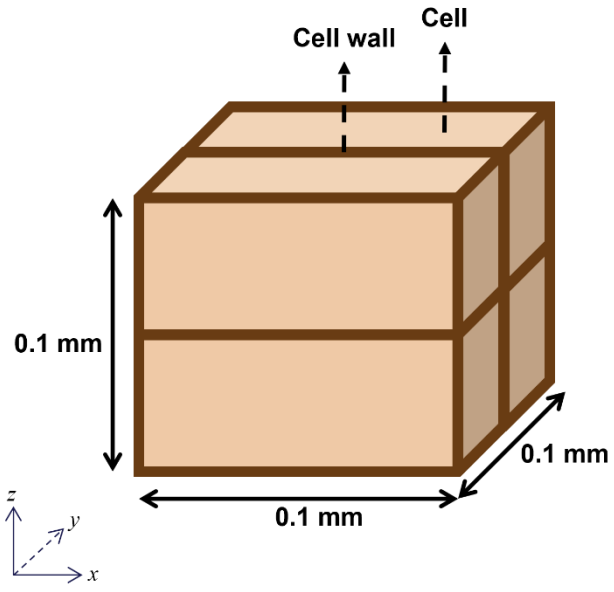


Figure 7.9 – A cubic biomass cluster with 1x2x2 cells and particle size of 0.1 mm

Parameter & value range	$\varepsilon''_{biomass} = 0 - 30$	$k = 0.01 - 0.1$ $Wm^{-1}K^{-1}$	$Q_s = 0 - 5\ Ks^{-1}$	$\rho_W = 1000$ kgm^{-3}	$\rho_S = 1500 - 3000$ kgm^{-3}	$Mr_W = 18$ $gmol^{-1}$	$Mr_S = 100 - 500$ $gmol^{-1}$	$s_{W(T_0)} = 70\ Jmol^{-1}K^{-1}$	$s_{S(T_0)} = 0 - 20$ $Jmol^{-1}K^{-1}$
Justification	Fair for edibles at 2.45 GHz (Sipahioglu and Barringer, 2003)	Fair for some biomasses given their porosity (Erić et al., 2016)	$5\ Ks^{-1}$ represents a very high heating rate	Typical (NIST, 2017)	Polymeric solutes; denser than water	–	Solutes originating from polymeric sources	Typical (Engineering Toolbox, 2005)	Polymeric solutes; more orderly than water
Parameter & value range	$C_p = 70$ $Jmol^{-1}K^{-1}$	$T_{extraction} = 100$ °C	$S_s = 0.00075 - 0.1\ g_s g_W^{-1}$	$D_W = 10^{-10} - 10^{-8}$ m^2s^{-1}	$D_{s1} = 0 - 10^{-8}$ m^2s^{-1}	$D_{s2} = 0 - 10^{-8}$ m^2s^{-1}	$n = 0.5 - 2$	$\%_{s-c} = 0 - 1$ (vol%)	$\%_{s-cw} = 0 - 1$ (mass%)
Justification	Typical for water (Rogers and Mayhew, 1995)	–	Even smaller cellulose values reported (Strachan, 1938)	See point 1	Depending on the degree of polymerisation, solute diffusivity may range from zero to the value of water		Covers a reasonable range of real solution behaviour	Cells may be 0-100% filled with water	Solutes may constitute 0-100% of the cell wall
Parameter & value range	$\%_{w-cw} = 0 - 1.5$ (mass%)	$\%_{s-s} = 0 - 1$ (mass%)	$S_R = 5 - 30$ mLg^{-1}	$D^R_{s1} = 0 - 10^{-8}$ m^2s^{-1}	$D^R_{s2} = 0 - 10^{-8}$ m^2s^{-1}	$P^R{}_C = 50 - 70$ $barg$	$P^R{}_{CW} = 0 - 10$ $barg$	$\Phi_{CW} = 0 - 1$	Cell cluster size = 1 cell onwards
Justification	See point 2	Solvent may be 0-100% water	Used empirically (Galan et al., 2017)	Rupture diffusivity may assume any normal diffusivity value		Reasonable for epidermal cells (section 5.3.2)	Arbitrary; cell walls are smaller than cells	Cell wall pores may occupy 0-100% of the cell wall volume	–
Parameter & value range	Cell dimensions = $25 - 200\ \mu m$	$t_{CW_0} = 1 - 10$ μm	$Y_{0-C} = 100 - 5000$ MPa	$Y_{0-CW} = 1 - 10$ MPa	$\varepsilon''_{solvent} = 0 - 10$	$\delta_p = 1 - 10$ cm	$F = 2.45$ GHz	$\varepsilon_0 = 8.854 \times 10^{-12} Fm^{-1}$	$T_{initial} = 30$ °C
Justification	Fair with imaging and models (Zamil et al., 2013; Zamil, Yi and Puri, 2017)	Fair (Devlin and Witham, 1983; Pieczywek and Zdunek, 2014)	Fair for some hydrated/un-hydrated cell walls (Zamil, Yi and Puri, 2015)	Arbitrary; cell wall pores are smaller and weaker than cells	Fair for water at 2.45 GHz (Datta, Sumnu and Raghavan, 2005)	Typical order for water (Pueschner, 2015)	Typical frequency value	–	–
Parameter & value range	$T_0 = 25$ °C	$\alpha_0 = 1$	$\mu_0 = 0$ $Jmol^{-1}$	$R = 8.314$ $Jmol^{-1}K^{-1}$					
Justification	–	–	–	–					

1- Knudsen model relates molecular diffusivity to an effective diffusivity given the medium porosity (Saravacos, 2005). D_W estimated in Chapter 5 is an effective diffusivity in a negligibly porous medium. Hence, magnifying this by 10^3 is reasonable to attain molecular diffusivity. Molecular and effective diffusivities are arguably of the same order here, due to the significant cell wall porosity.

2- The reported figures are as high as 1.5 (Gaff and Carr, 1961), but too high values cause positive initial pressure.

Table 7.3 – Typical value ranges for the various model parameters

Parameter & selected base value	$\varepsilon''_{biomass} = 20$	$k = 0.01$ $Wm^{-1}K^{-1}$	$Q_s = 1\,Ks^{-1}$ (See point 1)	$\rho_W = 1000$ kgm^{-3}	$\rho_s = 2000$ kgm^{-3}	$Mr_W = 18$ $gmol^{-1}$	$Mr_s = 200$ $gmol^{-1}$	$s_{W(T_0)} = 70$ $Jmol^{-1}K^{-1}$	$s_{s(T_0)} = 10$ $Jmol^{-1}K^{-1}$
Sensitivity analysis in…	Section 7.4.2			Effects of ρ already discussed in Chapter 5		–	–	Effects of s discussed in Chapter 5	
Parameter & selected base value	$C_p = 70$ $Jmol^{-1}K^{-1}$	$T_{extraction} = 100\,°C$	$S_s = 0.01\ g_s g_W{}^{-1}$	$D_W = 10^{-9}$ m^2s^{-1}	$D_{s1} = 10^{-10}$ m^2s^{-1}	$D_{s2} = 10^{-10}$ m^2s^{-1}	$n = 1$	$\%_{s-C} = 0.00025$ (vol%)	$\%_{s-CW} = 0.25$ (mass%)
Sensitivity analysis in…	Effects of C_p discussed in Chapters 3 and 5	Effects of $T_{extraction}$ discussed in Chapter 5	Sections 7.3.1, 7.3.2, 7.4.3, and 7.4.4	–	Sections 7.3.3, 7.4.3, and 7.4.4		Section 7.3.6 (for solutes)	–	Section 7.3.8
Parameter & selected base value	$\%_{W-CW} = 0.1$ (mass%)	$\%_{s-s} = \sim 0$ (mass%)	$S_R = 10$ mLg^{-1}	$D^R{}_{s1} = 10^{-10}$ m^2s^{-1}	$D^R{}_{s2} = 10^{-10}$ m^2s^{-1}	$P^R{}_C = 70$ $barg$	$P^R{}_{CW} = 5$ $barg$	$\Phi_{CW} = 0.5$	Cell cluster size = 0.1 mm
Sensitivity analysis in…	–	Section 7.3.7	Section 7.3.4	Section 7.4.4 (presented as scenarios)		–	–	–	Section 7.3.5
Parameter & selected base value	Cell dimensions: Length=100 μm Width/height=50 μm	$t_{CW_0} = 2.5$ μm	$Y_{0-C} = 800$ MPa	$Y_{0-CW} = 1$ MPa	$\varepsilon''_{solvent} = 5$	$\delta_p = 1$ cm	$F = 2.45$ GHz	$\varepsilon_0 = 8.854 \times 10^{-12} Fm^{-1}$	$T_{initial} = 30$ °C
Sensitivity analysis in…	Effects discussed in Chapter 5		Effects of Y_0 discussed in Chapter 5		Effects discussed in Chapter 3			–	–
Parameter & selected base value	$T_0 = 25$ °C	$\alpha_0 = 1$	$\mu_0 = 0$ $Jmol^{-1}$	$R = 8.314$ $Jmol^{-1}K^{-1}$					
Sensitivity analysis in…	–	–	–	–					

1- For the case of room temperature extraction $Q_s = 0\,Ks^{-1}$.

Table 7.4 – Selected baseline values for the various model parameters

Cell wall fragments within a biomass can be distinguished into two categories, namely, an "outer layer" comprising fragments that are in direct contact with the solvent phase; and an "inner layer" including wall fragments that are exclusively in contact with other biomass phases. As seen in Figure 7.10, the outer layer is adjacent to the solvent; hence, extraction is likely to be rapid and largely independent of the conditions of the inner biomass. However, for extraction to occur from within the inner layer and from cells, suitable conditions should exist in the outer cell wall fragments, as these act as a conducting medium between the inner biomass and the solvent phase. This categorisation of biomass phases is essential to understanding the results presented in this work.

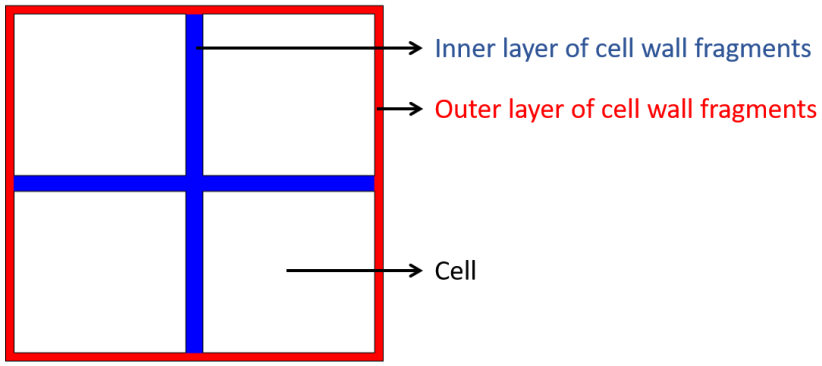


Figure 7.10 – Biomass cell cluster cross-section, demonstrating inner biomass and outer cell wall layers

Results arising from the base scenario (Table 7.4) are presented in Figure 7.11 as a yield-time plot, but also in Figure 7.12 as an osmotic potential diagram showing gradients in temperature, activities, pressure, and chemical potentials between the solvent phase, outer/inner cell wall layers, and cells. For further demonstration, the osmotic potential diagrams are supplemented with water activity (α_W)-time and solute activity (α_s)-time plots. Percentage yield is defined in Equation (7.18), and as seen in Figure 7.11 it is around 25% for both solutes, which is to be expected because both solutes are characterised by the same diffusivity in this case (i.e., $D_{s1} = D_{s2}$). However, it is evident from Figure 7.12 that, activity values α_W and α_s remain uniform and constant across the biomass for the full extraction duration (including inner/outer layers and cells), as they only change in the solvent phase. This is due to the significant amounts of undissolved solutes existing within the cell walls, which maintain constant activity values (section 7.2.2.3), and, thereby, inhibit any intra-biomass diffusion (Figure 7.12). As such, mass transfer occurs exclusively between the solvent and the

outer cell wall layer, due to the fact that activity gradients exist between these two entities exclusively. Moreover, owing to the small activity gradient amounting to just 0.001 in this case (due to low S_s), mass equilibrium is achieved with limited diffusion between the solvent and the outer cell wall layer, without the need to dissolve/extract all solutes available in the in this outer layer. Therefore, α_W and α_s remain uniform within the biomass throughout the process, as neither water penetrates the biomass deeper than the outer cell wall layer, nor solutes get extracted from the inner biomass. This fact is translated into Figure 7.11 as a small yet rapidly achieved equilibrium yield (around 25% achieved in less than 2 s). To further demonstrate these outcomes, the extraction process envisaged here is additionally conceptualised in Figure 7.13 as a schematic.

$$\%\ yield = \frac{Solute\ moles\ in\ solvent - Initial\ solute\ moles\ in\ solvent}{Initial\ solute\ moles\ in\ biomass} \times 100 \qquad \textbf{(7.18)}$$

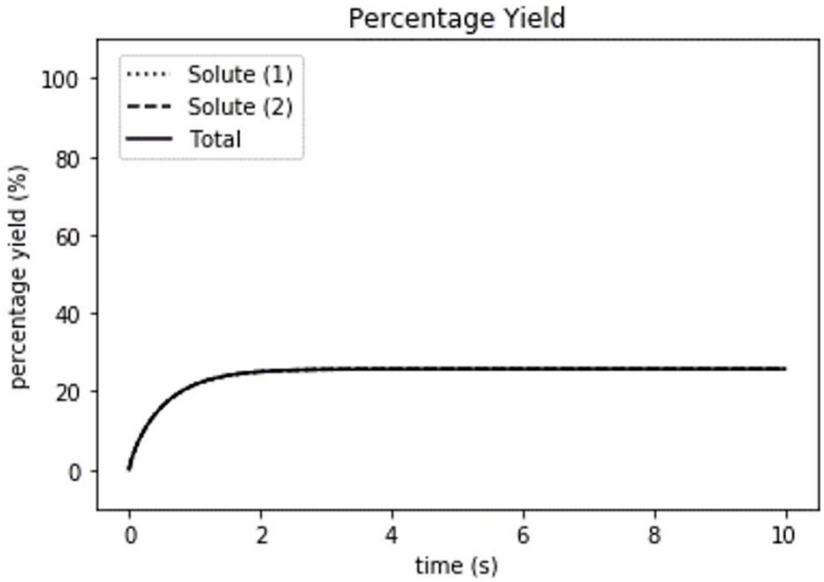


Figure 7.11 – Yield-time plot for the room temperature extraction base case

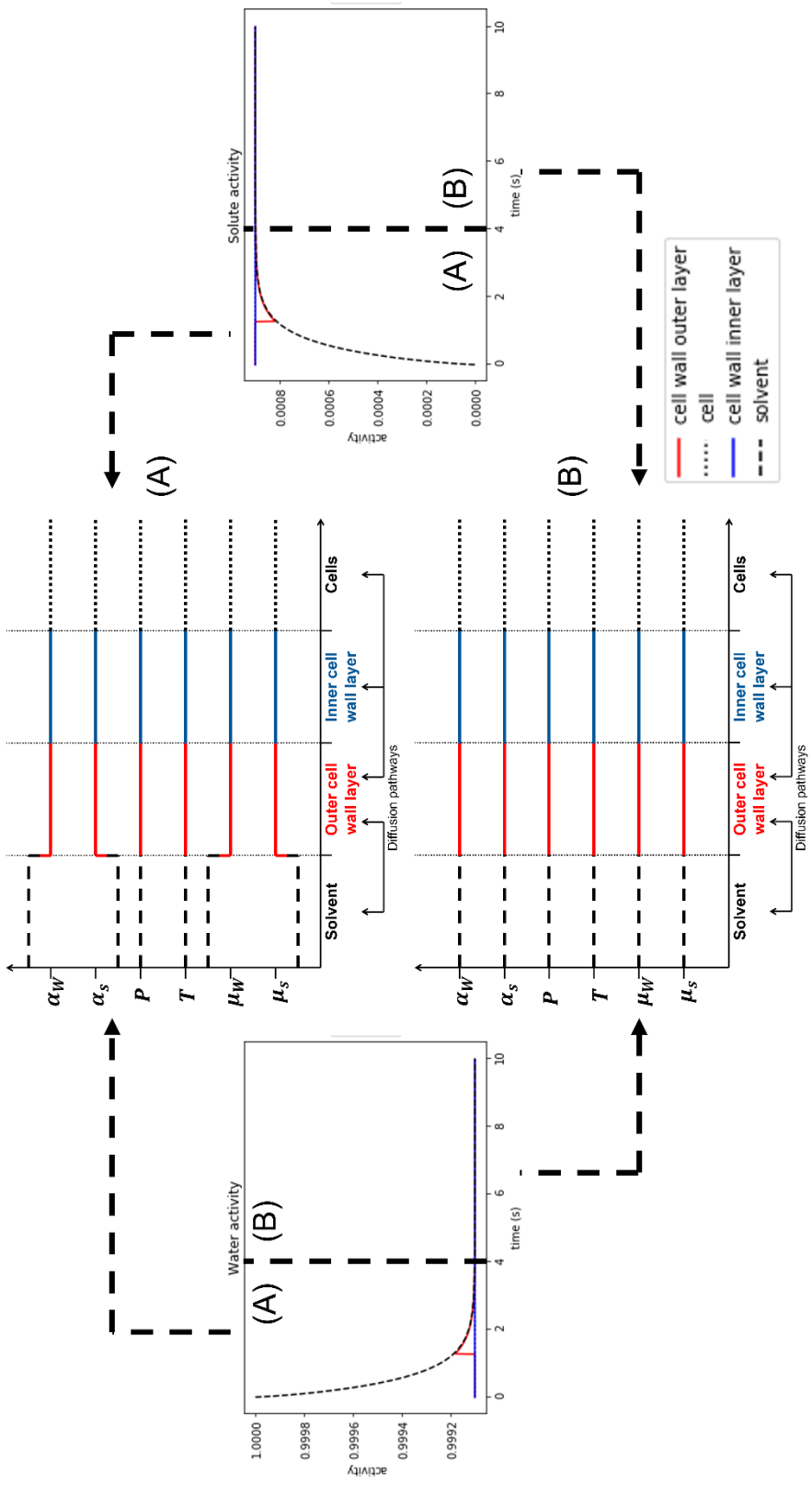


Figure 7.12 – Osmotic potential diagrams for the room temperature extraction base case. Diagrams show gradients in activities, pressure, temperature, and chemical potentials between solvent, outer cell wall layer, inner cell wall layer, and cells. (A) initial condition; (B) final/equilibrium condition. Diagrams are supplemented with water/solute activity-time plots, where each cell wall layer is represented by a single cell wall fragment

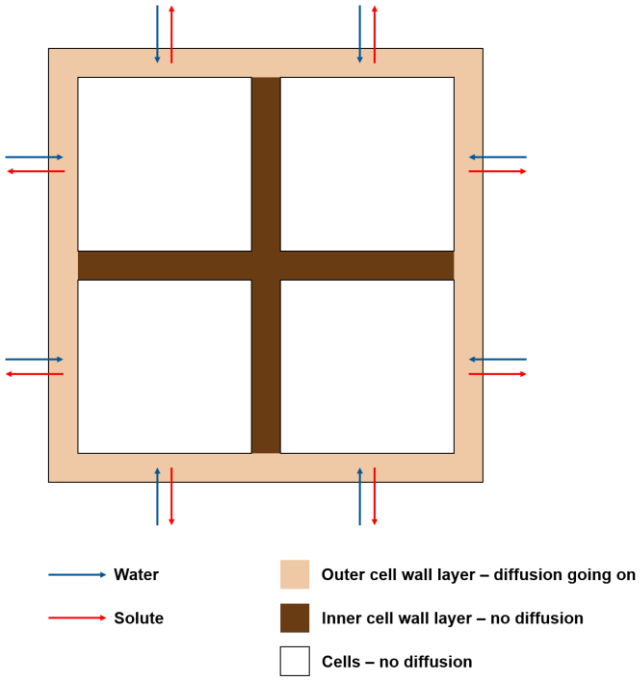


Figure 7.13 – Schematic for the room temperature extraction base case. Mass transfer only takes place between the solvent phase and the outer layer of cell wall fragments. These solutes cannot be fully dissolved by the available water; hence, activities remain constant in the outer layer and uniform across the biomass, thereby inhibiting any intra-biomass diffusion and restricting extraction to the outer layer only

On the other hand, consider a change in solubility S_s from its base quantity of 0.01 $g_S g_W{}^{-1}$ to a value of 0.04 $g_S g_W{}^{-1}$, while keeping all other parameters constant as shown in Table 7.4. Increasing S_s results in a higher capacity of water to dissolve components, which, in turn, indicates a higher tendency of solutes held within the outer cell wall layer to dissolve in the available water/moisture. This aspect is reflected into the yield-time outcome of this scenario (Figure 7.14), as an increase in the equilibrium yield to around 90%, compared with just 25% when $S_s = 0.01\ g_S g_W{}^{-1}$ (Figure 7.11). As it improves water's dissolving capacity, higher S_s magnifies the activity gradients existing between the solvent and the outer cell wall layer (section 7.2.2.3), causing enhanced water influx into the outer layer as well as increased solute diffusion towards the solvent phase. However, with such increase in S_s and the activity gradients, mass equilibrium cannot be achieved even as the outer layer solutes get dissolved/extracted completely, due to the finite quantity of these solutes. Therefore, a full extraction of the outer layer solutes does not cease mass transfer, but rather it allows the outer layer activities to change (Equation (7.6); Figure 7.5), ultimately driving them to become equivalent to the activities of the solvent phase. This is

demonstrated in the osmotic diagrams and supplementary activity-time plots shown in Figure 7.15. These diagrams/plots demonstrate a rapid and complete dissolution of the outer layer solutes, and as can be seen, this induces an intra-biomass activity gradient between the outer layer and the inner cells/cell walls, driving water towards these inner phases and solutes out of them. Unlike the case comprising $S_s = 0.01\ g_S g_W{}^{-1}$, Figure 7.14 and Figure 7.15 indicate extraction from both the outer layer and inner biomass, which explains the observed increase in the extraction yield. However, any extraction from the inner biomass must incorporate solutes flowing through the outer layer and into the solvent phase, and the very small activity gradients between the latter two entities limits the rate of such extraction from the inner biomass (Figure 7.15). Hence, solute diffusion from the inner biomass is a time-consuming process, compared with the extraction of solutes originating from the outer layer. This renders extraction a two-step process (Figure 7.14) where, initial solute liberation from the outer layer constitutes an inaugural sharp increase in yield, but the subsequent acquisition of solutes from the inner biomass gives rise to a much slower approach to mass equilibrium.

Furthermore, Figure 7.15 shows that the inner cell wall fragments sustain constant activities for the full duration of extraction, which is consistent with the fact that, these fragments maintain the presence of undissolved solutes throughout the process. In other words, it is sufficient in this scenario to only extract a portion of the inner layer solutes to bring about mass equilibrium, without the need to fully dissolve/extract these solutes. Note, however, that cells do not enclose any undissolved solutes at the initial state in this model (section 7.2.5.1); therefore, unlike the inner cell walls, cells exhibit changes in their activities shortly after achieving full dissolution of the outer layer solutes. As seen in Figure 7.15, cell activities in this specific case acquire an intermediate magnitude between the values of the outer and inner layers, which is consistent with their intermediate location in the biomass between the two cell wall layers. Depending on the specific biomass structure and other physical conditions, diffusion pathways within the inner biomass may differ, with water/solutes flowing from/to cells/cell walls. Nevertheless, regardless of the diffusion pathways established within the biomass, the overall extraction process is governed by the significant activity gradients induced between the outer layer and the inner biomass (Figure 7.15). These gradients ensure a continuous general influx of water deeper into the material,

and an overall extraction of solutes from the inner biomass towards the solvent phase. To further demonstrate these outcomes, the extraction process envisaged here is additionally conceptualised in Figure 7.16 as a schematic.

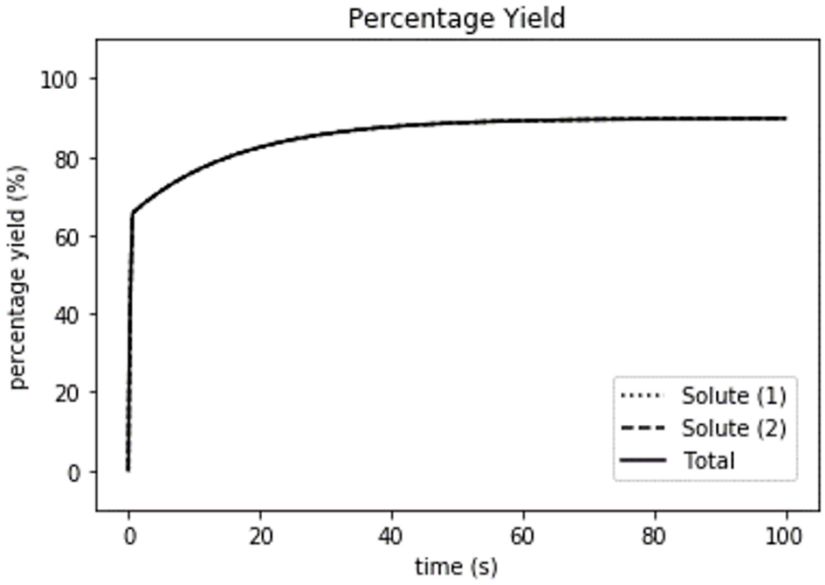


Figure 7.14 – Yield-time plot for room temperature extraction where $S_s = 0.04\ g_S g_W^{-1}$ (other parameters fixed as shown in Table 7.4)

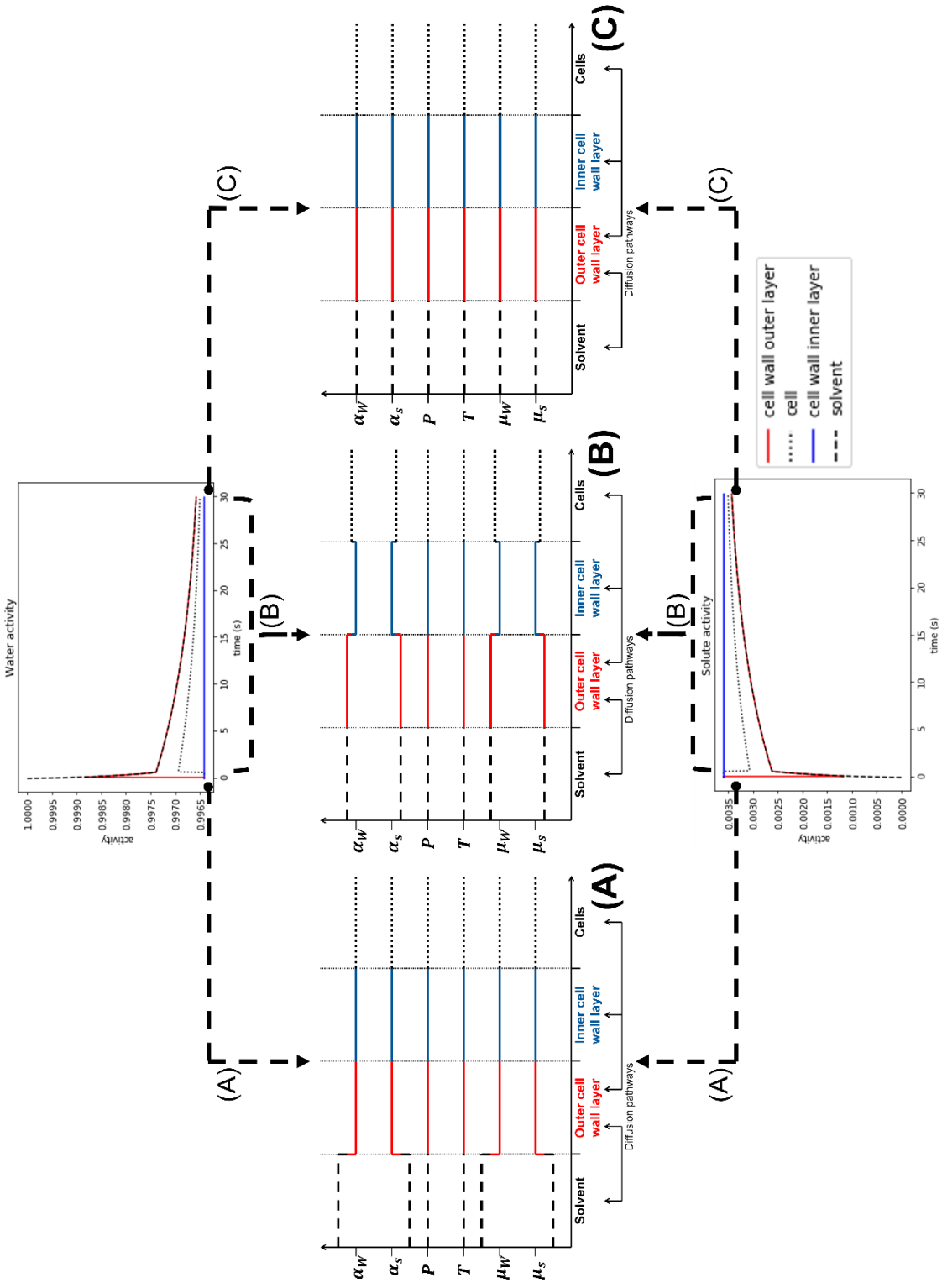


Figure 7.15 – Osmotic potential diagrams for room temperature extraction with $S_s = 0.04\ g_S g_W{}^{-1}$. Diagrams show gradients in activities, pressure, temperature, and chemical potentials between solvent, outer cell wall layer, inner cell wall layer, and cells. (A) initial condition; (B) complete dissolution of solutes in outer cell wall layer; (C) final/equilibrium condition. Diagrams are supplemented with water/solute activity-time plots, where each cell wall layer is represented by a single cell wall fragment

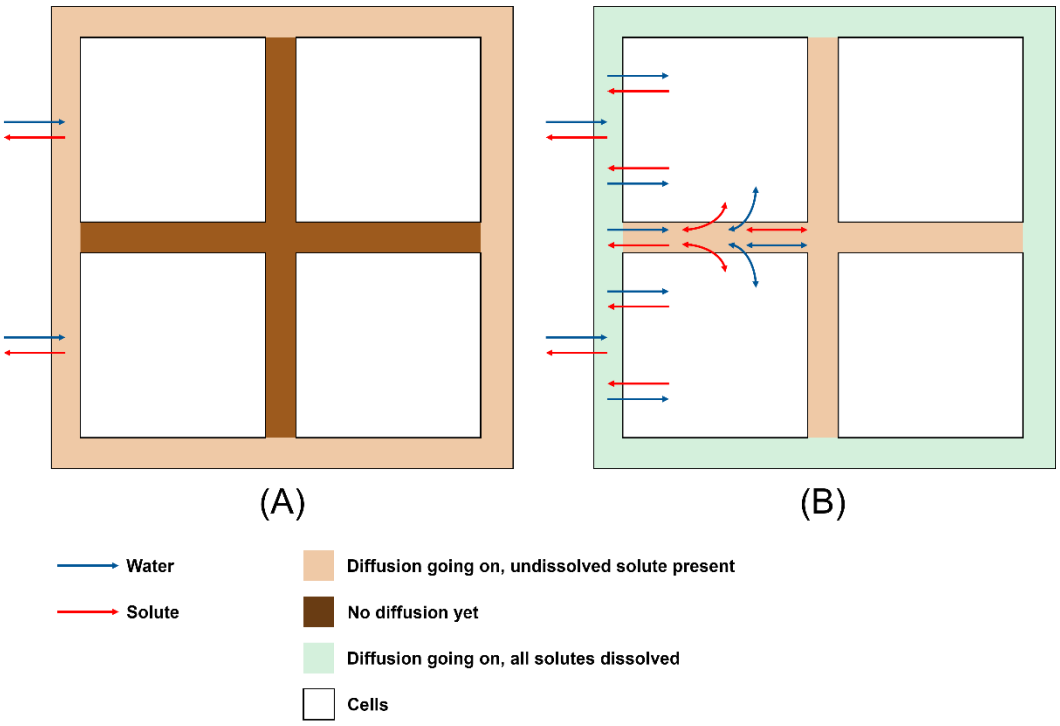


Figure 7.16 – Schematic for room temperature extraction under high S_s; (A) initially, mass transfer only takes place between the solvent and the outer cell wall layer due to the presence of undissolved solutes; (B) mass equilibrium is not established even as all solutes in the outer cell wall layer get fully dissolved; hence, intra-biomass diffusion is triggered where solutes are extracted from the inner cell wall layer and from cells. Water/solute exchange within the inner biomass (cells/cell walls) depends on the established local gradients. Nonetheless, the overall diffusion process is regulated by the significant gradients between the outer layer and the inner biomass, which generally drive water diffusion deeper into the biomass and solutes towards the solvent phase. This occurs regardless of the specific pathways taken by water/solutes within the inner biomass

It is clear from these outcomes that, the extent of extraction is governed by the solubility of solutes; the larger the value of S_s the more likely water will penetrate deeper into the biomass and solutes will be liberated from the inner layers. The layer-by-layer, solubility-specific extraction envisaged in this section, is summarised in the flow diagram shown in Figure 7.17. Additionally, a more comprehensive sensitivity analysis on S_s is presented in section 7.3.2.

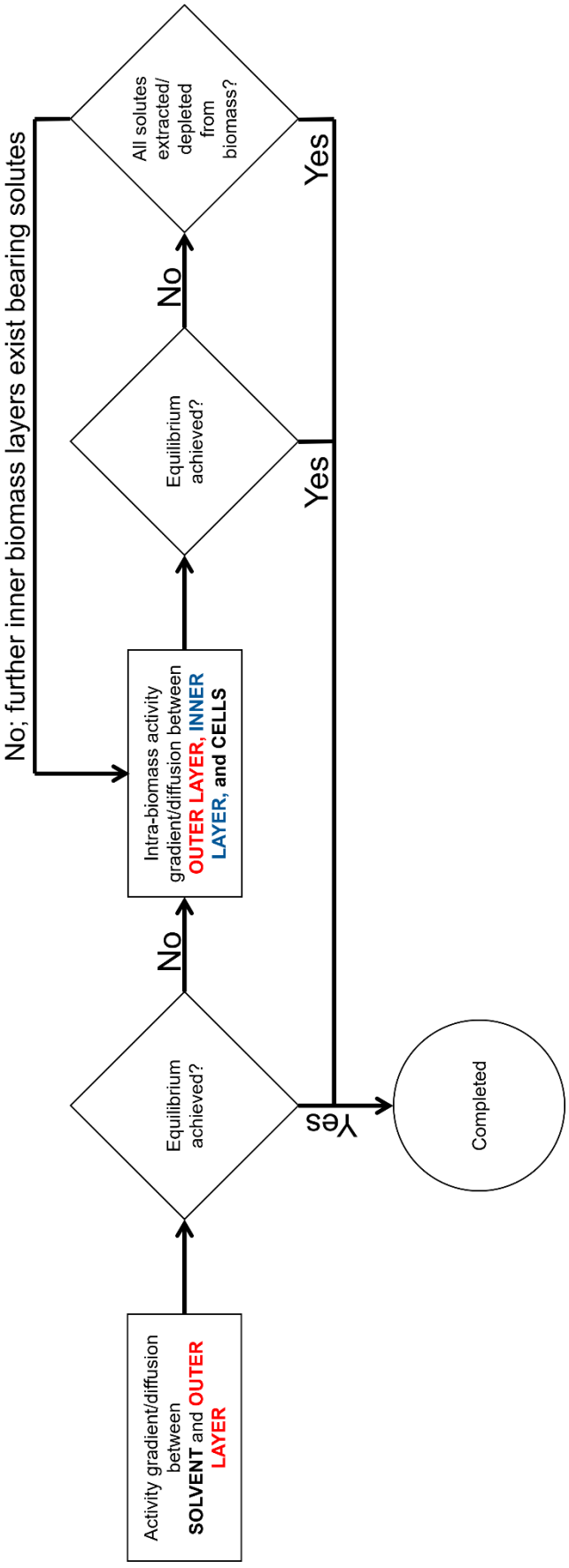


Figure 7.17 – Flow diagram summarising the layer-by-layer extraction process occurring at room temperature

7.3.2 Effect of solubility (S_s)

The effect of solubility (S_s) was investigated by varying this parameter between 0.001 $g_S g_W{}^{-1}$ and 0.1 $g_S g_W{}^{-1}$, while keeping all other parameters fixed as shown in Table 7.4. Table 7.5 presents the results including percentage yield at equilibrium and time required to achieve 95% of this equilibrium value (t_{95-M}).

S_s ($g_s g_W{}^{-1}$)	Yield (%)	t_{95-M} (s)
0.001	6.1	4.0
0.01	25.7	1.7
0.02	47.3	1.6
0.03	68.7	1.6
0.04	89.8	28.0
0.05	100.0	22.4
0.1	100.0	4.2

Table 7.5 – Percentage yield and time required to achieve 95% of mass equilibrium, for variable solubility (other parameters fixed as shown in Table 7.4)

As S_s is increased from 0.001 $g_S g_W{}^{-1}$ to 0.03 $g_S g_W{}^{-1}$, yield increases from 6% to 69% and t_{95-M} decreases from 4 s to 1.6 s. This is to be expected since activity gradients between the biomass and the solvent increase with S_s (section 7.3.1), providing a stronger driving force for mass transfer. However, despite this initial decrease in t_{95-M}, a significant jump is observed in this parameter with increasing S_s from 0.03 $g_S g_W{}^{-1}$ to 0.04 $g_S g_W{}^{-1}$, which is because solutes start to get extracted from the inner biomass. Increasing S_s expands the activity gradient between biomass and solvent, and this eventually renders extracting the outer layer solutes alone insufficient to achieve mass equilibrium, due to the finite quantity of these solutes (section 7.3.1). Therefore, at sufficiently high S_s solutes get extracted from the outer layer until there are no more undissolved solutes remaining, which then allows activities in the outer layer to vary and, thereby, induces an activity gradient between the outer layer and the inner biomass (Figure 7.15 – Figure 7.17). This intra-biomass activity gradient drives extraction from the inner cell wall layer and cells, but this diffusion process is much slower compared with extraction from the outer layer, which is why a steep rise in t_{95-M} is observed going from 0.03 $g_S g_W{}^{-1}$ to 0.04 $g_S g_W{}^{-1}$. Further to this, yield and t_{95-M} continue to increase with S_s beyond 0.04 $g_S g_W{}^{-1}$,

until the physical yield limit of 100% is approached (i.e., all solutes are extracted from the biomass); hence, t_{95-M} soon starts to drop thereafter as the activity gradients raised further through increasing S_s.

It is clear from these results and from those in section 7.3.1 that, S_s is a key limiting parameter in mass transfer and extraction. This parameter restricts water penetration into a biomass and limits solute extraction from within the material. Higher S_s values reflect an enhancement in water's capacity to dissolve biomass components, inducing higher biomass-solvent activity gradients and, thereby, enabling deeper water penetration into the biomass as well as improved solute extraction from inner phases. This limitation imposed by S_s may be overcome through various means, such as continuously replenishing the solvent to preserve the activity gradients; or heating as S_s is known to increase with temperature. In fact, the relationship between S_s and temperature may explain why some extraction studies have found the yield to increase with temperature (Galan et al., 2017; Nkhili et al., 2009). Moreover, this chapter will attempt to explain how the limitation imposed by S_s may also be overcome through microwave heating (section 7.4).

7.3.3 Effect of diffusivity (D)

This analysis is divided into two parts, the first of which investigates the effect of varying both D_{s1} and D_{s2} (i.e., $D_{s1} = D_{s2}$), while the second part investigates the effect of varying D_{s2} only (i.e., $D_{s1} \neq D_{s2}$). In accordance with the base values prescribed in Table 7.4, $D_W = 10^{-9}\, m^2 s^{-1}$ in all cases, and $D_{s1} = 10^{-10}\, m^2 s^{-1}$ throughout the second part.

7.3.3.1 Equal solute diffusivities (D_{s1}=D_{s2})

Results are presented in Table 7.6 where yield, t_{95-M}, and maximum pressure recorded in the biomass (P_{max}) are shown for D_s ranging from $0\, m^2 s^{-1}$ to $10^{-8}\, m^2 s^{-1}$. All other parameters were fixed as shown in Table 7.4.

D_s $(m^2 s^{-1})$	Yield (%)	t_{95-M} (s)	P_{max} $(barg)$
0	0.0	N/A	1.27
10^{-13}	23.3	1469.1	1.24
10^{-12}	24.7	157.4	1.17
10^{-11}	25.2	16.4	0.82
10^{-10}	25.7	1.7	0.00

$\mathbf{10^{-9}}$	25.8	0.2	0.00
$\mathbf{10^{-8}}$	25.8	0.02	0.00

Table 7.6 – Percentage yield, time required to achieve 95% of mass equilibrium, and maximum biomass pressure, for variable solute diffusivity (other parameters fixed as shown in Table 7.4)

At higher D_s an increase in the yield and a decrease in t_{95-M} are observed. As expected, a ten-fold increase in D_s generally results in a proportional decrease in t_{95-M}, which is because diffusivity primarily describes the resistance to mass transfer. On the other hand, the yield is much less sensitive to D_s and becomes increasingly less sensitive as D_s increases. At very low D_s, the yield will understandably be low as solute diffusion encounters significant resistance, and instead more water flows into the biomass, waiving the need to extract much solute to achieve equilibrium. However, as D_s increases the resistance to solute diffusion drops down, and the water and solute diffusion rates become more comparable such that D_s is less effective in dictating the equilibrium position. Hence, the yield increases significantly going from $D_s = 0\ m^2 s^{-1}$ to $D_s = 10^{-13}\ m^2 s^{-1}$, but for all practical purposes the yield remains constant beyond the latter D_s value. On the other hand, since water flows more considerably into the biomass at low D_s compared to solute diffusing out, the likelihood of developing pressure within the structure is increased. At sufficiently low D_s, the biomass absorbs water in amounts large enough to induce positive pressures (Table 7.6), and if $D_s = 0\ m^2 s^{-1}$ (i.e., no extraction), equilibrium is solely achieved through a balance between activity and biomass pressure (Figure 7.18), which is analogous to the model presented in Chapter 5. It should be noted that, all pressures induced in the biomass (except where $D_s = 0\ m^2 s^{-1}$), are limited here to the outer cell wall layer, because with $S_s = 0.01\ g_s {g_W}^{-1}$ mass transfer is not possible with the inner biomass under the current setup and physical conditions (section 7.3.2).

When $D_s = 0\ m^2 s^{-1}$, pressure induced in the outer layer drives water towards the inner biomass, in which pressure may also be induced as a result. Inner cell wall fragments can develop pressure easily, due to the presence of undissolved solutes maintaining constant activities in the voids of these fragments (section 7.2.2.3), but also due to the small size of these fragments compared with cells (section 7.2.4). Therefore, as seen in Figure 7.18, mass equilibrium when $D_s = 0\ m^2 s^{-1}$ must incorporate positive pressures in the cell walls, as these pressures balance the

otherwise unchangeable activity gradients in the system (i.e., unchangeable because solutes are both undissolved and cannot diffuse). However, this analogy does not necessarily apply to cells, where although the solutes are still immobile, in this work they are fully dissolved in the available moisture initially (section 7.2.5.1). Hence, activities vary in cells in response to any water influx, meaning that mass equilibrium does not necessarily require positive pressures in cells. Rather, attaining positive cell pressures depends on whether these cells are turgid initially, or they can still accommodate additional water without any pressure increase. In Figure 7.18, no positive cell pressure is required to bring about mass equilibrium, which is consistent with the fact that, in this work, cells contain minimal quantities of water and solutes at the initial state (Table 7.4). As such, sufficient quantities of water may diffuse into cells and alter their activities so as to bring about mass equilibrium, without the need to fully occupy these cells. In contrast, the base case in Chapter 5 (section 5.3.2) incorporated fully occupied cells at the initial state, allowing for an immediate pressure build-up upon water influx, be it under microwave heating or otherwise.

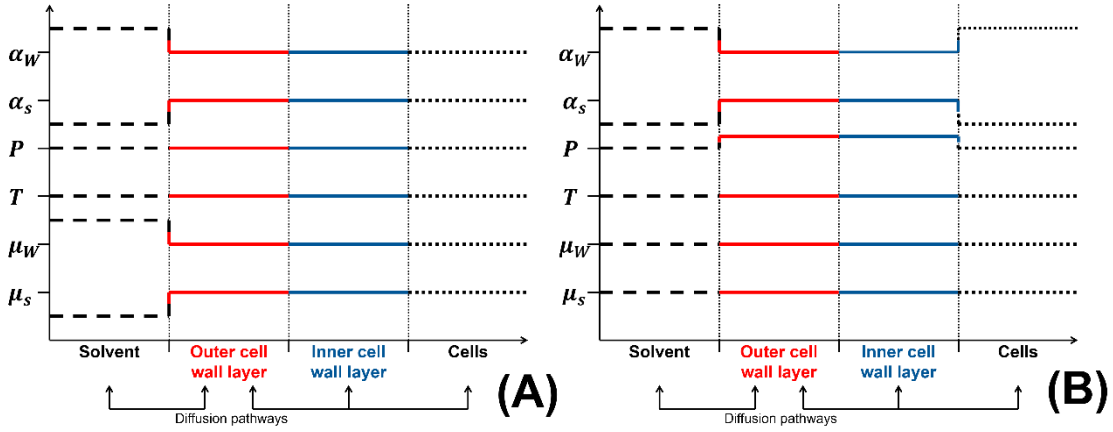


Figure 7.18 – Osmotic potential diagrams for room temperature extraction with $D_s = 0\ m^2 s^{-1}$ (i.e., solutes do not flow in the system; only water does). Diagrams show gradients in activities, pressure, temperature, and chemical potentials between solvent, outer cell wall layer, inner cell wall layer, and cells. (A) initial condition; (B) final/equilibrium condition

7.3.3.2 Unequal solute diffusivities ($D_{s1} \neq D_{s2}$)

Results are presented in Table 7.7 where yield and t_{95-M} are shown for each solute individually, together with the collective yield of both solutes. D_{s2} was varied between $5 \times 10^{-13}\ m^2 s^{-1}$ and $10^{-10}\ m^2 s^{-1}$, while all other parameters were fixed as shown in Table 7.4.

D_{s2} (m^2s^{-1})	Solute 1 yield (%)	$t_{95-M-s1}$ (s)	Solute 2 yield (%)	$t_{95-M-s2}$ (s)	Combined yield (%)
5×10^{-13}	50.9	3.5	0.3	3.6	25.6
10^{-12}	50.6	3.5	0.5	3.5	25.6
5×10^{-12}	48.7	3.3	2.5	3.4	25.6
10^{-11}	46.5	3.1	4.8	3.2	25.6
5×10^{-11}	34.2	2.2	17.1	2.2	25.7
10^{-10}	25.7	1.7	25.7	1.7	25.7

Table 7.7 – Percentage yield and time required to achieve 95% of mass equilibrium, for variable diffusivity of solute (2). $D_W = 10^{-9}\ m^2s^{-1}$, $D_{s1} = 10^{-10}\ m^2s^{-1}$, and $S_s = 0.01\ g_s{g_W}^{-1}$ (other parameters fixed as shown in Table 7.4)

At lower D_{s2}, the yield of solute (1) increases whereas that of solute (2) decreases. To understand this, it is vital to recall that both solutes are represented by the same activity and chemical potential here, following the assumption that they behave similarly in solution (section 7.2.2.2). Therefore, both solutes flow down a single potential gradient, and mass equilibrium is achieved with extracting either one or both solutes. This is proven with the fact that; the combined yield remains consistent regardless of how the individual solute yields change. The yield of solute (1) increases with decreasing D_{s2} because, at such condition solute (1) experiences lower resistance to diffusion than solute (2) does. Therefore, larger quantities of solute (1) get extracted at the expense of solute (2), but the combined yield remains consistent as changes in diffusivity do not alter the driving force of diffusion, given that diffusivity is not very low (section 7.3.3.1). These results show a competition between the two solutes to get extracted. If both solutes possess the same D_s value they will be extracted in equal proportions, but if the resistance to diffusion encountered by one solute is lower compared with the other, the former will then be extracted more readily at the expense of the latter. Figure 7.19 shows yield-time plots for D_{s2} values of $10^{-10}\ m^2s^{-1}$, $5 \times 10^{-11}\ m^2s^{-1}$, and $10^{-12}\ m^2s^{-1}$.

Furthermore, t_{95-M} increases for both solutes with decreasing D_{s2}, because on one hand solute (2) diffuses more slowly, and on the other hand the larger quantities of solute (1) being extracted require longer timeframes to be achieved. Nevertheless, both

t_{95-M} values remain roughly equal for both solutes under all D_{s2}, because both solutes diffuse down a single gradient and so they achieve mass equilibrium collectively.

It is shown here that extraction amongst similar solutes is conducted in a competitive manner, where solutes experiencing lower resistance to mass transfer are extracted in larger quantities at the expense of others. If the diffusivity of specific solutes varies with temperature, it could be possible to favour the extraction of specific components at given temperatures/heating conditions. The effect of temperature on extraction selectivity may be intuitive, but the underpinning cause of such selectivity has rarely been characterised quantitatively before. For instance, it is yet to be firmly established why certain extracts exhibit optimum extraction temperatures, and whether this is influenced by the presence of other solutes in the biomass. This section has demonstrated that, extraction selectivity amongst similar solutes is attributable to the differences in their diffusivities. This novel approach may allow future studies to quantitatively predict extraction selectivity trends in biomass-solvent systems at various temperatures.

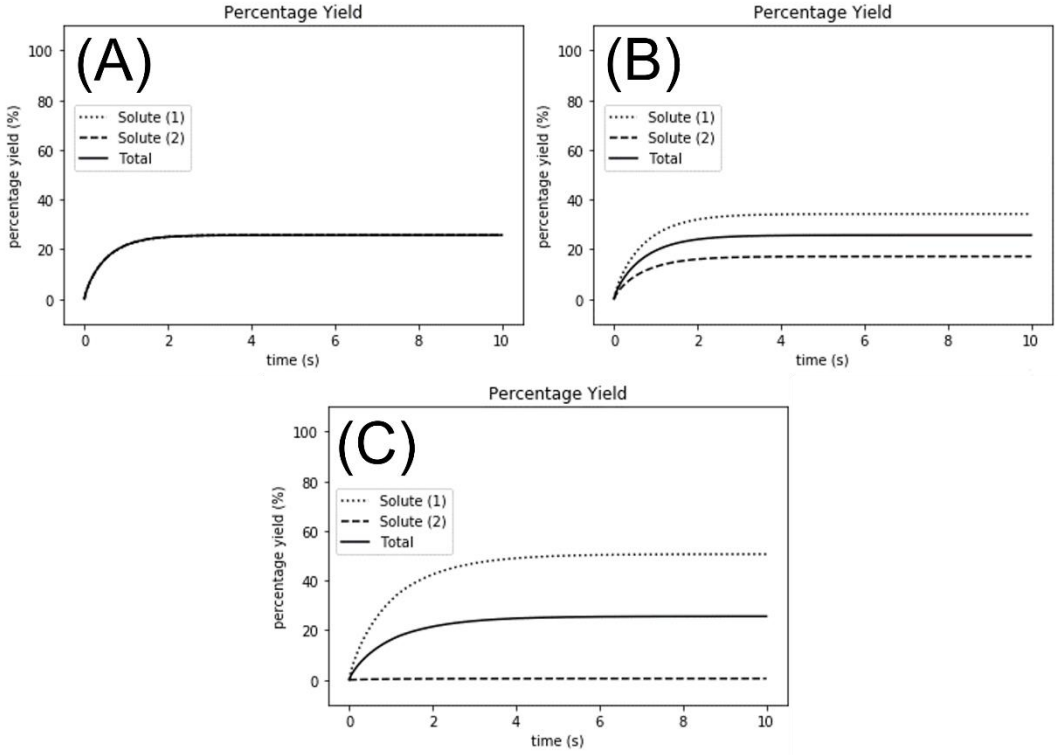


Figure 7.19 – Yield-time plots for $D_{s1} = 10^{-10}\ m^2 s^{-1}$ and (A) $D_{s2} = 10^{-10}\ m^2 s^{-1}$; (B) $D_{s2} = 5 \times 10^{-11}\ m^2 s^{-1}$; (C) $D_{s2} = 10^{-12}\ m^2 s^{-1}$ (other parameters fixed as shown in Table 7.4)

Table 7.7 has used the base S_s value of 0.01 $g_S g_W{}^{-1}$ which, as shown previously, is insufficient to induce extraction from the inner biomass in this specific setting and under the current physical conditions (section 7.3.2). However, given that solute (1) yield increases with decreasing D_{s2}, it remains unclear whether solute (1) could eventually be extracted from the inner biomass at sufficiently low D_{s2}. Therefore, the analysis in Table 7.7 was repeated with $S_s = 0.02\ g_S g_W{}^{-1}$ which, as shown in section 7.3.2, increases the yield but still does not permit diffusion from the inner biomass at the base diffusivity values. Hence, this scenario (Table 7.8) demonstrates more clearly whether changes in diffusivity can eventually allow extraction from the inner biomass, thereby overriding the limitation imposed by S_s (section 7.3.2).

D_{s2} $(m^2 s^{-1})$	Solute 1 yield (%)	$t_{95-M-s1}$ (s)	Solute 2 yield (%)	$t_{95-M-s2}$ (s)	Combined yield (%)
5×10^{-13}	68.5	1.1	21.4	486.6	44.2
10^{-12}	68.5	1.2	22.3	275.9	45.4
5×10^{-12}	67.5	1.2	25.4	60.0	46.4
10^{-11}	67.5	1.3	25.5	29.3	46.5
5×10^{-11}	62.0	2.1	32.3	2.2	47.1
10^{-10}	47.3	1.6	47.3	1.6	47.3

Table 7.8 – Percentage yield and time required to achieve 95% of mass equilibrium, for variable diffusivity of solute (2). $D_{s1} = 10^{-11}\ m^2 s^{-1}$ and $S_s = 0.02\ g_s g_W{}^{-1}$ (other parameters fixed as shown in Table 7.4)

As seen in Table 7.8, although all solute (1) gets extracted from the outer layer at low enough D_{s2} (maximum possible yield is around 68%), none gets further extracted from the inner biomass. Instead, any further decrease in D_{s2} only delays achieving mass equilibrium, but it does not alter the composition of extracts. Therefore, for solutes behaving similarly (i.e., represented with a single activity), it is insufficient to extract one solute completely from the outer layer to achieve more of it from the next. Rather, all solutes should be extracted from the outer layer first before mass transfer can be initiated with the inner biomass. In real-world situations, this means that certain desired solutes may not be achievable until some other undesired solutes sharing similar chemical/physical characteristics, are extracted first. Furthermore, if these other undesired solutes possess high diffusivities, exist in abundant amounts, or are

located closer to the biomass-solvent boundary, the desired solutes might simply not be extractable in any significant quantities.

It is clear from the results attained so far that S_s and D_s constitute major barriers to extraction, with the former limiting extractability to certain layers of the biomass material, and the latter favouring the extraction of certain solutes at the expense of others, thereby possibly limiting the extractability of desired components. To enhance extraction, manipulating the physical conditions should be focussed on tuning S_s and D_s to maximise the yields of desired components. S_s can be increased by solvent selection and through controlling the pH (as done in some studies (Mao et al., 2019)), but also through heating as solubility is known to increase with temperature. D_s can be manipulated through temperature as well; moreover, it can also be altered with physical rupture of biomass cells and cell walls (see section 7.2.4.2). Extraction can also be enhanced with increasing S_R (section 7.3.4), under which the increased volume of solvent demands more extraction to achieve mass equilibrium. Furthermore, semi-continuous processes entailing steady replenishment of the solvent may also improve extraction, as these preserve the activity gradients between biomass and solvent, thereby enhancing mass transfer in the system. On the other hand, extraction can also be enhanced with microwave heating, as this constitutes unique mass transfer patterns which overcome the limitations imposed by S_s and D_s. This will be discussed in detail in section 7.4.

7.3.4 Effect of solvent-to-solid ratio (S_R)

Table 7.9 shows the results including yield and t_{95-M}, for varying S_R between 5 mLg^{-1} and 30 mLg^{-1}. All other parameters were fixed as shown in Table 7.4.

S_R (mLg^{-1})	Yield (%)	t_{95-M} (s)
5	12.9	0.8
10	25.7	1.7
20	51.4	3.5
30	75.3	38.8

Table 7.9 – Percentage yield and time required to achieve 95% of mass equilibrium, for variable solute-to-solvent ratio (other parameters fixed as shown in Table 7.4)

Both yield and t_{95-M} increase with S_R, due to the increased solvent volume with which more solutes should be extracted to change α_W and α_s in the solvent phase, and

thereby achieve mass equilibrium. Furthermore, at some threshold ratio (between 20 and 30 mLg^{-1} in this case) all solutes in the outer layer get extracted yet mass equilibrium is still not achieved; therefore, extraction is initiated from the inner biomass. This additional step induces a sharp increase in t_{95-M}, which is because extraction from the inner biomass is a time-consuming process, as the relevant cells/cell walls are not in direct contact with the solvent phase (section 7.3.1; Figure 7.10). Therefore, in real-world situations entailing limited extraction timeframes, it is expected to observe a reduced influence of S_R on yield as the former increases. A flattening yield-S_R curve has been observed in some empirical studies utilising biomass particle sizes similar to those used this work (Galan et al., 2017).

7.3.5 Effect of biomass particle size

Table 7.10 shows the results including yield and t_{95-M}, for varying biomass particle size between 1 cell and 0.3 mm. Figure 7.9 demonstrates a biomass particle sized 0.1 mm; moreover, increasing the particle size is analogous to introducing more cells (and surrounding cell wall fragments) into the biomass. All other parameters were fixed as shown in Table 7.4.

Particle size	Yield (%)	t_{95-M} (s)
1 cell	25.7	1.0
0.1 mm	25.7	1.7
0.2 mm	25.7	3.4
0.3 mm	25.7	30.9

Table 7.10 – Percentage yield and time required to achieve 95% of mass equilibrium, for variable biomass particle size (other parameters fixed as shown in Table 7.4)

Particle size has no effect on the yield because S_R is constant, meaning that as the biomass grows here, the quantity of solutes it possesses increases proportionally with the increase in solvent volume. This proportional increase gives a constant percentage yield, although the quantity of solutes extracted (as opposed to percentage) increases with particle size and solvent volume. However, t_{95-M} is clearly affected by the particle size as it is higher for larger particles. Increasing the size from 1 cell to 0.2 mm (32 cells) raises t_{95-M} three-fold from 1 s to 3.4 s, and this is to be expected because the quantity of solutes extracted increases (although percentage yield remains constant), requiring longer timeframes to be achieved. Interestingly, however, t_{95-M}

increases ten-fold from 3.4 s to 30.9 s as the particle size grows from 0.2 mm to 0.3 mm (108 cells). This is a very significant increase given the extent to which the particle has grown here (i.e., only 3 times larger), compared with the earlier growth from 1 cell to 0.2 mm (i.e., 32 times larger). This unproportioned rise in t_{95-M} takes place since, going from 0.2 mm to 0.3 mm, the quantity of solutes available in the outer biomass layer becomes insufficient to constitute mass equilibrium. This is because, the inner solutes represent an increasingly larger percentage of the total solutes as the biomass grows, meaning that eventually the outer layer solutes will not suffice to achieve the required yield for mass equilibrium. As such, at a threshold particle size, all outer layer solutes get extracted without approaching mass equilibrium, and instead solute extraction is initiated from within the inner biomass. As stated earlier, this diffusion process requires significantly longer timeframes, thereby bringing about a sharp increase in t_{95-M}.

These results signify that particle size has no effect on percentage yield, but rather it only influences the time needed to complete an extraction process. Furthermore, particle sizes can be categorised into groups, where each group exhibits similar extraction timeframes, but there exist significant differences in the timeframes going from one group to another. As shown here, particle sizes of 1 cell – 0.2 mm exhibit similar extraction timeframes all within the order of 1 s, but a size of 0.3 mm is affiliated to a separate group requiring a significantly higher range of timeframes at least within the order of 10 s. This means that, if a 0.3 mm particle is chopped into either 108 cells or three 0.1 mm particles, the same yield can be achieved within significantly shorter timeframes which are similar in both cases, provided S_R remains constant. Given that empirical studies are time-limited, it is likely to observe yield decreasing as the particle size is increased, and such an observation has been reported (Chupin et al., 2015; Kaufmann, Christen and Veuthey, 2001).

7.3.6 Effect of solute activity-mole fraction relationship (n)

Table 7.11 shows the results including yield and t_{95-M}, for varying n (the activity-mole fraction relationship parameter, i.e., $\alpha = X^n$; Equation (7.5)) of solutes between 0.5 and 1.75. The value of n for water was maintained at 1 here, while all other parameters were fixed as shown in Table 7.4.

n (for solutes)	Yield (%)	t_{95-M} (s)

0.5	25.6	3.3
0.75	25.7	2.2
1	25.7	1.7
1.5	25.7	1.1
1.75	25.7	1.0

Table 7.11 – Percentage yield and time required to achieve 95% of mass equilibrium, for variable activity-mole fraction relationship for solutes (other parameters fixed as shown in Table 7.4)

Increasing n accelerates the extraction process due to a reduction in the activity gradient between biomass and solvent (i.e., for a given mole fraction, activity is smaller at larger n; Equation (7.5)). However, the variation in activity due to changing n does not affect the yield in this case, which is because n remains uniform throughout the biomass-solvent system. Therefore, the same quantity of solutes should still be extracted to achieve mass equilibrium, and so the yield remains constant here. Further studies can be conducted where n is assigned unequal values in amongst biomass and solvent. Such analysis, which can be carried out using the current model, may demonstrate varying yield trends based on the different combinations and distributions of n.

7.3.7 Effect of initial solvent purity ($\%_{s\text{-}S}$)

Table 7.12 shows the results including yield and t_{95-M}, for varying $\%_{s-S}$ between 0 and 0.01. All other parameters were fixed as shown in Table 7.4.

$\%_{s-S}$	**Yield (%)**	t_{95-M} (s)
~ 0	25.7	1.7
0.001	20.5	1.7
0.002	15.3	1.7
0.003	10.2	1.7
0.01	0.0	N/A

Table 7.12 – Percentage yield and time required to achieve 95% of mass equilibrium, for variable initial mass percentage of solutes in solvent (other parameters fixed as shown in Table 7.4)

Increasing $\%_{s-S}$ signifies raising the initial quantity of solutes dissolved in the solvent, making this phase increasingly impure. The more impure the solvent is, the smaller the activity gradient between biomass and solvent, the less the extraction required to achieve mass equilibrium. This results in a decrease in yield with

increasing $\%_{s-S}$, coupled with a consistent t_{95-M} even though the yield is decreasing, which indicates slower extraction.

Moreover, at $\%_{s-S} = 0.01$, no mass transfer takes place in the system, which is because the solvent is saturated and the available solute quantities are beyond the solvent's capacity to dissolve. Therefore, due to the assumption that solubility (S_s) is the same throughout the biomass-solvent system, the initial activity values in the biomass are equal to those in the solvent. This means that no mass transfer is required in this case, as the system exbibits mass equilibrium right from the start. Therefore, these results indicate that extraction only takes place if the solvent is not fully saturated. If, however, the solvent phase bears solutes in excess of its ability to dissolve, then extraction will not take place due to the absence of any driving force/activity gradient. In such cases, extraction may only be initiated through altering the physical conditions, such as heating, solvent replenishment, etc. Microwave heating can also induce extraction as it constitutes unique mass transfer patterns (section 7.4).

7.3.8 Effect of initial solute quantity in cell wall ($\%_{s\text{-}CW}$)

This section is aimed at understanding the effect of solute distribution amongst cells and cell walls, while maintaining a constant total initial solute quantity in the biomass. To conduct this, solutes are "removed" from cell walls and "relocated" to cells, through decreasing the initial mass fraction of solutes in the cell walls ($\%_{s-CW}$) from its base value of 0.25 (Table 7.4), and computing the solute quantity equivalent to the difference between 0.25 and the modified $\%_{s-CW}$. This excess solute quantity is then distributed evenly amongst cells, thereby achieving the desired relocation but also maintaining a constant initial solute mass within the biomass. Note that, as discussed in section 7.2.5.1 cells are assumed to contain a saturated solution initially, meaning that the initial amount of water in cells must increase as more solutes are added. Therefore, this analysis was limited to cases where the initial cell water volume is smaller than that of the cell itself, thus maintaining zero cell pressure initially. Furthermore, solvent-to-solid ratio (S_R) was varied in this analysis to maintain a constant initial volume of the solvent phase. This is because, with the initial cell water volume permitted to change based on solute distribution, a fixed S_R would result in variable solvent volume which interferes with the outcomes through altering the

extraction trends. Hence, it is key to maintain a constant solvent volume through varying S_R, to ensure a fair analysis.

Table 7.13 shows the results including yield and t_{95-M}, for varying $\%_{s-CW}$ between 0.232 and 0.25. The initial volume percentage of water in cells is also shown. All other parameters (except S_R) were fixed as shown in Table 7.4.

$\%_{s-CW}$	**Initial % vol of cells occupied by water**	**Yield (%)**	t_{95-M} (s)
0.232	0.96	25.7	1.7
0.235	0.81	25.7	1.7
0.24	0.55	25.7	1.7
0.245	0.30	25.7	1.7
0.25	0.05	25.7	1.7

Table 7.13 – Percentage yield and time required to achieve 95% of mass equilibrium, for variable initial mass percentage of solutes in cell wall. $S_s = 0.01\ g_S g_W{}^{-1}$. Other parameters, except solvent-to-solid ratio, are fixed as shown in Table 7.4)

In Table 7.13, solute distribution amongst cells and cell walls has no effect on either the yield or t_{95-M}. This is because, $\%_{s-CW}$ is only varied by small amounts here that are insufficient to bring about any significant change to the extraction patterns. In cells, the initial volume of water rises dramatically with a small decrease in $\%_{s-CW}$, which is because solubility (S_s) is low, and so large amounts of water are required to dissolve any surplus solutes introduced to cells. Therefore, low S_s restricts this analysis to a limited range of $\%_{s-CW}$ values, which if decreased further would constitute an unrealistic initial condition comprising large cell pressures.

To better understand the effect of solute redistribution on extraction, the current analysis was repeated with a high S_s value of 0.1 $g_S g_W{}^{-1}$. Table 7.14 shows the results including yield and t_{95-M}, for varying $\%_{s-CW}$ between 0.06 and 0.25. The initial volume percentage of water in cells is also shown.

$\%_{s-CW}$	**Initial % vol of cells occupied by water**	**Yield (%)**	t_{95-M} (s)

0.06	0.96	74.3	5.5
0.075	0.89	76.2	5.2
0.1	0.76	79.4	4.7
0.15	0.51	86.7	4.1
0.2	0.26	95.0	3.9
0.25	0.01	100.0	4.2

Table 7.14 – Percentage yield and time required to achieve 95% of mass equilibrium, for variable initial mass percentage of solutes in cell wall. $S_s = 0.1\ g_S g_W{}^{-1}$. Other parameters, except solvent-to-solid ratio, are fixed as shown in Table 7.4)

With $S_s = 0.1\ g_S g_W{}^{-1}$ the initial cell water volume is less sensitive to $\%_{s-CW}$; hence, the analysis spans a wider range of $\%_{s-CW}$ values. Yield clearly decreases with decreasing $\%_{s-CW}$ (i.e., as more solutes get relocated to cells), which is due to the reduction in the quantities of undissolved solutes in the biomass (i.e., which originate from the cell walls). With smaller amounts of undissolved solutes, the cell walls cannot maintain constant activity values (α_W and α_s) for long durations, because the undissolved solutes get depleted more quickly. To further illustrate, Figure 7.20 shows water activity (α_W)-time plots for $\%_{s-CW}$ values of 0.2 and 0.06, where in the former case the cell wall activity is held constant for a longer duration than it is in the latter case. The longer the cell wall activity can be held constant (due to the presence of undissolved solute), the longer an activity gradient is sustained between biomass and solvent; hence, the more extraction is achieved. Since cells are assumed here not to possess any undissolved solutes, the more these solutes get redistributed to cells the less the extraction yield at equilibrium. On the other hand, due to the reduced activity gradient achieved with lower $\%_{s-CW}$, which suppresses the diffusion driving force, t_{95-M} also increases slightly from 3.9 s to 5.5 s as $\%_{s-CW}$ is decreased from 0.2 to 0.06. However, an exception occurs when decreasing $\%_{s-CW}$ from 0.25 to 0.2, as t_{95-M} decreases from 4.2 s to 3.9 s. This is because the yield approaches 100% at $\%_{s-CW} = 0.25$, requiring slightly longer timeframes to readjust to the physical limit imposed on the extraction process.

These results signify that cell wall components are potentially easier to extract compared with solutes originating from cells. Furthermore, it has been demonstrated here that cell solutes are likely to be more soluble than cell wall components, otherwise cells should accommodate unrealistically large amounts of water and permanent

positive pressures. This is a logical outcome given that cell walls carry out structural functions in the biomass, while cells conduct metabolic functions in liquid media (Chapter 2; section 2.2). Extracting cell components is more challenging, but nonetheless, the extraction process can generally be enhanced with microwave heating, as will be shown in section 7.4.

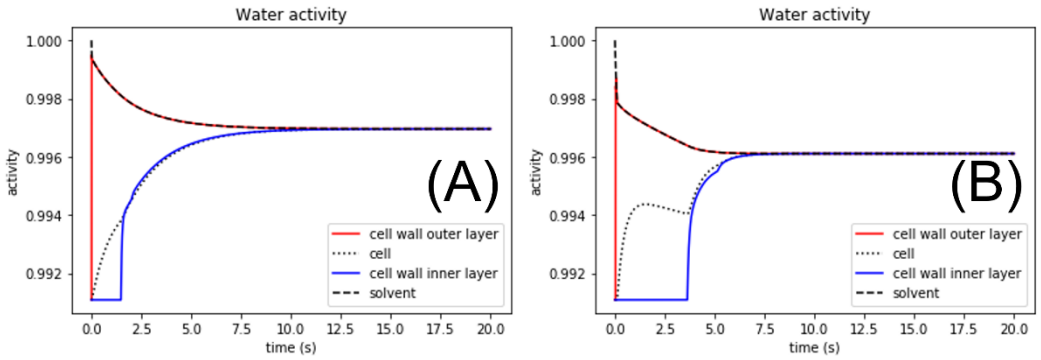


Figure 7.20 – Water activity-time plots for $S_s = 0.1\ g_S g_W{}^{-1}$ and different cell wall solute contents ($\%_{s-CW}$); (A) $\%_{s-CW} = 0.06$; (B) $\%_{s-CW} = 0.2$ (other parameters, except solvent-to-solid ratio, are fixed as shown in Table 7.4)

7.4 Predicted extraction trends with heating

In section 7.3, extraction was investigated at room temperature to understand the underlying effects of mass transfer parameters, including solubility (S_s), diffusivity (D), solvent-to-solid ratio (S_R), biomass particle size, solvent purity, solute distribution in biomass, and the non-ideal behaviour of solutions (i.e., activity-mole fraction relationship). This section extends the previous analyses through investigating the effects exercised by microwave and conventional heating on extraction patterns. This will allow differentiating between the two heating methods and, thereby, understanding whether they impose variable extraction trends in a biomass-solvent system.

As in section 7.3, the number of solutes existing in the system is limited to two throughout this section.

7.4.1 Base case

This case comprises the smallest possible cubic-shaped biomass cluster (1x2x2 cells; Figure 7.9), surrounded by a solvent with $S_R = 10\ mL g^{-1}$. The analysis incorporates two scenarios, one of which depicts microwave heating (i.e., $\varepsilon''_{biomass} = 20$) while the other resembles conventional heating (i.e., $\varepsilon''_{biomass} = 0$). In both

scenarios, Q_s and k were maintained at 1 Ks^{-1} and 0.01 $Wm^{-1}K^{-1}$, respectively, and all other heating and non-heating parameters were also fixed as shown in Table 7.4.

Results for the two scenarios are presented in Figure 7.21 as yield-time plots where, the equilibrium yield is clearly higher under microwave heating than it is under conventional heating. As briefly highlighted in section 7.3, heating may improve extraction through altering mass transfer parameters such as solubility (S_s) and diffusivity (D). However, since all input parameters were maintained here at constant values, it becomes understandable why conventional heating does not alter extraction in any significant way, compared with the room temperature extraction base scenario (section 7.3.1). However, microwave heating raises the equilibrium yield dramatically from its initial 25% all the way up to the 100% mark, indicating the occurrence of a unique microwave-induced diffusion pattern capable of enhancing extraction significantly (four-fold in this case).

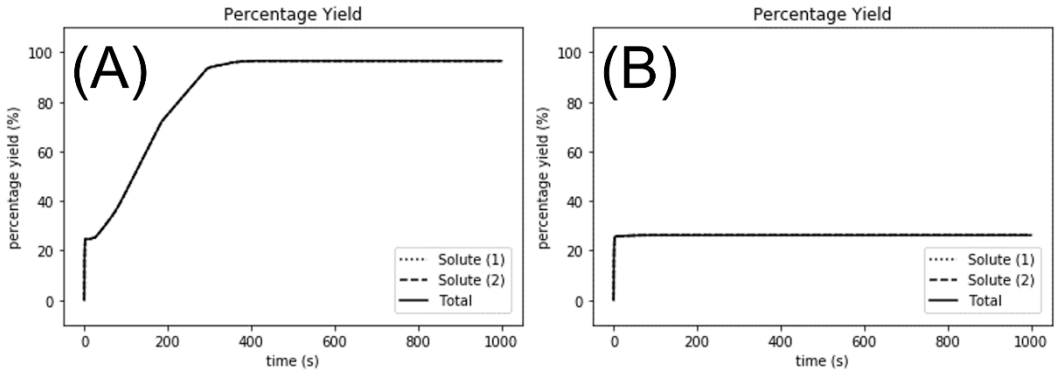


Figure 7.21 – Base results for the heating case presented as yield-time plots; (A) $\varepsilon''_{biomass} = 20$ (microwave heating); (B) $\varepsilon''_{biomass} = 0$ (conventional heating) (other parameters fixed as shown in Table 7.4)

In Figure 7.21, the yield under microwave heating increases initially to 25% and it tends to flatten at this value, thereby matching conventional heating up to this stage. Interestingly, however, this flattening in yield is followed by a dramatic second increase up to the 100% mark, indicating a microwave-induced interference to the original equilibrium position. This change in equilibrium is brought about by the temperature gradients induced in the system between biomass and solvent. As discussed previously in this thesis, such gradients provide an additional driving force for mass transfer, where higher temperatures in the biomass can induce a surplus water influx into cells/cell walls from the solvent phase. Figure 7.22 shows the temperature gradients induced between the biomass and the solvent in this case, under both

microwave and conventional heating. As can be seen, microwaves sustain higher biomass temperatures compared with that of the solvent, whereas conventional heating induces a short-lived temperature non-uniformity only applicable during the heat-up phase, where the biomass temperatures are lower than that of the solvent.

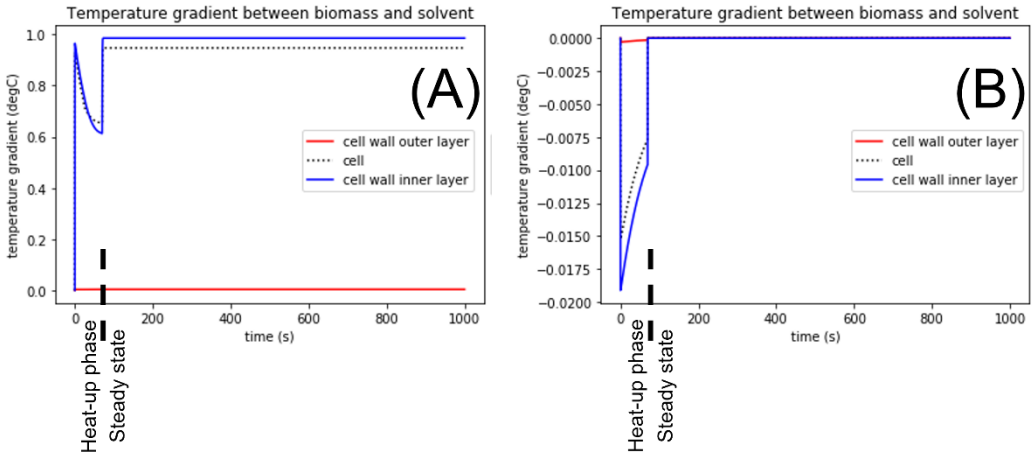


Figure 7.22 – Base results for the heating case presented as temperature gradient-time plots (difference in temperature between biomass phases and solvent); (A) $\varepsilon''_{biomass} = 20$ (microwave heating); (B) $\varepsilon''_{biomass} = 0$ (conventional heating). Other parameters are fixed as shown in Table 7.4, and each cell wall layer is represented by a single fragment

As seen in Figure 7.22, the maximum temperature gradient attained under microwave heating in this case is just below 1 ℃, indicating that even small temperature discrepancies between biomass and solvent can induce a significant change in extraction. This matches the observations reported in Chapter 5 and in literature (Lee et al., 2016), where small temperature gradients were also shown to induce significant cell pressures and increase the likelihood of cell rupture. However, attaining enhanced extraction here clearly does not require cell rupture, but instead, it results from a direct interference exercised by temperature gradients on the underpinning diffusion patterns. This matches some empirical results from Chapter 6, where continuous microwave heating was shown to result in a sharp second increase in the extraction yield. This observation could have been attributed to cell rupture, but with the current results, such attribution is clearly not required. In fact, a question may be raised on whether cell rupture is the primary phenomenon responsible for enhanced extraction, as generally perceived in literature (section 7.1).

To understand the effect of microwaves on extraction, observe Figure 7.23 where a set of osmotic potential diagrams is presented for the process, supplemented with

water activity-time and biomass pressure-time plots. As can be seen, α_W of the solvent drops initially until it is equal to the value in the inner/outer cell walls, thereby matching the room temperature extraction base case (section 7.3.1), and, in effect, also matching the conventional heating scenario. This initial similarity in the activity trends results in comparable initial yield-time profiles, where the yield flattens at around 25% under both microwave and conventional heating. However, due to the temperature gradients uniquely imposed and sustained under microwave heating, water in this case continues to flow into the biomass in significant quantities, even after the initial 25% yield has been achieved. As can be seen, this causes α_W in cells to increase, but a similar response is delayed in the cell walls (especially the inner fragments), as these contain undissolved solutes that can maintain constant α_W for longer durations (section 7.2.2.3). As water continues to flow into the biomass, driven by the temperature gradients but also supported by the activity gradients induced between the cells and cell walls, pressure builds up within the structure. This non-uniform positive pressure induced in the biomass, being highest where the temperature is high (i.e., inner biomass) and lowest where the temperature is low (i.e., outer layers), drives additional solute extraction from high pressure areas to low pressure areas, and eventually into the solvent phase. As can be seen in Figure 7.23, the biomass pressures induced in this manner can be maintained as long as the temperature gradients are preserved, explaining why the yield increases gradually yet significantly beyond its initial flattening value of 25% (in this case). Mass equilibrium is established here through attaining a comprehensive balance between the activities, pressures, and temperatures of the different phases. This is as opposed to the room temperature base case (section 7.3.1) where, due to the uniform temperature across the system and the restricted water flow into the biomass, mass equilibrium is established simply with an activity balance (i.e., when activities are equal throughout the system).

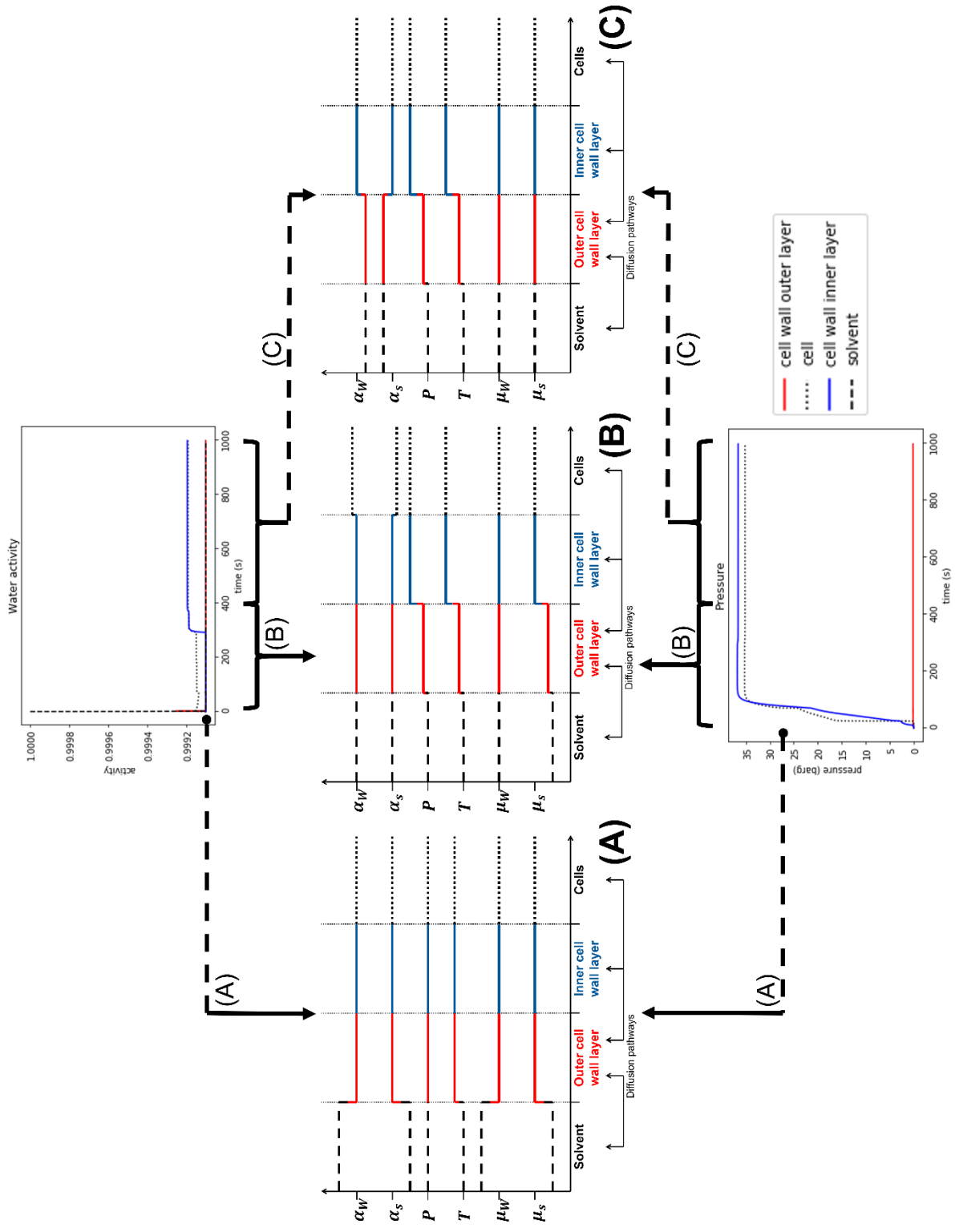


Figure 7.23 – Osmotic potential diagrams for the microwave extraction base scenario. Diagrams show gradients in activities, pressure, temperature, and chemical potentials between solvent, outer cell wall layer, inner cell wall layer, and cells. (A) initial condition; (B) pressure build-up in the biomass leading to a fresh increase in the yield; (C) final/equilibrium condition. Diagrams are supplemented with water activity-time and biomass pressure-time plots, where each cell wall layer is represented by a single cell wall fragment

A fundamental mechanism is proposed in this section explaining how microwaves can improve extraction in biomass-solvent systems without any cell rupture, but instead, through direct interference of the heating method with mass transfer patterns. The need for such mechanism has been highlighted in Chapter 6, where cell rupture was deemed unlikely to be responsible for all the extraction trends observed under microwave heating. This mechanism explains many of the trends observed in Chapter 6, including: the sharp increases in yield under continuous microwave heating, which occur after some time from starting the process; the existence of a threshold power to enhance extraction under ramp microwave heating (section 7.4.4.1.2); and, the gradual acceleration in extraction observed under continuous microwave heating, which occurs due to higher temperatures but also because of higher biomass pressures. In addition, this mechanism still acknowledges rupture as a possible cause of altering extraction dynamics (section 7.4.4), but it does not adopt cell rupture as a rate-limiting step in the process.

The proposed mechanism is further represented schematically in Figure 7.24. It is summarised from this section that microwave heating facilitates unique mass transfer mechanisms, which overcome key rate-limiting steps in extraction constituted by parameters like solubility (S_s) and diffusivity (D) (see section 7.3). This enhancement is not offered with conventional heating, as this method lacks the ability to induce/sustain temperature gradients in the system, where the biomass possesses higher temperatures than the solvent. As such, under conventional heating water is unlikely to flow into the biomass in quantities large enough to induce positive pressures and drive additional solute extraction.

The extent to which microwaves enhance extraction depends on the physical parameters defining the biomass-solvent system in question. This is further detailed in the following sections.

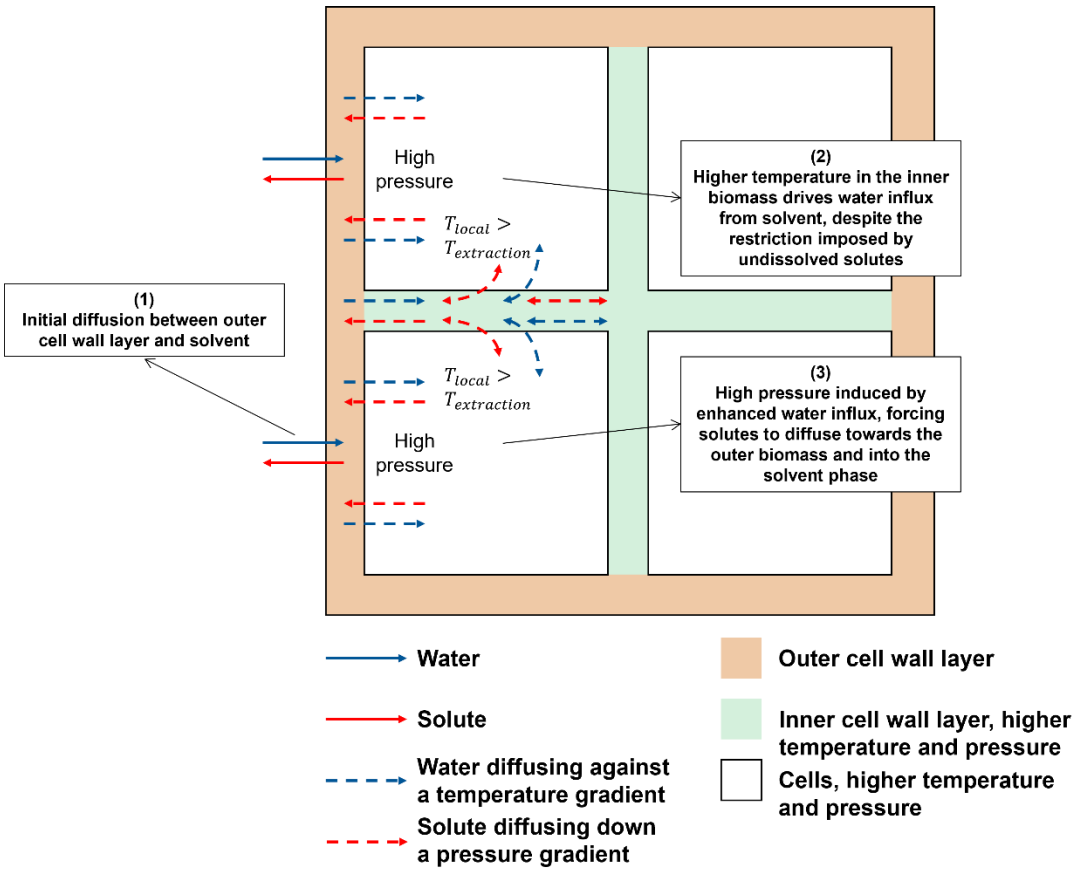


Figure 7.24 – Schematic describing extraction under microwave heating. In addition to normal mass transfer between solvent and outer biomass, water flows towards the inner biomass against the established temperature gradient, inducing high pressure and forcing solute extraction from the inner cell wall layer and cells. Water/solute exchange within the inner biomass (cells/cell walls) depends on the chemical potential gradients. Nonetheless, the overall water inward diffusion and solute extraction are governed by the temperature and pressure gradients, respectively, existing between the biomass and the solvent. Regardless of the specific pathways taken by water/solutes within the inner biomass, water generally diffuses into the biomass and solutes generally flow towards the solvent

7.4.2 Effects of microwave heating parameters

Microwave extraction (section 7.4.1) was studied with variable Q_s, $\varepsilon''_{biomass}$, and k, to investigate the effects of these parameters on the outcomes. All other parameters were fixed as shown in Table 7.4. Results are shown in Table 7.15 including percentage yield, t_{95-M}, and the maximum temperature gradient recorded between the biomass and the solvent (ΔT_{max}). Moreover, Figure 7.25 presents an example of the steady state temperature distribution in a biomass sized 0.3 mm, with $Q_s = 5\ Ks^{-1}$, $\varepsilon''_{biomass} = 30$, and $k = 0.01\ Wm^{-1}K^{-1}$. As can be seen, in cases where the biomass is sized 0.3 mm or smaller, the maximum temperature occurs around the centre of the biomass cluster.

Heating parameters		Yield (%)	t_{95-M} (s)	ΔT_{max} (℃)
Base case		96.6	285.2	1.03
Q_s (Ks^{-1})	**0.5**	97.7	556.8	0.51
	5	94.2	69.3	5.13
$\varepsilon''_{biomass}$	**0**	26.1	1.9	0.00
	30	96.2	193.5	1.54
k $(Wm^{-1}K^{-1})$	**0.005**	95.8	160.8	2.05
	0.05	98.4	1378.0	0.21

Table 7.15 – Yield, time required to achieve 95% of mass equilibrium, and maximum temperature gradient between biomass and solvent, for variable solvent heating rate, dielectric loss factor of biomass, and thermal conductivity. Base case values: $Q_s = 1\ Ks^{-1}$; $\varepsilon''_{biomass} = 20$; $k = 0.01\ Wm^{-1}K^{-1}$ (other parameters fixed as shown in Table 7.4)

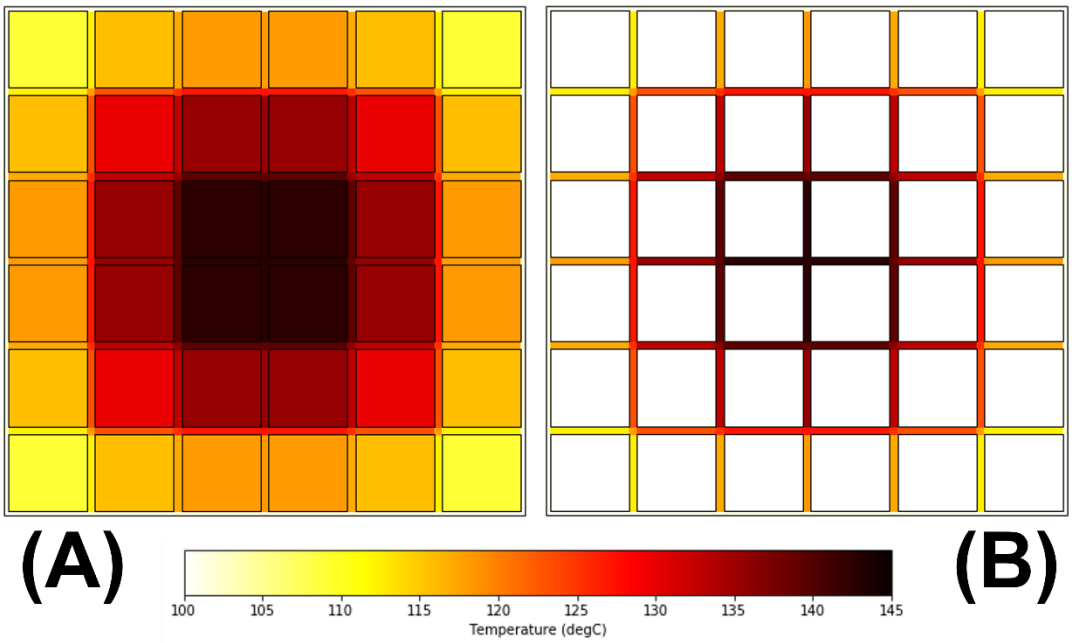


Figure 7.25 – Steady state temperature distribution of a YZ cross-section of a 0.3 mm cubic biomass within a biomass-solvent system. $\varepsilon''_{biomass} = 30$; $k = 0.01\ Wm^{-1}K^{-1}$; $Q_s = 5\ Ks^{-1}$; and all other parameters are fixed as shown in Table 7.4. (A) general temperature map of the biomass including both cells and cell walls; (B) temperature map for the cell walls only. A maximum biomass temperature of around 145 ℃ occurs around the centre of the cluster

As seen in Table 7.15, every change in the heating parameters to increase ΔT_{max}, results in a slight decrease in the yield and a noticeable reduction in t_{95-M}. The only exception is when $\varepsilon''_{biomass}$ increases from 0, because in such a case the heating mode is changed from conventional to microwave heating, raising both the yield and t_{95-M}

as discussed in section 7.4.1. During microwave heating, an increase in ΔT_{max} is observed at higher Q_s and $\varepsilon''_{biomass}$ and lower k, which matches the heat transfer observations made earlier in Chapter 3. Higher ΔT_{max} drives larger quantities of water into the biomass, thereby inducing higher pressures (as in Chapter 5) and accelerating solute extraction (i.e., decreasing t_{95-M}). On the other hand, the yield decreases with increasing ΔT_{max} because, like water, temperature gradients also favour solute diffusion into the biomass. However, this decrease in yield remains miniscule in this case, because here the entropy of solutes ($s_{s(T_0)}$) is much smaller than that of water ($s_{W(T_0)}$), meaning that any temperature-induced diffusion will be more pronounced on water than on solutes (Equation (4.63)). In this work, $s_{s(T_0)}$ was assumed to be smaller than $s_{W(T_0)}$ due to the more organised and polymeric structure/nature of solutes compared to water. Hence, it can be predicted that solutes possessing significantly high $s_{s(T_0)}$ may tend to recalcitrate within the biomass under microwave heating, rather than getting extracted into the solvent phase. This is because, increasing $s_{s(T_0)}$ induces a more pronounced effect of temperature gradient on solutes, forcing larger solute quantities to remain within high temperature areas (i.e., in the biomass). While this suppresses solute extraction, the effect may be overcome if the temperature gradients also induce high biomass pressures due to enhanced water influx, balancing the temperature gradient driving force and resulting in a net driver for solute extraction from the biomass. In other words, temperature gradients can only enhance extraction if they induce large enough biomass pressures, so as to overcome the increased tendency of solutes to recalcitrate within the biomass, due to the same temperature gradients imposed upon the system. Entropy is clearly a key parameter in microwave extraction, and a more in-depth study is intended for future work.

7.4.3 Effect of dielectric loss distribution (whether $\varepsilon''_{biomass} > \varepsilon''_{solvent}$)

For extraction to be enhanced under microwave heating, a temperature gradient of sufficient magnitude should be established between the biomass and the solvent, where the biomass is to attain the higher temperature. As discussed in sections 7.4.1 and 7.4.2, such event is a prerequisite for inducing positive biomass pressures which, in turn, enhance solute extraction. It has been suggested that temperature gradients are affected by the dielectric loss distribution in a biomass-solvent system, as the biomass attains a higher temperature than the solvent if $\varepsilon''_{biomass} > \varepsilon''_{solvent}$ (Galan et al., 2017; Lee et al., 2016; Mao, Robinson and Binner, 2021). This was investigated in

section 3.3.1.1, where ε'' was shown to dictate temperature distribution only during the heat-up phase (i.e., when temperature is increasing in the system). However, at thermal steady state, the biomass was shown to possess higher temperatures than the solvent as long as $\varepsilon''_{biomass} > 0$, regardless of whether or not $\varepsilon''_{biomass} > \varepsilon''_{solvent}$.

Insofar, section 3.3.1.1 only described the effect of dielectric loss distribution from a heat transfer perspective, meaning that mass transfer was not incorporated and, thereby, the analysis was incomplete. Temperature distribution in a biomass-solvent system is arguably affected by the mass of biomass and the diffusion rate between cells/cell walls and the solvent phase. This is because, temperature induced in a material for a given input energy, is dependent upon the amount of matter present and how fast this amount varies. Hence, the effect exercised by ε'' on temperature distribution should itself be influenced by mass transfer parameters. The heat transfer model was extended in Chapter 5 to incorporate mass transfer and cell pressure build-up. However, since extraction was assumed to occur at thermal steady state (section 7.1), it was still not possible to understand the effect of dielectric loss distribution beyond the initial analysis shown in section 3.3.1.1. Nevertheless, the current model overcomes the limitation in Chapter 5 by allowing heat and mass transfer to occur simultaneously. As such, this section attempts to understand the effect of dielectric loss distribution (i.e., whether or not $\varepsilon''_{biomass} > \varepsilon''_{solvent}$) on temperature distribution in biomass-solvent systems (i.e., whether biomass temperature is larger than that of the solvent), from a combined heat and mass transfer perspective.

Initially, temperature was studied in a hypothetical system with $\varepsilon''_{biomass} = 30$, $\varepsilon''_{solvent} = 5$ (i.e., $\Delta\varepsilon'' = 25$), and $Q_s = 7.5\ Ks^{-1}$, while all other parameters were fixed as shown in Table 7.4. This extreme heating scenario is not intended to replicate a physical case, but rather it enables a clear demonstration of the temperature-time profile while differentiating between cells and the inner/outer cell walls. Figure 7.26 presents the temperature-time profile for this scenario, together with a plot entailing the temperature gradients between the different biomass phases and the solvent. As can be seen, the biomass attains higher temperatures than the solvent throughout the process, with the highest temperature being located within the inner biomass, which matches the multitude of observations already made in this thesis. However, Figure 7.26 indicates that the temperature gradients in the system are not constant during the heat-up phase, but rather they change in magnitude. At the beginning of the heating

process, a maximum temperature gradient of around 10 ℃ is observed, but this figure drops down to just 6 ℃ after 10 s of heating. This reduction in temperature gradient is attributable to the diffusion of water from the solvent to the biomass, which increases the structure's mass and, thereby, progressively decelerates the rate of temperature increase in cells/cell walls. Despite this, the temperature gradient increases once again beyond 10 s, as the system approaches thermal steady state. Biomass temperature distribution at steady state is independent of any mass transfer parameters, as it only depends on $\varepsilon''_{biomass}$ (section 3.3.1.1). This explains why the maximum gradient quantity rises again to near its initial value of 10 ℃, as thermal steady state is approached in the system.

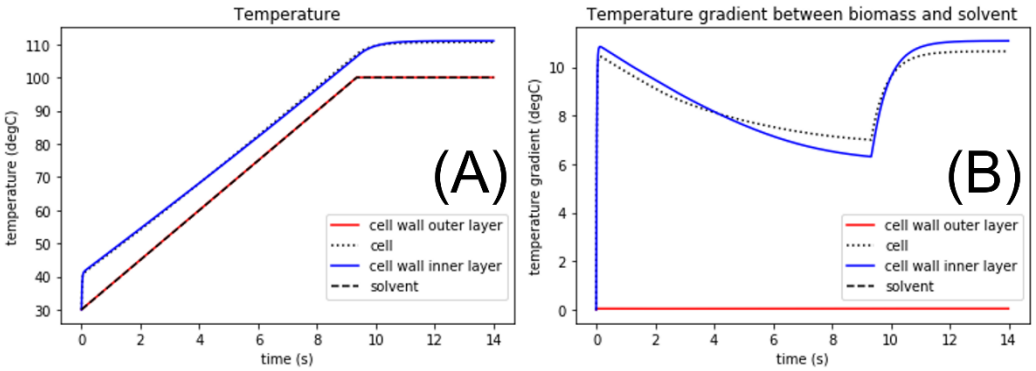


Figure 7.26 – (A) Temperature-time plot and (B) temperature gradient-time plot (difference in temperature between biomass phases and solvent) for a biomass-solvent system comprising a 0.1 mm cubic biomass material, with $\boldsymbol{\varepsilon''_{biomass} = 30}$; $\boldsymbol{\varepsilon''_{solvent} = 5}$ (i.e., $\boldsymbol{\Delta\varepsilon'' = 25}$); $\boldsymbol{Q_s = 7.5\ Ks^{-1}}$; and all other parameters fixed as shown in Table 7.4. Each cell wall layer is represented by a single cell wall fragment

The series of events described in Figure 7.26 demonstrate that mass transfer influences temperature gradients significantly, due to the dynamics of energy dissipation under variable mass. However, this effect is only applicable during the heat-up phase, as once steady state is achieved in the system the temperature gradient becomes solely dependent upon $\varepsilon''_{biomass}$. Some of the key mass transfer parameters influencing the heating process include: (i) diffusivity (D) which describes the resistance to diffusion and, thereby, the rate of water influx into the biomass; and (ii) solubility (S_s) which indirectly represents the initial mass of the biomass material (i.e., larger S_s signifies smaller amounts of water needed to dissolve solutes). The effects of D and S_s were investigated at $\varepsilon''_{biomass} = 2.5$, $\varepsilon''_{solvent} = 5$ (i.e., $\Delta\varepsilon'' = -2.5$), while all other parameters including Q_s were fixed as shown in Table 7.4. Figure 7.27

and Figure 7.28 present the results for variable D and S_s, respectively. The outcomes are demonstrated as a set of temperature gradient-time plots, where although $\Delta\varepsilon'' < 0$ here, in most cases the biomass temperature remains higher than that of the solvent throughout the heat-up phase. This is neither in agreement with section 3.3.1.1, nor is it with the general argument that $\Delta\varepsilon'' < 0$ induces a biomass temperature lower than that of the solvent (Galan et al., 2017; Lee et al., 2016; Mao, Robinson and Binner, 2021). Nevertheless, this result demonstrates that the effect of dielectric loss distribution (i.e., whether or not $\varepsilon''_{biomass} > \varepsilon''_{solvent}$) on the system's temperature, is in itself highly dependent upon mass transfer parameters and diffusion patterns. As seen in Figure 7.27, increasing D suppresses the temperature gradients between biomass and solvent, which is because, at higher D water diffuses faster into the biomass, increasing its mass quickly and decelerating the rate of temperature increase more significantly. At very high D (e.g., Figure 7.27B), the deceleration in biomass heating may even lead to negative temperature gradients, indicating a swap in the temperature distribution as the biomass becomes cooler than the solvent after it had been warmer. On the other hand, decreasing S_s (Figure 7.28) also results in a reduced temperature gradient, and with sufficiently low S_s, a negative gradient is recorded as the solvent attains a higher temperature than the biomass. In this analysis, smaller S_s means that more water is required initially in cells to dissolve the existing solutes (sections 7.2.5.1 and 7.3.8). This signifies a heavier biomass material and, thereby, lower heating rates for a given input microwave power. Note that, any parameter other than S_s influencing the mass of the biomass material (e.g., density), is also expected to exhibit similar trends.

The temperature distribution at thermal steady state is uniform throughout Figure 7.27 and Figure 7.28, since $\varepsilon''_{biomass}$ is the same in all cases.

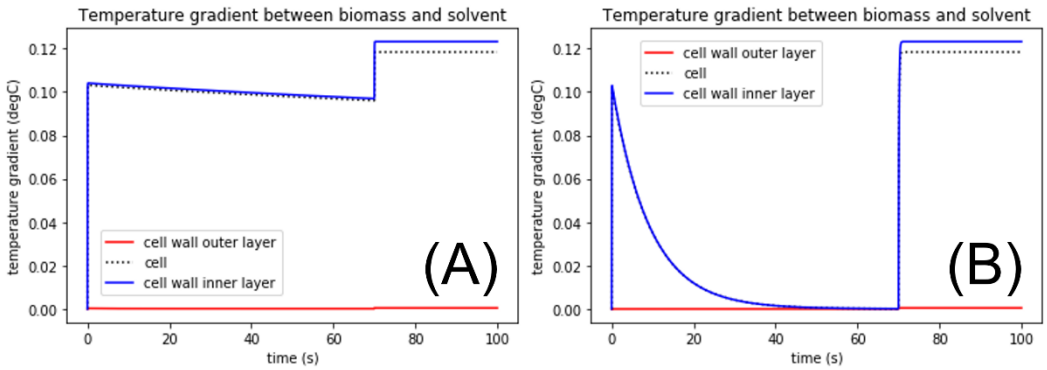


Figure 7.27 – Temperature gradient-time plots (difference in temperature between biomass phases and solvent) for $\Delta\varepsilon'' = -2.5$ and variable D. (A) $D_W, D_s = 10^{-10}, 10^{-11}\ m^2 s^{-1}$; (B) $D_W, D_s = 10^{-8}, 10^{-9}\ m^2 s^{-1}$. All other parameters are as shown in Table 7.4. Each cell wall layer is represented by a single cell wall fragment

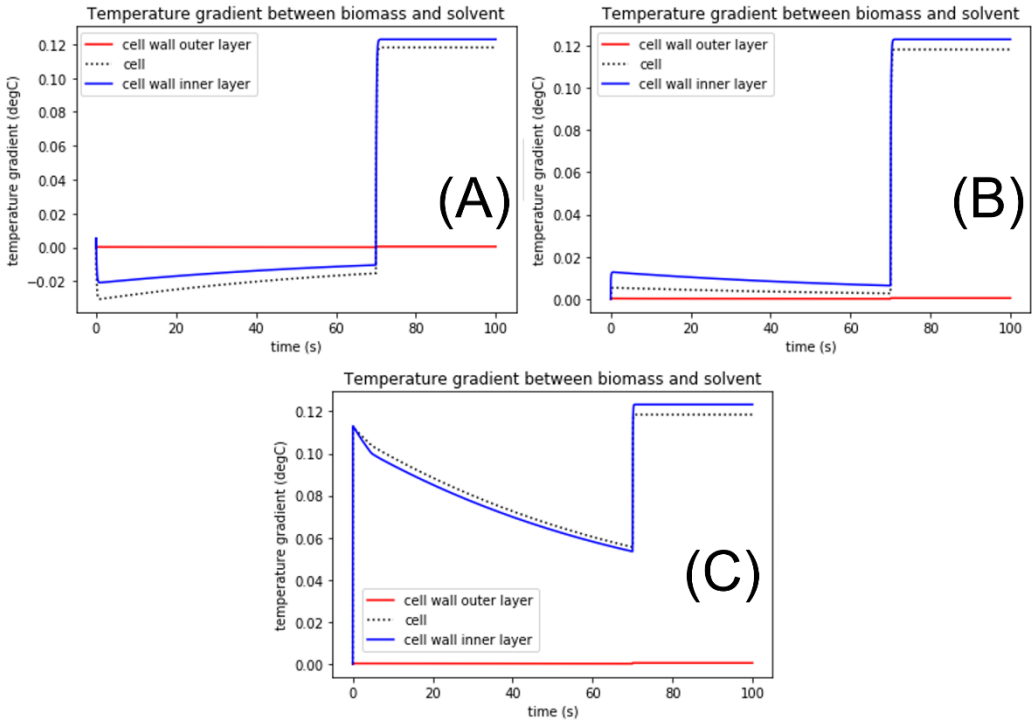


Figure 7.28 – Temperature gradient-time plots (difference in temperature between biomass phases and solvent) for $\Delta\varepsilon'' = -2.5$ and variable S_s. (A) $S_s = 0.00075\ g_s g_W^{-1}$; (B) $S_s = 0.001\ g_s g_W^{-1}$; (C) $S_s = 0.1\ g_s g_W^{-1}$. All other parameters are as shown in Table 7.4. Each cell wall layer is represented by a single cell wall fragment

Mass transfer parameters such as D and S_s, dictate the $\Delta\varepsilon''$ value required for the biomass to attain higher temperatures than the solvent. This novel finding extends the arguments in section 3.3.1.1 and literature (Galan et al., 2017; Lee et al., 2016; Mao, Robinson and Binner, 2021), by demonstrating that the effect of dielectric loss distribution on temperature and extraction, is not universal but rather it is case-specific. In some cases, the temperature gradient required for enhanced extraction can be established even if $\varepsilon''_{biomass} < \varepsilon''_{solvent}$, whereas in other situations the biomass may not attain higher temperatures even if $\varepsilon''_{biomass} > \varepsilon''_{solvent}$. In other words, attaining the temperature gradient required for enhanced microwave extraction does not necessarily occur when $\Delta\varepsilon'' > 0$, as opposed to the previous suggestions in literature. These outcomes indicate that two biomass materials with comparable dielectric properties, may not necessarily behave similarly under microwave heating.

Instead, the material's mass and its diffusion properties play a significant role in dictating whether microwave heating would enhance extraction. Since these complex phenomena only occur during the heat-up phase (i.e., when temperature is increasing in the system), one way to overcome this challenge is to apply continuous heating to the extraction system as demonstrated in Chapter 6. As opposed to "ramp microwave heating," this approach drives the system to thermal steady state while still maintaining a constant input power, allowing the biomass to always attain higher temperatures than the solvent given that $\varepsilon''_{biomass} > 0$. In contrast, with ramp microwave heating, the input power is lowered significantly on approaching a sub-saturation temperature set-point, which essentially means that temperature gradients are only maintained during the heat-up phase (Figure 6.2). Although this clearly poses a limitation to the process, many empirical studies have adopted a ramp heating approach. Therefore, to allow benchmarking those studies with the current work, Table 7.16 presents the likely solvent heating rates (Q_s) required to maintain a hotter biomass throughout the heat-up phase, where the temperature gradient in the representative inner cell wall fragment (blue line in Figure 7.28) is at least 0.25 ℃. Predicted Q_s values are shown for variable $\varepsilon''_{biomass}$, D, and S_s, but if the Q_s value needed to maintain 0.25 ℃ is higher than 15 Ks^{-1}, the required temperature gradient is deemed unachievable.

		D_W, D_s $(m^2 s^{-1})$		
		$10^{-10}, 10^{-11}$	$10^{-9}, 10^{-10}$	$10^{-8}, 10^{-9}$
S_s $(g_s g_W^{-1})$	**0.001**	Unachievable; 2.5; 1.0; 0.5	Unachievable; 4.0; 1.5; 0.5	Unachievable; Unachievable; 1.5; 0.5
	0.01	3.0; 2.0; 1.0; 0.5	5.0; 2.5; 1.0; 0.5	Unachievable; Unachievable; 1.5; 0.5
	0.1	2.5; 1.5; 1.0; 0.5	6.5; 3.0; 1.0; 0.5	Unachievable; Unachievable; 1.5; 0.5
		Q_s (Ks^{-1}) for $\varepsilon''_{biomass} = 2.5$; 5; 10; 20		

Table 7.16 – Threshold solvent heating rate (Q_s) required to maintain a temperature gradient of at least 0.25 ℃, between the representative inner cell

wall fragment (blue line in Figure 7.28) and the solvent, during the heat-up phase. Q_s values are shown in increments of $0.5\ Ks^{-1}$ for variable D, S_s, and $\varepsilon''_{biomass}$. If $Q_s > 15\ Ks^{-1}$, the required temperature gradient is deemed unachievable. $\varepsilon''_{solvent} = 5$ throughout, and other parameters are fixed as shown in Table 7.4

7.4.4 Extraction scenarios under variable solubility/diffusivity/heating

This section presents a set of scenarios highlighting the effects of solubility (S_s), solute diffusivity (D_s), and heating (Q_s and heating mode) on extraction in systems with two solutes. On approaching the rupture pressure in any biomass phase ($P^R{}_C$ for cells and $P^R{}_{CW}$ for cell walls), the parameter $D^R{}_s$ (i.e., ruptured solute diffusivity) is used for solute diffusion in that phase, instead of D_s (i.e., unruptured solute diffusivity). This enables studying some of the effects that rupture may have on extraction. Where $D_s = D^R{}_s$, rupture remains ineffective on diffusion, but if $D_s \neq D^R{}_s$, achieving rupture in any given phase alters the resistance to solute diffusion in that phase. In the latter case, extraction trends may be changed if widespread rupture is achieved within the biomass, as $D^R{}_s$ becomes applicable to an increasing number of cells/cell walls at the expense of D_s. The values of $P^R{}_C$ and $P^R{}_{CW}$ are fixed throughout this section at 70 bar and 5 bar, respectively, as per indicated in Table 7.4.

Different scenarios were conducted with different solvent heating rates (Q_s) and under three heating modes, namely continuous microwave heating, ramp microwave heating, and conventional heating. As discussed in Chapter 6, ramp microwave heating signifies applying microwave power onto the biomass-solvent system only during the heat-up phase, but once the solvent approaches its target temperature ($T_{extraction}$), the input power is readjusted to zero. On the other hand, continuous microwave heating denotes applying microwave power continuously, even after achieving $T_{extraction}$.

This section is divided into two subsections, the first of which presents selected extraction scenarios aimed at highlighting key effects, while the second displays a series of generalised scenarios given variable solubility (S_s), unruptured/ruptured solute diffusivity (D_s, $D^R{}_s$), heating mode, and solvent heating rate (Q_s). Apart from these, all other parameters were fixed as shown in Table 7.4.

7.4.4.1 Selected extraction scenarios

7.4.4.1.1 Continuous heating vs ramp heating

This scenario compares extraction under continuous and ramp microwave heating, using a typical process setting comprising low solubility (i.e., $S_s = 0.01\ g_s g_W{}^{-1}$);

equal resistance to diffusion experienced by both solutes (i.e., $D_{s1} = D_{s2} = 10^{-10}\ m^2 s^{-1}$); and negligible effect of rupture on diffusion dynamics (i.e., $D_s = D^R{}_s$ for both solutes). Results are shown in Figure 7.29 as yield-time plots attained under the two microwave heating modes plus conventional heating, where $Q_s = 1\ Ks^{-1}$ in all cases.

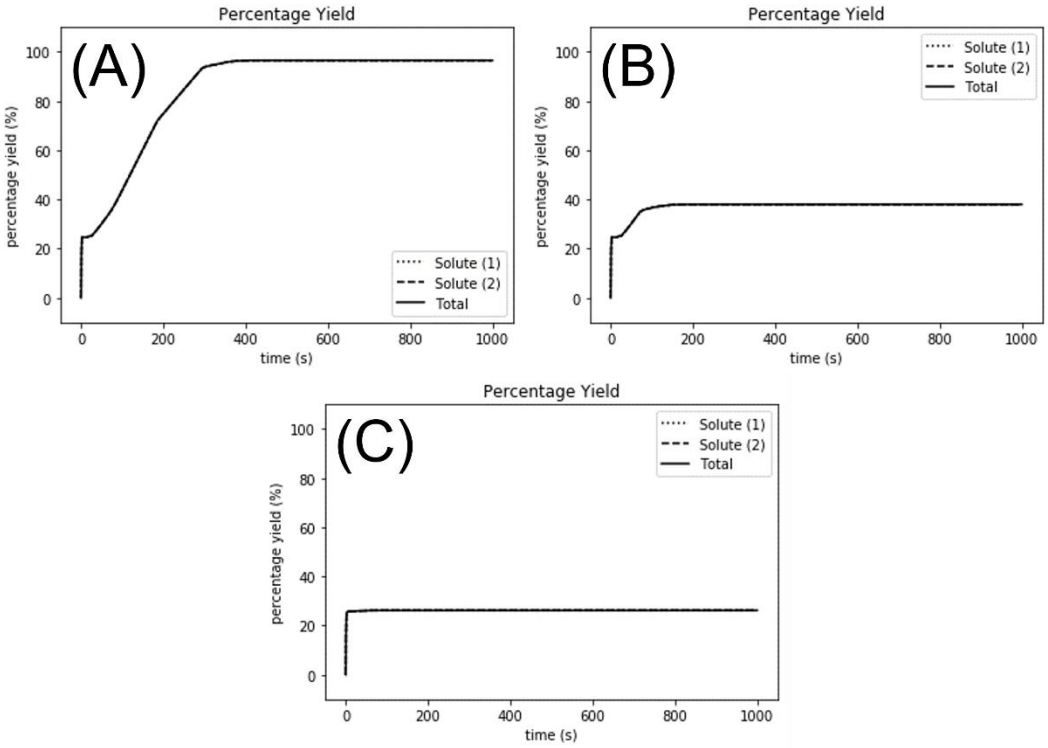


Figure 7.29 – Yield-time plots under (A) continuous microwave heating, (B) ramp microwave heating, and (C) conventional heating. $Q_s = 1\ Ks^{-1}$; $S_s = 0.01\ g_s g_W{}^{-1}$; $D_{s1} = D_{s2} = D^R{}_s = 10^{-10}\ m^2 s^{-1}$; other parameters fixed as shown in Table 7.4

Microwave heating clearly improves extraction compared with conventional heating, but this improvement is much more pronounced under continuous microwave heating, as this sustains the temperature gradients throughout extraction. In contrast, ramp microwave heating results in smaller yields because the temperature gradients are only maintained during the time-limited heat-up phase. This restricts temperature-induced water influx to the biomass and does not allow large pressures to be induced within cells/cell walls, thereby capping the maximum attainable yield.

7.4.4.1.2 Ramp heating at variable heating rates (no rupture effect)

This scenario comprises extraction under ramp microwave heating, conducted using variable heating rates (Q_s). It is vital to study extraction under ramp heating

since, unlike continuous microwave heating, this mode only sustains temperature gradients during the heat-up phase. Such difference in the heating pattern may alter the attainable extraction trends.

This scenario comprises low solubility (i.e., $S_s = 0.01\ g_s {g_W}^{-1}$); equal resistance to diffusion experienced by both solutes (i.e., $D_{s1} = D_{s2} = 10^{-10}\ m^2 s^{-1}$); and negligible effect of rupture on diffusion dynamics (i.e., $D_s = {D^R}_s$ for both solutes). Table 7.17 shows the yields achieved for variable Q_s, and for comparison, it also presents the corresponding yields achieved under conventional heating. This scenario is intended to depict realistic experimental situations; therefore, a maximum extraction time of 1000 s has been allocated for all simulation runs. Capping the process timeframe as such is a sensible practice experimentally, as it can be challenging to extend the process for long durations.

$\boldsymbol{Q_s}$ $\boldsymbol{(Ks^{-1})}$	**Yield after 1000 s of extraction (%)**	
	Ramp microwave heating	Conventional heating
0	25.7	25.7
0.005	25.6	25.7
0.01	25.7	25.8
0.05	33.9	26.1
0.1	39.5	26.1
0.5	38.6	26.1
1	38.0	26.1
5	35.4	26.1
10	33.7	26.1

Table 7.17 – Yields achieved after 1000 s of extraction, under ramp microwave heating and conventional heating, for variable Q_s. Other parameters fixed as shown in Table 7.4

As seen in Table 7.17, ramp heating only enhances extraction beyond some threshold heating rate, where in this case $Q_s > 0.01\ Ks^{-1}$ is needed. Such threshold is required because, at low Q_s, the short-lived temperature gradients are also small in magnitude, meaning that they cannot facilitate enhanced extraction. Nevertheless, the temperature gradients increase with Q_s, eventually leading to enhanced solute extraction once a sufficiently high Q_s value is applied. This threshold power analogy has been observed empirically, e.g., in Chapter 6 where a certain power input acted as a threshold to improve the yield under ramp heating; but also in literature where ramp heating was also shown to accelerate extraction only beyond a certain input power (Mao, Robinson and Binner, 2021). However, as seen in Table 7.17, increasing Q_s

even further (beyond $0.1\,Ks^{-1}$ here) causes the yield to drop again, due to the shortened timeframes at which the temperature gradients are maintained (i.e., higher Q_s signifies faster approach to thermal steady state). Hence, a trade-off exists between the magnitude of temperature gradients and the duration in which they are maintained, thereby manifesting an optimum Q_s for achieving the highest yield under ramp microwave heating. In the current scenario, a peak yield of $\sim 40\%$ is achieved when $Q_s = 0.1\,Ks^{-1}$ (i.e., optimum heating rate), but otherwise the yield remains smaller than the peak value for both higher and lower Q_s. Although the yields attainable under continuous microwave heating can be much higher than those achieved here (sections 7.4.1 and 7.4.4.1.1), the $\sim 40\%$ yield is still an improvement from conventional extraction. The latter returns a constant yield of $\sim 26\%$ in Table 7.17, which because the physical parameters affecting extraction have been made independent of temperature in the current analysis (i.e., they are fixed as shown in Table 7.4). As such, the enhanced microwave extraction observed here is solely attributable to the temperature gradients uniquely induced under microwave heating.

Furthermore, it can be argued here that, a threshold Q_s is only required to enhance extraction under ramp microwave heating, but not with continuous microwave heating. Continuous heating sustains temperature gradients throughout the process, meaning that even low Q_s values are capable of enhancing extraction (section 7.4.2). Despite this, however, the results from Chapter 6 (Figure 6.5A) still show that continuous heating enhances extraction beyond a threshold power, causing a sharp second increase in the yield. This threshold is arguably but a result of the limited extraction timeframes that were applied in Figure 6.5; in other words, should the process be allowed to proceed indefinitely, then all input powers would cause a second increase in the yield (under the current conditions). Therefore, the differences in extraction between continuous and ramp heating (under the current physical conditions) can be summarised in two points: (i) continuous heating generally results in higher yields as in section 7.4.4.1.1; and, (ii) ramp heating demands a threshold power to improve extraction, while also demonstrating a peak yield at a given optimum power value. Note, however, that certain physical conditions may alter these outcomes, such as when the solutes being extracted are highly soluble (section 7.4.4.1.4).

7.4.4.1.3 Ramp heating at variable heating rates (with rupture effect)

This scenario repeats that presented in section 7.4.4.1.2, but while incorporating cell/cell wall rupture as a cause for increasing solute diffusivity in the respective ruptured phases. In this scenario, solute diffusivity in a phase increases with rupture, from an ordinary value of $D_{s1} = D_{s2} = 10^{-10}\ m^2 s^{-1}$ to a ruptured value of $D^R{}_{s1} = D^R{}_{s2} = 10^{-9}\ m^2 s^{-1}$, thereby accelerating mass transfer ten-fold in any ruptured cell/cell wall. All other physical inputs are as shown in section 7.4.4.1.2, and the results for this scenario are presented in Table 7.18.

$\boldsymbol{Q_s}$ $(\boldsymbol{Ks^{-1}})$	**Yield after 1000 s of extraction (%)**	
	Ramp microwave heating	Conventional heating
0	25.7	25.7
0.005	25.6	25.7
0.01	25.7	25.8
0.05	33.9	26.1
0.1	39.5	26.1
0.5	38.6	26.1
1	38.0	26.1
5	73.3	26.1
10	87.3	26.1

Table 7.18 – Yields achieved after 1000 s of extraction, under ramp microwave heating and conventional heating, for variable $\boldsymbol{Q_s}$, and where $\boldsymbol{D^R{}_{s1} = D^R{}_{s2} = 10^{-9}\ m^2 s^{-1}}$. Other parameters fixed as shown in Table 7.4

All results in Table 7.18 match those presented in section 7.4.4.1.2, except where ramp heating is applied with $Q_s > 1\ Ks^{-1}$. Under such high Q_s, a dramatic step-change in extraction is observed, as the yield increases from 38% at $Q_s = 1\ Ks^{-1}$ to 87% at $Q_s = 10\ Ks^{-1}$. This increase occurs due to a widespread rupture in the biomass caused by the high temperature gradients (due to large Q_s), which drive large quantities of water into cells/cell walls. In this scenario, rupturing more phases makes $D^R{}_s$ increasingly more applicable at the expense of D_s, thereby lowering the overall resistance to diffusion experienced by solutes, and raising their diffusion rate. This allows more solutes to be extracted when the temperature gradient exists (i.e., during heat-up), leading to a dramatic increase in the yield as observed in Table 7.18.

It can be summarised here that, the effect of rupture on extraction depends on how it alters the relevant diffusion parameters; in this scenario rupture increased solute diffusivity, so it increased the extraction yield.

7.4.4.1.4 Extracting highly soluble components (equal diffusivities)

This scenario demonstrates the extraction of highly soluble components (i.e., $S_s = 0.1\ g_s{g_W}^{-1}$), where an equal resistance to diffusion is experienced by both solutes (i.e., $D_{s1} = D_{s2} = 10^{-10}\ m^2s^{-1}$), and the effect of rupture on diffusion dynamics is negligible (i.e., $D_s = {D^R}_s$ for both solutes). Results are shown in Figure 7.30 as yield-time plots attained under the two microwave heating modes plus conventional heating, where $Q_s = 5\ Ks^{-1}$ in all cases.

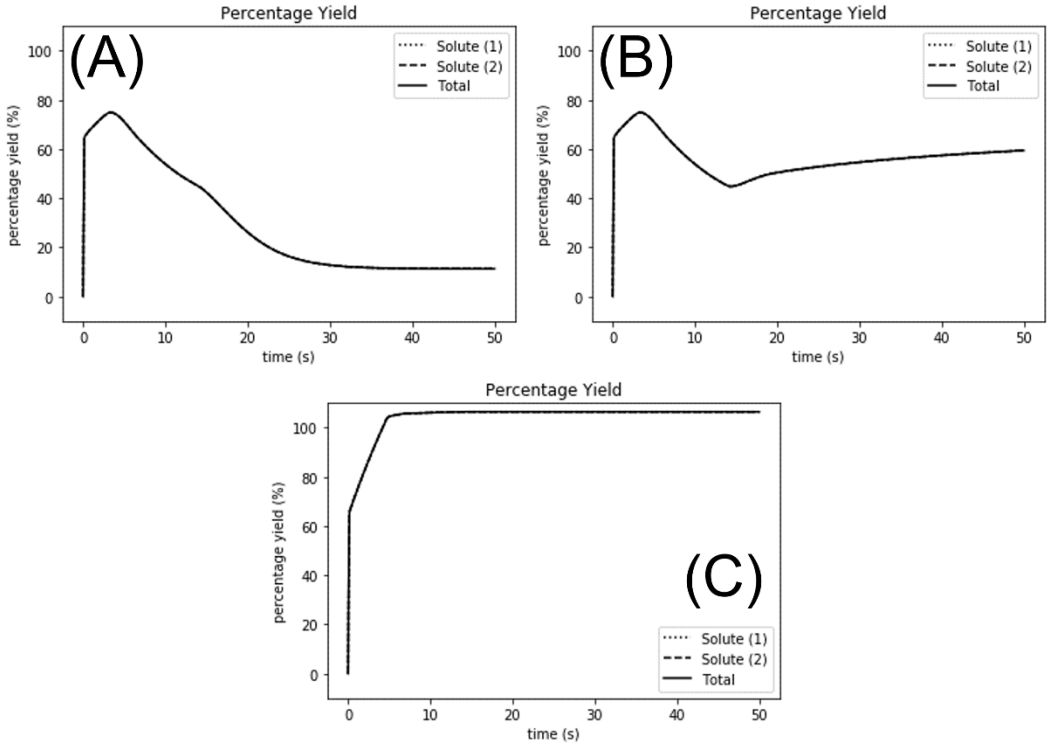


Figure 7.30 – Yield-time plots under (A) continuous microwave heating, (B) ramp microwave heating, and (C) conventional heating. $Q_s = 5\ Ks^{-1}$; $S_s = 0.1\ g_s{g_W}^{-1}$; $D_{s1} = D_{s2} = {D^R}_s = 10^{-10}\ m^2s^{-1}$. Other parameters fixed as shown in Table 7.4

The high S_s value of 0.1 $g_s{g_W}^{-1}$ has been shown to return yields as high as 100 %, at room temperature extraction and under the current physical conditions (section 7.3.2). As expected, therefore, such high yields are also observable here with conventional heating, but interestingly, they are not with microwave heating which evidently supresses extraction. In this case, microwave heating is not needed to enhance extraction, as the high S_s value itself results in high yields. However, since the microwave-induced temperature gradients still enhance water influx to the biomass, the already extracted solutes eventually get reabsorbed due to the increased solute activity (α_s) in the solvent phase. The reabsorption of solutes causes a decline

in the yield beyond a peak value (Figure 7.30), and while such a phenomenon is recognised in literature, it is commonly attributed to solute degradation (Lee et al., 2016; Veggi, Martinez and Meireles, 2013; Wang et al., 2010), which is also possible under microwave heating (Tao and Xu, 2008). Arguably, however, degradation itself cannot decrease the total yield of extracts, unless some of these extracts disappear by means of evaporation or reabsorption into the biomass, or if the apparatus/procedure incorporate a systematic error preventing full measurement of the degraded extracts. Evaporation requires a disintegration of the extracts into gaseous components, which is unlikely at the current solvent temperature of 100 ℃. Alternatively, solutes may get reabsorbed into the biomass, and the current outcomes propose a link between high solute solubility and reabsorption. This further indicates the importance of understanding solubility patterns in biomass-solvent systems.

Solute reabsorption signifies that microwave heating is better suited for low solubility components, which are also more difficult to extract by conventional means. This reabsorption is applicable to both continuous and ramp heating modes, but as can be seen in Figure 7.30, the yield increases again under ramp heating. This is because, ramp heating maintains the temperature gradients for a limited timeframe, only during the heat-up phase.

7.4.4.1.5 Extracting highly soluble components (unequal diffusivities)

As in the previous scenario (section 7.4.4.1.4), it is aimed here to study the extraction of highly soluble components, however while applying unequal diffusivities to the two solutes (i.e., $D_{s1} \neq D_{s2}$). D_{s1} and D_{s2} and fixed here at $10^{-10}\ m^2 s^{-1}$ and $10^{-11}\ m^2 s^{-1}$, respectively; moreover, $D_s = D^R{}_s$ is maintained for both solutes, signifying that rupture exercises negligible effect on extraction in this case. Results are shown in Figure 7.31 as yield-time plots attained under the two microwave heating modes plus conventional heating, where $Q_s = 5\ Ks^{-1}$ in all cases.

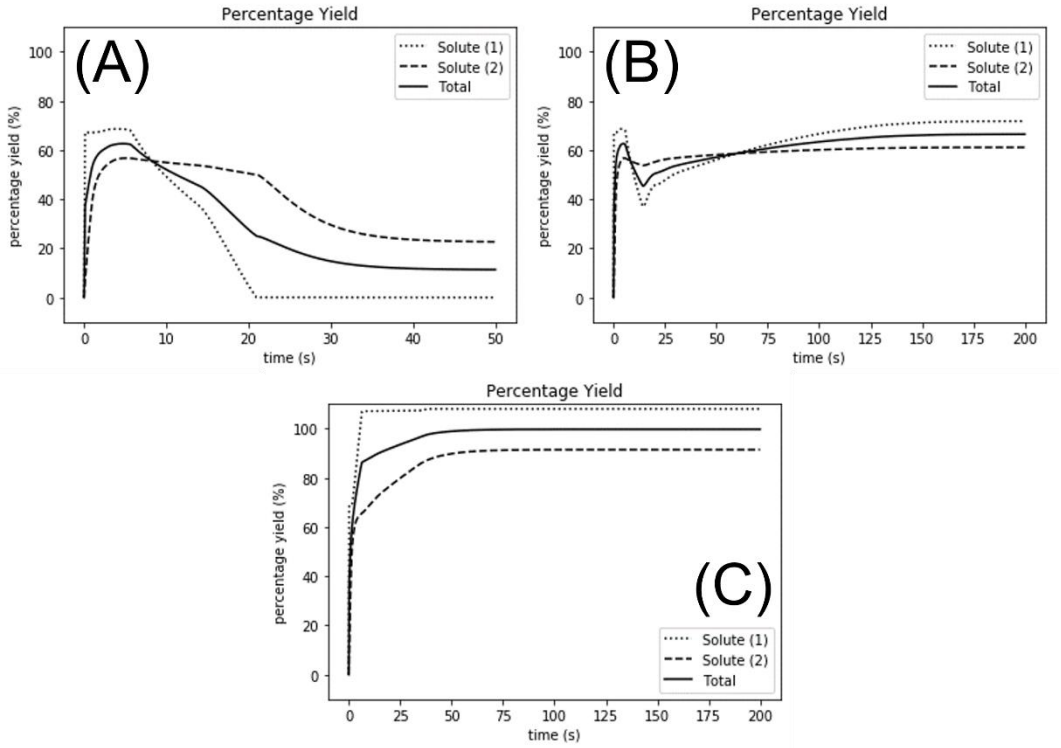


Figure 7.31 – Yield-time plots under (A) continuous microwave heating, (B) ramp microwave heating, and (C) conventional heating. $Q_s = 5\ Ks^{-1}$; $S_s = 0.1\ g_s g_W{}^{-1}$; $D_{s1} = 10^{-10}\ m^2 s^{-1}\ m^2 s^{-1}$; $D_{s2} = 10^{-11}\ m^2 s^{-1}\ m^2 s^{-1}$; $D_{s1} = D^R{}_{s1}$; $D_{s2} = D^R{}_{s2}$

Yield in this case is higher under conventional heating than it is under microwave heating, which is to be expected given the high S_s value (section 7.4.4.1.4). Moreover, the two solute yields are not equal, which is also an expected outcome given that $D_{s1} \neq D_{s2}$. Initially under continuous microwave heating, solute (1) gets extracted more readily compared with solute (2), which is because $D_{s1} > D_{s2}$ (section 7.3.3.2), but interestingly, solute (1) also gets reabsorbed more readily due to the same reason. This is an important observation, because although the process had started with larger amounts of solute (1) extracted, it ended with larger amounts of solute (2) extracted at a later stage. In fact, with the high heating rate used in Figure 7.31 ($Q_s = 5\ Ks^{-1}$), solute (1) gets reabsorbed fully under continuous microwave heating, as the final yield composition incorporates solute (2) only. On the other hand, ramp microwave heating only induces solute reabsorption as long as the temperature gradients are maintained in the system (i.e., during the heat-up phase). As such, the ramp extraction process starts with larger amounts of solute (1), which swaps to larger amounts of solute (2) due to reabsorption, but then reverts back to larger quantities of solute (1) as thermal steady state is approached.

7.4.4.2 Further/general extraction scenarios

A broad range of scenario is presented here for variable solubilities, solute diffusivities, and heating rates/modes. As opposed to section 7.4.4.1 where specific extraction situations were presented, this subsection presents more generalised outcomes offering nonexclusive trends.

All scenarios present yield-time plots attained under the two microwave heating modes plus conventional heating, where $Q_s = 0.5, 1,$ and $5\ Ks^{-1}$ in all cases. The solubility (S_s) and solute diffusivity (D_s; $D^R{}_s$) values used are summarised in Table 7.19, while all other parameters are summarised in Table 7.4.

Scenario	$\boldsymbol{S_s}$ $(\boldsymbol{g_s g_W{}^{-1}})$	$\boldsymbol{D_{s1}; D_{s2}}$ $(\boldsymbol{m^2 s^{-1}})$	$\boldsymbol{D^R{}_{s1}; D^R{}_{s2}}$ $(\boldsymbol{m^2 s^{-1}})$	**Rupture affects diffusion?**
1	0.01 (low)	10^{-10}; 10^{-10}	10^{-10}; 10^{-10}	No
2	0.1 (high)	10^{-10}; 10^{-10}	10^{-10}; 10^{-10}	
3	0.01 (low)	10^{-10}; 10^{-11}	10^{-10}; 10^{-11}	
4	0.1 (high)	10^{-10}; 10^{-11}	10^{-10}; 10^{-11}	
5	0.01 (low)	10^{-10}; 10^{-10}	10^{-9}; 10^{-9}	Yes, diffusivities increase in magnitude
6	0.1 (high)	10^{-10}; 10^{-10}	10^{-9}; 10^{-9}	
7	0.01 (low)	10^{-9}; 10^{-10}	10^{-10}; 10^{-9}	Yes, diffusivity magnitudes swap
8	0.1 (high)	10^{-9}; 10^{-10}	10^{-10}; 10^{-9}	

Table 7.19 – Solubilities and diffusivities used in the various scenarios

7.4.4.2.1 Scenario 1: low S_s; D_{s1}=D_{s2}

Key outcomes in bullet points:

- Extraction is enhanced under microwave heating compared with conventional heating (section 7.4.1), but the yields achieved under continuous microwave heating are far superior than those attained with ramp microwave heating (section 7.4.4.1.1).
- Under both microwave heating modes, higher Q_s accelerates the process while slightly lowering the equilibrium yield (sections 7.4.2 and 7.4.4.1.2).

$\boldsymbol{Q_s}$ $(\boldsymbol{Ks^{-1}})$	**(A) Continuous heating**	**(B) Ramp heating**

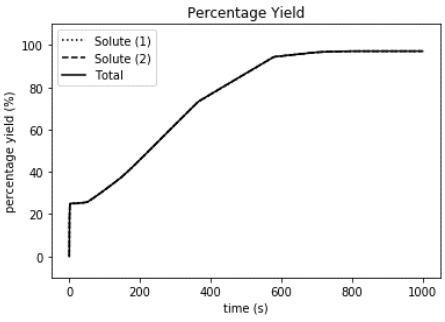
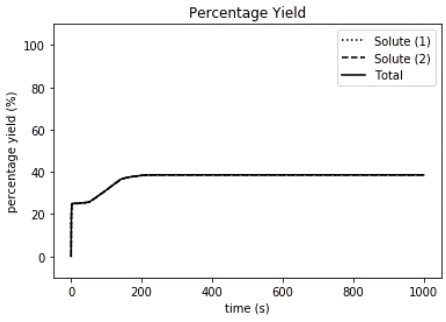
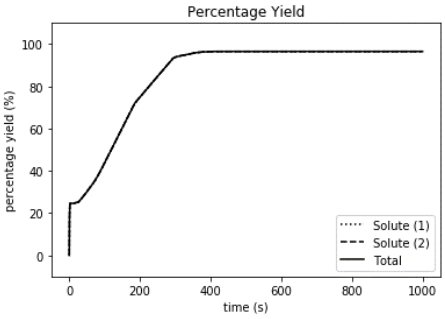
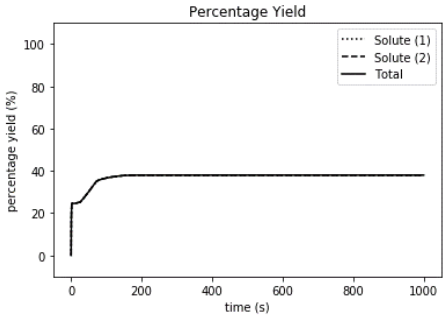
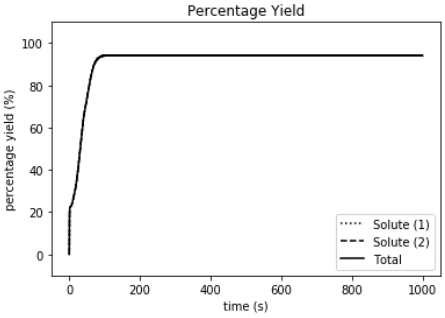
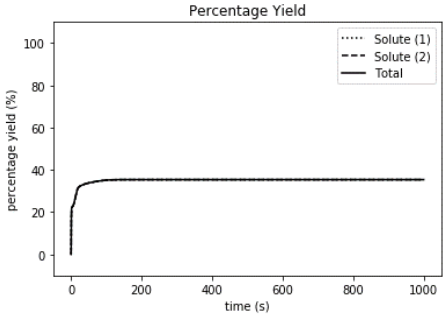
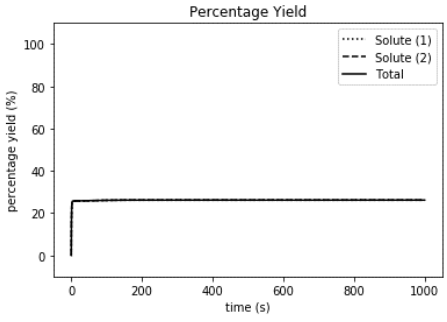
0.5		
1.0		
5.0		
Conventional heating		

Table 7.20 – Yield-time plots for scenario 1

7.4.4.2.2 *Scenario 2: high S_s; D_{s1}=D_{s2}*

Key outcomes in bullet points:

- Microwave heating suppresses the extraction of highly soluble solutes (section 7.4.4.1.4), which can otherwise be naturally extracted in high quantities (section 7.3.2).
- Microwaves cause a reabsorption of solutes into the biomass, and the rate of such reabsorption is higher at larger Q_s.

- The reabsorption occurs so long as the temperature gradients are maintained in the system; hence, the yield increases again on approaching thermal steady state under ramp heating.

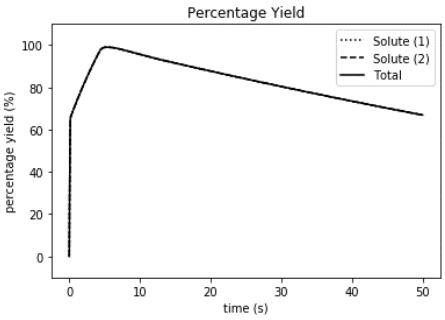
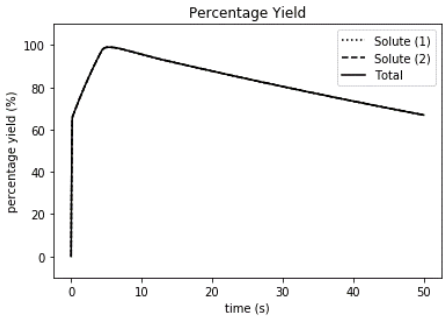
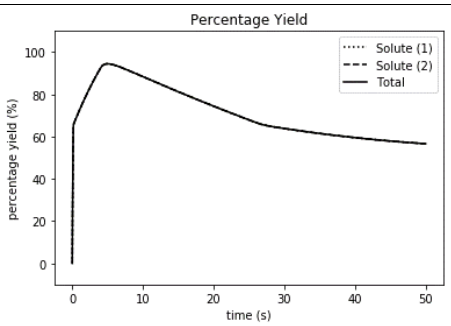
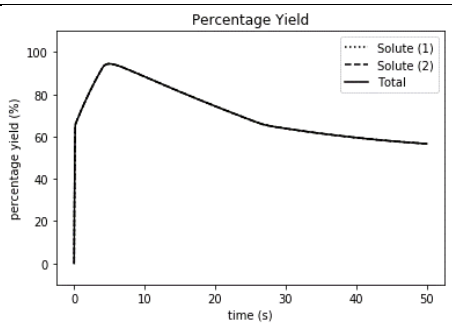
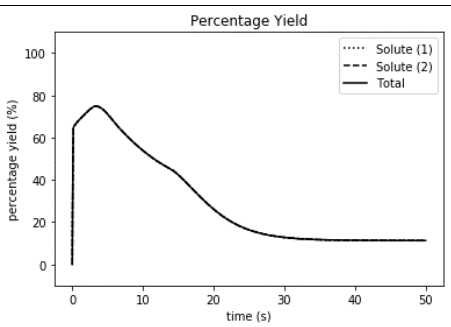
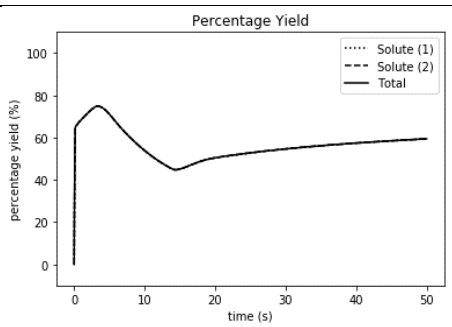
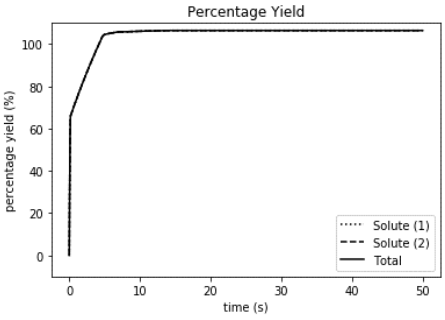
Q_s (Ks^{-1})	**(A) Continuous heating**	**(B) Ramp heating**
0.5		
1.0		
5.0		
Conventional heating		

Table 7.21 – Yield-time plots for scenario 2

7.4.4.2.3 *<u>Scenario 3: low S_s; $D_{s1} \neq D_{s2}$</u>*

All outcomes described in scenario 1 (section 7.4.4.2.1) are applicable here, however while also noting that solute (1) surpasses solute (2) in terms of yield, which is because $D_{s1} > D_{s2}$ (section 7.3.3.2).

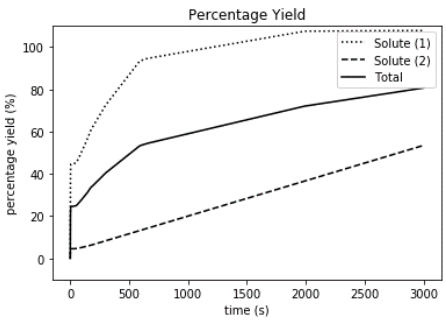
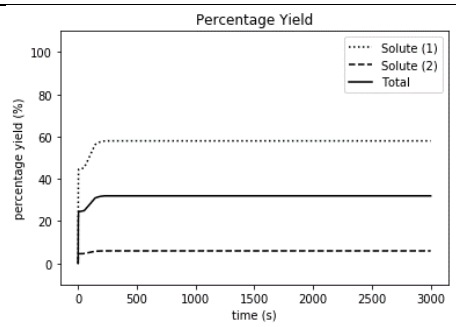
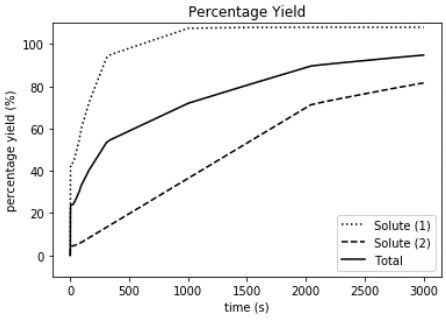
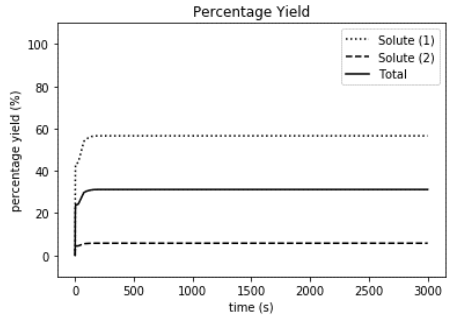
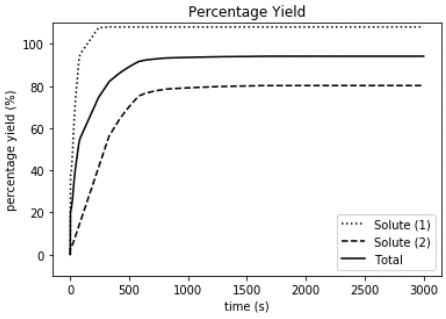
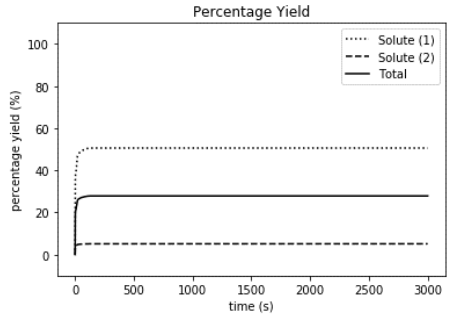
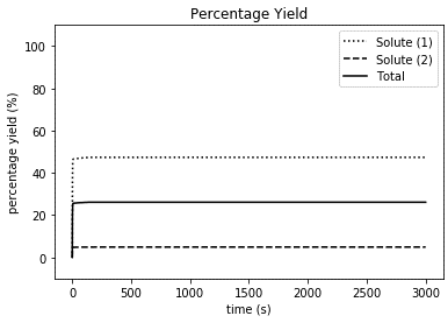
Q_s (Ks^{-1})	(A) Continuous heating	(B) Ramp heating
0.5		
1.0		
5.0		
Conventional heating		

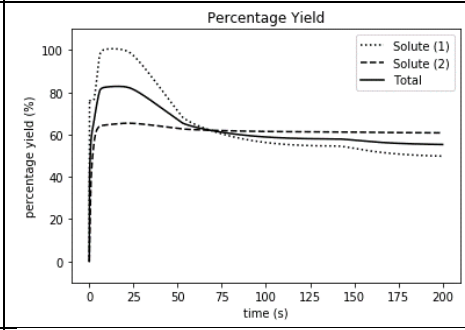
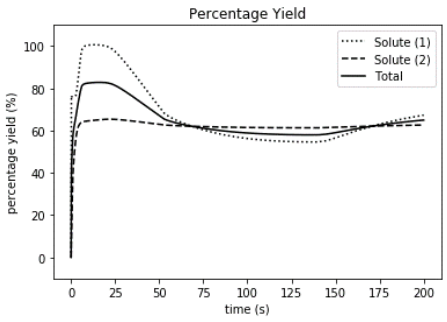
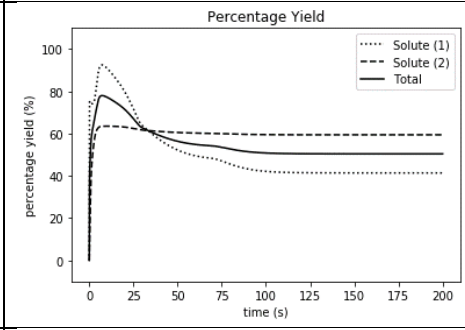
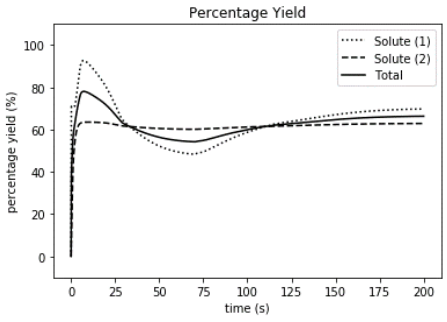
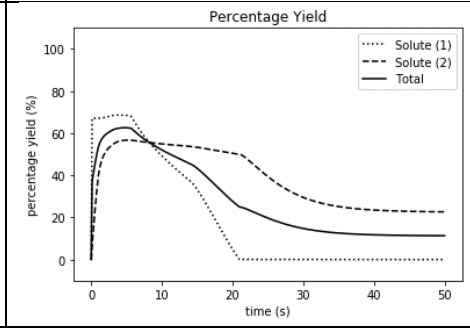
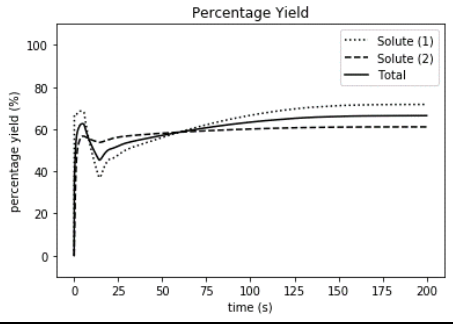
Table 7.22 – Yield-time plots for scenario 3

7.4.4.2.4 *<u>Scenario 4: high S_s; $D_{s1} \neq D_{s2}$</u>*

Key outcomes in bullet points:

- Due to their high solubility, solutes under microwave heating get reabsorbed into the biomass; therefore, the yield is higher under conventional heating (section 7.4.4.1.4).

- Under microwave heating, solute (1) gets reabsorbed more readily than solute (2), which is because $D_{s1} > D_{s2}$. Hence, the yield composition incorporates more of solute (1) at the beginning and more of solute (2) at later stages (section 7.4.4.1.5).
- Solute reabsorption occurs as long as the temperature gradients are maintained in the system. As such, the ramp heating process starts with an extracted mass incorporating more solute (1), which swaps later to larger amounts of solute (2) due to reabsorption. However, the extracts revert once again to larger quantities of solute (1) as thermal steady state is approached (section 7.4.4.1.5).
- Under microwave heating, increasing Q_s accelerates the process but it also causes more significant reabsorption, thereby reducing the overall yield. In this case, applying a high Q_s value of $5\,Ks^{-1}$ under continuous heating, results in a pure solute (2) extract, although the yield composition initially incorporated more solute (1).

Q_s (Ks^{-1})	**(A) Continuous heating**	**(B) Ramp heating**
0.5		
1.0		
5.0		

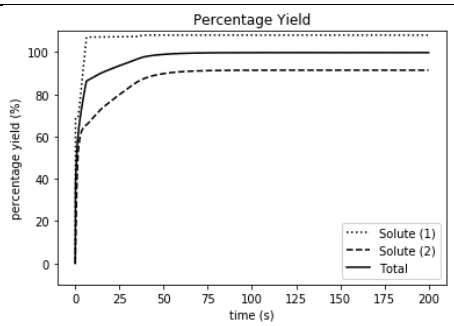
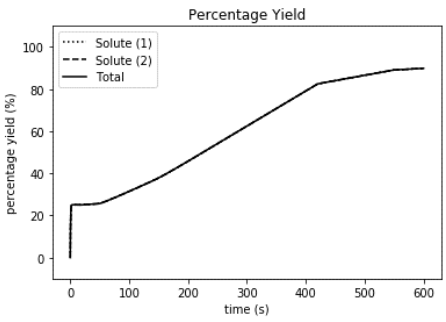
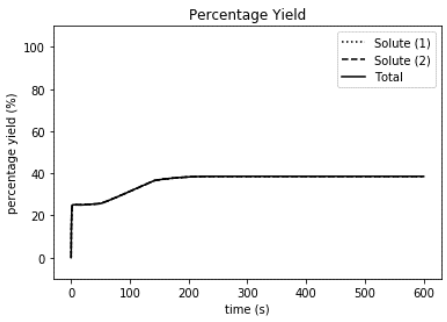
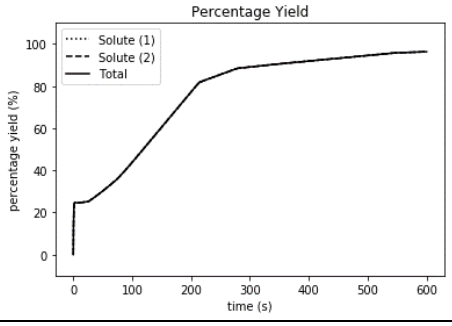
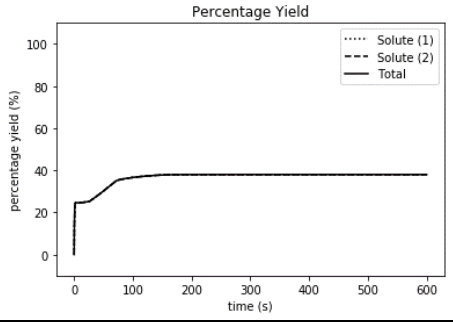
Conventional heating	

Table 7.23 – Yield-time plots for scenario 4

7.4.4.2.5 *Scenario 5: low S_s; D_{s1}=D_{s2} & both increase with rupture*

Key outcomes in bullet points:

- All outcomes described in scenario 1 (section 7.4.4.2.1) are applicable to cases where $Q_s = 0.5 - 1\ Ks^{-1}$.
- Widespread rupture occurs within the biomass on increasing Q_s to high values (beyond $1\ Ks^{-1}$ here). In this scenario, rupture is associated with increasing the diffusivity of solutes, which, under ramp heating, brings about a dramatic step-increase in the yield as Q_s is raised (section 7.4.4.1.3). On the other hand, given that the yields attainable here with continuous heating are already high, they cannot be further increased with rupture. Instead, rupture greatly accelerates the approach to mass equilibrium.

Q_s (Ks^{-1})	(A) Continuous heating	(B) Ramp heating
0.5		
1.0		

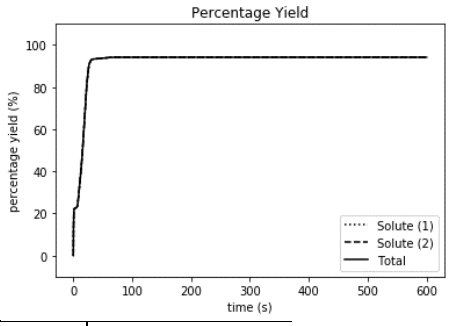
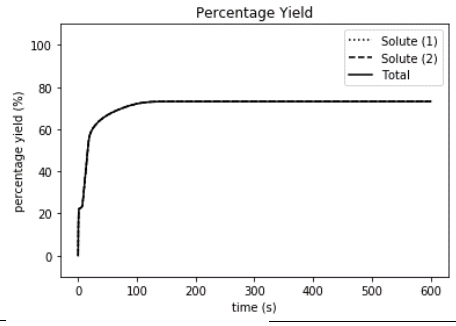
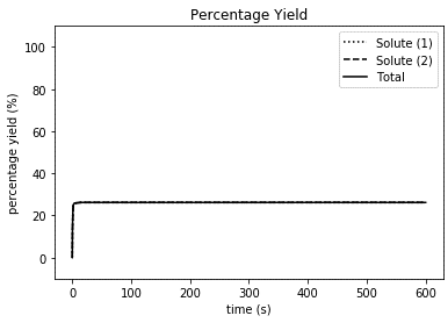
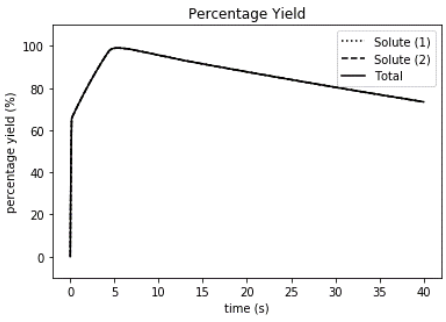
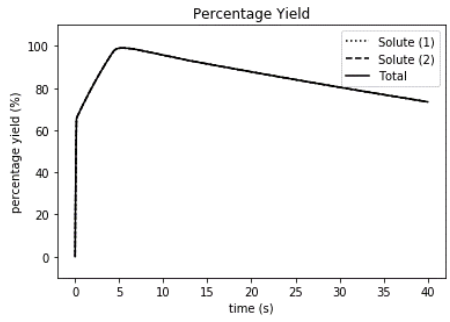
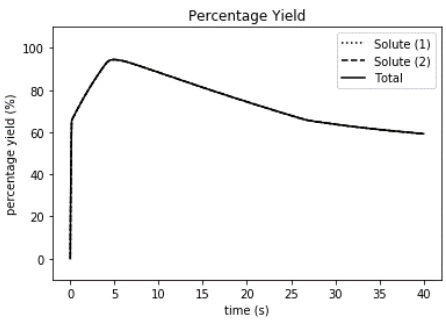
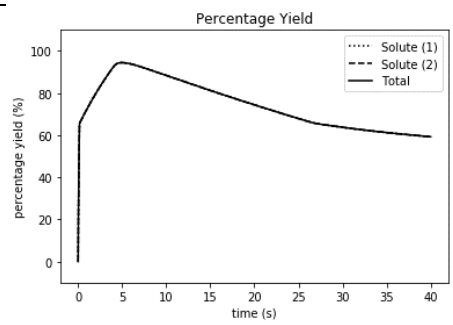
5.0		
Conventional heating		

Table 7.24 – Yield-time plots for scenario 5

7.4.4.2.6 *<u>Scenario 6: high S_s; D_{s1}=D_{s2} & both increase with rupture</u>*

Key outcomes in bullet points:

- Due to the high solubility of solutes, all outcomes described in scenario 2 (section 7.4.4.2.2) are applicable here.
- Although widespread rupture still occurs here at $Q_s > 1\ Ks^{-1}$ as it did in scenario 5 (section 7.4.4.2.5), the effect is not visible because the solutes are being reabsorbed rather than extracted.

Q_s (Ks^{-1})	(A) Continuous heating	(B) Ramp heating
0.5		
1.0		

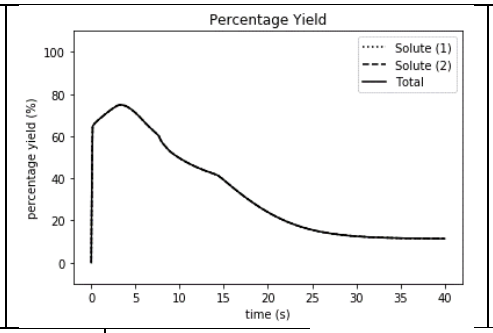
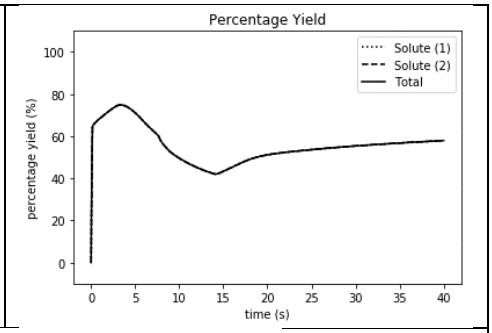
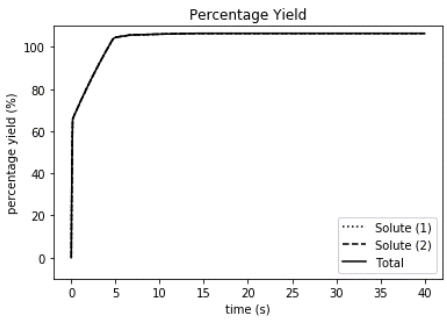
5.0		
Conventional heating		

Table 7.25 – Yield-time plots for scenario 6

7.4.4.2.7 *Scenario 7: low S_s; $D_{s1} \neq D_{s2}$ & values swap with rupture*

Key outcomes in bullet points:

- Due to the low solubility of solutes, microwave heating enhances extraction compared with conventional heating, especially when applying continuous microwave heating (sections 7.4.1 and 7.4.4.1.1).
- For $Q_s \leq 1\ Ks^{-1}$, solute (1) is extracted in larger quantities than solute (2), which is because $D_{s1} > D_{s2}$ (section 7.3.3.2).
- For $Q_s > 1\ Ks^{-1}$, widespread rupture occurs such that the diffusivity pattern changes from $D_{s1} > D_{s2}$ to ${D^R}_{s1} < {D^R}_{s2}$. Hence, at $Q_s = 5\ Ks^{-1}$ (continuous heating) the yield composition swaps from having higher solute (1) quantities initially, to incorporating more of solute (2) at mass equilibrium. On the other hand, rupture still occurs at $Q_s = 5\ Ks^{-1}$ under ramp heating, but due to the time-limited temperature gradients the solute yields do not swap in this case, but instead their magnitudes come closer.

$\boldsymbol{Q_s}$ $\boldsymbol{(Ks^{-1})}$	**(A) Continuous heating**	**(B) Ramp heating**

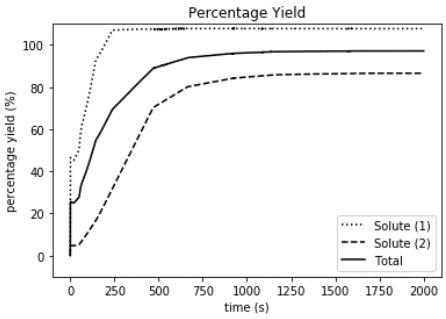
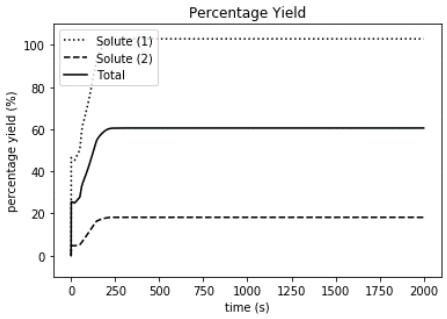
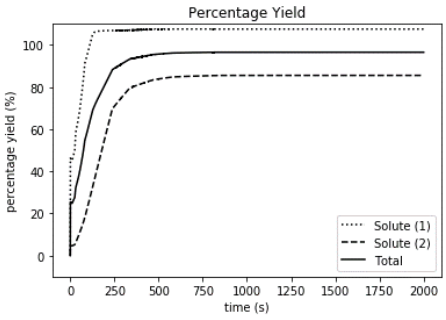
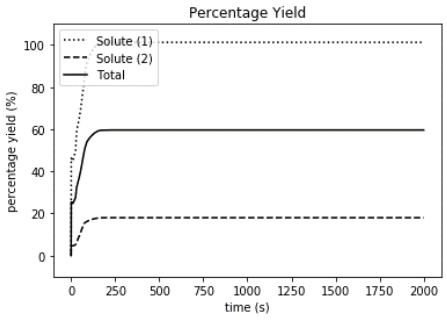
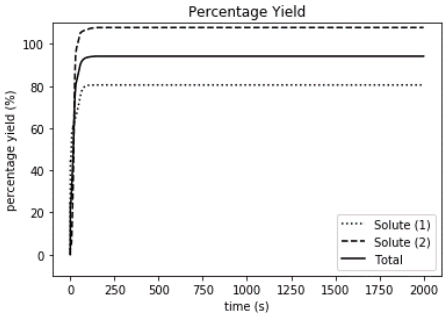
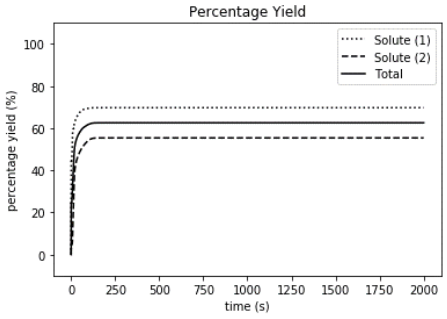
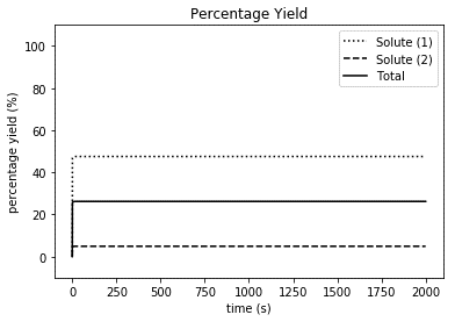
0.5		
1.0		
5.0		
Conventional heating		

Table 7.26 – Yield-time plots for scenario 7

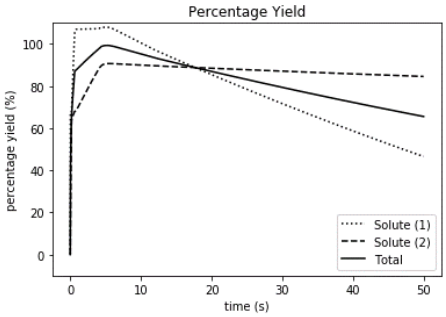
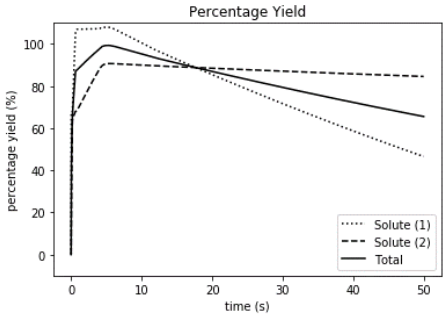
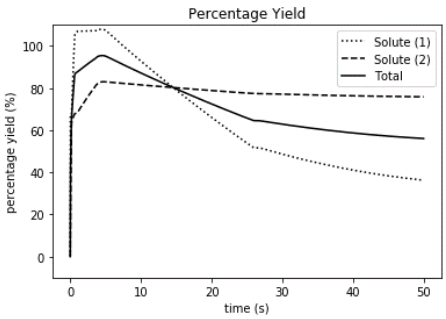
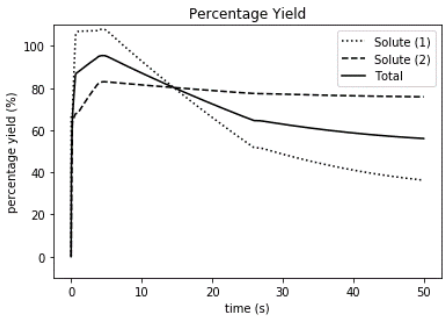
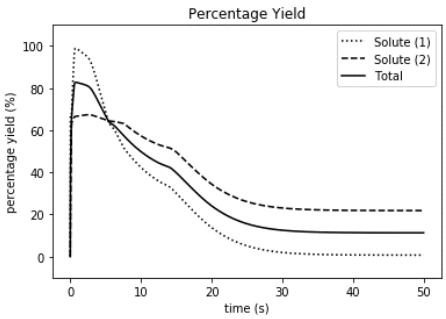
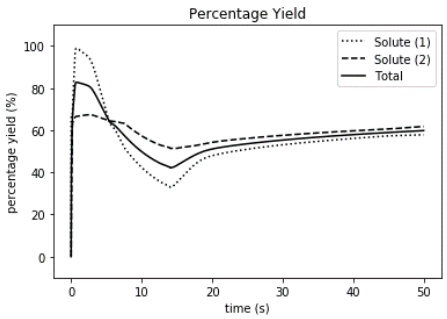
7.4.4.2.8 *<u>Scenario 8: high S_s; $D_{s1} \neq D_{s2}$ & values swap with rupture</u>*

Key outcomes in bullet points:

- Due to the high solubility of solutes, microwave heating suppresses extraction compared with conventional heating. Furthermore, all outcomes described in scenario 4 (section 7.4.4.2.4) are applicable here to cases where $Q_s = 0.5 - 1\ Ks^{-1}$.
- With $Q_s = 5\ Ks^{-1}$ (continuous heating), widespread rupture causes the diffusivities to swap from $D_{s1} > D_{s2}$ to $D^R{}_{s1} < D^R{}_{s2}$. As such, solute (2) gets reabsorbed more readily compared with the case in scenario 4 (section 7.4.4.2.4),

resulting here in a narrower disparity between the yields of the two solutes at mass equilibrium.

- With $Q_s = 5\ Ks^{-1}$ (ramp heating), the yield initially incorporates more of solute (1), which then changes to more of solute (2) as reabsorption is triggered. However, unlike the case in scenario 4 (section 7.4.4.2.4), the yield here does not revert back to higher solute (1) quantities as thermal steady state is approached. This is due to the widespread rupture achieved with which the diffusivities are changed from $D_{s1} > D_{s2}$ to $D^R{}_{s1} < D^R{}_{s2}$. This allows solute (2) to be extracted at higher rates compared with solute (1), thereby preventing a second swap in the extract composition.

Q_s (Ks^{-1})	**(A) Continuous heating**	**(B) Ramp heating**
0.5		
1.0		
5.0		

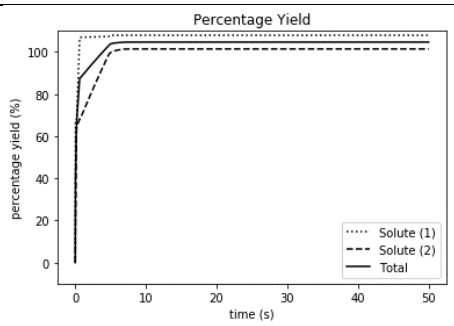
Conventional heating	

Table 7.27 – Yield-time plots for scenario 8

7.5 Summary

In this chapter, it was studied whether enhanced extraction can be achieved without the need for cell rupture, which is widely considered as a rate-limiting step in the process. The analysis was conducted with an improved version of the extraction model developed in Chapter 5, whose key limitations were readdressed here to redefine extraction in biomass-solvent systems away from cell rupture as a rate-limiting step. Some of the modifications introduced include the following: (i) devising a separate differential equation for solute diffusion in the system, which allows solute extraction to be quantified directly; (ii) incorporating the cell walls as independent phases in the system in which both water and solutes can exist, and through which they can flow; (iii) mass transfer has been made possible even during the system's heat-up phase, which enables more accurate understanding of the effects of heating on mass transfer; (iv) expressing heat input to the system in terms of the solvent's heating rate (Q_s), which is physically measurable but also allows fair comparison between microwave and conventional heating. Table 7.1 summarises the key limitations of the model from Chapter 5 and how they were readdressed here. Moreover, the model has been supplemented with additional features, allowing more accurate analyses to be conducted; some of these include: (i) redefining the mass equations to adhere to physical limits, which expands the domain of physical conditions that can be investigated without computing physically meaningless results; (ii) redefining activity (α_W; α_s) in terms of solubility (S_s), which is a more widely available parameter in literature, and more easily measured physically; (iii) allowing solute diffusivities (D_s) to change as physical rupture is achieved in a given phase, thereby enabling the study of some effects that rupture may have on extraction (without it being the rate-limiting step); (iv) enabling thermal conductivity (k) and water/solute diffusivities to vary from one phase to another, thereby delivering the potential for many further investigations to be conducted with this model; (v) introducing the option for non-ideal behaviour of

water/solutes in solution; (vi) supporting an infinite number of solutes in the system each flowing separately (the larger the capacity of the computing machine, the more solutes can be incorporated).

Initially, the model was employed to study extraction at room temperature, where water penetration into the biomass and solute extraction from it were found to occur gradually. At first, mass transfer of water/solutes occurs exclusively between the outermost biomass layer and the solvent, because the biomass otherwise maintains uniform activities within its cells/cell walls, preventing any intra-biomass diffusion. Later on, if the solutes existing within the outermost layer are dissolved completely yet mass equilibrium has not yet been achieved with the solvent phase, then activity gradients get established gradually deeper in the biomass, enabling extraction from within the cell cluster. This process continues getting deeper into the biomass material until either mass equilibrium is achieved with the solvent phase, or all of the available solutes in the material get depleted. This process of gradual extraction limits the recovery of solutes, as the small solute quantities in the outer layer of the biomass could be sufficient to bring about equilibrium to the system. Nevertheless, extraction from the inner biomass can be improved by increasing solubility (S_s), solvent-to-solid ratio (S_R), and solvent purity. Extraction can also be higher when smaller biomass particles are used, and where solutes exist in the cell walls in higher proportions compared with cells. On the other hand, the biomass contains many types of solutes, and some of these will be very similar to each other such that their flow can be described using the same activity/potential gradients. Such solutes compete for extraction, as the component experiencing the lowest resistance to diffusion (i.e., possessing the highest diffusivity) will be extracted in higher quantities at the expense the other solutes. Nevertheless, despite the variety of extract compositions attainable in this case, the total yield will remain consistent as it results from a single activity/potential gradient describing all the similar solutes being extracted.

The model was employed to investigate extraction under microwave and conventional heating. The latter was found to return the same outcomes as in the room temperature extraction case, which is because, in this work, the mass transfer parameters (e.g., solubility, diffusivity, etc) had been kept independent of temperature. Maintaining such condition is necessary to isolate and characterise any unique microwave effects on extraction, not entailing any temperature-induced changes in the

mass transfer parameters. From this, microwaves were shown to improve extraction significantly, causing a dramatic increase in the yield beyond the equilibrium value attained under conventional heating. This improvement can be attributed to the temperature gradients uniquely induced and sustained by microwaves, with which the biomass is consistently warmer than the solvent at thermal steady state. These temperature gradients enhance water influx to biomass cells/cell walls, overriding the gradual layer-by-layer diffusion otherwise observed under non-microwave extraction settings. The enhanced water influx induces high biomass pressures which, in turn, drive additional solute extraction, thereby improving the attainable yield. Even small temperature gradients inducing low positive biomass pressures were shown to improve the yield dramatically; but nonetheless, higher temperature gradients accelerate the process, which is a key advantage in time-limited experiments. However, increasing the temperature gradients may also reduce the maximum attainable yields, since these gradients favour solutes remaining within the biomass, in the same way as they enhance water influx to the material. Hence, the currently discussed microwave extraction mechanism is limited to cases where, the temperature gradients cause more water influx to the biomass than they inhibit solute extraction from it. This gives rise to a pressure force driving solutes outwards, which is larger than the temperature gradient force favouring solutes remaining within the biomass; hence, a net surplus yield is achieved.

The currently discussed microwave extraction mechanism does not require cell rupture, but rather it shows a direct effect exercised by temperature gradients on diffusion, leading to enhanced extraction. Nevertheless, rupture can still be achieved in cells/cell walls upon inducing sufficiently high pressures, and as demonstrated, such event may influence extraction, either through improving the yield or otherwise. In this work, solute diffusivities were allowed to vary upon achieving rupture in a cell/cell wall, but further examples as to how rupture may affect diffusion can be explored in future endeavours beyond this thesis. The key point here is that rupture is not the rate-limiting step in extraction, even though it may affect the process.

The model was used to study different microwave and conventional extraction scenarios incorporating various combinations of solubility (S_s), solute diffusivity (D_s), and heating rate (Q_s) values. It was shown that, microwave heating only enhances extraction at low S_s values, but as S_s is increased extraction gets suppressed, and the

yields eventually become lower than those attainable under conventional heating. This happens because, extraction is naturally enhanced with increasing S_s; however, coupling such enhancement with temperature gradients causes the already extracted solutes to be reabsorbed, following a discrepancy in the activity gradients caused by water flowing into the biomass. Therefore, as S_s is raised the extraction process gets increasingly dominated by a trend where, the yield approaches a maximum and drops thereafter. The maximum yield at a given S_s decreases at higher heating rates (Q_s), as the final yield can also approach 0% at sufficiently high Q_s values. Once again, extraction was shown to favour solutes with higher diffusivities (D_s), but additionally, higher D_s also induces faster reabsorption where such an event takes place. Hence, in cases comprising high S_s, the favoured reabsorption of solutes possessing higher D_s, allows for a selective extraction of the solutes possessing lower D_s.

In addition to the above, extraction was also investigated under ramp microwave heating, as this heating mode could alter the attainable yield trends. Continuous microwave heating sustains the temperature gradients throughout the extraction process, whereas ramp microwave heating only preserves these gradients during the time-limited heat-up phase. The differences in extraction observed between the two modes tend to be case-specific, but generally, ramp heating limits the attainable yields at low S_s and improves them at high S_s, compared with continuous heating. Moreover, enhancing the extraction of low S_s solutes under ramp heating, was found to demand a threshold Q_s. This matches the findings from Chapter 6 and wider literature; however, it is not caused by cell rupture as previously proposed, but instead, it is a direct result of the effects exercised by temperature gradients on diffusion patterns. As Q_s is increased beyond its threshold, the yield increases towards a maximum value before declining once again, as the timeframes during which the temperature gradients are maintained become increasingly shorter. On the other hand, the effects of rupture on extraction are also felt differently under continuous and ramp microwave heating, due to the differences in temperature gradients.

The model was improved from Chapter 5 to enable diffusion to occur not only at thermal steady state, but also during the heat-up phase of the system. This allowed conducting further analyses to understand the effects of mass transfer parameters on microwave heating patterns. All heating patterns observed at thermal steady state match those previously obtained in this thesis; however, the outcomes attained during

the heat-up phase do not match Chapters 3 and 5 or the wider literature. Temperature distribution during heat-up does not only depend on the distribution of dielectric properties, but it is also influenced by mass transfer parameters. For instance, while having $\varepsilon''_{biomass} > \varepsilon''_{solvent}$ is commonly regarded as a condition for attaining higher biomass temperatures during heat-up, such condition was shown here not to hold true in all cases. Instead, the biomass may attain higher temperatures than the solvent even when $\varepsilon''_{biomass} < \varepsilon''_{solvent}$, depending on mass transfer parameters like solubility (S_s), diffusivity (D), and possibly others. This is because, such parameters dictate the amount of matter existing in a given phase, and the diffusion rate to/from it, which affects the rate temperature increase in the phase. In this study, higher S_s and lower D were shown to induce higher temperatures in the biomass than the solvent during heat-up, indicating lower input microwave powers needed to induce a desired temperature gradient. In this work, higher S_s signifies smaller amounts of water in cells initially, meaning that the biomass is lighter and easier to heat. On the other hand, increasing D induces more rapid water influx into the biomass, suppressing the rate of temperature increase and gradually lowering temperature gradients between the biomass and the solvent. Further to S_s and D, any other mass transfer parameter influencing the amount of matter or the rates of diffusion, is also expected to affect heating in similar ways. These results highlight the importance of understanding the interdependence between heat and mass transfer, as this will be necessary to attain the desired temperature distribution in biomass-solvent systems under microwave heating.

The multitude of results obtained from this model indicate its uniqueness and ability to investigate a wide domain of extraction scenarios. This model is the first of kind, as it combines various physical phenomena to propose a novel mechanism as to how microwaves influence extraction patterns.

7.6 Thesis recap

This thesis has discussed the current lack of understanding as to why microwave heating enhances biomass-solvent extraction compared with conventional heating techniques. The extreme heterogeneity of biomasses stipulates that a quantitative set of outcomes from a given experiment cannot be generalised to other studies and scales. As such, a first principles' model is required to conceptualise extraction thereby defining a universally applicable mechanism to explain how microwaves enhance the process. Yet, most models attempted in literature have been empirical in nature,

significantly relying on experimental data input rather than conceptualising the fundamental mechanisms of microwave action in biomass-solvent systems. This constitutes a significant limitation in the efforts aimed at understanding how microwaves enhance extraction, since the attempted models remain confined to the respective experiments and scales employed.

A biomass-solvent extraction model was developed in this thesis, combining microwave heating transfer, mass transfer, and cell expansion mechanics (Chapters 3 and 5). The model was developed at the cellular scale given that this is the smallest of scales relevant to the current work. Since all biomasses concerned here fundamentally consist of cell clusters, a model at this scale would address the following key aspects: (i) providing the ground for a generalised framework to predict extraction in a variety of biomass-solvent systems; and (ii) enabling multidirectional scale up efforts in the future based on the specific needs.

In Chapter 5, the model still accepted cell rupture as the rate-limiting step to achieving enhanced extraction. Hence, the model solely focussed on understanding cell pressure build-up within biomasses and inferring whether these are sufficient to cause widespread cell rupture, thereby enhancing component extraction. Unlike most literature arguments, it was shown that the popular Steam Rupturing hypothesis is not a viable explanation as to how microwaves may enhance cell rupture. Instead, the novel Temperature-Induced Diffusion hypothesis was presented as a more viable alternative, entirely capable of underpinning cell rupture given a variety of realistic physical conditions. This alternative hypothesis also demonstrated that enhanced cell rupture under microwave heating can only be achieved beyond some threshold input power.

A critical experiment was conducted in Chapter 6 to assess the viability of the model and the wider conception that cell rupture is the rate-limiting step of extraction. The experiment entailed conducting biomass-solvent extraction under two microwave heating modes, namely “continuous heating” where constant input power was maintained throughout the process; and “ramp heating” where the power was only maintained for limited periods. While ramp heating showed a step-increase in yield beyond a threshold input power (as predicted in Chapter 5), continuous heating demonstrated gradual extraction acceleration with increasing power, and a unique

steep increase in yield late in the process at high powers. These differing outcomes cannot both be attributed to a single cell rupture event; hence, a more suitable mechanism underpinning both extraction regimes should be conceptualised.

Given the results from Chapter 6, the model was further developed in the current chapter to drive away from cell rupture as the rate-limiting step of extraction. This was conducted by readdressing the key model assumptions made in Chapter 5, resulting in a framework defining extraction as a conventional diffusion process independent of cell rupture. The outcomes, entailing percentage yields rather than just biomass cell pressures, agreed entirely with the empirical results obtained in Chapter 6, both on using continuous and ramp microwave heating modes. Based on the model predictions made in the current chapter, two critical experiments can be conducted to validate the proposed framework: (i) extending the extraction procedure in Chapter 6 to incorporate more input powers and longer processing times (section 6.3.2); and (ii) undertaking mass balance on the solid and liquid components of the biomass-solvent system, to understand how the masses vary as extraction takes place (section 7.4.4.1.4). In experiment (i), if the yield trend for 135W in Figure 6.5A is observed (even if partially) under several powers, then the current mechanism will be suitable to describe extraction (section 6.3.2). Note, however, that the results in such experiment could be affected by a degradation of extracted components, lowering the measurable yields in some cases. On the other hand, if experiment (ii) indicates a gradual increase in the masses of dried solid during the extraction process, then reabsorption of extracted components will be evident. Such outcome will also support the currently proposed framework, as this predicts component reabsorption (section 7.4.4.1.4) unlike cell rupture which is not capable of such prediction.

This model is more suitable to describe and predict biomass-solvent extraction than many other works in literature, which is because, for the first time, it integrates various physical phenomena to conceptualise extraction from fundamental principles. Such approach largely overcomes the inherent problem of extreme heterogeneity in biomasses, which renders many other models and empirical works only applicable to the specific conditions and scales investigated. As such, this model also enables multidirectional scale up efforts in the future based on the specific needs, promising many advantages to the biomass-solvent extraction field.

7.7 Nomenclature

Symbols

ε''	$-$	Dielectric loss factor
ε_0	$\boldsymbol{Fm^{-1}}$	Permittivity of free space
k	$\boldsymbol{Wm^{-1}K^{-1}}$	Thermal conductivity
$\|E\|$	$\boldsymbol{Vm^{-1}}$	Electric field intensity
F	$\boldsymbol{Hz}$	Microwave frequency
δ_p	$\boldsymbol{m}$	Penetration depth
T	$\boldsymbol{K}$	Temperature
ΔT_{max}	$\boldsymbol{K}$	Maximum temperature difference at steady state
$T_{extraction}$	$\boldsymbol{K}$	Extraction temperature set-point; analogous to $T_{saturation}$
Q	$\boldsymbol{W}$	Power
Q_s	$\boldsymbol{Ks^{-1}}$	Heating rate in the solvent phase
C_p	$\boldsymbol{Jmol^{-1}K^{-1}}$	Specific heat capacity
t	$\boldsymbol{s}$	Time
t_{95-M}	$\boldsymbol{s}$	Time required to achieve 95% of mass equilibrium
δt	$\boldsymbol{s}$	Time-step for the numerical mass analysis
P	$\boldsymbol{bar}$	Pressure
P_{max}	$\boldsymbol{bar}$	Maximum pressure recorded in biomass
δP	$\boldsymbol{bar}$	Pressure-step for the numerical mechanical analysis
N	$\boldsymbol{mol}$	Number of particles/molar quantity
J	$\boldsymbol{mols^{-1}m^{-2}}$	Molar flux
L	$\boldsymbol{mol^2KJ^{-1}m^{-1}s^{-1}}$	Mass transfer/diffusion coefficient
D	$\boldsymbol{m^2s^{-1}}$	Diffusivity
$\mathcal{H}$	$-$	Heaviside function
s	$\boldsymbol{Jmol^{-1}K^{-1}}$	Specific entropy
μ	$\boldsymbol{Jmol^{-1}}$	Chemical potential
α	$-$	Activity
γ	$-$	Activity coefficient
n	$-$	Activity-mole fraction relationship exponential
X	$-$	Mole fraction
$\bar{X}$	$-$	Composition (including dissolved and undissolved components)
S_s	$\boldsymbol{g_s g_W^{-1}}$	Solute's solubility in water
R	$\boldsymbol{Jmol^{-1}K^{-1}}$	Universal gas constant (Avogadro's const. times Boltzmann's const.)
ρ	$\boldsymbol{kgm^{-3}}$	Density
Mr	$\boldsymbol{gmol^{-1}}$	Molecular weight
$\%_{s-C}$	$-$	Initial percentage of solutes in cells (volume basis)
$\%_{s-CW}$	$-$	Initial percentage of solutes in cell walls (dry mass basis)
$\%_{s-S}$	$-$	Initial percentage of solutes in solvent (mass basis)
$\%_{W-CW}$	$-$	Initial percentage of water in cell walls (surplus to dry cell wall mass)
σ	$\boldsymbol{MPa}$	Axial/normal stress

ϵ	$-$	Strain
Y_0	$\boldsymbol{MPa}$	Elastic modulus at zero strain
t_{CW}	$\boldsymbol{m}$	Cell wall thickness
A	$\boldsymbol{m^2}$	Cross-sectional area
Φ_{CW}	$-$	Cell wall void fraction
S_R	$\boldsymbol{mLg^{-1}}$	Solvent-to-solid ratio

Subscripts and superscripts

$()_{biomass}$	Biomass property
$()_{solvent}$	Solvent property
$()_0$	Incident/baseline value
$()_{initial}$	Initial value
$()_L$	Property of a condensed state
$()_C$	Property of a cell phase
$()_{CW}$	Property of a cell wall phase
$()^R$	Property of a ruptured phase, e.g., P^R is rupture pressure
$()_W$	Property of water
$()_s$	Property of solutes
$()_{s1}$	Property of solute 1
$()_{s2}$	Property of solute 2
$()^*$	Property at saturation, e.g., ${X_W}^*$ is saturated mole fraction of water
$()_{()}$	Property at a given condition, e.g., $s_{(T_0)}$ is entropy at temperature T_0
$()_x$	Applicable parallel to the *x-direction*
$()_y$	Applicable parallel to the *y-direction*
$()_z$	Applicable parallel to the z-*direction*
$()_{i/j}$	Property of a phase "i" or "j"
$()_{i-j}$	Property applicable across the boundary of phases "i" and "j"
$()_{ijk}$	Property of the spatial numerical point ijk, i in the *x-direction;* j in the y-*direction;* k in the z-*direction*

8 GENERAL CONCLUSIONS AND RECOMMENDATIONS

The aim of this chapter is to summarise the conclusions of the current work, and to outline recommendation for future work.

The format of this chapter is as follows:

8.1 Introduction 286
8.2 Model construction 286
8.2.1 Chapter 3: microwave heat transfer model 286
8.2.2 Chapter 5: heat-mass-mechanical model for cell rupture 287
8.2.3 Chapter 7: extraction model independent of cell rupture 287
8.2.4 Recommendations for future work 288
8.3 Heating/heat transfer in biomass-solvent systems 289
8.3.1 Chapter 3: distinctive characteristics of microwave heating 289
8.3.2 Chapter 7: microwave heating under variable mass 290
8.3.3 Recommendations for future work 291
8.4 Biomass-solvent extraction in the context of cell rupture 292
8.4.1 Chapter 4: temperature gradients and mass transfer 292
8.4.2 Chapter 5: Steam Rupturing vs Temperature-Induced Diffusion 292
8.4.3 Chapter 6: empirical evidence for cell rupture 293
8.4.4 Recommendations for future work 295
8.5 Biomass-solvent extraction away from cell rupture 295
8.5.1 Room temperature extraction 295
8.5.2 Thermal extraction 296
8.5.3 Recommendations for future work 298
8.6 Nomenclature 300

8.1 Introduction

The aim of this thesis was to understand the influence of microwave heating on extraction in biomass-solvent systems, and to establish whether microwaves can fundamentally alter the extraction patterns in these systems compared with conventional heating techniques. This work has mainly been focussed on developing a mathematical model for biomass-solvent extraction at the cellular scale, comprising electromagnetic heating, heat transfer, mass transfer, and cell/cell wall expansion mechanics. Such fundamental characterisation of extraction is currently lacking, but nonetheless, it is an essential step towards enabling process design, optimisation, and industrialisation. Hence, this model addresses a significant gap in knowledge, providing unprecedented insights as to how the various physical parameters influence extraction. Such level of detail is otherwise extremely challenging (if at all possible) to attain through experimentation, given the currently available tools and capabilities.

The objectives set out for this work can be summarised thus: (i) constructing a microwave heat transfer model for biomass-solvent systems capable of depicting their key geometrical features; (ii) understanding the link between heat transfer and diffusion, and incorporating this into the existing heat model, while also extending the model altogether to include mass transfer and pressure build-up; (iii) using the model to investigate the currently accepted hypotheses as to how microwaves enhance extraction through cell rupture; (iv) evaluating whether cell rupture is evident empirically, and then improving/modifying the existing model based on the attained outcomes.

8.2 Model construction

8.2.1 Chapter 3: microwave heat transfer model

A model was constructed to describe microwave heat transfer in biomass-solvent systems at the cellular scale, while also capturing some key geometrical features of biomass including cell geometry/arrangement and linkage through a network of cell walls.

This model enables microwave heat transfer to be simulated under a variety of heating and geometrical conditions, including $\varepsilon''_{biomass}$, $\varepsilon''_{solvent}$, δ_p, k, C_p, S_R, ρ_L, cell dimensions, cell cluster size, F, and $|E|_0$.

8.2.2 Chapter 5: heat-mass-mechanical model for cell rupture

The model developed in Chapter 3 was further expanded here to include mass transfer and cell expansion mechanics. The three elements of heat, mass, and mechanics were interlinked in two ways: firstly, the rate of diffusion was expressed in terms of the chemical potential, a parameter depending on activity, pressure, and temperature; secondly, cell pressure was made dependent upon the mass and density of water held within the cell, where such a dependency was established using an appropriate cell pressure-volume relationship.

With its ability to compute heat/mass transfer and cell mechanics simultaneously, this model enables understanding whether the enhanced extraction observed with microwave heating can be attributed to cell rupture. Following the intention to specifically study the likelihood cell rupture, some key assumptions were made here to draw a focussed analysis on the desired phenomenon, and to eliminate any further complications. These key assumptions can be summarised in the following points: (i) only water was permitted to diffuse in the system, and it was made to flow directly between cells and solvent, while assuming the cell walls to be part of the solvent phase; (ii) mass transfer was assumed to occur after thermal steady state had been achieved in the system.

This model predicts cell pressure build-up given a wide range of heat, mass, mechanical, and geometrical conditions, some of which include $\varepsilon''_{biomass}$, k, $|E|_0$, ρ_L, $s_{W(T_0)}$, C_p, $T_{extraction}$, $\alpha_{W_{initial}}$, Φ_C, D, S_R, cell dimensions, t_{CW_0}, Y_0, and others.

8.2.3 Chapter 7: extraction model independent of cell rupture

The model developed in Chapter 5 accepts beforehand that cell rupture is the rate-limiting step for achieving enhanced extraction under microwave heating. While this could be the case in some situations, it might not be true in others where cell rupture is not evident, yet microwaves can still enhance extraction. It was, therefore, necessary to further extend the model to predict extraction trends away from cell rupture, thereby widening its predictability to an even larger domain of biomass-solvent systems.

The model from Chapter 5 was improved here through readdressing its key assumptions, all of which followed the principal presumption on cell rupture. Some of these assumptions include disregarding solute diffusion; assuming the cell walls as part of the solvent phase for mass transfer purposes; assuming extraction occurs at

thermal steady state; and others. Furthermore, the model was also improved by introducing some physically measurable user inputs in the place of others that are less accessible experimentally. For example, the electric field intensity ($|E|_0$) was replaced with an input heating rate parameter describing solvent heating (Q_s); moreover, initial cell water activity ($\alpha_{W_{initial}}$) was replaced with an input solubility parameter dictating the extent to which solutes dissolve in water (S_s).

This improved model simulates extraction quantitatively at room temperature, but also under both microwave and conventional heating. It incorporates heat transfer, mass transfer of water/solutes, and pressure build-up within both cells and cell wall fragments. The model is also capable of altering the extraction trends (e.g., through changing solute diffusivity; D_s) on achieving physical rupture in any given phase, thereby allowing some understanding to be formulated on how rupture may affect extraction trends (see Table 7.1 for all model features). The model predicts extraction trends given a wide range of heat, mass, mechanical, and geometrical conditions, some of which include S_s, D_W, D_s, S_R, biomass particle size, ideal behaviour of solutions, $\%_{s-S}$, solute distribution amongst cells and cell walls, $\varepsilon''_{biomass}$, k, $|E|_0$, and others.

8.2.4 Recommendations for future work

Future work should focus on the following:

- Devising appropriate homogenisation techniques to expand the model to much larger scales, while preserving the currently attainable heat transfer, mass transfer, and mechanical trends/features.
- Further developing the system's geometry to better resemble different biomass materials, e.g., by incorporating cells of various shapes and arrangements, and through introducing capillaries into the structure of the biomass separating different cell clusters.
- Devising a more dynamic numerical solver capable of automatically adjusting its internal tolerances as the outcomes are being computed. Such solver would be well adapted to the current model specifically, reducing its demand for computational effort, but also enhancing its ability to compute extraction under more extreme scenarios which are currently inaccessible.
- Updating the model's numerical framework based on the demands set out by any attempts for homogenisation and/or alterations to the model's geometry.

- Expanding the model to incorporate solutes behaving independently, as opposed to their current collective behaviour in which they follow a single diffusion driving force.
- Expanding the definition of cell/cell wall rupture and introducing more sophisticated aspects as to how it may influence extraction patterns.

8.3 Heating/heat transfer in biomass-solvent systems

8.3.1 Chapter 3: distinctive characteristics of microwave heating

In this chapter, heat transfer was studied in the absence of mass transfer, meaning that the latter did not influence heating here.

Microwave heating was shown to induce a non-uniform temperature distribution in biomass materials at thermal steady state, with a maximum temperature around the centre of the cell cluster, and a minimum value at the biomass-solvent boundary. These temperature gradients arise from the competing effects of volumetric heating and normal heat transfer; therefore, such temperature distribution cannot be sustained with conventional heating techniques. It was shown here that, as long as $\varepsilon''_{biomass} > 0$, biomass materials of the investigated scales are likely to always attain higher temperatures than the solvent at thermal steady state. This finding does not agree with literature, where it has been suggested that the biomass will only attain higher temperatures than the solvent if $\varepsilon''_{biomass} > \varepsilon''_{solvent}$. Instead, it has been shown here that, this only applies prior to achieving thermal steady state (i.e., during heat-up); however, once steady state is achieved, sustaining a higher temperature in the biomass becomes solely dependent on whether or not $\varepsilon''_{biomass} > 0$.

On the other hand, the magnitudes of steady state temperature gradients are affected by the quantities of the various heating parameters, which include $\varepsilon''_{biomass}$, $\varepsilon''_{solvent}$, δ_p, k, C_p, S_R, ρ_L, cell dimensions, cell cluster size, F, and $|E|_0$. Of these, thermal conductivity (k) was particularly interesting to study, as this parameter has been shown to affect the steady state temperature magnitudes, despite such effect being otherwise non-applicable under conventional settings. Thermal conductivity (k) is normally only associated with heat transfer rates; however, biomass temperatures were shown here be highly sensitive to changes in k. This is especially true when larger biomass cell clusters are being heated with microwaves, or when the k value of such materials being irradiated is small (i.e., they are poor heat conductors). The effect

of k on the steady state biomass temperature, can even be more pronounced than that exercised by the dielectric loss factor of the material ($\varepsilon''_{biomass}$), yet this key parameter has rarely been considered in microwave heating studies. This constitutes a significant gap in understanding microwave heating patterns in biomass-solvent systems.

Further to dictating temperature magnitudes at thermal steady state, the various heating parameters also influence the time required to arrive at steady state. Of these, electric field intensity ($|E|_0$) was found to be the primary influencer on the heating duration required to arrive at steady state. This is a logical outcome given that, $|E|_0$ directly describes the input microwave power, which logically dictates the heating rate of the system. Interestingly, nonetheless, the model was shown to reasonably predict the heating timeframes for a large domain of $|E|_0$ values, when benchmarked against empirical findings. Although these timeframes vary in orders of magnitude with such large changes in $|E|_0$, the model yielded reasonable outcomes both with low $|E|_0$ used in some microwave extraction studies, and with high $|E|_0$ used in some microwave pyrolysis studies. This key feature confirms the model's robustness and enables its future adaptation to serve a wide range of microwave processes for biomass-solvent systems.

8.3.2 Chapter 7: microwave heating under variable mass

The model was extended in this chapter to enable both heat transfer and mass transfer to occur at the same time, making it possible to further analyse heating patterns under variable mass.

The previous observations regarding steady state temperature distribution (section 8.3.1) were all reconfirmed here, some of which include biomass possessing higher temperatures than solvent given that $\varepsilon''_{biomass} > 0$; thermal conductivity ($k$) significantly influencing the steady state temperature magnitudes; and the heating rate (Q_s) being the most influential parameter in dictating the heating duration required to achieve thermal steady state. However, unlike thermal steady state, the outcomes attained here during the heat-up phase (i.e., prior to achieving thermal steady state) do not match those from Chapter 3 or the wider literature. Temperature distribution during heat-up does not only depend on the distribution of dielectric properties, but it is also influenced by mass transfer parameters. For instance, while $\varepsilon''_{biomass} >$

$\varepsilon''_{solvent}$ is commonly regarded as a condition for attaining higher biomass temperatures during heat-up, such condition was shown here not to hold true in all cases. Instead, the biomass may attain higher temperatures than the solvent even when $\varepsilon''_{biomass} < \varepsilon''_{solvent}$, depending on mass transfer parameters like solubility (S_s), diffusivity (D), and possibly others. This is because, such parameters dictate the amount of matter existing in a given phase and the diffusion rate to/from it, which affects the rate temperature increase in the phase. In this study, higher S_s and lower D were shown to induce higher temperatures in the biomass during heat-up, indicating lower input microwave powers needed to induce a desired temperature gradient. Higher S_s in this work signifies smaller amounts of water in cells initially, meaning that the biomass is lighter and easier to heat up. On the other hand, increasing D induces more rapid water influx into the biomass, suppressing the rate of temperature increase and gradually lowering temperature gradients between the biomass and the solvent. Further to S_s and D, any other mass transfer parameter influencing the amount of matter or the rates of diffusion, is also expected to affect heating in similar ways.

These results highlight the importance of understanding the interdependence between heat and mass transfer, as this will be necessary to attain the desired temperature distribution in biomass-solvent systems under microwave heating.

8.3.3 Recommendations for future work

Future work should focus on the following:

- Adjusting the model's electric field to incorporate more meaningful patterns depicting different wave propagation modes in various microwave cavities. This will be necessary as the model gets homogenised and expanded to larger scales. It will also enable further analyses to be conducted.
- Introducing a framework whereby temperature can vary due to bulk flow. This will enable the model to be used in flow/semi-flow extraction settings, in addition to its current batch setting.
- Obtaining more dielectric and heating data for a variety of materials through empirical means. Such data will be of utmost benefit in conducting further heating/heat transfer studies using the model.

8.4 Biomass-solvent extraction in the context of cell rupture

8.4.1 Chapter 4: temperature gradients and mass transfer

It was conceptually demonstrated that, diffusion can occur between two phases possessing unequal temperatures, where particles are likely to flow from the cooler phase to the warmer phase. This is analogous to activity-driven diffusion (i.e., Fick's law) and pressure-driven diffusion (i.e., osmotic potential analogy); moreover, this description matches both empirical evidence (e.g., the Ludwig-Soret effect) and literature proposals.

The three driving forces for mass transfer, including activity, pressure, and temperature, were all condensed into a single mathematical expression describing the chemical potential (μ), which was subsequently used to quantitatively describe diffusion in the biomass-solvent extraction model (section 8.2.2).

8.4.2 Chapter 5: Steam Rupturing vs Temperature-Induced Diffusion

Microwave heating is mainly thought to enhance extraction by inducing structural alterations and cell rupture within biomass materials. However, the mechanisms through which such alterations are induced have mainly been discussed qualitatively, and this limits the ability to understand these mechanisms and apply them to various systems and scales. Nevertheless, some quantitative attempts have been made, such as in the Steam-Rupturing and Temperature-Induced Diffusion hypotheses. Both these hypotheses accept cell rupture as the rate-limiting step to achieving enhanced extraction; moreover, they both argue that cell rupture is more likely under microwave heating than it is under conventional heating. However, the two hypotheses differ in the mechanisms they propose as to how cell rupture can be achieved: (i) Steam-Rupturing stipulates the need to evaporate intracellular moisture, thereby generating steam at sufficient pressures to cause cell rupture; (ii) Temperature-Induced Diffusion proposes that the microwave-induced temperature gradients between biomass and solvent, are sufficient to drive surplus water influx into biomass cells, thereby inducing pressures high enough to cause cell rupture.

The two hypotheses were assessed in this thesis for their ability to explain cell rupture under microwave heating. The Steam-Rupturing hypothesis was investigated from a heat transfer viewpoint, as it was attempted to understand whether the highest attainable biomass temperatures can underpin intracellular steam generation at the required pressures for cell rupture. It was shown that, in all but the most extreme of

physical conditions, the biomass temperatures obtained under microwave heating did not suffice to underpin the Steam-Rupturing hypothesis. Cell rupture should, therefore, be caused by another mechanism.

Temperature-Induced Diffusion was assessed using the combined heat-mass-mechanical model developed in Chapter 5. It as shown that, this hypothesis can underpin cell rupture entirely when using a realistic set of input heating, diffusion, mechanical, and geometrical parameters. Furthermore, the various sensitivity analyses conducted also demonstrated the applicability of this hypothesis to a potentially wide range of biomass-solvent systems where cell rupture may occur. Therefore, if cell rupture is the governing mechanism for enhanced extraction under microwave heating, then Temperature-Induced Diffusion is the underpinning cause of this rupture.

On the other hand, achieving widespread cell rupture within biomasses was predicted to occur only beyond a threshold microwave power, whose magnitude depends on the physical conditions of the system. Input power can be represented with the electric field intensity ($|E|_0$); hence, a range of threshold $|E|_0$ values required for widespread cell rupture under various conditions, were presented in Table 5.10.

In summary, Temperature-Induced Diffusion was demonstrated as a more viable explanation as to how microwaves may induce cell rupture in biomass-solvent systems. This is a key outcome not only due to the novelty of the approach undertaken in this thesis, but also because the results challenge the Steam-Rupturing hypothesis, which is more popular compared with the recently proposed Temperature-Induced Diffusion hypothesis.

8.4.3 Chapter 6: empirical evidence for cell rupture

It had been summarised in Chapter 5 that, should cell rupture be the rate-limiting step to enhanced extraction, then Temperature-Induced Diffusion is the fundamental basis upon which such rupture can be achieved under microwave heating. In Chapter 6, a critical experiment was intended to observe whether extraction can be attributed to a rate-limited step like cell rupture. This is necessary as it indicates whether the underlying cell rupture mechanism should be re-evaluated, and whether the model from Chapter 5 should be further improved.

Extraction was investigated under two microwave heating modes, namely continuous microwave heating and ramp microwave heating. Continuous heating

denotes non-stop heating of the sample with a constant input power for the full extraction duration. In contrast, ramp microwave heating signifies maintaining a constant input power only as long as the sample's temperature is increasing, but once a target temperature is achieved, heating would be stopped or significantly suppressed. These two heating modes deliver energy to the sample differently; hence, the extraction trends obtained could also be different. Therefore, when attempting to evaluate the effect of cell rupture on extraction, it is necessary to understand the extraction trends under both continuous and ramp microwave heating.

This chapter investigated extraction of pectin from onion peels under both continuous and ramp microwave heating. The trends observed under ramp heating were fully explicable with cell rupture because, a step-increase in the yield was observed on increasing the input power to a threshold value. These outcomes match the predictions made in Chapter 5, as well as some literature studies investigating ramp microwave heating. However, the results achieved with continuous microwave heating do not fully match the idea of cell rupture. Firstly, extraction accelerates gradually on raising the input power under continuous heating, and this cannot be explained through cell rupture because a similar acceleration is not observed under ramp microwave heating. Secondly, a sharp increase in the yield was observed at sufficiently high input powers, but the cause of this effect is unclear as it cannot be matched with the step-change observed at the same input powers under ramp heating.

Extraction was also observed at room temperature, as yields were attained even through no thermally induced cell rupture could have occurred, albeit at very slow rates. Unlike what has been suggested in literature, this outcome indicates that polymers like pectin can be extracted even without any heating or structural modifications in the biomass. As such, proposing an alternative mechanism for microwave extraction away from cell rupture, would not violate the fundamental principles governing extraction.

These results hint towards an alternative mechanism governing enhanced extraction under microwave heating; hence, re-evaluation of the model from Chapter 5 is required. Extraction could still be affected by physical rupture, but this is not necessarily the rate-limiting step of the process.

8.4.4 Recommendations for future work

Future work should focus on the following:

- Improving the thermodynamics of mass transfer even further where necessary, and obtaining more comprehensive datasets for the entropies, activities, and vapour pressures of water and other solutes. This will enable further, more detailed mass transfer analyses to be conducted.
- Expanding the cell pressure-volume relationship to incorporate responses of collective tissues rather than single cells. This will enable model homogenisation and allow further coupling with experimental data.
- Expanding the investigations on pressure and cell rupture to incorporate lignocellulosic biomasses, which are currently not included. This will require revisiting the cell expansion mechanics to account for mechanical properties of rigid secondary cell walls.
- Conducting further experiments to investigate cell rupture and extraction, while implementing longer heating durations but also using a larger domain of biomass-solvent systems and input microwave powers. Expanding the analysis to incorporate conventional heating under reflux can also be carried out. These tasks will require detailed design/planning to arrive at a setup that is robust and safe.

8.5 Biomass-solvent extraction away from cell rupture

8.5.1 Room temperature extraction

Biomass-solvent extraction was re-investigated in Chapter 7 to understand how microwaves may enhance extraction without the need for cell rupture. For this purpose, the model from Chapter 5 was further developed through addressing its key limitations, and by introducing an appropriate framework to quantify solute extraction (section 8.2.3).

Initially, the model was used to investigate extraction at room temperature, where water penetration into a biomass and solute extraction from it were found to occur gradually. At first, mass transfer of water/solutes occurs exclusively between the outermost biomass layer and the solvent, as the biomass otherwise maintains uniform activities within its cells/cell walls, preventing any intra-biomass diffusion. Later on, activity gradients get established gradually deeper into the material, enabling extraction from within the cell cluster up to the point when mass equilibrium is achieved in the biomass-solvent system. This process of gradual extraction limits the

recovery of solutes, as the small solute quantities in the outer layer could be sufficient to induce equilibrium in the system. Nevertheless, extraction from the inner biomass can be improved through increasing solubility (S_s), solvent-to-solid ratio (S_R), and solvent purity. Extraction can also be higher when smaller biomass particles are used, and where the desired solutes exist in cell walls in higher proportions compared with cells. On the other hand, the biomass contains many types of solutes, and some of these will be very similar to each other such that their diffusion can be described using the same activity/potential gradients. Such solutes compete for extraction, as the component experiencing the lowest resistance to diffusion (i.e., possessing the highest diffusivity) will be extracted in higher quantities than the other solutes. Nevertheless, despite the variety of extract compositions attainable in this case, the total yield will remain consistent as it results from a single activity/potential gradient.

8.5.2 Thermal extraction

The model was employed to investigate extraction under microwave and conventional heating. The latter was found to induce the same outcomes as in the room temperature extraction case, which is because, in this work, the mass transfer parameters (e.g., solubility, diffusivity, etc) had been kept independent of temperature. Maintaining such condition is necessary to isolate and characterise any unique microwave effects on extraction, which do not entail any temperature-induced changes in the mass transfer parameters. From this, microwaves were shown to improve extraction significantly, causing a dramatic increase in the yield beyond the equilibrium value attained under conventional heating. This improvement can be attributed to the temperature gradients uniquely induced and sustained by microwaves, in which the biomass is consistently warmer than the solvent at thermal steady state. These temperature gradients enhance water influx to biomass cells/cell walls, overriding the gradual layer-by-layer diffusion otherwise observed under non-microwave extraction settings. The enhanced water influx induces high biomass pressures which, in turn, drive additional solute extraction, thereby improving the attainable yields. Even small temperature gradients inducing low positive biomass pressures were shown to improve the yield dramatically; but nonetheless, higher temperature gradients accelerate the process, which is a key advantage in time-limited experiments. However, increasing the temperature gradients may also reduce the maximum attainable yields, since these gradients favour solutes remaining within the

biomass just as they enhance water influx to the material. Hence, the currently discussed microwave extraction mechanism is limited to cases where, the temperature gradients cause more water influx to the biomass than they inhibit solute extraction from it. This gives rise to a pressure force driving solutes outwards, which is larger than the temperature gradient force favouring solutes remaining within the biomass; hence, a net surplus yield is achieved.

The currently discussed microwave extraction mechanism does not require cell rupture, but instead, it shows a direct effect exercised by temperature gradients on diffusion, leading to enhanced extraction. Nevertheless, rupture can still be achieved in cells/cell walls upon inducing sufficiently high pressures, and as demonstrated, such event may influence extraction either through improving the yields or otherwise. In this work, solute diffusivities were allowed to vary upon achieving rupture in a cell/cell wall, but further examples as to how rupture may affect diffusion can be explored in future endeavours beyond this thesis. The key point here is that rupture is not the rate-limiting step in extraction, even though it may affect the process.

The model was used to study different microwave and conventional extraction scenarios incorporating various combinations of solubility (S_s), solute diffusivity (D_s), and heating rate (Q_s) values. It was shown that, microwave heating only enhances extraction at low S_s values, but as S_s is increased extraction gets suppressed, and the yields eventually become lower than those attainable under conventional heating. This happens because, extraction is naturally enhanced with increasing S_s; however, coupling such enhancement with temperature gradients causes the already extracted solutes to get reabsorbed, following a discrepancy in the activity gradients caused by water flowing into the biomass. Therefore, as S_s is raised the extraction process gets increasingly dominated by a trend where, the yield approaches a maximum and it drops thereafter. The maximum yield at a given S_s decreases at higher heating rates (Q_s), as the final yield can also approach 0% at sufficiently high Q_s values. Once again, extraction was shown to favour solutes with higher diffusivities (D_s), but additionally, higher D_s also induces faster reabsorption where such an event takes place. Hence, in cases comprising high S_s, the favoured reabsorption of solutes possessing higher D_s allows for a selective extraction of the solutes possessing lower D_s.

In addition to the above, extraction was also investigated under ramp microwave heating, as this heating mode could alter the attainable yield trends. Continuous microwave heating sustains the temperature gradients throughout the extraction process, whereas ramp microwave heating only preserves these gradients during the time-limited heat-up phase. The differences in extraction observed between the two modes tend to be case-specific, but generally, ramp heating limits the attainable yields at low S_s and improves them at high S_s, compared with continuous heating. Moreover, enhancing the extraction of low S_s solutes under ramp heating, was found to demand a threshold Q_s. This matches the findings from Chapter 6 and wider literature; however, it is not caused by cell rupture as previously proposed, but instead, it is a direct result of the effects exercised by temperature gradients on diffusion patterns. As Q_s is increased beyond its threshold, the yield increases towards a maximum value before declining once again, as the timeframes during which the temperature gradients are maintained become increasingly shorter. On the other hand, the effects of rupture on extraction are also felt differently under continuous and ramp microwave heating, due to the differences in temperature gradients.

8.5.3 Recommendations for future work

Future work should focus on the following:

- Conducting critical experiments to validate the proposed extraction framework as summarised in section 7.6.
- Investigating extraction in systems with solutes behaving independently (i.e., each represented by its own activity and chemical potential values).
- Defining some input parameters in terms of others (e.g., dielectric loss and thermal conductivity as functions of water activity). This will lay the foundation for further extraction analyses and predictions.
- Further investigating the effect of solute entropy on whether microwaves enhance extraction.
- Further studying the effects on non-ideal solute behaviour on extraction (the model enables different degrees of ideal behaviour to be imposed upon solutes existing cells, cell walls, and solvent).
- Introducing thermal degradation of solutes into the extraction framework, in order to understand the effects this may have on the results, but also to resemble real-world situations more thoroughly.

- Expanding the cell/cell wall pressure-volume relationships to incorporate the response of collective tissues rather than single cells (section 8.4.4).
- Improving the model through homogenisation and upscaling; defining rupture more comprehensively; and further developing the system's geometry (section 8.2.4).
- Acquiring further experimental data on the solubility, diffusivity, entropy, dielectric properties, etc of various solutes, and establishing the temperature/activity dependence of these parameters more clearly.

8.6 Nomenclature

Symbols

ε''	$-$	Dielectric loss factor
δ_p	$\boldsymbol{m}$	Penetration depth
k	$\boldsymbol{Wm^{-1}K^{-1}}$	Thermal conductivity
C_p	$\boldsymbol{Jg^{-1}K^{-1}}$	Specific heat capacity
$\lvert E \rvert$	$\boldsymbol{Vm^{-1}}$	Electric field intensity
F	$\boldsymbol{Hz}$	Microwave frequency
$T_{extraction}$	$\boldsymbol{K}$	Extraction temperature set-point; analogous to $T_{saturation}$
Q_s	$\boldsymbol{Ks^{-1}}$	Heating rate in the solvent phase
S_R	$\boldsymbol{mLg^{-1}}$	Solvent-to-solid ratio
ρ	$\boldsymbol{kgm^{-3}}$	Density
s	$\boldsymbol{Jmol^{-1}K^{-1}}$	Specific entropy
μ	$\boldsymbol{Jmol^{-1}}$	Chemical potential
α	$-$	Activity
D	$\boldsymbol{m^2s^{-1}}$	Diffusivity
Φ_C	$-$	Initial cell void fraction
t_{CW}	$\boldsymbol{m}$	Cell wall thickness
Y_0	$\boldsymbol{MPa}$	Elastic modulus at zero strain
S_s	$\boldsymbol{g_s g_W^{-1}}$	Solute's solubility in water
$\%_{s-S}$	$-$	Initial percentage of solutes in solvent (mass basis)

Subscripts

$()_{biomass}$	Biomass property
$()_{solvent}$	Solvent property
$()_0$	Incident/baseline value
$()_{initial}$	Initial value
$()_L$	Property of a condensed state
$()_W$	Property of water
$()_s$	Property of solutes
$()_{()}$	Property at a given condition, e.g., $s_{(T_0)}$ is entropy at temperature T_0

APPENDIX A
Validation for the model developed in Chapter 3

The format of this appendix is as follows:

A.1 Background 301
A.2 No heating 301
A.3 Conventional heating 303

A.1 Background

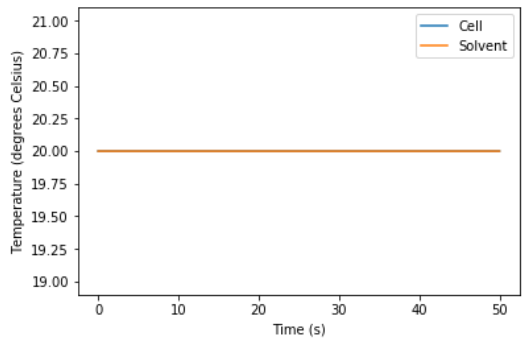
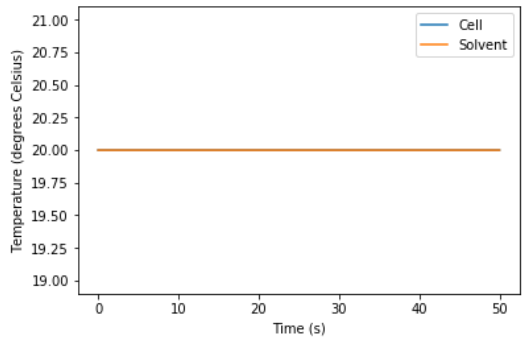
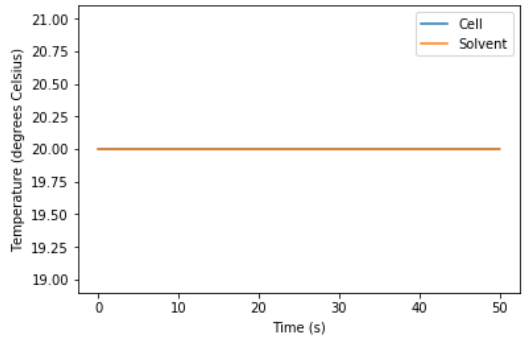
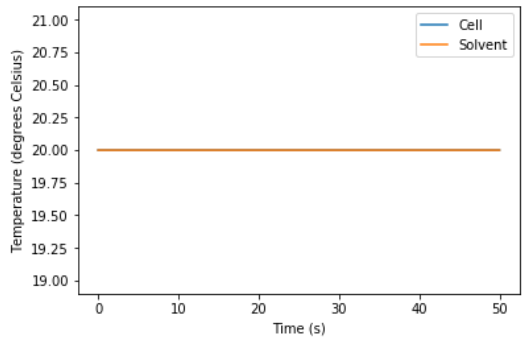
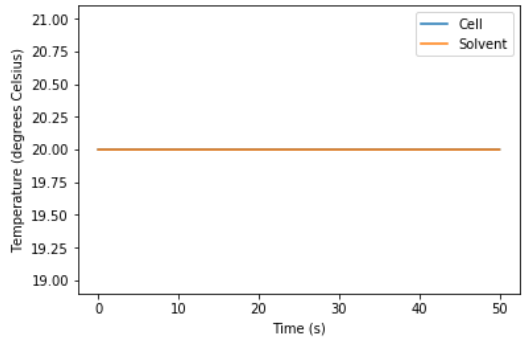
In the model presented in Chapter 3, heating is defined with a set of input microwave parameters such as electric field intensity ($|E|_0$), thermal conductivity (k), dielectric loss factors of biomass and solvent ($\varepsilon''_{biomass}$; $\varepsilon''_{solvent}$), and other parameters. Initial temperature ($T_{initial}$) and solvent boiling temperature ($T_{saturation}$) should also be defined by the user. Model validation was conducted here with a single-cell biomass-solvent system, for cases with no heating and with conventional heating. Different time-steps (δt) were employed in each case to assess computational accuracy. Table 3.1 summarises the baseline values for all parameters, while Table A.1 summarises the variables and constants for the different analyses conducted here. Results are in the sections below.

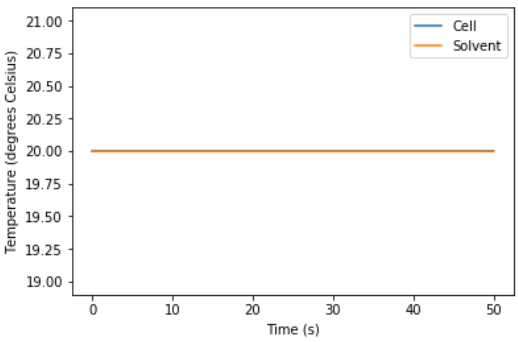
Figure/ Table	**Cell cluster size**	$\boldsymbol{\varepsilon''_{biomass}}$	$\boldsymbol{\varepsilon''_{solvent}}$	$\boldsymbol{\lvert E\rvert_0}$ ($\boldsymbol{Vm^{-1}}$)
Figure A.1	1 cell	0	0	0
Figure A.2	1 cell	0	5	5000
Figure A.3	1 cell	0	10	10000

Table A.1 – Variables and constants for the current model validation

A.2 No heating

With no heating, the temperature of the system must remain constant at its initial value ($T_{initial}$). The no heating condition is achieved either by setting $|E|_0 = 0\ Vm^{-1}$, or by setting both $\varepsilon''_{biomass} = 0$ and $\varepsilon''_{solvent} = 0$. The obtained temperature-time relationships for both the cell and the solvent are as expected (Figure A.1).

	(A) $\delta t = 0.00001\ s$
	(B) $\delta t = 0.0001\ s$
	(C) $\delta t = 0.001\ s$
	(D) $\delta t = 0.01\ s$
	(E) $\delta t = 0.1\ s$

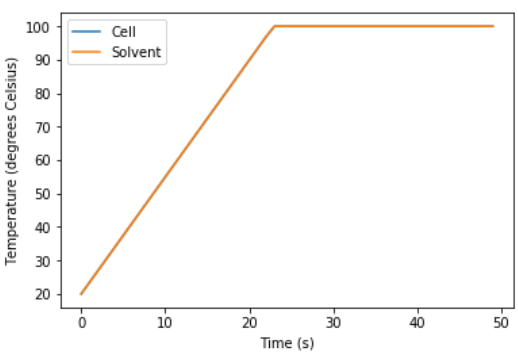


(F) $\delta t = 1\ s$

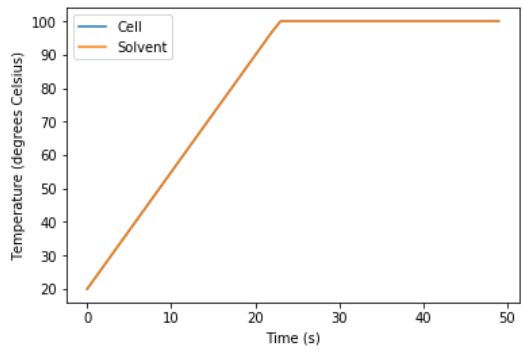
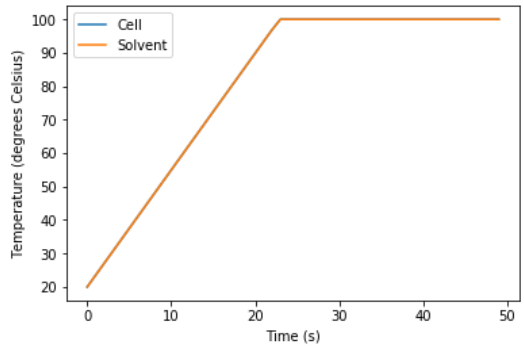
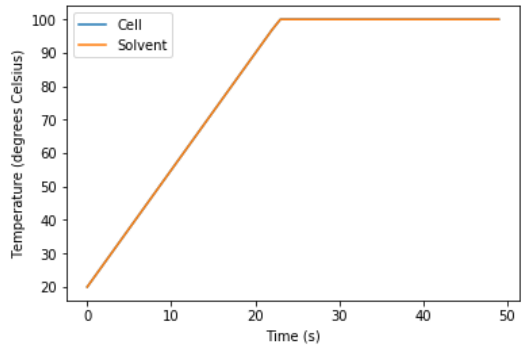
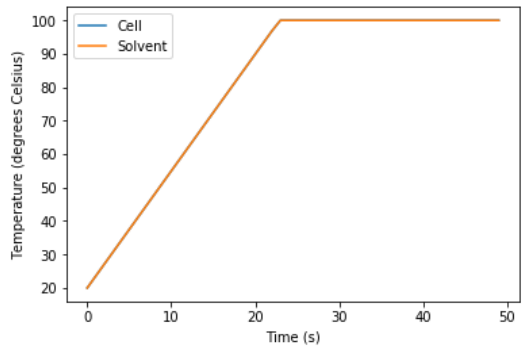
Figure A.1 – Temperature-time plots for the cell and solvent under the no-heating case and for different computational time intervals

A.3 Conventional heating

Conventional heating is achieved when heat is delivered to the biomass indirectly via the solvent phase. An analogous scenario to conventional heating is when microwaves are absorbed by the solvent phase only, but not by the biomass. This is achieved when $\varepsilon''_{biomass} = 0$, and in such a case the heating rate increases when either $\varepsilon''_{solvent}$ or $|E|_0$ are increased. However, regardless of the heating rate, the temperature in all of the system's phases should not exceed $T_{saturation}$, as this value represents the boiling point of the solvent. The outcomes are shown in Figure A.2 – Figure A.3 where, in Figure A.2 $|E|_0 = 5 \times 10^3\ Vm^{-1}$ and $\varepsilon''_{solvent} = 5$, while in Figure A.3 $|E|_0 = 10^4\ Vm^{-1}$ and $\varepsilon''_{solvent} = 10$. The expected trends are evident in the outcomes shown and with reasonable accuracy throughout the range of time-steps employed.



(A) $\delta t = 0.00001\ s$

	(B) $\delta t = 0.0001\ s$
	(C) $\delta t = 0.001\ s$
	(D) $\delta t = 0.01\ s$
	(E) $\delta t = 0.1\ s$

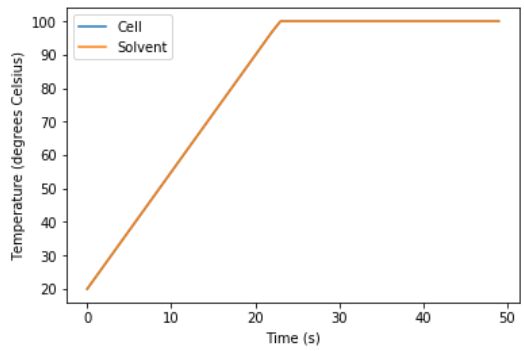
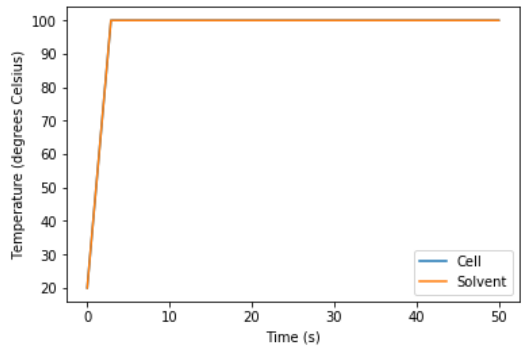
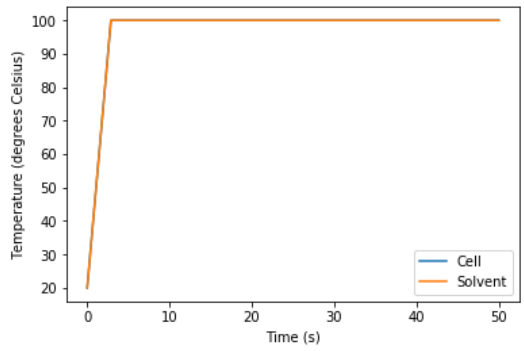
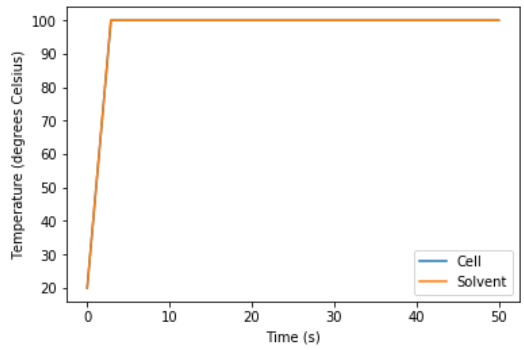
	(F) $\delta t = 1\ s$

Figure A.2 – Temperature-time plots for the cell and solvent under conventional heating where $|E|_0 = 5 \times 10^3\ Vm^{-1}$ and $\varepsilon''_{solvent} = 5$, and for different computational time intervals

	(A) $\delta t = 0.00001\ s$
	(B) $\delta t = 0.0001\ s$
	(C) $\delta t = 0.001\ s$

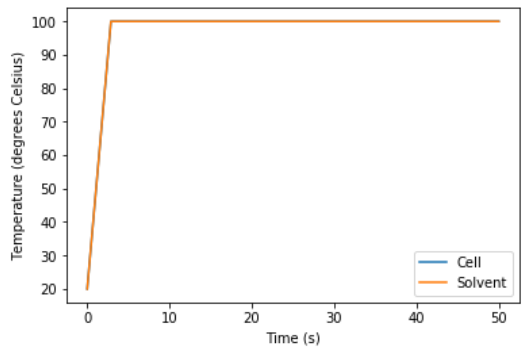
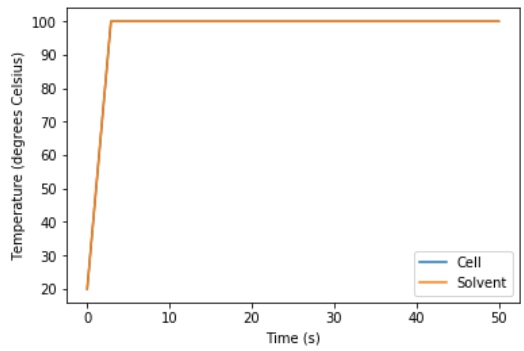
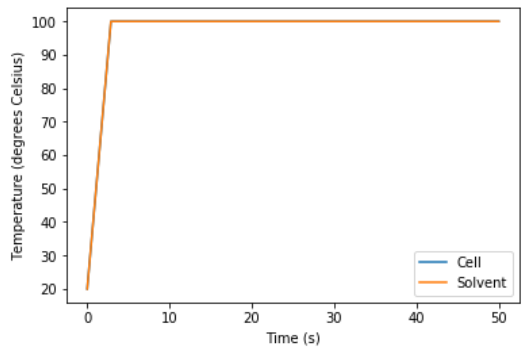
	(D) $\delta t = 0.01\ s$
	(E) $\delta t = 0.1\ s$
	(F) $\delta t = 1\ s$

Figure A.3 – Temperature-time plots for the cell and solvent under conventional heating where $|E|_0 = 10^4\ Vm^{-1}$ and $\varepsilon''_{solvent} = 10$, and for different computational time intervals

APPENDIX B
Validation for the model developed in Chapter 5

The format of this appendix is as follows:

B.1	**Background**	**307**
B.2	**Zero activity and temperature gradients**	**307**
B.3	**Nonzero activity gradient; zero temperature gradient**	**309**
B.4	**Nonzero activity and temperature gradients**	**315**

B.1 Background

In Chapter 5, the heat transfer model had been further developed to incorporate mass transfer of water, and expansion mechanics to quantify cell pressure upon water uptake. These additional elements were initially validated here at constant temperature, thus allowing them to be tested independently from heat transfer, but also ensuring that mass transfer works regardless of whether or not the system is being heated. Subsequently, the model was validated with a case incorporating temperature gradient, to ensure that the expected behaviour is observed. The manipulated parameters in this analysis are the initial cell water activity ($\alpha_{W_{initial}}$), and the incident electric field strength ($|E|_0$), whose values are shown in Table B.1. The analysis was conducted here with a single-cell biomass-solvent system, while using different time-steps (δt) in each case to assess computational accuracy. Table 5.5 summarises the baseline values used for all parameters other than $\alpha_{W_{initial}}$ and $|E|_0$.

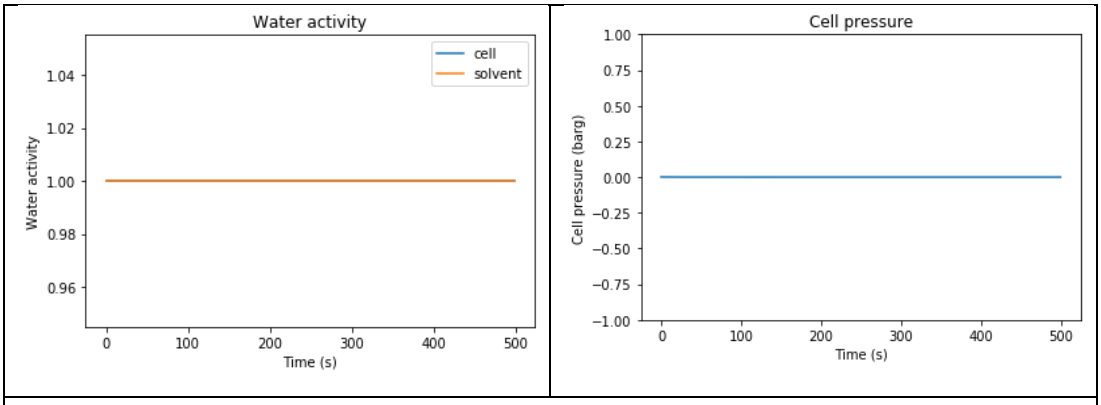
Figure/ Table	**Cell cluster size**	$\boldsymbol{\alpha_{W_{initial}}}$	$\boldsymbol{|E|_0}$ $(\boldsymbol{Vm^{-1}})$	**Constant cell pressure?**
Figure B.1	1 cell	1	0	No
Figure B.2	1 cell	0.99	0	No
Figure B.3	1 cell	0.98	0	No
Figure B.4	1 cell	0.98	0	Yes
Figure B.5	1 cell	0.98	10000	No

Table B.1 – Variables and constants for the current model validation

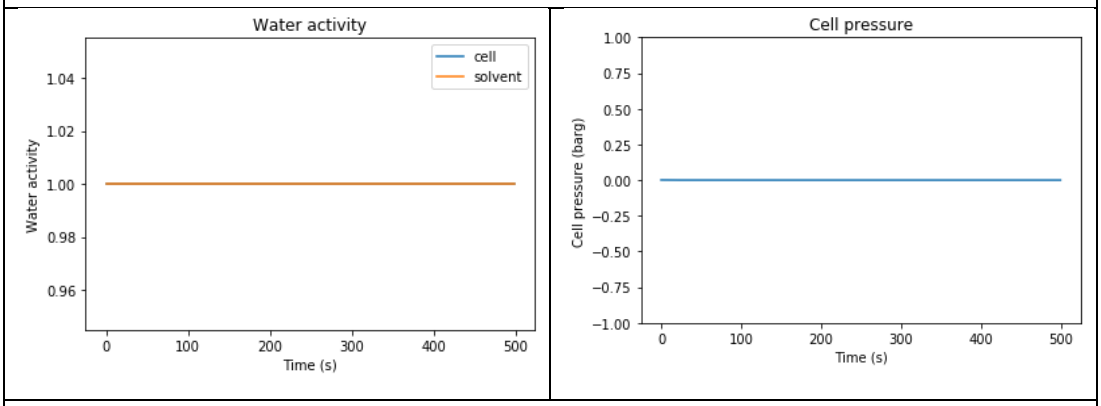
B.2 Zero activity and temperature gradients

When $\alpha_{W_{initial}} = 1$, there is no activity gradient between the cell and the solvent; hence, no mass transfer should take place and the cell pressure must remain constant

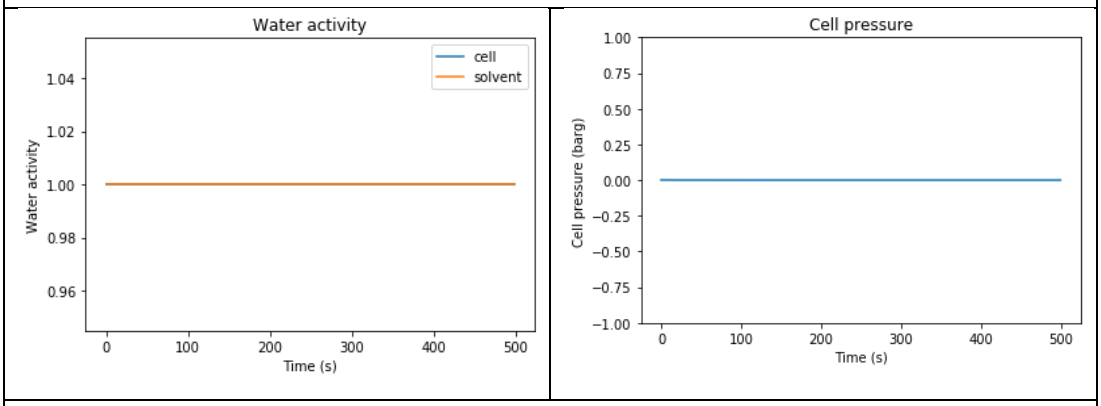
at its initial value. The obtained activity-time and pressure-time plots are as expected (Figure B.1).



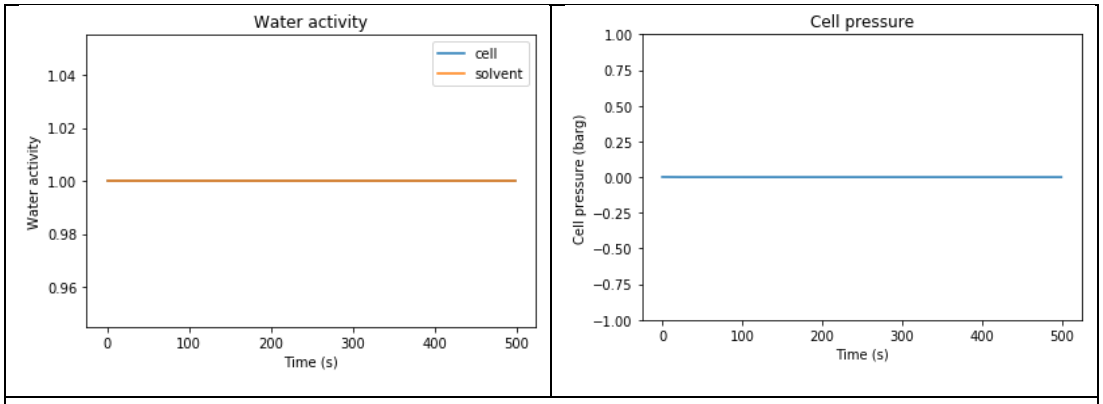
(A) $\delta t = 0.00001\ s$



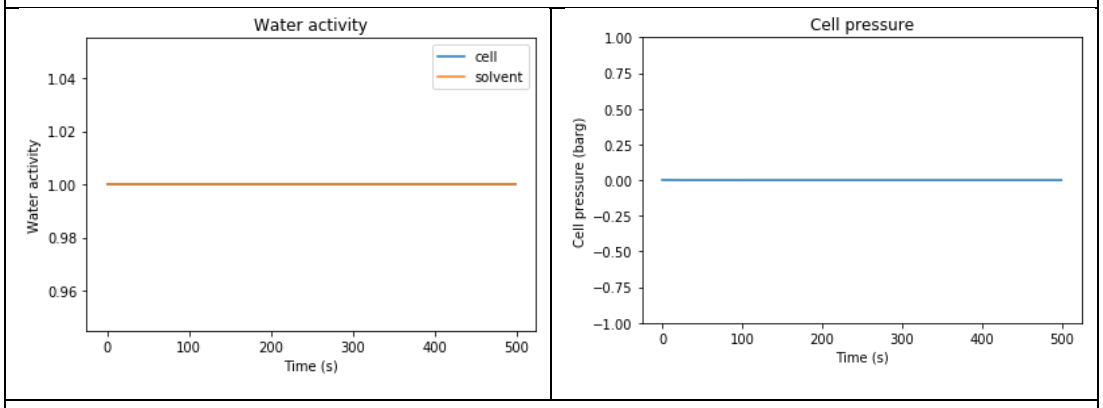
(B) $\delta t = 0.0001\ s$



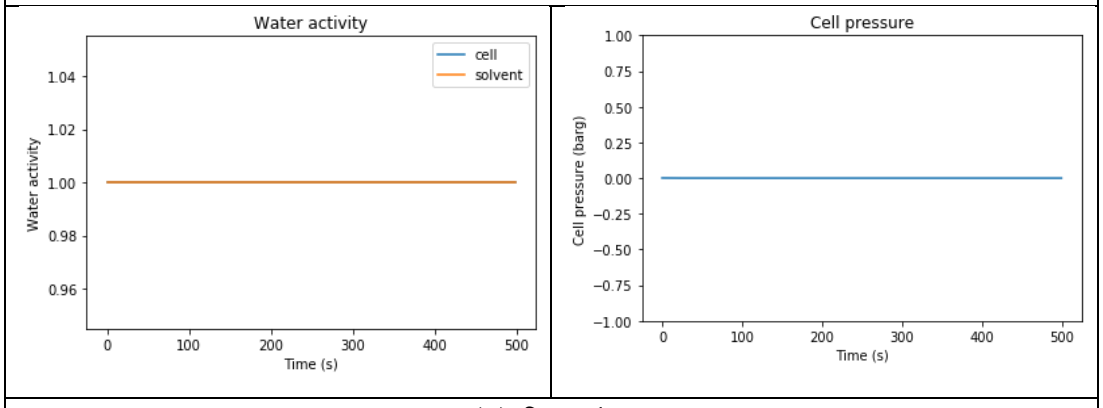
(C) $\delta t = 0.001\ s$



(D) $\delta t = 0.01\ s$



(E) $\delta t = 0.1\ s$



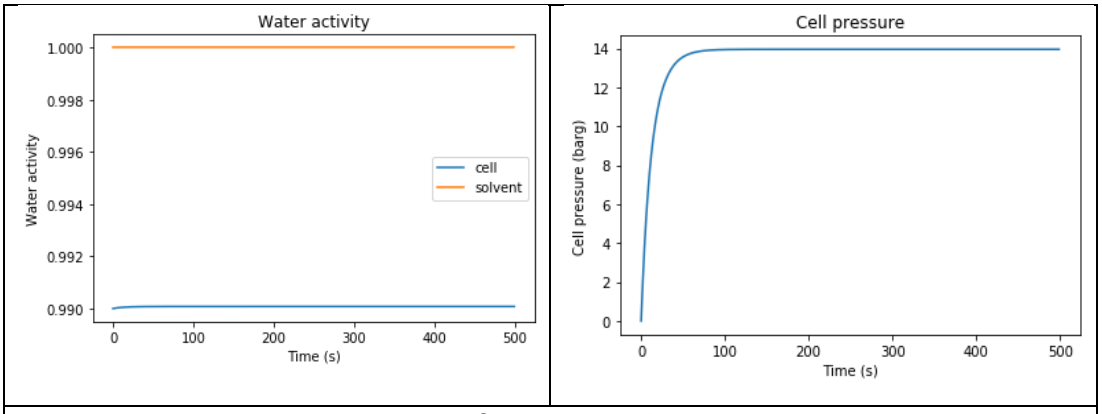
(F) $\delta t = 1\ s$

Figure B.1 – Water activity-time and cell pressure-time plots under the no-heating case where $\alpha_{W_{initial}} = 1$, and for different computational time intervals

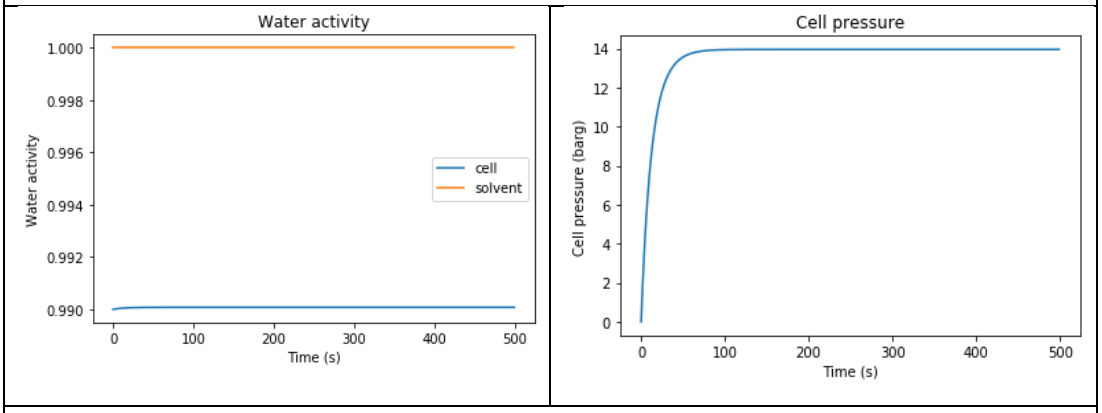
B.3 Nonzero activity gradient; zero temperature gradient

Readjusting $\alpha_{W_{initial}}$ to 0.99 introduces an activity gradient between the cell and the solvent, which should drive water diffusion from the latter to the former, increasing the cell pressure up to a point where mass equilibrium is established. Since the cell pressure is higher than that of the solvent at mass equilibrium, the equilibrium cell

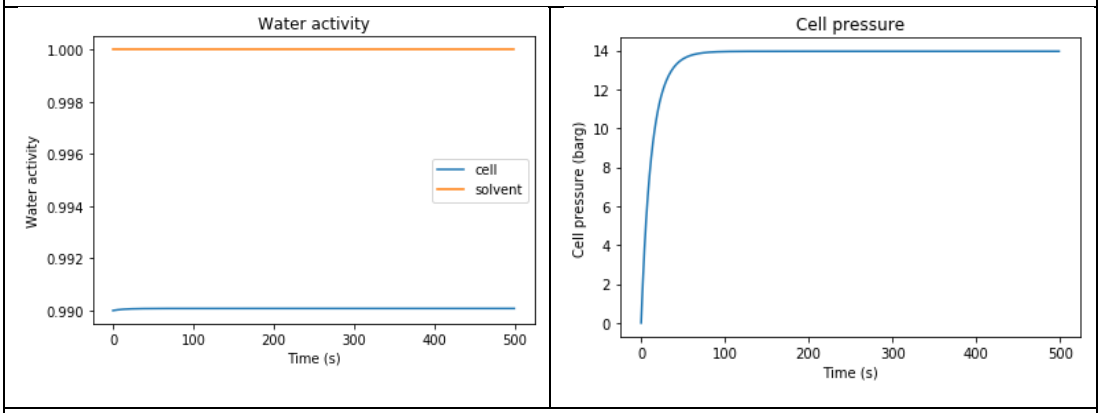
water activity should remain smaller than that of the solvent. The obtained activity-time and pressure-time trends are as expected (Figure B.2).



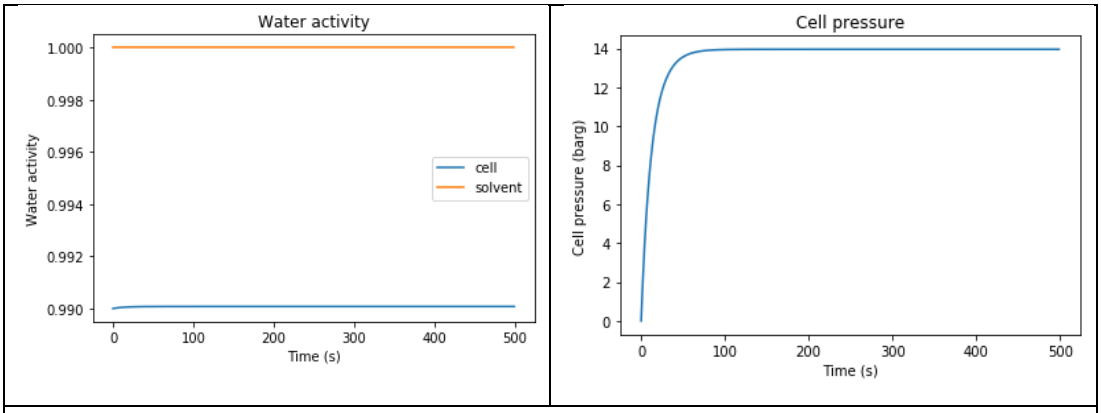
(A) $\delta t = 0.00001\ s$



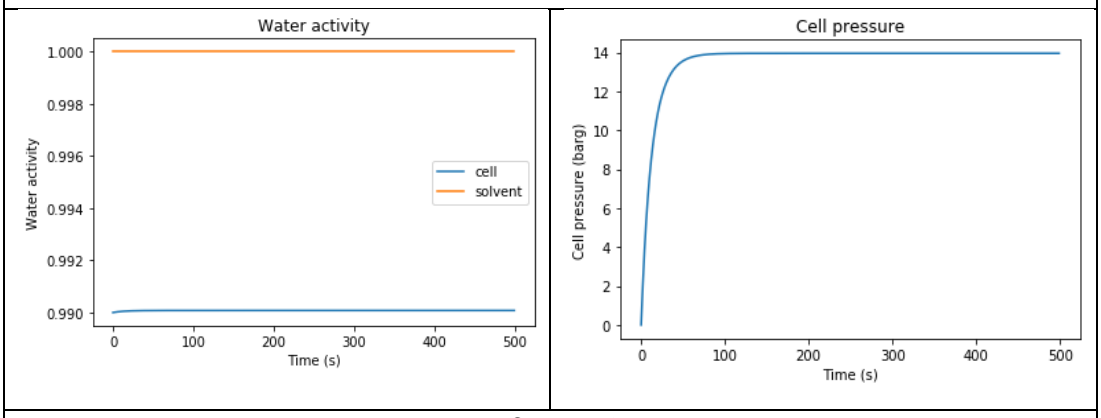
(B) $\delta t = 0.0001\ s$



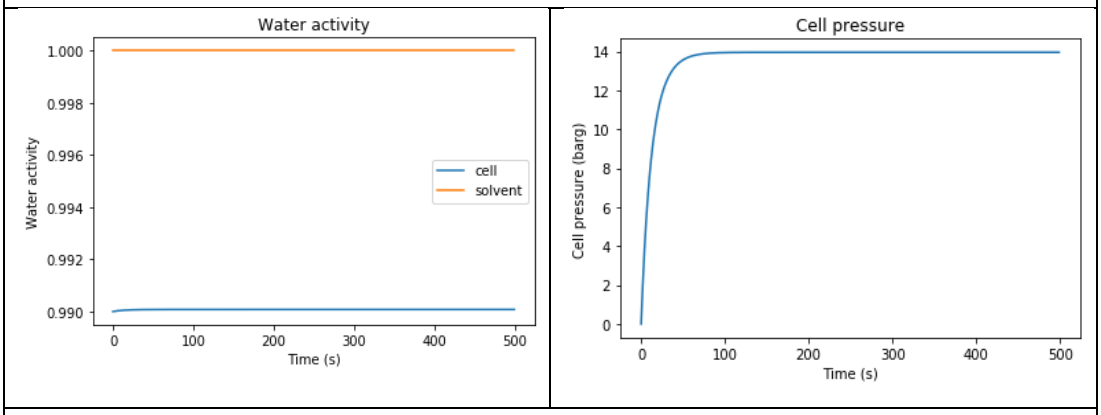
(C) $\delta t = 0.001\ s$



(D) $\delta t = 0.01\ s$



(E) $\delta t = 0.1\ s$

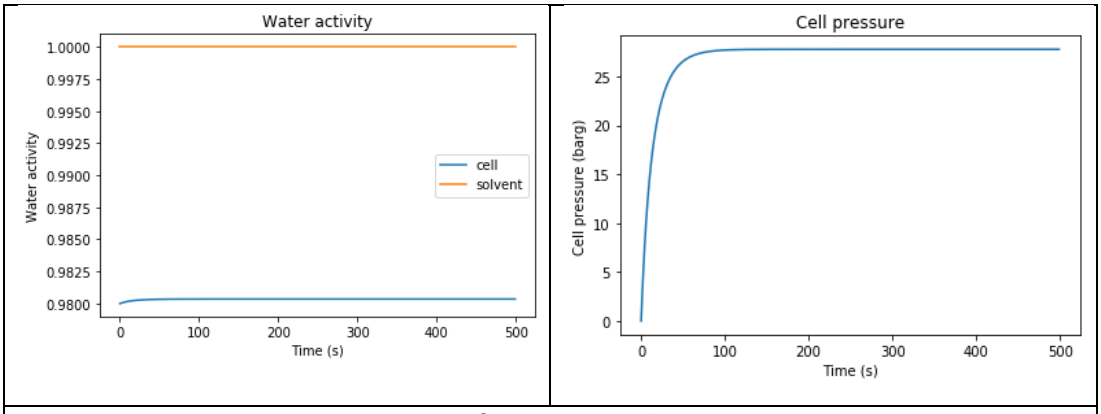


(F) $\delta t = 1\ s$

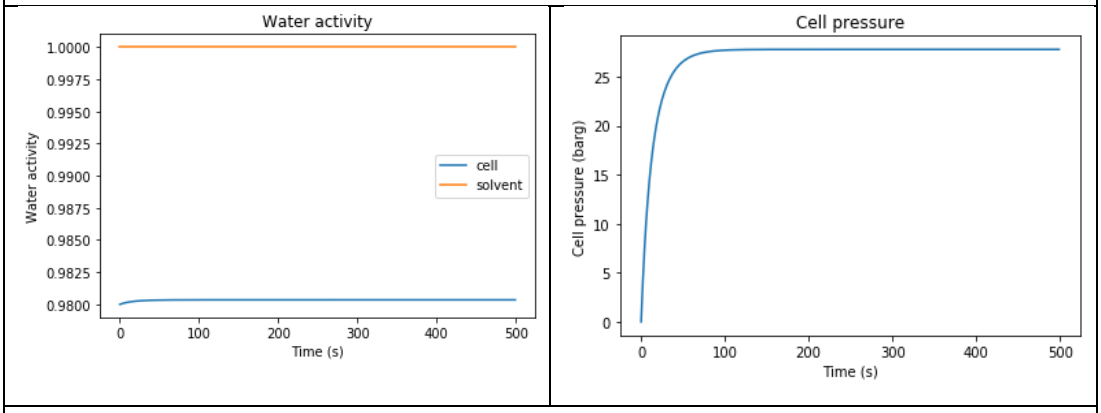
Figure B.2 – Water activity-time and cell pressure-time plots under the no-heating case where $\alpha_{W_{initial}} = 0.99$, and for different computational time intervals

As $\alpha_{W_{initial}}$ is further decreased to 0.98, the same observations should be made as those in Figure B.2, but with a larger equilibrium cell pressure due to the larger activity

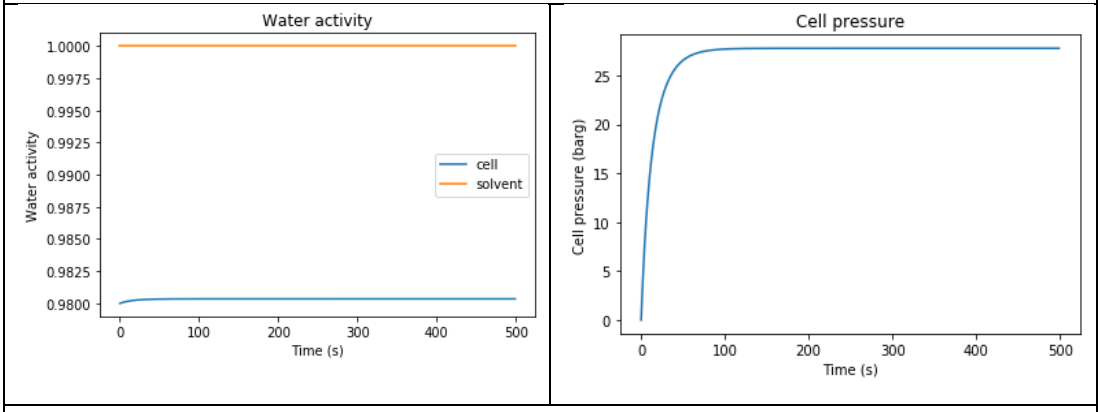
gradient in the system. The obtained activity-time and pressure-time trends are as expected (Figure B.3).



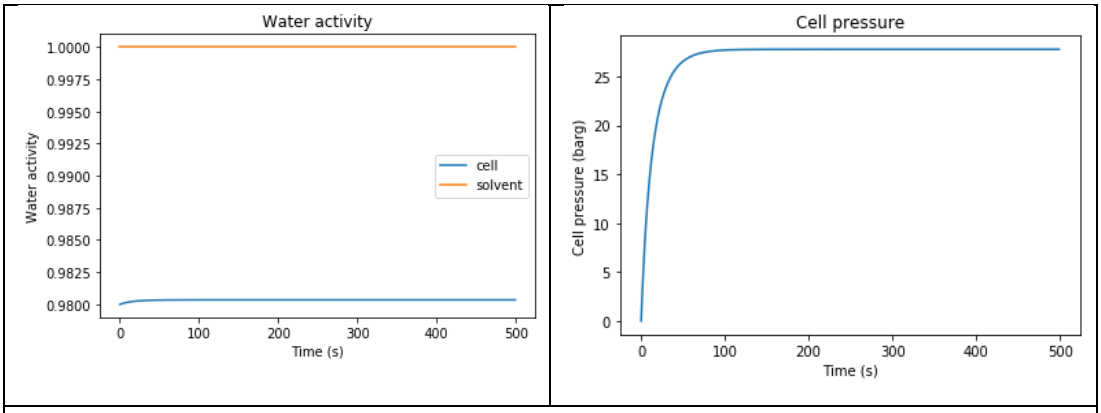
(A) $\delta t = 0.00001\ s$



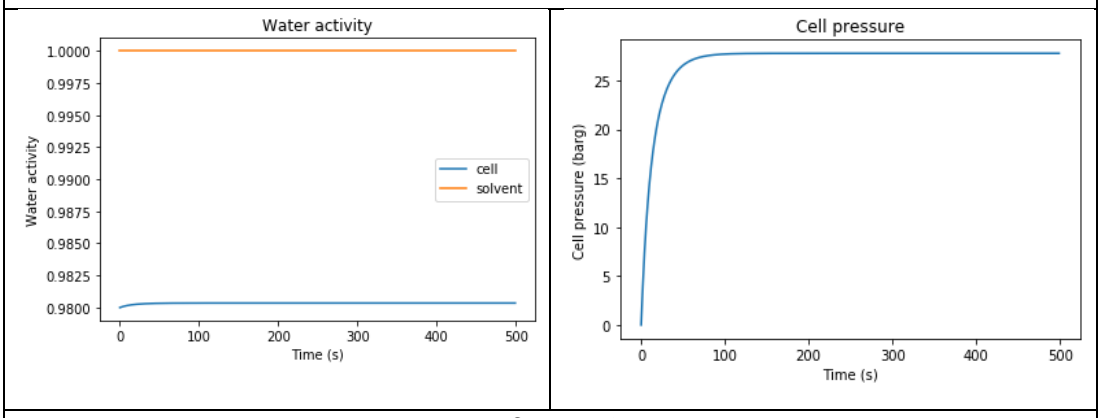
(B) $\delta t = 0.0001\ s$



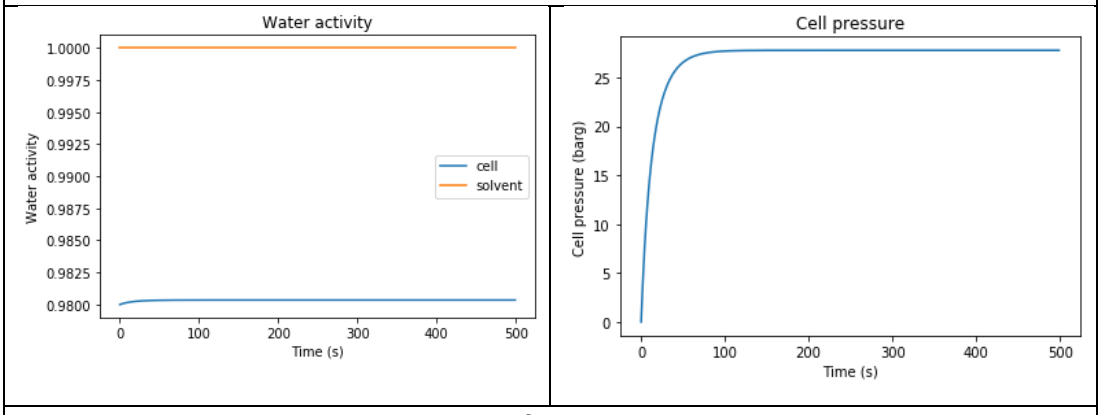
(C) $\delta t = 0.001\ s$



(D) $\delta t = 0.01\ s$



(E) $\delta t = 0.1\ s$



(F) $\delta t = 1\ s$

Figure B.3 – Water activity-time and cell pressure-time plots under the no-heating case where $\alpha_{W_{initial}} = 0.98$, and for different computational time intervals

The equilibrium cell pressures obtained with $\alpha_{W_0} = 0.99$ and $\alpha_{W_0} = 0.98$ are 14 $barg$ and 27.8 $barg$, respectively. These results were validated as shown below.

At constant temperature, the cell water chemical potential ($\mu_{W_{cell}}$) can be written as follows:

$$\mu_{W_{cell}} = \mu_{0(T)} + v_{L(T)}\left(P_L + P_{atm} - {P_{(T)}}^*\right) + RTln\left(\frac{\alpha_{W_{cell}}}{\alpha_0}\right) \quad \textbf{(B.1)}$$

At constant temperature and atmospheric pressure, the solvent water chemical potential ($\mu_{W_{solvent}}$) can be written as follows:

$$\mu_{W_{solvent}} = \mu_{0(T)} + v_{L(T)}\left(P_{atm} - {P_{(T)}}^*\right) + RTln\left(\frac{\alpha_{W_{solvent}}}{\alpha_0}\right) \quad \textbf{(B.2)}$$

At mass equilibrium, the chemical potentials of water in the cell and solvent are equal (due to constant temperature); therefore, Equations (B.1) and (B.2) can be written as follows:

$$P_L = \frac{RT}{v_{L(T)}} ln\left(\frac{\alpha_{W_{solvent}}}{\alpha_{W_{cell}}}\right) \quad \textbf{(B.3)}$$

All parameters in Equation (B.3) other than P_L and $\alpha_{W_{cell}}$ can be taken as constant. $R = 8.314\ Jmol^{-1}K^{-1}$; $T = 303\ K$; $v_{L(T)} = 1.8 \times 10^{-5}\ molm^{-3}$; and $\alpha_{W_{solvent}} = 1$. Therefore, Equation (B.3) can be expressed as follows:

$$P_L = -1.3995 \times 10^8\ ln(\alpha_{W_{cell}}) \quad \textbf{(B.4)}$$

Since $\alpha_{W_{cell}}$ does not vary significantly in Figure B.2 and Figure B.3, it can be substituted in Equation (B.4) with the initial cell water activity ($\alpha_{W_{initial}}$), resulting in the following expression:

$$P_L = -1.3995 \times 10^8\ ln(\alpha_{W_{initial}}) \quad \textbf{(B.5)}$$

From Equation (B.5), the P_L values corresponding to $\alpha_{W_{initial}} = 0.99$ and 0.98 are $14.1\ barg$ and $28.3\ barg$, respectively. These values are slightly higher than those obtained in Figure B.2 and Figure B.3, which is because cell water activities do change

slightly during mass transfer, leading to a miniscule reduction in the attainable equilibrium pressures. Nevertheless, the two sets of values attained here and from Figure B.2 and Figure B.3 are very close, and for all practical purposes they match closely.

On the other hand, it is clear from Equation (B.3) that if the cell pressure cannot be elevated (i.e., $P_L = 0\ barg$ always), then mass equilibrium can only be achieved if $\alpha_{W_{cell}} = \alpha_{W_{solvent}}$. It is not possible to satisfy this condition in the current model, due to the physical constraint dictating that cells incorporate a non-diffusible solutes, meaning that cell water activity can never approach unity. As such, it is expected that the model will not deliver a meaningful outcome if the cell pressure is restricted to $0\ barg$. Such an observation is clear in Figure B.4, through the activity-time and pressure-time plots obtained under this setting.

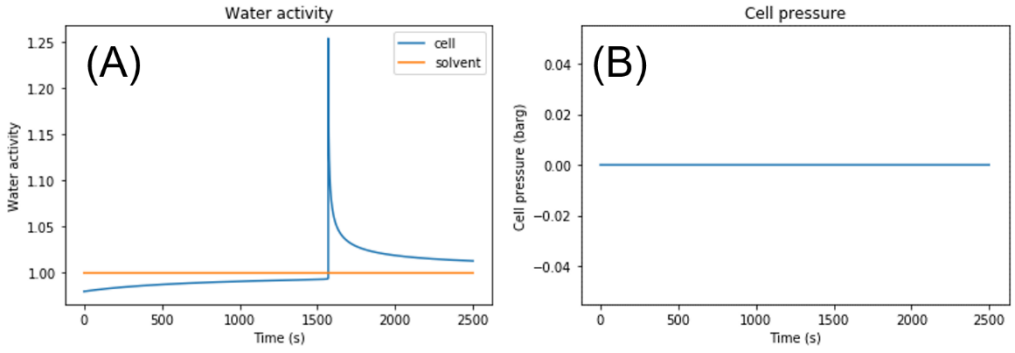
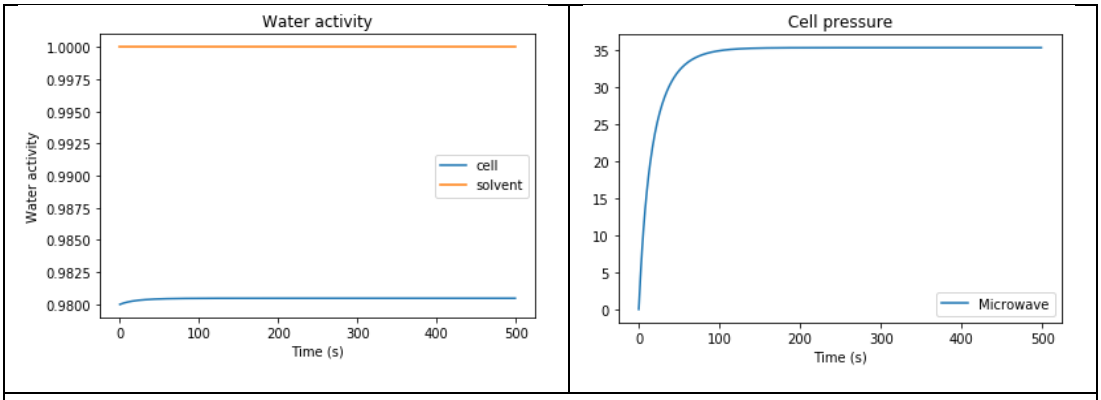


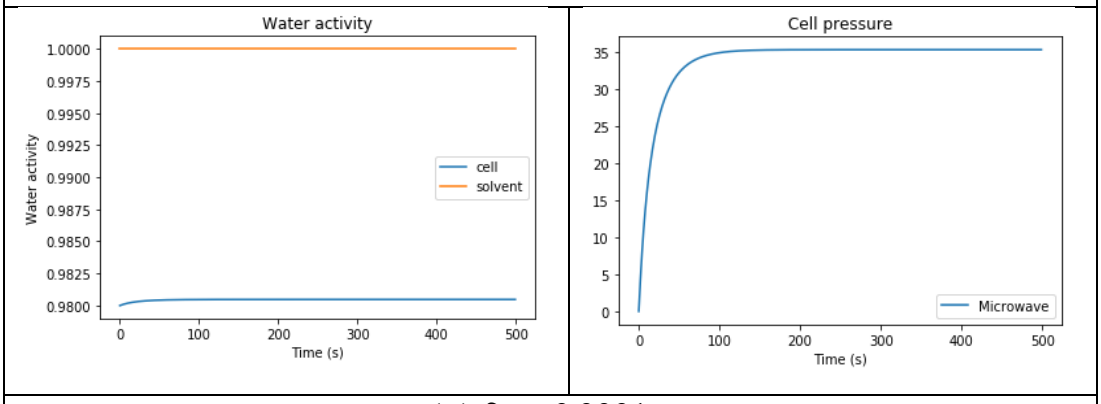
Figure B.4 – Water activity-time and cell pressure-time plots under the no-heating case where $\alpha_{W_{initial}} = 0.98$, where cell pressure is constrained to $0\ barg$ regardless of water diffusion

B.4 Nonzero activity and temperature gradients

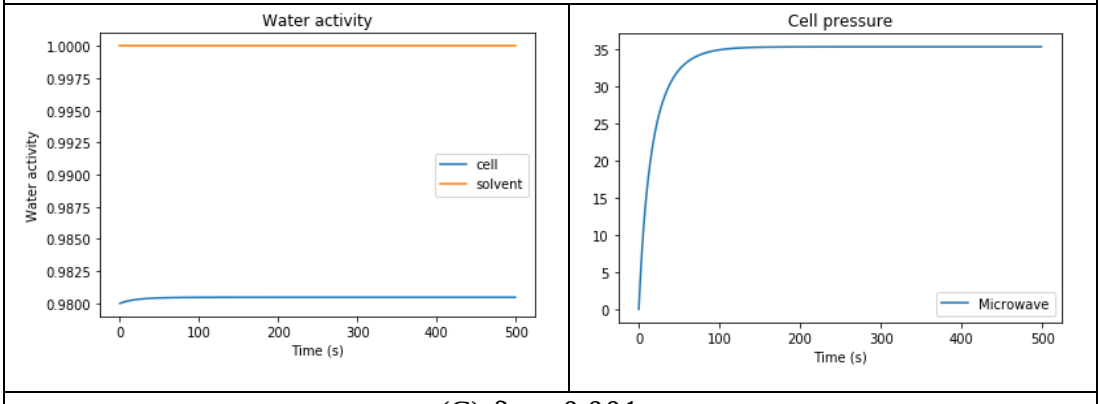
Finally, the model was validated under temperature gradient induced with $|E|_0 = 10^4\ Vm^{-1}$. As expected, a considerably higher equilibrium cell pressure is induced under a small temperature gradient (around 0.036 ℃ in this case). This is shown in Figure B.5.



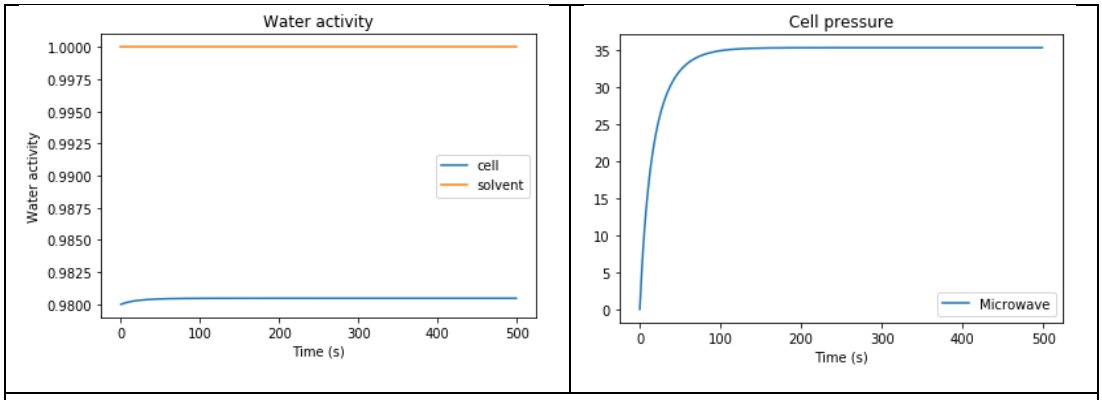
(A) $\delta t = 0.00001\ s$



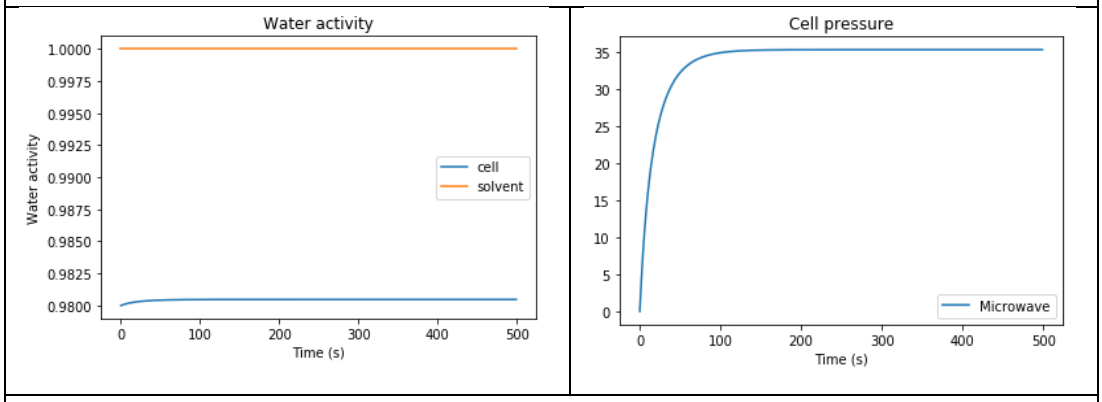
(B) $\delta t = 0.0001\ s$



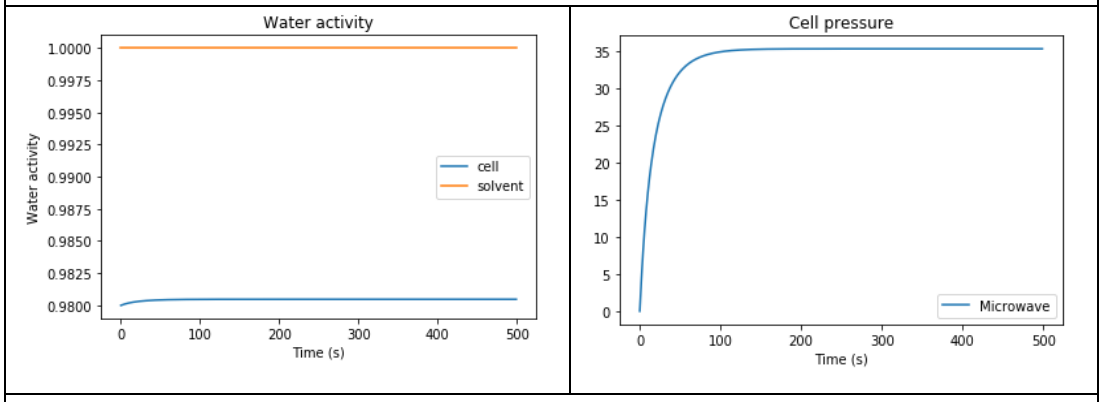
(C) $\delta t = 0.001\ s$



(D) $\delta t = 0.01\ s$



(E) $\delta t = 0.1\ s$



(F) $\delta t = 1\ s$

Figure B.5 – Water activity-time and cell pressure-time plots under a microwave heating case where $|E|_0 = 10^4\ Vm^{-1}$, $\alpha_{W_{initial}} = 0.98$, and for different computational time intervals

The equilibrium cell pressure obtained in Figure B.5 is 35.4 $barg$, and this value was validated as shown below.

The cell chemical potential-to-temperature ratio ($\mu_{W_{cell}}/T_{cell}$) can be written as follows:

$$\frac{\mu_{W_{cell}}}{T_{cell}} = \frac{\mu_0}{T_{cell}} + \frac{v_{L(T_0)}}{T_{cell}}\left(P_L + P_{atm} - {P_{(T_0)}}^*\right) - s_{W(T_0)}\left(1 - \frac{T_0}{T_{cell}}\right) + C_p\left[\left(1 - \frac{T_0}{T_{cell}}\right) - ln\left(\frac{T_{cell}}{T_0}\right)\right] + Rln\left(\frac{\alpha_{W_{cell}}}{\alpha_0}\right) \quad \textbf{(B.6)}$$

Similarly, the solvent chemical potential-to-temperature ratio ($\mu_{solvent}/T_{solvent}$) can be written as follows, assuming the pressure remains at the atmospheric value:

$$\frac{\mu_{W_{solvent}}}{T_{solvent}} = \frac{\mu_0}{T_{solvent}} + \frac{v_{L(T_0)}}{T_{solvent}}\left(P_{atm} - {P_{(T_0)}}^*\right) - s_{W(T_0)}\left(1 - \frac{T_0}{T_{solvent}}\right) + C_p\left[\left(1 - \frac{T_0}{T_{solvent}}\right) - ln\left(\frac{T_{solvent}}{T_0}\right)\right] + Rln\left(\frac{\alpha_{W_{solvent}}}{\alpha_0}\right) \quad \textbf{(B.7)}$$

At mass equilibrium, the parameters μ_{cell}/T_{cell} and $\mu_{solvent}/T_{solvent}$ are equal; therefore, Equations (B.6) and (B.7) can be written as follows:

$$P_L = \frac{RT_{cell}}{v_{L(T_0)}} ln\left(\frac{\alpha_{W_{solvent}}}{\alpha_{W_{cell}}}\right) + \beta \quad \textbf{(B.8)}$$

For a given temperature gradient, β is a constant defined as follows:

$$\beta = \left(\frac{T_{cell}}{T_{solvent}} - 1\right)\left(\frac{\mu_0}{v_{L(T_0)}} + P_{atm} - {P_{(T_0)}}^* + \frac{T_0}{v_{L(T_0)}} s_{W(T_0)} - \frac{T_0}{v_{L(T_0)}} C_p\right) + \frac{C_p T_{cell}}{v_{L(T_0)}} ln\left(\frac{T_{cell}}{T_{solvent}}\right) \quad \textbf{(B.9)}$$

All parameters in Equation (B.9) other than P_L and $\alpha_{W_{\text{cell}}}$ can be taken as constant. $\mu_0 = 0\, Jmol^{-1}K^{-1}$; $R = 8.314\, Jmol^{-1}K^{-1}$; $T_{\text{cell}} = 373.036\, K$ (as per the temperature gradient obtained from the analysis in Figure B.5); $T_{solvent} = 373\, K$; $v_{L(T)} = 1.8 \times 10^{-5}\, molm^{-3}$; $\alpha_{W_{solvent}} = 1$. $T_0 = 298\, K$; $C_p = 72\, Jmol^{-1}K^{-1}$; $s_{W(T_0)} = 70\, Jmol^{-1}K^{-1}$; $P_{atm} = 1.01325\, bar$; and ${P_{(T_0)}}^* = 0.03\, bar$. Therefore, Equation (B.9) can be expressed as follows:

$$P_L = -1.7230 \times 10^8 ln\left(\alpha_{W_{cell}}\right) + 1.4082 \times 10^5 \quad \textbf{(B.10)}$$

Since $\alpha_{W_{cell}}$ does not vary significantly in Figure B.5, it can be substituted in Equation (B.10) with the initial cell water activity ($\alpha_{W_{initial}}$), resulting in the following expression:

$$P_L = -1.7230 \times 10^8 ln\left(\alpha_{W_{initial}}\right) + 1.4082 \times 10^5 \quad \textbf{(B.11)}$$

From Equation (B.11), the P_L value corresponding to $\alpha_{cell} = 0.98$ is $36.2\ barg$. This value is slightly higher than that obtained in Figure B.5, which is because cell water activities do change slightly during mass transfer, leading to a miniscule reduction in the attainable equilibrium pressures. Nevertheless, the value attained here is very close to that obtained from Figure B.5, and for all practical purposes the two values match closely.

APPENDIX C
Validation for the model developed in Chapter 7

The format of this appendix is as follows:

C.1	**Background**	**320**
C.2	**Extractability of solutes**	**321**
C.3	**Dependence of activities on solubility and molar quantity**	**323**
C.4	**Elimination of negative molar quantities**	**327**

C.1 Background

In Chapter 7, the model was improved by introducing a means for quantifying solute extraction, which is a key advantage enabling direct benchmarking of the attainable outcomes with experimental data. This modified model also offers a novel microwave extraction mechanism not requiring cell rupture, thereby widening the model's predictive capability to a larger domain of biomass-solvent extraction scenarios. Improving the model required readdressing some of its pre-existing assumptions (Table 7.1); hence, the current appendix demonstrates some key testing steps undertaken to validate the new framework.

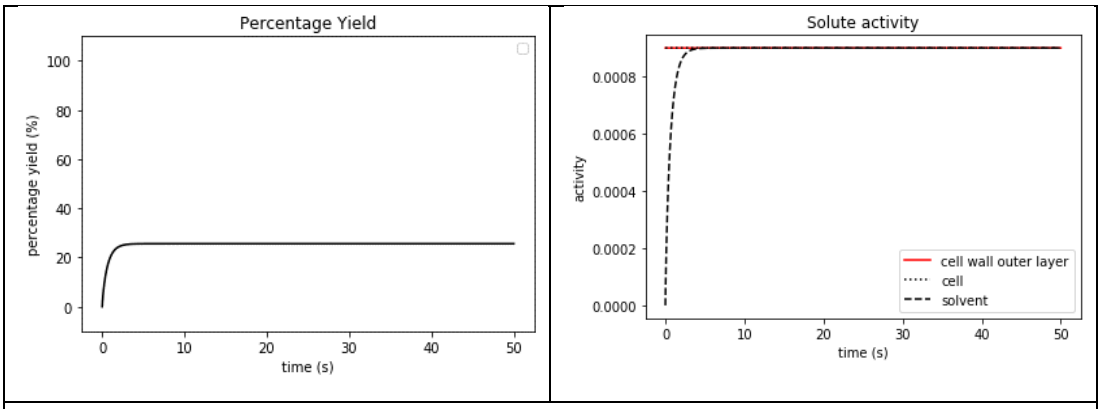
The manipulated parameters in this analysis are the solubility of solutes in water (S_s), and the mass percent of water in cell walls ($\%_{W-CW}$). The analysis was conducted here with a single-cell biomass-solvent system, while using different time-steps (δt) in each case to assess computational accuracy. The analysis was conducted at room temperature (i.e., $Q_s = 0\ Ks^{-1}$) to understand the fundamental behaviour of the model in the absence of microwave heating. The values used for S_s, $\%_{W-CW}$, and Q_s are summarised in Table C.1, while all other parameters were fixed as shown in Table 7.4.

Figure/ Table	**Cell cluster size**	$\boldsymbol{S_s}$ $(\boldsymbol{g_s g_W^{-1}})$	$\boldsymbol{\%_{W-CW}}$	$\boldsymbol{Q_s}$ $(\boldsymbol{Ks^{-1}})$
Figure C.1	1 cell	0.01	0.1	0
Figure C.2	1 cell	0.01; 0.03	0.1	0
Figure C.3	1 cell	0.01	0.01; 0.1	0
Figure C.4	1 cell	0.05	0.1	0

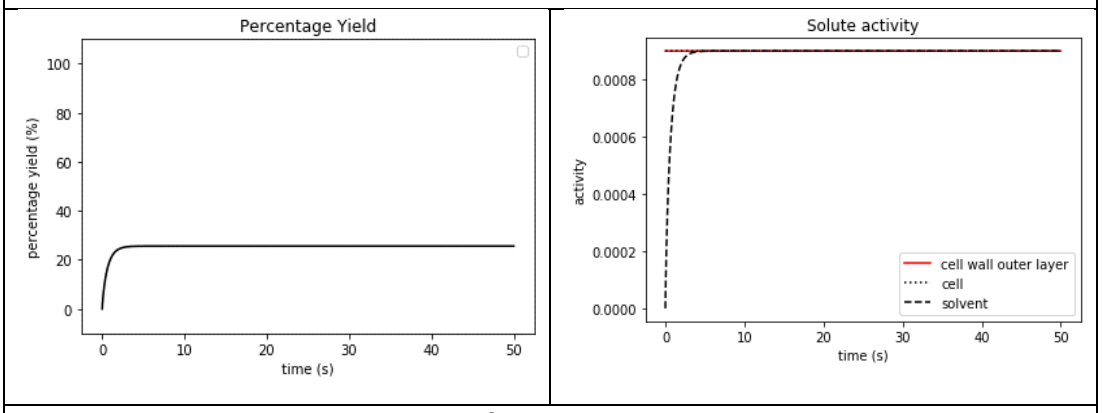
Table C.1 – Variables and constants for the current model validation

C.2 Extractability of solutes

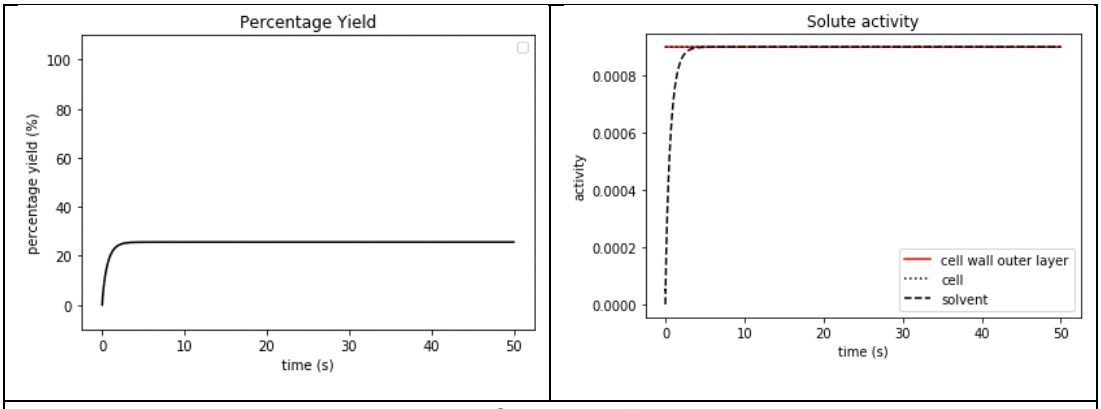
As the model incorporates diffusion of both water and solutes, it was necessary to investigate whether these diffusion patterns follow the expected trends. Initially, an elementary study was conducted to establish that solutes flow from the biomass to the solvent, resulting in a proportional increase in the percentage yield computed by the model. Figure C.1 presents a case where the single-cell biomass contains $1.5719 \times 10^{-10}\ mol$ of extractable solutes initially, of which $4.0240 \times 10^{-11}\ mol$ get liberated into the solvent phase during extraction. As can be seen, the solute diffuses from the biomass to the solvent as desired in this computational exercise, and the obtained yield of 25.6% matches the extracted quantity. Moreover, the model demonstrates a rapidly converging yield outcome as the computational time-step (δt) is decreased from $1\ s$ to $0.1\ s$, and a converging activity trend as δt is further decreased to $0.0001\ s$.



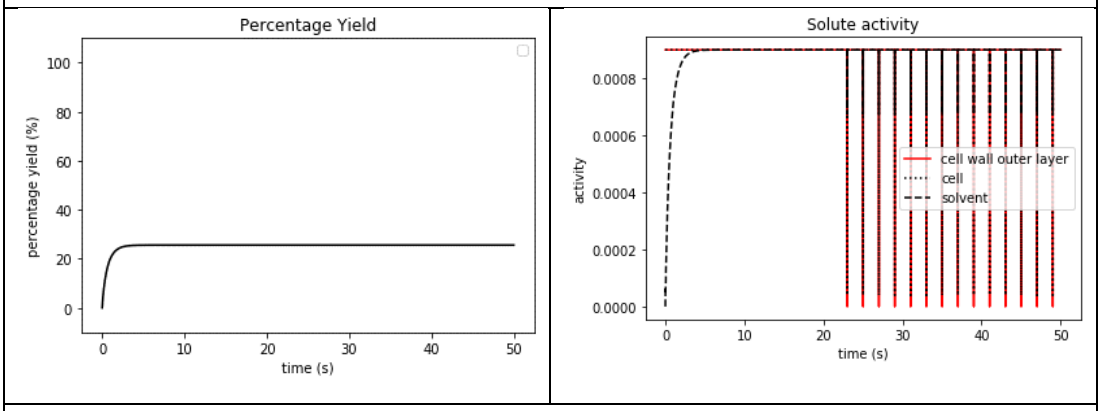
(A) $\delta t = 0.00001\ s$



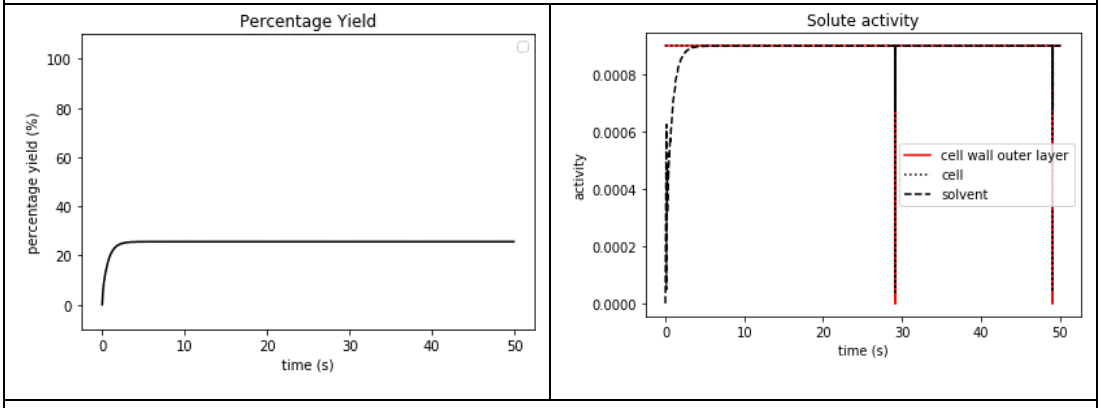
(B) $\delta t = 0.0001\ s$



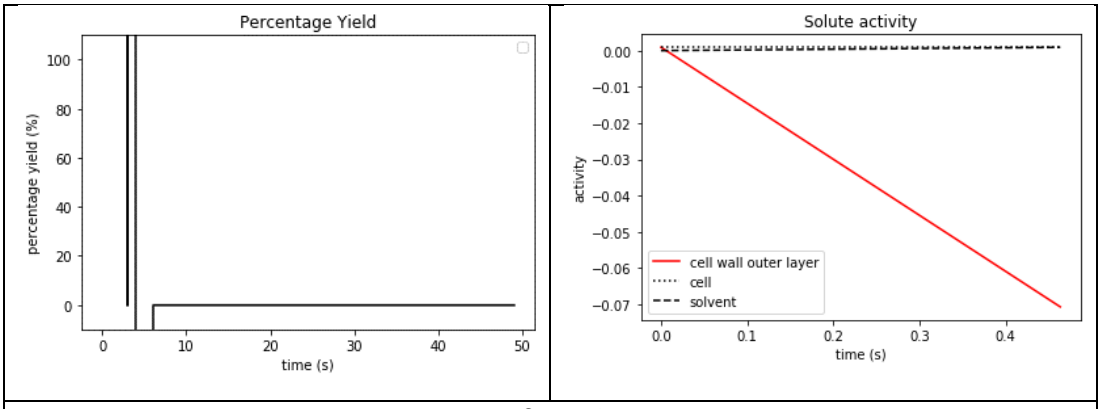
(C) $\delta t = 0.001\ s$



(D) $\delta t = 0.01\ s$



(E) $\delta t = 0.1\ s$

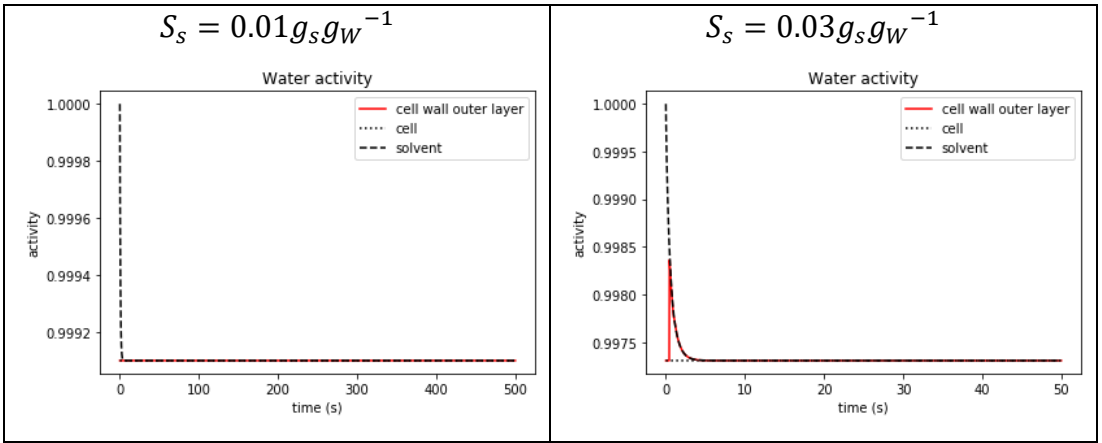


(F) $\delta t = 1\ s$

Figure C.1 – Percentage yield-time and solute activity-time plots under the no-heating case where $S_s = 0.01\ g_s g_W{}^{-1}$, and for different computational time intervals

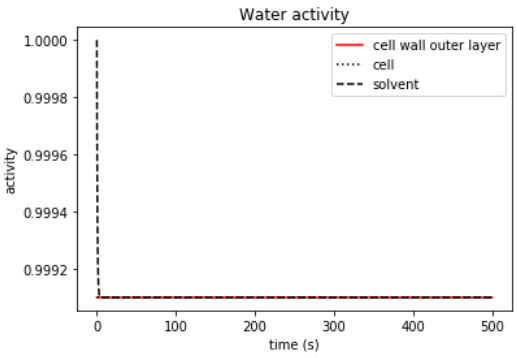
C.3 Dependence of activities on solubility and molar quantity

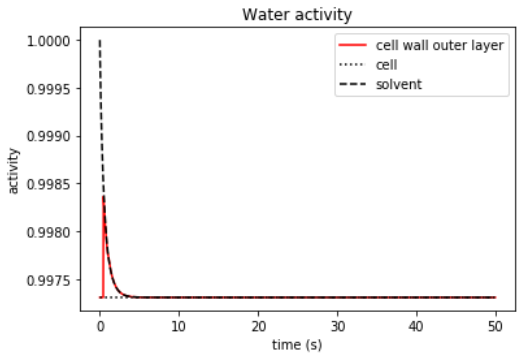
Furthermore, water and solute activities (α_W; α_s) were defined in this model through the solute's solubility (S_s), which is a more widely available and accessible parameter. This link dictates that, increasing S_s induces a larger activity gradient in the system, through lowering the initial water activity of the biomass, and raising its initial solute activity. This was assessed and has been proven as shown in Figure C.2 (demonstrates water activity-time plots). Moreover, the outcomes converge with decreasing the computational time-step (δt).



(A) $\delta t = 0.00001\ s$

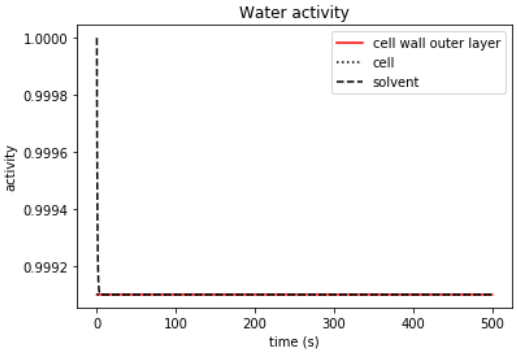
$S_s = 0.01 g_s g_W{}^{-1}$ $S_s = 0.03 g_s g_W{}^{-1}$



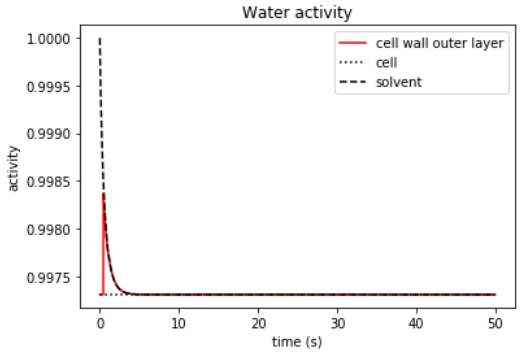


(B) $\delta t = 0.0001\ s$

$S_s = 0.01 g_s {g_W}^{-1}$

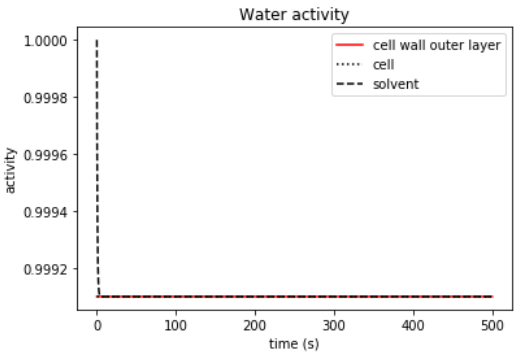


$S_s = 0.03 g_s {g_W}^{-1}$

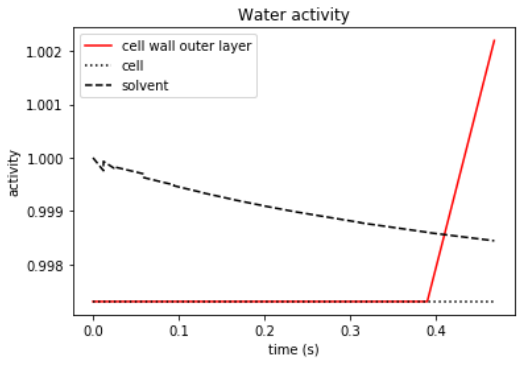


(C) $\delta t = 0.001\ s$

$S_s = 0.01 g_s {g_W}^{-1}$



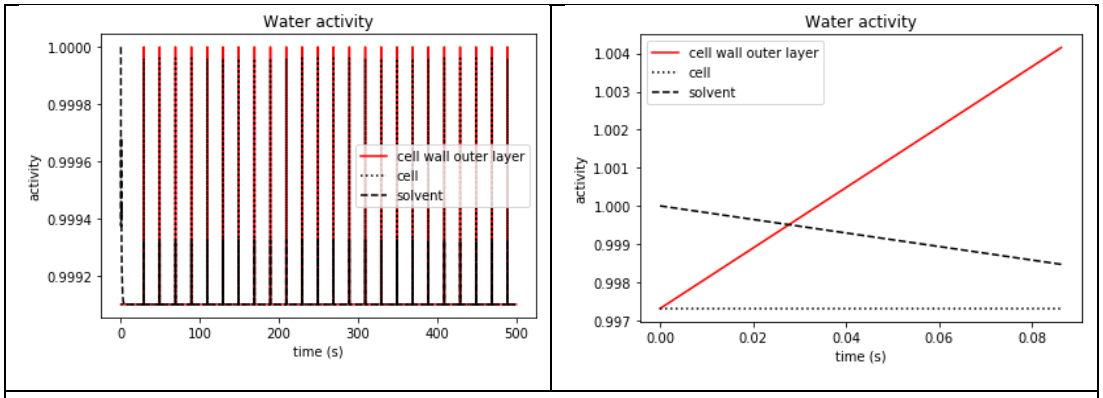
$S_s = 0.03 g_s {g_W}^{-1}$



(D) $\delta t = 0.01\ s$

$S_s = 0.01 g_s {g_W}^{-1}$

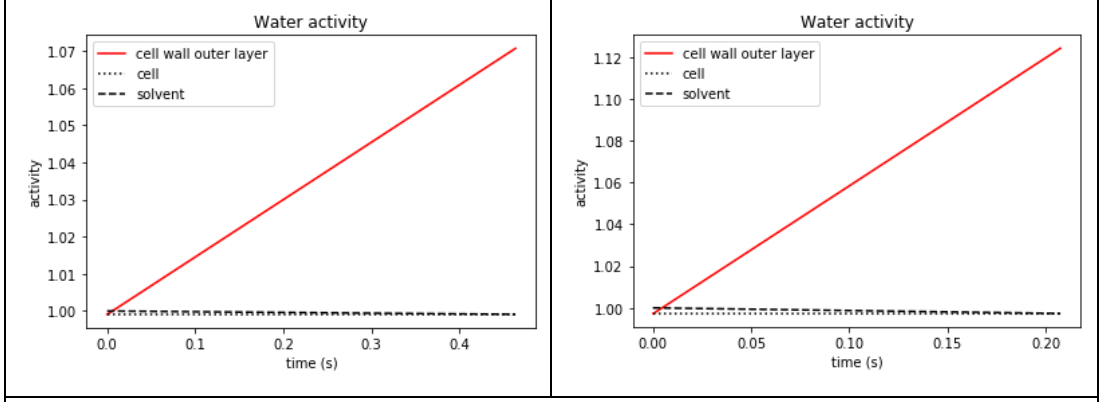
$S_s = 0.03 g_s {g_W}^{-1}$



(E) $\delta t = 0.1\ s$

$S_s = 0.01 g_s {g_W}^{-1}$

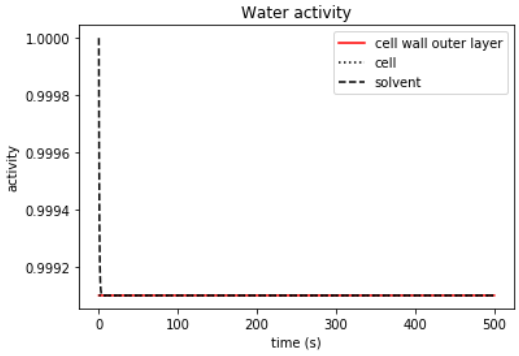
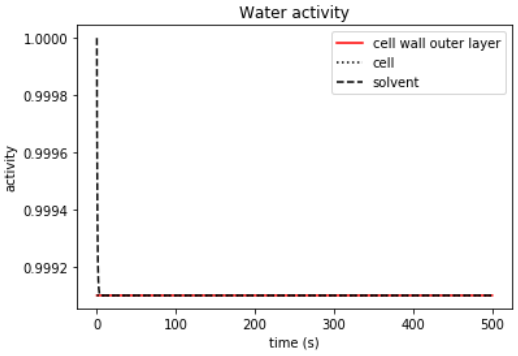
$S_s = 0.03 g_s {g_W}^{-1}$



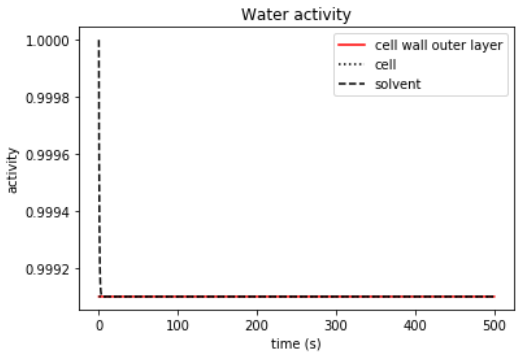
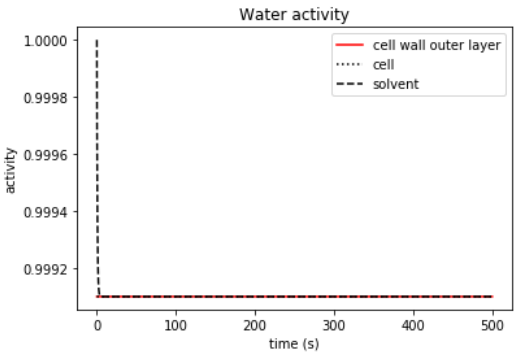
(F) $\delta t = 1\ s$

Figure C.2 – Water activity-time plots under the no-heating case where $S_s = 0.01\ g_s {g_W}^{-1}$ and $0.03\ g_s {g_W}^{-1}$, and for different computational time intervals

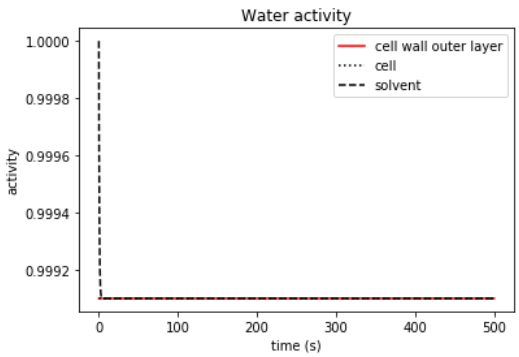
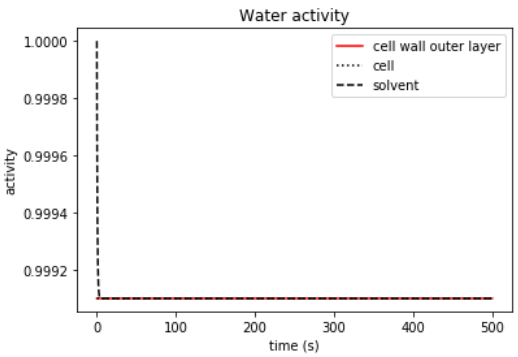
Establishing solubility (S_s) as an input model parameter allows activity values in the biomass to be defined reasonably even if the biomass incorporates small quantities of water, thereby giving flexibility to the computation. As discussed in Chapter 7 (section 7.2.2.3), S_s dictates the maximum amount of solutes that can be dissolved in water, as any excess solutes would precipitate out of solution. Hence, the water/solute activities remain constant in the respective phases until enough water diffuses inwards or S_s increases sufficiently, so as to dissolve all available solutes in the phase. The fact that activities should remain constant when decreasing the initial molar quantity of water in the biomass (at constant S_s), was assessed here. Figure C.3 demonstrates the case of cell wall fragments, where water activities clearly remain constant even as the initial water amounts are lowered. The amount of water is defined as the surplus mass percent added to the dry mass of the cell wall ($\%_{W-CW}$). Moreover, the outcomes converge with decreasing the computational time-step (δt).

$\%_{w-cw} = 0.01$	$\%_{w-cw} = 0.1$
	

(A) $\delta t = 0.00001\ s$

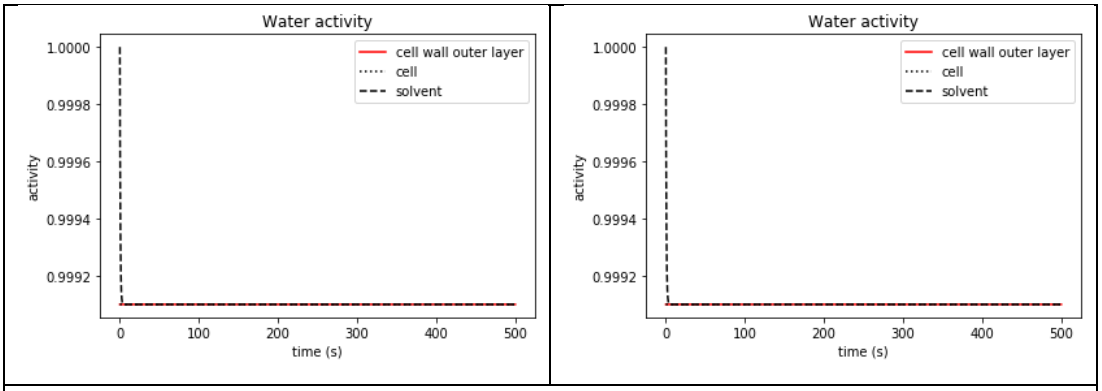
$\%_{w-cw} = 0.01$	$\%_{w-cw} = 0.1$
	

(B) $\delta t = 0.0001\ s$

$\%_{w-cw} = 0.01$	$\%_{w-cw} = 0.1$
	

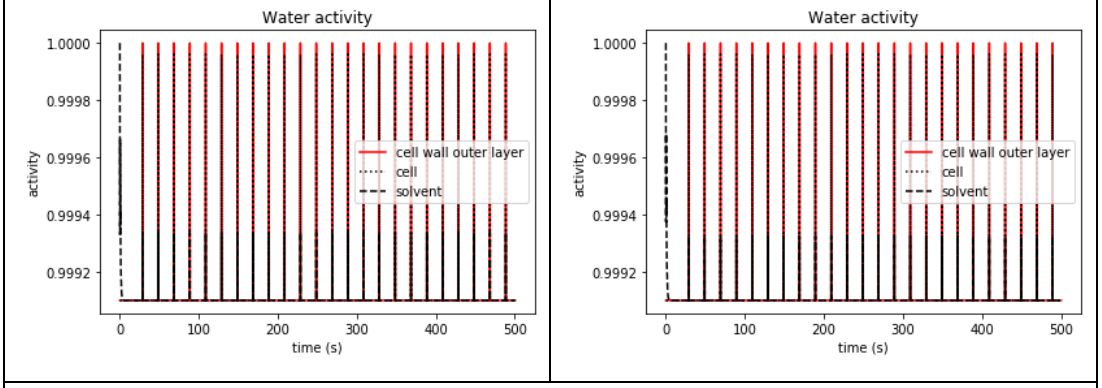
(C) $\delta t = 0.001\ s$

$\%_{w-cw} = 0.01$	$\%_{w-cw} = 0.1$



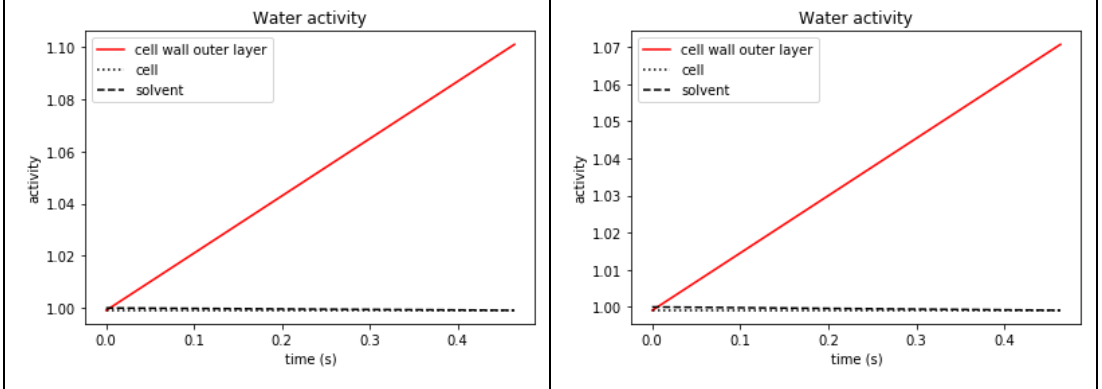
(D) $\delta t = 0.01\ s$

$\%_{W-CW} = 0.01$ $\%_{W-CW} = 0.1$



(E) $\delta t = 0.1\ s$

$\%_{W-CW} = 0.01$ $\%_{W-CW} = 0.1$



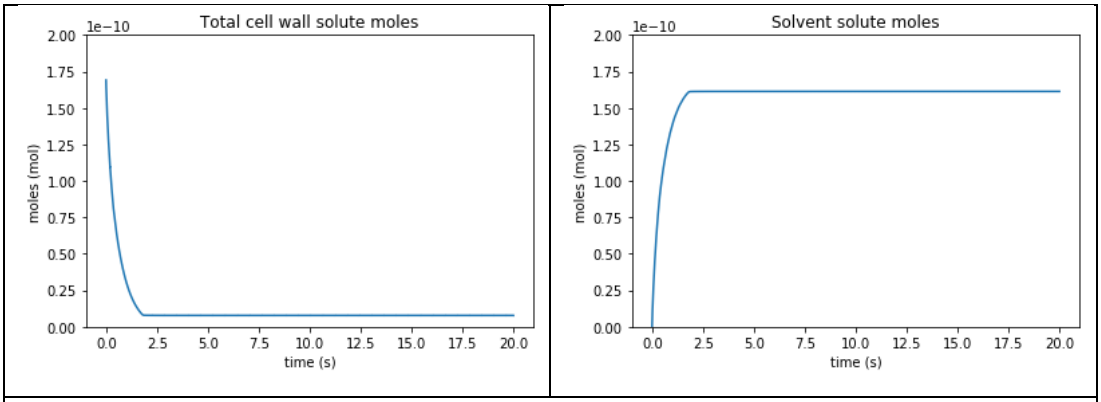
(F) $\delta t = 1\ s$

Figure C.3 – Water activity-time plots under the no-heating case where $\%_{W-CW} = 0.01$ and 0.1, and for different computational time intervals

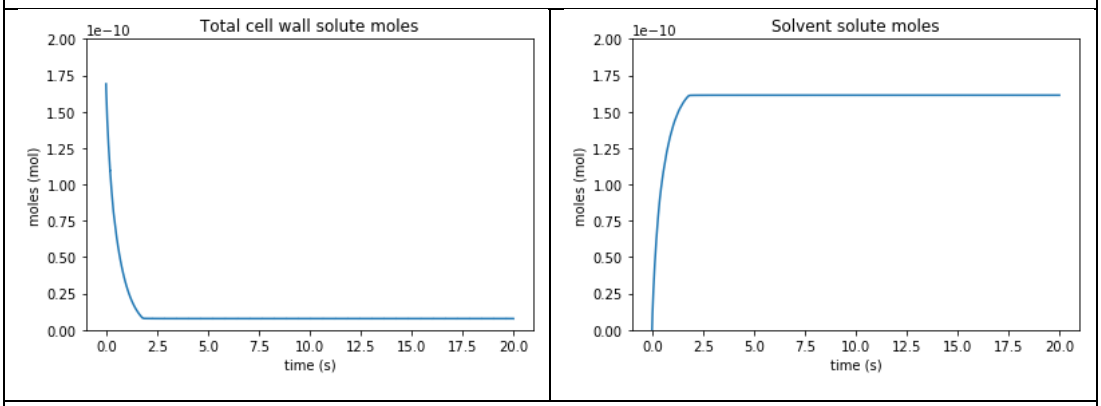
C.4 Elimination of negative molar quantities

The model had been constructed to avoid computing physically meaningless negative molar quantities. As described in Chapter 7 (section 7.2.2.1.2), such effort is necessary because mass transfer is independent of the absolute quantities of matter

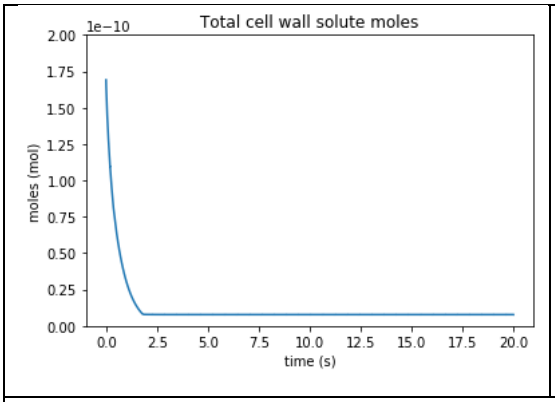
available, but rather it depends on intensive properties like mole fraction, pressure, and temperature. The model's ability to avoid negative molar quantities was assessed here through increasing the solubility (S_s), thereby increasing the activity gradients between biomass and solvent, and pushing all solutes available in the single-cell biomass to get extracted. Results are presented in Figure C.4, where extraction is clearly shown to cease as the molar quantity of solutes in the cell walls approaches a near-zero value. Moreover, the outcomes converge with decreasing the computational time-step (δt).

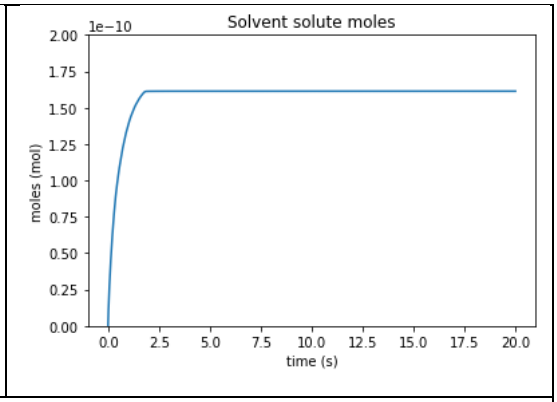


(A) $\delta t = 0.00001\ s$

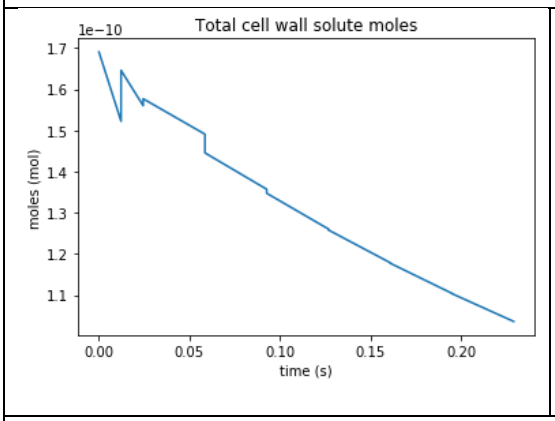


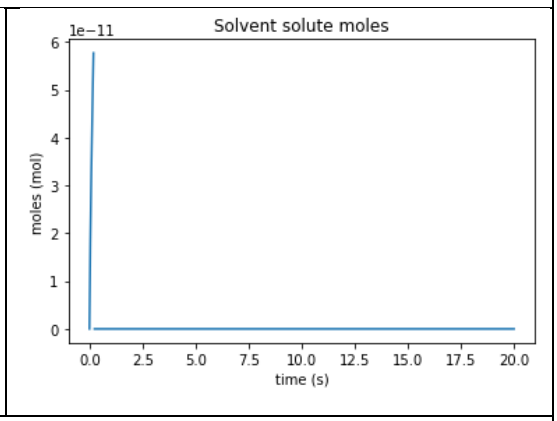
(B) $\delta t = 0.0001\ s$



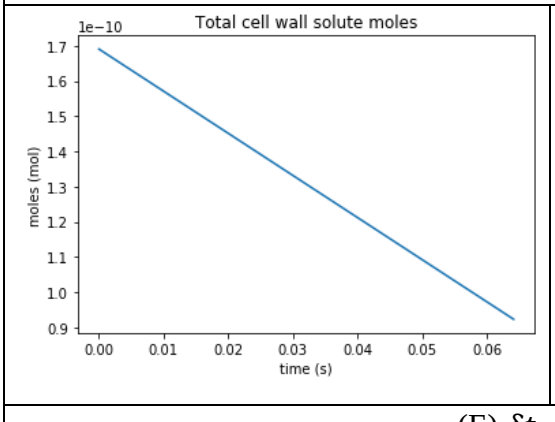


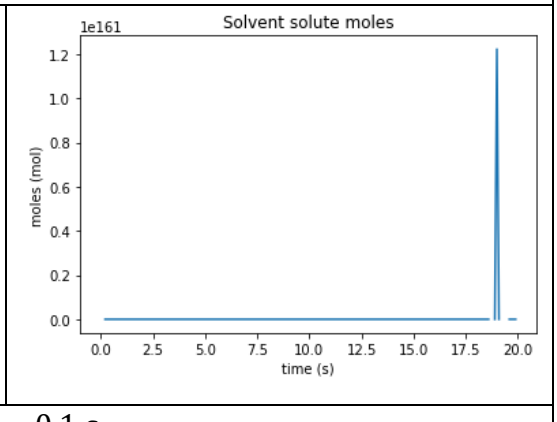
(C) $\delta t = 0.001\ s$



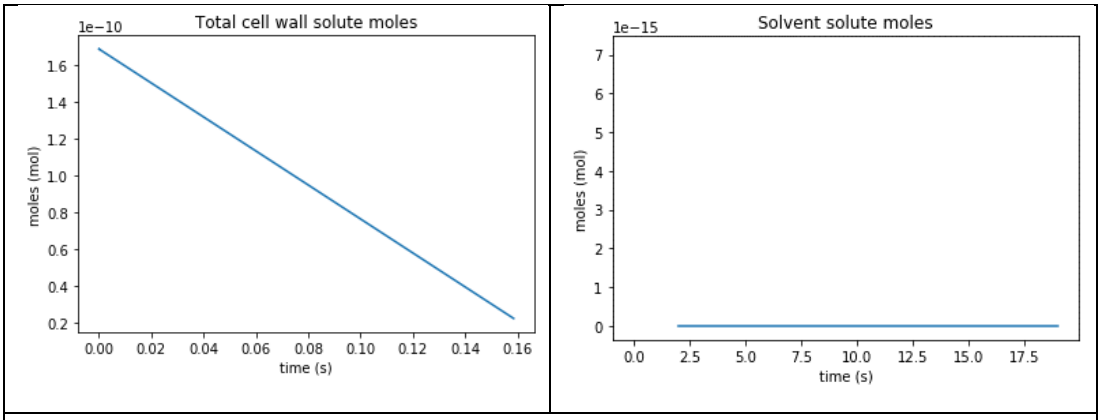


(D) $\delta t = 0.01\ s$





(E) $\delta t = 0.1\ s$



(F) $\delta t = 1\ s$

Figure C.4 – Solute quantity-time plots under the no-heating case, for different computational time intervals

APPENDIX D
Software implementation

The format of this appendix is as follows:

D.1 Background 331
D.2 Software implementation steps 331
D.2.1 Step 1: data acquisition 331
D.2.2 Step 2: expansion mechanics 331
D.2.3 Step 3: system geometry and initial values 332
D.2.4 Step 4: main computational analysis 333
D.2.5 Step 5: outcome presentation 333
D.3 Software structure 334
D.4 Libraries used in the model 336

D.1 Background

The model has been developed with Python™, but nonetheless, it can also be encoded using any other compatible programming language, or even be attempted manually where feasible. This appendix highlights the steps undertaken to implement the model as a computer software. The steps shown here complement the framework discussed in Chapter 7, as it represents the most up-to-date version of the model.

D.2 Software implementation steps

D.2.1 Step 1: data acquisition

The model requests a set of data defining all input parameters highlighted in Table 7.4, plus some additional parameters and Booleans to characterise various computational conditions such as the heating mode; the time-steps; tolerance of the numerical solver; whether some data should be treated as constants; whether to represent outcomes as figures/colour maps; and other similar functions. The code is written in an object-oriented fashion; therefore, all input data are stored in appropriate variables (e.g., arrays and dictionaries) to be used in the subsequent modules.

D.2.2 Step 2: expansion mechanics

At first, pressure-volume relationships are generated for cells and cell walls using the steps discussed in sections 5.3.1.2 and 7.2.4, respectively, and through the input mechanical/geometrical data defined by the user. The pressure-volume relationships for cells are generated separately from those generated for cell walls, but in each case, the output entails a list of polynomial coefficients to quantify pressure for a given

cell/cell wall volume. These outcomes are stored in appropriate variables (e.g., arrays and dictionaries) to be used in the subsequent modules. For observational purposes, the constructed relationships are also presented to the user as a series of figures, including stress-strain plots, stress-pressure plots, and other relevant representations.

D.2.3 Step 3: system geometry and initial values

Next, all relevant input data are used to fully define the geometry of the system, including number/orientation/arrangement of cells; locations of the numerical points and distances between them; and volume/dimensions of the solvent phase. Any symmetry in the geometry is also identified to homogenise the system, thus ensuring the elimination of all unnecessary subsequent mathematical operations. An example of such symmetry is presented in Figure D.1.

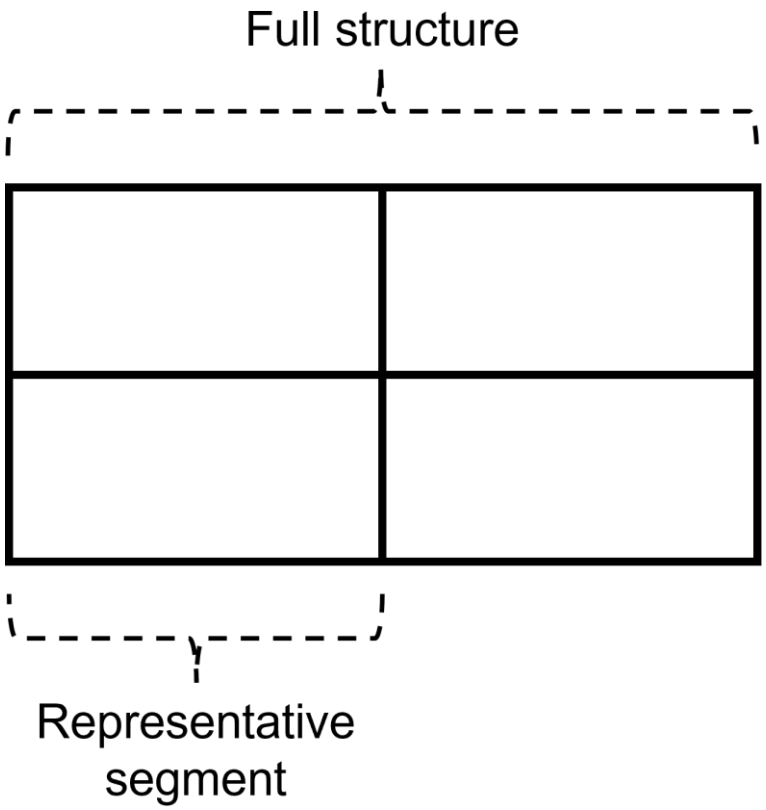


Figure D.1 – 2-dimensional structure showing perfect symmetry in the vertical and horizontal axes; therefore, the properties of the representative segment are identical to those throughout the other segments. Such symmetry can be utilised in the biomass-solvent extraction model to compute the relevant outcomes only in representative segments, thereby significantly reducing the demand for computational effort

Furthermore, each phase in the system gets assigned with initial temperature and water/solute quantities as per the user-defined input parameter. Initial temperature is defined directly by the user, whereas the water/solute quantities are computed indirectly based on other input parameters like dimensions, densities, mass percentages, solvent-to-solid ratio, etc. The model also computes the incident electric field intensity upon the system, using prior input data defining the desired heating rate in the solvent (Q_s), and the system's heating mode (i.e., continuous microwave heating, ramp microwave heating, or conventional heating).

All outcomes are stored in appropriate variables (e.g., arrays and dictionaries) to be used in subsequent modules. Additionally, for observational purposes the software generates a set of visualisations detailing the computed biomass geometry.

D.2.4 Step 4: main computational analysis

All input parameters together with the computed pressure-volume relationships (section D.2.2) and geometry/initial values (section D.2.3), are assembled to compute temporal changes in the system's temperatures, molar quantities, and pressures. This is the principal task of the model, and it is conducted numerically over a predefined time domain (Chapter 7; section 7.2.5.4). Each time-step entails defining pressures, activities, and potentials for all numerical points in the system, and subsequently computing the differentials in temperatures and molar quantities.

This process is repeated based on the number of analyses requested by the user initially, as the model allows multiple extraction simulations to be conducted in a single run, which is useful to compare the results at variable conditions and, e.g., plot them together.

All outcomes from this computational exercise stored in appropriate variables (e.g., arrays and dictionaries) to be displayed as results.

D.2.5 Step 5: outcome presentation

The analysis described in section D.2.4 returns a series of outcomes including the temporal changes of temperature, pressure, molar quantities, activities, and potentials in the biomass-solvent system. These outcomes are then used to extrapolate a further set of results including yield percentages, times needed to achieve thermal and mass equilibria, and others. The results are presented either in writing, as 2-dimensional plots, or in both forms, depending on the most practical method of presentation in each

case. If required by the user, colour maps are also generated to represent the distributions of temperature, pressure, and water activity in the system at a given time-step. An example of such colour map for temperature distribution at thermal steady state is shown in Figure 7.25 (Chapter 7).

Furthermore, when multiple analyses are requested in the same run (e.g., two analyses with different heating rates), the final yield-time data are plotted together on a single diagram, enabling efficient comparison between the different attained extraction outcomes.

D.3 Software structure

The model has been constructed in an object-oriented fashion; in that it incorporates several scripts linked with each other as demonstrated in Figure D.2.

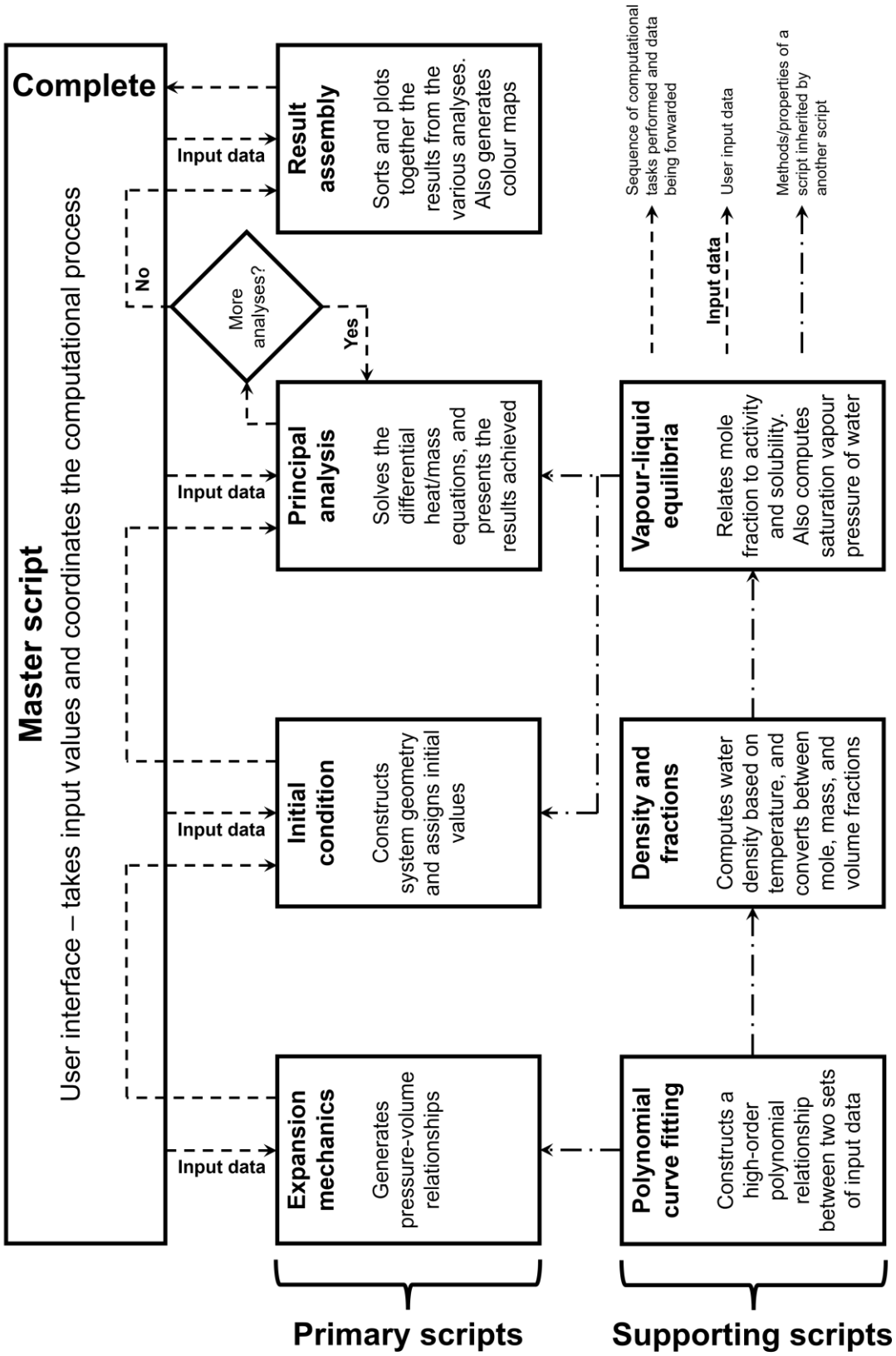


Figure D.2 – Software structure mapping the links between the various model elements, which are connected in an object-oriented fashion

D.4 Libraries used in the model

Table D.1 summarises the Python libraries used in this work.

Library	Use
NumPy (Harris et al., 2020)	To manage data, numbers, variables, and arrays, and to provide some mathematical functions: • Creating, appending, and modifying lists of data. • Extracting data from lists based on specific criteria (e.g., the n^{th} entry or the largest figure). • Conducting various mathematical operations such as summing all numbers in a list or quantifying the absolute magnitudes of given parameters. • Providing some mathematical constants like π and exp. • Providing some mathematical functions such as the natural logarithm and the Heaviside function.
SciPy (Virtanen et al., 2020)	To solve equations: • Solving the differential heat and mass equations numerically. • Finding roots of some functions that are otherwise difficult to solve/rearrange.
Matplotlib (Hunter, 2007)	To visualise outcomes and trends: • Constructing various 2-dimensional plots to display results, trends, and polynomial estimations. • Constructing colour maps to visualise system geometry as well as temperature, pressure, and water activity distributions across the system at a given time-step.
Time (Available with Python)	To measure the durations required for simulation runs: • Displaying local date/time at the start of a simulation run. • Measuring and displaying the total time taken to complete a simulation run. • Aiding in the dynamic estimation of time needed to complete an ongoing simulation run.
Sys (Available with Python)	To manipulate software environment during simulation runs: • Calling errors and stopping the simulation on detecting inaccurate/unsupported user inputs, which are otherwise not recognised as errors in the syntax/functionality of the programming language. • Aiding in the dynamic display of computational progress (percentage completion and estimated time remaining).
Os (Available with Python)	To save the visual outcomes of the model automatically when needed: • Accessing the machine's directory and creating folders based on a predefined arrangement. • Saving the figures generated by the model into the created folders in an organised manner.

Table D.1 – Python libraries used in this work

REFERENCES

Adam, M., Beneroso, D., Katrib, J., Kingman, S. and Robinson, J.P., 2017. Microwave fluidized bed for biomass pyrolysis. Part I: Process design. *Biofuels, Bioproducts and Biorefining*, 11, pp.601–612.

Adetunji, L.R., Adekunle, A., Orsat, V. and Raghavan, V., 2017. Advances in the pectin production process using novel extraction techniques: A review. *Food Hydrocolloids*, 62, pp.239–250.

Alcántara, M.Á.B., Dobruchowska, J., Azadi, P., García, B.D., Molina-Heredia, F.P. and Reyes-Sosa, F.M., 2016. Recalcitrant carbohydrates after enzymatic hydrolysis of pretreated lignocellulosic biomass. *Biotechnology for Biofuels*, 9.

Alexander, M.M. and Sulebele, G.A., 1973. Pectic substances in onion and garlic skins. *Journal of the Science of Food and Agriculture*, 24, pp.611–615.

Altarawneh, S., Al-Harahsheh, M., Buttress, A., Dodds, C., Rodriguez, J. and Kingman, S., 2021. Microwave selective heating of electric arc furnace dust constituents toward sustainable recycling: Contribution of electric and magnetic fields. *Journal of Industrial and Engineering Chemistry*, 104, pp.521–528.

Amarni, F. and Kadi, H., 2010. Kinetics study of microwave-assisted solvent extraction of oil from olive cake using hexane Comparison with the conventional extraction. *Innovative Food Science and Emerging Technologies*, 11, pp.322–327.

Anderson, C.T., Carroll, A., Akhmetova, L. and Somerville, C., 2010. Real-time imaging of cellulose reorientation during cell wall expansion in Arabidopsis roots. *Plant Physiology*, 152, pp.787–796.

Angiolillo, L., Del Nobile, M.A. and Conte, A., 2015. The extraction of bioactive compounds from food residues using microwaves. *Current Opinion in Food Science*, 5, pp.93–98.

Arrutia, F., Adam, M., Calvo-Carrascal, M.Á., Mao, Y. and Binner, E., 2020. Development of a continuous-flow system for microwave-assisted extraction of pectin-derived oligosaccharides from food waste. *Chemical Engineering Journal*, 395, p.125056.

Ayappa, K.G., Davis, H.T., Crapiste, G., Davis, E.A. and Gordon, J., 1991. Microwave heating: an evaluation of power formulations. *Chemical Engineering Science*, 46, pp.1005–1016.

Bagherian, H., Zokaee Ashtiani, F., Fouladitajar, A. and Mohtashamy, M., 2011. Comparisons between conventional, microwave- and ultrasound-assisted methods for extraction of pectin from grapefruit. *Chemical Engineering and Processing: Process Intensification*, 50, pp.1237–1243.

Bartley, I.M. and Knee, M., 1982. The chemistry of textural changes in fruit during storage. *Food Chemistry*, 9, pp.47–58.

Bashline, L., Lei, L., Li, S. and Gu, Y., 2014. Cell wall, cytoskeleton, and cell expansion in higher plants. *Molecular Plant*, 7, pp.586–600.

Baskin, T.I., 2005. Anisotropic expansion of the plant cell wall. *Annual Review of Cell and Developmental Biology*, 21, pp.203–222.

Beneroso, D., Albero-Ortiz, A., Monzó-Cabrera, J., Díaz-Morcillo, A., Arenillas, A. and Menéndez, J.A., 2016. Dielectric characterization of biodegradable wastes during pyrolysis. *Fuel*, 172, pp.146–152.

Beneroso, D., Monti, T., Kostas, E.T. and Robinson, J., 2017. Microwave pyrolysis of biomass for bio-oil production : Scalable processing concepts. *Chemical Engineering Journal*, 316, pp.481–498.

Bowley, R. and Sanchez, M., 1999. *Introductory Statistical Mechanics*. 2nd ed. Oxford: Clarendon Press.

BP, 2016. *BP energy outlook 2016*. [online] Available at: <https://www.bp.com/content/dam/bp/business-sites/en/global/corporate/pdfs/energy-economics/energy-outlook/bp-energy-outlook-2016.pdf>.

BP, 2017. *BP energy outlook 2017*. [online] Available at: <https://www.bp.com/content/dam/bp/business-sites/en/global/corporate/pdfs/energy-economics/energy-outlook/bp-energy-outlook-2017.pdf>.

BP, 2018. *BP energy outlook 2018*. [online] Available at: <https://www.bp.com/content/dam/bp/business-sites/en/global/corporate/pdfs/energy-economics/energy-outlook/bp-energy-outlook-2018.pdf>.

BP, 2019. *BP energy outlook 2019*. [online] Available at: <https://www.bp.com/content/dam/bp/business-sites/en/global/corporate/pdfs/energy-economics/energy-outlook/bp-energy-outlook-2019.pdf>.

BP, 2020. *BP energy outlook 2020*. [online] Available at: <https://www.bp.com/content/dam/bp/business-sites/en/global/corporate/pdfs/energy-economics/energy-outlook/bp-energy-outlook-2020.pdf>.

Brace, C.L., 2009. Microwave Ablation Technology: What Every User Should Know. *Current Problems in Diagnostic Radiology*, 38, pp.61–67.

Budarin, V.L., Clark, J.H., Lanigan, B.A., Shuttleworth, P. and Macquarrie, D.J., 2010. Microwave assisted decomposition of cellulose: A new thermochemical route for biomass exploitation. *Bioresource Technology*, 101, pp.3776–3779.

Bykov, Y. V., Rybakov, K.I. and Semenov, V.E., 2001. High-temperature microwave processing of materials. *Journal of Physics D: Applied Physics*, 34, pp.R55–R75.

Calinescu, I., Lavric, V., Asofiei, I., Gavrila, A.I., Trifan, A., Ighigeanu, D., Martin, D. and Matei, C., 2017. Microwave assisted extraction of polyphenols using a coaxial antenna and a cooling system. *Chemical Engineering and Processing: Process Intensification*, 122, pp.373–379.

Carpenter, D., Westover, T.L., Czernik, S. and Jablonski, W., 2014. Biomass feedstocks for renewable fuel production: A review of the impacts of feedstock and pretreatment on the yield and product distribution of fast pyrolysis bio-oils and vapors. *Green Chemistry*, 16, pp.384–406.

de Castro, M.D.L. and García-Ayuso, L.E., 1998. Soxhlet extraction of solid materials: An outdated technique with a promising innovative future. *Analytica Chimica Acta*, 369, pp.1–10.

Chan, C.-H., Yusoff, R. and Ngoh, G.-C., 2015. Assessment of scale-up parameters of microwave-assisted extraction via the extraction of flavonoids from cocoa leaves. *Chemical Engineering Technology*, 38, pp.489–496.

Chan, C., Yeoh, H.K., Yusoff, R. and Ngoh, G.C., 2016. A first-principles model for plant cell rupture in microwave-assisted extraction of bioactive compounds. *Journal of Food Engineering*, 188, pp.98–107.

Chan, C.H., Lim, J.J., Yusoff, R. and Ngoh, G.C., 2015. A generalized energy-based kinetic model for microwave-assisted extraction of bioactive compounds from plants. *Separation and Purification Technology*, 143, pp.152–160.

Chan, C.H., Yusoff, R., Ngoh, G.-C. and Kung, F.W.-L., 2011. Microwave-assisted extractions of active ingredients from plants. *Journal of Chromatography A*, 1218, pp.6213–6225.

Chan, C.H., Yusoff, R. and Ngoh, G.C., 2013. Modeling and prediction of extraction profile for microwave-assisted extraction based on absorbed microwave energy. *Food Chemistry*, 140, pp.147–153.

Chan, C.H., Yusoff, R. and Ngoh, G.C., 2014. Modeling and kinetics study of conventional and assisted batch solvent extraction. *Chemical Engineering Research and Design*, 92, pp.1169–1186.

Chandler, D., 1987. *Introduction to Modern Statistical Mechanics*. New York, Oxford: Oxford University Press.

Chandrasekaran, S., Ramanathan, S. and Basak, T., 2012. Microwave material processing - A review. *AIChE Journal*, 58, pp.330–363.

Chaplain, M.A.J., 1993. The strain energy function of an ideal plant cell wall. *Journal of Theoretical Biology*, 163, pp.77–97.

Cherubini, F., 2010. The biorefinery concept: Using biomass instead of oil for producing energy and chemicals. *Energy Conversion and Management*, 51, pp.1412–1421.

Chew, K.K., Khoo, M.Z., Ng, S.Y., Thoo, Y.Y., Wan Aida, W.M. and Ho, C.W.,

2011. Effect of ethanol concentration, extraction time and extraction temperature on the recovery of phenolic compounds and antioxidant capacity of Centella asiatica extracts. *International Food Research Journal*, 18, pp.1427–1435.

Chumnanpaisont, N., Niamnuy, C. and Devahastin, S., 2014. Mathematical model for continuous and intermittent microwave-assisted extraction of bioactive compound from plant material: Extraction of β-carotene from carrot peels. *Chemical Engineering Science*, 116, pp.442–451.

Chupin, L., Maunu, S.L., Reynaud, S., Pizzi, A., Charrier, B. and Charrier-EL Bouhtoury, F., 2015. Microwave assisted extraction of maritime pine (Pinus pinaster) bark: Impact of particle size and characterization. *Industrial Crops and Products*, 65, pp.142–149.

Clark, D.E., Folz, D.C. and West, J.K., 2000. Processing materials with microwave energy. *Materials Science and Engineering A*, 287, pp.153–158.

Clark, D.E. and Sutton, W.H., 1996. Microwave processing of materials. *Annual Review of Materials Science*, 26, pp.299–331.

Clark, J. and Deswarte, F., 2015. The Biorefinery Concept: An Integrated Approach. In: J.H. Clark and F. Deswarte, eds. *Introduction to Chemicals from Biomass*, 2nd ed. Chichester: John Wiley & Sons.

Cosgrove, D.J., 2014. Re-constructing our models of cellulose and primary cell wall assembly. *Current Opinion in Plant Biology*, 22, pp.122–131.

Cosgrove, D.J., 2016. Plant cell wall extensibility: Connecting plant cell growth with cell wall structure, mechanics, and the action of wall-modifying enzymes. *Journal of Experimental Botany*, 67, pp.463–476.

Coulson, J.M., Richardson, J.F., Backhurst, J.R. and Harker, J.H., 1999. *Coulson & Richardson's Chemical Engineering - Volume 1*. 6th ed. Oxford, Woburn: Butterworth-Heinemann.

Dahmoune, F., Nayak, B., Moussi, K., Remini, H. and Madani, K., 2015. Optimization of microwave-assisted extraction of polyphenols from Myrtus communis L. leaves. *Food Chemistry*, 166, pp.585–595.

Dahmoune, F., Spigno, G., Moussi, K., Remini, H., Cherbal, A. and Madani, K., 2014. Pistacia lentiscus leaves as a source of phenolic compounds: Microwave-assisted extraction optimized and compared with ultrasound-assisted and conventional solvent extraction. *Industrial Crops and Products*, 61, pp.31–40.

Dang, Y.-Y., Zhang, H. and Xiu, Z.-L., 2014. Microwave-assisted aqueous two-phase extraction of phenolics from grape (Vitis vinifera) seed. *Journal of Chemical Technology and Biotechnology*, 89, pp.1576–1581.

Datta, A., Sumnu, G. and Raghavan, G.S. V., 2005. Dielectric Properties of Foods. In: M.A. Rao, S.S.H. Rizvi and A.K. Datta, eds. *Engineering Properties of Foods*, 3rd ed. Boca Raton: Taylor & Francis.

Demain, A.L., Newcomb, M. and Wu, J.H.D., 2005. Cellulase, clostridia, and ethanol. *Microbiology and Molecular Biology Reviews*, 69, pp.124–154.

Devlin, R.M. and Witham, F.H., 1983. *Plant Physiology*. 4th ed. Belmont: PWS Publishers.

Dinulovic´, M. and Rašuo, B., 2011. Dielectric modeling of multiphase composites. *Composite Structures*, 93, pp.3209–3215.

Dotsenko, A.S., Dotsenko, G.S., Senko, O. V., Stepanov, N.A., Lyagin, I. V., Efremenko, E.N., Gusakov, A. V., Zorov, I.N. and Rubtsova, E.A., 2018. Complex effect of lignocellulosic biomass pretreatment with 1-butyl-3-methylimidazolium chloride ionic liquid on various aspects of ethanol and fumaric acid production by immobilized cells within SSF. *Bioresource Technology*, 250, pp.429–438.

Duan, D., Ruan, R., Wang, Y., Liu, Y., Dai, L., Zhao, Y., Zhou, Y. and Wu, Q., 2018. Microwave-assisted acid pretreatment of alkali lignin: Effect on characteristics and pyrolysis behavior. *Bioresource Technology*, 251, pp.57–62.

Eastman, P., 2019. *Introduction to statistical mechanics*. [online] Available at: <https://web.stanford.edu/~peastman/statmech/> [Accessed 1 Dec. 2019].

El-Nawawi, S.A. and Shehata, F.R., 1987. Extraction of pectin from Egyptian orange peel. Factors affecting the extraction. *Biological Wastes*, 20, pp.281–290.

Electronic Communications Committee, 2020. *The european table of frequency allocations and applications in the frequency range 8.3 kHz to 3000 GHz (ECA Table) - ERC report 25*.

Engineering Toolbox, 2003. *Thermal conductivity of some selected materials and gases*. [online] Available at: <https://www.engineeringtoolbox.com/thermal-conductivity-d_429.html> [Accessed 16 Feb. 2021].

Engineering Toolbox, 2005. *Standardized enthalpies and entropies*. [online] Available at: <https://www.engineeringtoolbox.com/enthalpy-entropy-d_998.html>.

Erić, A., Komatina, M., Nemoda, S., Dakić, D. and Repić, B., 2016. Determination of thermal conductivity of baled agricultural biomass. *Renewable and Sustainable Energy Reviews*, 58, pp.876–884.

FAO, 2011. *Global food losses and food waste: extent, causes and prevention*. [online] Available at: <http://www.fao.org/3/i2697e/i2697e.pdf>.

Farmer, T.J. and Mascal, M., 2015. Platform Molecules. In: J.H. Clark and F. Deswarte, eds. *Introduction to Chemicals from Biomass*, 2nd ed. Chichester: John Wiley & Sons.

Federal Communications Commission, 2021. *FCC online table of frequency allocations - 47 C.F.R. § 2.106 - Revised on February 1, 2021*.

Ferhat, M.A., Meklati, B.Y., Smadja, J. and Chemat, F., 2006. An improved microwave Clevenger apparatus for distillation of essential oils from orange peel.

Journal of Chromatography A, 1112, pp.121–126.

Flórez, N., Conde, E. and Domínguez, H., 2015. Microwave assisted water extraction of plant compounds. *Journal of Chemical Technology and Biotechnology*, 90, pp.590–607.

Fry, S.C., 1998. Oxidative scission of plant cell wall polysaccharides by ascorbate-induced hydroxyl radicals. *Biochemical Journal*, 332, pp.507–515.

Gabriel, C., Gabriel, S., Grant, E.H., Halstead, B.S.J. and Mingos, D.M.P., 1998. Dielectric parameters relevant to microwave dielectric heating. *Chemical Society Reviews*, 27, pp.213–224.

Gaff, D.F. and Carr, D.T., 1961. The quantity of water in the cell wall and its significance. *Australian Journal of Biological Sciences*, 14, pp.299–311.

Galan, A.M., Calinescu, I., Trifan, A., Winkworth-Smith, C., Calvo-Carrascal, M., Dodds, C. and Binner, E., 2017. New insights into the role of selective and volumetric heating during microwave extraction: Investigation of the extraction of polyphenolic compounds from sea buckthorn leaves using microwave-assisted extraction and conventional solvent extraction. *Chemical Engineering and Processing - Process Intensification*, 116, pp.29–39.

González-Nuñez, L.N. and Cañizares-Macías, M.P., 2011. Focused microwaves-assisted extraction of theobromine and caffeine from cacao. *Food Chemistry*, 129, pp.1819–1824.

Green, P.B., 1960. Multinet growth in the cell wall of Nitella. *The Journal of biophysical and biochemical cytology*, 7, pp.289–296.

Greenberg, J.T., 1996. Programmed cell death: A way of life for plants. *Proceedings of the National Academy of Sciences of the United States of America*, 93, pp.12094–12097.

Gujar, J.G., Wagh, S.J. and Gaikar, V.G., 2010. Experimental and modeling studies on microwave-assisted extraction of thymol from seeds of Trachyspermum ammi (TA). *Separation and Purification Technology*, 70, pp.257–264.

Gunawardena, A.H., Greenwood, J.S. and Dengler, N.G., 2007. Cell wall degradation and modification during programmed cell death in lace plant, Aponogeton madagascariensis (Aponogetonaceae). *American Journal of Botany*, 94, pp.1116–1128.

Gunawardena, A.H.L.A.N., Greenwood, J.S. and Dengler, N.G., 2004. Programmed cell death remodels lace plant leaf shape during development. *The Plant Cell*, 16, pp.60–73.

Guo, Q., Xia, Y., Sandig, M. and Yang, J., 2012. Characterization of cell elasticity correlated with cell morphology by atomic force microscope. *Journal of Biomechanics*, 45, pp.304–309.

Harris, C.., Millman, K.J., van der Walt, S.J., Gommers, R., Virtanen, P.,

Cournapeau, D., Wieser, E., Taylor, J., Berg, S., Smith, N.J. and Kern, R., 2020. Array programming with NumPy. *Nature*, 585, pp.357–362.

Herrero, M. and Ibañez, E., 2018. Green extraction processes, biorefineries and sustainability: Recovery of high added-value products from natural sources. *Journal of Supercritical Fluids*, 134, pp.252–259.

Hole, C.C., Drew, R.L.K. and Gray, D., 2000. Humidity and mechanical properties of onion skins. *Postharvest Biology and Technology*, 19, pp.229–237.

Hu, F. and Ragauskas, A., 2012. Pretreatment and lignocellulosic chemistry. *Bioenergy Research*, 5, pp.1043–1066.

Huang, H.J., Ramaswamy, S., Tschirner, U.W. and Ramarao, B. V., 2008. A review of separation technologies in current and future biorefineries. *Separation and Purification Technology*, 62, pp.1–21.

Huang, K., 1963. *Statistical Mechanics*. New York, London: John Wiley & Sons.

Hunter, J.D., 2007. Matplotlib: A 2D graphics environment. *Computing in Science and Engineering*, 9, pp.90–95.

Huray, P.G., 2010. *Maxwell's Equations*. New Jersey: John Wiley & Sons.

IEA, 2009a. *Bioenergy - A sustainable and reliable energy source*. [online] Available at: <http://www.globalbioenergy.org/uploads/media/0912_IEA_Bioenergy_-_MAIN_REPORT_-_Bioenergy_-_a_sustainable_and_reliable_energy_source._A_review_of_status_and_prospects.pdf>.

IEA, 2009b. *Biorefineries: Adding value to the sustainable utilisation of biomass*. [online] Available at: <https://www.ieabioenergy.com/wp-content/uploads/2013/10/Task-42-Booklet.pdf>.

Jawaid, M., Paridah, M.T. and Saba, N., 2017. Introduction to Biomass and its Composites. In: M. Jawaid, M.T. Paridah and N. Saba, eds. *Lignocellulosic Fible and Biomass-Based Composite Materials: Processing, Properties and Applications*. Duxford, Csmbridge, Kidlington: Elsevier.

Jiang, H., Liu, Z. and Wang, S., 2018. Microwave processing: Effects and impacts on food components. *Critical Reviews in Food Science and Nutrition*, 58, pp.2476–2489.

Job, G. and Herrmann, F., 2006. Chemical potential - a quantity in search of recognition. *European Journal of Physics*, 27, pp.353–371.

Jones, A.M., 2001. Programmed cell death in development and defense. *Plant Physiology*, 125, pp.94–97.

Jones, D.A., Lelyveld, T.P., Mavrofidis, S.D., Kingman, S.W. and Miles, N.J., 2002. Microwave heating applications in environmental engineering - A review.

Resources, Conservation and Recycling, 34, pp.75–90.

Jong, E. De and Jungmeier, G., 2015. Biorefinery Concepts in Comparison to Petrochemical Refineries. In: A. Pandey, R. Höfer, M. Taherzadeh, M. Nampoothiri and C. Larroche, eds. *Industrial Biorefineries and White Biotechnology*. Amsterdam, Oxford, Waltham: Elsevier B.V.

Kaatze, U., 1989. Complex permittivity of water as a function of frequency and temperature. *Journal of Chemical and Engineering Data*, 34, pp.371–374.

Kala, H.K., Mehta, R., Sen, K.K., Tandey, R. and Mandal, V., 2016. Critical analysis of research trends and issues in microwave assisted extraction of phenolics: Have we really done enough. *Trends in Analytical Chemistry*, 85, pp.140–152.

Kappe, C.O., 2004. Controlled microwave heating in modern organic synthesis. *Angewandte Chemie - International Edition*, 43, pp.6250–6284.

Kappe, C.O., Pieber, B. and Dallinger, D., 2013. Microwave effects in organic synthesis: Myth or reality? *Angewandte Chemie - International Edition*, 52, pp.1088–1094.

Kappe, C.O., Stadler, A. and Dallinger, D., 2012. *Microwaves in Organic and Medicinal Chemistry*. 2nd ed. *Methods and Principles in Medicinal Chemistry*, Weinheim: Wiley-VCH.

Karabegović, I.T., Stojičević, S.S., Veličković, D.T., Nikolić, N.Č. and Lazić, M.L., 2013. Optimization of microwave-assisted extraction and characterization of phenolic compounds in cherry laurel (Prunus laurocerasus) leaves. *Separation and Purification Technology*, 120, pp.429–436.

Kaufmann, B., Christen, P. and Veuthey, J.-L., 2001. Parameters affecting microwave-assisted extraction of withanolides. *Phytochemical Analysis*, 12, pp.327–331.

Kishikawa, Y., Shinohara, H., Maeda, K., Nakamura, Y., Wiegand, S. and Kita, R., 2012. Temperature dependence of thermal diffusion for aqueous solutions of monosaccharides, oligosaccharides, and polysaccharides. *Physical Chemistry Chemical Physics*, 14, pp.10147–10153.

Kostas, E.T., Beneroso, D. and Robinson, J.P., 2017. The application of microwave heating in bioenergy: A review on the microwave pre-treatment and upgrading technologies for biomass. *Renewable and Sustainable Energy Reviews*, 77, pp.12–27.

Koyama, T. and Tsukada, Y., 2021. Ludwig–Soret effect formulated from the grain-boundary-phase model. *Calphad*, 73, p.102269.

Kratchanova, M., Pavlova, E. and Panchev, I., 2004. The effect of microwave heating of fresh orange peels on the fruit tissue and quality of extracted pectin. *Carbohydrate Polymers*, 56, pp.181–185.

Kumar, C.S., Sivakumar, M. and Ruckmani, K., 2016. Microwave-assisted

extraction of polysaccharides from Cyphomandra betacea and its biological activities. *International Journal of Biological Macromolecules*, 92, pp.682–693.

Kumar, R., Singh, S. and Singh, O. V, 2008. Bioconversion of lignocellulosic biomass: biochemical and molecular perspectives. *Journal of Industrial Microbiology and Biotechnology*, 35, pp.377–391.

Leão, D.P., Botelho, B.G., Oliveira, L.S. and Franca, A.S., 2018. Potential of pequi (Caryocar brasiliense Camb.) peels as sources of highly esterified pectins obtained by microwave assisted extraction. *LWT - Food Science and Technology*, 87, pp.575–580.

Lee, C.S., Binner, E., Winkworth-Smith, C., John, R., Gomes, R. and Robinson, J., 2016. Enhancing natural product extraction and mass transfer using selective microwave heating. *Chemical Engineering Science*, 149, pp.97–103.

Lee, C.S., Chong, M.F., Robinson, J. and Binner, E., 2015. Optimisation of extraction and sludge dewatering efficiencies of bio-flocculants extracted from Abelmoschus esculentus (okra). *Journal of Environmental Management*, 157, pp.320–325.

Letellier, M. and Budzinski, H., 1999. Microwave assisted extraction of organic compounds. *Analusis*, 27, pp.259–271.

Li, Y., Fabiano-Tixier, A.S., Vian, M.A. and Chemat, F., 2013. Solvent-free microwave extraction of bioactive compounds provides a tool for green analytical chemistry. *Trends in Analytical Chemistry*, 47, pp.1–11.

Liu, J., Takada, R., Karita, S., Watanabe, T., Honda, Y. and Watanabe, T., 2010. Microwave-assisted pretreatment of recalcitrant softwood in aqueous glycerol. *Bioresource Technology*, 101, pp.9355–9360.

Lynd, L.R., 1996. Overview and evaluation of fuel ethanol from cellulosic biomass: Technology, economics, the environment, and policy. *Annual Review of Energy and the Environment*, 21, pp.403–465.

Mandal, S.C., Mandal, V. and Das, A.K., 2015. *Essentials of Botanical Extraction: Principles and Applications*. London, San Diego, Waltham, Oxford: Elsevier Academic Press.

Mao, Y., Lei, R., Ryan, J., Arrutia Rodriguez, F., Rastall, B., Chatzifragkou, A., Winkworth-Smith, C., Harding, S.E., Ibbett, R. and Binner, E., 2019. Understanding the influence of processing conditions on the extraction of rhamnogalacturonan-I “hairy” pectin from sugar beet pulp. *Food Chemistry: X*, 2, p.100026.

Mao, Y., Robinson, J. and Binner, E., 2021. Understanding heat and mass transfer processes during microwave-assisted and conventional solvent extraction. *Chemical Engineering Science*, 233, p.116418.

Maran, J.P. and Prakash, K.A., 2015. Process variables influence on microwave assisted extraction of pectin from waste Carcia papaya L. peel. *International Journal of Biological Macromolecules*, 73, pp.202–206.

Mehdizadeh, M., 2015. *Microwave/RF Applicators and Probes for Material Heating, Sensing, and Plasma Generation*. 2nd ed. Oxford, Waltham: Elsevier.

Menéndez, J.A., Arenillas, A., Fidalgo, B., Fernández, Y., Zubizarreta, L., Calvo, E.G. and Bermúdez, J.M., 2010. Microwave heating processes involving carbon materials. *Fuel Processing Technology*, 91, pp.1–8.

Meredith, R., 1998. *Engineers' Handbook of Industrial Microwave Heating*. *Engineers' Handbook of Industrial Microwave Heating*. Stevenage: Institution of Engineering and Technology 2007.

Metaxas, A.C., 1991. Microwave heating. *Power Engineering Journal*, 5, pp.237–247.

Metaxas, A.C. and Meredith, R.J., 1983. *Industrial Microwave Heating*. *Industrial Microwave Heating*. Stevenage: Institution of Engineering and Technology 2008.

Mishra, R.R. and Sharma, A.K., 2016. Microwave–material interaction phenomena: Heating mechanisms, challenges and opportunities in material processing. *Composites: Part A*, 81, pp.78–97.

Moyer, J.C. and Holgate, K.C., 1948. Determination of alcohol-insoluble solids and sugar contents of vegetables. *Analytical Chemistry*, 20, pp.472–474.

Mulakhudair, A.R., Hanotu, J. and Zimmerman, W., 2016. Exploiting microbubble-microbe synergy for biomass processing: Application in lignocellulosic biomass pretreatment. *Biomass and Bioenergy*, 93, pp.187–193.

Nelson, S.O., 1994. Measurement of microwave dielectric properties of particulate materials. *Journal of Food Engineering*, 21, pp.365–384.

Nesvadba, P., 2005. Thermal Properties of Unfrozen Foods. In: M.A. Rao, S.S.H. Rizvi and A.K. Datta, eds. *Engineering Properties of Foods*, 3rd ed. Taylor & Francis.

Ng, A. and Waldron, K.W., 1997. Effect of cooking and pre-cooking on cell-wall chemistry in relation to firmness of carrot tissues. *Journal of the Science of Food and Agriculture*, 73, pp.503–512.

NIST, 2017. *Thermophysical properties of fluid systems*. [online] Available at: <https://webbook.nist.gov/chemistry/fluid/> [Accessed 24 Sep. 2018].

Nkhili, E., Tomao, V., El Hajji, H., El Boustani, E., Chemat, F. and Dangles, O., 2009. Microwave-assisted water extraction of green tea polyphenols. *Phytochemical Analysis*, 20, pp.408–415.

Nomanbhay, S.M., Hussain, R. and Palanisamy, K., 2013. Microwave-assisted alkaline pretreatment and microwave assisted enzymatic saccharification of oil palm empty fruit bunch fiber for enhanced fermentable sugar yield. *Journal of Sustainable Bioenergy Systems*, 3, pp.7–17.

Ohmiya, K., Sakka, K., Kimura, T. and Morimoto, K., 2003. Application of

microbial genes to recalcitrant biomass utilization and environmental conservation. *Journal of Bioscience and Bioengineering*, 95, pp.549–561.

Oliveira, M.E.C. and Franca, A.S., 2002. Microwave heating of foodstuffs. *Journal of Food Engineering*, 53, pp.347–359.

Osaili, T.M., 2012. Developments in the Thermal Processing of Food. In: R. Bhat, A.K. Alias and G. Paliyath, eds. *Progress in Food Preservation*, 1st ed. Oxford, Chichester, Ames: Wiley-Blackwell.

Osepchuk, J.M., 1984. A history of microwave heating applications. *IEEE Transactions on Microwave Theory and Techniques*, 32, pp.1200–1224.

Pan, X., Niu, G. and Liu, H., 2003. Microwave-assisted extraction of tea polyphenols and tea caffeine from green tea leaves. *Chemical Engineering and Processing*, 42, pp.129–133.

Pandey, R. and Shrivastava, S.L., 2018. Comparative evaluation of rice bran oil obtained with two-step microwave assisted extraction and conventional solvent extraction. *Journal of Food Engineering*, 218, pp.106–114.

Park, Y.B. and Cosgrove, D.J., 2012a. A revised architecture of primary cell walls based on biomechanical changes induced by substrate-specific endoglucanases. *Plant Physiology*, 158, pp.1933–1943.

Park, Y.B. and Cosgrove, D.J., 2012b. Changes in cell wall biomechanical properties in the xyloglucan-deficient xxt1/xxt2 mutant of Arabidopsis. *Plant Physiology*, 158, pp.465–475.

Paudel, S.R., Banjara, S.P., Choi, O.K., Park, K.Y., Kim, Y.M. and Lee, J.W., 2017. Pretreatment of agricultural biomass for anaerobic digestion: Current state and challenges. *Bioresource Technology*, 245, pp.1194–1205.

Pavlović, M.D., Buntić, A. V., Šiler-Marinković, S.S. and Dimitrijević-Branković, S.I., 2013. Ethanol influenced fast microwave-assisted extraction for natural antioxidants obtaining from spent filter coffee. *Separation and Purification Technology*, 118, pp.503–510.

Peng, Z. and Hwang, J.Y., 2015. Microwave-assisted metallurgy. *International Materials Reviews*, 60, pp.30–63.

Philip, J.R., 1958. The osmotic cell, solute diffusibility, and the plant water economy. *Plant Physiology*, 33, pp.264–271.

Pieczywek, P.M. and Zdunek, A., 2014. Finite element modelling of the mechanical behaviour of onion epidermis with incorporation of nonlinear properties of cell walls and real tissue geometry. *Journal of Food Engineering*, 123, pp.50–59.

Prasanna, V., Prabha, T.N. and Tharanathan, R.N., 2007. Fruit ripening phenomena - An overview. *Critical Reviews in Food Science and Nutrition*, 47, pp.1–19.

Proestos, C. and Komaitis, M., 2008. Application of microwave-assisted extraction

to the fast extraction of plant phenolic compounds. *LWT - Food Science and Technology*, 41, pp.652–659.

Pueschner, 2015. *Penetration depths*. [online] Available at: <https://www.pueschner.com/en/microwave-technology/penetration-depths> [Accessed 24 Sep. 2018].

Puligundla, P., Oh, S.-E. and Mok, C., 2016. Microwave-assisted pretreatment technologies for the conversion of lignocellulosic biomass to sugars and ethanol: A review. *Carbon Letters*, 17, pp.1–10.

Rahman, M.A. and Saghir, M.Z., 2014. Thermodiffusion or Soret effect: Historical review. *International Journal of Heat and Mass Transfer*, 73, pp.693–705.

Ramachandriya, K.D., Kundiyana, D.K., Sharma, A.M., Kumar, A., Atiyeh, H.K., Huhnke, R.L. and Wilkins, M.R., 2016. Critical factors affecting the integration of biomass gasification and syngas fermentation technology. *AIMS Bioengineering*, 3, pp.188–210.

Reif, F., 1965. *Fundamentals of Statistical and Thermal Physics*. New York: McGraw-Hill.

Remya, N. and Lin, J.G., 2011. Current status of microwave application in wastewater treatment-A review. *Chemical Engineering Journal*, 166, pp.797–813.

Renard, C.M.G.C., 2005. Effects of conventional boiling on the polyphenols and cell walls of pears. *Journal of the Science of Food and Agriculture*, 85, pp.310–318.

Rizvi, S.S.H., 2005. Thermodynamic Properties of Foods in Dehydration. In: M.A. Rao, S.S.H. Rizvi and A.K. Datta, eds. *Engineering Properties of Foods*, 3rd ed. Boca Raton: Taylor & Francis.

Robinson, J., Binner, E., Saeid, A., Al-Harahsheh, M. and Kingman, S., 2014. Microwave processing of Oil Sands and contribution of clay minerals. *Fuel*, 135, pp.153–161.

Robinson, J., Dodds, C., Stavrinides, A., Kingman, S., Katrib, J., Wu, Z., Medrano, J. and Overend, R., 2015. Microwave pyrolysis of biomass: Control of process parameters for high pyrolysis oil yields and enhanced oil quality. *Energy and Fuels*, 29, pp.1701–1709.

Robinson, J., Kingman, S., Irvine, D., Licence, P., Smith, A., Dimitrakis, G. and Kappe, C.O., 2010. Understanding microwave heating effects in single mode type cavities - theory and experiment. *Physical Chemistry Chemical Physics*, 12, pp.4750–4758.

Robinson, J., Meehan, J., Taqi, A., Binner, E. and Tokay, B., 2019. Water desalination using a temperature gradient. *Desalination*, 464, pp.1–7.

Robinson, J.P., Kingman, S.W., Snape, C.E., Shang, H., Barranco, R. and Saeid, A., 2009. Separation of polyaromatic hydrocarbons from contaminated soils using microwave heating. *Separation and Purification Technology*, 69, pp.249–254.

Rodrigues, V.H., de Melo, M.M.R., Portugal, I. and Silva, C.M., 2018. Supercritical fluid extraction of Eucalyptus globulus leaves. Experimental and modelling studies of the influence of operating conditions and biomass pretreatment upon yields and kinetics. *Separation and Purification Technology*, 191, pp.173–181.

Rodriguez-Jasso, R.M., Mussatto, S.I., Pastrana, L., Aguilar, C.N. and Teixeira, J.A., 2011. Microwave-assisted extraction of sulfated polysaccharides (fucoidan) from brown seaweed. *Carbohydrate Polymers*, 86, pp.1137–1144.

Roelofsen, P.A. and Houwink, A.L., 1953. Architecture and growth of the primary cell wall in some plant hairs and in the Phycomyces sporangiophore. *Acta Botanica Neerlandica*, 2, pp.218–225.

Rogers, G.F.C. and Mayhew, Y.R., 1995. *Thermodynamic and Transport Properties of Fluids*. 5th ed. Oxford, Malden, Carlton: Blackwell Publishing.

Rombaut, N., Tixier, A.-S., Bily, A. and Chemat, F., 2014. Green extraction processes of natural products as tools for biorefinery. *Biofuels, Bioproducts and Biorefining*, 8, pp.530–544.

Rosana, M.R., Tao, Y., Stiegman, A.E. and Dudley, G.B., 2012. On the rational design of microwave-actuated organic reactions. *Chemical Science*, 3, pp.1240–1244.

Routray, W. and Orsat, V., 2012. Microwave-assisted extraction of flavonoids: A review. *Food and Bioprocess Technology*, 5, pp.409–424.

Ryynänen, S., 1995. The electromagnetic properties of food materials: A review of the basic principles. *Journal of Food Engineering*, 26, pp.409–429.

Sadeghi, A., Hassanzadeh, H. and Harding, T.G., 2017. Thermal analysis of high frequency electromagnetic heating of lossy porous media. *Chemical Engineering Science*, 172, pp.13–22.

Sahin, S. and Sumnu, S.G., 2006. *Physical Properties of Foods*. New York: Springer.

Salazar-González, C., San Martín-González, M.F., López-Malo, A. and Sosa-Morales, M.E., 2012. Recent studies related to microwave processing of fluid foods. *Food and Bioprocess Technology*, 5, pp.31–46.

Salmén, L., 2004. Micromechanical understanding of the cell-wall structure. *Comptes Rendus Biologies*, 327, pp.873–880.

Saravacos, G.D., 2005. Mass Transfer Properties of Foods. In: M.A. Rao, S.S.H. Rizvi and A.K. Datta, eds. *Engineering Properties of Foods*, 3rd ed. Boca Raton: Taylor & Francis.

Searcy, E., Flynn, P., Ghafoori, E. and Kumar, A., 2007. The relative cost of biomass energy transport. *Applied Biochemistry and Biotechnology*, 137, pp.639–652.

Shepherd, B.J., Ryan, J., Adam, M., Vallejo, D.B., Castaño, P., Kostas, E.T. and Robinson, J.P., 2018. Microwave pyrolysis of biomass within a liquid medium. *Journal of Analytical and Applied Pyrolysis*, 134, pp.381–388.

Sinha, K., Chowdhury, S., Saha, P. Das and Datta, S., 2013. Modeling of microwave-assisted extraction of natural dye from seeds of Bixa orellana (Annatto) using response surface methodology (RSM) and artificial neural network (ANN). *Industrial Crops and Products*, 41, pp.165–171.

Sinha, K., Saha, P. Das and Datta, S., 2012. Response surface optimization and artificial neural network modeling of microwave assisted natural dye extraction from pomegranate rind. *Industrial Crops and Products*, 37, pp.408–414.

Sipahioglu, O. and Barringer, S.A., 2003. Dielectric properties of vegetables and fruits as a function of temperature, ash, and moisture content. *Journal of Food Science*, 68, pp.234–239.

Soh, L. and Eckelman, M.J., 2016. Green solvents in biomass processing. *ACS Sustainable Chemistry and Engineering*, 4, pp.5821–5837.

Spigno, G. and De Faveri, D.M., 2009. Microwave-assisted extraction of tea phenols: A phenomenological study. *Journal of Food Engineering*, 93, pp.210–217.

Spigno, G., Tramelli, L. and De Faveri, D.M., 2007. Effects of extraction time, temperature and solvent on concentration and antioxidant activity of grape marc phenolics. *Journal of Food Engineering*, 81, pp.200–208.

Steer, M.B., 2008. Passive Microwave Devices. In: M. Golio and J. Golio, eds. *RF and Microwave Passive and Active Technologies*. Boca Raton: CRC Press.

Strachan, J., 1938. Solubility of cellulose in water. *Nature*, 141, pp.332–333.

Švarc-Gajić, J., Stojanović, Z., Carretero, A.S., Román, D.A., Borrás, I. and Vasiljević, I., 2013. Development of a microwave-assisted extraction for the analysis of phenolic compounds from Rosmarinus officinalis. *Journal of Food Engineering*, 119, pp.525–532.

Tan, S.N., Yong, J.W.H., Teo, C.C., Ge, L., Chan, Y.W. and Hew, C.S., 2011. Determination of metabolites in Uncaria sinensis by HPLC and GC–MS after green solvent microwave-assisted extraction. *Talanta*, 83, pp.891–898.

Tanongkankit, Y., Sablani, S.S., Chiewchan, N. and Devahastin, S., 2013. Microwave-assisted extraction of sulforaphane from white cabbages: Effects of extraction condition, solvent and sample pretreatment. *Journal of Food Engineering*, 117, pp.151–157.

Tao, Y. and Xu, W., 2008. Microwave-assisted solubilization and solution properties of hyperbranched polysaccharide. *Carbohydrate Research*, 343, pp.3071–3078.

Taqi, A., Farcot, E., Robinson, J.P. and Binner, E.R., 2020. Understanding microwave heating in biomass-solvent systems. *Chemical Engineering Journal*, 393, p.124741.

Thomas-Hillman, I., Laybourn, A., Dodds, C. and Kingman, S.W., 2018. Realising the environmental benefits of metal-organic frameworks: Recent advances in microwave synthesis. *Journal of Materials Chemistry A*, 6, pp.11564–11581.

Thostenson, E.T. and Chou, T.-W., 1999. Microwave processing: fundamentals and applications. *Composites: Part A*, 30, pp.1055–1071.

Trabelsi, S. and Nelson, S.O., 2006. Temperature-dependent behaviour of dielectric properties of bound water in grain at microwave frequencies. *Measurement Science and Technology*, 17, pp.2289–2293.

Tran, T.H., Nguyen, H.H.H., Nguyen, D.C., Nguyen, T.Q., Tan, H., Nhan, L.T.H., Nguyen, D.H., Tran, L.D., Do, S.T. and Nguyen, T.D., 2018. Optimization of microwave-assisted extraction of essential oil from Vietnamese basil (Ocimum basilicum L.) using response surface methodology. *Processes*, 6, p.206.

Tsubaki, S., Sakamoto, M. and Azuma, J. ichi, 2010. Microwave-assisted extraction of phenolic compounds from tea residues under autohydrolytic conditions. *Food Chemistry*, 123, pp.1255–1258.

UK Government, 2020. *The ten point plan for a green industrial revolution*. [online] Available at: <https://assets.publishing.service.gov.uk/government/uploads/system/uploads/attachment_data/file/936567/10_POINT_PLAN_BOOKLET.pdf>.

UN, 2015. *Paris agreement*. [online] Available at: <https://unfccc.int/sites/default/files/english_paris_agreement.pdf>.

Veggi, P.C., Martinez, J. and Meireles, M.A.A., 2013. Fundamentals of Microwave Extraction. In: F. Chemat and G. Cravotto, eds. *Microwave-assisted Extraction for Bioactive Compounds: Theory and Practice*. New York: Springer.

Venkatesh, M.S. and Raghavan, G.S. V., 2004. An overview of microwave processing and dielectric properties of agri-food materials. *Biosystems Engineering*, 88, pp.1–18.

Virtanen, P., Gommers, R., Oliphant, T.E., Haberland, M., Reddy, T., Cournapeau, D., Burovski, E., Peterson, P., Weckesser, W., Bright, J., van der Walt, S.J., Brett, M., Wilson, J., Millman, K.J., Mayorov, N., Nelson, A.R.J., Jones, E., Kern, R., Larson, E., Carey, C.J., Polat, İ., Feng, Y., Moore, E.W., VanderPlas, J., Laxalde, D., Perktold, J., Cimrman, R., Henriksen, I., Quintero, E.A., Harris, C.R., Archibald, A.M., Ribeiro, A.H., Pedregosa, F., van Mulbregt, P., Vijaykumar, A., Bardelli, A. Pietro, Rothberg, A., Hilboll, A., Kloeckner, A., Scopatz, A., Lee, A., Rokem, A., Woods, C.N., Fulton, C., Masson, C., Häggström, C., Fitzgerald, C., Nicholson, D.A., Hagen, D.R., Pasechnik, D. V., Olivetti, E., Martin, E., Wieser, E., Silva, F., Lenders, F., Wilhelm, F., Young, G., Price, G.A., Ingold, G.L., Allen, G.E., Lee, G.R., Audren, H., Probst, I., Dietrich, J.P., Silterra, J., Webber, J.T., Slavič, J., Nothman, J., Buchner, J., Kulick, J., Schönberger, J.L., de Miranda Cardoso, J.V., Reimer, J., Harrington, J., Rodríguez, J.L.C., Nunez-Iglesias, J., Kuczynski, J., Tritz, K., Thoma, M., Newville, M., Kümmerer, M., Bolingbroke, M., Tartre, M., Pak, M., Smith, N.J., Nowaczyk, N., Shebanov, N., Pavlyk, O., Brodtkorb, P.A., Lee, P.,

McGibbon, R.T., Feldbauer, R., Lewis, S., Tygier, S., Sievert, S., Vigna, S., Peterson, S., More, S., Pudlik, T., Oshima, T., Pingel, T.J., Robitaille, T.P., Spura, T., Jones, T.R., Cera, T., Leslie, T., Zito, T., Krauss, T., Upadhyay, U., Halchenko, Y.O. and Vázquez-Baeza, Y., 2020. SciPy 1.0: fundamental algorithms for scientific computing in Python. *Nature Methods*, 17, pp.261–272.

Vu, H.T., Scarlett, C.J. and Vuong, Q. V., 2019. Changes of phytochemicals and antioxidant capacity of banana peel during the ripening process; with and without ethylene treatment. *Scientia Horticulturae*, 253, pp.255–262.

Wainaina, S., Horváth, I.S. and Taherzadeh, M.J., 2018. Biochemicals from food waste and recalcitrant biomass via syngas fermentation: A review. *Bioresource Technology*, 248, pp.113–121.

Wang, J., Zhang, J., Zhao, B., Wang, X., Wu, Y. and Yao, J., 2010. A comparison study on microwave-assisted extraction of Potentilla anserina L. polysaccharides with conventional method: Molecule weight and antioxidant activities evaluation. *Carbohydrate Polymers*, 80, pp.84–93.

Wang, L. and Weller, C.L., 2006. Recent advances in extraction of nutraceuticals from plants. *Trends in Food Science and Technology*, 17, pp.300–312.

Wang, S., Chen, F., Wu, J., Wang, Z., Liao, X. and Hu, X., 2007. Optimization of pectin extraction assisted by microwave from apple pomace using response surface methodology. *Journal of Food Engineering*, 78, pp.693–700.

Whittles, D.N., Kingman, S.W. and Reddish, D.J., 2003. Application of numerical modelling for prediction of the influence of power density on microwave-assisted breakage. *International Journal of Mineral Processing*, 68, pp.71–91.

Wijmans, J.G. and Baker, R.W., 1995. The solution-diffusion model: a review. *Journal of Membrane Science*, 107, pp.1–21.

Williams, G., 2000. *Advanced Biology for You*. Cheltenham: Nelson Thornes.

Wood, L.A., 1977. Uniaxial extension and compression in stress-strain relations of rubber. *Journal of Research of the National Bureau of Standards*, 82, pp.57–63.

Wu, H.-I., Spence, R.D., Sharpe, P.J.H. and Goeschl, J.D., 1985. Cell wall elasticity: I. A critique of the bulk elastic modulus approach and an analysis using polymer elastic principles. *Plant, Cell and Environment*, 8, pp.563–570.

Wu, H.I., Spence, R.D. and Sharpe, P.J.H., 1988. Plant cell wall elasticity II: Polymer elastic properties of the microfibrils. *Journal of Theoretical Biology*, 133, pp.239–253.

Wyman, C.E., Dale, B.E., Elander, R.T., Holtzapple, M., Ladisch, M.R. and Lee, Y.Y., 2005. Coordinated development of leading biomass pretreatment technologies. *Bioresource Technology*, 96, pp.1959–1966.

Xiao, W., Han, L. and Shi, B., 2008. Microwave-assisted extraction of flavonoids from Radix Astragali. *Separation and Purification Technology*, 62, pp.614–618.

Xiao, X., Song, W., Wang, J. and Li, G., 2012. Microwave-assisted extraction performed in low temperature and in vacuo for the extraction of labile compounds in food samples. *Analytica Chimica Acta*, 712, pp.85–93.

Yakovlev, V. V., 2006. Examination of contemporary electromagnetic software capable of modeling problems of microwave heating. In: *Advances in Microwave and Radio Frequency Processing*. Berlin, Heidelberg: Springer.pp.178–190.

Yan, M.-M., Liu, W., Fu, Y., Zu, Y.-G., Chen, C.-Y. and Luo, M., 2010. Optimisation of the microwave-assisted extraction process for four main astragalosides in Radix Astragali. *Food Chemistry*, 119, pp.1663–1670.

Yang, H.W. and Gunasekaran, S., 2004. Comparison of temperature distribution in model food cylinders based on Maxwell's equations and Lambert's law during pulsed microwave heating. *Journal of Food Engineering*, 64, pp.445–453.

Yanık, D.K., 2017. Alternative to traditional olive pomace oil extraction systems: Microwave-assisted solvent extraction of oil from wet olive pomace. *LWT - Food Science and Technology*, 77, pp.45–51.

Yeoh, S., Shi, J. and Langrish, T.A.G., 2008. Comparisons between different techniques for water-based extraction of pectin from orange peels. *Desalination*, 218, pp.229–237.

Zamil, M.S., Yi, H., Haque, M.A. and Puri, V.M., 2013. Characterizing microscale biological samples under tensile loading: Stress-strain behavior of cell wall fragment of onion outer epidermis. *American Journal of Botany*, 100, pp.1105–1115.

Zamil, M.S., Yi, H. and Puri, V.M., 2014. Mechanical characterization of outer epidermal middle lamella of onion under tensile loading. *American Journal of Botany*, 101, pp.778–787.

Zamil, M.S., Yi, H. and Puri, V.M., 2015. The mechanical properties of plant cell walls soft material at the subcellular scale: the implications of water and of the intercellular boundaries. *Journal of Materials Science*, 50, pp.6608–6623.

Zamil, M.S., Yi, H. and Puri, V.M., 2017. A multiscale FEA framework for bridging cell-wall to tissue-scale mechanical properties: the contributions of middle lamella interface and cell shape. *Journal of Materials Science*, 52, pp.7947–7968.

Zhang, M., Zeng, G., Pan, Y. and Qi, N., 2018. Difference research of pectins extracted from tobacco waste by heat reflux extraction and microwave-assisted extraction. *Biocatalysis and Agricultural Biotechnology*, 15, pp.359–363.

Zhang, Z., Harrison, M.D., Rackemann, D.W., Doherty, W.O.S. and O'Hara, I.M., 2016. Organosolv pretreatment of plant biomass for enhanced enzymatic saccharification. *Green Chemistry*, 18, pp.360–381.

Zheng, X., Xu, X., Liu, C., Sun, Y., Lin, Z. and Liu, H., 2013. Extraction characteristics and optimal parameters of anthocyanin from blueberry powder under microwave-assisted extraction conditions. *Separation and Purification Technology*, 104, pp.17–25.

Zhongdong, L., Guohua, W., Yunchang, G. and Kennedy, J.F., 2006. Image study of pectin extraction from orange skin assisted by microwave. *Carbohydrate Polymers*, 64, pp.548–552.